

Concepts and Applied Principles of Bioinorganic Chemistry

Volume II

Warren Gibbs

Concepts and Applied Principles of Bioinorganic Chemistry

Volume II

"This page is Intentionally Left Blank"

Concepts and Applied Principles of Bioinorganic Chemistry

Volume II

Edited by Warren Gibbs

Published by Academic Pages,
5 Penn Plaza,
19th Floor,
New York, NY 10001, USA

Concepts and Applied Principles of Bioinorganic Chemistry: Volume II
Edited by Warren Gibbs

© 2017 Academic Pages

International Standard Book Number: 978-1-9789-2205-1

This book contains information obtained from authentic and highly regarded sources. Copyright for all individual chapters remain with the respective authors as indicated. A wide variety of references are listed. Permission and sources are indicated; for detailed attributions, please refer to the permissions page. Reasonable efforts have been made to publish reliable data and information, but the authors, editors and publisher cannot assume any responsibility for the validity of all materials or the consequences of their use.

Copyright of this ebook is with Academic Pages, rights acquired from the original print publisher, Callisto Reference.

The publisher's policy is to use permanent paper from mills that operate a sustainable forestry policy. Furthermore, the publisher ensures that the text paper and cover boards used have met acceptable environmental accreditation standards.

Trademark Notice: Registered trademark of products or corporate names are used only for explanation and identification without intent to infringe.

Contents

Preface	IX
Chapter 1 Sensitive Marker of the Cisplatin-DNA Interaction: X-Ray Photoelectron Spectroscopy of CL Fangxing Xiao, Xiaobin Yao, Qianhong Bao, Danzhen Li and Yi Zheng	1
Chapter 2 Computational Study of the Structure of a Sepiolite/Thioindigo Mayan Pigment Manuel Alvarado Jr., Russell C. Chianelli and Roy M. Arrowood	11
Chapter 3 A Comparison of Epithelial Cells, Fibroblasts, and Osteoblasts in Dental Implant Titanium Topographies Fu-Yuan Teng, Chia-Ling Ko, Hsien-Nan Kuo, Jin-Jia Hu, Jia-Horng Lin, Ching-Wen Lou, Chun-Cheng Hung, Yin-Lai Wang, Cheng-Yi Cheng and Wen-Cheng Chen	17
Chapter 4 Synthesis, Characterization and <i>In Vitro</i> Antibacterial Studies of Organotin(IV) Complexes with 2-Hydroxyacetophenone-2-methylphenylthiosemicarbazone ($H_2\text{dampt}$) M. A. Salam, M. A. Affan, Ramkrishna Saha, Fasihuddin B. Ahmad and Norrihan Sam	26
Chapter 5 SOD-Mimic Cu(II) Dimeric Complexes Involving Kinetin and Its Derivative: Preparation and Characterization Radka Novotná, Zdeněk Trávníček and Radovan Herchel	35
Chapter 6 Studies on Synthetic and Natural Melanin and Its Affinity for Fe(III) Ion T. G. Costa, R. Younger, C. Poe, P. J. Farmer and B. Szpoganicz	43
Chapter 7 Spectroscopic, Thermal, and Antimicrobial Studies of Co(II), Ni(II), Cu(II), and Zn(II) Complexes Derived from Bidentate Ligands Containing N and S Donor Atoms Kiran Singh, Yogender Kumar, Parvesh Puri and Gulab Singh	52
Chapter 8 Hydroxyapatite Coating of Titanium Implants Using Hydroprocessing and Evaluation of Their Osteoconductivity Kensuke Kuroda and Masazumi Okido	61
Chapter 9 DNA-Binding and Topoisomerase-I-Suppressing Activities of Novel Vanadium Compound Van-7 Xiao-mei Mo, Zhan-fang Chen, Xin Qi, Yan-tuan Li and Jing Li	68

Chapter 10	Antifungal and Antioxidant Activities of Pyrrolidone Thiosemicarbazone Complexes Ahmed A. Al-Amiry, Abdul Amir H. Kadhum and Abu Bakar Mohamad	77
Chapter 11	Immobilization of Laccase in Alginate-Gelatin Mixed Gel and Decolorization of Synthetic Dyes Mehdi Mogharabi, Nasser Nassiri-Koopaei, Maryam Bozorgi-Koushalshahi, Nastaran Nafissi-Varcheh, Ghodsieh Bagherzadeh and Mohammad Ali Faramarzi	83
Chapter 12	Analysis of the Release Characteristics of Cu-Treated Antimicrobial Implant Surfaces Using Atomic Absorption Spectrometry Carmen Zietz, Andreas Fritzsche, Birgit Finke, Vitezslav Stranak, Maximilian Haenle, Rainer Hipppler, Wolfram Mittelmeier and Rainer Bader	89
Chapter 13	Enhancement of Antibacterial Activity of Capped Silver Nanoparticles in Combination with Antibiotics, on Model Gram-Negative and Gram-Positive Bacteria Aruna Jyothi Kora and Lori Rastogi	94
Chapter 14	DNA-Platinum Thin Films for Use in Chemoradiation Therapy Studies Mohammad Rezaee, Elahe Alizadeh, Darel Hunting and Léon Sanche	101
Chapter 15	Spectroscopic Characterization and Biological Activity of Mixed Ligand Complexes of Ni(II) with 1,10-Phenanthroline and Heterocyclic Schiff Bases Y. Prashanthi, K. Kiranmai, Ira, Sathish kumar K, Vijay kumar Chityala and Shivaraj	110
Chapter 16	Cytotoxicity and <i>In Vitro</i> Antileishmanial Activity of Antimony (V), Bismuth (V), and Tin (IV) Complexes of Lapachol Marcele Neves Rocha, Paula Monalisa Nogueira, Cynthia Demicheli, Ludmila Gonçalvez de Oliveira, Meiriane Mariano da Silva, Frédéric Frézard, Maria Norma Melo and Rodrigo Pedro Soares	118
Chapter 17	Physicochemical Properties and Cellular Responses of Strontium-Doped Gypsum Biomaterials Amir Pouria, Hadis Bandegani, Milad Pourbaghi-Masouleh, Saeed Hesaraki and Masoud Alizadeh	125
Chapter 18	Synthesis, Characterization, Mössbauer Parameters, and Antitumor Activity of Fe(III) Curcumin Complex Mutasim Ibrahim Khalil, Aisha Mohamed Al-Zahem and Maha Hamad Al-Qunaibit	134
Chapter 19	Thermodynamic Investigation and Mixed Ligand Complex Formation of 1,4-Bis-(3-aminopropyl)-piperazine and Biorelevant Ligands Ahmed A. El-Sherif, Mohamed R. Shehata, Mohamed M. Shoukry and Mohammad H. Barakat	139

Chapter 20	Temporal Changes in Concentrations of Some Trace Elements in Muscle Tissue of Crayfish, <i>Astacus leptodactylus</i> (Eschscholtz, 1823), from Keban Dam Lake	149
	Onder Aksu, Ragip Adiguzel, Veysel Demir, Numan Yildirim, Durali Danabas, Sebahat Seker, Safak Seyhaneyildiz Can and Mustafa Ates	
Chapter 21	Synthesis, Spectral Characterization, and Antiproliferative Studies of Mixed Ligand Titanium Complexes of Adamantylamine	153
	Raj Kaushal, Nitesh Kumar, Ashun Chaudhary, Saroj Arora and Pamita Awasthi	
Chapter 22	Evaluation of DNA Binding, Cleavage, and Cytotoxic Activity of Cu(II), Co(II), and Ni(II) Schiff Base Complexes of 1-Phenylindoline-2,3-dione with Isonicotinohydrazide	165
	Ramadoss Gomathi, Andy Ramu and Athiappan Murugan	
Chapter 23	Novel Zinc(II) Complexes of Heterocyclic Ligands as Antimicrobial Agents: Synthesis, Characterisation, and Antimicrobial Studies	177
	Ramesh S. Yamgar, Y. Nivid, Satish Nalawade, Mustapha Mandewale, R. G. Atram and Sudhir S. Sawant	
Chapter 24	Synthesis, Characterization, Antimicrobial, DNA Cleavage, and <i>In Vitro</i> Cytotoxic Studies of Some Metal Complexes of Schiff Base Ligand Derived from Thiazole and Quinoline Moiety	187
	Nagesh Gunvanthrao Yernale and Mruthyunjayaswamy Bennikallu Hire Mathada	

Permissions

List of Contributors

"This page is Intentionally Left Blank"

Preface

Bioinorganic chemistry is a field of science that focuses on the examination of the role of metals in biology. This branch of chemistry is about the, function, mechanism and structure dynamics of any and all biologically relevant metal complexes and metal-containing proteins. Bioinorganic chemistry describes the shared relationship between the two sub-disciplines of biochemistry and inorganic chemistry, with emphasis on the function of inorganic substances and chemicals in living systems, as well as processes including the speciation, transport and mineralisation of inorganic materials, along with the use of inorganics in medicinal therapy and diagnosis. This field of study also studies the arena of both natural phenomena such as the behaviour of metallo-proteins as well as artificially introduced metals. These studies also include those that are non-essential metals and chemicals such as in medicine and toxicology. Bioinorganic chemistry is important in elucidating the consequences of substrate bindings and activation, electron-transfer proteins, atom and group transfer chemistry as well as metal properties in biological chemistry. Chemists in this arena use contemporary synthetic methods, theoretical calculations, biological manipulations and advanced characterization techniques that include ultrafast spectroscopy, single-molecule spectroscopy along with synchrotron-based x-ray spectroscopy and diffraction. This is a highly specialized branch of chemistry that requires skilled researchers and scientists to work on new developments and thus the need for newer research is also rapidly increasing.

This book attempts to compile and collate the research and data available in the field of bioinorganic chemistry. I am grateful to those who put in effort and hard work in this field. I am also thankful to those who supported me in this endeavour. I also wish to thank my family for their endless support in my life at every step.

Editor

"This page is Intentionally Left Blank"

Sensitive Marker of the Cisplatin-DNA Interaction: X-Ray Photoelectron Spectroscopy of CL

Fangxing Xiao, Xiaobin Yao, Qianhong Bao, Danzhen Li, and Yi Zheng

State Key Laboratory Breeding Base of Photocatalysis, Research Institute of Photocatalysis,
College of Chemistry and Chemical Engineering, Fuzhou University, Fuzhou 350002, China

Correspondence should be addressed to Yi Zheng, yizheng@fzu.edu.cn

Academic Editor: Nicholas P. Farrell

The development of cisplatin and Pt-based analogues anticancer agents requires knowledge concerning the molecular mechanisms of interaction between such drugs with DNA. However, the binding dynamics and kinetics of cisplatin reactions with DNA determined by traditional approaches are far from satisfactory. In this study, a typical 20-base oligonucleotide (CGTGACAGTTATTGCAGGCG), as a simplified model representing DNA, was mixed with cisplatin in different molar ratios and incubation time. High-resolution XPS spectra of the core elements C, N, O, P, and Cl were recorded to explore the interaction between cisplatin and DNA. From deconvoluted Cl spectra we could readily differentiate the covalently bound chlorine from ionic chloride species in the cisplatin-oligo complexes, which displayed distinct features at various reaction times and ratios. Monitoring the magnitude and energy of the photoelectron Cl 2p signal by XPS could act as a sensitive marker to probe the interaction dynamics of chemical bonds in the reaction of cisplatin with DNA. At 37°C, the optimum incubation time to obtain a stable cisplatin-oligo complex lies around 20 hrs. This novel analysis technique could have valuable implications to understand the fundamental mechanism of cisplatin cytotoxicity and determine the efficiency of the bonds in treated cancer cells.

1. Introduction

Cis-diamminedichloroplatinum (cisplatin) has become the most frequently used drugs in the chemotherapy treatment of most malignant cancers [1–4]. The enhancement of DNA damage by cisplatin in concomitant chemoradiation therapy further stresses the application of the cisplatin analogues drug in cancer treatment [5, 6]. Cisplatin kills cancer cells via apoptosis caused by its binding and cross-linking to nuclear DNA, in which different intermediate adducts formed when cisplatin binds to DNA are thought to be responsible for its cytotoxicity. Therefore, probing the molecular basis of such underlying interactions could have significant implications for the optimum clinical application of cisplatin and platinum-based antitumor drugs.

The process of Pt binding to nucleobases involves complex pathways which are kinetically controlled, rendering accurate identification of the reaction rates and products rather difficult. In this regard, a myriad of analyzing technologies to date have been harnessed to investigate the

manifold of adducts from the cisplatin—DNA reactions, including ionic exchanged chromatography [7], capillary electrophoresis (CE) [8–11], high-performance liquid (HPLC) [12, 13], X-ray diffraction [14–18], NMR spectroscopy [12, 19–21], extended X-ray absorption fine structure (EXAFS), Fourier transform infrared (FTIR) [22], a collection of mass spectroscopy (MS) techniques [8, 16, 17, 23–32], and time-resolved femtosecond laser spectroscopy [33]. These series of combinatorial studies have revealed that the reaction initiates predominantly from the aquation process of cisplatin to the monofunctional and bifunctional adducts on the time scale of days to weeks. The major configurations are the GpG and ApG intrastrand adducts that together account for 80–90% of the bound Pt. Despite the above joint techniques used for the determination of the products deriving from cisplatin binding to DNA, the challenge for elucidating the intermediate binding mechanism has met with limited success. Meanwhile, many other factors such as DNA sequence types and buffer can also affect the observed adduct profile. Hence, the interaction of cisplatin with DNA

at the molecular scale was found to be fairly intricate in addition to its significance in cancer therapy. In practice, the application of Pt-based chemotherapeutic drugs requires a simple and direct method to monitor such interaction process.

Previous studies revealed the cisplatin aquation and subsequent reactions to be mainly oriented toward the Pt binding process. Nonetheless, important information regarding the chloro ligands released from cisplatin is generally neglected because it is difficult to obtain *via* conventional HPLC-based techniques. Moreover, reports on the interaction of cisplatin with DNA, by monitoring the chlorine signal with X-ray photoelectron spectroscopy (XPS), have not yet been reported. In the present study, new insights into the interaction of cisplatin with DNA are obtained by monitoring chlorine instead of the more conventional Pt signal with XPS. XPS is one of the most powerful techniques of chemical characterization. Compared to traditional analytical methods mentioned above, not only does it allow quantitative elemental analysis of various sample films, but also, more significantly, provides relatively precise information with regard to the modification of chemical bonds and elemental chemical state.

XPS characterization of cisplatin-DNA interaction has not been reported apart from the tentative work performed by Millard et al. in 1975 [34]. Depending on the sensitive binding energy (BE) shift of DNA constituent elements, including N 1s, O 1s, and P 2p, the authors concluded that the cisplatin—DNA reaction was initiated by the attack of Pt at the N7 position and neighboring O6 sites of guanine (G). Compared to the result of other techniques, which showed that cisplatin preferentially bonds to N7 sites of purine [4, 14, 15, 35], it thus appears highly desirable to systematically compare the cisplatin—DNA to pure DNA by XPS again with current improved sensitivity and resolution. *With respect to the discrimination between aqua and chloroligands XPS is particularly well suited to detect the chemical changes of chlorine, which would be a powerful signal to monitor the kinetic interaction between cisplatin and DNA.*

Herein, in order to simply elucidate the general chemistry scenario of cisplatin and DNA, a typical 20-base oligonucleotide, that is, the “oligo,” CGTGACAGT TATTGCAGGCG, with 8 sites of G is devised and used as a proof-of-concept model to represent cellular DNA. Cisplatin-oligo complexes are prepared with different ratios of cisplatin and reaction time at 37°C, as it does in most *in vitro* reactions [36, 37]. High-resolution spectra of the principal elements of oligonucleotide (C, N, O, P and Cl) with and without binding to cisplatin are accurately measured by XPS to probe the detailed chemical bond transformation of oligo in the dynamic process of cisplatin binding to DNA as compared with pure DNA. The significant differences of high-resolution spectra of Cl demonstrate that monitoring the chloro ligand by XPS could provide an easily accessible and effective way to disclose the detailed reaction dynamics of cisplatin. More significantly, the technique may be extended to other Pt-relating anticancer drugs used in chemotherapy. We also specifically discuss for the first time the compositional alterations of DNA in relation to its

binding with cisplatin. It is hoped that our current work could motivate explorations focused on the mechanical analysis between platinum-based antitumor drugs and DNA with XPS.

2. Materials and Methods

2.1. Materials. The HPLC purified 20-mer oligo (CGTGAC AGTTATTGCAGGCG, molecular weight 6063) was purchased from Invitrogen. The amount of oligo was determined by measuring its UV absorption at 260 nm of 28.5 µg/OD provided by Invitrogen. *Cis*-diammineplatinum (II) dichloride (cisplatin) was obtained from Sigma Aldrich and used without any further purification. The tantalum substrates (Alfa Aesar, 99.95%) were cleaned by ultrasonic with ethanol and deionized water (ddH₂O, Milipore, 18.2 MΩ·cm resistivity) for three times and dried in glove box at room temperature prior to each deposition of DNA.

2.2. Preparation of Oligo and Cisplatin-Oligo Films. 10 µL of oligo solution (100 µM) were deposited on the tantalum foil forming a drop with 2 mm radius and dried in glove box under nitrogen atmosphere at room temperature. Assuming a uniform distribution of the oligo on the substrate and a density of 1.7 g cm⁻³, the thickness of the film was estimated to be 50 molecular layers (ML).

0.1 mg of cisplatin was dissolved in 500 µL dd H₂O at 55°C for 30 minutes to obtain the cisplatin solution. Subsequently, the cisplatin solution was mixed with oligos to prepare the cisplatin-oligo complexes with different ratios (R_i), where R_i is defined as the molar ratio of platinum atom to oligo molecule. In brief, 5.2 µL of 100 µM oligo were mixed with 1.56 µL of cisplatin with different concentration (from 100 to 2000 ng/µL) to get the final cisplatin-oligo complexes with molar ratios of 1:1, 2:1, 4:1, 8:1, 10:1, 12:1, 20:1, respectively. The cisplatin-oligo complexes were simultaneously incubated at 37°C in the dark for 4 h in PCR (GeneAmp PCR System 9700). Finally, the aqueous cisplatin-oligo solution was deposited on a tantalum substrate and dried in glove box with nitrogen atmosphere at room temperature to form the films of cisplatin-oligo complexes with different ratios. With the same amount of oligos in the complexes the thickness of all the cisplatin-oligo films was estimated to be 26 ML.

For the experiment of various incubation times, similarly, cisplatin-oligo complexes with ratio of 8:1 were incubated at 37°C from 0 to 24 h with 4 h time interrupt in between. Each sample was immediately removed from PCR at given time and formed the corresponding films for further XPS analysis.

2.3. XPS Measurement. XPS measurements were conducted using a commercial XPS system (Thermo Scientific ESCALAB 250) equipped with a dual anode X-ray gun, a concentric hemispherical electron energy analyzer, and a magnetic electron lens. The apparatus was operated with a monochromatic Al K α beam as the excitation source ($h\nu = 1486.6$ eV) with the energy resolution of 0.45 eV. The emission current was kept at 6 mA under a base pressure

of 3.8×10^{-10} mbar. The XPS spot size and analyzer field were below 1 mm². The neutralizing electron gun was turned on in the low energy mode with emission current of 100 mA to eliminate the charging of the samples during X-ray irradiation. Before the measurements each film was first etched by Argon ion operated at 2 KV and 1 μ A for 30 s. The material removed was estimated to be approximately 1.2 nm ($0.4 \text{ \AA/s} \times 30 \text{ s} = 1.2 \text{ nm}$). No difference is observed in the P 2p spectra before and after Ar etching, while three monitored spots are randomly chosen on each sample surface (See Supporting Information Figure S1 in Supplementary Material available online at doi:10.1155/2012/649640). It indicates that the applied Ar etching does not affect the chemical composition of oligo and oligo-Pt complex on the Ta substrate under the present conditions. Instead it can helpfully remove surface contaminants and expose the fresh sample particularly for C, O, and N spectra. Since the XPS probing length is approximately 10 nm (3–5 ML) on a sample surface [38], the thickness of oligo and cisplatin oligo films with profile of 50 and 26 ML in the present study is found to be sufficient for the XPS characterization.

The hemispherical electron energy analyzer input axis was normal to the sample surface. XPS survey spectra from BE of 0 to 1200 eV were recorded in the fixed analyzer transmission mode with a pass energy of 100 eV and energy steps of 1 eV. The typical peaks of elements, C 1s, N 1s, O 1s, P 2p, Cl 2p, and Pt 4f, were recorded separately with pass energy of 50 eV and energy steps of 0.05 eV. The energy scale of XPS spectra was calibrated according to the standard C 1s BE line of 285.0 eV, which corresponds to standard hydrocarbon energy of C–H and C–C bonds. The work function of the system was 4.38 eV.

2.4. XPS Peak Analysis. Commercial XPS analysis software (Advantage 4.37) was used to calculate the peak area and deconvolute the peaks of high-resolution spectra. The atomic ratios of composition elements in the film were calculated according to the corresponding fitted peak area and corrected by the instrument sensitivity factors (SF), leading to the more reliable result with error of 5%. The convolution of Lorentzian and Gaussian line shapes were employed to fit the core-level spectra of individual peaks as well as the Shirley function to model the background.

3. Results and Discussion

3.1. The Reaction Process of Cisplatin with Oligos during the Incubation Time. Generally, two chemical states of chlorine exist in any compound, that is, the covalent-bound and the ionic states [39]. Figure 1(a) exhibits the core-level Cl 2p spectra of cisplatin in the solid phase (top curve) and in H₂O (bottom curve). The individual Cl 2p peaks could be deconvoluted according to the chemical characteristics of chlorine. With the angular momentum coupling the 2p orbital of each type of chlorine consists of the spin-orbit-split doublet, that is, 2p_{3/2} and 2p_{1/2} [40]. Thus, the spectra of Cl 2p are curve fitted to two doublet subpeaks assigning to covalent (dashed upper curve in Figure 1(a))

and both covalent and ionic chlorine (dashed curves in lower Figure 1(a) and in Figure 1(b)).

For cisplatin in the solid, without the perturbation of aquation all chlorine is expected to be covalently bound to Pt. In other words, the spectrum of solid state cisplatin represents the characteristic covalent Cl with BE of 199.6 and 201.1 eV (Figure 1(a)). When cisplatin is dissolved in H₂O, it is known that the kinetic of the aquation process involves the replacement of Cl by H₂O subsequently in two steps, resulting the coexistence of two types of Cl: ionic and covalent, around the bulk of cisplatin [25, 41]. The ionic Cl arises from the release of covalently bound chlorine from cisplatin and exists owing to the remaining electrostatic interaction, indicating that the BE of ionic chlorine is smaller than that of covalently bonded. This scenario is demonstrated in Figure 1(a) for cisplatin in water, where a strong signal of ionic Cl is observed and the covalent Cl signal remains. The latter is evidently seen with the identical BE as that of in solid cisplatin. The similar assignation of Cl is applied to the spectra of cisplatin-oligo complex.

Figure 1(b) shows the core-level Cl 2p spectra of the cisplatin-oligo complex at molar ratio of 8 : 1 as a function of incubation time, ranging from 0 to 24 h at interval of 4 h. The high-resolution spectra of Cl 2p display dramatically different features with reaction time prolonging. At 0 h, which means that cisplatin is only mixed with oligos without the incubation at 37°C, two main peaks are observed corresponding to covalent and ionic Cl with characteristic BEs of 200.15 and 198.48 eV, respectively. The feature of the two main peaks remains after incubation for 4 h with the shift of related BEs to lower energies of 199.24 eV and 197.71 eV, respectively. With longer reaction time, the Cl spectra appear as a prominent broader peaks except at 24 h where the feature of the two peaks could be observed again to some extent. Applying the same principle of peak deconvolution, two types of Cl could be assigned in each spectrum with respect to various incubation times. The result clearly displayed that the BE of covalent Cl remained almost the same from 4 to 24 h, whereas the BE of ionic Cl decreased with a final relative increase of 0.27 eV at 24 h. The BE of ionic Cl as a function of incubation time is specified in Figure 1(c).

When cisplatin is mixed with oligos, the reaction channel of cisplatin directly interacting with oligos is expected to be competitive with the simultaneous aquation of cisplatin. In the process of hydrolysis, the chloride ions are progressively replaced by water (H₂O) ligand, resulting in the production of cationic monofunctional and bifunctional adducts [41]. NMR studies have determined the half-time of cisplatin hydrolysis is *ca.* 2 h with *cis*-[Pt(NH₃)₂Cl(H₂O)]⁺ as the dominant species which compromise *ca.* 8% of the total platinum complex within 2 h [41]. As revealed in Figure 1(a), the Cl spectrum of cisplatin-oligos at 0 h is similar to that of pure cisplatin, indicating a similar initial status of the reaction system. For pure cisplatin after 4 h of incubation the covalent component in the Cl spectra could be mainly assigned to the *cis*-[Pt(NH₃)₂Cl(H₂O)]⁺ species with featured BE of 199.82 eV. Under identical reaction conditions, however, the Cl spectrum of the cisplatin-oligo complex varies substantially from the pure cisplatin with a pronounced BE

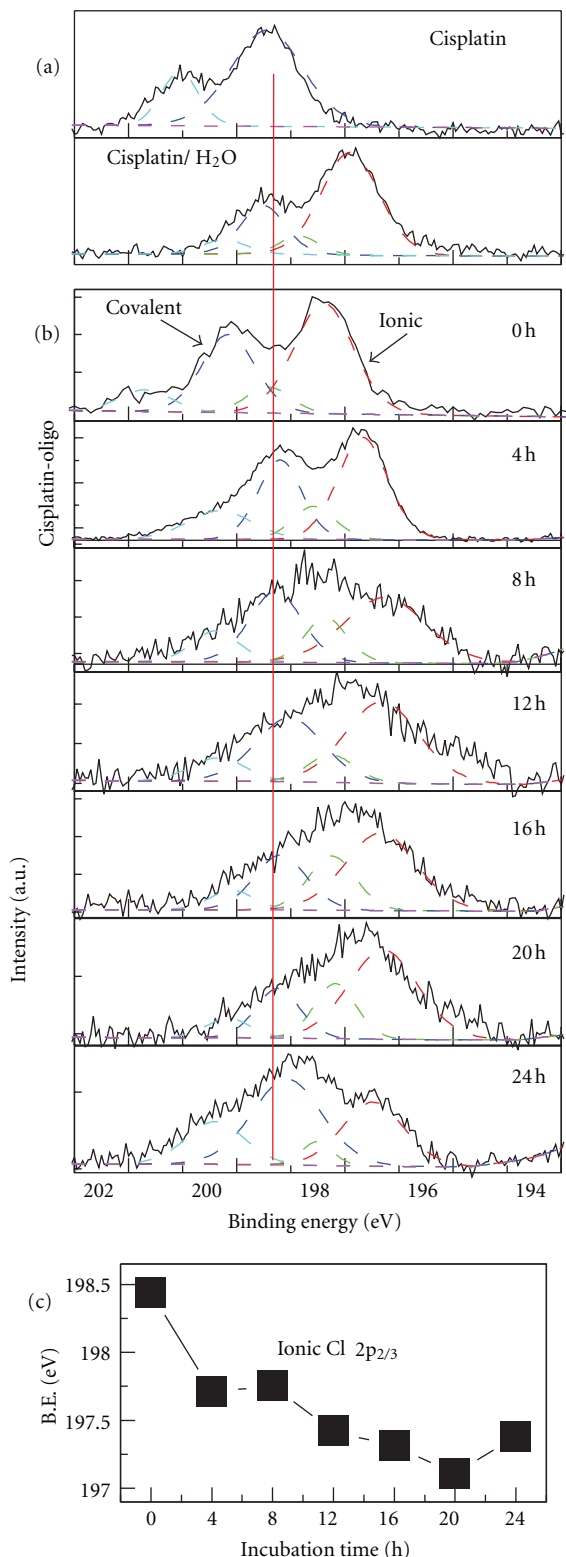


FIGURE 1: (a) High-resolution XPS spectra of Cl 2p for cisplatin in solid phase and in H₂O. (b) Cl 2p spectra for cisplatin-oligo complex at ratio of 8:1 with the increasing incubation time. The peaks are deconvoluted to covalent and ionic Cl (two coupled dashed lines), respectively. The straight line is used to point out the relative position of covalent Cl. (c) The binding energy of ionic Cl 2p_{3/2} corresponding to (b) as a function of incubation time.

shift of covalent-bound Cl (i.e., 199.18 eV versus 199.82 eV). Although it could not be accurately determined whether the formation of *cis*-Pt(NH₃)₂Cl-oligo adduct was due to the direct replacement of Cl ligand in cisplatin by oligos or replacement of water in *cis*-[Pt(NH₃)₂Cl(H₂O)]⁺ by oligos, the significant difference of the spectra along with substantial BE shift simultaneously suggest that in the cisplatin-oligo system formation of *cis*-[Pt(NH₃)₂Cl (oligo)]⁺ adduct is the main pathway as compared with hydrolysis. In other words, cisplatin could react easily with oligos leading to irreversible DNA binding.

Notably, the full width at half-maximum (FWHM) for covalent and ionic Cl peaks at 4 h is approximately 1.0 and 1.1 eV, respectively. With the reaction time processing, the broadening of the Cl peaks, especially for the ionic Cl, is obvious in Figure 1(b). The enlargement of the peak reflects the increase of the inelastic electron scattering with the longer reaction time, which further demonstrates the formation of chemical bond between Pt and oligo bases as well as the release of ionic Cl. Evidence of ionic Cl release is reflected by the gradual decrease of BE for the ionic Cl 2p_{3/2} from 0 to 20 h (Figure 1(c)). The negative BE shift of ionic Cl indicates that Cl⁻ could be increasingly released with the binding of cisplatin to oligo. Around 20 h, it is expected that nearly all Cl ligands of the Pt species are replaced by oligo forming the *cis*-Pt(NH₃)₂GG, giving the major feature of ionic Cl in the spectra. At 24 h, the increase of the Cl⁻ BE and the recovered feature of two main peaks with characteristic BEs of 199.47 eV and 197.38 eV suggests that the interaction of cisplatin with oligos stabilizes around the incubation time of 20 h. Another explanation of the two-peak reappearance is the possible formation of bridged dinuclear platinum adducts, as reported by Davies et al. [41]. They reported that indication of the formation of bridged dinuclear platinum adducts is around 26 h [41].

The present result of high-resolution Cl spectra as a function of reaction time is consistent with the well-known cisplatin-DNA reaction schemes. In addition, it discloses that the process of cisplatin binding to DNA at a temperature of 37°C over a time scale of 24 h is more kinetically than thermodynamically controlled. Compared to previous studies focused on the Pt bonding, the signal of Cl by XPS technique could be a sensitive marker to directly reflect the dynamics of cisplatin reaction with DNA.

3.2. The Effect of the Molar Ratio of Cisplatin to Oligo. The Cl spectra of the complexes with various cisplatin/oligo ratios are illustrated in Figure 2 together with the pure cisplatin under the identical incubation time of 4 h. For better comparison, the amount of oligos was kept the same in the measurement; that is, only the amount of cisplatin increases. Accordingly, the amount of cisplatin with ratio of 2 is equal to 1 nmol, which is close to the detection limit of the XPS signal thereby leading to a broad Cl peak with relatively high signal-to-noise. Thus, with the exception of the ratio of 2 each Cl spectrum could be deconvoluted into two doublet 2p peaks assigned to covalent and ionic Cl, respectively

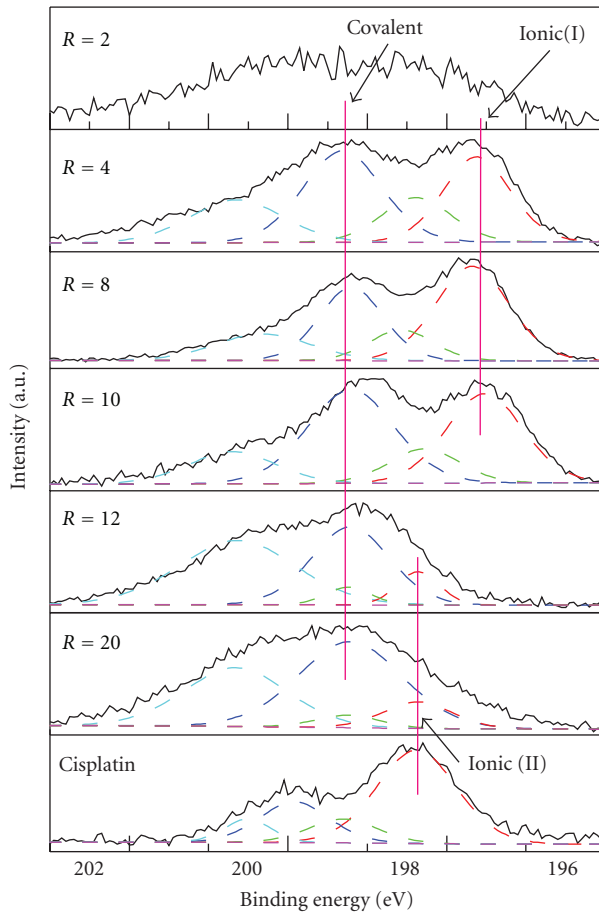


FIGURE 2: High-resolution XPS spectra of Cl 2p for cisplatin-oligo complexes with ratios (R) from 2 to 20 with identical amount (3.1 μg) of oligo. All samples are taken after incubation at 37°C for 4 hrs. The three straight lines are used to assign the position of covalent and ionic (I) Cl bond position of cisplatin-oligo complexes as well as the ionic (II) Cl of cisplatin, respectively.

(Figure 2). The Cl spectra of cisplatin-oligo complexes with ratios of 4, 8, and 10 exhibit similarly two main $2p_{3/2}$ peaks with BE of 199.2 and 197.7 ± 0.1 eV for covalent and ionic Cl, respectively. The assignment is consistent with the previous studies on the Cl containing compounds [42–51]. Moreover, the integrated peak area of each type of Cl indicated a relative percentage of ionic to covalent Cl of approximately $50\% \pm 10\%$ for ratios of 4, 8, and 10.

When the ratio increased to 12 and 20, a broader peak with higher BE is displayed. The result of reaction time has indicated that the BE of ionic Cl to the oligo is around 197.7 eV or lower. Compared to the spectra of cisplatin-oligos with lower ratios, it is surprising to find that the peak which could be resolved to similar ionic Cl (ionic I) does not exist in the cisplatin-oligo complex with ratios of 12 and 20. With such high BE, the broad peaks of cisplatin-oligo complex with ratios of 12 and 20 could only be assigned to covalent bond Cl. This assignment seems contrary to the previous result, indicating that cisplatin could react easily with oligos leading to the release of ionic Cl. How can we understand the apparent disappearance of the ionic Cl in Figure 2?

Noteworthily, the 20-base oligo (CGTGACAGTTATT GCAGGGCG) used in this study has 11 purines (G, A) indicating there are a total of 11 interaction sites for one cisplatin. Thus, in the case of mole ratio of cisplatin to oligo lower than 11, cisplatin could react completely, that is, binding to one of G or A bases and release Cl^- as indicated in Figure 1. When the ratio increases beyond 11, there is an oversupply of cisplatin with respect to the reaction sites. In other words, the system contains more cisplatin which cannot react with oligos and has to follow the aquation process. The increase in the amount of cisplatin results in the change of chemical environment in the cisplatin-oligo complex, leading to shift of the Cl spectra to higher BE. In fact, the Cl spectrum of pure cisplatin under identical conditions is resolved to covalent and ionic Cl with BE of 199.82 and 198.37 eV, respectively. Thereby, it is reasonable to deconvolute the spectra of Cl with ratio of 12 and 20 to the ionic Cl in pure cisplatin, as ionic (II) Cl shown in Figure 2. Moreover, multiple reactions could also occur in the system with ratios of 12 and 20 which is demonstrated by the broader peaks of Cl spectra compared to that of ratios lower than 11.

Determination of the platination of DNA with Pt-based drugs is usually confined to complicated inductively coupled plasma mass spectroscopy (ICPMS) which may not provide sufficient information on the specific interaction process [52]. Our results strongly evince that peak intensity and detailed chemical compositions deconvoluted from the Cl spectra are well correlated with the ratio of cisplatin to oligo. The covalently bound chlorine ($-Cl$) and ionic chloride (Cl^-) species in different reaction procedures and in the presence of varied molar ratios of cisplatin could be readily differentiated solely from the high-resolution Cl spectra. That is, the Cl XPS spectrum could exhibit distinct features at different molar ratio levels, thus, making it an alternative *in situ* approach to trace the platination process of DNA. It also suggested that the characterization of Cl by XPS could be applied to monitor the interaction of chemotherapeutic agent cisplatin with DNA.

3.3. Chemical Bond Transformation of DNA Induced by Cisplatin. In addition to the Cl spectrum, XPS could also be used to characterize the chemical bond transformations of DNA induced by cisplatin. The high-resolution spectra recorded for the four principal elements, C, N, O, and P of DNA (C 1s, N 1s, O 1s, and P 2p regions of cisplatin-oligo and oligo) are presented in Figure 3. A number of peaks are chosen to fit each elemental region corresponding to particular chemical bonding. The assignment of the spectral peaks is carried out according to the known substituent effects of core electron binding energies [53]. The XPS characterization of thymus DNA [54] and self-assembled monolayer DNA [55, 56] has also been reported previously. Due to structural similarity of oligo to DNA and for better comparison, we apply the same peak assignments referring to the work of Ptasińska et al. [54]. The specific chemical bond species relating to C, N, and O in the framework of oligonucleotide are displayed in the supporting information.

The C 1s spectra of cisplatin-oligo and oligo (Figure 3(a)) are curve-fitted to assign four types of carbon species: (1) urea [$N-C(=O)-N$], (2) amide ($N-C=O$), (3) alcohol/cyclic ether/carbon bond to nitrogen ($C-OH/C-O-C/C-N/N=C-C$), and (4) hydrocarbon ($C-C/C-H$). In the present study, the samples are sputtered with Ar ions before each measurement to obtain minimum carbon contamination in the XPS spectra. Thus, the C 1s spectra exhibit features uniquely due to the different contributions of carbon species in the bulk sample. The XPS C 1s spectrum of oligo shows faithful agreement with the previously reported single-strand DNA [55]. From the convoluted peak areas of the different carbon species, the percentage of corresponding 1–4 carbon components is found to change from 7.13%, 17.73%, 38.19%, and 36.95%, to 3.18%, 15.24%, 29.77%, and 51.18%, respectively, with the ratio of cisplatin to oligo increasing from 0 to 10. The constituent of C 1s spectrum varies appreciably for component 4 and the intensities greatly increase with the addition of cisplatin to oligo. It suggested that the binding of cisplatin may violently perturb the regular structure of oligonucleotides leading to the alternation of chemical environment. More specifically, with the inter- and

intrastrand binding of cisplatin to DNA bases, greater effect of structural change, such as the perturbation of hydrogen bonding between bases, is expected to occur in the well-defined double-strand DNA.

The principal N 1s core-level peak consists of two-component structure for DNA with BE of 400.8 and 399.3 eV, respectively, consistent with published results [55]. The higher energy peak is attributed to amino N sites connected with single bonds, and the peak at the lower BE is assigned to imino species that include a double $N=C$ bond. The N 1s spectrum of cisplatin-oligo displays different features in comparison with pure oligo: the increase of the intensity to a narrower peak and the shift of the peak to higher BE. It is known that cisplatin binds preferentially to the N7 sites of G or A yielding cisplatin-DNA adducts, and moreover, *in vitro* studies have shown that *cis*- $Pt(NH_3)_2GG$ and *cis*- $Pt(NH_3)_2AG$ intrastrand cross-link adducts account for 65% and 25%, respectively, in the total Pt-DNA species [57, 58]. Hence, it is expected that the peak 1 of N 1s for cisplatin-oligo includes the new contribution of the Pt–N bond. Compared to oligos, BEs of the amino and imino for cisplatin-oligos increased to 401.8 and 400.1 eV, respectively, indicating the formation of stronger chemical bond.

The O 1s spectrum of oligo is consistent with the previous report, including two main peaks and a relatively small peak with BE of 534.3, 532.8, and 531.1 eV, respectively. The small peak is deconvoluted according to the procedure of Dinsmore and Lee and assigned to the C-OH bond [55]. Nevertheless, for oligos, the alcohol is the smallest component in all the O species, which is negligible as indicated in [55]. A relative symmetric peak is observed in the O 1s spectrum of cisplatin-oligos. Similarly, it can be deconvoluted to three peaks having BE of 534.5, 533, and 532 eV. One possible explanation in terms of the change of O 1s spectra is that cisplatin could also react with carbonyl group near the N7 sites of guanine, as suggested by Macquet and Theophanides [59], which may contribute to the change of carboxyl/carbamido (2) species. Furthermore, it is noticeable that peak 3, which is assigned to oxygen in the phosphate group, is substantially shifted to higher BE by 0.9 eV. Since there is no bonding of cisplatin to the backbone, it is speculated that cisplatin binding to DNA bases may exert influence on the chemical bond environment of sites neighboring the backbone. In the case of P 2p spectra, a peak with increased BE of 0.2 eV is observed for cisplatin-oligo. In this regard, we speculate that the binding of cisplatin may authentically affect the backbone in that P 2p spectra can only be attributed to the phosphate of backbone; this result is in agreement with the interpretation of the result of O 1s spectra.

To recapitulate, significant changes are clearly observed in the XPS survey spectra of cisplatin-oligo complexes compared to that of pure oligo (Figure S5). It was explicitly demonstrated that the BEs and peak intensity in oligos with regard to the C 1s, N 1s, O 1s orbitals were perturbed with the addition of cisplatin, a phenomenon which lies at the basis of the mechanism for the cytotoxicity of cisplatin in cell.

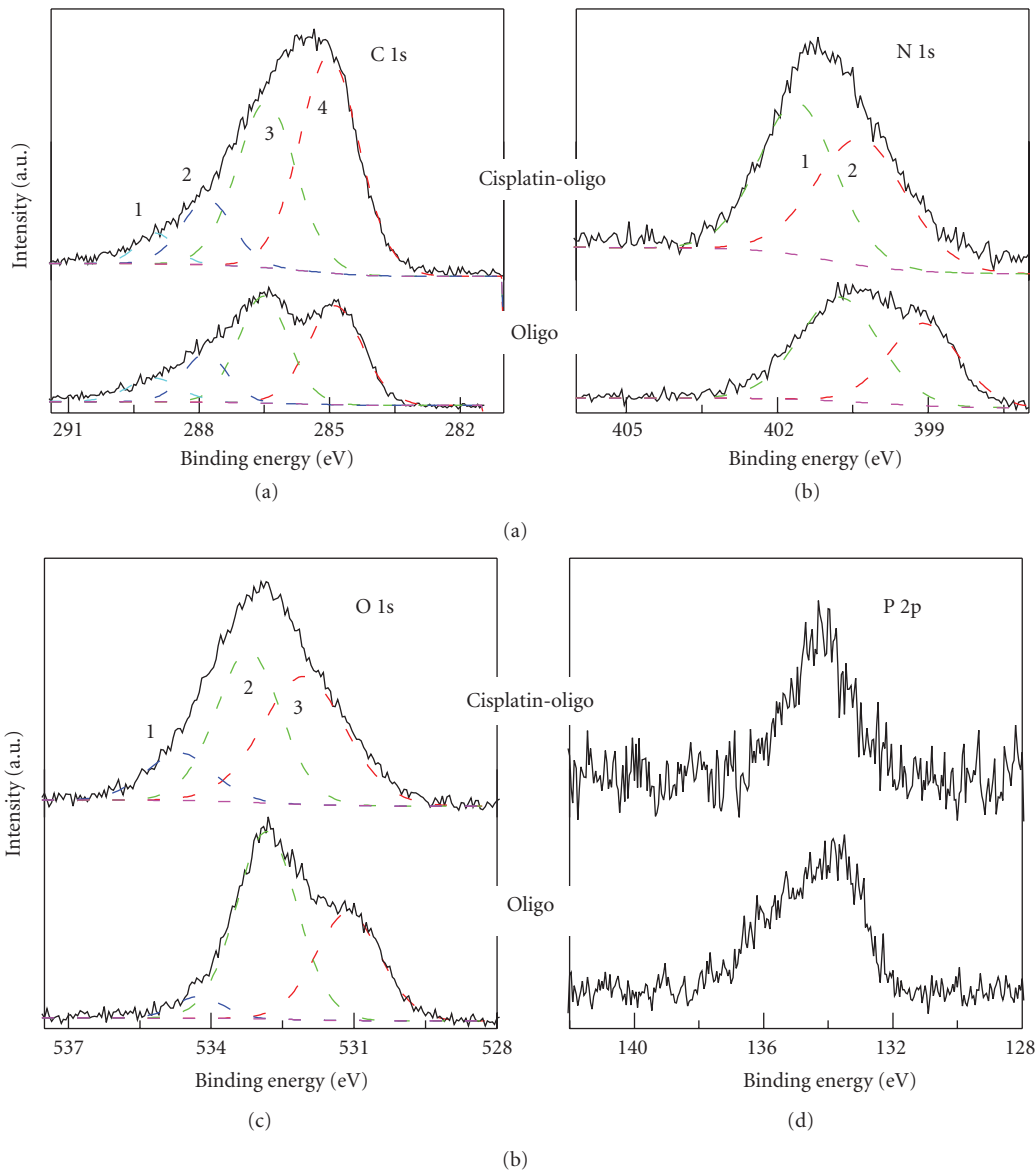


FIGURE 3: High-resolution XPS spectra of C 1s, N 1s, O 1s, and P 2p regions for pure oligos and cisplatin-oligo complexes at a ratio of 10 with the same amount of oligos in the films. The incubation time for the cisplatin-oligo complex is 4 hr. The peaks (solid curve) were deconvoluted into specific components of the oligo (dashed line) including (a) C 1s, urea (peak 1), amide (2), C=N/C—O—C/C—OH/N=C—C (3), and hydrocarbon (4); (b) N 1s, amino (1) and imino (2); (c) O 1s, C—OH (1), C=O/N=O (2), and phosphate group (3); (d) P 2p, the phosphate group. Note that the spectra in each figure are on the same scale, but offset for clarity.

3.4. DNA Chemical Bond Transformation during the Incubation Time. In addition to Cl spectra, chemical bond transformation during the incubation time could be related to the C, N, O, and P spectra. Applying the similar Gaussian curvefitting shown in Figure 3, the relative peak percentage of different components for C, N, and O species at various incubation times could be obtained. The relative percentage of O in phosphate (O 1s-3), N in imino (N 1s-2), and C in urea (C 1s-1) as a function of incubation time from 8 to 24 h is illustrated in Figure 4. The peak percentage of the typical

three bonds of C, N, and O displays a similar trend, that is, decreasing dramatically from incubation time of 8 to 12 h along with relative saturation from 16 to 24 h. It indicates that no matter to what extent cisplatin binding influences the O, C, and N bonding in DNA, the chemical bond is more stable with the incubation time longer than 16 h. Thus, to get better equilibrium of chemical reaction between cisplatin and DNA and obtain stable cisplatin-DNA complexes for further radiation study, we suggest an optimum incubation time for cisplatin of about 20 h. The result also implies that

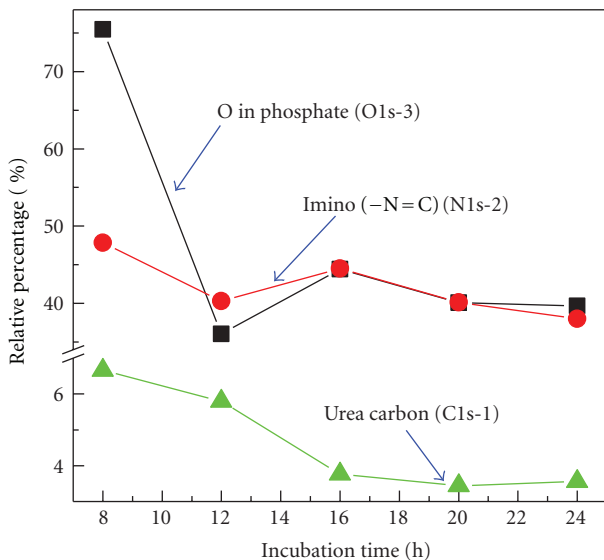


FIGURE 4: The relative percentage of O-P (■), N=C (●), and C-N (▲) bonds for a cisplatin-oligo complex with ratio of 10 deconvoluted from the corresponding O 1s, N 1s, and C 1s peaks as a function of incubation time. The percentages were obtained from a similar Gaussian deconvolution procedure as shown in Figure 3.

for concomitant chemoradiation therapy involved Pt-based drugs the optimum uptake of cisplatin could occur within one day after injection.

4. Conclusion

The dynamics of cisplatin interaction with a 20-mer oligo have been systematically monitored by XPS technique. High-resolution XPS spectra of Cl in cisplatin-oligo complexes showed characteristic features with respect to different reaction time and ratios of cisplatin to oligo. The result indicated that characteristic Cl signal obtained by XPS could be employed as a sensitive marker to disclose the reaction dynamics of cisplatin binding with DNA, which at 37°C mimics the process in chemotherapy. By accurate measuring the spectra of other principal compositional elements of oligo (i.e., C, N, O, and P), the shift of the BE as well as peak intensity with the binding of cisplatin were, for the first time, observed. Since the structural and chemical bond modifications may provide information related to the cytotoxicity of cisplatin in cell, our results would point to promising vistas on XPS as a novel characterization platform to investigate the dynamics of specific processes in the reaction of cisplatin with DNA, along with complementary results from traditional methods. In fact, the technique may have widespread applications to monitor the reaction dynamics of other Pt-based therapeutic agents, such as carboplatin and oxaliplatin. Recently, engineering of cisplatin nanoparticles with glycol-functionalized copolymer exhibit improved antitumor efficacy [60], indicating the continuous opening of the development of novel cisplatin drugs. Further systematic work along this line on interaction between Pt-anticancer drugs and DNA is in progress in our lab.

Acknowledgments

The support by the National Natural Science Foundation of China (20973039), the Award Program for Minjiang Scholar Professorship, Program for Changjiang Scholarship and Innovative Research Team in University (PCSIRT0818), and the National Basic Research Program of China (973 Program: 2007CB613306) is greatly acknowledged.

References

- V. T. Devita, S. Hellman, and S. A. Rosenberg, *Cancer: Principle and Practice of Oncology*, Lippincott Williams and Wilkins, New York, NY, USA, 2001.
- D. Wang and S. J. Lippard, "Cellular processing of platinum anticancer drugs," *Nature Reviews Drug Discovery*, vol. 4, no. 4, pp. 307–320, 2005.
- L. Kelland, "The resurgence of platinum-based cancer chemotherapy," *Nature Reviews Cancer*, vol. 7, no. 8, pp. 573–584, 2007.
- E. Wong and C. M. Giandomenico, "Current status of platinum-based antitumor drugs," *Chemical Reviews*, vol. 99, no. 9, pp. 2451–2466, 1999.
- Y. Zheng, D. J. Hunting, P. Ayotte, and L. Sanche, "Role of secondary low-energy electrons in the concomitant chemoradiation therapy of cancer," *Physical Review Letters*, vol. 100, no. 19, pp. 198101–198104, 2008.
- L. Sanche, "Role of secondary low energy electrons in radiobiology and chemoradiation therapy of cancer," *Chemical Physics Letters*, vol. 474, no. 1–3, pp. 1–6, 2009.
- A. J. Fichtinger-Schepman, A. T. van Oosterom, P. M. Lohman, and F. Berends, "cis-Diamminedichloroplatinum(II)-induced DNA adducts in peripheral leukocytes from seven cancer patients: quantitative immunochemical detection of the adduct induction and removal after a single dose of cis-diamminedichloroplatinum(II)," *Cancer Research*, vol. 47, no. 11, pp. 3000–3004, 1987.
- C. G. Hartinger, P. Schuluga, M. Galanski, A. R. Timerbaev, and B. K. Keppler, "Tumor-inhibiting platinum(II) complexes with aminoalcohol ligands: comparison of the mode of action by capillary electrophoresis and electrospray ionization-mass spectrometry," *Electrophoresis*, vol. 24, no. 12–13, pp. 2038–2044, 2003.
- C. G. Hartinger and B. K. Keppler, "CE in anticancer metallodrug research—an update," *Electrophoresis*, vol. 28, no. 19, pp. 3436–3446, 2007.
- A. Zenker, M. Galanski, T. L. Bereuter, B. K. Keppler, and W. Lindner, "Capillary electrophoretic study of cisplatin interaction with nucleoside monophosphates, di- and trinucleotides," *Journal of Chromatography A*, vol. 852, no. 1, pp. 337–346, 1999.
- C. G. Hartinger, A. R. Timerbaev, and B. K. Keppler, "Capillary electrophoresis in anti-cancer metallodrug research: advances and future challenges," *Electrophoresis*, vol. 24, no. 12–13, pp. 2023–2037, 2003.
- F. Reeder, Z. Guo, P. D. S. Murdoch et al., "Platination of a GG site on single-stranded and double-stranded forms of a 14-base oligonucleotide with diaqua cisplatin followed by NMR and HPLC. Influence of the platinum ligands and base sequence on 5'-G versus 3'-G platination selectivity," *European Journal of Biochemistry*, vol. 249, no. 2, pp. 370–382, 1997.
- E. Volckova, L. P. Dudones, and R. N. Bose, "HPLC determination of binding of cisplatin to DNA in the presence

- of biological thiols: implications of dominant platinum-thiol binding to its anticancer action," *Pharmaceutical Research*, vol. 19, no. 2, pp. 124–131, 2002.
- [14] S. E. Sherman, D. Gibson, A. H. J. Wang, and S. J. Lippard, "X-ray structure of the major adduct of the anticancer drug cisplatin with DNA: Cis-[Pt(NH₃)₂(d(pGpG))]," *Science*, vol. 230, no. 4724, pp. 412–417, 1985.
- [15] S. E. Sherman, D. Gibson, A. H. J. Wang, and S. J. Lippard, "Crystal and molecular structure of cis-[Pt(NH₃)₂[d(pGpG)]], the principal adduct formed by cis-diamminedichloroplatinum(II) with DNA," *Journal of the American Chemical Society*, vol. 110, no. 22, pp. 7368–7381, 1988.
- [16] P. M. Takahara, A. C. Rosenzweig, C. A. Frederick, and S. J. Lippard, "Crystal structure of double-stranded DNA containing the major adduct of the anticancer drug cisplatin," *Nature*, vol. 377, no. 6550, pp. 649–652, 1995.
- [17] P. M. Takahara, C. A. Frederick, and S. J. Lippard, "Crystal structure of the anticancer drug cisplatin bound to duplex DNA," *Journal of the American Chemical Society*, vol. 118, no. 49, pp. 12309–12321, 1996.
- [18] S. Komeda, T. Moulaei, K. K. Woods, M. Chikuma, N. P. Farrell, and L. D. Williams, "A third mode of DNA binding: phosphate clamps by a polynuclear platinum complex," *Journal of the American Chemical Society*, vol. 128, no. 50, pp. 16092–16103, 2006.
- [19] C. J. Van Garderen and L. P. A. Van Houtte, "The solution structure of a DNA duplex containing the *cis*-Pt(NH₃)₂[d(GTG)-N7(G), N7(G)] adduct, as determined with high-field NMR and molecular mechanics/dynamics," *European Journal of Biochemistry*, vol. 225, no. 3, pp. 1169–1179, 1994.
- [20] H. Huang, L. Zhu, B. R. Reid, G. P. Drobny, and P. B. Hopkins, "Solution structure of a cisplatin-induced DNA interstrand cross-link," *Science*, vol. 270, no. 5243, pp. 1842–1845, 1995.
- [21] S. O. Ano, F. P. Intini, G. Natile, and L. G. Marzilli, "A novel head-to-head conformer of d(GpG) cross-linked by Pt: new light on the conformation of such cross-links formed by Pt anticancer drugs," *Journal of the American Chemical Society*, vol. 120, no. 46, pp. 12017–12022, 1998.
- [22] D. Bouvet, A. Michalowicz, S. Crauste-Manciet, D. Brossard, and K. Provost, "EXAFS and IR structural study of platinum-based anticancer drugs' degradation by diethyl dithiocarbamate," *Inorganic Chemistry*, vol. 45, no. 8, pp. 3393–3398, 2006.
- [23] J. L. Beck, M. L. Colgrave, S. F. Ralph, and M. M. Sheil, "Electrospray ionization mass spectrometry of oligonucleotide complexes with drugs, metals, and proteins," *Mass Spectrometry Reviews*, vol. 20, no. 2, pp. 61–87, 2001.
- [24] A. Dorcier, C. G. Hartinger, R. Scopelliti, R. H. Fish, B. K. Kepler, and P. J. Dyson, "Studies on the reactivity of organometallic Ru-, Rh- and Os-p-ta complexes with DNA model compounds," *Journal of Inorganic Biochemistry*, vol. 102, no. 5–6, pp. 1066–1076, 2008.
- [25] C. G. Hartinger, Y. O. Tsybin, J. Fuchser, and P. J. Dyson, "Characterization of platinum anticancer drug protein-binding sites using a top-down mass spectrometric approach," *Inorganic Chemistry*, vol. 47, no. 1, pp. 17–19, 2008.
- [26] C. S. Allardyce, P. J. Dyson, J. Coffey, and N. Johnson, "Determination of drug binding sites to proteins by electrospray ionisation mass spectrometry: the interaction of cisplatin with transferrin," *Rapid Communications in Mass Spectrometry*, vol. 16, no. 10, pp. 933–935, 2002.
- [27] C. G. Hartinger, W. H. Ang, A. Casini, L. Messori, B. K. Kepler, and P. J. Dyson, "Mass spectrometric analysis of ubiquitin-platinum interactions of leading anticancer drugs: MALDI versus ESI," *Journal of Analytical Atomic Spectrometry*, vol. 22, no. 8, pp. 960–967, 2007.
- [28] M. Groessl, C. G. Hartinger, K. Polec-Pawlak, M. Jarosz, and B. K. Kepler, "Capillary electrophoresis hyphenated to inductively coupled plasma-mass spectrometry: a novel approach for the analysis of anticancer metallodrugs in human serum and plasma," *Electrophoresis*, vol. 29, no. 10, pp. 2224–2232, 2008.
- [29] R. Da Col, L. Silvestro, C. Baiocchi, D. Giacosa, and I. Viano, "High-performance liquid chromatographic-mass spectrometric analysis of cis-dichlorodiamineplatinum-DNA complexes using an ionspray interface," *Journal of Chromatography*, vol. 633, no. 1–2, pp. 119–128, 1993.
- [30] U. Warnke, C. Rappel, H. Meier et al., "Analysis of platinum adducts with DNA nucleotides and nucleosides by capillary electrophoresis coupled to ESI-MS: indications of guanosine 5'-monophosphate O⁶-N₇ chelation," *ChemBioChem*, vol. 5, no. 11, pp. 1543–1549, 2004.
- [31] J. Will, A. Kyas, W. S. Sheldrick, and D. Wolters, "Identification of (η^6 -arene)ruthenium(II) protein binding sites in *E. coli* cells by combined multidimensional liquid chromatography and ESI tandem mass spectrometry: specific binding of [$(\eta^6$ -p-cymene) RuCl₂(DMSO)] to stress-regulated proteins and to helicases," *Journal of Biological Inorganic Chemistry*, vol. 12, no. 6, pp. 883–894, 2007.
- [32] S. S. Hah, K. M. Stivers, R. W. de Vere White, and P. T. Henderson, "Kinetics of carboplatin-DNA binding in genomic DNA and bladder cancer cells as determined by accelerator mass spectrometry," *Chemical Research in Toxicology*, vol. 19, no. 5, pp. 622–626, 2006.
- [33] Q. B. Lu, "Molecular reaction mechanisms of combination treatments of low-dose cisplatin with radiotherapy and photodynamic therapy," *Journal of Medicinal Chemistry*, vol. 50, no. 11, pp. 2601–2604, 2007.
- [34] M. M. Millard, J. P. Macquet, and T. Theophanides, "X ray photoelectron spectroscopy of DNA. Pt complexes. Evidence of O⁶ (Gua). N₇ (Gua) chelation of DNA with cis dichlorodiamine platinum (II)," *Biochimica et Biophysica Acta*, vol. 402, no. 2, pp. 166–170, 1975.
- [35] M. Crul, J. H. M. Schellens, J. H. Beijnen, and M. Maliepaard, "Cisplatin resistance and DNA repair," *Cancer Treatment Reviews*, vol. 23, no. 5–6, pp. 341–366, 1997.
- [36] J. Malina, O. Vrana, and V. Brabec, "Mechanistic studies of the modulation of cleavage activity of topoisomerase I by DNA adducts of mono- and bi-functional PtII complexes," *Nucleic Acids Research*, vol. 37, no. 16, pp. 5432–5442, 2009.
- [37] G. B. Onoa and V. Moreno, "Study of the modifications caused by cisplatin, transplatin, and Pd(II) and Pt(II) mepirizole derivatives on pBR322 DNA by atomic force microscopy," *International Journal of Pharmaceutics*, vol. 245, no. 1–2, pp. 55–65, 2002.
- [38] C. D. Wagner, W. M. Riggs, L. E. Davis, J. F. Moulder, and G. E. Muilenberg, *Handbook of X-Ray Photoelectron Spectroscopy*, Perkin-Elmer, Eden Prairie, Minn, USA, 1979.
- [39] E. S. Olson, C. R. Crocker, S. A. Benson, J. H. Pavlish, and M. J. Holmes, "Surface compositions of carbon sorbents exposed to simulated low-rank coal flue gases," *Journal of the Air and Waste Management Association*, vol. 55, no. 6, pp. 747–754, 2005.
- [40] T. Balakrishnan and E. Murugan, "Preparation and spectroscopic characterization of surface-enriched (with active sites) polymer-supported phase-transfer catalysts and their

- efficiency in organic addition reactions: a kinetic study," *Journal of Polymer Science A*, vol. 41, no. 2, pp. 347–364, 2003.
- [41] M. S. Davies, S. J. Berners-Price, and T. W. Hambley, "Slowing of cisplatin aquation in the presence of DNA but not in the presence of phosphate: improved understanding of sequence selectivity and the roles of monoaquated and diaquated species in the binding of cisplatin to DNA," *Inorganic Chemistry*, vol. 39, no. 25, pp. 5603–5613, 2000.
- [42] W. H. Yu, E. T. Kang, and K. G. Neoh, "Functionalization of hydrogen-terminated Si(100) substrate by surface-initiated RAFT polymerization of 4-vinylbenzyl chloride and subsequent derivatization for photoinduced metallization," *Industrial and Engineering Chemistry Research*, vol. 43, no. 17, pp. 5194–5202, 2004.
- [43] J. F. Moulder, W. F. Stickle, P. E. Sobol, K. D. Bomben, and J. Chastian, *X-Ray Photoelectron Spectroscopy*, Perkin-Elmer, Eden Prairie, Minn, USA, 1992.
- [44] G. Beamson and D. Briggs, *High-Resolution XPS of Organic Polymers: The Scienta ESCA300 Database*, John Wiley, Chichester, UK, 1992.
- [45] K. G. Neoh and E. T. Kang, "Structural study of polyaniline films in reprotonation/deprotonation cycles," *The Journal of Physical Chemistry*, vol. 95, no. 24, pp. 10151–10157, 1991.
- [46] K. L. Tan, B. T. G. Tan, E. T. Kang, and K. G. Neoh, "X-ray photoelectron spectroscopy studies of the chemical structure of polyaniline," *Physical Review B*, vol. 39, no. 11, pp. 8070–8073, 1989.
- [47] S. J. Yuan, F. J. Xu, E. T. Kang, and S. O. Pehkonen, "Modification of surface-oxidized copper alloy by coupling of viologens for inhibiting microbiologically influenced corrosion," *Journal of the Electrochemical Society*, vol. 154, no. 11, pp. C645–C657, 2007.
- [48] K. G. Neoh, E. T. Kang, and K. L. Tan, "Limitations of the X-ray photoelectron spectroscopy technique in the study of electroactive polymers," *Journal of Physical Chemistry B*, vol. 101, no. 5, pp. 726–731, 1997.
- [49] G. Chamoulaud and D. Bélanger, "Chemical modification of the surface of a sulfonated membrane by formation of a sulfonamide bond," *Langmuir*, vol. 20, no. 12, pp. 4989–4995, 2004.
- [50] S. Tan, A. L. Forgue, and D. Belanger, "Characterization of a cation-exchange/polyaline composite membrane," *Langmuir*, vol. 19, no. 3, pp. 744–751, 2003.
- [51] X. Liu, K. G. Neoh, and E. T. Kang, "Redox-sensitive micro-porous membranes prepared from poly(vinylidene fluoride) grafted with viologen-containing polymer side chains," *Macromolecules*, vol. 36, no. 22, pp. 8361–8367, 2003.
- [52] E. E. M. Brouwers, M. Tibben, H. Rosing, J. H. M. Schellen, and J. H. Beijnen, "The application of inductively coupled plasma mass spectrometry in clinical pharmacological oncology research," *Mass Spectrometry Reviews*, vol. 27, no. 2, pp. 67–100, 2008.
- [53] C. Y. Lee, P. Gong, G. M. Harbers, D. W. Grainger, D. G. Castner, and L. J. Gamble, "Surface coverage and structure of mixed DNA/Alkylthiol monolayers on gold: characterization by XPS, NEXAFS, and fluorescence intensity measurements," *Analytical Chemistry*, vol. 78, no. 10, pp. 3316–3325, 2006.
- [54] S. Ptasińska, A. Stypczyńska, T. Nixon, N. J. Mason, D. V. Klyachko, and L. Sanche, "X-ray induced damage in DNA monitored by X-ray photoelectron spectroscopy," *Journal of Chemical Physics*, vol. 129, no. 6, pp. 129–134, 2008.
- [55] M. J. Dinsmore and J. S. Lee, "Characteristic differences in the X-ray photoelectron spectrum between B-DNA and M-DNA monolayers on gold," *Journal of Inorganic Biochemistry*, vol. 102, no. 8, pp. 1599–1606, 2008.
- [56] M. R. Vilar, A. M. B. do Rego, A. M. Ferraria et al., "Interaction of self-assembled monolayers of DNA with electrons: HREELS and XPS studies," *Journal of Physical Chemistry B*, vol. 112, no. 23, pp. 6957–6964, 2008.
- [57] V. M. Sharma and W. R. Wilson, "Radiosensitization of advanced squamous cell carcinoma of the head and neck with cisplatin during concomitant radiation therapy," *European Archives of Oto-Rhino-Laryngology*, vol. 256, no. 9, pp. 462–465, 1999.
- [58] A. J. Fichtinger-Schepman, A. T. Van Oosterom, P. H. M. Lohman, and F. Berends, "Cis-Diamminedichloroplatinum(II)-induced DNA adducts in peripheral leukocytes from seven cancer patients: quantitative immunochemical detection of the adduct induction and removal after a single dose of cis-diamminedichloroplatinum(II)," *Cancer Research*, vol. 47, no. 11, pp. 3000–3004, 1987.
- [59] J. P. Macquet and T. Theophanides, "DNA platinum interactions in vitro with trans and cis $\text{Pt}(\text{NH}_3)_2\text{Cl}_2$," *Bioinorganic Chemistry*, vol. 5, no. 1, pp. 59–66, 1975.
- [60] A. Paraskar, S. Soni, S. Basu et al., "Rationally engineered polymeric cisplatin nanoparticles for improved antitumor efficacy," *Nanotechnology*, vol. 22, no. 26, Article ID 265101, 2011.

Computational Study of the Structure of a Sepiolite/Thioindigo Mayan Pigment

Manuel Alvarado Jr.¹ Russell C. Chianelli,¹ and Roy M. Arrowood²

¹Materials Research and Technology Institute, The University of Texas at El Paso, El Paso, TX 79912, USA

²Department of Metallurgical & Materials Engineering, The University of Texas at El Paso, El Paso, TX 79912, USA

Correspondence should be addressed to Russell C. Chianelli, chianell@utep.edu

Academic Editor: Ian Butler

The interaction of thioindigo and the phyllosilicate clay sepiolite is investigated using density functional theory (DFT) and molecular orbital theory (MO). The best fit to experimental UV/Vis spectra occurs when a single thioindigo molecule attaches via Van der Waals forces to a tetrahedrally coordinated Al^{3+} cation with an additional nearby tetrahedrally coordinated Al^{3+} also present. The thioindigo molecule distorts from its planar structure, a behavior consistent with a color change. Due to the weak interaction between thioindigo and sepiolite we conclude that the thioindigo molecule must be trapped in a channel, an observation consistent with previous experimental studies. Future computational studies will look at the interaction of indigo with sepiolite.

1. Introduction

Among the ruins of the Mayan civilization are many examples of murals displaying a very vivid and beautiful blue paint known as Maya Blue (Figure 1). For more than 50 years this pigment has been the subject of much interest and debate among the scientific community [1, 2]. In 1931, Merwin published photographs of the ruins of a mural at Chichen Itza, noting that a blue pigment was very distinct among the other colors present [3]. The term Maya Blue was first coined in 1946 by Gettens and Stout [4] as this pigment was believed to exist exclusively on relics of the Mayan civilization in the Yucatan Peninsula region. Since these first investigations this paint has been identified in many other Mesoamerican artifacts found outside this region but is still known by its original designation, Maya Blue.

This fascinating material, composed of a fibrous clay material (palygorskite) and an organic dye (indigo), has long been renowned for its chemical stability and vivid color. Maya Blue is of great interest due to its resistance to solvents, oxidants, reducing agents, alkalis, extreme humidity, acids, and exposure to ultraviolet radiation. Even more remarkable is the fact that Maya Blue contains no heavy metal content.

This material is synthesized using a very simple process involving grinding the clay, mixing with the organic dye, and heating the mixture to a temperature above the boiling point of water (typically 120°C to 190°C), which may have been the method used by Mayan craftsmen [5]. We now know that in addition to indigo a large variety of organic dyes can be used to create similar pigments, with the choice of the dye determining the color of the finished product [6]. Additionally, other phyllosilicate materials (such as sepiolite and montmorillonite) have led to results which are similar as those obtained in palygorskite-based Mayan pigments [7], leading to a situation where an almost innumerable variety of clay/dye mixtures and corresponding colors exist. In order to avoid a brute force approach where every new mixture must be physically synthesized to determine its color there is a strong inspiration to model and predict the color resulting from such new combinations of these materials. This paper will propose a model for the binding for one such material, consisting of the clay sepiolite being combined with the organic dye thioindigo (the choice of material was purely determined by the availability of experimental UV/Vis data in order to validate the computational results).



FIGURE 1: A photograph of a monument in Chichen Itza, YUC (900 C.E.), Mexico, painted with Maya Blue, from [6].

1.1. Sepiolite. Sepiolite, like palygorskite, is a fibrous, colorless phyllosilicate material consisting of layers of SiO_4 tetrahedra (oriented such that unshared oxygen atoms are facing each other) bonded together with octahedrally coordinated magnesium atoms between these tetrahedral sheets [8–10]. The unit cell of the clay, shown in Figure 2, has orthorhombic symmetry with lattice parameters $a = 13.5 \text{ \AA}$, $b = 27.0 \text{ \AA}$, and $c = 5.30 \text{ \AA}$ [10]. Like palygorskite, rectangular channels forms parallel the c -axis of the unit cell and often contain zeolitic water or hydroxyl groups. A trivalent cation (Mn^{3+} , Al^{3+} , or Fe^{3+}) is often found as a substitutional impurity occupying a silicon site in a tetrahedral sheet [9]. Additional water molecules are present in the octahedral magnesium layers (structural water, as opposed to zeolitic water).

The larger channel size in sepiolite compared to palygorskite makes channel diffusion and adsorption of dye molecules a more probable process in sepiolite. Ovarlez et al. [11] found that indigo did not react with sepiolite until the clay was heated well above the boiling point of water (180°C – 550°C), concluding that both zeolitic and structural water groups must be removed from sepiolite before indigo is bonded with sepiolite due to bond energies appearing in FTIR spectra. Giustetto et al. [12] found evidence of chemical bonding between indigo and sepiolite when the clay had been heated to 190°C (enough to remove zeolitic but not structural water) using IR and RAMAN spectroscopy, noting that a weak bond existed between the clay and C=O and N–H functional groups in indigo. Furthermore, this group concluded that this weak chemical bond could show surprising stability when formed within channels where the adsorbed indigo was difficult to reach and thus remove. In these cited studies there was evidence that indigo was present in its dehydroindigo form, allowing more structural flexibility of the dye molecule. As dehydroindigo is a strong chemical analogue to thioindigo we expect thioindigo to diffuse and bond in a similar fashion as dehydroindigo, especially if Van der Waals bonding is the predominant chemical attraction.

1.2. Color Changes in Clay/Dye Complexes. A key measure of the formation of the clay/dye complex is a dramatic color change, as shown in Figure 3. These color changes occur

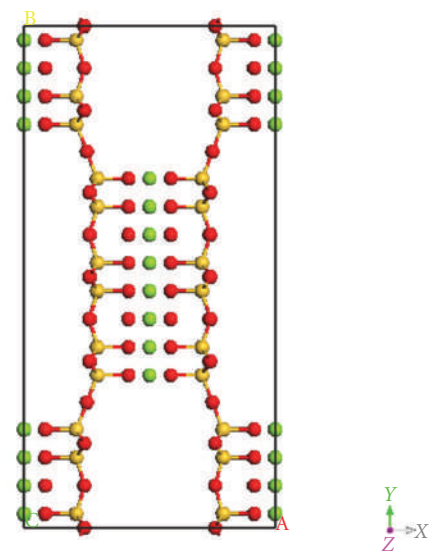


FIGURE 2: Unit cell of sepiolite, showing magnesium (green) octahedrally coordinated between chains of SiO_4 (silicon shown in orange, oxygen in white). View is along the c -axis.

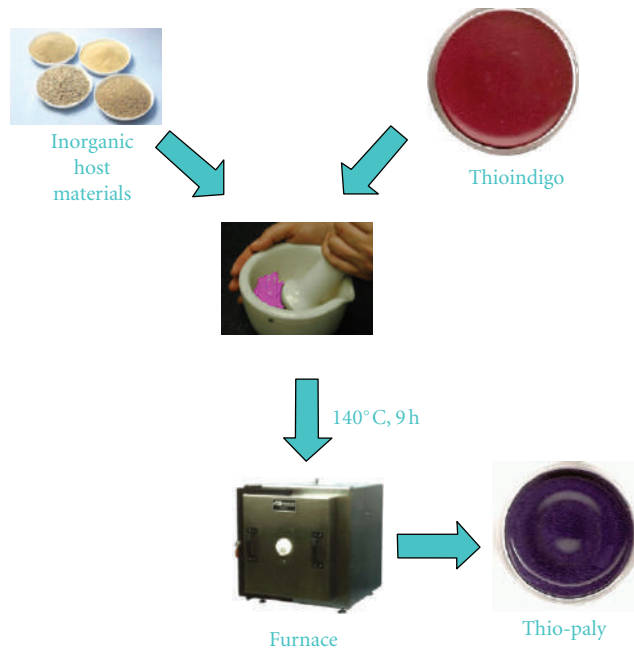


FIGURE 3: Color change of clay/dye complex during synthesis, in this case palygorskite/thioindigo.

only as the temperature of the clay/dye mixture is heated and a chemical interaction takes place. The blue of indigo, for example, changes to the classic Maya Blue color upon heating, a nonreversible change (a strong indication of the presence of the dehydroindigo form of the indigo molecule). Although the figure shows an example of a color change with a palygorskite/thioindigo complex these color changes have been observed for a wide range of both clays (palygorskite, sepiolite and montmorillonite) and dye molecules (indigo,

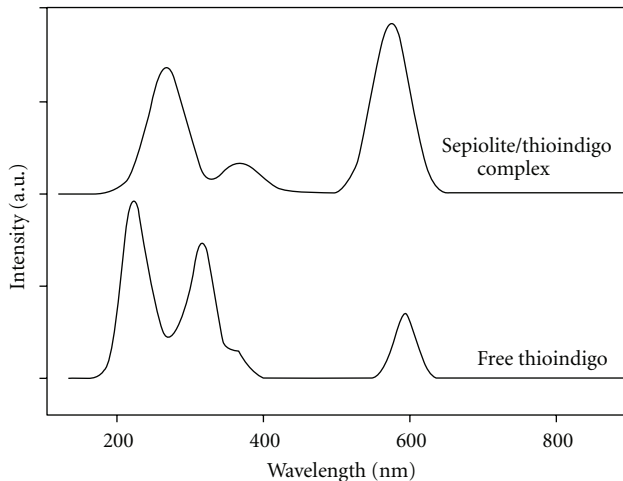


FIGURE 4: Computational color change in sepiolite-bonded thioindigo. The UV-Vis spectra are displaced vertically for clarity.

thioindigo, vat orange 5, yellow 33, etc.). This color change is seen as evidence of a chemical interaction between the dye and clay, an assertion confirmed by IR and XRD spectra, HRTEM analysis, and DTA analysis [13]. An example of the color change seen in our computational model is shown in Figure 4.

2. Preliminary Chemical Model for a Synthetic Sepiolite/Thioindigo Complex

Most studies on the structural characterization of sepiolite-based dye complexes have drawn a parallel with palygorskite-based complexes. For these structures, two significant and related issues are (1) whether surface biding or channel “tucking” is the predominant means of interaction and (2) the presence of zeolitic water in these channels. The process of synthesizing sepiolite-based dye complexes involves mixing the dye with sepiolite and heating the mixture to temperatures above 120°C, resulting in a mass loss of 6–10% in the mixture, which has been attributed to loss of zeolitic water molecules by thermogravimetric analysis (TGA) [14]. Although sepiolite has been observed to undergo structural collapse and loss of channels with removal of structural water [15], the temperatures required to achieve this (approximately 800°C) are far in excess of the temperatures used in the synthesis of this material. We therefore proceed on the assumption that the channels in sepiolite are clear of water and are capable of having thioindigo molecules diffusing into these channels, as the channel size is more than large enough to accommodate the dye molecule. Our preliminary chemical model is shown in Figure 5.

3. Computational Modeling Procedure

The computational methodology used for this study is as follows. The proposed structure was optimized using a plane-wave pseudopotential density functional theory (DFT) code, CASTEP [16]. A Gaussian smearing width of each

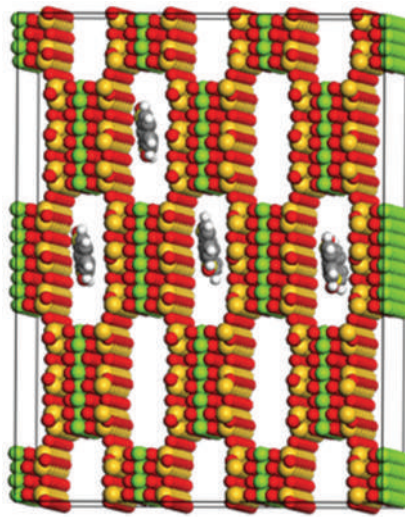


FIGURE 5: Crystal structure of sepiolite with zeolitic water removed and thioindigo tucked into several channels. The model was generated using the Sorption module in Materials Studio 4.0.

energy level is introduced to eliminate a discontinuity in the energy when an electron band crosses a Fermi level during calculation. This width is subsequently halved upon the convergence of energy values to the parameter specified by a Self-Consistent Field (SCF) condition, in which the field experienced by an atom depends on the global distribution of atoms. The calculation is then repeated and the process continues in this manner until the smearing width converges to a specific minimum value. The initial smearing width of each calculation was set to 1 eV, as this value offered a reasonable compromise between speed and accuracy. It should be noted that the CASTEP graphic user interface allows for a range of values for the smearing width varying between 4.0 eV and 0.1 eV.

A pseudopotential chosen for these preliminary calculations was a norm-conserving nonlocal pseudopotential as described by Lin et al. [17]. Although additional pseudopotentials are available through the CASTEP GUI, it was decided to limit these initial calculations to a single pseudopotential due to the computation time involved.

The plane-wave expansion of electronic wavefunctions used by CASTEP requires the input of a kinetic cut-off energy for these wavefunctions. It was determined that specifying a cut-off energy of no less than 200 eV provided the optimum balance between computation time and precision, as cut-off energies below this value did not yield significantly varying energies. The resulting constraint on spacing of cells in reciprocal space used to generate k-point by a Monkhorst-Pack scheme 42 was set at 0.07 Å⁻¹. These parameters were employed in all calculations.

The CASTEP calculations consisted of both energy calculations for fixed structures and geometry optimizations for structures without fixed parameters. The geometry optimizations in CASTEP involve the movement of atoms in a crystal structure until a geometry is achieved that minimizes the energy. An additional investigation involved the varying

of the lattice parameters resulting from each geometry optimization to within 0.1 Å of the optimized values to ensure the convergence of the energy to an absolute as opposed to a local minimum. This procedure was employed in all cases to test the validity of optimized lattice parameters.

For MO calculations, the molecular orbital (MO) method VAMP [18] was used on the nonperiodic version of the organic/inorganic complex. First, the energy of the optimized structure (as optimized in a periodic version of the structure by CASTEP) was calculated. A ZINDO (Zerner's Intermediate Neglect of Differential Overlap) Hamiltonian, which uses INDO to handle differential overlap, was used [19]. A full Configuration Interaction (CI) scheme, which allows all available permutations of electronic excitations in each orbital, was applied. The SCF tolerance in the calculation was 5×10^{-7} eV/atom (fine criterion within the VAMP GUI). Once the energy was calculated for the structure these same constraints were applied to calculate the UV/Vis spectrum using a Gaussian integration scheme and applying a smearing width of 30 nm FWHM in order to simulate instrumental broadening.

4. DFT and MO Results for Calculation of Optical Spectra for Sepiolite/Thioindigo Complex

We modeled the sepiolite-thioindigo system by first optimizing the structure geometry using CASTEP, and then calculating the optical spectrum using VAMP. The proposed structures (with approximate geometries provided by the Sorption module in Cerius² [20] as a starting point) were modeled as a surface by taking a 14×3 lattice of adjacent silica rings (mimicking the morphology along a wall of a channel in sepiolite) and introducing a substitutional impurity at a silicon site (based on spectroscopic data, aluminum, iron, and magnesium were used in our simulations). Using this proposed surface complex as a basis we constructed a three-dimensional unit cell as required by CASTEP for geometry optimizations (Figure 6). By allowing the unit cell to have a very large lattice parameter perpendicular to the surface we are able to simulate a surface interaction while satisfying three-dimensional periodicity required by CASTEP as the simulation becomes one of modeling a series of noninteracting parallel planes (confirmed by the fact that the total electronic energy converged to a constant value as this lattice parameter is increased). Once the model converged to an optimum geometry by CASTEP using a generalized gradient approximation (GGA) functional the structure is reduced to a nonperiodic structure (required for a VAMP calculation) consisting of 3 adjacent silica rings and the attached dye molecule as structures larger than this were prohibitively expensive in terms of computational power. A VAMP molecular orbital simulation employing a neglect of diatomic differential overlap (NDDO) Hamiltonian with a full configuration interaction (CI) scheme was then used to calculate UV/Vis spectra and compare to experimental data. This process was repeated using single and multiple substitutional metallic impurity sites using the aforementioned

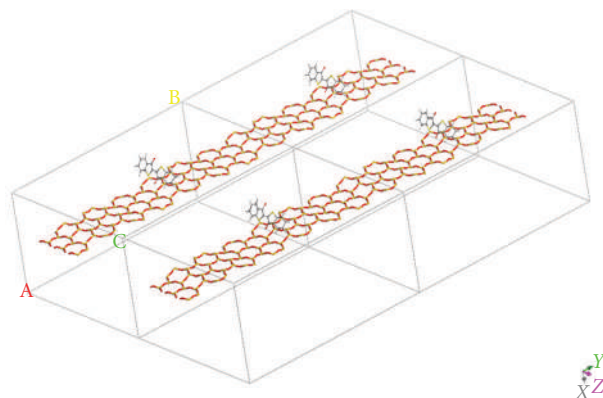


FIGURE 6: Periodic structure of sepiolite/thioindigo complex used for CASTEP calculation.

metals found in sepiolite as well as monomer, dimer, and trimer thioindigo complexes. We found the best agreement between computational and experimental spectra when the structures had the following characteristics:

- (i) tetrahedral bonding of thioindigo to an aluminum impurity site;
- (ii) a single thioindigo molecule bonded to an aluminum site in the nonperiodic surface mesh;
- (iii) distortion of the thioindigo molecule from its planar structure. This has been associated with the observed color changes in the synthesis of mayan pigments and related materials [13].

The first two observations ran contrary to our findings with a palygorskite/thioindigo complex, which saw the best UV/Vis spectral fit for octahedral binding and a dimer thioindigo structure attaching to the surface mesh. The results for the optical spectrum for the thioindigo/sepiolite complex are shown in Figure 7, showing excellent agreement in both visible and near-UV regions between the computational and experimental results. The optimized molecular structure corresponding to this result is shown in Figure 8. Two interesting features of this structure are (1) unlike palygorskite-based mayan pigments which display a dimer structure on the adsorbed dye molecules, only a single dye molecule bonds to the surface mesh, and (2) the dye molecule is bonded to the surface via a Van der Waals interaction. While such an interaction would seem to be at odds with the resistance to color fading of mayan pigments we must consider the added stability of channel bonding sites within the clay as due to physical confinement of the dye molecules within these channels in a manner analogous to layer intercalation in catalytic materials such as MoS₂ [21]. An additional argument in support of channel bonding is the fact that the maximum concentrations of dye are less than those possible in palygorskite-based complexes [22] in which the dye is known to bond to the clay predominantly at surface sites.

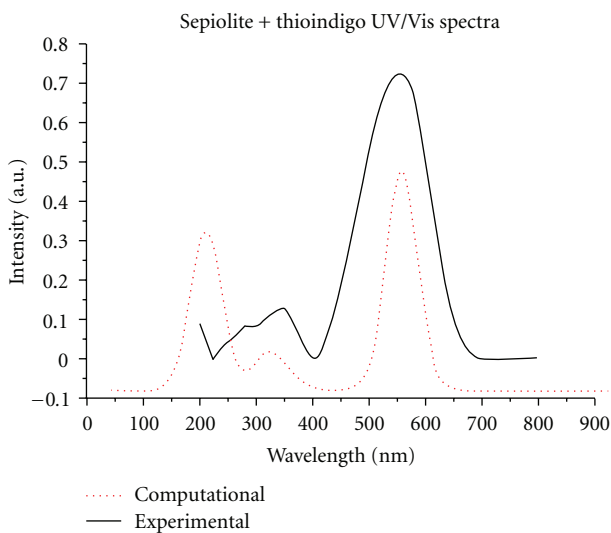


FIGURE 7: Comparison of computational and experimental UV/Vis spectrum of the thioindigo/sepiolite complex.

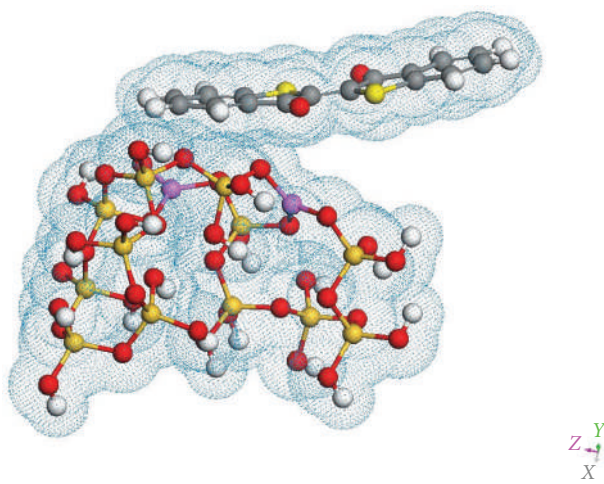


FIGURE 8: Optimized thioindigo/sepiolite structure with Van der Waals surface displayed. Note the distortion of the planar geometry of the thioindigo molecule.

5. Conclusions

In this paper we have presented a model for the chemical interaction between sepiolite and thioindigo in a clay/dye complex similar in nature to palygorskite/dye based Mayan pigment complexes. During synthesis sepiolite loses its zeolitic water content, opening up channels for the insertion of thioindigo molecules. The experimentally reported concentration of dye in this complex is consistent with channel absorption of the dye. Thioindigo attaches to the channel at an aluminum impurity site, with an additional but noninteracting aluminum impurity site nearby. The interaction is of a Van der Waals nature. The simulated model showed a significant distortion of the planar geometry of thioindigo, a characteristic of the well-known color changes in Mayan pigment-type materials. The UV/Vis spectrum of

the model was simulated using both DFT and MO methods and is in excellent agreement with experimental results for the spectrum. Future studies will develop a model for a sepiolite/indigo complex.

References

- [1] M. J. Yacaman and M. C. S. Puche, "High resolution electron microscopy of maya blue paint," *Materials Research Society Symposium Proceedings*, vol. 352, pp. 3–11, 1995.
- [2] R. Kleber, L. Masschelein-Kleiner, and J. Thissen, "Étude et identification du Bleu Maya," *Studies in Conservation*, vol. 12, no. 2, pp. 41–56, 1967.
- [3] H. E. Merwin, *Temple Warriors at Chitzen Itza*, vol. 406, Carnegie Institution of Washington, Washington, DC, USA, 1931.
- [4] R. J. Gettens and G. L. Stout, *Paint Materials: A Short Encyclopedia*, D. van Nostrand, New York, NY, USA, 1946.
- [5] H. Van Olphen, "Maya Blue: a clay-organic pigment?" *Science*, vol. 154, no. 3749, pp. 645–646, 1966.
- [6] R. R. Chianelli and L. A. Polette, "Color Compositions," US Patent 7,052,541, 2006.
- [7] A. Ramírez, C. Sifuentes, F. S. Manciu, S. Komarneni, K. H. Pannell, and R. R. Chianelli, "The effect of Si/Al ratio and moisture on an organic/inorganic hybrid material: thioindigo/montmorillonite," *Applied Clay Science*, vol. 51, no. 1-2, pp. 61–67, 2011.
- [8] A. Alvarez, *Palygorskite-Sepiolite: Occurrences, Genesis, and Uses*, Elsevier, New York, NY, USA, 1984.
- [9] D. L. Bish and G. D. Guthrie, "Mineralogy of clay and zeolite dusts (exclusive of 1 : 1 layer silicates)," *Reviews in Mineralogy*, vol. 28, pp. 139–184.
- [10] K. Hansen and B. T. Mossman, "Generation of superoxide (O_2^-) from alveolar macrophages exposed to asbestosiform and nonfibrous particles," *Cancer Research*, vol. 47, no. 6, pp. 1681–1686, 1987.
- [11] S. Ovarlez, F. Giulieri, F. Delamare, N. Sbirrazzuoli, and A. M. Chaze, "Indigo-sepiolite nanohybrids: temperature-dependent synthesis of two complexes and comparison with indigo-palygorskite systems," *Microporous and Mesoporous Materials*, vol. 142, no. 1, pp. 371–380, 2011.
- [12] R. Giustetto, K. Seenivasan, and S. Bordiga, "Spectroscopic characterization of a sepiolitebased Maya Blue pigment," *Periodico di Mineralogia*, vol. 79, pp. 21–37, 2010.
- [13] L. A. Polette-Niewold, F. S. Manciu, B. Torres, M. Alvarado, and R. R. Chianelli, "Organic/inorganic complex pigments: ancient colors maya blue," *Journal of Inorganic Biochemistry*, vol. 101, no. 11-12, pp. 1958–1973, 2007.
- [14] S. Ovarlez, A. M. Chaze, F. Giulieri, and F. Delamare, "Indigo chemisorption in sepiolite. Application to Maya blue formation," *Comptes Rendus Chimie*, vol. 9, no. 10, pp. 1243–1248, 2006.
- [15] J. J. Beaudoin and P. E. Grattan-Bellew, "Collapse of structure in sepiolite and other layered silicate systems," *Cement and Concrete Research*, vol. 10, no. 3, pp. 347–359, 1980.
- [16] M. C. Payne, M. P. Teter, D. C. Allan, T. A. Arias, and J. D. Joannopoulos, "Iterative minimization techniques for ab initio total-energy calculations: molecular dynamics and conjugate gradients," *Reviews of Modern Physics*, vol. 64, no. 4, pp. 1045–1097, 1992.
- [17] I. Stich, M. C. Payne, R. D. King-Smith, J.-S. Lin, and L. J. Clarke, "Ab initio total-energy calculations for extremely large systems: application to the Takayanagi reconstruction of

- Si(111)," *Physical Review Letters*, vol. 68, no. 9, pp. 1351–1354, 1992.
- [18] J. Hafner, "Ab-initio simulations of materials using VASP: density-functional theory and beyond," *Journal of Computational Chemistry*, vol. 29, pp. 2044–2078, 2008.
- [19] M. Zerner, *Reviews in Computational Chemistry*, vol. 2, Edited by K. B. Lipkowitz and D. B. Boyd, VCH, New York, NY, USA, 1991.
- [20] N. Metropolis, A. W. Rosenbluth, M. N. Rosenbluth, A. H. Teller, and E. Teller, "Equation of state calculations by fast computing machines," *The Journal of Chemical Physics*, vol. 21, no. 6, pp. 1087–1092, 1953.
- [21] K. E. Dungey, M. D. Curtis, and J. E. Penner-Hahn, "Structural characterization and thermal stability of MoS₂ intercalation compounds," *Chemistry of Materials*, vol. 10, no. 8, pp. 2152–2161, 1998.
- [22] S. Ovarlez, A. M. Chaze, F. Giulieri, and F. Delamare, "A chemical comprehension of the colour centres in Maya blue green palette. A study of indigo chemisorption in sepiolite," in *Proceedings of the Dyes in History and Archaeology Conference*, Suceava, Romania, 2006.

A Comparison of Epithelial Cells, Fibroblasts, and Osteoblasts in Dental Implant Titanium Topographies

Fu-Yuan Teng,^{1,2} Chia-Ling Ko,² Hsien-Nan Kuo,³ Jin-Jia Hu,⁴ Jia-Horng Lin,⁵ Ching-Wen Lou,⁶ Chun-Cheng Hung,² Yin-Lai Wang,¹ Cheng-Yi Cheng,² and Wen-Cheng Chen⁷

¹Department of Dentistry, Kaohsiung Armed Forces General Hospital, Kaohsiung 802, Taiwan

²School of Dentistry, College of Dental Medicine, Kaohsiung Medical University, Kaohsiung 807, Taiwan

³Medical Device Development Division, Metal Industries Research & Development Centre, Kaohsiung 82151, Taiwan

⁴Department of Biomedical Engineering, National Cheng Kung University, Tainan 701, Taiwan

⁵Laboratory of Fiber Application and Manufacturing, Department of Fiber and Composite Materials, Feng Chia University, School of Chinese Medicine, China Medical University, Taichung 40724, Taiwan

⁶Institute of Biomedical Engineering and Material Science, Central Taiwan University of Science and Technology, Taichung 40601, Taiwan

⁷Department of Fiber and Composite Materials, College of Engineering, Feng Chia University, 100 Wenhwa Road., Seatwen, Taichung 40724, Taiwan

Correspondence should be addressed to Wen-Cheng Chen, chernlin2@gmail.com

Academic Editor: Ivano Bertini

The major challenge for dental implants is achieving optimal esthetic appearance and a concept to fulfill this criterion is evaluated. The key to an esthetically pleasing appearance lies in the properly manage the soft tissue profile around dental implants. A novel implant restoration technique on the surface was proposed as a way to augment both soft- and hard-tissue profiles at potential implant sites. Different levels of roughness can be attained by sandblasting and acid etching, and a tetracalcium phosphate was used to supply the ions. In particular, the early stage attaching and repopulating abilities of bone cell osteoblasts (MC3T3-E1), fibroblasts (NIH 3T3), and epithelial cells (XB-2) were evaluated. The results showed that XB-2 cell adhesive qualities of a smooth surface were better than those of the roughened surfaces, the proliferative properties were reversed. The effects of roughness on the characteristics of 3T3 cells were opposite to the result for XB-2 cells. E1 proliferative ability did not differ with any statistical significance. These results suggest that a rougher surface which provided calcium and phosphate ions have the ability to enhance the proliferation of osteoblast and the inhibition of fibroblast growth that enhance implant success ratios.

1. Introduction

Successful dental implant treatment depends on three components: bone, connective tissue, and epithelium. Each plays an important function; for example, connective tissue cannot anchor the implant surface having mechanical attachments as bone does because inadequate peri-implant epithelium function can lead to the creation of deep pockets and invasion of bacteria [1–3]. In addition, the fundamental esthetic outcomes associated with dental implant treatments are related to the healing characteristics of both the epithelium and connective tissue [4]. Different surface designs of

materials can also cause varying levels of peri-implant hard and soft tissues [4, 5]. Accordingly, the chemical composition and physical properties of the implant's surface can affect peri-implant tissues behavior [6, 7].

Many methods are used to create a rough implant surface. To create a three dimensional roughness on the implant surface for improving bone anchorage, differential ways such as titanium plasma spraying, grit or sandblasting, acid-etching, and anodization were used [7–9]. Among these, a most popular way of the sandblasting and acid etching (SLA) have been reported. The SLA treatment showed the properties of earlier osseointegration and decreased bone loss than

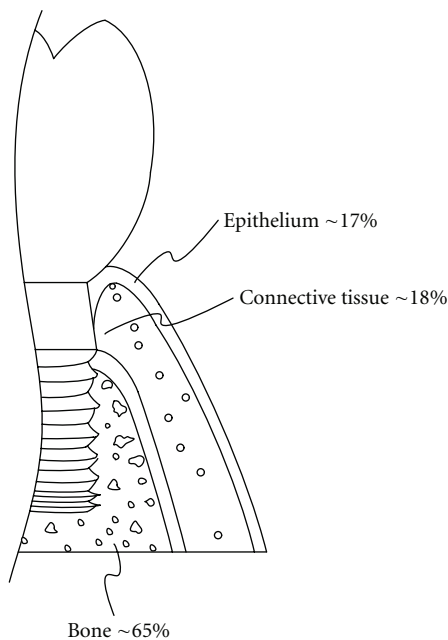


FIGURE 1: A diagrammatic illustration showing the relationship of the interfacial parts between periodontal tissues and an implant (length: 5.7 mm). The relationship between the bone of the alveolar process, the gingival connective tissue and junctional epithelium are shown, at the level where the implants and tissues contact.

other surface treatment ways [10]. However, harmful metal ion dissolution and particles such as aluminum remain in the processes by SLA surface treating and lead to local or systemic toxic effects [11–13].

Peri-implant soft tissues play an important role, as they might encompass over one-third of the height area of short implants (Figure 1). After implantation, two distinct responses may occur on the implant surface. The bone tissue can contact the implant surface with a proper biological width, signaling a successful treatment with complete osseointegration. Another response is fibrous encapsulation involving the soft tissue covering the entire implant surface. These responses involve the three aforementioned cell types, which have distinct growth patterns and varying abilities of adhesion to the implant surface and the early stage attaching and repopulating abilities of cells is a common technique for evaluating initial stability of the implant [14–16].

Because implant surface treatment is usually only concerned with integration of bone tissues and neglects soft tissues, the surfaces contacting the implant and surrounding tissues deviates from the originally intended design leading to implantation failure. For this reason, current techniques are insufficient to achieve controlled success. Hence, the purpose of this study is to find the cells relationship to develop a proper tissue architecture on the pure Ti implant surfaces that is almost identical to the patient's original after tooth extraction and implantation. The process was to treat the different roughen surfaces, and then samples were cultured with bone cells, fibroblasts, and epidermal

cells to evaluate the differential early stage cell attaching and repopulating abilities.

2. Materials and Methods

2.1. Materials—Surface Treatment. Commercially pure, grade II titanium (cp Ti) samples (Buehler Ltd, USA) measuring $6 \times 5 \times 1$ mm in respective length, width, and thickness of constant surface areas of 30 mm^2 within 2.5% standard deviation (SD) were used. The samples were embedded into an epoxy resin to be polished by sandpaper of decreasing grain sizes: 400, 1200 and 2000. Then the samples were washed following with ethanol, acetone, and distilled water using ultrasonic oscillation for each 5 min. The Ti metal surface, a control group, controlled an Ra value of 0.12 micrometer (μm) within 5.0% SD.

Testing groups, in which the surfaces of the control group were sandblasted for 10, 20, and 30 sec with aluminum (Al_2O_3) particles (mean size $54.5 \pm 32.1 \mu\text{m}$). The sandblasting used an air compressor with 7 kg/m^2 of powder blasted over a 0.5 mm distance. After sandblasting, the samples were acid-etched for 30 sec. An etching solution of the HCl (37%, Panreac, Barcelona, Spain) to H_2SO_4 (95–98%, Panreac, Barcelona, Spain) to H_2O volume ratio of 1:1:1 was used. Testing groups were after different blasting times and following acid-etching processes (SLA) for constant time 30 sec were presented as the symbols of 10/30, 30/30, and 60/30 groups ($n = 10$). To clarify the ion effect of 10/30 testing group, a comparative group receiving secondary grit-blasting using TTCP particles (10 sec), which was prepared in-house and had a mean particle size of $10.1 \pm 0.7 \mu\text{m}$ [17], was present as a SLA 10/30/TTCP group. The 10/30/TTCP group was dry-heat sterilized at 160°C for 2 h and the other samples were sterilized in an autoclave.

2.2. Surface Characterizations. The average surface roughness was measured using a roughness tester (SJ-301 Mitutoyo Ltd, Japan) and presented in Ra. Topographies and the anchored/residual particles were analyzed by a scanning electron microscope (SEM, Hitachi S-3000N, Japan) equipped with an energy dispersive X-ray spectrometer (EDS, Horiba EX220, Japan).

2.3. Cell Abilities and Morphologies. Three cell lines of the bone (MC3T3-E1, abbreviated E1), fibroblast (NIH 3T3, abbreviated 3T3), and epidermal (XB-2) cells were provided by the National Institute of Health (NIH) in Taiwan. E1 was derived from newborn mouse calvaria and were cultured in a 10 mL of *alfa*-modified Eagle's medium (MEM) containing 10% fetal bovine serum (FBS) (Biological Industries, Haemek, Israel), and 1% penicillin (100 units/mL)/streptomycin (100 $\mu\text{g/mL}$) (Gibco, Invitrogen Taiwan Ltd., MD). 3T3 was derived from newborn mouse fibroblasts and cultured in Dulbecco's modified Eagle's medium (DMEM) (Gibco, Invitrogen Taiwan Ltd., MD) containing 10% bovine serum (BS) (Biological Industries, Haemek, Israel). XB-2 was derived from newborn mouse keratinized cells and cultured as in the study [18]. XB-2 cells

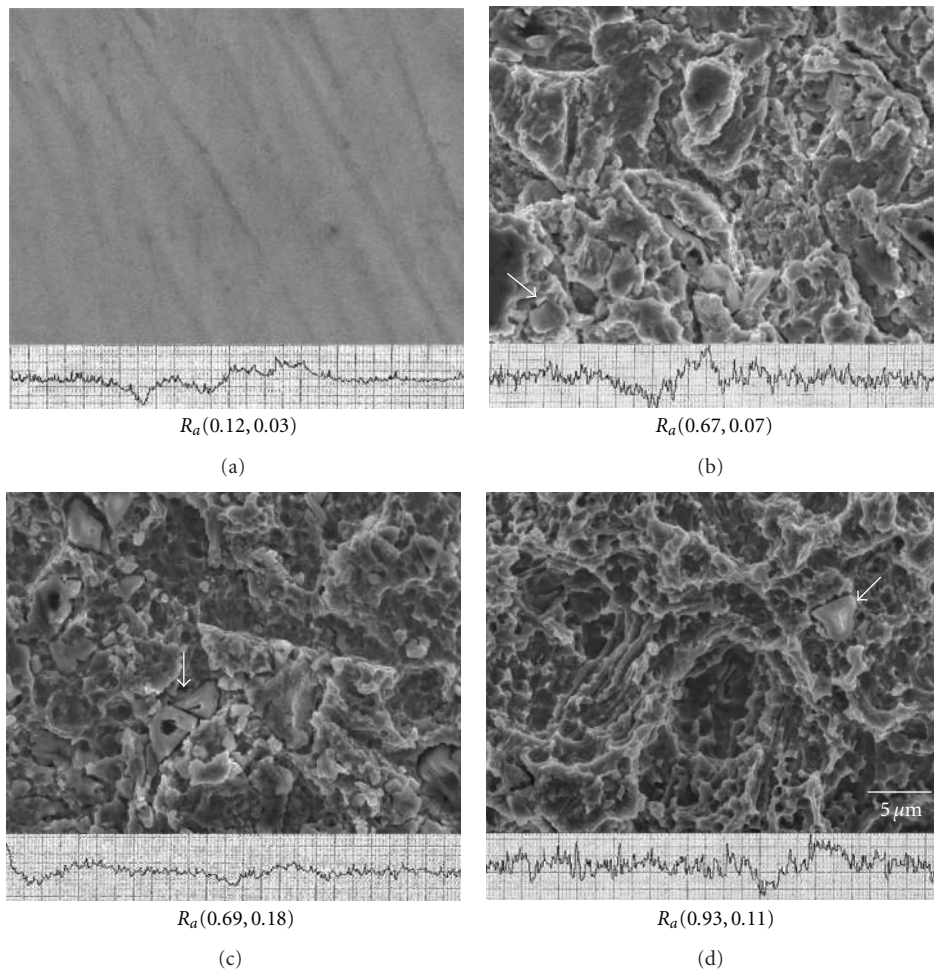


FIGURE 2: The different topographies of cp Ti surfaces and their respective levels of roughness after blasting/etching for various times (sec). (a) Control and (b) 10/30, (c) 30/30, (d) 60/30 test groups. Ra: average roughness (mean, SD), units: micrometers. Arrowhead: surface-trapped alumina.

were grown in the presence of 3T3 cells, which were briefly cultured on a 0.1% gelatin-coated plate (G932-500G, Sigma Co., St. Louis, USA) before culturing in DMEM containing mitomycin C ($10 \mu\text{g}/\text{mL}$) for 2.5–3 h. Subsequently, XB-2 cells were cultured in DMEM containing 20% FBS. All cells were cultured in a humidified atmosphere in a 5% CO_2 incubator. The culture medium was replaced every 2–3 days. After the cultured cells were harvested, cells were counted and seeded on the prepared surfaces at 1×10^5 cells/sample.

An XTT Cell Viability Assay Kit provided a simple method to count live cells using an absorbance reader. The cells' adhesive and repopulative abilities were measured at two early stage time points of 1 h and 24 h. After the cultured time, the cells on the samples' surface were washed with phosphate-buffered saline (PBS) and transferred to a $200 \mu\text{L}$ culture medium with a $100 \mu\text{L}$ XTT kit and were incubated for another 4 h. The reaction medium was then measured spectrophotometrically at 490 nm using an ELISA microplate reader UVM-340 (ASYS Hitech GmbH, Eugendorf, Austria). Finally, the cell numbers were determined from a plot of absorbance (OD values) versus the respective E1, 3T3, and

XB-2 cells after adjustment via XTT assays. Each experiment was performed five times ($n = 5$).

After being cultured, the samples were washed and fixed with a mixture of 2% paraformaldehyde and 2.5% glutaraldehyde for 2 h. After dehydration in a graded series of ethanol, the samples were treated with iso-amyl acetate and dried using a critical point dryer. The specimens were sputter-coated with gold and the cell morphology was observed using SEM. To compensate for the ion effects in the medium, TTCP was extracted at a ratio of 1 g TTCP to 10 mL culture medium. The three cells were cultured in the extraction and on the selected 10/30/TTCP surfaces for 24 h. The statistical analysis was performed using JMP 6.0 software (SAS Institute Inc., Cary, NC, USA) with statistical significance set at $P < 0.05$.

3. Results

3.1. Topographies and Elements Mapping. The flattest surface was observed in the control group and the etching effects on the Ti surfaces became more significant as the blasting time

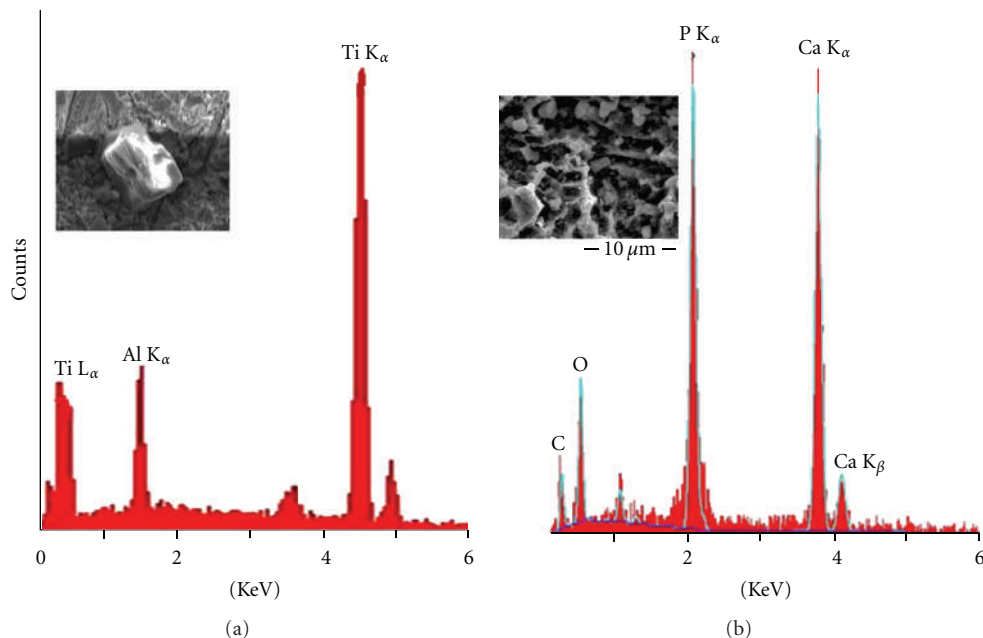


FIGURE 3: (a) Results of spectrum showing the surfaces having alumina particles in the test groups after 10/30 sec of blasting/etching. (b) EDS showing the surfaces having high levels of Ca and P atoms without alumina through secondary blasting of TTCP particles.

was increased in Figures 2(b)–2(d). The SLA 60/30 group obviously increases the roughness more than other groups. Al_2O_3 particles are still captured or anchored on the surface even after 5 min ultrasonic cleaning accompanied by 30 sec etching. However, Al_2O_3 particles were not found after the secondary grit-blasting using TTCP particles (Figure 3(b)), where only calcium and phosphorus elements were found and reduce the Ra values in the groups from SLA test group to SLA 10, 30, and 60/30/TTCP (Ra 0.62 ± 0.07 , 0.63 ± 0.09 , and 0.71 ± 0.08).

3.2. Early Stage Cell Properties. Cells were cultured for 1 h and 24 h each to determine their adhesive and initial proliferative abilities. Statistical analysis of all the groups was shown in the Table 1.

Accordingly to the OD values (Figures 4(a) and 4(b)), higher Ra values would reduce the OD values of the E1 and 3T3 cells, however, XB-2 cells were unaffected in all measurements. When the cell numbers were aligned and counted after 1 h (Figure 4(c)), the XB-2 cells on the flattest surface was shown to be four times larger than on the rough SLA 60/30 surface. After 24 h, XB-2, and 3T3 cells behaved differently depending on the Ra values. As such, the behavior of 3T3 cells was not obviously different after 1 h and 24 h of SLA 60/30. The epidermal cells proliferate faster on the rough surface and the fibroblasts displayed a contrary proliferation tendency on a surface with 60/30 SLA treatment, the number of XB-2 cells obtained after 1 h increased 2.6 times after 24 h (Table 1).

3.3. Morphologies of Cells. XB-2 and 3T3 cells displayed a round morphology and the filopodia of E1 demonstrated

a spider shape originally. The XB-2 and 3T3 cells in the control group were spindle-shaped and especial the XB-2 cells, proliferated on the largest Ra samples, had an entirely different morphology (Figure 5). The filopodia were extended and evenly distributed over the surface. This phenomenon of altered epithelial morphology is indicating that XB-2 cells have a better growth rate on the rough surface [19].

3.4. Ions Effect. Proliferative patterns of XB-2 and 3T3 cells were no different among SLA 10/30, SLA 10/30/TTCP, and TTCP-extracted medium groups and the conditions of E1 cells deteriorated with anchored SLA 10/30/TTCP group ($P < 0.05$) (Figure 6). However, TTCP-extracted culture medium is basically aid for the E1 early stage proliferation at 24 h cultured. Hence, in the early stages of cell repopulation, surface conditions are clearly more important for bone cells than the effects of ions.

4. Discussion

To view the SLA procedures, Al_2O_3 is widely used as sandblasting particles for surface cleaning or developing roughness. These particles, which were entrapped in the Ti surface, were difficult to remove through a popular used single acid-etching process. Moreover, this has been proved that can cause poor osseointegration, and a high density of Al ions on the Ti alloy may be related to Alzheimer's disease [20–22]. Fortunately these particles can be replaced by a secondary sandblasting technique, which has a smaller particle size distribution than Al_2O_3 .

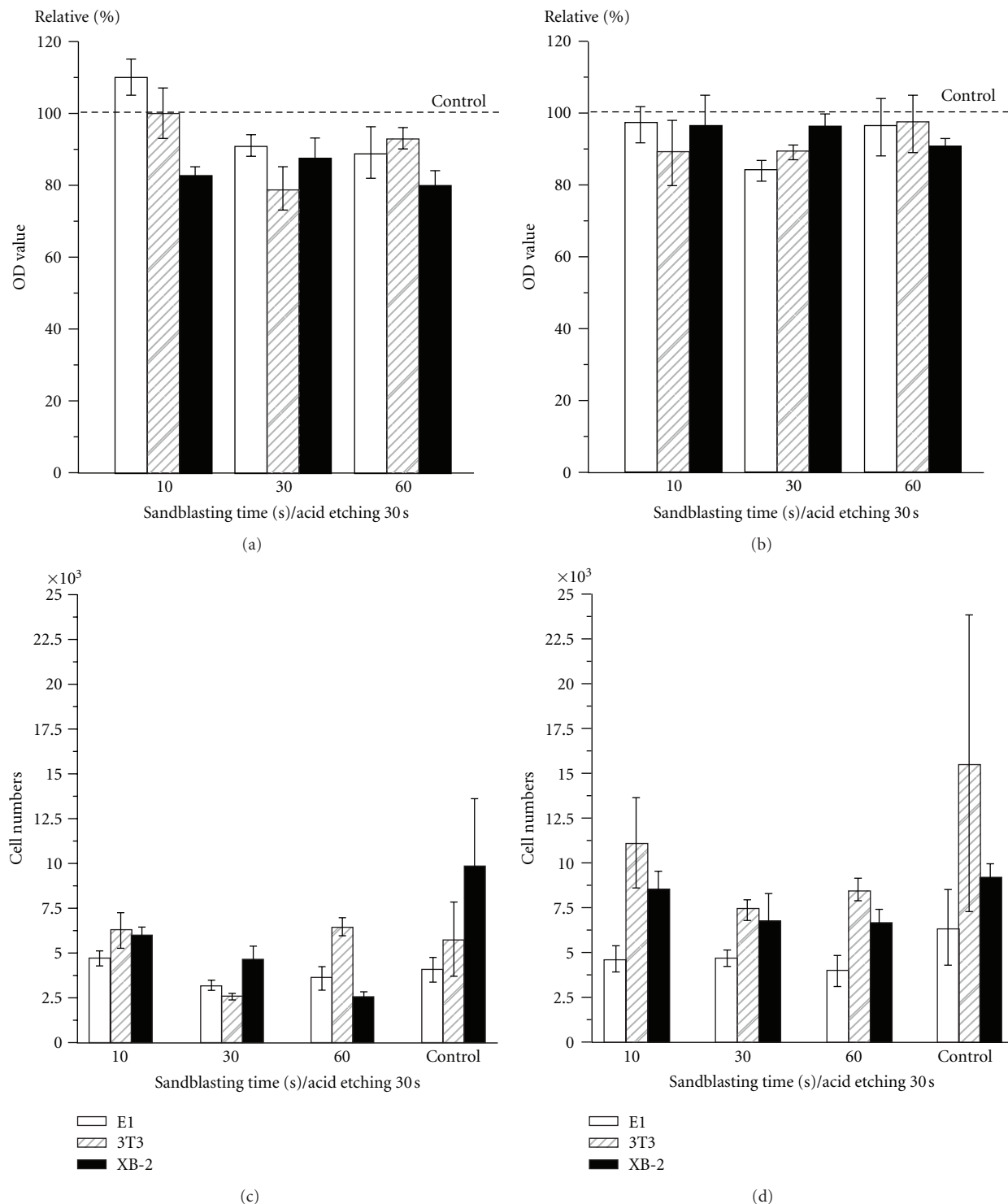


FIGURE 4: Different cells cultured on a variety of topographies: OD values after (a) 1 h of adhesion and (b) 24 h of proliferation were compared with the control group and the cell numbers were counted after 1 h (c) and 24 h (d).

After placement of the dental implant, the complications of infection and fibrous encapsulation may occur during the healing process. The success of dental implants cannot merely be defined by the efficacy of osseointegration between the bone and the implant. Rather, a proper biological

interaction to obtain healthy gingiva is essential as shown in Figure 1. Among both of these contact parts between the tissues and the implant, epithelium linking would lead to the absence of inflammation [14]. The integration of soft tissue provides a beneficial strategy where the epithelium linking is

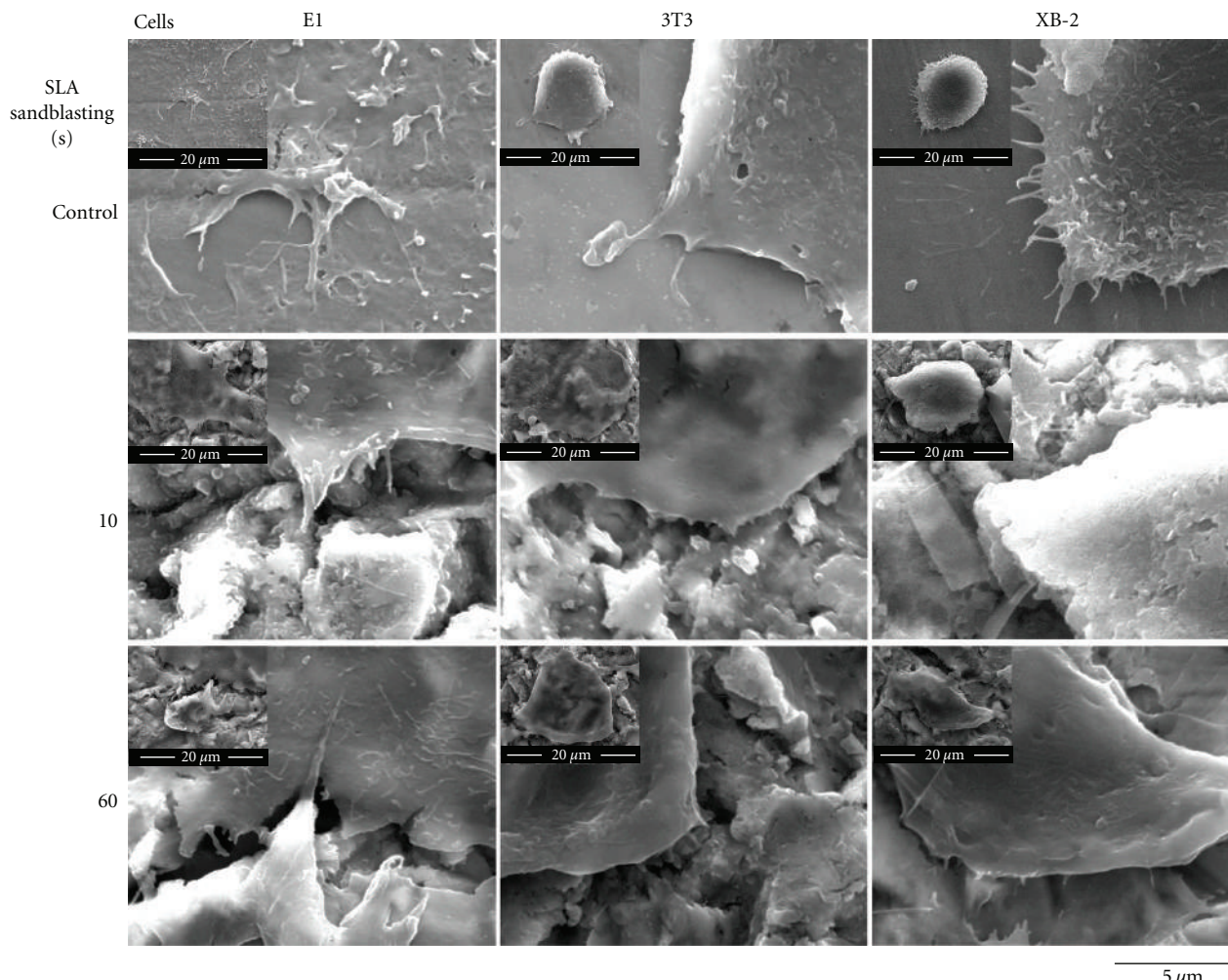


FIGURE 5: SEM images showing the proliferative morphologies of the various cells growing on areas of varying roughness in the control and test groups after 10, 30, and 60/30 sec of blasting and etching after 24 h.

enhanced while the contact part of the gingival connective tissues is suppressed.

Unlike the case with their early stage adhesive and proliferative behavior, the XB-2 and 3T3 cells acted differently than each other in respect to their reaction to surface roughness. Based on the analysis in Figures 4(c) and 4(d), 3T3 cells cultured on the smooth surface of the control group after 1 h were not significantly different from the largest roughness SLA 60/30 testing group (Table 1). However, in the control group, after 24 h cultured, the 3T3 cells went largely beyond testing groups with rough surfaces and were a 2.7-fold increase in cell numbers at 1 h culturing. Contrary to the results obtained with the 3T3 cells, the XB-2 cells had a statistical significance in roughness after 1 h of culturing; the control group displayed the best cell adhesive ability. However, after the XB-2 cells were allowed to proliferate at early stage for 24 h, there were no significant differences between the control and test groups ($P > 0.05$). This early stage result indicates that epithelial cells cultured on roughened surfaces have better proliferative abilities than those cultured on smooth surfaces. The proliferative rate of

XB-2 cells increased 2.6-fold from 1 h to 24 h of culturing for the SLA 60/30 testing, though the control group showed no specific statistical change. XB-2 cell's qualities in the control group after 1 h culturing were better than those of the roughened surfaces, the proliferative properties after 24 h culturing were reversed.

Early stage cell abilities such as adhesion and proliferation to the substrates can vary according to surface topography, which in turn influences cytoskeletal components [19, 23]. Sandblasting was thought to induce stress on the surface, whereas acid etching was thought to release the resulting residual stresses. Several related experiments [16, 24–26] reported that surface conditions can affect different types of cell morphology, and this is referred to as cell-specific discrepancies [27]. Surface characteristics have been shown to regulate how the different cells reach clinically appropriate proportions with respect to the implant. For example, one of the main challenges in implant treatment lies in achieving an esthetic appearance, involving a physiological outcome [28–30]. For soft-tissue integration involving epithelium cells adhesion and proliferation, roughened topographies should

TABLE 1: One-way ANOVA statistical analysis of the control group (0 sec) and test groups using 30 sec of acid etching after 10, 30, and 60 sec of sandblasting for samples from bone E1, fibroblast 3T3, and an epidermal cell XB-2 cells after 1 and 24 h ($n = 5$).

Statistical analysis*	Variations	(a)								
		0 ^b			Time of sandblasting (sec)			60		
		Groups	Cells	P value	Group comparisons ^a	P value	Groups	Group comparisons	P value	Group comparisons
1 h cell adhesion	3T3/E1/XB-2	0.0161	XB-2 > E1	0.0077	3T3 > E1 XB-2 > E1	0.0013	XB-2 > E1 XB-2 > 3T3	<0.0001	3T3 > E1 3T3 > XB-2 XB-2 > E1	
24 h cell proliferation	3T3/E1/XB-2	0.0705	none	0.0026	3T3 > E1 XB-2 > E1	0.0231	XB-2 > E1	<0.0001	3T3 > E1 3T3 > XB-2 XB-2 > E1	

Statistical analysis*	Variations	(b)								
		E1 bone cell			3T3 fibroblast cell			XB-2 epidermal cell		
		Groups	0 sec ^b and through 30 sec etching after 10, 30, and 60 sec blasting	P value	Group comparisons ^a	P value	Group comparisons ^a	P value	Group comparisons ^a	
1 h cell adhesion	0/10/30/60			0.0025	30 > 0, 10, 60	0.0026	10 > 30 60 > 10	0.0005	0 > 10, 30, 60 10 > 60	
24 h cell proliferation	0/10/30/60			0.0510	none	0.0791	none	0.2788	none	

* Groups significantly differ at $P < 0.05$; ^a“none” indicates the group comparisons are not significantly different at $P > 0.05$; ^b“0 sec” indicates the control group without the blasting/etching treatment.

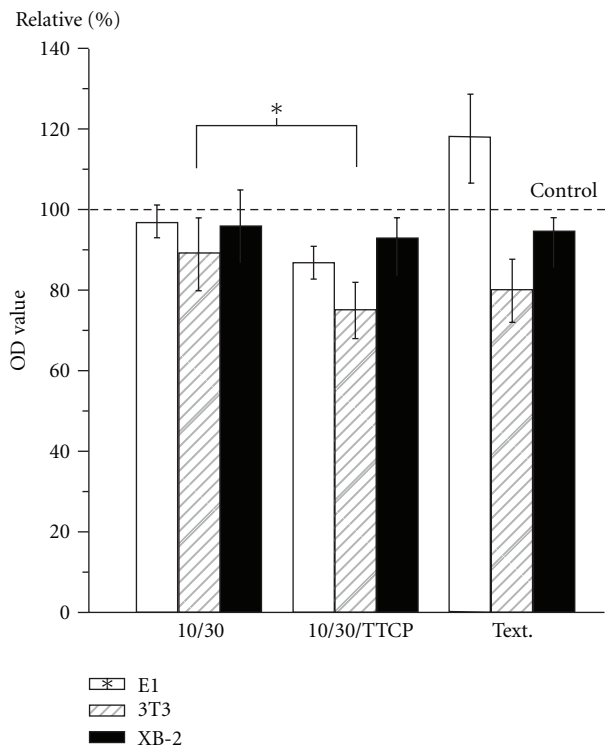


FIGURE 6: A diagram indicating the OD values after 24 h cell proliferations of the test groups: SLA 10/30, 10/30/TTCP and TTCP extraction cells culture medium (Text.) (*: a statistically significant difference in the group comparisons, $P < 0.05$).

be recommended, as they can increase linking and inhibit the risk of fibrous encapsulation by connective tissues.

The ion effects are demonstrated in Figure 6. The early stage cell proliferative ability in the extracted cultured medium was significantly increased ($P < 0.05$) in E1 cells but decreased in 3T3 cells. However, when the ionic effect was combined with the effect of topography in the comparative SLA 10/30/TTCP group, the proliferative ability of E1 cells was shown to be significant lower ($P < 0.05$) than in the SLA 10/30 group. The calcium and phosphate ions became incorporated into the apatite that formed in an intimate association with the organic component, leading to bone formation [31, 32]. Figure 6 showed the promoted E1 bone cell growth was largely due to the topography rather than the ions. The ion effect played a less important role than the roughness with respect to E1 cell proliferation. The existence of calcium phosphates in a thin film coating can play a mediatory role between implants and natural bone tissues, but such properties did not lead to clinical success [33, 34]. Rough surfaces enhanced the ability to act as essential factors for bone cell adhesion and proliferation. The contacting surfaces between implants and the soft tissues should be roughened and ions releasing from TTCP hydrolysis should also be commented. This study clearly confirms the hypothesis that roughness and ion effects would impact the initial implant stability by the early stage cell interactions. The results had demonstrated that TTCP as the ions releasing medium could be a potential application in bone regeneration and prevention of the fibrous encapsulation of implants.

5. Conclusions

Techniques necessary to harmonize the early stage adhesion and proliferation of osteoblasts and epithelial cells on the implant are important. The optimal implant can be designed with a smooth surface in the top area of implant, which is closer to the gingival surface, to promote rapid epithelial cell adhesion that could lead to prevent inflammation after implantation. A rougher surface anchored with TTCP can replace Al_2O_3 particles in the sandblasting process and provide soluble ions to enhance the early stage proliferation of osteoblast cells. Such results suggest that an active surface can be prepared to achieve appropriate implant biological widths. In summary, we emphasize a concept whereby an implant actively regulates cells rather than undergoing a passive healing process, at the same time eliminating the dangers of fibrous encapsulation at an early implant stage.

Acknowledgments

Financial support was received via Grants from Kaohsiung Medical University Research Foundation and Taiwan and Kaohsiung Medical Device Special Zone in Southern Taiwan Science Park, under Contracts Q098001 and CZ-02-07-22-98, respectively. This financial support is greatly appreciated. W.-C. Chen contributed equally to this work as first authors.

References

- [1] K. Kieswetter, Z. Schwartz, D. D. Dean, and B. D. Boyan, "The role of implant surface characteristics in the healing of bone," *Critical Reviews in Oral Biology and Medicine*, vol. 7, no. 4, pp. 329–345, 1996.
- [2] H. P. Weber and D. L. Cochran, "The soft tissue response to osseointegrated dental implants," *Journal of Prosthetic Dentistry*, vol. 79, no. 1, pp. 79–89, 1998.
- [3] R. Glauser, P. Schupbach, J. Gottlow, and C. H. F. Hammerle, "Soft Tissue Integration of a TiUnite implant. The image shows junctional epithelium at the implant surface and a shallow sulcus lined by sulcular epithelium," *Clinical Implant Dentistry and Related Research*, vol. 7, supplement 1, pp. 44–51, 2005.
- [4] I. Abrahamsson, T. Berglundh, J. Wennström, and J. Lindhe, "The peri-implant hard and soft tissues at different implant systems: a comparative study in the dog," *Clinical Oral Implants Research*, vol. 7, no. 3, pp. 212–219, 1996.
- [5] I. Abrahamsson, T. Berglundh, P. O. Glantz, and J. Lindhe, "The mucosal attachment at different abutments: an experimental study in dogs," *Journal of Clinical Periodontology*, vol. 25, no. 9, pp. 721–727, 1998.
- [6] D. C. Smith, "Dental implants: materials and design considerations," *The International Journal of Prosthodontics*, vol. 6, no. 2, pp. 106–117, 1993.
- [7] L. Le Guehenneuc, A. Soueidan, P. Layrolle, and Y. Amouriq, "Surface treatments of titanium dental implants for rapid osseointegration," *Dental Materials*, vol. 23, no. 7, pp. 844–854, 2007.
- [8] A. B. Novaes, V. Papalexiou Jr., M. F. Grisi, S. S. Souza, M. Taba, and J. K. Kajiwara, "Influence of implant microstructure on the osseointegration of immediate implants placed in periodontally infected sites: a histomorphometric study in dogs," *Clinical Oral Implants Research*, vol. 15, no. 1, pp. 34–43, 2004.
- [9] C. M. Stanford, "Surface modification of biomedical and dental implants and the processes of inflammation, wound healing and bone formation," *International Journal of Molecular Sciences*, vol. 11, no. 1, pp. 354–369, 2010.
- [10] D. L. Cochran, R. K. Schenk, A. Lussi, F. L. Higginbottom, and D. Buser, "Bone response to unloaded and loaded titanium implants with a sandblasted and acid-etched surface: a histometric study in the canine mandible," *Journal of Biomedical Materials Research*, vol. 40, no. 1, pp. 1–11, 1998.
- [11] M. Browne and P. J. Gregson, "Effect of mechanical surface pretreatment on metal ion release," *Biomaterials*, vol. 21, no. 4, pp. 385–392, 2000.
- [12] C. Aparicio, F. Javier Gil, C. Fonseca, M. Barbosa, and J. A. Planell, "Corrosion behaviour of commercially pure titanium shot blasted with different materials and sizes of shot particles for dental implant applications," *Biomaterials*, vol. 24, no. 2, pp. 263–273, 2003.
- [13] S. Szumukler-Moncler, D. Perrin, V. Ahossi, G. Magnin, and J. P. Bernard, "Biological properties of acid etched titanium implants: effect of sandblasting on bone anchorage," *Journal of Biomedical Materials Research: Part B*, vol. 68, no. 2, pp. 149–159, 2004.
- [14] M. A. Listgarten, "Soft and hard tissue response to endosseous dental implants," *Anatomical Record*, vol. 245, no. 2, pp. 410–425, 1996.
- [15] C. Blaschke and U. Volz, "Soft and hard tissue response to zirconium dioxide dental implants—a clinical study in man," *Neuroendocrinology Letters*, vol. 27, supplement 1, pp. 69–72, 2006.
- [16] D. W. Hamilton, B. Chehroudi, and D. M. Brunette, "Comparative response of epithelial cells and osteoblasts to micro-fabricated tapered pit topographies in vitro and in vivo," *Biomaterials*, vol. 28, no. 14, pp. 2281–2293, 2007.
- [17] N. Eidelman, L. C. Chow, and W. E. Brown, "Calcium phosphate phase transformations in serum," *Calcified Tissue International*, vol. 41, no. 1, pp. 18–26, 1987.
- [18] K. L. Blacker, M. L. Williams, and M. Goldyne, "Mitomycin C-treated 3T3 fibroblasts used as feeder layers for human keratinocyte culture retain the capacity to generate eicosanoids," *Journal of Investigative Dermatology*, vol. 89, no. 6, pp. 536–539, 1987.
- [19] M. Di Carmine, P. Toto, C. Feliciani et al., "Spreading of epithelial cells on machined and sandblasted titanium surfaces: an in vitro study," *Journal of Periodontology*, vol. 74, no. 3, pp. 289–295, 2003.
- [20] Y. S. Chang, M. Oka, M. Kobayashi et al., "Significance of interstitial bone ingrowth under load-bearing conditions: a comparison between solid and porous implant materials," *Biomaterials*, vol. 17, no. 11, pp. 1141–1148, 1996.
- [21] A. Ignatius, M. Peraus, S. Schorlemmer et al., "Osseointegration of alumina with a bioactive coating under load-bearing and unloaded conditions," *Biomaterials*, vol. 26, no. 15, pp. 2325–2332, 2005.
- [22] W. C. Chen, C. P. Ju, Y. C. Tien, and J. H. C. Lin, "In vivo testing of nanoparticle-treated TTCP/DCPA-based ceramic surfaces," *Acta Biomaterialia*, vol. 5, no. 5, pp. 1767–1774, 2009.
- [23] F. Rupp, L. Scheideier, N. Olshanska, M. de Wild, M. Wieland, and J. Geis-Gerstorfer, "Enhancing surface free energy and hydrophilicity through chemical modification of microstructured titanium implant surfaces," *Journal of*

- Biomedical Materials Research: Part A*, vol. 76, no. 2, pp. 323–334, 2006.
- [24] D. M. Brunette, “Fibroblasts on micromachined substrata orient hierarchically to grooves of different dimensions,” *Experimental Cell Research*, vol. 164, no. 1, pp. 11–26, 1986.
 - [25] D. M. Brunette, “In vitro models of biological responses to implants,” *Advances in Dental Research*, vol. 13, pp. 35–37, 1999.
 - [26] S. A. Biela, Y. Su, J. P. Spatz, and R. Kemkemer, “Different sensitivity of human endothelial cells, smooth muscle cells and fibroblasts to topography in the nano-micro range,” *Acta Biomaterialia*, vol. 5, no. 7, pp. 2460–2466, 2009.
 - [27] M. M. Stevens and J. H. George, “Exploring and engineering the cell surface interface,” *Science*, vol. 310, no. 5751, pp. 1135–1138, 2005.
 - [28] L. C. Chow, M. Markovic, S. A. Frukhtbeyn, and S. Takagi, “Hydrolysis of tetracalcium phosphate under a near-constant-composition condition—effects of pH and particle size,” *Biomaterials*, vol. 26, no. 4, pp. 5393–5401, 2005.
 - [29] Y. Oshida, E. B. Tuna, O. Aktören, and K. Gençay, “Dental implant systems,” *International Journal of Molecular Sciences*, vol. 11, no. 4, pp. 1580–1678, 2010.
 - [30] R. M. Wazen, L. P. Lefebvre, E. Baril, and A. Nanci, “Initial evaluation of bone ingrowth into a novel porous titanium coating,” *Journal of Biomedical Materials Research*, vol. 94, no. 1, pp. 64–71, 2010.
 - [31] L. Fassina, E. Saino, M. G. Cusella De Angelis, G. Magenes, F. Benazzo, and L. Visai, “Low-power ultrasounds as a tool to culture human osteoblasts inside cancellous hydroxyapatite,” *Bioinorganic Chemistry and Applications*, vol. 2010, Article ID 456240, 2010.
 - [32] S. Raynaud, E. Champion, D. Bernache-Assollant, and P. Thomas, “Calcium phosphate apatites with variable Ca/P atomic ratio I. Synthesis, characterisation and thermal stability of powders,” *Biomaterials*, vol. 23, no. 4, pp. 1065–1072, 2002.
 - [33] J. E. Davies, “Understanding peri-implant endosseous healing,” *Journal of Dental Education*, vol. 67, no. 8, pp. 932–949, 2003.
 - [34] J. E. Ellingsen, P. Thomsen, and S. P. Lyngstadaas, “Advances in dental implant materials and tissue regeneration,” *Periodontology*, vol. 41, no. 1, pp. 136–156, 2000.

Synthesis, Characterization and *In Vitro* Antibacterial Studies of Organotin(IV) Complexes with 2-Hydroxyacetophenone-2-methylphenylthiosemicarbazone ($H_2\text{dampt}$)

M. A. Salam,¹ M. A. Affan,¹ Ramkrishna Saha,² Fasihuddin B. Ahmad,¹ and Norrihan Sam¹

¹Faculty of Resource Science and Technology, Universiti Malaysia Sarawak, 94300 Kota Samarahan, Sarawak, Malaysia

²Department of Chemistry, Shahjalal University of Science and Technology, Sylhet 3114, Bangladesh

Correspondence should be addressed to M. A. Salam, salambpx@yahoo.com

Academic Editor: Virtudes Moreno

Five new organotin(IV) complexes of 2-hydroxyacetophenone-2-methylphenylthiosemicarbazone [$H_2\text{dampt}$, (1)] with formula $[\text{RSnCl}_{n-1}(\text{dampt})]$ (where R = Me, n = 2 (2); R = Bu, n = 2 (3); R = Ph, n = 2 (4); R = Me₂, n = 1 (5); R = Ph₂, n = 1 (6)) have been synthesized by direct reaction of $H_2\text{dampt}$ (1) with organotin(IV) chloride(s) in absolute methanol. The ligand (1) and its organotin(IV) complexes (2–6) were characterized by CHN analyses, molar conductivity, UV-Vis, FT-IR, ¹H, ¹³C, and ¹¹⁹Sn NMR spectral studies. $H_2\text{dampt}$ (1) is newly synthesized and has been structurally characterized by X-ray crystallography. Spectroscopic data suggested that $H_2\text{dampt}$ (1) is coordinated to the tin(IV) atom through the thiolate-S, azomethine-N, and phenoxide-O atoms; the coordination number of tin is five. The *in vitro* antibacterial activity has been evaluated against *Staphylococcus aureus*, *Enterobacter aerogenes*, *Escherichia coli*, and *Salmonella typhi*. The screening results have shown that the organotin(IV) complexes (2–6) have better antibacterial activities and have potential as drugs. Furthermore, it has been shown that diphenyltin(IV) derivative (6) exhibits significantly better activity than the other organotin(IV) derivatives (2–5).

1. Introduction

Thiosemicarbazones and their metal complexes have received considerable attention in chemistry and biology, primarily because of their marked and various biological properties [1–3]. The pharmacological profiles of 2-formyl, 2-acetyl, and 2-benzoylpyridine thiosemicarbazones have been investigated [4]. Seena and Kurup [5] have synthesized and characterized dioxomolybdenum(IV) complexes with 2-hydroxyacetophenone-*N*(4)-cyclohexyl and *N*(4)-phenyl thiosemicarbazone which suggested that the Mo(IV) complex is pentacoordinated [5]. For the past few years, studies of the coordination chemistry of thiosemicarbazone involved complexes with transition metal ions [6–8]. Organotin(IV) complexes have been the subject of interest for some time because of their biomedical and commercial applications including *in vitro* and *in vivo* antitumor activity

[9, 10]. Many organotin(IV) complexes have been found to be as effective as or even better than traditional anticancer drugs [11–14]. Organotin(IV) chelates with nitrogen, sulfur, and oxygen donor ligands have gained attention during the last few years [15]. The coordination chemistry of tin is extensive with various geometries and coordination numbers known for both inorganic and organometallic complexes [16, 17]. In our previous work, we have reported some new organotin(IV) complexes with heterocyclic-*N*(4)-cyclohexylthiosemicarbazone ligands [18, 19]. The results revealed that thiosemicarbazones derived from 2-benzoylpyridine and 2-acetylpyrazine and their tin (IV)/organotin(IV) complexes have been characterized by different spectroscopic techniques. From the literature survey, the studies on the organotin(IV) complexes derived from substituted thiosemicarbazone ligands containing ONS-donor atoms are still lacking.

To the best of our knowledge, there was no report on the organotin(IV) complexes of the 2-hydroxyacetophenone-2-methylphenylthiosemicarbazone. In this view, we have synthesized a series of organotin(IV) complexes with 2-hydroxyacetophenone-2-methylphenylthiosemicarbazone. These complexes have been characterized by elemental analysis, ^1H , ^{13}C , and ^{119}Sn NMR spectroscopy. X-ray crystal structure of 2-hydroxyacetophenone-2-methylphenylthiosemicarbazone (**1**) is also described. Their biological activity data has also been reported.

2. Experimental

2.1. Materials and Methods. All reagents were purchased from Fluka, Aldrich, and JT Baker. All solvents were purified according to standard procedures [20]. UV-Vis spectra were recorded in CHCl_3 solution with a Perkin Elmer Lambda 25 UV-Visible spectrometer. Infrared spectra were recorded on KBr discs using a Perkin Elmer Spectrum GX Fourier-Transform spectrometer in the range $4000\text{--}370\text{ cm}^{-1}$ at room temperature. ^1H , ^{13}C , and ^{119}Sn NMR spectra were recorded on a JEOL 500 MHz-NMR spectrometer; chemical shifts were given in ppm relative to SiMe_4 and SnMe_4 in CDCl_3 solvent. CHN analyses were obtained with a Flash EA 1112 series CHN elemental analyzer. Molar conductivity measurements were carried out with Jenway 4510 conductivity meter using DMF solvent mode.

2.2. Synthesis of 2-Hydroxyacetophenone-2-Methylphenylthiosemicarbazone ($H_2\text{dampt}$) (1**).** The 2-methylphenylisothiocyanate (0.746 g, 5 mmol) and hydrazine hydrate (0.253 g, 5 mmol), each dissolved in 10 mL ethanol, were mixed with constant stirring. The stirring was continued for 30 min and the white product, 2-methylphenylthiosemicarbazide, formed was washed with ethanol and dried *in vacuo*. A solution of the isolated 2-methylphenylthiosemicarbazide (0.540 g, 3 mmol) in 10 mL methanol was then refluxed with a methanolic solution of 2-hydroxyacetophenone (0.408 g, 3 mmol) for 5 h after adding 1-2 drops of glacial acetic acid (Scheme 1). On cooling the solution to room temperature, light-yellow microcrystals were separated and washed with methanol. The microcrystals were recrystallized from methanol and dried *in vacuo* over silica gel. Yield: 0.74 g, 78%; M.p.: 178–180°C; UV-Visible (CHCl_3) $\lambda_{\text{max/nm}}$: 226, 318, 359; FT-IR (KBr disc, cm^{-1}) ν_{max} : 3175 (s, OH), 3000 (s, NH), 1583 (m, C=N), 1298 (m, C=O), 943 (m, N=N), 1371, 861 (w, C=S). ^1H NMR (CDCl_3) δ : 10.82 (s, 1H, OH), 9.02 (s, 1H, N-H), 7.31–7.25 (m, 8H, phenyl ring), 2.56 (s, 3H, N=C-CH₃), 2.29 (s, 3H, CH₃), 1.19 (s, 1H, SH). ^{13}C NMR (CDCl_3) δ : 185.20 (NH-C=S), 165.32 (C=N), 145.30–136.21 (aromatic ring), 10.45 (CH₃). Anal. Calc. for $\text{C}_{16}\text{H}_{17}\text{N}_3\text{OS}$: C, 64.21; H, 5.73; N, 14.04%. Found: C, 64.17; H, 5.67; N, 14.01%.

2.3. Synthesis of [Me₂SnCl(dampt)] (2**).** $H_2\text{dampt}$ (0.299 g, 1.0 mmol) was dissolved in absolute methanol (10 mL) in a Schlenk round bottom flask under a nitrogen atmosphere. Then, a methanolic solution of methyltin(IV) trichloride

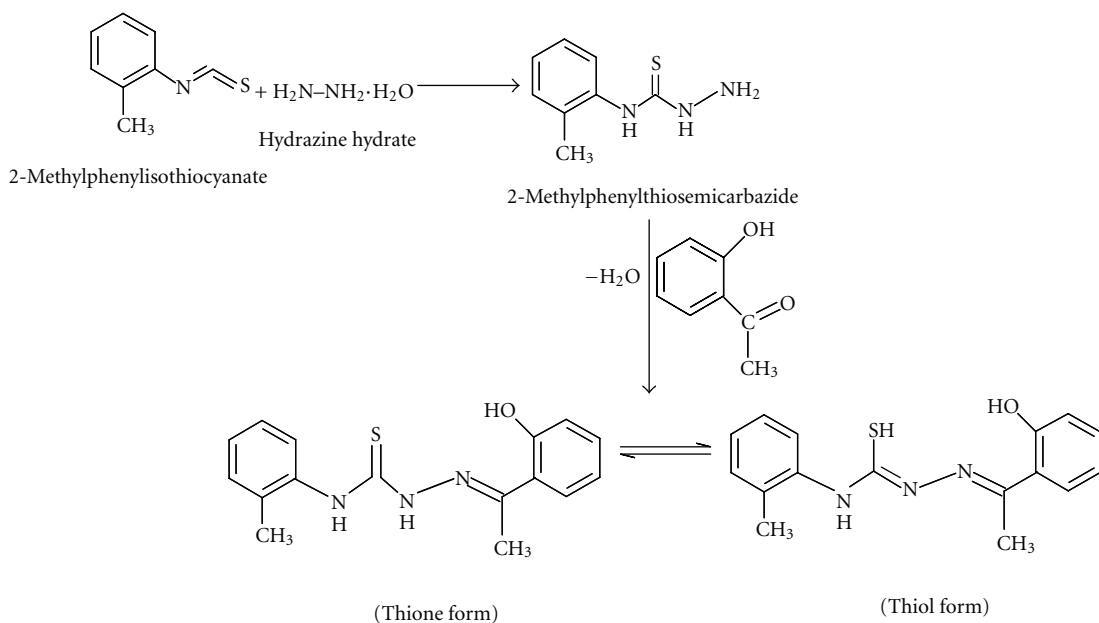
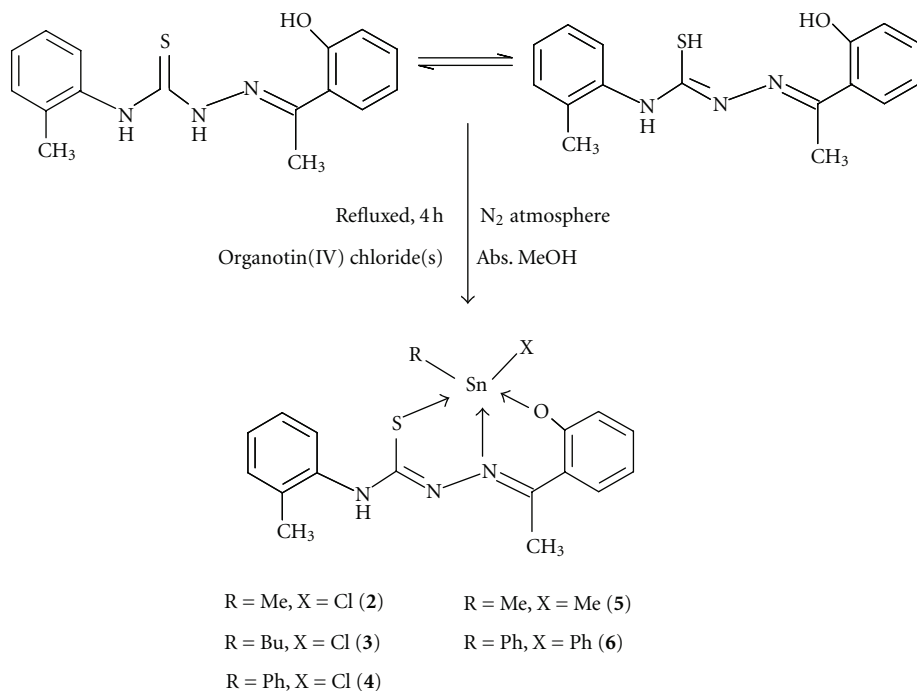
(0.24 g, 1.0 mmol) was added dropwise. The resulting reaction mixture was refluxed for 4 h (Scheme 2) and cooled to room temperature. The microcrystals were filtered off, washed with a small amount of cold methanol, and dried *in vacuo* over silica gel. Yield: 0.41 g, 76%; Mp.: 222–224°C; Molar conductance (DMF) $\Omega^{-1}\text{ cm}^2\text{ mol}^{-1}$: 7.1; UV-Visible (CHCl_3) $\lambda_{\text{max/nm}}$: 262, 328, 367, 384; FT-IR (KBr, cm^{-1}) ν_{max} : 3378 (s, NH), 1595 (m, C=N-N=C), 1268 (m, C=O), 1026 (w, N-N), 1306, 822 (m, C-S), 612 (w, Sn-C), 570 (w, Sn-O), 449 (w, Sn-N). ^1H NMR (CDCl_3 , $^2\text{J}[^{119}\text{Sn}, ^1\text{H}]$) δ : 9.08 (s, 1H, N-H), 7.26–6.94 (m, 8H, phenyl ring), 2.95 (s, 3H, N=C-CH₃), 2.30 (s, 3H, CH₃), 1.09 (s, 3H, Sn-CH₃), [74.4 Hz]. ^{13}C NMR (CDCl_3) δ : 180.55 (N=C-S), 170.88 (C=N), 144.35–135.60 (aromatic ring), 18.70 (CH₃), 12.80 (Sn-CH₃). ^{119}Sn NMR (CDCl_3) δ : -168.5. Anal. Calc. for $\text{C}_{17}\text{H}_{18}\text{N}_3\text{SOSnCl}$: C, 43.76; H, 3.88; N, 9.00%. Found: C, 43.71; H, 3.82; N, 8.95%.

The other complexes (**3–6**) were synthesized using a similar procedure to organotin(IV) complex (**2**) using appropriate organotin(IV) chloride(s) (Scheme 2).

2.4. Synthesis of [Bu₂SnCl(dampt)] (3**).** Yield: 0.43 g, 74%; Mp.: 226–228°C; Molar conductance (DMF) $\Omega^{-1}\text{ cm}^2\text{ mol}^{-1}$: 9.1; UV-Visible (CHCl_3) $\lambda_{\text{max/nm}}$: 262, 328, 382, 397; FT-IR (KBr, cm^{-1}) ν_{max} : 3374 (s, NH), 1599 (m, C=N-N=C), 1254 (m, C=O), 1014 (w, N-N), 1299, 835 (m, C-S), 605 (w, Sn-C), 568 (w, Sn-O), 443 (w, Sn-N). ^1H NMR (CDCl_3) δ : 9.07 (s, 1H, N-H), 7.25–7.97 (m, 8H, phenyl ring), 2.62 (s, 3H, N=C-CH₃), 2.30 (s, 3H, CH₃), 2.28–2.15 (t, 2H, Sn-CH₂-CH₂-CH₂-CH₃), 2.14–1.73 (m, 2H, Sn-CH₂-CH₂-CH₂-CH₃), 1.24–1.22 (m, 2H, Sn-CH₂-CH₂-CH₂-CH₃), 0.99–0.86 (t, 3H, Sn-CH₂-CH₂-CH₂-CH₃). ^{13}C NMR (CDCl_3) δ : 178.99 (N=C-S), 168.36 (C=N), 145.20–136.22 (aromatic ring), 32.78, 26.31, 24.18, 20.11 (Sn-CH₂-CH₂-CH₂-CH₃), 16.44 (CH₃). ^{119}Sn NMR (CDCl_3) δ : -149.6. Anal. Calc. for $\text{C}_{20}\text{H}_{24}\text{N}_3\text{SOSnCl}$: C, 45.10; H, 4.54; N, 7.88%. Found: C, 45.00; H, 4.51; N, 7.81%.

2.5. Synthesis of [Ph₂SnCl(dampt)] (4**).** Yield: 0.48 g, 79%; Mp.: 218–220°C; Molar conductance (DMF) $\Omega^{-1}\text{ cm}^2\text{ mol}^{-1}$: 3.11; UV-Visible (CHCl_3) $\lambda_{\text{max/nm}}$: 263, 335, 381, 410; FT-IR (KBr, cm^{-1}) ν_{max} : 3184 (s, NH), 1598 (m, C=N-N=C), 1240 (m, C=O), 1035 (w, N-N), 1300, 838 (m, C-S), 601 (w, Sn-C), 522 (w, Sn-O), 471 (w, Sn-N). ^1H NMR (CDCl_3) δ : 9.01 (s, 1H, N-H), 7.24–6.95 (m, 13H, phenyl ring), 2.76 (s, 3H, N=C-CH₃), 2.29 (s, 3H, CH₃). ^{13}C NMR (CDCl_3) δ : 180.12 (N=C-S), 173.97 (C=N), 144.84–136.60 (aromatic ring), 16.88 (CH₃). ^{119}Sn NMR (CDCl_3) δ : -174.73. Anal. Calc. for $\text{C}_{22}\text{H}_{20}\text{N}_3\text{SOSnCl}$: C, 49.98; H, 3.81; N, 7.94%. Found: C, 48.92; H, 3.77; N, 7.90%.

2.6. Synthesis of [Me₂Sn(dampt)] (5**).** Yield: 0.41 g, 78%; Mp.: 210–212°C; Molar conductance (DMF) $\Omega^{-1}\text{ cm}^2\text{ mol}^{-1}$: 5.2; UV-Visible (CHCl_3) $\lambda_{\text{max/nm}}$: 266, 338, 378, 414; FT-IR (KBr, cm^{-1}) ν_{max} : 3320 (s, NH), 1605 (m, C=N-N=C), 1252 (m, C=O), 1036 (w, N-N), 1300, 832 (m, C-S), 603 (w, Sn-C), 523 (w, Sn-O), 499 (w, Sn-N). ^1H NMR (CDCl_3 , $^2\text{J}[^{119}\text{Sn}, ^1\text{H}]$) δ : 9.08 (s, 1H, N-H), 7.26–6.94 (m,

SCHEME 1: Synthesis of 2-hydroxyacetophenone-2-methylphenylthiosemicarbazone ($H_2\text{dampt}$) ligand (1).

SCHEME 2: Reaction scheme for the synthesis of organotin(IV) complexes (2–6).

8H, phenyl ring), 2.98 (s, 3H, N=C–CH₃), 2.30 (s, 3H, CH₃), 0.98 (s, 3H, Sn–CH₃), [77.5 Hz]. ¹³C NMR (CDCl₃, [¹J (¹³C–¹¹⁹Sn)]) δ: 181.10 (N=C–S), 178.45 (C=N), 145.68–137.20 (aromatic ring), 17.5 (CH₃), 14.97 (Sn–CH₃) [557 Hz]. ¹¹⁹Sn NMR (CDCl₃) δ: –182.45. Anal. Calc. for C₁₈H₂₁N₃SOSn: C, 48.54; H, 4.74; N, 9.41%. Found: C, 48.50; H, 4.71 N, 9.38%.

2.7. Synthesis of [Ph₂Sn(dampt)] (6). Yield: 0.48 g, 75%; Mp.: 258–260°C; Molar conductance (DMF) $\Omega^{-1} \text{cm}^2 \text{ mol}^{-1}$: 8.17; UV-Visible (CHCl₃) λ_{max} /nm: 268, 327, 373, 402; FT-IR (KBr, cm^{–1}) ν_{max} : 3383 (s, NH), 1592 (m, C=N–N=C), 1265 (m, C=O), 1039 (w, N–N), 1307, 821 (m, C=S), 601 (w, Sn–C), 570 (w, Sn–O), 448 (w, Sn–N). ¹H NMR (CDCl₃) δ: 9.02

(*s*, 1H, N–H), 7.30–6.97 (*m*, 13H, phenyl ring), 2.67 (*s*, 3H, N=C–CH₃), 2.29 (*s*, 3H, CH₃). ¹³C NMR (CDCl₃, [¹J (¹³C–¹¹⁹Sn]) δ : 179.98 (N=C–S), 171.75 (C=N), 142.20–138.21 (aromatic ring), 15.88 (CH₃) [546 Hz]. ¹¹⁹Sn NMR (CDCl₃) δ : –185.32. Anal. Calc. for C₂₈H₂₅N₃SOSn: C, 58.97; H, 4.41; N, 7.36%. Found: C, 58.92; H, 4.38; N, 7.30%.

2.8. Antibacterial Test. The synthesized ligand (**1**) and its organotin(IV) complexes (**2–6**) were screened *in vitro* for their antibacterial activity against *Staphylococcus aureus*, *Enterobacter aerogenes*, *Escherichia coli*, and *Salmonella typhi* bacterial strains using agar-well diffusion method [21]. Wells (size of well 6 mm in diameter) were dug in the media with the help of a sterile metallic borer with centers at least 24 mm. Eight-hour old bacterial inoculums containing 10⁴–10⁶ colony-forming units (CFU)/mL were spread on the surface of the nutrient agar using a sterile cotton swab. Recommended concentration of the test sample (200 mg/mL in DMSO) was introduced in the respective wells. Other wells supplemented with DMSO and reference drug (doxycycline) served as negative and positive controls, respectively. The plates were incubated immediately at 37°C for 20 h. Activity was determined by measuring the diameter of zones showing complete inhibition (mm). Growth inhibition was calculated with reference to the positive control.

3. Results and Discussion

3.1. Synthesis. 2-Hydroxyacetophenone-2-methylphenylthiosemicarbazone ($H_2\text{dampt}$) was synthesized by the condensation reaction of 2-hydroxyacetophenone and 2-methylphenylthiosemicarbazide in absolute methanol in 1:1 mole ratio. It has two tautomers within the structure, existing as either thione or thiol tautomer (Scheme 1). The present organotin(IV) complexes (**2–6**) were obtained by direct reaction of organotin(IV) chloride(s) and $H_2\text{dampt}$ (**1**) in absolute methanol under N₂ atmosphere (Scheme 2). The physical properties and analytical data of $H_2\text{dampt}$ (**1**) and its organotin(IV) complexes (**2–6**) are given in the experimental section. All complexes (**2–6**) were stable under N₂ atmosphere and soluble in CHCl₃, CH₂Cl₂, DMF, DMSO, and MeCN solvents except methanol, ethanol, hexane, pentane, THF, and ether. The molar conductances values of the complexes (**2–6**) are 9.1–3.1 Ω^{–1} cm² mol^{–1}, respectively, indicate that the complexes behave as nonelectrolytes [22].

3.2. UV-Visible Spectra. The UV-Vis spectra of ligand (**1**) and its organotin(IV) complexes (**2–6**) were carried out in CHCl₃ (1×10^{-4} mol L^{–1}) at room temperature. The free ligand (**1**) exhibited three absorption bands at 262, 318, and 359 nm assigned to the HOMO/LUMO transition of phenolic group, azomethine, and thiolate function, respectively [23]. After complexation, the UV-Vis spectra of the complexes (**2–6**) exhibited four absorption bands in the region at 262–268, 327–338, 367–382, and 384–414 nm, respectively. In the electronic spectra of the complexes (**2–6**), the intraligand transition is shifted to higher wavelength as a result of coordination. In the spectra of organotin(IV)

complexes (**2–6**), one new absorption band appeared at 384–414 nm which is assigned to the ligand → metal charge transfer (LMCT) [24]. The shift of the λ_{\max} band from the ligand to the complex is supported by the coordination of ligand (**1**) to the tin(IV) ion.

3.3. IR Spectra. The IR spectrum of free ligand (**1**) showed absorption bands at 3175 and 3000 cm^{–1}, which are due to the stretching vibrations of the OH and NH groups, respectively. The absorption bands at 1583, 1298, 943, and 1371, 861 cm^{–1} are due to ν (C=N), ν (C–O), ν (N–N), and ν (C=S), respectively. Several significant changes with respect to the free ligand (**1**) bands on complexation suggest coordination through phenolic group, azomethine, and sulfur of the thiolic form of the ligand. The strong stretching band at 3375 cm^{–1} that corresponds to the ν (OH) group in the spectrum of ligand (**1**) has disappeared in the spectra of complexes (**2–6**) due to the deprotonation, indicating coordination through the phenolic oxygen to tin(IV) atom. The free ligand (**1**) showed a band at 1298 cm^{–1} which is due to ν (C–O). This band is shifted to lower wave numbers at 1240–1268 cm^{–1} in the complexes (**2–6**), indicating the coordination of O[–] to the tin(IV) atom [25]. The newly formed ν (C=N–N=C) bond showed medium-to-strong absorption peaks in the range at 1592–1605 cm^{–1} in the spectra of the complexes (**2–6**), indicating coordination of azomethine nitrogen to tin(IV) atom [26]. A sharp band at 943 cm^{–1} is due to ν (N–N) for ligand (**1**) is shifted to higher frequencies at 1014–1039 cm^{–1} in the spectra of organotin(IV) complexes ((**2–6**). The increase in the frequency of this band in the spectra of complexes (**2–6**) due to an increase in the bond length again confirms coordination *via* the azomethine nitrogen atom [27]. The bands at 1371 and 861 cm^{–1} in the free ligand (**1**) due to ν (C=S) stretching vibrations are shifted to lower frequencies at 1299–1307 cm^{–1} and 821–838 cm^{–1} in the spectra of the complexes (**2–6**), suggesting coordination through the thiolate sulfur with tin(IV) atom [28]. The IR bands observed in the range at 570–522 cm^{–1} in the spectra of the complexes (**2–6**) suggest the presence of Sn–O bonding in their structure. The ν (Sn–C) and ν (Sn–N) bands are tentatively assigned to absorptions in the regions 612–601 cm^{–1} and 443–499 cm^{–1}, respectively. Based on the infrared spectra analyses of ligand (**1**) and its organotin(IV) complexes (**2–6**), it was suggested that ligand (**1**) was coordinated to the tin(IV) core through the phenoxide-O, azomethine-N, and thiolato-S atoms.

3.4. ¹H NMR Spectra. ¹H NMR spectrum of free ligand (**1**) showed resonance signals at 10.82, 9.02, 7.31–7.25, 2.56, 2.29, and 1.19 ppm are due to OH, NH, phenyl ring protons, N=C–CH₃, CH₃, and SH, respectively. After complexation, the resonance signal of OH proton was absent in the spectra of the complexes (**2–6**), indicating deprotonation of the phenolic proton and supported the phenolic oxygen atom was coordinated with tin(IV) atom. The resonance signal of SH is not found in the spectra of complexes (**2–6**) which suggested the deprotonation of the SH proton and confirming that the ligand coordinated to the tin(IV) in the

thiolate form. The azomethine proton ($\text{N}=\text{C}-\text{CH}_3$) signal appears at 2.56 ppm in the free ligand (**1**) which is shifted to high frequency at 2.98–2.62 ppm in the complexes (**2–6**), supporting the coordination of azomethine nitrogen to the central tin(IV) atom. The resonance signals for the protons of phenyl moiety of the ligand (**1**) were observed at 7.31–7.25 ppm, which is shifted to low frequency at 7.30–6.94 ppm in the complexes (**2–6**). This is due to the electron withdrawal tendency from the aromatic ring owing to coordination with tin(IV). The methyl group attached to the tin(IV) in complexes **2** and **5** gave a singlet at 1.09 and 0.98 ppm with $^2J[\text{Sn}^{119}, \text{H}]$ coupling constant value equal to 74.4 and 77.5 Hz, respectively, supporting the five-coordinate environment around tin(IV) [29]. The three butyl groups attached to the tin(IV) moiety in the organotin(IV) complex **3** gave four resonance signals, namely, 2.28–2.15 ppm (triplet, $\text{Sn}-\text{CH}_2-\text{CH}_2-\text{CH}_2-\text{CH}_3$), 2.14–1.73 ppm (multiplet, $\text{Sn}-\text{CH}_2-\text{CH}_2-\text{CH}_2-\text{CH}_3$), 1.24–1.22 ppm (multiplet, $\text{Sn}-\text{CH}_2-\text{CH}_2-\text{CH}_2-\text{CH}_3$), and 0.99–0.86 ppm (triplet, $\text{Sn}-\text{CH}_2-\text{CH}_2-\text{CH}_2-\text{CH}_3$). ^1H NMR information also supported the IR data of the complexes (**2–6**).

3.5. ^{13}C NMR Spectra. The ^{13}C -{ ^1H } NMR spectrum of free ligand (**1**) showed the resonance signals at 185.20, 165.32, 145.30–136.21, and 10.45 ppm are due to the $\delta(\text{NH}-\text{C}=\text{S})$, $\delta(\text{C}=\text{N})$, δ (aromatic ring carbon) and $\delta(\text{CH}_3)$, respectively. After complexation, the carbon signals of the $\text{N}=\text{C}-\text{S}$ group shifted to low frequency at 179.99–181.10 ppm in all the complexes (**2–6**) compared to ligand (**1**), indicating participation of the $\text{N}=\text{C}-\text{S}$ group in coordination to tin(IV) atom. The chemical shifts of carbon in $\text{C}=\text{N}$ and CH_3 in the free ligand (**1**) were observed at 165.32 and 10.45 ppm which were shifted to high frequency at 168.36–178.45 and 16.44–18.70 ppm, respectively, in the complexes (**2–6**). This results supported the azomethine-N is coordinated to the tin(IV) atom [30]. After complexation, the δ value of carbon atoms in the aromatic ring did not have much change in the complexes (**2–6**) as compared to the free ligand. Besides, the butyl group attached to the organotin(IV) moiety in complex **3** gave four resonance signals at 32.78, 26.31, 24.18, and 20.11 ppm. In the ^{13}C -{ ^1H } NMR spectra of the organotin(IV) complexes **2** and **5**, a sharp singlet resonance signal appeared at 12.80 ppm [$(\text{Sn}-\text{CH}_3)$] and 14.97 [$\text{Sn}-(\text{CH}_3)_2$] ppm, respectively [31]. In organotin(IV) compounds, the $^1J[\text{Sn}^{119}, \text{C}]$ value is an important parameter to assess the coordination number of the Sn atom. The calculated coupling constants for dimethyltin(IV) (**4**) and diphenyltin(IV) (**5**) compounds were found to be 557 and 546 Hz, which described the penta-coordinate environment about the Sn atom in these compounds [32]. All these statements are also supported by the ^1H NMR spectra analyses.

3.6. ^{119}Sn NMR Spectra. ^{119}Sn NMR spectra can be used as an indicator of the coordination number of the tin atom. ^{119}Sn NMR of all the complexes (**2–6**) shows only one resonance signals in the range of –149.60 to –185.32 ppm. ^{119}Sn NMR values are characteristic for the five-coordinated

TABLE 1: Summary of crystal data and structure refinement parameters for ligand (**1**).

Compound	H ₂ dampf (1)
Empirical formula	$\text{C}_{16}\text{H}_{17}\text{N}_3\text{OS}$
Formula weight	299.39
Temperature (K)	100 (2)
Wavelength (Å)	0.71073
Crystal system	Monoclinic
Space group	$P2_1/c$
Unit cell dimensions	
a (Å)	14.6966(8)
b (Å)	7.3586(4)
c (Å)	14.0926(8)
α (°)	90.00
β (°)	94.358(5)
γ (°)	90.00
Volume (Å ³)	1519.66(15)
Z	4
Calculated density (mg/m ³)	1.309
Radiation type λ (Å)	Mo K\alpha
F (000)	632
Crystal size (mm)	0.30 × 0.1 × 0.05
Crystal colour	Light-yellow
Scan range θ (°)	2.8–29.3
Absorption coefficient (μ) (mm ⁻¹)	0.225
Max. and min. transm	1.00 and 0.419
Goodness of fit on F ²	0.995
Data/restrains/ parameters	3375/3/201
Final R indices [$I > 2\sigma(I)$]	$R_1 = 0.0599, wR_2 = 0.1324$
R indices (all data)	$R_1 = 0.110, wR_2 = 0.1738$

tin atom observed in the organotin(IV) complexes (**2–6**) [33–36].

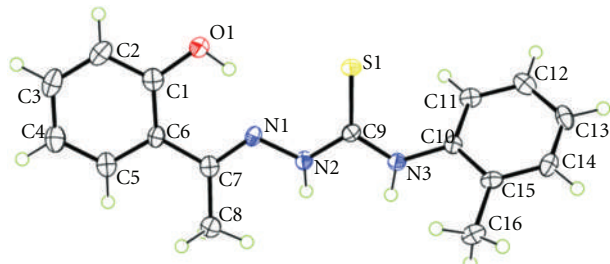
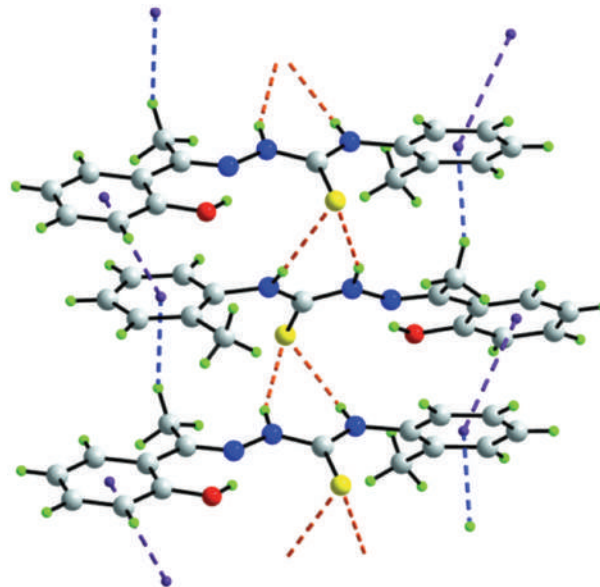
3.7. X-Ray Crystallography Diffraction Analysis. The molecular structure of the ligand (**1**) with atom numbering scheme is depicted in Figure 1. The main crystal parameters are reported in Table 1. Selected bond lengths and bond angles are given in Table 2. The compound crystallizes into monoclinic crystal system with a space group of $P2_1/c$. In the title substituted thiosemicarbazone, $\text{C}_{16}\text{H}_{17}\text{N}_3\text{OS}$, the hydroxy- and methyl-substituted benzene rings form dihedral angles of 9.62 (12) and 55.69 (6)°, respectively, with the central CN₃S chromophore (r.m.s. deviation = 0.0117 Å) in ($\text{C}_{16}\text{H}_{17}\text{N}_3\text{OS}$) (Figure 1) and the OH- and Me-benzene rings are twisted as seen in the respective dihedral angles of 9.62 (12) and 55.69 (6)°. The almost coplanarity of the central atoms is ascribed to the formation of an intramolecular hydroxyl-O-H· · · N-imine hydrogen bond (Table 3). The N1–N2 bond length (1.375 Å) is closer to single bond length (1.45 Å) than to double bond length (1.25 Å) [37]. The C9–S1 bond distance (1.694 Å) is close to that expected of a C=S double bond (1.60 Å) [37] and the C7–N1 bond length (1.295 Å) is nearly the same as that of the

TABLE 2: Selected bond lengths (Å) and bond angles (°) of ligand [$H_2\text{dampt}$] (1).

Bond lengths (Å)			
S1–C9	1.694 (3)	O1–C1	1.357 (4)
N1–C7	1.295 (4)	N1–N2	1.375 (3)
N2–C9	1.352 (4)	N3–C9	1.344 (3)
C7–C8	1.500 (4)	C6–C7	1.473 (4)
Bond angles (°)			
C7–N1–N2	119.0 (2)	C9–N2–N1	120.6 (2)
C9–N3–C10	127.7 (2)	N3–C9–N2	113.2 (2)
N3–C9–S1	124.3 (2)	N2–C9–S1	122.4 (2)
O1–C1–C2	116.8 (3)	O1–C1–C6	123.2 (3)

TABLE 3: Hydrogen-bond geometry (Å, °)

D–H···A	D–H	H···A	D···A	D–H···A
O1–H1o···N1	0.84 (1)	1.81 (2)	2.551 (3)	145 (3)
N2–H2n···S1 ⁱ	0.88 (1)	2.51 (2)	3.323 (2)	154 (3)
N3–H3n···S1 ⁱ	0.88 (1)	2.49 (2)	3.286 (3)	151 (2)
C8–H8b···Cg1 ⁱ	0.98	2.59	3.501 (3)	155

Symmetry codes: $-x + 1, y + 1/2, -z + 1/2$.FIGURE 1: The molecular structure of $H_2\text{dampt}$ (1) showing the atom-labelling scheme and displacement ellipsoids at the 50% probability level.FIGURE 2: A view of the helical supramolecular chain aligned along the b axis in (I). The N – H ··· S hydrogen bonds are shown as orange dashed lines. Further stabilization to the chain is provided by C – H ··· π and π – π interactions, shown as blue and purple dashed lines, respectively.

$C=N$ double bond (1.28 Å) [38]. These bond distances are in strong support of the existence of 2-hydroxyacetophenone-2-methylphenylthiosemicarbazone in the thione form in the solid state. The H atoms of the NH groups are *syn*, and the conformation about the $N1=C7$ double bond [1.295 (4) Å] is *E*. The *syn* arrangement in ($C_{16}H_{17}N_3OS$) contrast the *anti*arrangement often seen in such derivatives but is readily explained in terms of the intramolecular O – H ··· N -imine hydrogen bond in ($C_{16}H_{17}N_3OS$) by contrast to the normally observed intramolecular N – H ··· N -imine hydrogen bond [39, 40]. Helical supramolecular chains along the b axis dominate the crystal packing (Figure 2 and Table 3). These arise as a result of the thione-S interacting with both N–H atoms of a neighboring molecule thereby forming six-membered hydrogen-bond-mediated rings.

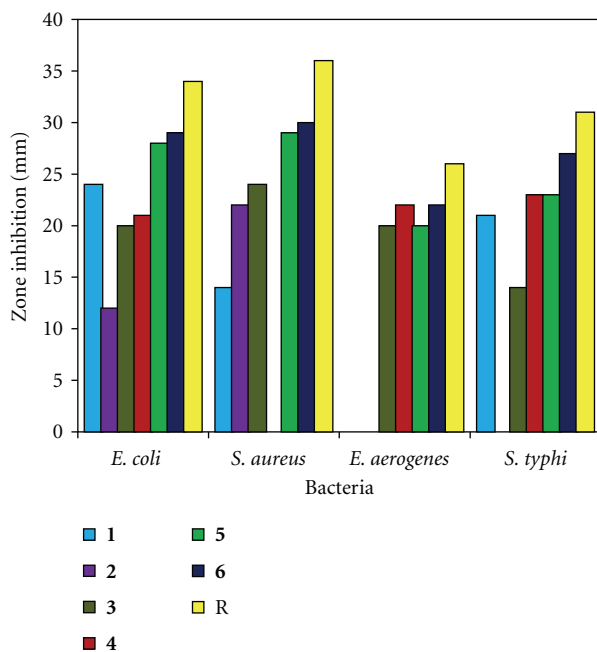
3.8. Antibacterial Activity. The synthesized ligand (1) and its organotin(IV) complexes (2–6) were tested against

Escherichia coli, *Staphylococcus aureus*, *Enterobacter aerogenes*, and *Salmonella typhi* bacterial strains for their antibacterial activity using agar-well diffusion method and data are shown in Table 4 and Figure 3. The doxycycline was used as a reference drug. The results showed that the substituted thiosemicarbazone ligand (1) possessed moderate antibacterial activity. The antibacterial studies of the compounds (2–6) showed relatively better activity against

TABLE 4: Antibacterial activity^{a,b} of the free ligand (**1**) and its organotin(IV) complexes **2–6** (inhibition zone in mm).

Bacterium	Clinical implication	Zone of Inhibition (mm)						
		(1)	(2)	(3)	(4)	(5)	(6)	R
<i>Escherichia coli</i>	Infection of wounds, urinary tract, and dysentery	24	12	20	21	28	29	34
<i>Staphylococcus aureus</i>	Food poisoning, scaled skin syndrome, endocarditis	14	22	24	—	29	30	36
<i>Enterobacter aerogenes</i>	Lower respiratory tract infections, skin and soft-tissue infections	—	—	20	22	20	22	26
<i>Salmonella typhi</i>	Typhoid fever, localized infection	21	—	14	23	23	27	31

^a *In vitro*, agar-well diffusion method, conc. 200 mg/mL of DMSO. ^b Reference drug (R), doxycycline, dash indicate inactivity.

FIGURE 3: Antibacterial activity of compounds **1–6** against various bacteria.

the selected bacteria than the free ligand (**1**), but low activities as compared to the reference drug. Among all the organotin(IV) derivatives, the bactericidal activities of **5** and **6** are fairly good. Complex **2** is the least active among all the organotin(IV) complexes, while complex **4** was found to be active against all the studied strains except *Staphylococcus aureus*. The most probable reason for this difference might be due to chelation which reduces the polarity of the central Sn atom because of the partial sharing of its positive charge with donor groups and possible π -electron delocalization within the whole chelating ring. As a result, the lipophilic nature of the central Sn atom increases, which favours the permeation of the complexes through the lipid layer of the cell membrane [41]. In addition, among the organotin(IV) complexes (**2–6**), complex (**6**) is found to be more active and it can be attributed to the presence of bulky phenyl groups which facilitate binding to biological molecules π - π interactions.

4. Conclusion

The ligand (**1**) and its organotin(IV) complexes (**2–6**) have been synthesized and fully characterized by different spectroscopic techniques. The ligand ($H_2\text{dampt}$) exists in thione form in a solid state but it takes on a thiol form when it is in solution. All organotin(IV) complexes (**2–6**) of $H_2\text{dampt}$ were proposed to be five coordinated and the ligand binds to the central tin(IV) atom in dinegative tridentate form. Single crystal X-ray analysis of newly synthesized ligand (**1**) has been reported. The *in vitro* antibacterial activities of the synthesized complexes against the selected bacterial strains have been established. All compounds have been found biologically active, while the studies have confirmed that compounds **5** and **6** are more active and have the potency to be used as antibacterial agents. Trials to obtain single crystals suitable for structure determination by X-ray crystallography were in vain due to the amorphous nature of the complexes.

Acknowledgment

This work was financially supported by the Ministry of Science Technology and Innovation (MOSTI) under a Research Grant (no. 06-01-09-SF0046). The authors would like to thank Universiti Malaysia Sarawak (UNIMAS) for the facilities to carry out the research work.

References

- [1] B. D. Wang, Z. Y. Yang, M. H. Lü, J. Hai, Q. Wang, and Z. N. Chen, “Synthesis, characterization, cytotoxic activity and DNA binding Ni(II) complex with the 6-hydroxy chromone-3-carbaldehyde thiosemicarbazone,” *Journal of Organometallic Chemistry*, vol. 694, no. 25, pp. 4069–4075, 2009.
- [2] S. Padhye, Z. Afrasiabi, E. Sinn, J. Fok, K. Mehta, and N. Rath, “Antitumor metallothiosemicarbazones: structure and anti-tumor activity of palladium complex of phenanthrenequinone thiosemicarbazone,” *Inorganic Chemistry*, vol. 44, no. 5, pp. 1154–1156, 2005.
- [3] C. R. Kowol, R. Trondl, P. Heffeter et al., “Impact of metal coordination on cytotoxicity of 3-aminopyridine-2- carbox-aldehyde thiosemicarbazone (Triapine) and novel insights into terminal dimethylation,” *Journal of Medicinal Chemistry*, vol. 52, no. 16, pp. 5032–5043, 2009.
- [4] H. Beraldo and D. Gambino, “The wide pharmacological versatility of semicarbazones, thiosemicarbazones and their metal complexes,” *Mini-Reviews in Medicinal Chemistry*, vol. 4, no. 1, pp. 31–39, 2004.

- [5] E. B. Seena and M. R. P. Kurup, "Synthesis of mono- and binuclear dioxomolybdenum(VI) complexes derived from N(4)-substituted thiosemicarbazones: X-ray crystal structures of $[(\text{MoO}_2\text{L}^1)_2]$, $[\text{MoO}_2\text{L}^1\text{py}]$ and $[\text{MoO}_2\text{L}^2\text{py}]$," *Polyhedron*, vol. 26, no. 14, pp. 3595–3601, 2007.
- [6] M. R. Maurya, A. Kumar, M. Abid, and A. Azam, "Dioxovanadium(V) and μ -oxo bis[oxovanadium(V)] complexes containing thiosemicarbazone based ONS donor set and their antiamoebic activity," *Inorganica Chimica Acta*, vol. 359, no. 8, pp. 2439–2447, 2006.
- [7] K. Alomar, M. A. Khan, M. Allain, and G. Bouet, "Synthesis, crystal structure and characterization of 3-thiophene aldehyde thiosemicarbazone and its complexes with cobalt(II), nickel(II) and copper(II)," *Polyhedron*, vol. 28, no. 7, pp. 1273–1280, 2009.
- [8] M. Vieites, L. Otero, D. Santos et al., "Platinum-based complexes of bioactive 3-(5-nitrofuryl)acroleine thiosemicarbazones showing anti-Trypanosoma cruzi activity," *Journal of Inorganic Biochemistry*, vol. 103, no. 3, pp. 411–418, 2009.
- [9] A. Tarassoli and T. Sedaghat, in *Organometallic Chemistry Research Perspectives*, R. P. Irwin, Ed., p. 7, Nova Science, New York, NY, USA, 2007.
- [10] Y. Arakawa, in *Chemistry of Tin*, P. J. Smith, Ed., Blackie, London, UK, 2nd edition, 1998.
- [11] M. Carcelli, C. Pelizzi, G. Pelizzi, P. Mazza, and F. Zani, "The different behaviour of the di-2-pyridylketone 2-thenoylhydrazone in two organotin compounds. Synthesis, X-ray structure and biological activity," *Journal of Organometallic Chemistry*, vol. 488, pp. 55–61, 1995.
- [12] M. Gielen, "Organotin compounds and their therapeutic potential: a report from the Organometallic Chemistry Department of the Free University of Brussels," *Applied Organometallic Chemistry*, vol. 16, no. 9, pp. 481–494, 2002.
- [13] M. Gielen, "Tin-based antitumour drugs," *Coordination Chemistry Reviews*, vol. 151, pp. 41–51, 1996.
- [14] M. Nath, S. Pokharia, and R. Yadav, "Organotin(IV) complexes of amino acids and peptides," *Coordination Chemistry Reviews*, vol. 215, no. 1, pp. 99–149, 2001.
- [15] M. S. Singh, "Synthesis and characterisation of organotin(IV) derivatives of benzilmonohydrazone," *Indian Journal of Chemistry—Section A*, vol. 37, no. 10, pp. 911–914, 1998.
- [16] E. Katsoulakou, M. Tiliakos, G. Papaefstathiou et al., "Diorganotin(IV) complexes of dipeptides containing the α -aminoisobutyryl residue (Aib): preparation, structural characterization, antibacterial and antiproliferative activities of $[(n\text{-Bu})_2\text{Sn}(\text{H}-1\text{L})]$ (LH = H-Aib-L-Leu-OH, H-Aib-L-Ala-OH)," *Journal of Inorganic Biochemistry*, vol. 102, no. 7, pp. 1397–1405, 2008.
- [17] T. S. Basu Baul, C. Masharing, G. Ruisi et al., "Self-assembly of extended Schiff base amino acetate skeletons, 2-[(2Z)-(3-hydroxy-1-methyl-2-but enylidene)]aminophenylpropionate and 2-[(E)-1-(2-hydroxyaryl) alkylidene] aminophenylpropionate skeletons incorporating organotin(IV) moieties: synthesis, spectroscopic characterization, crystal structures, and *in vitro* cytotoxic activity," *Journal of Organometallic Chemistry*, vol. 692, no. 22, pp. 4849–4862, 2007.
- [18] M. A. Salam, M. A. Affan, F. B. Ahmad, R. B. Hitam, Z. Gal, and P. Oliver, "Synthesis and characterization of tin(IV)/organotin(IV) complexes with 2-benzoylpyridine-N(4)-cyclohexylthiosemicarbazone [HBPCT]: X-ray crystal structure of $[\text{SnCl}_3(\text{BPCT})]$," *Journal of Coordination Chemistry*, vol. 64, no. 14, pp. 2409–2418, 2011.
- [19] M. A. Affan, M. A. Salam, F. B. Ahmad, J. Ismail, M. B. Sham-suddin, and H. M. Ali, "Synthesis and spectroscopic characterization of organotin(IV) complexes with 2-benzoylpyridine-N(4)-cyclohexylthiosemicarbazone (HBPCT): X-ray crystal structure of $[\text{PhSnCl}_2(\text{BPCT})]$," *Inorganica Chimica Acta*, vol. 366, no. 1, pp. 227–232, 2011.
- [20] W. L. F. Armarego and D. D. Perrin, *Purification of Laboratory Chemicals*, Butterworth Heinemann, Oxford, UK, 4th edition, 1996.
- [21] A. Rahman, M. I. Choudry, and W. J. Thomsen, *Bioassay Techniques for Drug Development*, Harwood Academic, Amsterdam, The Netherlands, 2001.
- [22] C. M. Sharaby, "Synthesis, spectroscopic, thermal and antimicrobial studies of some novel metal complexes of Schiff base derived from $[\text{N}^1\text{-}(4\text{-methoxy-1,2,5-thiadiazol-3-yl})\text{sulfanilamide}]$ and 2-thiophene carboxaldehyde," *Spectrochimica Acta—Part A*, vol. 66, no. 4–5, pp. 1271–1278, 2007.
- [23] A. P. Rebollo, G. M. De Lima, L. N. Gambi et al., "Tin(IV) complexes of 2-benzoylpyridine N(4)-phenylthiosemicarbazone: spectral characterization, structural studies and anti-fungal activity," *Applied Organometallic Chemistry*, vol. 17, no. 12, pp. 945–951, 2003.
- [24] M. R. Maurya, M. N. Jayaswal, V. G. Puranik, P. Chakrabarti, S. Gopinathan, and C. Gopinathan, "Dioxomolybdenum(VI) and dioxotungsten(VI) complexes of isomeric ONO donor ligands and the X-ray crystal structure of $[\text{MoO}_2(o\text{-OC}_6\text{H}_4\text{CH=NCH}_2\text{C}_6\text{H}_4\text{O})(\text{MeOH})]_2 \cdot \text{MeOH}$," *Polyhedron*, vol. 16, no. 23, pp. 3977–3983, 1997.
- [25] O. A. Rajan and A. Chakravorty, "Molybdenum complexes. 1. Acceptor behavior and related properties of MoVIO_2 (tridentate) systems," *Inorganic Chemistry*, vol. 20, no. 3, pp. 660–664, 1981.
- [26] R. F. F. Costa, A. P. Rebollo, T. Matencio et al., "Metal complexes of 2-benzoylpyridine-derived thiosemicarbazones: structural, electrochemical and biological studies," *Journal of Coordination Chemistry*, vol. 58, no. 15, pp. 1307–1319, 2005.
- [27] B. S. Garg, M. R. Prathapachandra Kurup, S. K. Jain, and Y. K. Bhoon, "Spectroscopic studies on copper(II) complexes derived from a substituted 2-acetylpyridine thiosemicarbazone," *Transition Metal Chemistry*, vol. 13, no. 4, pp. 309–312, 1988.
- [28] I. C. Mendes, J. P. Moreira, A. S. Mangrich, S. P. Balena, B. L. Rodrigues, and H. Beraldo, "Coordination to copper(II) strongly enhances the *in vitro* antimicrobial activity of pyridine-derived N(4)-tolyl thiosemicarbazones," *Polyhedron*, vol. 26, no. 13, pp. 3263–3270, 2007.
- [29] T. P. Lockhart and W. F. Manders, "Structure determination by NMR spectroscopy. Correlation of $-2J(^{119}\text{Sn}, ^1\text{H})$ and the Me-Sn-Me angle in methyltin(IV) compounds," *Inorganic Chemistry*, vol. 25, no. 7, pp. 892–895, 1986.
- [30] E. Labisbal, L. Rodríguez, A. Sousa-Pedrares et al., "Synthesis, characterisation and X-ray structures of diorganotin(IV) and iron(III) complexes of dianionic terdentate Schiff base ligands," *Journal of Organometallic Chemistry*, vol. 691, no. 7, pp. 1321–1332, 2006.
- [31] H. D. Yin and S. W. Chen, "Synthesis and characterization of organotin(IV) compounds with Schiff base of o-vanillin-2-thiophenylhydrazone," *Journal of Organometallic Chemistry*, vol. 691, no. 13, pp. 3103–3108, 2006.
- [32] T. P. Lockhart and F. Davidson, "Methyltin(IV) structure determination by NMR. X-ray and NMR structural analyses

- of three $\text{Me}_2\text{Sn}(\text{chelate})_2$ compounds bearing five-membered chelate rings," *Organometallics*, vol. 6, no. 12, pp. 2471–2478, 1987.
- [33] J. Holeček, K. Handlir, M. Nadvorník, and A. Lycka, " ^{13}C and ^{119}Sn NMR study of some triphenyl tin(IV) carboxylates," *Journal of Organometallic Chemistry*, vol. 258, pp. 147–153, 1983.
- [34] J. Holeček, M. Nadvorník, K. Handlir, and A. Lycka, " ^{13}C and ^{119}Sn NMR spectra of Di-n-butyltin(IV) compounds," *Journal of Organometallic Chemistry*, vol. 315, pp. 299–308, 1986.
- [35] B. Sarkar, A. K. Choudhury, A. Roy et al., "Crystal structure, anti-fungal activity and phytotoxicity of diorganotin compounds of dihalo-substituted [(2-hydroxyphenyl) methylidene]neamino]thiourea," *Applied Organometallic Chemistry*, vol. 24, no. 12, pp. 842–852, 2010.
- [36] I. U. Din, M. Mazhar, K. C. Molloy, and K. M. Khan, "Synthesis, structural characterization of some germanium substituted chiral diethyltin derivatives," *Journal of Organometallic Chemistry*, vol. 691, no. 8, pp. 1643–1648, 2006.
- [37] J. E. Huheey, E. A. Keiter, and R. L. Keiter, *Inorganic Chemistry, Principles of Structure and Reactivity*, Harper Collins College, New York, NY, USA, 4th edition, 1993.
- [38] J. March, *Advanced Organic Chemistry, Reactions, Mechanisms and Structure*, John Wiley & Sons, New York, NY, USA, 4th edition, 1992.
- [39] E. Normaya, Y. Farina, S. N. A. Halim, and E. R. T. Tiekkink, "3-(2-Hydroxyphenyl)-1-(E)-[1-(pyrazin-2-yl)ethylidene]aminothiourea monohydrate," *Acta Crystallographica Section E*, vol. 67, pp. o943–o944, 2011.
- [40] M. A. Salam, M. A. Affan, F. B. Ahmad, S. W. Ng, and E. R. T. Tiekkink, "1-Cyclohexyl-3-(E)-[1-(pyridin-2-yl)ethylidene]aminothiourea," *Acta Crystallographica Section E*, vol. 67, article o955, 2010.
- [41] R. S. Srivastava, "Pseudotetrahedral Co(II), Ni(II) and Cu(II) complexes of N1-(O-chlorophenyl)-2-(2',4'-dihydroxyphenyl)-2-benzylazomethine their fungicidal and herbicidal activity," *Inorganica Chimica Acta*, vol. 56, pp. 65–67, 1981.

SOD-Mimic Cu(II) Dimeric Complexes Involving Kinetin and Its Derivative: Preparation and Characterization

Radka Novotná, Zdeněk Trávníček, and Radovan Herchel

Department of Inorganic Chemistry, Regional Centre of Advanced Technologies and Materials, Faculty of Science, Palacký University, 17. listopadu 12, 771 46 Olomouc, Czech Republic

Correspondence should be addressed to Zdeněk Trávníček, zdenek.travnicek@upol.cz

Academic Editor: Spyros Perlepes

Two SOD-mimic active dimeric Cu(II) chlorido complexes of the compositions $[\text{Cu}_2(\mu\text{-HL}^1)_4\text{Cl}_2]\text{Cl}_2$ (**1**) and $[\text{Cu}_2(\mu\text{-HL}^2)_2(\mu\text{-Cl})_2(\text{HL}^2)_2\text{Cl}_2] \cdot 4\text{H}_2\text{O}$ (**2**) involving the cosmetologically relevant cytokinin kinetin (N6-furfuryladenine, HL¹) and its derivative N6-(5-methylfurfuryl)adenine (HL²) have been synthesized and characterized by elemental analysis, infrared, and electronic spectroscopy, ESI+ mass spectrometry, conductivity and temperature dependence of magnetic susceptibility measurements, and thermogravimetric (TG) and differential thermal (DTA) analyses. The results of these methods, particularly the temperature dependence of magnetic susceptibility, showed the complexes to be dimeric with a strong antiferromagnetic exchange ($J = -290 \text{ cm}^{-1}$ for complex **1** and $J = -160 \text{ cm}^{-1}$ for **2**). The complexes have been identified as auspicious SOD-mimics, as their antiradical activity evaluated by the *in vitro* SOD-mimic assay resulted in the IC₅₀ values equal to 8.13 μM (**1**) and 0.71 μM (**2**).

1. Introduction

The metalloenzyme copper, zinc-superoxide dismutase (Cu, Zn-SOD), plays a crucial role in the cell protection against the damage of physiological functions caused by the reactive oxygen species in mammals [1]. The SOD enzyme catalyses the disproportionation of the cytotoxic superoxide radical to oxygen and hydrogen peroxide [2]. The overproduction or destructive effect of superoxide is a basic characteristic of more than 100 diseases, including neurodegenerative [3, 4], diabetes [5], inflammatory or carcinogenetic related processes [6]. The Cu, Zn-SOD enzyme, which is the organism's first line of antioxidant defence, contains a bimetallic active site with zinc(II) and copper(II) bridged by deprotonated imidazole. The presence of the redox active copper atom is essential for the superoxide dismutase mechanism and if zinc is replaced by copper, the dicopper derivative has the same activity as the native enzyme [7]. The unique role of this enzyme in the organism protection has made it a model compound for the design of low molecular antioxidants on the basis of copper complexes mimicking the active site of the metalloenzyme, thus achieving SOD-like activity.

Metallotherapeutics based on such SOD-mimics could then be supplemented in the treatment of diseases connected with the oxidative stress. This assumption that low molecular SOD-mimic Cu(II) complexes could have a potential to become future pharmaceuticals has recently been confirmed by results of our laboratory. The dimeric perchlorate Cu(II) complexes $[\text{Cu}_2(\mu\text{-HL}^x)_4(\text{ClO}_4)_2](\text{ClO}_4)_2$ involving variously benzyl-substituted derivatives of N6-benzyladenine (HL^x), a natural phytohormone, exhibited promising SOD-mimic activity (IC₅₀ = 8.67–41.45 μM) [8]. Moreover, the complexes of the same basic composition, however, with the chloride anions instead of perchlorate, showed dramatically increased activity (IC₅₀ = 0.687–1.090 μM) and in the case of structurally different $[\text{Cu}_2(\mu\text{-2MeOHL}^x)_2(\mu\text{-Cl})_2\text{Cl}_2]$ even better (IC₅₀ = 0.253 μM) than the native bovine Cu, Zn-SOD (0.48 μM); 2MeOHL^x = N6-(2-methoxybenzyl)adenine [9]. Additionally, the pharmaceutical potential of the latter complexes involving the methoxy-benzyl-derived N6-benzyladenines was confirmed in the antidiabetic activity testing (cytoprotective effect against the alloxan-induced diabetes), in which they also exhibited significant antioxidant activity *in vivo* [9]. The last mentioned promising

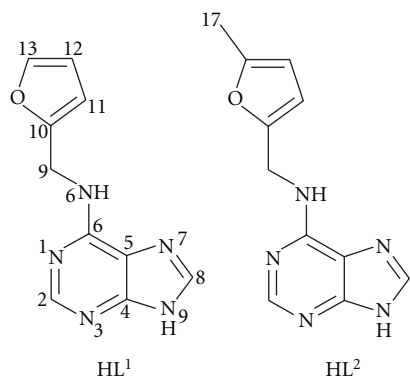


FIGURE 1: The organic compounds (N6-furfuryladenine, left; N6-(methylfurfuryl)adenine, right) used as ligands in the presented complexes.

results motivated us to try to prepare Cu(II) chlorido complexes involving the molecule of kinetin. Kinetin (N6-furfuryladenine) belongs among naturally occurring phytohormones called cytokinins. Apart from its action in plants, it has been shown to possess strong antiaging activity in fruit flies and also human fibroblasts, for which it is presently used in cosmetic pharmaceuticals. As for the suggested mode of kinetin action, various evidence indicates that kinetin can act both as an inhibitor of the radical oxygen species (ROS) formation and as a scavenger of ROS [10]. Taking into consideration these intrinsic antioxidant properties of kinetin and the high antioxidant activity of the above-mentioned Cu chlorido complexes of N6-benzyladenine [9], Cu(II) chlorido complexes involving the molecule of kinetin as a ligand could exhibit high SOD-mimic activity based on the possible synergic effect of the ligand and redox active copper centres.

2. Experimental

2.1. Materials and Methods. Chemicals and solvents were obtained from commercial sources (Sigma-Aldrich Co., Acros Organics Co.) and were used as received. N6-furfuryladenine (HL^1) and its derivative, N6-(5-methylfurfuryl)adenine (HL^2), (Figure 1), were synthesized using the modified previously reported procedures [11].

Elemental analyses (C, H, N) were measured on a ThermoScientific Flash 2000 CHNS-O Analyser. Conductivity measurements (10^{-3} M DMF solutions; 25°C) were obtained on a Cond 340i/SET (WTW) conductometer. The copper content was measured by chelatometric titration with murexide as an indicator. After mineralizing the complexes in concentrated HNO_3 , the resulting suspension was dissolved in distilled water. Then a few drops of a buffer (1 M NH_3) were added and the solution turned dark blue, after which the indicator murexide was added to obtain a brown colour. The resulting solution was titrated with a solution of complexon III until a purple colour. The diffuse reflectance and electronic absorption spectra (10^{-3} M DMF and DMSO solutions of complexes) were measured on a Perkin-Elmer

Lambda35 spectrometer (200–1000 nm). FTIR spectra were recorded on a Nexus 670 FT-IR (ThermoNicolet) using the ATR (400–4000 cm^{-1}) and Nujol techniques (150–600 cm^{-1}). The mass spectra were measured on a LCQ Fleet Ion Mass Trap mass spectrometer (Thermo Scientific). A SQUID magnetometer (Quantum Design) was used for the magnetic susceptibility measurements in the temperature range of 2–300 K with the applied field of 1 T. The diamagnetic corrections were calculated using Pascal constants [12] and the correction for the temperature-independent paramagnetism $\chi_{\text{TIP}} = +0.75 \text{ m}^3 \text{ mol}^{-1}$ per a Cu(II) ion was applied. Thermogravimetric (TG) and differential thermal analyses (DTA) were taken on an Exstar TG/DTA 6200 (Seiko Instruments Inc.) thermal analyzer in a ceramic crucible in dynamic air atmosphere (150 mL min^{-1}) up to 1000°C ($2.5^\circ\text{C min}^{-1}$ gradient).

2.2. SOD-Mimic Activity Testing. The SOD-mimic activity of the complexes **1** and **2** was evaluated by a modified indirect chemical method, which was described previously [13]. The method involves the competitive reaction between the tested compounds and 2,3-bis(2-methoxy-4-nitro-5-sulfophenyl)-2H-tetrazolium-5-carboxanilide sodium salt [the XTT dye] with the saturated DMSO solution of KO_2 . The concentration of orange XTT-formazane, as the product of the reaction of XTT with superoxide, was determined by UV-Vis spectra measurements at 470 nm. The percentage of inhibition of XTT reduction was calculated using the equation, %INH = $100 * (A_b - A_s)/A_b$, where A_b (blank) and A_s (sample) are absorbances at 470 nm. The IC_{50} values were then calculated from the linearized dependence of %INH on a logarithm of molar concentration (first order equation). The concentration that caused 50% inhibition of the XTT-formazane formation (IC_{50}) was compared to the standard of bovine Cu, Zn-superoxide dismutase.

2.3. Syntheses of Cu(II) Complexes

2.3.1. $[\text{Cu}_2(\mu_2-\text{HL}^1)_4\text{Cl}_2]\text{Cl}_2$ (1). The ligand HL^1 (1 mmol) was dissolved in 50 mL methanol under reflux and then, $\text{CuCl}_2 \cdot 2\text{H}_2\text{O}$ dissolved in a minimum of warm distilled water was added. The resulting mixture immediately turned into thick dark green suspension, which was then slowly filtered off and washed with cold methanol and diethyl ether and dried under an infrared lamp.

$[\text{Cu}_2(\mu_2-\text{HL}^1)_4\text{Cl}_2]\text{Cl}_2$ (1): yield: 73% [with respect to (wrt) copper], Anal. Calc. for $\text{Cu}_2\text{Cl}_4\text{C}_{40}\text{H}_{36}\text{N}_{20}\text{O}_4$ ($\text{Mr} = 1129.8$): C, 42.5; H, 3.2; N, 24.8; Cu, 11.2. Found: C, 42.4; H, 3.6; N, 24.5; Cu, 11.6%. Λ_M (DMF solution, $\text{S cm}^2 \text{ mol}^{-1}$): 131.3. FTIR (Nujol, cm^{-1}): 278 s (Cu–N), 331 s (Cu–Cl). FTIR (ATR, cm^{-1}): 1504 w, 1540 m, 1592 sh (C=C), 1616 s, 1642 s (C=N), 2933 m (C–H)_{al}, 3057 w, 3124 m (C–H)_{ar}, 3271 m (N–H). λ_{max} (solid state, nm): 611. λ_{max} (10^{-3} M DMF solution, nm)/ ϵ ($\text{M}^{-1} \text{ cm}^{-1}$): 636/97. ESI + MS (m/z): 136, 148, 216, 278, 493, 527, 557, 591.

2.3.2. $[\text{Cu}_2(\mu-\text{HL}^2)_2(\mu-\text{Cl})_2(\text{HL}^2)_2\text{Cl}_2] \cdot 4\text{H}_2\text{O}$ (2). The modification of the previously described procedure established

by Mikulski et al. for adenine complexes with divalent 3d metal chlorides was applied [14]. Hydrated copper chloride (1.4 mmol) was dissolved in a mixture of methanol (35 mL) and triethylorthoformate (15 mL) and stirred at 50°C for 1 h. Subsequently, the organic compound HL^2 (2.5 mmol) was added and the resultant mixture was refluxed for 6 days. After mixing the reactants, the clear solution turned to green suspension, which gradually thickened and darkened during the reaction time. The dark green powder product was then filtered off and washed with cold methanol and diethyl ether and dried under an infrared lamp.

$[\text{Cu}_2(\mu\text{-}\text{HL}^2)_2(\mu\text{-Cl})_2(\text{HL}^2)_2\text{Cl}_2] \cdot 4\text{H}_2\text{O}$ (**2**): Yield: 57% (wrt copper), Anal. Calc. for $\text{Cu}_2\text{Cl}_4\text{C}_{44}\text{H}_{52}\text{N}_{20}\text{O}_8$ ($M_r = 1257.9$): C, 42.0; H, 4.2; N, 22.3; Cu, 10.1. Found: C, 41.5; H, 3.9; N, 22.2; Cu 9.7%. Λ_M (DMF solution, $\text{S cm}^2 \text{ mol}^{-1}$): 49.2. FTIR (Nujol, cm^{-1}): 279 m (Cu–N), 315 s (Cu–Cl). FTIR (ATR, cm^{-1}): 1536 m, 1592 m (C=C), 1639 s (C=N), 2920 m (C–H)_{al}, 3057 m (C–H)_{ar}, 3306 m (N–H). λ_{max} (solid state, nm): 637. λ_{max} (10^{-3} M DMF solution, nm)/ ϵ ($\text{M}^{-1} \text{ cm}^{-1}$): 649/95. ESI + MS (m/z): 236, 148, 230, 293, 521, 556, 654.

In an effort to obtain single crystals of the studied complexes suitable for single crystal X-ray analysis, the dark green powder products were subjected to varied crystallization attempts, such as recrystallizations from DMF or DMSO, diffusions of diethyl ether/acetone/methanol into DMF solutions and gel crystallization from tetramethoxysilane according to [15]. Unfortunately, none of these crystallization efforts were successful and the products were at best obtained in the microcrystalline forms. However, on the basis of the results following from other techniques as well as the similarity of the presented complexes with those formerly crystallographically determined we believe that there are no doubts about the composition and stereochemistry of the studied complexes.

3. Results and Discussion

3.1. General Characteristics. The presented Cu(II) complexes $[\text{Cu}_2(\mu_2\text{-}\text{HL}^2)_4\text{Cl}_2]$ (**1**) and $[\text{Cu}_2(\mu\text{-}\text{HL}^2)_2(\mu\text{-Cl})_2(\text{HL}^2)_2\text{Cl}_2] \cdot 4\text{H}_2\text{O}$ (**2**) were obtained as powder products of the reactions of copper(II) chloride with the corresponding ligands (Figure 1). The differences in the synthetic procedures used lead to diverse structural types of the compounds, that is, with the bridging moieties $\{\text{Cu}(\mu\text{-HL}^n)_4\text{Cu}\}$ and $\{\text{Cu}(\mu\text{-HL}^n)_2(\mu\text{-Cl})_2\text{Cu}\}$ in **1**, and **2**, respectively. It should be pointed out that the two synthetic patterns were used for both ligands, however; the obtained solids could not be characterized as magnetically pure products. The complexes were found to be well soluble in dimethyl sulfoxide (DMSO) and *N,N'*-dimethylformamide (DMF) and otherwise insoluble in other common organic solvents (acetone, alcohols). Various attempts to crystallize the compounds were performed to obtain single crystals of the complexes suitable for single crystal X-ray analysis (recrystallization from DMF or DMSO, diffusion of diethyl ether/acetone/methanol into DMF solutions, and gel crystallization from tetramethoxysilane according to [15]); however, still the compounds were

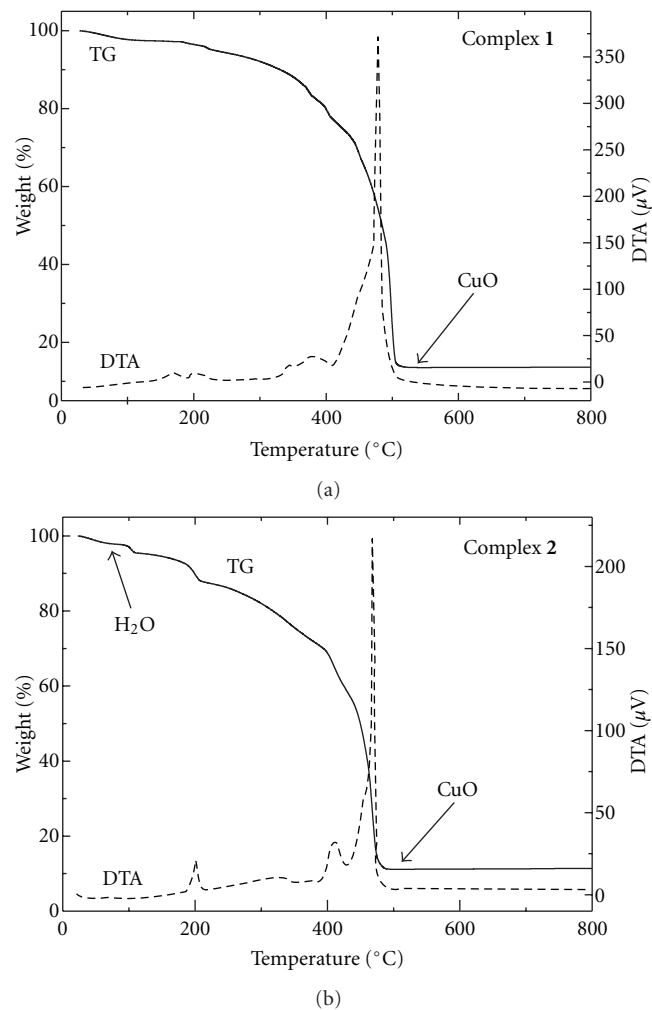


FIGURE 2: TG and DTA curves showing the thermal behaviour of complex **1** (a) and **2** (b).

obtained as polycrystalline solids. The molar conductivity values measured in the 10^{-3} M DMF solutions showed the complex **1** to be a 1:2 electrolyte ($131.3 \text{ S cm}^2 \text{ mol}^{-1}$) and the complex **2** as a nonelectrolyte ($49.2 \text{ S cm}^2 \text{ mol}^{-1}$) [16]. The simultaneous thermogravimetric (TG) and differential thermal analysis (DTA) study of **1** confirmed the complex to be nonsolvated, and the study of **2** proved the presence of four water molecules of crystallization. The final products of thermal decomposition (Figure 2) were calculated to be CuO (complex **1**: calcd./found 14.1/13.6%; complex **2**: the loss of 4 H₂O molecules; small *endo*-effect at 38.1°C, calcd./found 5.7/6.5%; CuO, calcd./found 12.6/11.7%).

3.2. Spectral Characterisations. The characteristic IR bands of the corresponding organic molecules (HLⁿ) were observed in the IR spectra of **1** and **2**. The most intensive $\nu(\text{C}=\text{N})_{\text{aromatic}}$ vibration in the spectra of the complexes was detected at 1642 and 1639 cm^{-1} in **1** and **2**, respectively. The vibration was shifted by ca 20 cm^{-1} with respect to the spectra of free organic molecules, thus suggesting on

TABLE 1: Magnetic and electronic spectral data for complexes **1** and **2**.

Compound	$J[\text{cm}^{-1}]$	g	Diffuse-reflectance spectra [nm]	UV-Vis spectra (fresh DMF solution) [nm] ($\epsilon [\text{M}^{-1}/\text{cm}]$)	UV-Vis spectra (24 h old DMF solution) [nm] ($\epsilon [\text{M}^{-1}/\text{cm}]$)
1	-290	2.03	611	636 (97)	640 ^a , 860 (195)
2	-162	2.05	637	649 (95)	652 ^a , 840 (150)

^aDetected as a shoulder of the band at higher wavelength.

changes in the vicinity of heterocyclic nitrogens, most likely connected with coordination to copper. In the region of the wave numbers higher than 2900 cm^{-1} , the middle intensive maxima of the $\nu(\text{C}-\text{H})_{\text{aromatic}}$ stretching vibrations were detected between 3057 and 3124 cm^{-1} , while the peaks connected with the $\nu(\text{C}-\text{H})_{\text{aliphatic}}$ were found at 2920 – 2933 cm^{-1} . The spectra of the complexes exhibited the peaks attributable to $\nu(\text{N}-\text{H})$ at 3271 and 3306 cm^{-1} for **1** and **2**, respectively. Regarding the far-IR region, the new bands, as compared to the spectra of uncoordinated organic compounds, observed at 278 (in **1**) and 279 (in **2**) cm^{-1} can be attributed to the $\nu(\text{Cu}-\text{N})$ vibrations thus supporting the conclusions about coordination of the organic molecules to the central ion. The prominent $\nu(\text{Cu}-\text{Cl})$ vibration was observed at 331 cm^{-1} in the spectrum of **1** and at 315 cm^{-1} for **2**, thus agreeing with the suggested bridging mode of the chlorides in **2**, because the bridging stretching $\nu(\text{Cu}-\text{Cl})$ vibrations generally appear lower than the terminal ones [17].

The diffuse reflectance and UV-Vis spectra (10^{-3} DMF and DMSO solutions) of the presented Cu(II) complexes were measured in the 200 – 1000 nm region. The spectra obtained in the solid state showed only one maximum corresponding to the $d-d$ transition typical of the Cu(II) complexes [18]. The maxima were observed at 611 and 637 nm in the cases of **1** and **2**, respectively. This fact indirectly suggested a different coordination environment around the metal centre in **1** and **2**. The spectra of the fresh 10^{-3} DMF (or analogically DMSO) solutions (as well as of 1 – 3 h old solutions) of the complexes exhibited a qualitatively similar course, still the maxima were shifted to higher wavelengths by 25 and 12 nm for **1** and **2**, respectively. The calculated values of molar absorption coefficients equalled 97 (**1**) and 95 (**2**) $\text{M}^{-1} \text{ cm}^{-1}$ and correspond to the $d-d$ transitions (Table 1). The solvent effect on the coordination environment of copper was clearly observable after 24 h standing of the DMF solutions, when the changes in the spectra of **1** and **2** were very significant. The intensity of the band around 640 nm decreased and a new broad peak at ca. 850 nm was observed, whose values of molar absorption coefficients also corresponded to the $d-d$ transitions ($\sim 200 \text{ M}^{-1} \text{ cm}^{-1}$). The fact that the complexes partially and gradually decompose in the DMF solution could be related to the somewhat higher values of molar conductivity, especially in the case of **2**. The comparison of the diffuse reflectance and UV-Vis spectra of complex **1** are shown in Figure 3. The behaviour of the complexes in the DMSO solutions was analogical, only the peak shifts were less pronounced indicating a less significant effect of this solvent on the coordination environment.

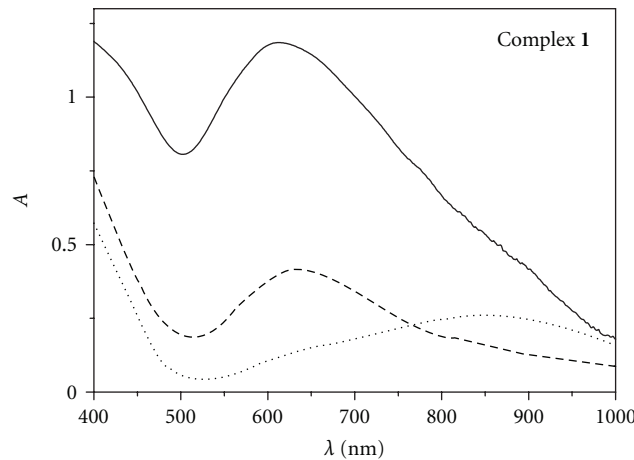


FIGURE 3: Diffuse-reflectance (solid line) and electronic (10^{-3} DMF solution) spectra of complex **1**; dashed line: freshly made solution, dotted line: after 24 h .

ESI+ mass spectrometry unambiguously confirmed the presence of the organic ligands (HL^1 and HL^2) in the complexes **1** and **2**, as the spectra revealed prominent peaks at 216 and 230 m/z , respectively. Then, the fragmentation of the organic molecules was also observed, as in both spectra the peaks at 136 m/z (adenine) and 148 m/z ($\text{C}_5\text{H}_4\text{N}_5=\text{CH}_2$; HL^{1x}) were assigned. The molecular peak of neither complex cation of **1** nor complex **2** was detected in the mass spectra. The peaks in the ESI+ mass spectra of **1** at 278 , 493 , 557 and 591 m/z may be assigned to $[\text{Cu}(\text{HL}^1)]^+$, $[\text{Cu}(\text{HL}^1)_2]^+$, $[\text{Cu}_2(\text{HL}^1)_2]^+$, and $[\text{Cu}_2(\text{HL}^1)_2\text{Cl}]^+$. Additionally, a dicopper particle involving a fragmented organic ligand was detected at 527 m/z ; $[\text{Cu}_2(\text{HL}^{1x})_2\text{Cl}_3]^+$. A dicopper fragment was also observed in the negative mode spectrum, that is, $[\text{Cu}_2(\text{L}^1)\text{Cl}_2]^-$. Similarly, fragmentation was detected also in the spectrum of **2**. The peaks at 292 , 521 , 556 and 654 m/z may be related to the fragments $[\text{Cu}(\text{HL}^2)]^+$, $[\text{Cu}(\text{HL}^2)_2]^+$, $[\text{Cu}(\text{HL}^2)_2\text{Cl}]^+$, and $[\text{Cu}_2(\text{HL}^2)_2\text{Cl}]^+$, respectively. Another dicopper fragment was identified in the spectrum measured in the negative mode, that is, $[\text{Cu}_2(\text{L}^2)\text{Cl}_2]^-$ at 426 m/z . The fragmentation of the peak at 591 m/z , the fragment $[\text{Cu}_2(\text{HL}^1)_2\text{Cl}]^+$ of complex **1**, is shown in Figure 4.

3.3. Magnetic Properties. The structural parameters of the presented compounds have been proposed particularly based on the data resulting from the magnetochemical characterizations. The temperature dependence of magnetic susceptibility for both compounds has the typical course for the dimers with strong antiferromagnetic coupling between

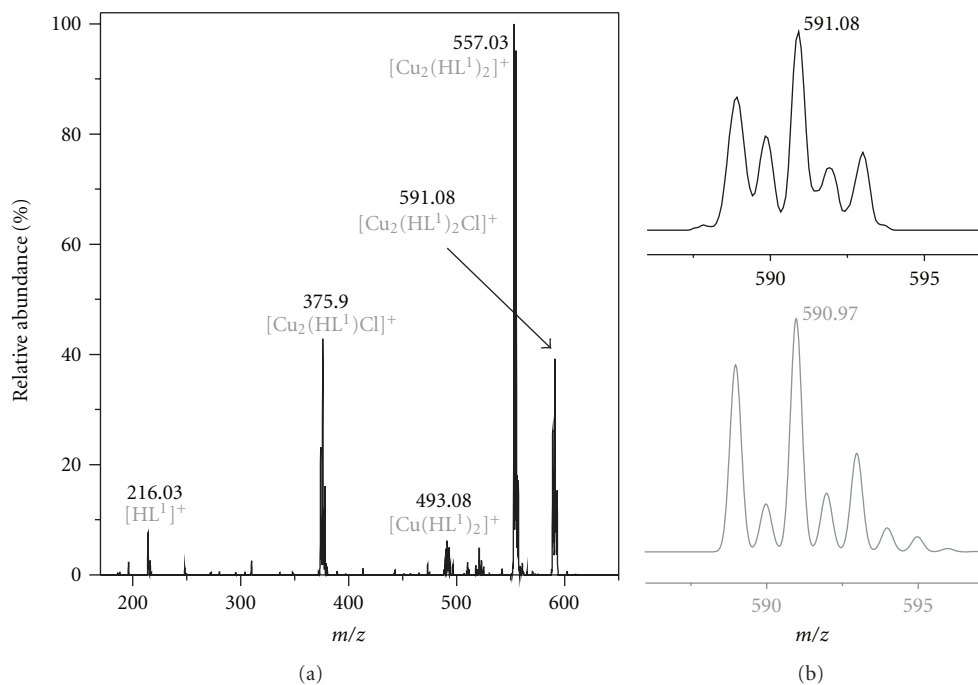


FIGURE 4: The MS^2 spectrum showing the fragmentation of the peak $591 \text{ } m/z$, the $[\text{Cu}_2(\text{HL}^1)_2\text{Cl}]^+$ fragment of **1** (left); the comparison of the measured (up) and calculated (down, in grey) isotope pattern of $591 \text{ } m/z$.

the copper centres characterized by maxima at M_{mol} versus T curves, $T_{\text{max}} = 235$, and 175 K for **1** and **2**, respectively (Figure 5). The magnetic data were thus analyzed with the spin Hamiltonian describing the magnetic behaviour of antiferromagnetic coupled dimers with a small amount of the monomeric paramagnetic impurity [19]:

$$\hat{H} = -J(\vec{S}_A \cdot \vec{S}_B) + \mu_B g (\hat{S}_{z,A} + \hat{S}_{z,B}), \quad (1)$$

where the J parameter determines the energy gap between the singlet ($S = 0$) and triplet states ($S = 1$), resulting from the coupling of two local spins $S_A = S_B = 1/2$. The temperature dependence of the molar magnetization of complexes **1** and **2** were treated with simple relationship derived for such dimer [20]:

$$M_{\text{mol}} = \frac{\mu_B g N_A [\exp((J+x)/kT) - \exp((J-x)/kT)]}{[1 + \exp((J+x)/kT) + \exp(J/kT) + \exp((J-x)/kT)]}, \quad (2)$$

where $x = \mu_B g B$. The total magnetization of the powder sample was calculated as the sum of the contributions of a dimer and monomeric paramagnetic impurity, $M_{\text{mol}} = (1 - x_{\text{PI}})M_{\text{dimer}} + 2x_{\text{PI}}M_{\text{mono}}$. The best-fitted parameters of **1** were $J = -290 \text{ cm}^{-1}$, $g = 2.03$, and $x_{\text{PI}} = 5.2\%$ (Table 1, Figure 5). The resulting J value for **1** is comparable to those [$J = (-285) - (-329) \text{ cm}^{-1}$] reported for the Cu(II) dimers with four NCN bridges, for which the X-ray structures have been determined, for example, $[\text{Cu}_2(\mu\text{-AzabH})_4\text{Cl}_2]\text{Cl}_2 \cdot 3\text{CH}_3\text{OH}$

[21], $[\text{Cu}_2(\mu\text{-AdeH})_4\text{Cl}_2]\text{Cl}_2 \cdot 6\text{H}_2\text{O}$ [22, 23], $[\text{Cu}_2(\mu\text{-AdeH})_4(\text{H}_2\text{O})_2](\text{ClO}_4)_4 \cdot 2\text{H}_2\text{O}$ [23, 24], and $[\text{Cu}_2(\mu\text{-4CILH}^x)_4(\text{ClO}_4)_2](\text{ClO}_4)_2 \cdot 2\text{EtOH} \cdot \text{H}_2\text{O}$ [8]; AzabH = 4-azabenzimidazole, AdeH = adenine, 4CILH x = N6-(4-chlorobenzyl)adenine. The experimental data of **2** were fitted with $J = -162 \text{ cm}^{-1}$, $g = 2.05$, and $x_{\text{PI}} = 0.7\%$ (Table 1, Figure 5), which means that the antiferromagnetic exchange for **2** was found to be substantially smaller than that for **1**. Therefore, a different exchange pathway, that is, bridging, between the Cu(II) centres is present. It has already been established that the coupling in Cu(II) dimers bridged by only chlorido bridges is generally very weak [25], therefore this cannot be the case in **2**. A similar value of J (-139 cm^{-1}) as in **2** was found for the dimeric complex $[\text{Cu}_2(\mu\text{-Nphtd})_2(\mu\text{-Cl})_2\text{Cl}_2]$ (Nphtd = 1,8-naphthyridine), where the Cu(II) atoms are bridged by two NCN bridges and two chlorides, that is, the $\{\text{Cu}(\mu\text{-HL}^n)_2(\mu\text{-Cl})_2\text{Cu}\}$ moiety is present, which was determined by single crystal X-ray analysis [26, 27].

Based on the above analytical methods and literature research, for complex **1**, we propose the 1:2 ionic composition of the complex cation $[\text{Cu}_2(\mu\text{-LH}^1)_4\text{Cl}_2]^{2+}$, with four $\mu\text{-N}_3\text{N}_9$ bridging kinetin molecules and two terminal chlorides coordinated to Cu(II), whose charge is compensated by two chloride anions. The proposed structure for **2** involves the dimeric core $\{\text{Cu}(\mu\text{-HL}^n)_2(\mu\text{-Cl})_2\text{Cu}\}$ with the copper centres bridged by two $\mu\text{-N}_3\text{N}_9$ HL^2 molecules and two chlorides, with one terminal N_9 -coordinated HL^2 and one chloride bonded to each Cu(II) (Figure 6), as was analogically reported previously for $[\text{Cu}_2(\mu\text{-nClHL}^x)_2(\mu\text{-Cl})_2(\text{nCILH}^x)_2\text{Cl}_2] \cdot 2\text{H}_2\text{O}$ ($\text{nClHL}^x = \text{N}_6\text{-}(n\text{-chlorobenzyl})\text{adenine}$; $n = 2, 3$) [28, 29].

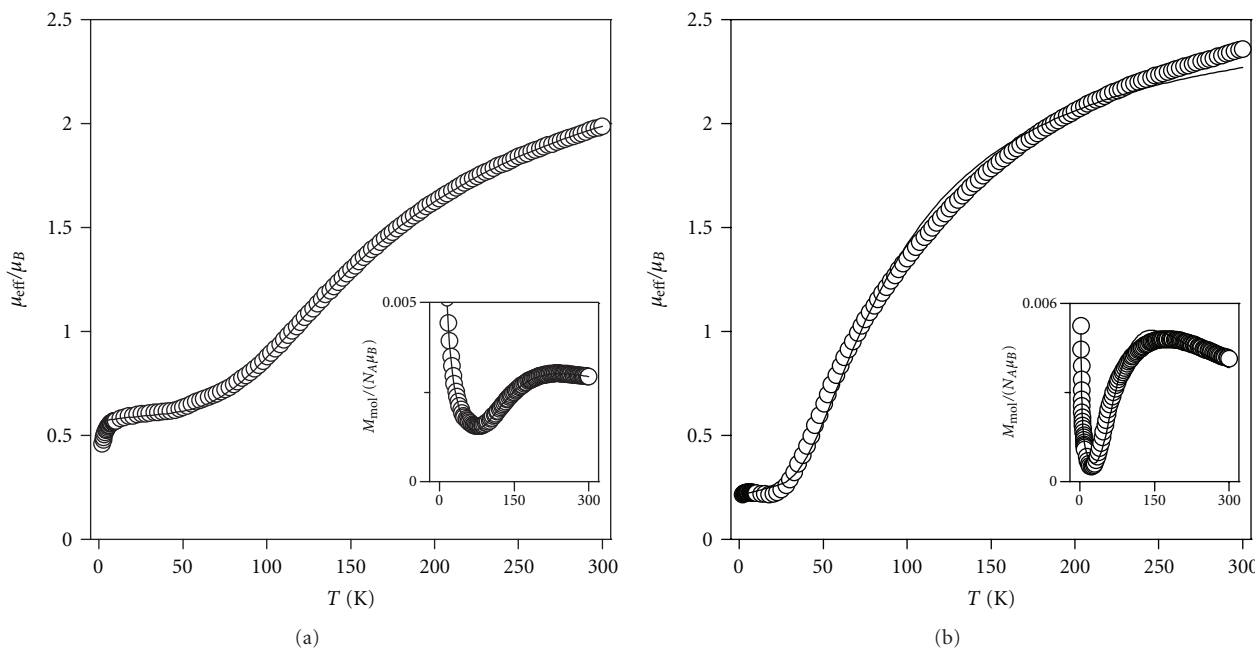


FIGURE 5: The magnetic data for complexes **1** (a) and **2** (b): the temperature dependence of the effective magnetic moment and molar magnetization measured at $B = 1$ T (inset). Empty circles: experimental data, full lines: calculated data using (1) and $J = -290$ cm $^{-1}$, $g = 2.03$ and $x_{\text{Pl}} = 5.2\%$ for **1** and $J = -162$ cm $^{-1}$, $g = 2.05$, and $x_{\text{Pl}} = 0.7\%$ for **2**.

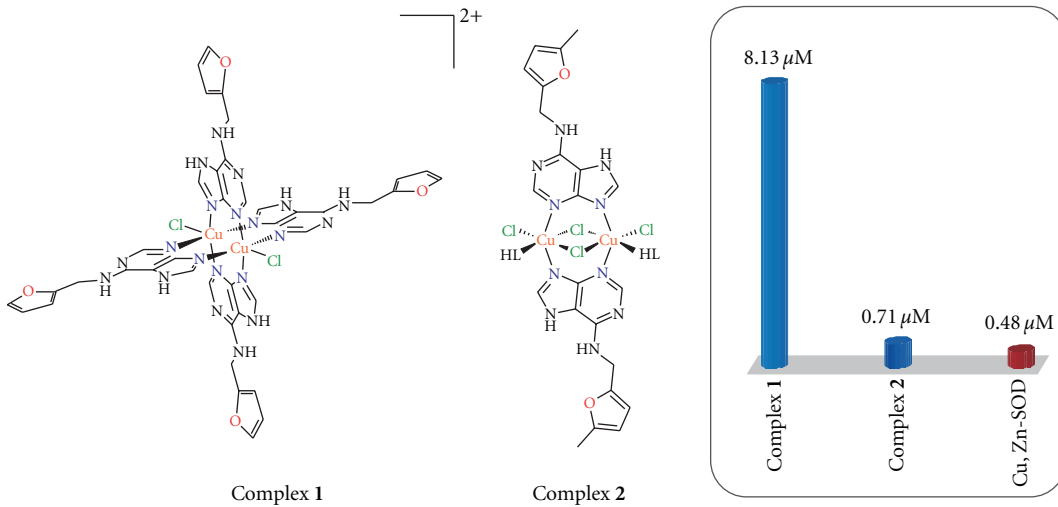


FIGURE 6: Proposed structures of the presented complexes **1** and **2** with their *in vitro* SOD-mimic activity (expressed as the IC_{50} values).

3.4. Evaluation of SOD-Mimic Activity. The antiradical activity was evaluated for the presented compounds by the *in vitro* SOD-mimic test performed by a slightly modified indirect chemical method [13]. The results for the tested Cu(II) complexes, as compared with native bovine Cu, Zn-SOD ($IC_{50} = 0.48 \mu\text{M}$, [13]), indicated that these compounds could be considered good SOD-mimics (Figure 6) because the IC_{50} values equalled 8.13 (for **1**) and 0.71 μM (**2**). The more potent compound **2** exhibited the activity of the same order of magnitude as Cu, Zn-SOD as well as the most active Cu(II) complexes with adenine derived N-donor ligands ($IC_{50} = 0.253\text{--}1.250 \mu\text{M}$) prepared previously

in our laboratory and having additionally strong *in vivo* antidiabetic activity [9]. Direct comparisons of SOD-mimic activity results of complexes **1** and **2** with other Cu(II) complexes reported before are somewhat complicated by diverse methodology used for the generation of superoxide. What can only be compared is the ratio of the activity of the studied compound and the native SOD determined by the same procedure. Using this logic, the activity of the herein presented complex **1** (17 \times higher IC_{50} than native bovine Cu, Zn-SOD) is comparable or even better than various reported Cu(II) complexes exhibiting pharmacological properties connected to the dismutation of the superoxide

radical. For example, the Cu(II) complex used as a SOD mimic in veterinary practice [$\text{Cu}_2(\text{indo})_4(\text{DMSO})_2$] (indo = indomethacin) was in the testing found to have ca 6 × higher IC₅₀ than SOD [30], while the Cu(II) complexes possessing antirheumatic activity involving D-penicillamine (200 × higher IC₅₀ than SOD) or 2-merkaptopropionylglycine (150 × higher IC₅₀ than SOD) [31] can be in this comparison understood as worse SOD-mimics than complex **1**.

From the general point of view of the SOD-mimic active types of Cu(II) complexes, it has already been shown that the dimeric compounds tend to be more active than the mononuclear ones. It was previously proven for example for the dimeric and monomeric Cu(II) complexes with tripodal polypyridyl-amine ligands, where the monomeric complexes (IC₅₀ = 5.02–140.0 μM) were significantly less antioxidant active than the dimeric ones (IC₅₀ = 0.54–0.76 μM) [32]. It is generally explained by the possible cooperation of both Cu(II) centres in electron transfer and binding of free radicals. This finding can be also demonstrated by data recently acquired in our laboratory concerning the SOD-mimic activity of Cu(II) complexes involving various derivatives of the title molecule kinetin. The mononuclear complex [$\text{Cu}(\text{H}_2\text{O})_2(\text{L}^a)_2(\text{phen})$] exhibited a very low antioxidant effect (IC₅₀ = 189.6 μM). The dimeric complex [$\text{Cu}_2(\mu_2\text{-Ac})_4(\text{HL}^b)_2$] bridged by four acetate groups was more active (57.4 μM) [33], however, still not reaching the activity exhibited by the herein presented compounds; HL^a = 2-chloro-N6-furfuryladenine, HL^b = 2-chloro-N6-furfuryl-9-isopropyladenine.

The active site of Cu, Zn-SOD has the Cu(II) atom coordinated by four imidazole moieties from the histidine molecules and by one water molecule in the distorted square pyramid, with the CuN₄O chromophore [34]. The copper and zinc metal centres are bridged by the deprotonated N-donor imidazole moiety from one of the histidine molecules. In complex **1**, each Cu(II) atom is also pentacoordinated by four nitrogen atoms from the N-donor bridging organic ligands (HL¹) and by one chlorido ligand, thus forming the CuN₄Cl chromophore. On the other hand, in complex **2**, the Cu(II) atoms are octahedrally coordinated by three nitrogen atoms from the bridging and terminal organic ligands (HL²), two bridging and one terminal chlorido ligands in the CuN₃Cl₃ donor set. There are two aspects from the structural point of view that could help to explain the higher SOD-mimic activity of the herein presented complexes as compared to the previously reported Cu(II) complexes involving kinetin derivatives [33]. Firstly, the higher activity of **1** and **2** might be connected with the type of bridging between the copper centres, which is different from the previously described dimeric complexes (acetato bridges). Therefore, the presence of the bridging bidentate N-donor HLⁿ molecules in **1** and **2** (similarly to bridging imidazole in native Cu, Zn-SOD) might help to mimic, to some extent, the structure of the active centre of SOD-enzyme and thus be able to, just like the bridging imidazole, participate in the mechanism of dismutation. Secondly, besides the type of bridging; what clearly also influences the antioxidant activity of a Cu(II) complex is the

accessibility of the metal ion for superoxide [32]. This might be the reason why the previously reported dimeric Cu(II) chlorido complexes of N6-benzyladenines are more than twenty times more active than the analogical perchlorate compounds both involving the same type of bridging bidentate N-donor ligands [8, 9]; for example, [$\text{Cu}_2(\mu_2\text{-4MeOHL}^x)_4\text{Cl}_2\text{Cl}_2\cdot 2\text{H}_2\text{O}$] (IC₅₀ = 0.687 μM) contrary to [$\text{Cu}_2(\mu_2\text{-4MeOHL}^x)_4(\text{ClO}_4)_2](\text{ClO}_4)_2$ (IC₅₀ = 14.41 μM); 4MeOHL^x = N6-(4-methoxybenzyl)adenine. The bulky ClO₄⁻ anionic ligand makes it more difficult for superoxide to access the metal centre and to substitute this ligand on copper in the suggested first phase of the dismutation process [8]. The same logic might be applied when explaining the different activity of the herein presented compounds **1** and **2**. The compound **1** is more than ten times less active than **2**, because the copper centre accessibility could be lower in the dimeric core of **1** due to the presence of four bulky N3,N9-bridging kinetin molecules, while the bridging in **2** is formed by two N3,N9-bridging HL² molecules and two bridging chlorides with higher bond length and angle flexibility. The higher activity of **2** with the {Cu(μ-HLⁿ)₂(μ-Cl)₂Cu} bridging moiety is in agreement with the finding that the most active Cu(II) compound involving an adenine derivative has the composition [$\text{Cu}_2(\mu\text{-HL}^a)_2(\mu\text{-Cl})_2\text{Cl}_2$] [9] with the same bridging unit as **2**.

4. Conclusion

In conclusion, this work presents synthesis and characterization of two Cu(II) complexes of the compositions [$\text{Cu}_2(\mu_2\text{-HL}^1)_4\text{Cl}_2$] (1) and [$\text{Cu}_2(\mu\text{-HL}^2)_2(\mu\text{-Cl})_2(\text{HL}^2)_2\text{Cl}_2\cdot 4\text{H}_2\text{O}$] (2), where HL¹ stands for kinetin and HL² for methyl-derived kinetin (N6-(5-methylfurfuryl)adenine). The complexes were evaluated for their antiradical activity, which resulted in the IC₅₀ values equalling 8.13 μM (complex **1**) and 0.71 μM (**2**), therefore the presented compounds might be characterized as auspicious SOD-mimics.

Acknowledgments

The authors would like to thank the Operational Program Research and Development for Innovations—European Regional Development Fund (CZ.1.05/2.1.00/03.0058), the Operational Program Education for Competitiveness—European Social Fund (Project CZ.1.07/2.3.00/20.0017) and Palacký University (Student Project PrF_2011_014 and PrF_2012_009) for financial support, Dr. Pavel Štarha for TG/DTA thermal measurements, Mrs. Pavla Richterová for performing the CHN elemental analyses.

References

- [1] I. Fridovich, "Superoxide dismutases," *Annual Review of Biochemistry*, vol. 44, pp. 147–159, 1975.
- [2] K. Y. Xu and P. Kuppusamy, "Dual effects of copper-zinc superoxide dismutase," *Biochemical and Biophysical Research Communications*, vol. 336, no. 4, pp. 1190–1193, 2005.
- [3] J. J. A. Hendriks, C. E. Teunissen, H. E. De Vries, and C. D. Dijkstra, "Macrophages and neurodegeneration," *Brain Research Reviews*, vol. 48, no. 2, pp. 185–195, 2005.

- [4] I. Margaill, M. Plotkine, and D. Lerouet, "Antioxidant strategies in the treatment of stroke," *Free Radical Biology and Medicine*, vol. 39, no. 4, pp. 429–443, 2005.
- [5] D. Jay, H. Hitomi, and K. K. Griendling, "Oxidative stress and diabetic cardiovascular complications," *Free Radical Biology and Medicine*, vol. 40, no. 2, pp. 183–192, 2006.
- [6] R. Govindarajan, M. Vijayakumar, and P. Pushpangadan, "Antioxidant approach to disease management and the role of 'Rasayana' herbs of Ayurveda," *Journal of Ethnopharmacology*, vol. 99, no. 2, pp. 165–178, 2005.
- [7] K. G. Strothkamp and S. J. Lippard, "Chemistry of the imidazolate-bridged bimetallic center in the Cu-Zn superoxide dismutase and its model compounds," *Accounts of Chemical Research*, vol. 15, no. 10, pp. 318–326, 1982.
- [8] A. Klanicová, Z. Trávníček, J. Vančo, I. Popa, and Z. Šindelář, "Dinuclear copper(II) perchlorate complexes with 6-(benzylamino)purine derivatives: synthesis, X-ray structure, magnetism and antiradical activity," *Polyhedron*, vol. 29, no. 13, pp. 2582–2589, 2010.
- [9] P. Štarha, Z. Trávníček, R. Herchel, I. Popa, P. Suchý, and J. Vančo, "Dinuclear copper(II) complexes containing 6-(benzylamino)purines as bridging ligands: synthesis, characterization, and in vitro and in vivo antioxidant activities," *Journal of Inorganic Biochemistry*, vol. 103, no. 3, pp. 432–440, 2009.
- [10] J. Barciszewski, S. I. S. Rattan, G. Siboska, and B. F. C. Clark, "Kinetin—45 years on," *Plant Science*, vol. 148, no. 1, pp. 37–45, 1999.
- [11] J. A. Kuhnle, G. Fuller, J. Corse, and B. E. Mackey, "Antisenescent activity of natural cytokinins," *Physiologia Plantarum*, vol. 41, pp. 14–21, 1977.
- [12] E. König and G. König, *Magnetic Properties of Coordination and Organometallic Transition Metal Compounds*, vol. 10 of *Landolt-Börnstein: Numerical Data and Functional Relationships in Science and Technology*, Springer, Berlin, Germany, 1966.
- [13] J. Vančo, O. Švajlenová, E. Račanská, J. Muselík, and J. Valentová, "Antiradical activity of different copper(II) Schiff base complexes and their effect on alloxan-induced diabetes," *Journal of Trace Elements in Medicine and Biology*, vol. 18, no. 2, pp. 155–161, 2004.
- [14] C. M. Mikulski, S. Cocco, N. De Franco, T. Moore, and N. M. Karayannis, "Adenine complexes with divalent 3D metal chlorides," *Inorganica Chimica Acta*, vol. 106, no. 2, pp. 89–95, 1985.
- [15] H. Arend and J. J. Connelly, "Tetramethoxysilane as gel forming agent in crystal growth," *Journal of Crystal Growth*, vol. 56, no. 3, pp. 642–644, 1982.
- [16] W. J. Geary, "The use of conductivity measurements in organic solvents for the characterisation of coordination compounds," *Coordination Chemistry Reviews*, vol. 7, no. 1, pp. 81–122, 1971.
- [17] K. Nakamoto, *Infrared and Raman Spectra of Inorganic and Coordination Compounds*, Wiley-Interscience, New York, NY, USA, 5th edition, 1997.
- [18] E. I. Solomon and A. B. P. Lever, *Inorganic Electronic Structure and Spectroscopy, Applications and Case Studies*, vol. 2, Wiley, New York, NY, USA, 1999.
- [19] O. Kahn, *Molecular Magnetism*, Wiley, New York, NY, USA, 1993.
- [20] R. Boča, *Theoretical Foundation of Molecular Magnetism*, Elsevier, Amsterdam, The Netherlands, 1999.
- [21] G. A. van Albada, I. Mutikainen, U. Turpeinen, and J. Reedijk, "Crystal structure, magnetism and spectroscopy of two strongly antiferromagnetically coupled dinuclear Cu(II) paddlewheel-like compounds with 4-azabenzimidazole as a ligand," *Polyhedron*, vol. 25, no. 17, pp. 3278–3284, 2006.
- [22] P. De Meester and A. C. Skapski, "Crystal structure of dichlorotetra- μ -adenine-dicopper(II) chloride hexahydrate," *Journal of the Chemical Society A*, pp. 2167–2169, 1971.
- [23] D. Sonnenfroh and R. W. Krelick, "Exchange coupling in copper dimers with purine ligands," *Inorganic Chemistry*, vol. 19, no. 5, pp. 1259–1262, 1980.
- [24] A. Terzis, A. L. Beauchamp, and R. Rivest, "Crystal and molecular structure of tetra- μ -adenine-diaquodiacopper(II) perchlorate dihydrate, $[\text{Cu}_2(\text{C}_5\text{H}_5\text{N}_5)_4(\text{H}_2\text{O})_2](\text{ClO}_4)_4 \cdot 2\text{H}_2\text{O}$," *Inorganic Chemistry*, vol. 12, no. 5, pp. 1166–1170, 1973.
- [25] A. M. Schuitema, A. F. Stassen, W. L. Driessens, and J. Reedijk, "Synthesis, magnetic properties, and crystal structure of dinuclear antiferromagnetic $[\text{Cu}_2(5\text{-aminomethyl-3-methylpyrazole})_2\text{Cl}_4]$," *Inorganica Chimica Acta*, vol. 337, pp. 48–52, 2002.
- [26] K. Emerson, A. Emad, R. W. Brookes, and R. L. Martin, "Two magnetically subnormal copper halide complexes with 1,8-naphthyridine," *Inorganic Chemistry*, vol. 12, no. 5, pp. 978–981, 1973.
- [27] C. Mealli and F. Zanobini, "X-ray crystal structure of the anti-ferromagnetic binuclear dichloro- μ -dichloro- μ -di(1,8-naphthyridine)-dicopper complex," *Journal of the Chemical Society, Chemical Communications*, no. 2, pp. 97–98, 1982.
- [28] M. Maloň, Z. Trávníček, M. Maryško et al., "Metal complexes as anticancer agents 2. Iron(III) and copper(II) bio-active complexes with N⁶-benzylaminopurine derivatives," *Inorganica Chimica Acta*, vol. 323, no. 1-2, pp. 119–129, 2001.
- [29] Z. Trávníček, M. Maloň, Z. Šindelář et al., "Preparation, physicochemical properties and biological activity of copper(II) complexes with 6-(2-chlorobenzylamino)purine (HL_1) or 6-(3-chlorobenzylamino)purine (HL_2). The single-crystal X-ray structure of $[\text{Cu}(\text{H}^+\text{L}_2)_2\text{Cl}_3]\text{Cl} \cdot 2\text{H}_2\text{O}$," *Journal of Inorganic Biochemistry*, vol. 84, no. 1-2, pp. 23–32, 2001.
- [30] J. E. Weder, C. T. Dillon, T. W. Hambley et al., "Copper complexes of non-steroidal anti-inflammatory drugs: an opportunity yet to be realized," *Coordination Chemistry Reviews*, vol. 232, no. 1-2, pp. 95–126, 2002.
- [31] N. A. Roberts and P. A. Robinson, "Copper chelates of antirheumatic and anti-inflammatory agents: their superoxide dismutase-like activity and stability," *British Journal of Rheumatology*, vol. 24, no. 2, pp. 128–136, 1985.
- [32] K. Jitsukawa, M. Harata, H. Arii, H. Sakurai, and H. Masuda, "SOD activities of the copper complexes with tripodal polypyridylamine ligands having a hydrogen bonding site," *Inorganica Chimica Acta*, vol. 324, no. 1-2, pp. 108–116, 2001.
- [33] R. Novotná, R. Herchel, and Z. Trávníček, "Structurally varied Cu(II) complexes involving kinetin and its derivatives: synthesis, characterization and evaluation of SOD-mimic activity," *Polyhedron*, vol. 34, pp. 56–66, 2012.
- [34] A. F. Miller, "Superoxide dismutases: active sites that save, but a protein that kills," *Current Opinion in Chemical Biology*, vol. 8, no. 2, pp. 162–168, 2004.

Studies on Synthetic and Natural Melanin and Its Affinity for Fe(III) Ion

T. G. Costa,¹ R. Younger,² C. Poe,³ P. J. Farmer,³ and B. Szpoganicz¹

¹Department of Chemistry, Federal University of Santa Catarina, CP476, 88040-900 Florianópolis, SC, Brazil

²Department of Chemistry, University of California, Irvine, Irvine, CA 96729, USA

³Department of Chemistry and Biochemistry, Baylor University, Waco, TX 76706, USA

Correspondence should be addressed to B. Szpoganicz, bruno.s@ufsc.br

Academic Editor: Viktor Brabec

In this work, we measured the metal-binding sites of natural and synthetic dihydroxyindole (DHI) melanins and their respective interactions with Fe(III) ions. Besides the two acid groups detected for the DHI system: catechol (Cat) and quinone-imine (QI), acetate groups were detected in the natural oligomer by potentiometric titrations. At acidic pH values, Fe(III) complexation with synthetic melanin was detected in an $\text{Fe(OH)}(\text{CatH}_2\text{Cat})$ interaction. With an increase of pH, three new interactions occurred: dihydroxide diprotonated catechol, $\text{Fe(OH)}_2(\text{CatH}_2\text{Cat})^-$, dihydroxide monoprotonated catechol, $[\text{Fe(OH)}_2(\text{CatHCat})]^{2-}$, and an interaction resulting from the association of one quinone-imine and a catechol group, $[\text{Fe(OH)}_2(\text{Qi}^-)(\text{CatHCat})]^{3-}$. In the natural melanin system, we detected the same interactions involving catechol and quinone-imine groups but also the metal interacts with acetate group at pH values lower than 4.0. Furthermore, interactions in the synthetic system were also characterized by infrared spectroscopy by using the characteristic vibrations of catechol and quinone-imine groups. Finally, scanning electronic microscopy (SEM) and energy-dispersive X-ray (EDS) analysis were used to examine the differences in morphology of these two systems in the absence and presence of Fe(III) ions. The mole ratio of metal and donor atoms was obtained by the EDS analysis.

1. Introduction

Melanin is an ubiquitous oligomeric pigment found in plants and in the hair, skin (*eumelanins*), and brain (*neuromelanins*) of animals. The two major chemical monomers are 5,6-dihydroxyindole (DHI) and 5,6-dihydroxyindole-2-carboxylic acid (DHICA) as shown in Figure 1 [1, 2]. The pigment can be synthesized, usually by auto-oxidation of catechols or by tyrosinase-catalyzed oxidation of tyrosine or Dopa [3, 4], to give oligomeric sheets as illustrated in Figure 2. In this work, we also use an enzymatic process for the isolation of *eumelanin* from human black hair, first described by Novellino et al. [5], which allows isolation of intact pigment particles for structural characterization.

Previous reports have shown that the affinity of divalent metals like Cu(II) and Zn(II) for melanin has a significant effect on the structure of melanin aggregates [6]. The binding of metal ions to melanin also accelerates its bleaching under

air or peroxide; for example, melanin-copper complexation has been implicated in Fenton-like catalytic oxidations [7]. Other researchers have studied the binding of Fe(III) by melanins [8–10] and shown that this ion accelerates the air oxidation of DHI and DHICA and suggested that a similar increase in iron-promoted oxidative stress in the substantia nigra is linked to the loss of melanin observed during Parkinson's disease [11–15]. In related studies, we have shown that metal ion complexes, which induce passive uptake of the metal ions into cells, show significant toxicity towards melanin-producing melanoma cells [16].

In this work, we measure the interaction of synthetic melanin (DHI) and natural melanin with Fe(III) ions using potentiometric titrations in combination with mathematical fitting functions. The results are correlated with infrared spectroscopy and scanning electronic microscopy with energy-dispersive X-ray analysis to quantify the binding

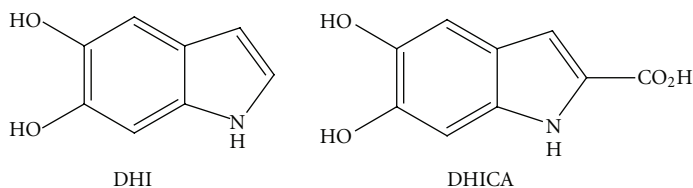


FIGURE 1: Precursors of the melanin oligomers.

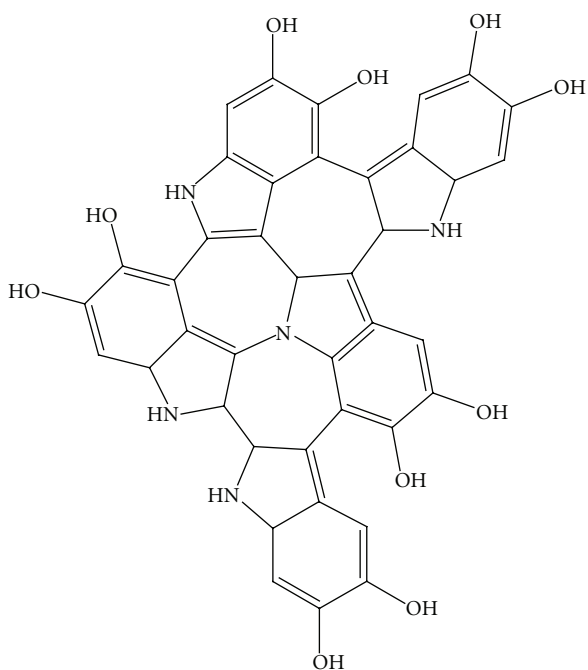


FIGURE 2: Model of DHI melanin oligomerization.

sites and to see the morphological differences in these types of melanin.

2. Experimental

2.1. DHI Melanin. Stock solutions of synthetic melanin were derived from air oxidation of 5,6-dihydroxyindole (DHI), generated *in situ* by hydrolysis of 5,6-diacetoxyindole (DAI) obtained from TCI America, Portland. The DAI starting material (120 mg, 0.5145 mmol) was treated with 20% molar excess of KOH (1.28 mmol in 250 mL in deionized water), and the mixture was vigorously stirred until the DAI was completely reacted [6]. DAI is not very soluble in water, but as the reaction progresses over 6 hours, all of the DAI is consumed.

2.2. Natural Melanin Extraction. Hair melanin was obtained by the method described by Novellino et al. [5]. Locks of black hair were washed several times with acetone, distilled water, and a few portions of chloroform. Afterwards, the hair was dried at room temperature and cut to bands of about 5 cm. About 5 g of hair was homogenized with a

glass pestle in 50 mL of 0.1 M phosphate buffer at pH 7.5, and the homogenate was submitted to the following treatments: dithiothreitol (0.5 g) was added and the resulting mixture stirred at 37°C under a stream of argon for 18 h. Then, proteinase K (10 mg) and dithiothreitol (0.5 g) were added to the mixture and left stirring at 37°C under argon for an additional 18 h. The mixture was centrifuged for 10 min, and the resulting pellet extensively rinsed with water. The precipitate was then suspended in 30 mL of 0.1 M phosphate buffer pH 7.5, with papain (10 mg) and dithiothreitol (50 mg). This mixture was stirred for 18 h at 37°C under argon and centrifuged as earlier. The black pellet collected, after 6 washings with water, was resuspended in 10 mL of 0.1 M phosphate buffer, pH 7.5, with protease (10 mg) and dithiothreitol (20 mg) added, and the mixture was stirred for 18 h at 37°C under an argon stream. An oxygen-free solution of 2% w/v Triton X-100 was added, and the mixture was stirred for 4 h at room temperature under argon and then centrifuged (4000 rpm) for 20 min. After washing once with water:methanol 1 : 1 v/v, and four times with water, the black pellet was treated again with protease and dithiothreitol as described earlier. The pigment pellet, collected by centrifugation (4000 rpm for 20 min), was dried over NaOH in presence of CaCl₂ for 24 h to give 200 mg of melanin.

2.3. Potentiometric Titration. The potentiometric studies were carried out in water solution with a Metrohm Titrino plus 350 automatic titrator combined with an Ag/AgCl electrode. The experimental samples were analyzed in a 50 mL sealed thermostated cell that was maintained at 25°C, bubbled with argon to ensure an inert atmosphere. The pH of the experimental solution (20 mL of DHI melanin) was adjusted to 11 with 0.100 M KOH (CO₂ free, Backer Dilut-It) and back-titrated with 0.100 M HCl. For the native melanin, a 40 mg sample of the melanin particles extracted from hair was dispersed in 20 mL of twice-distilled water. For the Fe(III)-treated samples, melanin solutions were titrated in the presence of metal ions in melanin:metal ion molar ratio of 2 : 1. The Fe(III) solutions were standardized with EDTA [17], and the amount of added HCl to avoid metal hydrolysis was determined by Gran's Plot [18]. The melanin samples were homogenized for 30 minutes to guarantee total equilibration before measurements. The pH of the experimental solutions was brought to 11.0 and back titrated with aliquots of 0.100 M HCl until pH 3.0. The time to reach the equilibrium in each experimental data was about 15 minutes.

2.4. Infrared Studies. For the IR studies, synthetic melanin was first complexed with Fe(III) by Korytowski method [19] with little modification; this method is used for complexes formed with oligomers and bimolecular systems. A portion of stock DHI solution (40 mL) was mixed with 5 mL of 0.01 M FeCl_3 solution, and the pH of solutions was brought to 4.0 and 10.0, adjusted by 0.1 M HCl or 0.1 M NaOH solution. $\text{FeCl}_3 \cdot 6\text{H}_2\text{O}$, (Vetec Ltd.) was used. The mixtures after 3 h were precipitate at 0°C and filtered, the solid was washed with twice-distilled water and dried at vacuum.

The analysis was carried out in KBr pellets with approximately 5–10 mg of the samples at spectrometer Perkin-Elmer FT-IR 1600 with computer detect system, in the region of 500 to 4000 cm^{-1} .

2.5. Scanning Electron Microscopy and EDS Analysis. The samples with pure synthetic melanin and those coordinated to Fe(III) (as described in 2.4) were prepared with silver glass and coated with gold. A Philips XL 30 SEM was used to examine the samples at 30 kV and a 20° tilt. Images were captured using the digital software image acquisition, accolade with the SEM. The EDS spectrum was obtained in the same instrument.

2.6. Electrochemical Studies. A 6.0 mg portion of 5,6-diacetoxyindole was dissolved in 12.5 mL degassed ethanol in a glovebox under nitrogen, to which 0.55 mL 0.1 M NaOH was added. The solution was stirred and stood for 1 hour, then diluted up to 25 mL with pH 7.0, 50 mM phosphate buffer. An ITO plate was submerged in the solution, and polymerization of DHI on the plate was done using cyclic voltammetry for 15 cycles at a sweep rate of 50 mV s^{-1} from -0.4 V to 0.6 V versus Ag/AgCl. Solutions of 0.1 M CuCl_2 , $\text{ZnSO}_4 \cdot 7\text{H}_2\text{O}$, FeCl_3 , and $\text{Fe}(\text{SO}_4)_2(\text{NH}_4)_2 \cdot 6\text{H}_2\text{O}$ were prepared in atmosphere, degassed, and loaded into glovebox. Freshly made poly-DHI films were soaked in the metal ion solutions overnight, then rinsed with deionized water and stored under nitrogen. UV-Vis spectra were recorded using a 2-neck UV-Vis electrochemical cell in a solution of 0.1 M LiCl, pH 7, 50 mM phosphate buffer. Electrodes were attached, and spectroelectrochemical measurements were made using bulk electrolysis at various potentials versus Ag/AgCl.

3. Results and Discussion

3.1. DHI Melanin System. The titration curves for the DHI melanin in the presence and absence of Cu(II), Zn(II), and Fe(III) are shown in Figure 3. The buffer region above pH 9 in the free DHI melanin can be attributed to the acid-base equilibrium involving catecholic groups which are present in melanin. The strong buffer below pH 7 can be attributed to the acid-base equilibrium of quinone-imine group [6]. The acetate molecules present in the solution due to DAI hydrolysis were included in the calculation of the DHI pKa's and the interaction constants with Fe(III) ion. The amount of each group was calculated using the best-fit equilibrium constants in the Best7 program. Also

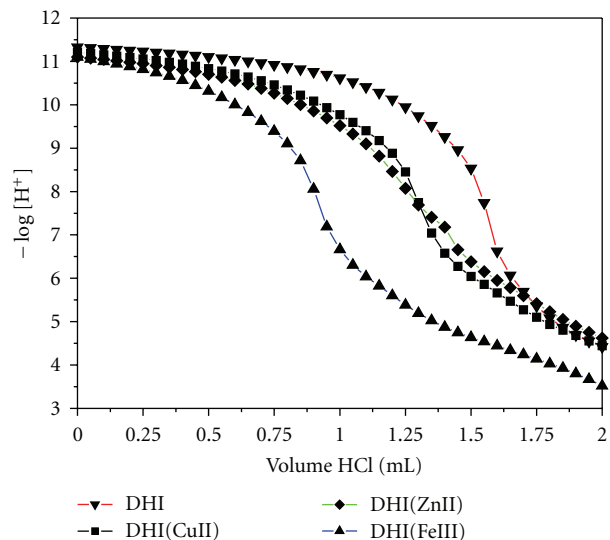


FIGURE 3: The titration curves of DHI melanin in the absence and presence of metals.

the interaction distribution curves of the Fe(III)-complexed sites in the DHI-melanin were calculated using the Species program [20].

The metal curves (Figure 3) are below the free DHI melanin curve. The curve in the presence of Fe(III) is much lower than those in the presence of Cu(II) and Zn(II) ions, indicating that the Fe(III) ion interacts more strongly than Cu(II) or Zn(II) ions with melanin. The experimental data was analyzed with the BEST7 [20] program and the equilibrium constants that were determined are shown in Table 1. The equilibrium constants of the interactions with Cu(II) and Zn(II) ions were calculated previously [6]. The equilibriums detected in the DHI system with Fe(III) are shown in Scheme 1.

The distribution curves of the interactions in the DHI melanin system (Figure 4) show that at acidic pH values, the monohydroxide $\text{Fe(OH)}(\text{CatH}_2\text{Cat})$ interaction predominates. At higher pH values, the dihydroxide $[\text{Fe(OH)}_2(\text{CatH}_2\text{Cat})]^-$ interaction increases and is the predominant interaction at pH 8.4–10.3. At pH values above 9, two other interactions appear: the dihydroxide Fe(III) monoprotonated catechol, $[\text{Fe(OH)}_2(\text{CatHCat})]^-$, and the dihydroxide Fe(III) quinone-imine monoprotonated catechol, $[\text{Fe(OH)}_2(\text{Qi}^-)(\text{CatHCat})]^{3-}$. These equilibriums are shown in Figure 4.

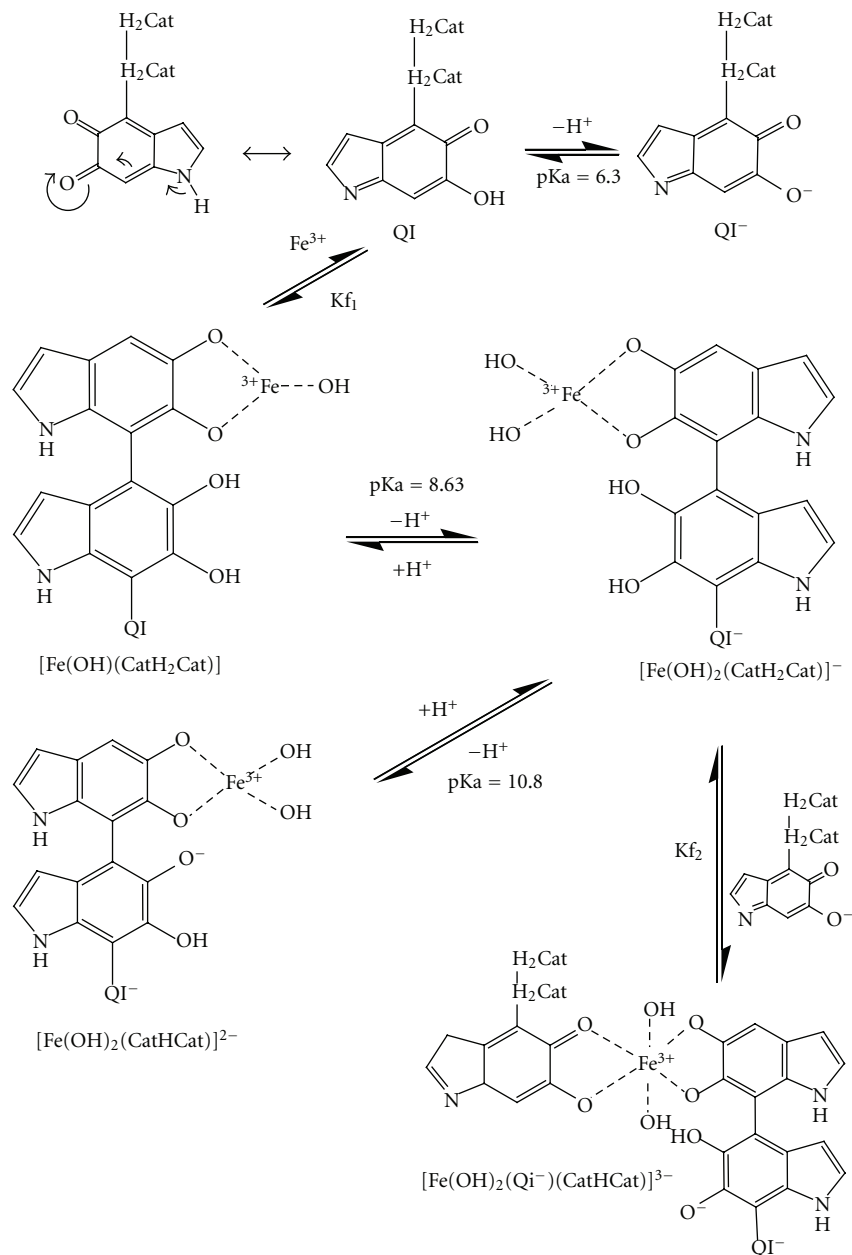
3.2. Natural Melanin System. As with synthetic melanin, the natural melanin shows the same buffer region above pH 9 which is a characteristic of the presence of catechol groups (Figure 5). The interaction of Fe(III) ion is shown by comparing the two curves (in the presence and absence of the metal ion). Also, we can see the buffer in pH 6 on the melanin Fe(III) curve; it represents the complexation of Fe(III) with the quinone-imine groups.

In natural melanin, the major group is catechol, and the amount of this group found by potentiometric titration

TABLE 1: Equilibrium constants for the interactions of DHI melanin-Fe(III) systems*.

Equilibria	$\log K$ (SD)
$[\text{Fe}(\text{OH})(\text{CatH}_2\text{Cat})][\text{H}^+]/[\text{Fe}^{3+}][\text{CatH}_2\text{Cat}^{2-}]$	42.52 (1.03)
$[\text{Fe}(\text{OH})_2(\text{CatH}_2\text{Cat})^-][\text{H}^+]/[\text{Fe}(\text{OH})(\text{CatH}_2\text{Cat})]$	-8.63 (0.11)
$[\text{Fe}(\text{OH})_2(\text{CatH}_2\text{Cat})^{2-}][\text{H}^+]/[\text{Fe}(\text{OH})_2(\text{CatH}_2\text{Cat})^-]$	-10.80 (0.09)
$[\text{Fe}(\text{OH})_2(\text{Qi}^-)(\text{CatH}_2\text{Cat})]^{3-}/[\text{Fe}(\text{OH})_2(\text{CatH}_2\text{Cat})^{2-}][\text{Qi}^-]$	5.0 (0.2)

* Obtained by fitting the average of three or more titrations. SD is standard deviation.

SCHEME 1: Chemical equilibria involving all of the species detected, where QI/QI⁻ and H₂Cat/HCat⁻/Cat²⁻ are protonated and deprotonated forms of quinone-imine and catechol groups.

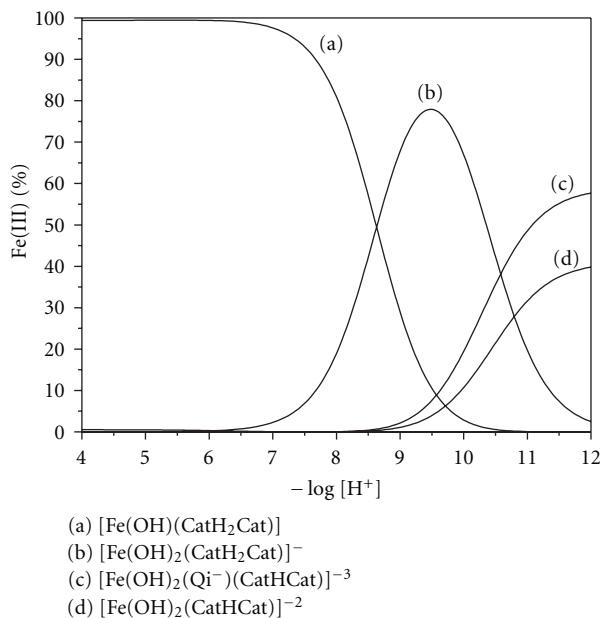


FIGURE 4: Interaction distribution curves of a DHI melanin solution containing 2.00 mM of DHI melanin (in a 2.0:0.5 ratio of catechol:quinone-imine) and 0.99 mM of Fe(III) ions at 25.0°C.

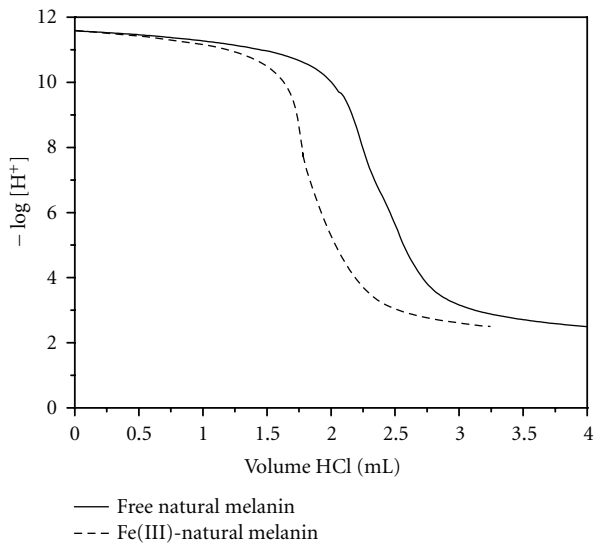


FIGURE 5: The titration curves for natural melanin in the absence and presence of Fe(III).

is 3.977 mmol per gram of melanin; the explanation for the major group is that the precursor of natural melanin is the natural amino acid tyrosine, which by hydroxylation reaction catalyzed by tyrosinase leads to the formation of catechol groups in the melanin structure. We also detect quinone-imine 0.300 mmol per gram and 1.188 mmol of acetate groups per gram of melanin. The pKa values for the major groups present in the natural melanin are given in Table 2.

TABLE 2: Dissociation constants of major groups in natural melanin*.

Equilibria	$-\log K_a$ (SD)
$[\text{Ac}^-][\text{H}^+]/[\text{HAc}]$	4.35 (0.10)
$[\text{Qi}^-][\text{H}^+]/[\text{HQi}]$	6.30 (0.08)
$[\text{HCat}^-][\text{H}^+]/[\text{H}_2\text{Cat}]$	10.50 (0.12)
$[\text{Cat}^{2-}][\text{H}^+]/[\text{HCat}^-]$	12.81 (0.09)

* Obtained by fitting the average of three or more titrations.

The distribution curves of the interactions detected by potentiometric titration are shown in Figure 6. The interactions detected in low pH values 2–4 are resulting from the competition of Fe(III) by quinone-imine, acetate, and catechol groups (a, b, and c), represented by $\text{Fe}(\text{Ac})^{2+}$, $\text{Fe}(\text{Qi})^{2+}$, and $\text{Fe}(\text{OH})(\text{Cat})^+$. The interactions of Fe(III) with catechol group predominate at pH values above 3.0. Those interactions are represented by $\text{Fe}(\text{OH})(\text{Cat})$, $\text{Fe}(\text{OH})(\text{Cat})(\text{Qi})^-$, $\text{Fe}(\text{OH})_2(\text{Cat})(\text{Qi})^{2-}$, and $\text{Fe}(\text{OH})_2(\text{Cat})_2^{3-}$, and the equilibrium constants of all interactions detected are shown in Table 3.

The strong complexation of melanin by Fe(III) in solution was shown by Franz and colleagues [8] using brain melanins, *neuromelanins*, where it was found that acidic pH in the melanin is 1:1 coordination with Fe(III). In our work, we detail the coordinate groups in this pH range in this proportion: $\text{Fe}(\text{Ac})^{2+}$, $\text{Fe}(\text{Qi})^{2+}$, and $\text{Fe}(\text{OH})(\text{Cat})^+$, at pH 4–8, the formation of melanin 2:1 species melanin:metal, in our system represented by the species $\text{Fe}(\text{OH})(\text{Cat})(\text{Qi})^-$, and higher pH values promote the formation of dihydroxy species.

3.3. Infrared Studies. The IR spectra of synthetic melanin in the absence and presence of Fe(III) ions are shown in Figure 7. Shurygina et al. [21] did one of the first IR analyses of melanin and identified three characteristic peaks: $\sim 3300 \text{ cm}^{-1}$, representative of catechol groups, $\sim 1625 \text{ cm}^{-1}$, representative of aromatic C=C and/or carboxylate groups as well as nitrogen containing heterocycles, and $\sim 1470 \text{ cm}^{-1}$, representative of o-hydroxy quinone groups. The complexation of Fe(III) is identified by the shift of the 3313 cm^{-1} peak, characteristic of melanin in the absence of Fe(III), to 3395 cm^{-1} at pH 4 and 3407 cm^{-1} at pH 10 for melanin in the presence of the metal ion. The presence of quinone-imine is shown at 1472 cm^{-1} for melanin alone. In the presence of metal ions, this peak shifts to lower wavenumbers (1468 cm^{-1} at pH 4 and 1350 cm^{-1} at pH 10). A shift in the C=O stretching in organic compounds to lower wavenumbers by metal complexation was reported by Nakamoto et al. [22]. The interaction of Fe(III) with the quinone-imine group was found in the potentiometric study (Figure 3).

3.4. Scanning Electron Microscopy and EDS Analysis. The scanning electron microscopy images of synthetic and natural melanin are shown in Figures 8 and 9. Simon et al. [23] used SEM to examine the structure of natural and synthetic eumelanins. It was reported that the synthetic

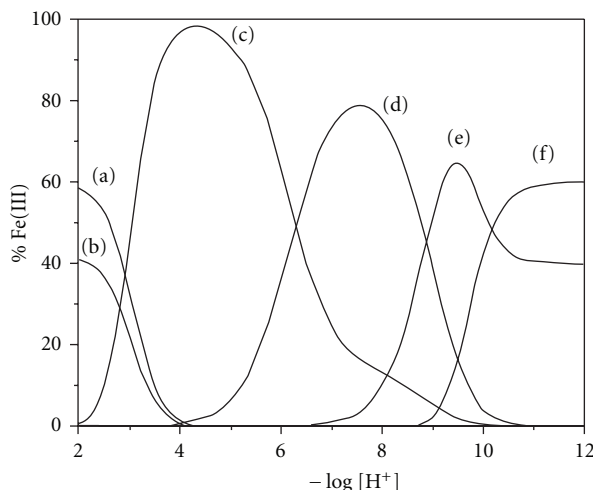


FIGURE 6: Interaction distribution curves of a natural melanin solution containing 0.00994 mmol of Fe(III) ions and 0.0370 mmol of melanin (40 mg of natural melanin) at 25.0°C., where (a) = $\text{Fe}(\text{Ac})^{2+}$, (b) = $\text{Fe}(\text{Qi})^{2+}$, (c) = $\text{Fe}(\text{OH})(\text{Cat})$, (d) = $\text{Fe}(\text{OH})(\text{Cat})(\text{Qi})^-$, (e) = $\text{Fe}(\text{OH})_2(\text{Cat})(\text{Qi})^{2-}$, and (f) = $\text{Fe}(\text{OH})_2(\text{Cat})_2^{3-}$.

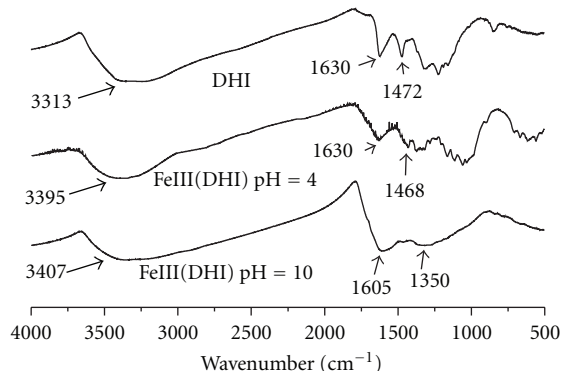


FIGURE 7: IR spectra of synthetic melanin in the absence and presence of Fe(III) ions at different pH values.

TABLE 3: Equilibrium constants for the interactions of natural melanin-Fe(III)*.

Equilibrium	$\log K$ (SD)
$[\text{Fe}(\text{Ac})]^{2+}/[\text{Fe}^{3+}][\text{Ac}^-]$	5.20 (0.20)
$[\text{Fe}(\text{Qi})^{2+}]/[\text{Fe}^{3+}][\text{Qi}^-]$	5.73 (0.22)
$[\text{Fe}(\text{OH})(\text{Cat})][\text{H}^+]/[\text{Fe}^{3+}][\text{Cat}^{2-}]$	23.53 (0.18)
$[\text{Fe}(\text{OH})(\text{Cat})(\text{Qi})^-]/[\text{Fe}(\text{OH})(\text{Cat})][\text{Qi}^-]$	5.66 (0.15)
$[\text{Fe}(\text{OH})_2(\text{Cat})(\text{Qi})^{2-}][\text{H}^+]/[\text{Fe}(\text{OH})(\text{Cat})(\text{Qi})^-]$	-8.89 (0.05)
$[\text{Fe}(\text{OH})_2(\text{Cat})_2^{3-}][\text{H}^+]/[\text{Fe}(\text{OH})(\text{Cat})][\text{Cat}^{2-}]$	4.1 (0.08)

*Obtained by fitting the average of three or more titrations.

samples appear to be amorphous solids while the natural samples appear to be small spheres. In our studies, the synthetic melanin appears to be amorphous, organized layers of melanin. The natural melanin extracted from hair appears to be small batons rather than spheres as reported in the

literature [18]. In the presence of the Fe(III) ions, the layers of synthetic melanin are destroyed (Figure 10), and the amorphous organization predominated.

3.5. EDS Analysis

3.5.1. Melanin Complexes with Fe(III). Potentiometric results at pH 7 for the catechol complex, $[\text{Fe}(\text{OH})(\text{CatH}_2\text{Cat})]$, with a C: Fe atom ratio of 15:1 are shown in Scheme 1. Table 4 shows semiquantitative analysis, and Figure 11 shows the EDS spectra of the DHI melanin complexed with Fe(III), which gives a 15.1:1 atom ratio for C:Fe (atom % column), confirming the potentiometric results. These results confirm that the structure remains the same in both solution and solid states. The presence of potassium is due to isolation of the solid in presence of KCl, and the peak at 2 keV is due to Au, that was used as sample support for EDS analysis.

3.6. Electrochemical Studies. The redox activity of melanin is difficult to study in solution, [6, 7] but it has been shown that melanin can be polymerized onto an electrode, whereby the electrochemical properties of melanin can be better studied [7, 24]. Indium-tin-oxide (ITO) electrodes coated with a polymerized DHI film and treated with Cu(II) and Zn(II) had been previously studied [7]. For comparison, treatments of synthetic melanin with Cu(II), and with Fe(II) and Fe(III) as well, were characterized both by UV-Vis spectroscopy and spectroelectrochemical equilibrium studies.

Simply treating the poly-DHI ITO plates with metal ion solution tended to increase the overall absorbance of the melanin, as shown in Figure 12. The Fe(III)-treated plates had an absorbance at ~500 nm while the Cu(II)-treated plates had an additional absorbance at ~680 nm. These results are consistent with previous reports, which were interpreted as metal ion coordination changing the equilibration of the QI/Cat redox states within the melanin, thus affecting its strong absorbance at 500 nm [7]. Treatment of the poly-DHI films with Fe(II) caused a loss of film stability; the films degraded and tended to delaminate off the surface even when handled anaerobically. But notably, measurements on Fe(II)-treated films showed a loss of absorbance at 500 nm.

The change in absorbance at 500 nm between poly-DHI melanin plates with and without applied potential from -700 to +500 mV is shown in Figure 13. These absorbance values are obtained after the poly-DHI plate electrodes have equilibrated at the applied potential, typically 10 min after initial charging. The resulting spectroelectrochemical absorbance versus potential curves can be interpreted as the effect of metal ion binding on the different redox states of the melanin. The behavior for poly-DHI melanin and the Cu-treated melanin is similar, with two apparent redox equilibria (ca. -150 mV and between -500 and -600 mV).

The behavior of the Fe(III)-treated sample is unique, and a very distinct transition is observed at about -250 mV, at lower potential than similar transitions for the poly-DHI and Cu-treated melanins. The sharp absorbance increase

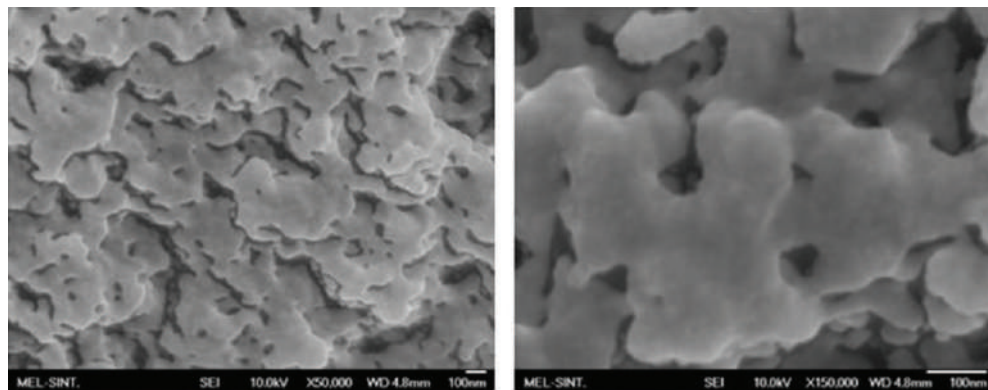


FIGURE 8: SEM images of synthetic melanin.

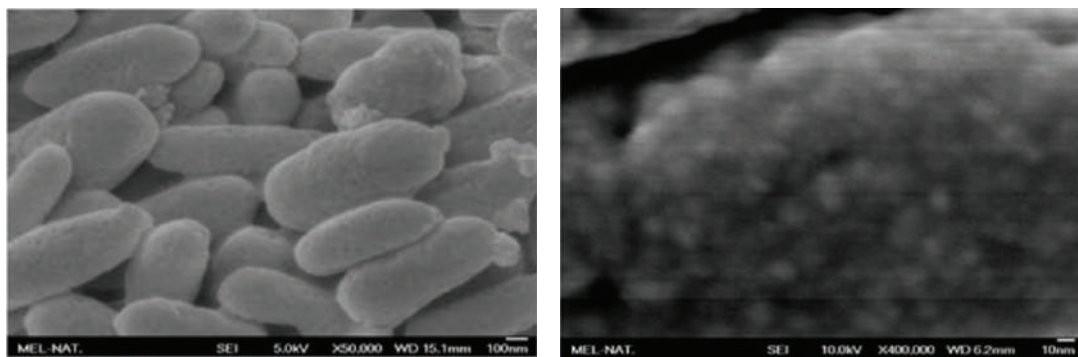


FIGURE 9: SEM images of the natural melanin used in the experiments.

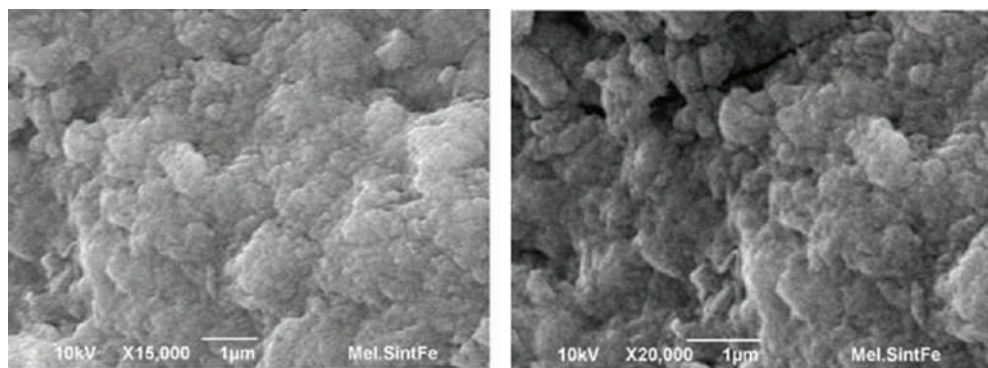


FIGURE 10: SEM images of the synthetic melanin complex with Fe(III).

TABLE 4: EDS results for the Fe(III)-DHI system.

Element line	Weight %	Weight % error	Atom %	Atom % error
C	60.54	±0.98	75.96	±1.23
O	19.70	±0.59	18.55	±0.56
K	1.29	±0.25	0.50	±0.10
Fe	18.48	±2.14	4.99	±0.58
Total	100.00		100.00	

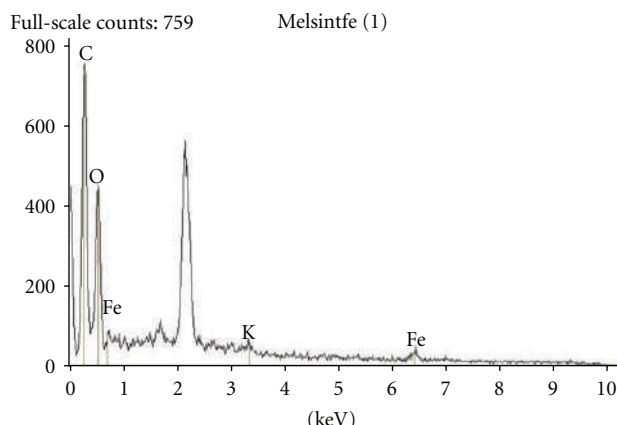


FIGURE 11: EDS analysis of Fe(III)-DHI.

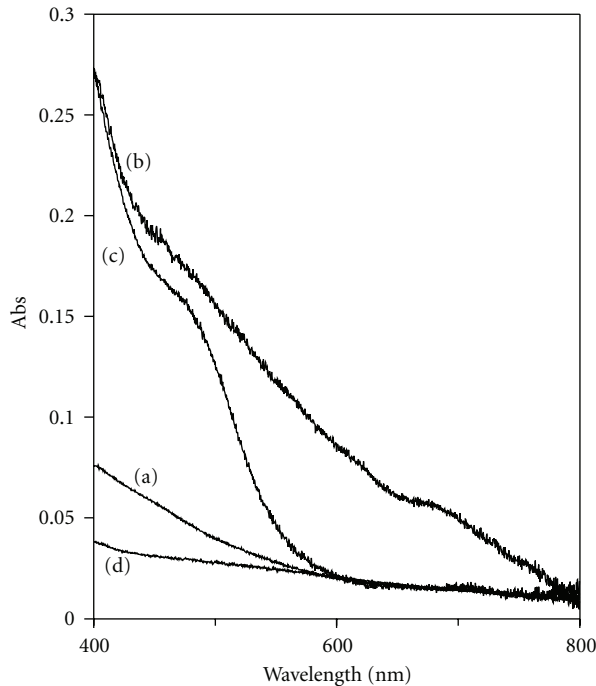


FIGURE 12: UV-Vis spectra of (a) poly-DHI film, (b) Cu-treated poly-DHI film, (c) Fe(III)-treated poly-DHI film, and (d) Fe(II)-treated poly-DHI film.

within about 60 mV span also implies a uniformity in the Fe binding sites within the poly-DHI, which is in agreement with the SEM and EDS results which suggest that the melanin reorganizes upon exposure to Fe(III), perhaps a greater binding affinity for one of quinone tautomers. The lower apparent $E_{1/2}$ value for Fe(III)-treated melanin indicates that it is more easily reduced, but again we attribute this to a melanin-based reduction and not one involving the Fe(III/II) redox couple.

4. Conclusion

In this work, potentiometric titrations, combined with IR spectroscopy and EDS, were used to quantify donor groups

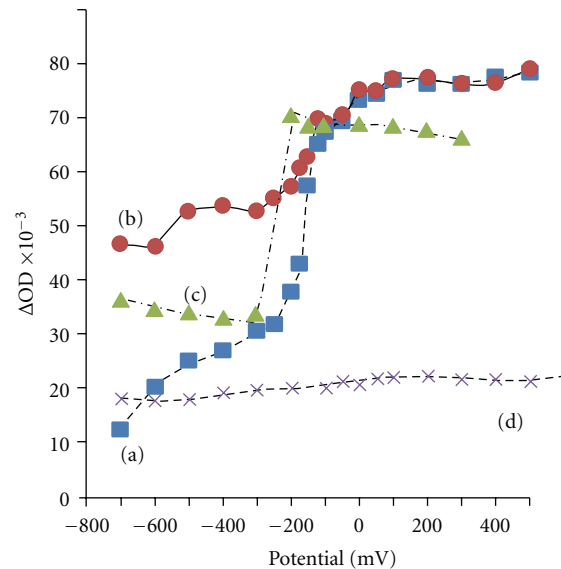


FIGURE 13: Plot of absorbance at 500 nm versus applied potential for (a) poly-DHI film, (b) Cu-treated poly-DHI film, (c) Fe(III)-treated poly-DHI film, and (d) Fe(II)-treated poly-DHI film.

and characterize the interactions of synthetic and natural melanin with Fe(III). This ion has a great affinity for the donor groups of both melanins, which is reflected by the equilibrium constants of the interactions. Catechol is the major group interacting with Fe(III) in both forms of melanin. For natural melanin, the interaction products at neutral and basic pH values are $[Fe(OH)_2(Cat^{2-})]^-$ and $[Fe(OH)_2(Cat^-)_2]^{3-}$, respectively. In this system appears the species $[Fe(Qi)]^{2+}$ at pH above 4, but in the DHI melanin, the species present in this pH was not calculated because of the precipitation of the oligomers. The IR spectroscopy results show the characteristic bands for the formation of the species: 3300 cm^{-1} attributed to catechol group, 1625 cm^{-1} and 1470 cm^{-1} attributed to the quinone-imine group, and the interactions of these groups with the metal ions.

The SEM images show that synthetic DHI melanin is an amorphous solid while natural melanin has a baton shape. However, in the presence of Fe(III) ion, the melanin layers are destroyed and an amorphous organization is kept. Electrochemical measurements confirm that the melanin is reorganized by treatment with Fe^{3+} . EDS analysis shows the mole ratio of atoms present in the metal system, confirming the results of $Fe(OH)(Cat_2H_2Cat)$ interaction that were detected by potentiometric titrations.

Acknowledgment

The authors thank the Central Laboratory of Electron Microscope of UFSC and CNPq (Brazil) for scholarship.

References

- [1] R. A. Nicolaus, "Melanins," in *Methodicum Chimicum*, F. Korte, Ed., vol. 11, pp. 190–199, 1978.

- [2] G. Prota, *Melanins and Melanogenesis*, Academic Press, San Diego, Calif, USA, 1992.
- [3] H. Z. Hill, "The function of melanin or six blind people examine an elephant," *Bioessays*, vol. 14, pp. 49–55, 1992.
- [4] E. V. Gan, H. F. Haberman, and I. A. Menon, "Oxidation of NADH by melanin and melanoproteins," *Biochimica et Biophysica Acta*, vol. 370, no. 1, pp. 62–69, 1974.
- [5] L. Novellino, A. Napolitano, and G. Prota, "Isolation and characterization of mammalian eumelanins from hair and irides," *Biochimica et Biophysica Acta*, vol. 1475, no. 3, pp. 295–306, 2000.
- [6] B. Szpoganicz, S. Gidanian, P. Kong, and P. Farmer, "Metal binding by melanins: studies of colloidal dihydroxyindole-melanin, and its complexation by Cu(II) and Zn(II) ions," *Journal of Inorganic Biochemistry*, vol. 89, no. 1-2, pp. 45–53, 2002.
- [7] S. Gidanian and P. J. Farmer, "Redox behavior of melanins: direct electrochemistry of dihydroxyindole-melanin and its Cu and Zn adducts," *Journal of Inorganic Biochemistry*, vol. 89, no. 1-2, pp. 54–60, 2002.
- [8] K. Franz and L. Charkoudian, "Fe(III)-coordination properties of neuromelanin components: 5,6-dihydroxyindole and 5,6-dihydroxyindole-2-carboxylic acid," *Inorganic Chemistry*, vol. 45, pp. 3657–3664, 2006.
- [9] Y. Liu, L. Hong, V. R. Kempf, K. Wakamatsu, S. Ito, and J. D. Simon, "Ion-exchange and adsorption of Fe(III) by Sepia melanin," *Pigment Cell Research*, vol. 17, no. 3, pp. 262–269, 2004.
- [10] L. Hong, Y. Liu, and J. D. Simon, "Binding of metal ions to melanin and their effects on the aerobic reactivity," *Photochemistry and Photobiology*, vol. 80, no. 3, pp. 477–481, 2004.
- [11] W. Korytowski and T. Sarna, "Bleaching of melanin pigments. Role of copper ions and hydrogen peroxide in autoxidation and photooxidation of synthetic dopa-melanin," *Journal of Biological Chemistry*, vol. 265, no. 21, pp. 12410–12416, 1990.
- [12] D. Ben-Shachar and M. B. H. Youdim, "Iron, melanin and dopamine interaction: relevance to Parkinson's disease," *Progress in Neuro-Psychopharmacology and Biological Psychiatry*, vol. 17, no. 1, pp. 139–150, 1993.
- [13] B. Pilas, T. Sarna, B. Kalyanaraman, and H. M. Swartz, "The effect of melanin on iron associated decomposition of hydrogen peroxide," *Free Radical Biology & Medicine*, vol. 4, no. 5, pp. 285–293, 1988.
- [14] L. Zecca, M. B. H. Youdim, P. Riederer, J. R. Connor, and R. R. Crichton, "Iron, brain ageing and neurodegenerative disorders," *Nature Reviews Neuroscience*, vol. 5, no. 11, pp. 863–873, 2004.
- [15] A. Pezzella, A. Napolitano, M. d'Ischia, G. Prota, R. Seraglia, and P. Traldi, "Identification of partially degraded oligomers of 5,6-dihydroxyindole-2-carboxylic acid in sepius melanin by matrix-assisted laser desorption/ionization mass spectrometry," *Rapid Communications in Mass Spectrometry*, vol. 11, no. 4, pp. 368–372, 1997.
- [16] P. J. Farmer, S. Gidanian, B. Shahandeh, A. J. Di Bilio, N. Tohidian, and F. L. Meyskens, "Melanin as a target for melanoma chemotherapy: pro-oxidant effect of oxygen and metals on melanoma viability," *Pigment Cell Research*, vol. 16, no. 3, pp. 273–279, 2003.
- [17] G. Schwarzenbach and H. Flaschka, *Complexometric Titration*, Methuen, London, UK, 1969.
- [18] F. J. C. Rossotti and H. Rossotti, "Potentiometric titrations using Gran plots: a textbook omission," *Journal of Chemical Education*, vol. 42, p. 375, 1965.
- [19] W. Korytowski, [Ph.D. thesis], Jagiellonian University, Cracow, Poland, 1982.
- [20] A. E. Martell and R. I. Motekaitis, *The Determination and Use of Stability Constants*, Wiley-VCH, New York, NY, USA, 1992.
- [21] E. A. Shurygina, N. K. Larina, M. A. Chubarova, and M. M. Kononova, "Differential thermal analysis (DTA) and thermogravimetry (TG) of soil humus substances," *Geoderma*, vol. 6, no. 3, pp. 169–177, 1971.
- [22] K. Nakamoto, V. Morimoto, and A. E. Martell, "Infrared spectra of aqueous solutions. I. Metal chelate compounds of amino acids," *Journal of the American Chemical Society*, vol. 83, no. 22, pp. 4528–4532, 1961.
- [23] J. D. Simon, S. E. Forest, L. M. Eibest et al., "Probing the building blocks of eumelanins using scanning electron microscopy," *Pigment Cell Research*, vol. 13, pp. 179–184, 2000.
- [24] J. McGinness, P. Corry, and P. Proctor, "Amorphous semiconductor switching in melanins," *Science*, vol. 183, no. 4127, pp. 853–855, 1974.

Spectroscopic, Thermal, and Antimicrobial Studies of Co(II), Ni(II), Cu(II), and Zn(II) Complexes Derived from Bidentate Ligands Containing N and S Donor Atoms

Kiran Singh,¹ Yogender Kumar,¹ Parvesh Puri,¹ and Gulab Singh²

¹Department of Chemistry, Kurukshetra University, Kurukshetra 136 119, India

²Department of Microbiology, Kurukshetra University, Kurukshetra 136 119, India

Correspondence should be addressed to Kiran Singh, kiransinghkuk@yahoo.co.in

Academic Editor: Claudio Pettinari

Two new heterocyclic Schiff bases of 4-amino-5-mercaptopropyl-1,2,4-triazole and 5-nitrofurfuraldehyde [HL^{1-2}] and their cobalt, nickel, copper, and zinc complexes have been synthesized and characterized by elemental analyses, spectral (UV-Vis, IR, ^1H NMR, Fluorescence, and ESR) studies, thermal techniques, and magnetic moment measurements. The heterocyclic Schiff bases act as bidentate ligands and coordinate with metal ions through nitrogen and sulphur of the thiol group. The low molar conductance values in DMF indicate that the metal complexes are nonelectrolytes. The magnetic moments and electronic spectral data suggest octahedral geometry for the Co(II), Ni(II), and Zn(II) complexes and square planar for Cu(II) complexes. Two Gram-positive bacteria (*Staphylococcus aureus* MTCC 96 and *Bacillus subtilis* MTCC 121), two Gram-negative bacteria (*Escherichia coli* MTCC 1652 and *Pseudomonas aeruginosa* MTCC 741), and one yeast, *Candida albicans*, were used for the evaluation of antimicrobial activity of the newly synthesized compounds.

1. Introduction

Recently, for the rapid development of drug resistance, new antimicrobial agent should be designed and synthesized with chemical characteristics clearly different from those of existing ones. 1,2,4-triazoles and their fused heterocyclic derivatives have received considerable attention owing to their synthetic and effective biological importance such as analgesic [1], antitumor [2], anticancer [3, 4], antimicrobial [5–7], anticonvulsant [8, 9], and antiproliferative activities [10]. In addition, 1,2,4-triazole and, in particular, its derivatives exhibit a strong property of acting as a bridging ligand between two metal centers [11] and can provide 1,2-bridging as well as 2,4-bridging form in case of 4-unsubstituted 1,2,4-triazoles.

Schiff bases represent an important class of compounds because they are utilized as starting materials in the synthesis of industrial products [12]. Schiff bases derived from 3-substituted-4-amino-5-mercaptopropyl-1,2,4-triazoles show analgesic, antimicrobial, anti-inflammatory, and antidepressant activities [13]. When bioorganic molecules or drugs are bound to

metal ions, there is a drastic change in their biomimetic properties, therapeutic effects, and pharmacological properties. Metal complexes of Schiff bases derived from triazoles have been synthesized, and it has been observed that antimicrobial activity of the Schiff bases is significantly enhanced when coordinated to metal ions [14, 15]. The metal complexes containing substituted 1,2,4-triazole ligands have spin-crossover properties and can be used as molecular-based memory devices, display and optical switches [16, 17].

Keeping in view medicinal and industrial applications of triazoles and potential chemistry of transition metals; new heterocyclic Schiff bases of 4-amino-5-mercaptopropyl-1,2,4-triazole with 5-nitrofurfuraldehyde [HL^{1-2}] and their metal complex with Co(II), Ni(II), Cu(II), and Zn(II) ions have been synthesized. The synthesized ligands and their metal complexes were characterized by different techniques like elemental analyses, spectral studies (UV-Vis, IR, ^1H NMR, Fluorescence, ESR), TGA, and magnetic and conductance measurements. The newly synthesized compounds were evaluated for their antimicrobial studies.

2. Experimental

2.1. Materials. All starting precursor were of analytical grade. The reagents and solvents were purchased commercially and used without further purification unless otherwise noted. 4-Amino-5-mercaptop-1,2,4-triazole (AMT) and 4-amino-5-mercaptop-3-propyl-1,2,4-triazole (AMPT) were prepared by reported literature method [18].

2.2. Syntheses of Schiff Bases

2.2.1. 4-((5-Nitrofuran-2-yl)methyleneamino)-5-mercaptop-1,2,4-triazole (HL^1). 4-Amino-5-mercaptop-1,2,4-triazole (0.61 g, 5.06 mmol) dissolved in warm ethanol (20 mL) was added to an ethanol solution (30 mL) containing 5-nitrofurfuraldehyde (0.72 g, 5.06 mmol). The mixture was refluxed for 5 hrs. The reaction mixture was then cooled to room temperature and the yellow solid formed was filtered. It was then recrystallized from ethanol and dried.

m.p. 168–170°C, (Found: C, 35.01; H, 2.11; N, 29.28%. Calcd. for $C_7H_5N_5O_3S$: C, 35.15; H, 2.11; N, 29.28%).

2.2.2. 4-((5-Nitrofuran-2-yl)methyleneamino)-5-mercaptop-3-propyl-1,2,4-triazole (HL^2). To a solution of 5-nitrofurfuraldehyde (0.52 g, 3.68 mmol) in ethanol (30 mL), 4-amino-5-mercaptop-3-propyl-1,2,4-triazole (0.58 g, 3.68 mmol) in ethanol (20 mL) was added. The mixture was refluxed for 6 h. The reaction mixture was then cooled to room temperature and the reddish yellow solid formed was filtered. It was then recrystallized from ethanol and dried.

m.p. 142–144°C, (Found: C, 42.70; H, 3.33; N, 24.33%. Calcd. for $C_{10}H_{11}N_5O_3S$: C, 42.70; H, 3.94; N, 24.90%).

2.3. Syntheses of Metal Complexes

2.3.1. Metal Complexes of 4-((5-Nitrofuran-2-yl)methyleneamino)-5-mercaptop-1,2,4-triazole (HL^1). The metal complexes were synthesized by reacting aqueous ethanolic solutions of acetates of Co(II) (0.14 g, 0.57 mmol), Ni(II) (0.14 g, 0.57 mmol), Cu(II) (0.11 g, 0.57 mmol), and Zn(II) (0.13 g, 0.57 mmol) with the hot ethanolic solutions of the HL^1 (0.27 g, 1.14 mmol). The solid complexes formed were filtered off and washed several times with warm water, aqueous ethanol to remove unreacted metal acetates or ligands, and finally with acetone and vacuo dried.

$Co(L^1)_2 \cdot 2H_2O$: (Found: C, 29.21; H, 2.01; N, 24.11; Co, 10.13% Calcd. for $C_{14}H_{12}CoN_{10}O_8S_2$: C, 29.43; H, 2.12; N, 24.51; Co, 10.31%).

$Ni(L^1)_2 \cdot 2H_2O$: (Found: C, 29.12; H, 2.02; N, 24.08; Ni, 10.11% Calcd. for $C_{14}H_{12}NiN_{10}O_8S_2$: C, 29.44; H, 2.12; N, 24.52; Ni, 10.28%).

$Cu(L^1)_2$: (Found: C, 31.00; H, 1.39; N, 25.88; Cu, 11.40% Calcd. for $C_{14}H_8CuN_{10}O_6S_2$: C, 31.14; H, 1.49; N, 25.94; Cu, 11.77%).

$Zn(L^1)_2 \cdot 2H_2O$: (Found: C, 28.96; H, 1.99; N, 24.20; Zn, 11.31% Calcd. for $C_{14}H_{12}N_{10}O_8S_2Zn$: C, 29.10; H, 2.09; N, 24.24; Zn, 11.32%).

2.3.2. Metal Complexes of 4-((5-Nitrofuran-2-yl)methyleneamino)-5-mercaptop-3-propyl-1,2,4-triazole (HL^2). The metal acetates of Co(II) (0.17 g, 0.67 mmol), Ni(II) (0.17 g, 0.67 mmol), Cu(II) (0.13 g, 0.67 mmol), and Zn(II) (0.15 g, 0.67 mmol) in aqueous ethanol were treated with hot ethanolic solution of the HL^2 (0.37 g, 1.34 mmol). The colored complexes formed were filtered off and washed several times with warm water, aqueous ethanol to remove unreacted metal acetates or ligands, and finally with acetone and vacuo dried.

$Co(L^2)_2 \cdot 2H_2O$: (Found: C, 36.22; H, 3.47; N, 21.23; Co, 8.23% Calcd. for $C_{20}H_{24}CoN_{10}O_7S_2$: C, 36.64; H, 3.69; N, 21.37; Co, 8.99%).

$Ni(L^2)_2 \cdot 2H_2O$: (Found: C, 36.53; H, 3.51; N, 21.18; Ni, 8.53% Calcd. for $C_{20}H_{24}NiN_{10}O_7S_2$: C, 36.66; H, 3.69; N, 21.37; Ni, 8.96%).

$Cu(L^2)_2$: (Found: C, 38.15; H, 3.18; N, 22.13; Cu, 10.23% Calcd. for $C_{20}H_{20}CuN_{10}O_6S_2$: C, 38.49; H, 3.23; N, 22.44; Cu, 10.18%).

$Zn(L^2)_2 \cdot 2H_2O$: (Found: C, 36.06; H, 3.43; N, 21.15; Zn, 9.43% Calcd. for $C_{20}H_{24}N_{10}O_7S_2Zn$: C, 36.29; H, 3.65; N, 21.16; Zn, 9.88%).

2.4. Analyses and Instrumentation. Elemental analyses (C, H, and N) were performed on Perkin-Elmer 2400 Elemental Analyzer available at SAIF, Punjab University, Chandigarh. The metal contents were determined gravimetrically by a literature procedure [19] after digesting the organic matter with aqua regia and evaporating the residue to dryness. IR spectra (4000–250 cm^{-1}) of the ligands and their metal complexes were recorded on an MB-3000 ABB Spectrometer. The electronic absorption spectra were recorded on T 90 (PG Instruments Ltd) UV/Vis spectrometer in the region 1100–200 nm. ^1H NMR spectra were recorded in DMSO-d_6 on a Bruker ACF 300 spectrometer at 300 MHz using “tetramethyl silane” as the internal standard. Magnetic moment measurements were carried out at room temperature on vibrating sample magnetometer (Model 155) at Institute Instrumentation Centre, IIT Roorkee. The Perkin Elmer (Pyris Diamond) instrument was used to carry out thermal analysis of metal complex in atmospheric air (50–800°C) at a heating rate of 10°C min^{-1} using a reference to alumina powder. The fluorescence studies of Schiff bases and their metal complexes were recorded on SHIMADZU RF-5301PC spectrophotometer. The solutions of 10⁻³ M concentration were prepared in HPLC-grade DMF, and the experiment was carried out at room temperature. ESR spectra were recorded on X-Band at frequency of 9.1 GHz under the magnetic field 3000 Guass on a varian E-112 ESR spectrometer at SAIF, IIT Bombay.

2.5. Antimicrobial Assay

2.5.1. Test Microorganisms. Two Gram-positive bacteria (*Staphylococcus aureus* MTCC 96 and *Bacillus subtilis* MTCC

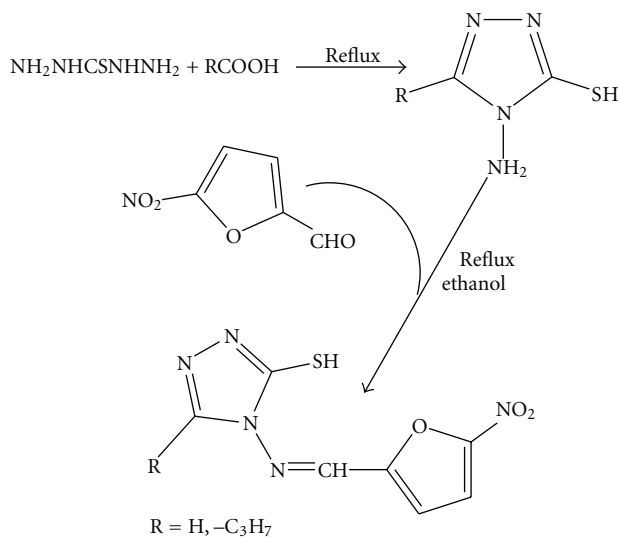


FIGURE 1: Scheme for the syntheses of Schiff bases.

121), two Gram-negative bacteria (*Escherichia coli* MTCC 1652 and *Pseudomonas aeruginosa* MTCC 741), and one Yeast *Candida albicans* were used in the present study for evaluation of antimicrobial activity of the synthesized compounds. All the bacterial cultures were procured from Microbial Type Culture Collection (MTCC), IMTECH-Chandigarh. Medium used for the antimicrobial testing was Muller Hilton agar media and autoclaved at 15 lbs/in² for 15 min.

2.5.2. Antimicrobial Activity. The antimicrobial activity of the newly synthesized compounds was assayed by using agar wells diffusion technique [20, 21]. For the evaluation of antimicrobial activity, the size of inoculum was adjusted to approximately 10⁸ colony-forming units (cfu/mL) by suspending the culture in sterile distilled water. Petri dishes containing 20 mL of Muller Hilton agar medium were swabbed with a culture of the respective microbial strains and kept for 15 min for the absorption of culture. Sterile borer is used to create the wells (6 mm in diameter), and we added 100 μL solution of each compound of 4.0 mg/mL concentration reconstituted in the DMSO on the preinoculated plates. All the plates were incubated at 37°C for 24 hrs. Antimicrobial activity of all the synthesized compounds was determined by measuring the zone of inhibition around the wells. DMSO was used as a negative control, whereas Ciprofloxacin was used as positive control. This procedure was performed in three replicate plates for each organism.

2.5.3. Determination of Minimum Inhibitory Concentration (MIC). MIC of all the compounds was determined by the modified agar well diffusion method [22]. Different concentrations ranging from 10 to 1000 $\mu\text{g}/\text{mL}$ of synthesized compounds were made from the stock solution of 4 mg/mL in DMSO. A 100 μL volume of each dilution was introduced into wells (in triplicate) in the agar plates already seeded with 100 μL of standardized inoculum (10⁸ cfu/mL) of the

test microbial strain. These plates were incubated at 37°C for 24 h and observed for the inhibition zones. Ciprofloxacin antibiotic was taken as positive control.

3. Results and Discussion

The scheme for the syntheses of Schiff bases is represented in Figure 1. The complexes are soluble in DMF and DMSO and are insoluble in common organic solvents. The elemental analyses data show that the metal to ligand ratio is 1 : 2 in all the complexes. The complexes are powdery solids, colored, and nonhygroscopic in nature. The molar conductance values of the complexes (measured in 10⁻³ M DMF) at room temperature lie in the range 6.8–11.3 ohm⁻¹ cm² mol⁻¹, which suggest that they are nonelectrolytes [23, 24]. The purity of ligands and their metal complexes has been checked by TLC.

3.1. ^1H NMR and ^{13}C NMR Spectra. The ^1H NMR spectral data of Schiff bases (HL^{1-2}) and their Zn(II) complexes have been given in Table 1 [14, 15, 25]. In the spectra of free ligands, signals observed at δ 14.10 (HL^1) and 13.91 (HL^2) can be assigned to the SH protons. These signals disappeared in the spectra of metal complexes, which confirms the coordination of ligand to metal ion through the deprotonated thiol group. In the spectra of Schiff bases, signals at δ 9.86 and 10.42 are assigned to azomethine protons. The characteristic signal due to azomethine proton shifted downfield in the spectra of metal complexes indicating coordination through the azomethine nitrogen. The aromatic protons present in the ligands (HL^{1-2}) are found in the region δ 7.55–7.84 ppm. The triazole-H of HL^1 appeared as singlet at 8.97 ppm and propyl group protons of HL^2 Schiff base appeared as triplet δ 0.93 ($-\text{CH}_3$), triplet δ 2.69 ($-\text{CH}_2-$), and multiplet at δ 1.66 ($-\text{CH}_2-$) ppm. These protons signals of Schiff bases show a slight shift upon coordination with metal ions.

The ^{13}C NMR spectral data of Schiff bases (HL^{1-2}) and their Zn(II) complexes have been given in Table 1. Schiff bases show signal at δ 163.34 (HL^1) and 161.9 (HL^2) for their azomethine carbons, and they shift downfield in their corresponding zinc(II) complexes due to the coordination through azomethine nitrogen.

3.2. IR Spectra. The bonding of the ligands to metal ions has been judged by careful comparison of the infrared spectra of the complexes with those of the free ligand (Table 2). Some important bands have been selected to observe the effect on ligand vibration in the complexes. The formation of ligand is confirmed by the absence of stretching vibrations due to aldehyde $\nu(\text{CHO})$ and amino $\nu(\text{NH}_2)$ moiety of triazole and instead of this a strong new band appeared at 1622–1625 cm⁻¹ corresponding to the azomethine $\nu(\text{HC=N})$ group. After complexation, the band due azomethine vibration shifted to lower frequency (10–15 cm⁻¹), thus indicating the coordination of the azomethine-N to metal ions [26]. The ligands show a characteristic strong band at 2739–2770 cm⁻¹, which is attributed to $\nu(\text{SH})$, disappeared in the spectra of metal complexes, confirming deprotonation and coordination of thiol group [27]. This is further supported by

TABLE 1: ^1H NMR and ^{13}C NMR spectral data of Schiff bases and their metal complexes.

Compounds	^1H NMR (DMSO-d ₆) (ppm)	^{13}C NMR (DMSO-d ₆) (ppm)
HL ¹ [C ₇ H ₅ N ₅ O ₃ S]	7.55 (d, 1H, Ar–H), 7.84 (d, 1H, Ar–H), 8.97 (s, triazole–H), 9.86 (s, 1H, –N=CH–), 14.10 (s, 1H, –SH)	114.37, 120.34, 139.44, 146.98, 149.43, 152.12 (Aromatic), 163.34 (–N=CH–)
Zn(L ¹) ₂ ·2H ₂ O [C ₁₄ H ₁₂ N ₁₀ O ₈ S ₂ Zn]	7.42 (d, 2H, Ar–H), 7.66 (d, 2H, Ar–H), 9.05 (s, 2H, triazole–H), 10.12 (s, 2H, –N=CH–) 0.93 (t, 3H, –CH ₃), 1.66 (m, 2H, –CH ₂ –), 2.69 (t, 2H, –CH ₂ –), 7.63 (d, 1H, Ar–H), 7.84 (d, 1H, Ar–H), 10.42 (s, 1H, –N=CH–), 13.91 (s, 1H, –SH)	114.31, 121.02, 139.28, 146.76, 150.22, 152.38 (Aromatic), 171.18 (–N=CH–)
HL ² [C ₁₀ H ₁₁ N ₅ O ₃ S]	0.80 (t, 6H, –CH ₃), 1.57 (m, 4H, –CH ₂ –), 2.63 (t, 4H, –CH ₂ –), 7.69 (d, 2H, Ar–H), 7.85 (d, 2H, Ar–H), 10.83 (s, 2H, –N=CH–)	13.84 (–CH ₃), 19.21 (–CH ₂ –), 26.69 (–CH ₂ –), 114.32, 120.4, 148.28, 149.50, 151.97, 153.52 (Aromatic), 161.9 (–N=CH–)
Zn(L ²) ₂ ·2H ₂ O [C ₂₀ H ₂₄ N ₁₀ O ₇ S ₂ Zn]	0.80 (t, 6H, –CH ₃), 1.57 (m, 4H, –CH ₂ –), 2.63 (t, 4H, –CH ₂ –), 7.69 (d, 2H, Ar–H), 7.85 (d, 2H, Ar–H), 10.83 (s, 2H, –N=CH–)	13.74 (–CH ₃), 19.63 (–CH ₂ –), 26.79 (–CH ₂ –), 114.22, 121.5, 148.75, 152.87, 153.50, 153.70 (Aromatic), 169.72 (–N=CH–)

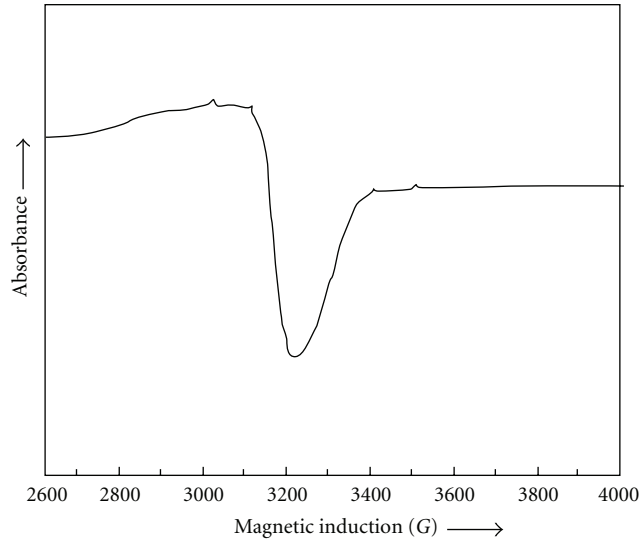
TABLE 2: Important IR spectral bands (cm⁻¹) of Schiff bases and their metal complexes.

Compound	$\nu(\text{N}=\text{CH})$	$\nu(\text{C}-\text{S})$	$\nu(\text{S}-\text{H})$	$\nu(\text{H}_2\text{O}/\text{OH})$	$\nu(\text{M}-\text{S})$	$\nu(\text{M}-\text{N})$
HL ¹	1622	—	2739	—	—	—
Co(L ¹) ₂ ·2H ₂ O	1613	733	—	3441	360	502
Ni(L ¹) ₂ ·2H ₂ O	1607	734	—	3356	347	512
Cu(L ¹) ₂	1612	715	—	—	351	497
Zn(L ¹) ₂ ·2H ₂ O	1610	717	—	3425	361	511
HL ²	1625	—	2770	—	—	—
Co(L ²) ₂ ·2H ₂ O	1613	735	—	3440	355	493
Ni(L ²) ₂ ·2H ₂ O	1611	730	—	3410	347	490
Cu(L ²) ₂	1609	710	—	—	362	503
Zn(L ²) ₂ ·2H ₂ O	1606	718	—	3395	353	510

the lower frequency band appeared at 710–735 cm⁻¹ in the metal complexes due to $\nu(\text{C}-\text{S})$. A broad band in the region 3355–3445 cm⁻¹ assigned as $\nu(\text{OH})$ indicates the presence of water molecules in the complexes. The metal ligand bands appear in the region 347–362 cm⁻¹ and 490–515 cm⁻¹ in all the complexes that have been assigned to $\nu(\text{M}-\text{S})$ and $\nu(\text{M}-\text{N})$, respectively [24, 28].

3.3. ESR Spectra. The electronic paramagnetic resonance spectra of Cu(L¹)₂ (Figure 2) and Cu(L²)₂ were recorded in solid state at room temperature to obtain further information about their stereochemistry. The g -tensor values of the Cu(L¹)₂ ($g_{||} = 2.12$, $g_{\perp} = 2.05$, $g_{\text{av}} = 2.07$, $G = 2.46$) and Cu(L²)₂ ($g_{||} = 2.13$, $g_{\perp} = 2.05$, $g_{\text{av}} = 2.07$, $G = 2.66$) complexes can be used to derive the ground state. In square planar complexes, the unpaired electron lies in dx^2-y^2 orbital giving $^2B_{1g}$ as the ground state with $g_{||} > g_{\perp} > 2$, while the unpaired electron lies in the dz^2 orbital giving $^2A_{1g}$ as the ground state with $g_{\perp} > g_{||} > 2$. In the present case, $g_{||} > g_{\perp} > 2$, therefore the unpaired electron is likely to be in the dx^2-y^2 orbital, indicating square planar geometry around the copper(II) ion [29, 30]. No signal at half field was observed in the spectrum, ruling out the possibility of a dimeric form [31].

3.4. Magnetic Moment Measurements and Electronic Spectra. The observed electronic transitions and calculated ligand

FIGURE 2: X-Band ESR spectrum of Cu(L¹)₂.

field parameters of the metal complexes are listed in Table 3. The electronic spectra provided enough information regarding the arrangements of the ligands around the metal ions. Co(II) complexes of HL¹⁻² at room temperature show magnetic moments 4.11 and 4.20 BM, respectively [25, 27]. These values are in good agreement with those reported

TABLE 3: Electronic spectral data (in DMF) and ligand field parameters of metal complexes.

Compound	Transitions (cm^{-1})			Dq (cm^{-1})	B (cm^{-1})	ν_2/ν_1	β	$\beta\%$	μ_{eff} (BM)
	ν_1	ν_2	ν_3						
$\text{Co(L}^1\text{)}_2 \cdot 2\text{H}_2\text{O}$	10599	22425*	20809	1182.6	762.4	2.11	0.78	22	4.20
$\text{Co(L}^2\text{)}_2 \cdot 2\text{H}_2\text{O}$	10913	23063*	20998	1215.0	754.8	2.11	0.77	22	4.11
$\text{Ni(L}^1\text{)}_2 \cdot 2\text{H}_2\text{O}$	9907	16226	24372	990.7	725.1	1.63	0.69	31	3.79
$\text{Ni(L}^2\text{)}_2 \cdot 2\text{H}_2\text{O}$	9933	16283	23415	993.3	659.9	1.63	0.63	37	3.73
$\text{Cu(L}^1\text{)}_2$	17981			—	—	—	—	—	1.86
$\text{Cu(L}^2\text{)}_2$	18121			—	—	—	—	—	1.92

* Calculated value.

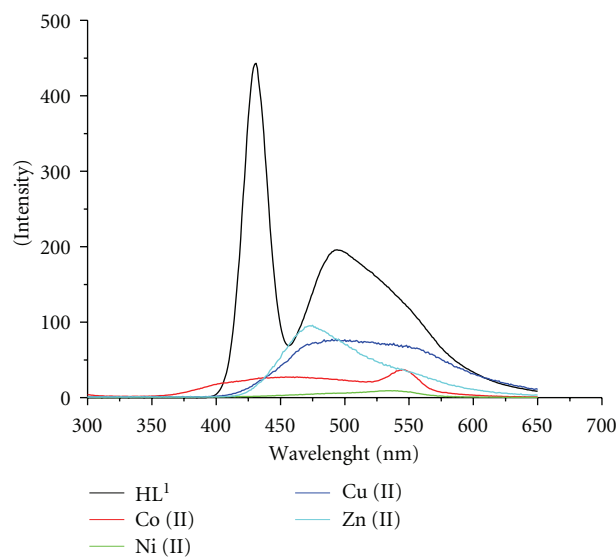
for octahedral Co(II) complexes. The Co(II) complexes exhibited two distinct absorptions in the regions $10599\text{--}10913\text{ cm}^{-1}$ and $20809\text{--}20998\text{ cm}^{-1}$ assigned to ${}^4\text{T}_{1g}(\text{F}) \rightarrow {}^4\text{T}_{2g}(\text{F})$ (ν_1) and ${}^4\text{T}_{1g}(\text{F}) \rightarrow {}^4\text{T}_{1g}(\text{P})$ (ν_3) transitions, respectively, which suggests octahedral geometry around the Co(II) ion [14, 25, 27]. ν_2 is not observed, but it is calculated by using relation $\nu_2 = \nu_1 + 10Dq$, which is very close to (ν_3) transition [32].

The Ni(II) complex reported herein are high spin with room temperature magnetic moment value ~ 3.75 BM, which is in the normal range observed for octahedral complexes. The electronic spectra of Ni(II) complexes displayed three bands in the regions $9907\text{--}9933\text{ cm}^{-1}$, $16226\text{--}16283\text{ cm}^{-1}$, and $23415\text{--}24372\text{ cm}^{-1}$, assigned to ${}^3\text{A}_{2g}(\text{F}) \rightarrow {}^3\text{T}_{2g}(\text{F})$ (ν_1), ${}^3\text{A}_{2g}(\text{F}) \rightarrow {}^3\text{T}_{1g}(\text{F})$ (ν_2), and ${}^3\text{A}_{2g}(\text{F}) \rightarrow {}^3\text{T}_{1g}(\text{P})$ (ν_3) transitions, respectively [24–26]. These are the characteristic bands of octahedral environment around Ni(II) ion.

The Band-fitting equations [32, 33] have been used to calculate the ligand field parameters (Dq , B , β , and $\beta\%$) for Co(II) and Ni(II) complexes indicated significant covalent character of metal ligand bonds (Table 3). The value of Rachah parameter (B) is less than free ion value, suggesting an orbital overlap and delocalization of electron on the metal ion. The nephelauxetic ratio (β) for the metal complexes is less than one suggesting partial covalency in the metal ligand bond.

The copper complexes of HL^{1-2} Schiff bases show band at 17981 and 18121 cm^{-1} , respectively, which can be assigned to ${}^2\text{B}_{1g} \rightarrow {}^2\text{A}_{1g}$ (ν_1) transition. It is a characteristic band of square planar geometry around the Cu(II) [25, 34]. The room temperature magnetic moment value $1.86\text{--}1.92$ BM falls in the range normally observed for square planar complexes.

3.5. Fluorescence Spectra. In order to investigate the effect of M(II) ions on the fluorescence of the ligands, the fluorescence spectra of ligands (HL^{1-2}) and their metal complexes have been recorded in 10^{-3} M DMF solution. The overlapping spectra of the ligands and their Co(II), Ni(II), Cu(II), and Zn(II) complexes are given in Figures 3 and 4. HL^1 exhibits two strong fluorescence emission bands at 431 and 494 nm (Ex 280 nm), and its metal complexes show fluorescence emission bands at 463 , 545 nm for Co(II), 403 , 536 nm for Ni(II), 493 nm for Cu(II), and 475 nm for Zn(II).

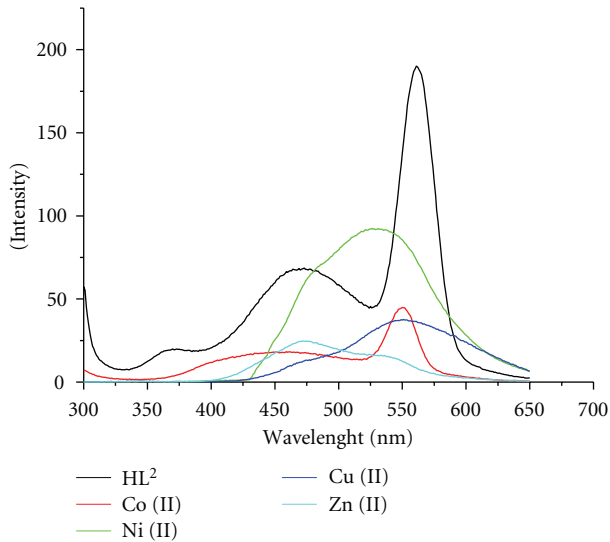
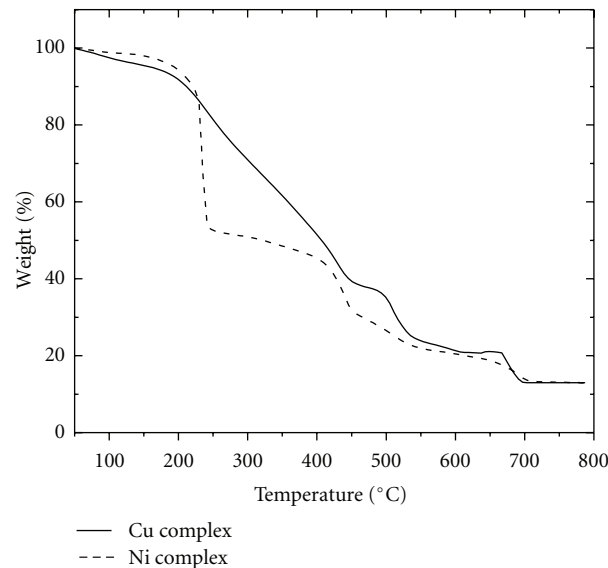
FIGURE 3: Fluorescence spectra of HL^1 and its metal complexes.

HL^2 shows one weak emission band at 370 nm and two strong fluorescence emission bands at 473 and 561 nm (Ex. 275 nm), while its metal complexes show emission bands at 451 , 550 nm for Co(II), 526 nm for Ni(II), 551 nm for Cu(II), and 475 nm for Zn(II). It has been observed from the fluorescence emission spectra that transition metal ions decrease the fluorescence intensity of free ligands. The results of our study are in accordance with the reports of earlier workers [26, 35], which also observed partial fluorescence quenching phenomena in the metal complexes. Magnetic perturbation, redox activity, and so forth. have been invoked in the past to rationalize fluorescence quenching by transition metal ions [36].

3.6. Thermal Studies. Thermogravimetric analyses of the complexes $\text{Ni(L}^1\text{)}_2 \cdot 2\text{H}_2\text{O}$ and $\text{Cu(L}^1\text{)}_2$ are given in Table 4. The correlations between the different decomposition steps of the complexes with their corresponding mass losses are discussed in terms of the proposed formulae of the complexes. The results show good agreement with the formulae suggested from the analytical data. The TG curve of $\text{Ni(L}^1\text{)}_2 \cdot 2\text{H}_2\text{O}$ (Figure 5) consists mainly of three steps in the temperature range $50\text{--}190$, $190\text{--}424$, and $424\text{--}750^\circ\text{C}$. The first step seems to be consistent with the evolution

TABLE 4: Thermogravimetric data of $\text{Ni}(\text{L}^1)_2 \cdot 2\text{H}_2\text{O}$ and $\text{Cu}(\text{L}^1)_2$ complexes.

Compound	Decomposition stages and assignment	Temp. (°C)	% Weight loss found (Calcd.)
$\text{Ni}(\text{L}^1)_2 \cdot 2\text{H}_2\text{O}$ [$\text{C}_{14}\text{H}_{12}\text{N}_{10}\text{NiO}_8\text{S}_2$]	(1) Water molecules	50–190	6.9 (6.3)
	(2) Organic moiety	190–424	48.2 (48.6)
	(3) Triazoles moiety	424–750	34.5 (34.6)
$\text{Cu}(\text{L}^2)_2$ [$\text{C}_{14}\text{H}_8\text{CuN}_{10}\text{O}_6\text{S}_2$]	(1) Organic moiety	50–245	46.9 (46.3)
	(2) Triazole moiety	245–445	20.1 (20.9)
	(3) Triazole moiety	445–750	20.3 (20.9)

FIGURE 4: Fluorescence spectra of HL^2 and its metal complexes.FIGURE 5: Thermogravimetric Curves of $\text{Ni}(\text{L}^1)_2 \cdot 2\text{H}_2\text{O}$ and $\text{Cu}(\text{L}^1)_2$ complexes.

of two water molecules (calcd. 6.3%, found 6.9%). The second TG step represents a mass loss (calcd. 48.6%, found 48.2%) corresponding to the removal of organic moiety [$\text{C}_{10}\text{H}_6\text{N}_4\text{O}_6$]. The final step corresponds to decomposition of triazole molecules at 424–750°C with mass loss of 34.5% (calcd. 34.6%) of the ligand leaving metal oxide as residue. The TG curve of the $\text{Cu}(\text{L}^1)_2$ complex shows three stages of decomposition within the temperature range 50–750°C. The first stage at 50–245°C correspond to loss of organic moiety with mass loss of 46.9% (calcd. 46.3%). The second and third steps corresponds to removal of two triazole molecules in the temperature range 245–750°C with a total mass loss of 40.4% (calcd. 41.8%). The decomposition of all the complexes ended with oxide formation [24, 25, 27].

3.7. In Vitro Antimicrobial Discussion. The ligands (HL^{1-2}), metal complexes, standard drugs, and DMSO solvent were screened separately for their antimicrobial activity against Gram-positive (*Staphylococcus aureus*, *Bacillus subtilis*) and Gram-negative (*Escherichia coli*, *Pseudomonas aeruginosa*) bacteria and against yeast *Candida albicans*. The microbial results are summarized in Tables 5 and 6. The comparative studies of the Schiff bases and their metal complexes indicate that the complexes showed significantly enhanced antimicrobial activity against microbial strains in comparison to the

free ligands. Positive controls (Standard drug) produced significantly sized inhibition zones against the tested bacteria; however, negative control (DMSO) produced no observable inhibitory effect against any of the test organisms.

The newly synthesized compounds showed zone of inhibition ranging from 12.6 mm to 19.6 mm against the Gram positive bacteria and 12.7 mm to 21.2 mm against Gram negative bacteria. On the basis of zone of inhibition produced against the test bacterium, it is observed that $\text{Cu}(\text{L}^1)_2$ shows antibacterial activity comparable to standard drug in case of *Pseudomonas aeruginosa*. However, some of the compounds in this series were not effective against some bacterial strains. All the compounds showed good antimicrobial activity against *Candida albicans* ranging from 14.6 mm to 19.5 mm each. $\text{Co}(\text{L}^1)_2 \cdot 2\text{H}_2\text{O}$ and $\text{Cu}(\text{L}^1)_2$ were found to be most effective against *Candida albicans* with zone of inhibition of 19.5 mm. MIC results also revealed that the metal complexes are slightly more effective against the antimicrobial strains as compared to the Schiff bases. $\text{Co}(\text{L}^1)_2 \cdot 2\text{H}_2\text{O}$ was found to be the best antimicrobial agent exhibited the lowest MIC 100 µg/mL against *Bacillus subtilis* and *Candida albicans* (Table 6). The results of our study are in accordance with the reports of earlier workers [25, 26],

TABLE 5: Antimicrobial activity of the synthesized compounds.

Compound	Diameter of growth of inhibition zone (mm)				
	<i>Staphylococcus aureus</i>	<i>Bacillus subtilis</i>	<i>Escherichia coli</i>	<i>Pseudomonas aeruginosa</i>	<i>Candida albicans</i>
HL ¹	17.3	19.6	15.2	12.7	15.2
Co(L ¹) ₂ ·2H ₂ O	17.4	16.5	16.3	—	19.5
Ni(L ¹) ₂ ·2H ₂ O	18.2	16.9	15.4	—	16.5
Cu(L ¹) ₂	17.2	18.4	17.6	21.2	19.5
Zn(L ¹) ₂ ·2H ₂ O	15.4	16.8	17.4	17.6	15.8
HL ²	15.4	12.6	15.4	13.7	15.3
Co(L ²) ₂ ·2H ₂ O	—	14.6	19.4	17.3	14.8
Ni(L ²) ₂ ·2H ₂ O	—	14.8	16.2	17.3	17.9
Cu(L ²) ₂	—	—	19.2	17.4	14.6
Zn(L ²) ₂ ·2H ₂ O	15.4	—	13.3	12.4	15.7
Ciprofloxacin	23.0	24.0	23.0	20.0	nt

—: Indicates no activity, nt: not tested.

TABLE 6: Minimum inhibitory concentration (MIC) ($\mu\text{g/mL}$) of synthesized compounds.

Compounds	<i>Staphylococcus aureus</i>	<i>Bacillus subtilis</i>	<i>Escherichia coli</i>	<i>Pseudomonas aeruginosa</i>	<i>Candida albicans</i>
NFMT	300	200	400	800	200
Co(L ¹) ₂ ·2H ₂ O	300	100	200	—	100
Ni(L ¹) ₂ ·2H ₂ O	100	400	200	—	200
Cu(L ¹) ₂	200	200	200	500	200
Zn(L ¹) ₂ ·2H ₂ O	400	500	500	700	500
NFMPT	500	800	300	500	700
Co(L ²) ₂ ·2H ₂ O	—	800	500	700	700
Ni(L ²) ₂ ·2H ₂ O	—	500	800	400	700
Cu(L ²) ₂	—	—	100	600	500
Zn(L ²) ₂ ·2H ₂ O	200	—	500	800	200
Ciprofloxacin	5	5	5	5	—

—: Not tested.

which also showed that the antimicrobial activity of ligands is greatly enhanced when it is coordinated to metal ions.

The overtone's concept [37] and Tweedy's chelation theory [38] can be used to explain the enhanced in antimicrobial activity of the metal complexes. According to the Overtone's concept of cell permeability, the lipid membrane surrounding the cell favors the passage of only lipid-soluble materials; therefore, liposolubility is an important factor which controls the antimicrobial activity. On chelation, polarity of the metal ion is reduced to a greater extent due the overlapping of the ligand orbital and partial sharing of the positive charge of the metal ion with donor groups. Moreover, delocalization of the π -electrons over the whole chelate ring is increased, and lipophilicity of the complexes is enhanced. The increased lipophilicity enhances the penetration of the complexes into the lipid membranes and blocks the metal binding sites in the enzymes of microorganisms. These complexes also disturb the respiration process of the cell and thus block the synthesis of proteins, which restricts further growth of the organism.

In general, metal complexes are more active than ligands as they may serve as principal cytotoxic species.

4. Conclusions

The synthesized Schiff bases act as bidentate ligands and coordinated to metal ion through azomethine nitrogen and sulphur of thiol group. The bonding of ligand to metal ion is confirmed by elemental analyses, spectral studies (UV-Vis, IR, ^1H NMR, ESR, Fluorescence), TGA, and magnetic and conductance measurements. The spectral studies suggested octahedral geometry for the Co(II), Ni(II), and Zn(II) complexes and square planar for Cu(II) complexes (Figure 6). No signal at half field was observed in the ESR spectrum, ruling out the possibility of a dimeric form. The antimicrobial studies suggested that the Schiff bases were found to be biologically active and their metal complexes show significantly enhanced antimicrobial activity against microbial strains in comparison to the free ligands. Thus,

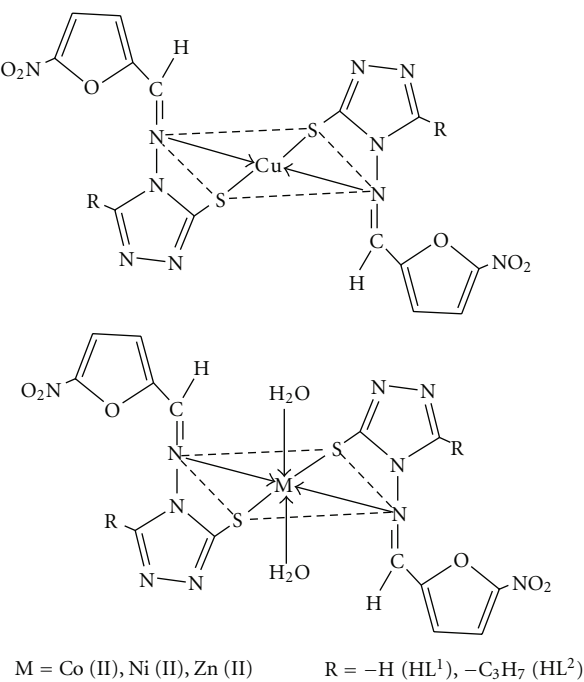


FIGURE 6: Structures of Metal Complexes.

exhibiting their broad spectrum nature can be further used in pharmaceutical industry for mankind, as an antimicrobial agent, after testing its toxicity to human beings.

Acknowledgments

Y. Kumar is highly thankful to University Grant Commission, New Delhi, for providing Senior Research Fellowship (SRF) and Department of Chemistry, Kurukshetra University Kurukshetra, for providing facilities to carry out this research work.

References

- [1] M. Amir and K. Shikha, "Synthesis and anti-inflammatory, analgesic, ulcerogenic and lipid peroxidation activities of some new 2-[(2,6-dichloroanilino) phenyl]acetic acid derivatives," *European Journal of Medicinal Chemistry*, vol. 39, no. 6, pp. 535–545, 2004.
- [2] Y. A. Al-Soud, N. A. Al-Masoudi, and A. E. R. S. Ferwanah, "Synthesis and properties of new substituted 1,2,4-triazoles: potential antitumor agents," *Bioorganic & Medicinal Chemistry*, vol. 11, no. 8, pp. 1701–1708, 2003.
- [3] B. S. Holla, B. Veerendra, M. K. Shivananda, and B. Poojary, "Synthesis characterization and anticancer activity studies on some Mannich bases derived from 1,2,4-triazoles," *European Journal of Medicinal Chemistry*, vol. 38, no. 7-8, pp. 759–767, 2003.
- [4] O. Bekircan, M. Küçük, B. Kahveci, and S. Kolayli, "Convenient synthesis of fused heterocyclic 1,3,5-triazines from some N-Acyl imidates and heterocyclic amines as anticancer and antioxidant agents," *Archiv der Pharmazie*, vol. 338, no. 8, pp. 365–372, 2005.
- [5] K. Singh, Y. Kumar, P. Puri, C. Sharma, and K. R. Aneja, "Antimicrobial, spectral and thermal studies of some transition metal complexes derived from bidentate ligands containing N and S donor atoms," *Phosphorus, Sulfur, and Silicon and the Related Elements*, vol. 187, no. 12, pp. 1498–1509, 2012.
- [6] M. S. Karthikeyan, D. J. Prasad, B. Poojary, K. S. Bhat, B. S. Holla, and N. S. Kumari, "Synthesis and biological activity of Schiff and Mannich bases bearing 2,4-dichloro-5-fluorophenyl moiety," *Bioorganic & Medicinal Chemistry*, vol. 14, no. 22, pp. 7482–7489, 2006.
- [7] Z. H. Chohan, S. H. Sumrra, M. H. Youssoufi, and T. B. Hadda, "Metal based biologically active compounds: design, synthesis, and antibacterial/antifungal/cytotoxic properties of triazole-derived Schiff bases and their oxovanadium(IV) complexes," *European Journal of Medicinal Chemistry*, vol. 45, no. 7, pp. 2739–2747, 2010.
- [8] X. S. Cui, J. Chen, K. Y. Chai, J. S. Lee, and Z. S. Quan, "Synthesis and anticonvulsant evaluation of 3-substituted-4-(4-hydroxyphenyl)-4H-1,2,4-triazoles," *Medicinal Chemistry Research*, vol. 18, no. 1, pp. 49–58, 2009.
- [9] J. Chen, X. Y. Sun, K. Y. Chai, J. S. Lee, M. S. Song, and Z. S. Quan, "Synthesis and anticonvulsant evaluation of 4-(4-alkoxylphenyl)-3-ethyl-4H-1,2,4-triazoles as open-chain analogues of 7-alkoxyl-4,5-dihydro[1,2,4]triazolo[4,3-a]quinoxelines," *Bioorganic & Medicinal Chemistry*, vol. 15, no. 21, pp. 6775–6781, 2007.
- [10] S. Manfredini, C. B. Vicentini, M. Manfrini et al., "Pyrazolotriazoles as light activable dna cleaving agents," *Bioorganic & Medicinal Chemistry*, vol. 8, no. 9, pp. 2343–2346, 2000.
- [11] J. G. Haasnoot, "Mononuclear, oligonuclear and polynuclear metal coordination compounds with 1,2,4-triazole derivatives as ligands," *Coordination Chemistry Reviews*, vol. 200–202, pp. 131–185, 2000.
- [12] A. M. El-Sayed and O. A. Abd Allah, "Synthetic and biological studies on coumarin hydrazone derivatives," *Phosphorus, Sulfur and Silicon and Related Elements*, vol. 170, no. 1, pp. 75–86, 2001.
- [13] O. Bekircan and H. Bektas, "Synthesis of new bis-1,2,4-triazole derivatives," *Molecules*, vol. 11, no. 6, pp. 469–477, 2006.
- [14] K. Singh, D. P. Singh, M. S. Barwa, P. Tyagi, and Y. Mirza, "Antibacterial Co(II), Ni(II), Cu(II) and Zn(II) complexes of Schiff bases derived from fluorobenzaldehyde and triazoles," *Journal of Enzyme Inhibition and Medicinal Chemistry*, vol. 21, no. 5, pp. 557–562, 2006.
- [15] K. Singh, D. P. Singh, M. S. Barwa, P. Tyagi, and Y. Mirza, "Some bivalent metal complexes of Schiff bases containing N and S donor atoms," *Journal of Enzyme Inhibition and Medicinal Chemistry*, vol. 21, no. 6, pp. 749–755, 2006.
- [16] Y. Garcia, P. J. Van Koningsbruggen, E. Codjovi, R. Lapouyade, O. Kahn, and L. Rabardel, "Non-classical Fe^{II} spin-crossover behaviour leading to an unprecedented extremely large apparent thermal hysteresis of 270 K: application for displays," *Journal of Materials Chemistry*, vol. 7, no. 6, pp. 857–858, 1997.
- [17] O. Kahn and C. J. Martinez, "Spin-transition polymers: from molecular materials toward memory devices," *Science*, vol. 279, no. 5347, pp. 44–48, 1998.
- [18] S. Bala, R. P. Gupta, M. L. Sachdeva, A. Singh, and H. K. Pujari, "Heterocyclic systems containing bridgehead nitrogen atom: part III—synthesis of s-Triazolo [3,4-b][1,3,4] thiadiazine, s-triazolo-[3,4-b][1,3,4]thiadiazino[6,7-b] quinoxaline & astriazino-[3,4-b] [1,3,4] thiadiazines," *Indian Journal of Chemistry*, vol. 16, pp. 481–483, 1978.
- [19] A. I. Vogel, *A Text Book of Quantitative Chemical Analysis*, Addison Wesley, London, UK, 1999.

- [20] I. Ahmad and A. Z. Beg, "Antimicrobial and phytochemical studies on 45 Indian medicinal plants against multi-drug resistant human pathogens," *Journal of Ethnopharmacology*, vol. 74, no. 2, pp. 113–123, 2001.
- [21] J. M. Andrews, "Determination of minimum inhibitory concentrations," *Journal of Antimicrobial Chemotherapy*, vol. 48, no. 1, pp. 5–16, 2001.
- [22] M. I. Okeke, C. U. Iroegbu, E. N. Eze, A. S. Okoli, and C. O. Esimone, "Evaluation of extracts of the root of Landolphia overrience for antibacterial activity," *Journal of Ethnopharmacology*, vol. 78, no. 2-3, pp. 119–127, 2001.
- [23] W. J. Geary, "The use of conductivity measurements in organic solvents for the characterisation of coordination compounds," *Coordination Chemistry Reviews*, vol. 7, no. 1, pp. 81–122, 1971.
- [24] K. Singh, Y. Kumar, P. Puri, C. Sharma, and K. R. Aneja, "Metal based biologically active compounds: synthesis, spectral and antimicrobial studies of cobalt, nickel, copper and zinc complexes of triazole derived Schiff bases," *Bioinorganic Chemistry and Applications*, vol. 2011, Article ID 901716, 10 pages, 2011.
- [25] K. Singh, Y. Kumar, P. Puri, M. Kumar, and C. Sharma, "Cobalt, nickel, copper and zinc complexes with 1, 3-diphenyl-1H-pyrazole-4-carboxaldehyde Schiff bases: antimicrobial, spectroscopic, thermal and fluorescence studies," *European Journal of Medicinal Chemistry*, vol. 52, pp. 313–321, 2012.
- [26] S. A. Patil, S. N. Unki, A. D. Kulkarni, V. H. Naik, and P. S. Badami, "Co(II), Ni(II) and Cu(II) complexes with coumarin-8-yl Schiff-bases: spectroscopic, in vitro antimicrobial, DNA cleavage and fluorescence studies," *Spectrochimica Acta A*, vol. 79, no. 5, pp. 1128–1136, 2011.
- [27] K. Singh, Y. Kumar, P. Puri, C. Sharma, and K. R. Aneja, "Synthesis, spectroscopic, thermal and antimicrobial studies of Co(II), Ni(II), Cu(II) and Zn(II) complexes with Schiff base derived from 4-amino-3-mercaptopro-6-methyl-5-oxo-1,2,4-triazine," *Medicinal Chemistry Research*, vol. 21, pp. 1708–1716, 2012.
- [28] A. K. Singh, O. P. Pandey, and S. K. Sengupta, "Synthesis, spectral characterization and biological activity of zinc(II) complexes with 3-substituted phenyl-4-amino-5-hydrazino-1, 2, 4-triazole Schiff bases," *Spectrochimica Acta A*, vol. 85, no. 1, pp. 1–6, 2012.
- [29] O. I. Singh, M. Damayanti, N. R. Singh, R. K. H. Singh, M. Mohapatra, and R. M. Kadam, "Synthesis, EPR and biological activities of bis(1-n-butylamidino-O- alkylurea)copper(II)chloride complexes: EPR evidence for binuclear complexes in frozen DMF solution," *Polyhedron*, vol. 24, no. 8, pp. 909–916, 2005.
- [30] H. A. El-Boraey, R. M. Abdel-Rahman, E. M. Atia, and K. H. Hilmy, "Spectroscopic, thermal and toxicity studies of some 2-amino-3-cyano-1, 5-diphenylpyrrole containing Schiff bases copper (II) complexes," *Central European Journal of Chemistry*, vol. 8, no. 4, pp. 820–833, 2010.
- [31] N. Raman, R. Jeyamurugan, M. Subbulakshmi, R. Boomianthan, and C. R. Yuvarajan, "Synthesis, DNA binding, and antimicrobial studies of novel metal complexes containing a pyrazolone derivative Schiff base," *Chemical Papers*, vol. 64, no. 3, pp. 318–328, 2010.
- [32] F. A. Cotton, G. Willikinson, C. A. Murillo, and M. Bochman, *Advanced Inorganic Chemistry*, John Wiley & Sons, New York, NY, USA, 6th edition, 2003.
- [33] A. B. P. Lever, *Inorganic Spectroscopy*, Elsevier, Amsterdam, The Netherlands, 2nd edition, 1984.
- [34] K. A. Melha, "Antimicrobial, spectral, magnetic and thermal studies of Cu(II), Ni(II), Co(II), UO₂(VI) and Fe(III) complexes of the Schiff base derived from oxalylhydrazide," *Journal of Enzyme Inhibition and Medicinal Chemistry*, vol. 23, no. 2, pp. 285–295, 2008.
- [35] Q. H. Wang, W. Weng, J. M. Liu, L. Z. Cai, and G. C. Guo, "Synthesis, crystal structure, and fluorescence properties of several schiff-base compounds," *Journal of Coordination Chemistry*, vol. 59, no. 5, pp. 485–492, 2006.
- [36] A. W. Varnes, R. B. Dodson, and E. L. Wehry, "Interactions of transition-metal ions with photoexcited states of flavins. Fluorescence quenching studies," *Journal of the American Chemical Society*, vol. 94, no. 3, pp. 946–950, 1972.
- [37] N. Raman, A. Kulandaisamy, and K. Jeyasubramanian, "Synthesis, structural characterization, redox and antimicrobial studies of Schiff base copper(II), nickel(II), cobalt(II), manganese(II), zinc(II) and oxovanadium(II) complexes derived from benzil and 2-aminobenzyl alcohol," *Polish Journal of Chemistry*, vol. 76, no. 8, pp. 1085–1094, 2002.
- [38] N. Dharmaraj, P. Viswanathamurthi, and K. Natarajan, "Ruthenium(II) complexes containing bidentate Schiff bases and their antifungal activity," *Transition Metal Chemistry*, vol. 26, no. 1-2, pp. 105–109, 2001.

Hydroxyapatite Coating of Titanium Implants Using Hydroprocessing and Evaluation of Their Osteoconductivity

Kensuke Kuroda and Masazumi Okido

Department of Materials Science and Engineering, Graduate School of Engineering, Nagoya University, Nagoya 464-8603, Japan

Correspondence should be addressed to Kensuke Kuroda, kkuroda@numse.nagoya-u.ac.jp

Academic Editor: Ian Butler

Many techniques for the surface modification of titanium and its alloys have been proposed from the viewpoint of improving bioactivity. This paper contains an overview of surface treatment methods, including coating with hydroxyapatite (HAp), an osteoconductive compound. There are two types of coating methods: pyroprocessing and hydroprocessing. In this paper, hydroprocessing for coating on the titanium substrate with HAp, carbonate apatite ($\text{CO}_3\text{-Ap}$), a $\text{CO}_3\text{-Ap/CaCO}_3$ composite, HAp/collagen, and a HAp/gelatin composite is outlined. Moreover, evaluation by implantation of surface-modified samples in rat tibiae is described.

1. Introduction

Titanium (Ti) and its alloys are used as artificial joints and teeth roots in orthopedic and dental settings because they have the advantage that their mechanical properties are closer to those of bone than are those of stainless steel or cobalt-chromium alloys. However, the difference in mechanical properties between Ti and natural bone leads to negative effects, such as stress shielding. To mitigate these effects, many new Ti alloys have been developed for hard tissue implants, with a focus on controlling the alloy element and its content, phase, and other characteristics.

When implants do not undergo surface modification to enhance the osteoconductivity, it takes a relatively long time to fix the metallic implant to bone such that it is stable. There are many approaches for improving the osteoconductivity of Ti and its alloys. These approaches can be classified into the following two techniques: (1) bioactive compounds that accelerate bone formation are coated on metallic implants and (2) a rough surface at the macrol level is formed on the metallic implants, and the ingrowth of bone results in anchorage of the implants. These techniques have achieved a certain level of success, and the surface-modified implants

have been used clinically. However, there are still weaknesses with the coating that need resolution, as well as unclear points regarding the effect of the surface properties on the osteoconductivity. Since hydroprocessing can be used to prepare the coating on complex-shaped substrates with complex topography, which many implants have, we focus on the use of hydroprocessing in many techniques for coating the bioactive compound, especially hydroxyapatite (HAp), and expound on the characteristics of the techniques and issues. Moreover, we describe in detail the evaluation of the osteoconductivity of implants coated with HAp, using *in vivo* testing in rat tibiae.

2. HAp Coating

HAp ($\text{Ca}_{10}(\text{PO}_4)_6(\text{OH})_2$), which is the main inorganic component in the mammal bone or tooth [1], has attracted attention as a surface-coating compound because of its high osteoconductivity. Many pyroprocessing methods of forming HAp and other calcium phosphate coatings on metallic substrates have been reported (e.g., plasma spraying [2, 3], sol-gel method [4, 5], electron beam sputtering method [6], and ion beam sputtering method [7]). However, all have weak points in relation to coating with HAp

on complex-shaped implants. Plasma spraying remains the most commonly used technique for HAp coating on a Ti or Ti alloy substrate in the fabrication of artificial joint replacements [1] and in endosseous dental implants [2]. On the other hand, many hydrocoating techniques (e.g., cathodic electrolysis method [8–10], electrophoretic method [11, 12], and thermal substrate method [13–18]) have been proposed as approaches to forming thin-film coatings on metallic substrates. The cathodic electrolysis and thermal substrate methods are single-step coating techniques in an aqueous solution, and they coat the HAp directly from the solution. The electrophoretic method is omitted from this paper because it uses HAp formed by other methods in advance, despite the hydroprocessing. Therefore, in this paper, we describe the cathodic electrolysis and thermal substrate methods.

2.1. Theory of HAp Coating Using Hydroprocessing. It is known that the solubility of HAp in an aqueous solution decreases with increasing temperature and that the relationship between the HAp solubility product, $K_{SP}/(\text{mol dm}^{-3})^9$, and the temperature, T/K , is given by [19]

$$\log K_{SP} = -\frac{8219.41}{T} - 1.6657 - 0.098215 T. \quad (1)$$

Therefore, heating an aqueous solution containing Ca^{2+} and PO_4^{3-} ions results in the precipitation of calcium phosphates, such as HAp, in the solution.

The ionic product of HAp, $K_{IP}/(\text{mol L}^{-1})^9$, is expressed as follows:

$$K_{IP} = [\text{Ca}^{2+}]^5 [\text{PO}_4^{3-}]^3 [\text{OH}^-], \quad (2)$$

where $[X]$ indicates the molar concentration (mol L^{-1}) of ionic species X . The increase in $[\text{Ca}^{2+}]$ or $[\text{PO}_4^{3-}]$ content or pH value in the solution initiates the precipitation of HAp because K_{IP} achieves K_{SP} . Moreover, $[\text{PO}_4^{3-}]$ increases with increasing pH value (Figure 1). Therefore, the increase in pH directly accelerates the precipitation of HAp, which indirectly increases the $[\text{PO}_4^{3-}]$ content.

Figure 2 shows the solubility curves of various compounds on calcium orthophosphosphate [19]; as shown, there are many compounds other than HAp. This figure indicates that CaHPO_4 (DCPA) is the most stable compound at $\text{pH} < 5$, with HAp the most stable at $\text{pH} > 5$. Therefore, HAp can be easily obtained in a solution where $\text{pH} > 5$ and where the ion content and temperature are controlled. However, HAp cannot precipitate in a solution of $\text{pH} < 5$, and hydroprocessing using the precipitation phenomenon in the aqueous solution cannot give $\beta\text{-Ca}_3(\text{PO}_4)_2$ ($\beta\text{-TCP}$), a bioactive compound.

2.2. Thermal Substrate Method in Aqueous Solution [13]. This process involves passing an alternating current through a metallic sample immersed in an aqueous solution. The immersed metallic sample heats up to more than 100°C by Joule heating, even though the hydroprocessing occurs at atmospheric pressure (Figure 3). Therefore, this method

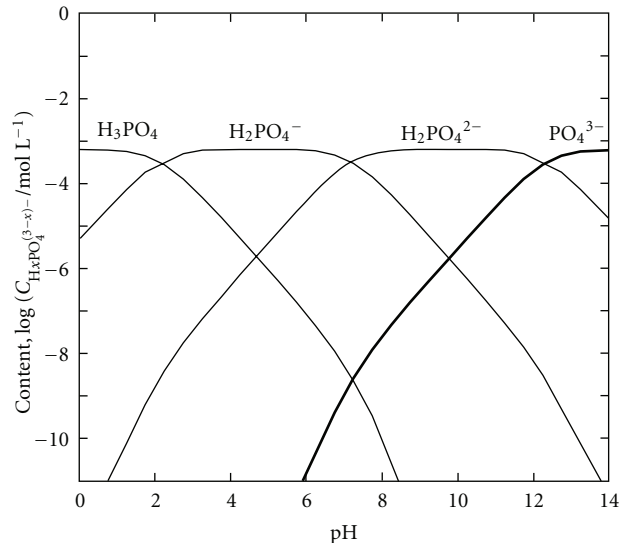


FIGURE 1: Logarithmic concentration diagram for orthophosphoric acid.

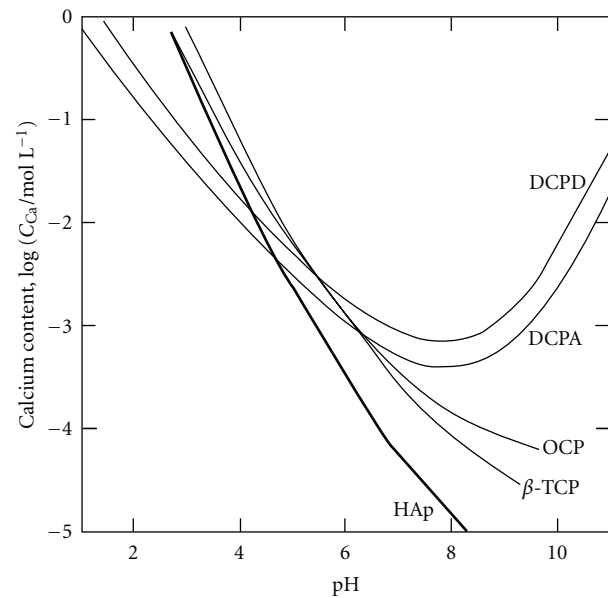


FIGURE 2: Solubility curves of calcium orthophosphoric compounds at 37°C , depending on pH in aqueous solution. HAp: hydroxyapatite ($\text{Ca}_{10}(\text{PO}_4)_6(\text{OH})_2$), TCP: calcium phosphate ($\text{Ca}_3(\text{PO}_4)_2$), OCP: octacalcium phosphate ($\text{Ca}_8\text{H}_2(\text{PO}_4)_6 \cdot 5\text{H}_2\text{O}$), DCPA: dicalcium phosphate anhydrous (CaHPO_4), DCPD: dicalcium phosphate dihydrate ($\text{CaHPO}_4 \cdot 2\text{H}_2\text{O}$).

can produce the special reaction conditions ($>100^\circ\text{C}$ in an aqueous solution) by not using the pressure vessel.

When the thermal substrate method in an aqueous solution is used, the fact that the solubility of HAp decreases with increasing temperature means that HAp precipitation occurs only on the substrate. It is important to coat HAp while controlling the concentration of the solute and the pH value of the solution and temperature, because they affect the degree of supersaturation of HAp in the

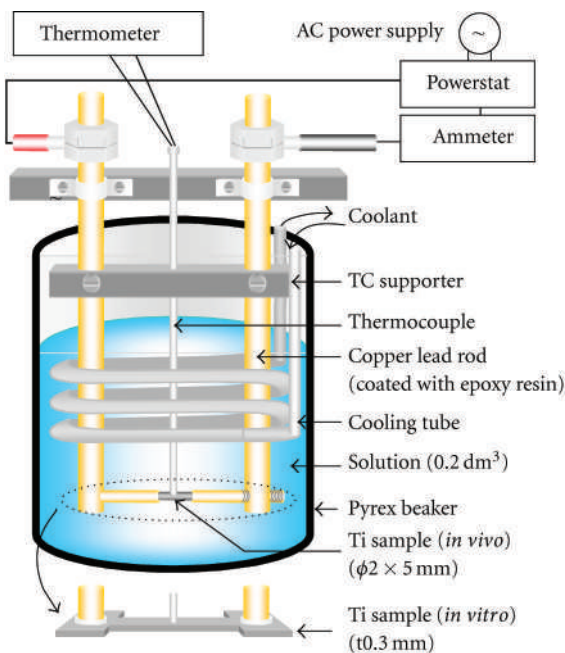


FIGURE 3: Experimental apparatus for HAp coating.

solution (Equations (1) and (2)). Figures 4(a)–4(d) show the change in the surface morphology of the samples coated with HAp under controlled pH and temperature, whose factors determined the degree of the supersaturation with respect to HAp [14, 15, 17, 18]. The precipitate at pH = 4.0 (Figure 4(a)) appeared to pile up like bricks and was identified as DCPA, which is a stable compound. On the other hand, in the solution at pH = 8.0, the precipitate was composed of HAp (Figures 4(b)–4(d)). From the EDX analysis, the molar ratio of calcium to phosphorous (Ca/P) of HAp was 1.41–1.43. This shows the coated HAp was calcium deficient. The pH dependence of the solubility of the calcium phosphate compounds explains why the precipitate changed with increasing pH of the solution, that is, the solubility curves of DCPA and HAp cross at approximately pH = 5 for various compounds of calcium phosphate [19]. The surface morphology of the precipitated HAp strongly depends on coating temperature: low temperature (40°C) gave net-like HAp (Figure 4(b)); high temperature (140°C) gave needle-like HAp (Figure 4(d)); mid temperature (60°C) gave plate-like HAp (Figure 4(c)). That is, by using hydroprocessing, we can control the crystalline form, which could not have been achieved using traditional methods. Figure 5 shows the scanning electron microscopy (SEM) photographs of the HAp-coated samples on porous Ti alloy surfaces formed by sintering Ti6Al4V particles (ca. 100 μm in diameter) on cpTi substrates [16]. Heating at 100°C for 15 min. in a pH = 7 solution led to HAp precipitation over the entire surface of the Ti6Al4V sintered particles (on both front and back faces) and on the base cpTi substrate of the experimental samples. In particular, it was found that HAp precipitate was also detected at the sinter neck regions of adjacent particles and on the base substrate, while the original open-pored geometry was maintained. Therefore, this method can be

used to apply the HAp coating to a substrate with complex topography.

Biological apatite in natural bone does not appear in the form of pure HAp, and it contains a considerable amount of carbonate ions [20] (about 7.4 mass% with respect to total bone and 11.4 mass% with respect to the inorganic component in natural bone [21]). Carbonate apatite ($\text{CO}_3\text{-Ap}$), which replaces PO_4^{3-} and/or OH^- ions with CO_3^{2-} ions, is similar to the inorganic component of bone, and it seems to be a more promising bioactive material than stoichiometric HAp, because $\text{CO}_3\text{-Ap}$ has greater solubility than pure HAp [20]. In addition, it has been reported that CaCO_3 displays bioactivity, such as cell compatibility and hard tissue compatibility [22, 23]; that is, CO_3^{2-} is expected to influence biological reactivity and osteoconductive properties. It is also well known that the solubility of CaCO_3 in an aqueous solution decreases with increasing temperature [24]. In the solution, when CO_3^{2-} ions are added, $\text{CO}_3\text{-Ap}$ or $\text{CO}_3\text{-Ap}/\text{CaCO}_3$ composite films are easily obtained on a substrate. Typical SEM photographs of the surface of the samples are shown in Figures 4(e)–4(f), coated in a solution of pH = 8 with <0.5 mM NaHCO₃ added at 140°C for a period of 15 min., and after the steam autoclaving treatment (5 mass% CO₃ in this film) [25, 26]. The precipitates coated from the solution with >0.5 mM NaHCO₃ added contained CO₃-Ap and CaCO₃ at all temperatures, and the X-ray diffraction spectra showed a mixture of calcite, vaterite, and aragonite. The crystalline form of CO₃-Ap was changed, depending on the added NaHCO₃ content, as well as coating temperature. In particular, adding a significant amount of NaHCO₃ (>5 mM) brought about sphere-like CO₃-Ap (Figure 4(f)) in the 140°C coating. In CO₃-Ap films, FT-IR analysis revealed that CO₃²⁻ was substituted for PO₄³⁻ (Type B CO₃-Ap) in advance, which was similar to biological apatite [27], and adding more CO₃²⁻ to the solution gave the substitution for OH⁻ (type A). Therefore, in the samples with <0.5 mM NaHCO₃ added, type B CO₃-Ap was obtained, and in the samples with >5 mM NaHCO₃ added (i.e., having the binary phase of CO₃-Ap/CaCO₃), type AB CO₃-Ap was formed.

Natural bone contains CO₃-Ap and a considerable amount of organic components, such as collagen (about 23 mass% [21]). It is known that the hybrid organic-inorganic structure initiates pliable bone. Some researchers have reported the preparation of nanocomposites of HAp/collagen and HAp/gelatin [28–30], as natural bone is considered a nanocomposite of mineral and proteins. Moreover, immobilization of collagen on implants displays a tighter fixation with the surrounding tissue, since the collagen behaves as an adhesive protein with cells because of the amino groups in the collagen molecules [31, 32]. From the viewpoint of osteoconductivity, we expected that preparing the HAp/collagen composite coating would be a more promising approach than using an individual coating of either CO₃-Ap or HAp. In the solution to which acid-soluble collagen is added, HAp/collagen or HAp/gelatin composite films are easily obtained on a substrate, depending on coating temperature. In general, as mammalian collagen rapidly denatures to gelatin at >45°C, HAp/collagen composite

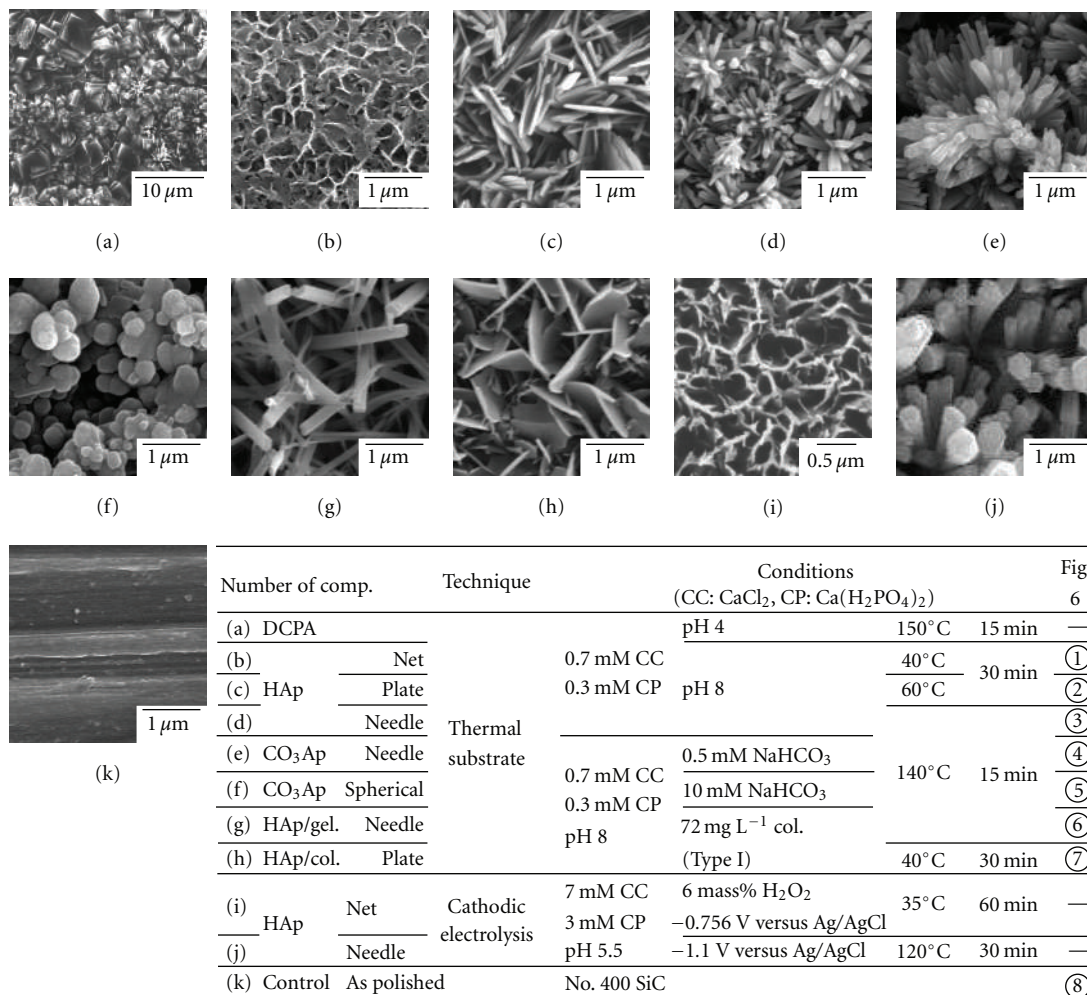


FIGURE 4: SEM photographs of the surface of the samples treated by various methods.

can be obtained at <40°C and HAp/gelatin composite at >50°C. Figures 4(g)-4(h) show the surface of the samples coated in a solution of pH = 8 with 72 mg L⁻¹ collagen, derived from calf, at 140°C and 40°C (10–15 mass% collagen or gelatin in the film) [33]. The surface morphologies of HAp/collagen and HAp/gelatin significantly depend on the coating temperature and are not affected by whether the composite film contains collagen or gelatin. That is, collagen and gelatin have only a small effect on the HAp crystal growth of the adsorption onto HAp. Hydroprocessing can be used to form HAp/collagen and HAp/gelatin composite films, which could not be formed using high-temperature processing, and the content of collagen and gelatin in the films can be controlled up to 60 mass%.

2.3. Cathodic Electrolysis in Aqueous Solution [8–10]. In the electrochemical technique, a redox reaction produces supersaturation of OH⁻ ions near the electrode in the aqueous solution containing Ca²⁺ and PO₄³⁻ in the same manner as in the thermal substrate method. This local effect induces heterogeneous nucleation on the metal substrate serving as the electrode. The addition of hydrogen peroxide

to the solution prevents H₂ gas generation at the cathodic electrode and promotes nucleation and growth of the HAp coating. Adding H₂O₂ to electrolytes enhances the formation of OH⁻ ions at the solution-electrode interface at a lower cathodic potential, as described in the following reaction [10]:



In this method, the surface morphology of the precipitated HAp greatly depends on coating temperature [34] in the same manner as in the thermal substrate method. The effect of temperature on the surface morphology of coated samples is shown in Figures 4(i)-4(j). The HAp crystals had a similar shape to those formed using the thermal substrate method, although the size of HAp crystals differed between the cathodic electrolysis and the thermal substrate methods. The molar ratio (Ca/P) of HAp was almost same as that using the thermal substrate method. The coatings at >100°C were conducted in the pressure vessel. When using the electrolysis solution, to which CO₃²⁻ or collagen are added, CO₃-Ap, HAp/collagen, or HAp/gelatin composite films are formed on a substrate, depending on coating temperature.

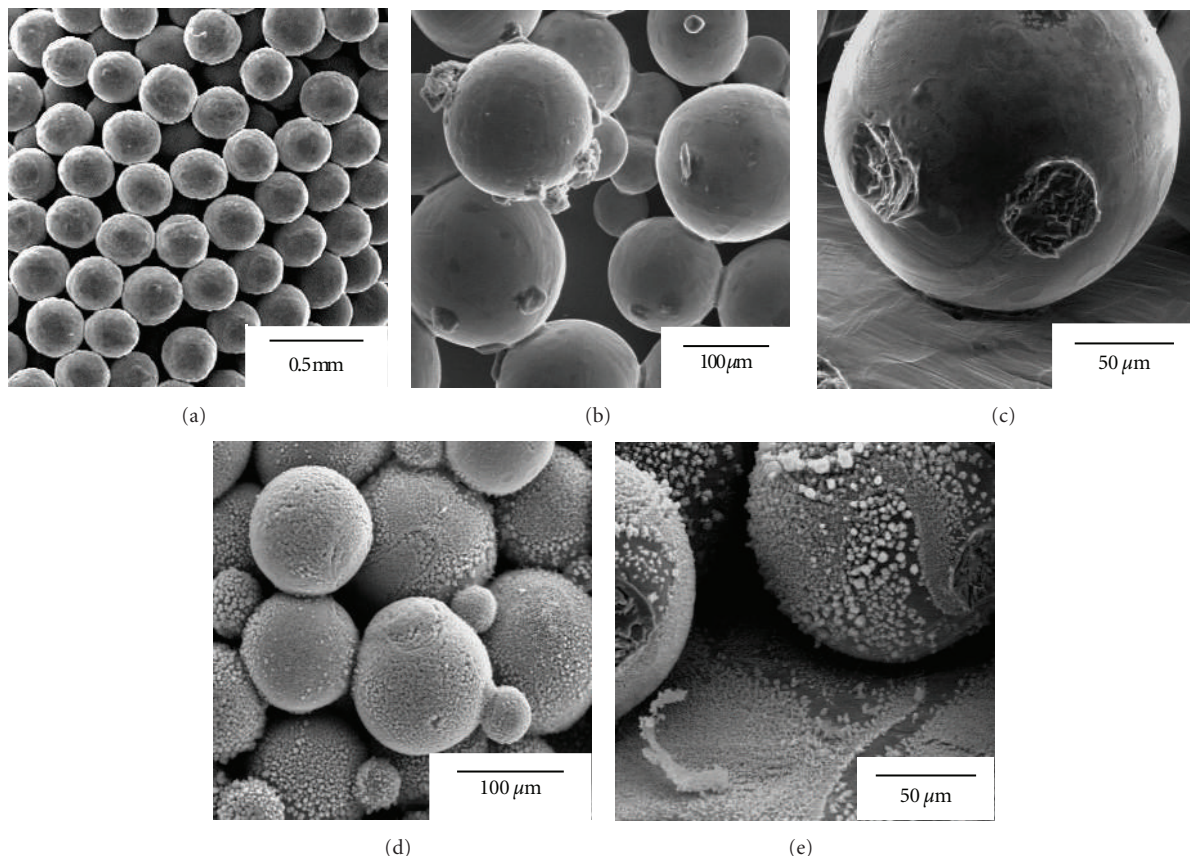


FIGURE 5: Surface and/or cross-sectional views of the samples with surface roughness. (a)–(c) bead-sintered porous samples (as sintered), (d)–(e) bead-sintered porous samples coated with HAp (thermal substrate method, 0.7 mM CaCl₂ + 0.3 mM Ca(H₂PO₄)₂, pH 7, 100°C, 15 min.).

3. Evaluation of Osteoconductivity

The evaluation methods for the bioactivity of the implants are classified into *in vitro* and *in vivo* methods. In this review, the *in vivo* evaluation method is described. In *in vivo* evaluation, many types of animals at different ages were used in various studies, and different researchers used a different implanted part of the animals. Moreover, a unified quantification criterion has not yet been established, and the criteria used in various studies are not compatible with one

another. Therefore, we use the bone-implant contact ratio, R_{B-I} , as an osteoconductive index based on the observation of body tissue on the implants. Bone-implant contact was determined by linear measurement of direct bone contact with the implant surface. The sum of the length of the bone formation on the implant surface was measured and expressed as a percentage of the total implant length (bone-implant contact ratio) in the cancellous bone and the cortical bone parts [17, 18, 25, 26, 33].

$$R_{B-I} (\%) = \frac{\text{sum of the length of the part of bone formation on the implant surface}}{\text{total implant length}} \times 100. \quad (4)$$

Figure 6 shows the bone-implant contact ratios, R_{B-I} , of the samples coated under the various conditions mentioned above and classified based on the following four surface morphologies: (A) needlelike, (B) platelike, (C) netlike, and (D) spherelike. The samples are then compared with the control implant ((E) noncoated Ti). In Figure 6, the samples are distinguished according to color based on whether or not the coating contained CaCO₃ and collagen or gelatin (white:

HAp; gray: CO₃-Ap or HAp/gelatin; black: CO₃-Ap/CaCO₃ or HAp/collagen). The R_{B-I} value of HAp-coated samples (white bar) is the same as or higher than that of the as-polished one (E). In particular, R_{B-I} in the cancellous bone part is highest in the sample coated with the needle-like HAp (A-1). The influence of the different surface morphologies on R_{B-I} is apparent [17, 18]. A small amount of CO₃ included in CO₃-Ap does not influence osteoconductivity, and an

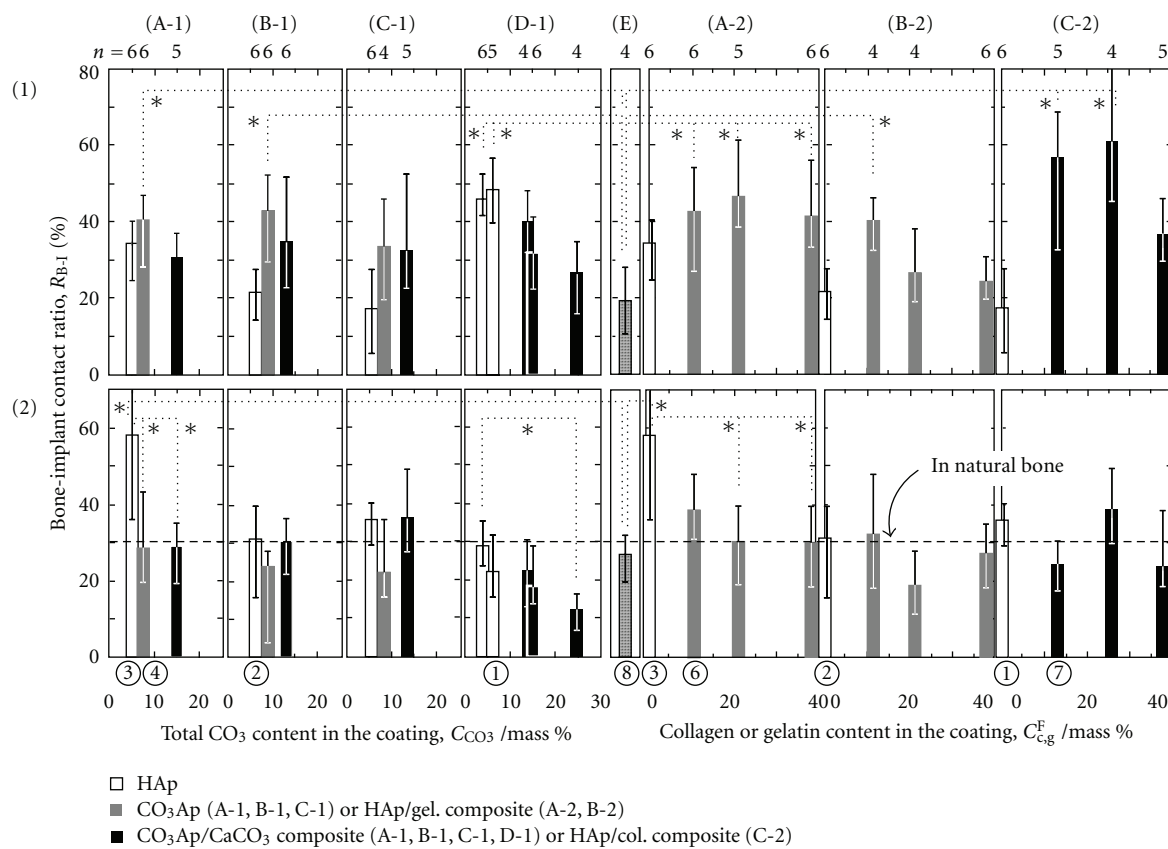


FIGURE 6: Bone-implant contact ratio, R_{B-I} , for the various surface-coated samples (rats' tibia, 14 days). * $P < 0.05$ (1) cortical bone part, (2) cancellous bone part. (A) needle-like, (B) plate-like, (C) net-like, (D) spherical-like, (E) as-polished Ti.

increased amount of CO_3 (>15 mass% CO_3), including that in $\text{CO}_3\text{-Ap}/\text{CaCO}_3$, has a negative effect on (black bar in (A-1), (B-1), (C-1), and (D-1)) [25, 26]. The R_{B-I} value of HAp/gelatin-coated samples is the same as that of HAp (gray and white bars in (A-2) and (B-2)), and we did not find a positive effect of the addition to HAp on the osteoconductivity, or any negative effects within the limit of gelatin content used. In the HAp/collagen films (C-2), osteoconductivity was improved, and maximum R_{B-I} was obtained when the collagen content was the same as that in natural bone. The addition of too much collagen, exceeding that amount of collagen content in natural bone, inhibited the improvement of the osteoconductivity [33].

4. Conclusion

The inside of the human body is equivalent to a water environment at room temperature, since the water content in the body is about 60%. It is thought that hydroformed HAp has greater osteoconductivity than HAp synthesized using pyroprocessing, because synthesized HAp in the aqueous solution at neutral pH and room temperature is similar to that formed in the body. In addition, titanium dioxide, TiO_2 , which does not exist in the human body, is a remarkable compound with respect to its osteoconductivity. It is important to research and improve the osteoconductivity of

substances such as HAp, TiO_2 , and CaTiO_3 . However, we need to pay attention to the properties of their compounds, such as surface roughness [35], crystallinity, and corrosivity, all of which influence osteoconductivity. Furthermore, the evaluation criterion for osteoconductivity has not been adequately established.

The development of implants with high functionality is an important problem that urgently needs to be solved, instead of merely making progress in medical technology. It is thought that nothing can compete with such implants in the progress and development of the individual technology. We hope that these important problems can be solved using the combination of the discovery of new bioactive compounds (organic and inorganic) and their coating techniques, alloy designs for the implants, and/or the growth of related surrounding techniques for them.

References

- [1] L. L. Hench and J. Wilson, *An Introduction to Bioceramics*, chapter 1, World Scientific Publishing, Singapore, 1993.
- [2] R. M. Pilliar, D. A. Deporter, P. A. Watson et al., "The effect of partial coating with hydroxyapatite on bone remodeling in relation to porous-coated titanium-alloy dental implants in the dog," *Journal of Dental Research*, vol. 70, no. 10, pp. 1338–1345, 1991.

- [3] S. W. K. Kweh, K. A. Khor, and P. Cheang, "Plasma-sprayed hydroxyapatite (HA) coatings with flame-spheroidized feedstock: microstructure and mechanical properties," *Biomaterials*, vol. 21, no. 12, pp. 1223–1234, 2000.
- [4] B. Mavis and A. C. Taş, "Dip coating of calcium hydroxyapatite on Ti-6Al-4V substrates," *Journal of the American Ceramic Society*, vol. 83, no. 4, pp. 989–991, 2000.
- [5] S. Langstaff, M. Sayer, T. J. N. Smith, S. M. Pugh, S. A. M. Hesp, and W. T. Thompson, "Resorbable bioceramics based on stabilized calcium phosphates. Part I: rational design, sample preparation and material characterization," *Biomaterials*, vol. 20, no. 18, pp. 1727–1741, 1999.
- [6] D. H. Kim, Y. M. Kong, S. H. Lee et al., "Composition and crystallization of hydroxyapatite coating layer formed by electron beam deposition," *Journal of the American Ceramic Society*, vol. 86, no. 1, pp. 186–188, 2003.
- [7] T. S. Chen and W. R. Lacefield, "Crystallization of ion beam deposited calcium phosphate coatings," *Journal of Materials Research*, vol. 9, no. 5, pp. 1284–1290, 1994.
- [8] H. Ishizawa and M. Ogino, "Thin hydroxyapatite layers formed on porous titanium using electrochemical and hydrothermal reaction," *Journal of Materials Science*, vol. 31, no. 23, pp. 6279–6284, 1996.
- [9] M. Okido, K. Kuroda, M. Ishikawa, R. Ichino, and O. Takai, "Hydroxyapatite coating on titanium by means of thermal substrate method in aqueous solutions," *Solid State Ionics*, vol. 151, no. 1–4, pp. 47–52, 2002.
- [10] M. Okido, K. Nishikawa, K. Kuroda, R. Ichino, Z. Zhao, and O. Takai, "Evaluation of the hydroxyapatite film coating on titanium cathode by QCM," *Materials Transactions*, vol. 43, no. 12, pp. 3010–3014, 2002.
- [11] X. Nie, A. Leyland, and A. Matthews, "Deposition of layered bioceramic hydroxyapatite/TiO₂ coatings on titanium alloys using a hybrid technique of micro-arc oxidation and electrophoresis," *Surface and Coatings Technology*, vol. 125, no. 1–3, pp. 407–414, 2000.
- [12] L. A. De Sena, M. C. De Andrade, A. M. Rossi, and G. A. De Soares, "Hydroxyapatite deposition by electrophoresis on titanium sheets with different surface finishing," *Journal of Biomedical Materials Research*, vol. 60, no. 1, pp. 1–7, 2002.
- [13] H. Ziani-Cherif, Y. Abe, K. Imachi, and T. Matsuda, "Hydroxyapatite coating on titanium by thermal substrate method in aqueous solution," *Journal of Biomedical Materials Research*, vol. 59, no. 2, pp. 390–397, 2002.
- [14] K. Kuroda, R. Ichino, M. Okido, and O. Takai, "Effects of ion concentration and pH on hydroxyapatite deposition from aqueous solution onto titanium by the thermal substrate method," *Journal of Biomedical Materials Research*, vol. 61, no. 3, pp. 354–359, 2002.
- [15] K. Kuroda, Y. Miyashita, R. Ichino, M. Okido, and O. Takai, "Preparation of calcium phosphate coatings on titanium using the thermal substrate method and their in vitro evaluation," *Materials Transactions*, vol. 43, no. 12, pp. 3015–3019, 2002.
- [16] K. Kuroda, S. Nakamoto, R. Ichino, M. Okido, and R. M. Pilliar, "Hydroxyapatite coatings on a 3D porous surface using thermal substrate method," *Materials Transactions*, vol. 46, no. 7, pp. 1633–1635, 2005.
- [17] K. Kuroda, S. Nakamoto, Y. Miyashita, R. Ichino, and M. Okido, "Osteoinductivity of HA films with different surface morphologies coated by the thermal substrate method in aqueous solutions," *Materials Transactions*, vol. 47, no. 5, pp. 1391–1394, 2006.
- [18] K. Kuroda, S. Nakamoto, Y. Miyashita, R. Ichino, and M. Okido, "Osteoinductivity of hydroxyapatite films with different surface morphologies coated by the thermal substrate method in aqueous solutions," *Journal of the Japan Institute of Metals*, vol. 71, no. 3, pp. 342–345, 2007.
- [19] J. C. Elliot, "Studied in inorganic chemistry 18," in *Structure and Chemistry of the Apatites and Other Calcium Orthophosphates*, chapter 1, Elsevier, New York, NY, USA, 1994.
- [20] R. Tang, Z. J. Henneman, and G. H. Nancollas, "Constant composition kinetics study of carbonated apatite dissolution," *Journal of Crystal Growth*, vol. 249, no. 3–4, pp. 614–624, 2003.
- [21] H. Aoki, *Marvelous Biomaterial, Apatite*, Ishiyaku Publishers, Tokyo, Japan, 1999.
- [22] D. Hanein, H. Sabanay, L. Addadi, and B. Geiger, "Selective interactions of cells with crystal surfaces. Implications for the mechanism of cell adhesion," *Journal of Cell Science*, vol. 104, no. 2, pp. 275–288, 1993.
- [23] H. Ohgushi, M. Okumura, T. Yoshikawa, K. Inoue, N. Senpuku, and S. Tamai, "Bone formation process in porous calcium carbonate and hydroxyapatite," *Journal of Biomedical Materials Research*, vol. 26, no. 7, pp. 885–895, 1992.
- [24] Nihon Kagaku Kai, *Kagaku Binran, Kiso-Hen*, Maruzen, Tokyo, Japan, 2004.
- [25] K. Kuroda, M. Moriyama, R. Ichino, M. Okido, and A. Seki, "Formation and in vivo evaluation of carbonate apatite and carbonate apatite/CaCO₃ composite films using the thermal substrate method in aqueous solution," *Materials Transactions*, vol. 49, no. 6, pp. 1434–1440, 2008.
- [26] K. Kuroda, M. Moriyama, R. Ichino, M. Okido, and A. Seki, "Formation and in vivo evaluation of carbonate apatite and carbonate apatite/CaCO₃ composite films using the thermal substrate method in aqueous solution," *Journal of the Japan Institute of Metals*, vol. 73, no. 5, pp. 346–353, 2009.
- [27] Q. Zhang, J. Chen, J. Feng, Y. Cao, C. Deng, and X. Zhang, "Dissolution and mineralization behaviors of HA coatings," *Biomaterials*, vol. 24, no. 26, pp. 4741–4748, 2003.
- [28] M. C. Chang, T. Ikoma, M. Kikuchi, and J. Tanaka, "Preparation of a porous hydroxyapatite/collagen nanocomposite using glutaraldehyde as a crosslinkage agent," *Journal of Materials Science Letters*, vol. 20, no. 13, pp. 1199–1201, 2001.
- [29] R. Z. Wang, F. Z. Cui, H. B. Lu, H. B. Wen, C. L. Ma, and H. D. Li, "Synthesis of nanophase hydroxyapatite/collagen composite," *Journal of Materials Science Letters*, vol. 14, no. 7, pp. 490–492, 1995.
- [30] M. C. Chang, C. C. Ko, and W. H. Douglas, "Preparation of hydroxyapatite-gelatin nanocomposite," *Biomaterials*, vol. 24, no. 17, pp. 2853–2862, 2003.
- [31] T. Ishii, M. Koishi, and T. Tsunoda, *Nure-Gijutsu Handbook*, chapter 16, Techno-System, Tokyo, Japan, 2001.
- [32] T. Okada and Y. Ikada, "Surface modification of silicone for percutaneous implantation," *Journal of Biomaterials Science*, vol. 7, no. 2, pp. 171–180, 1995.
- [33] K. Kuroda, M. Moriyama, R. Ichino, M. Okido, and A. Seki, "Formation and osteoconductivity of hydroxyapatite/collagen composite films using a thermal substrate method in aqueous solutions," *Materials Transactions*, vol. 50, no. 5, pp. 1190–1195, 2009.
- [34] S. Ban and S. Maruno, "Hydrothermal-electrochemical deposition of hydroxyapatite," *Journal of Biomedical Materials Research*, vol. 42, no. 3, pp. 387–395, 1998.
- [35] D. Yamamoto, I. Kawai, K. Kuroda, R. Ichino, M. Okido, and A. Seki, "Osteoconductivity of anodized titanium with controlled micron-level surface roughness," *Materials Transactions*, vol. 52, no. 8, pp. 1650–1654, 2011.

DNA-Binding and Topoisomerase-I-Suppressing Activities of Novel Vanadium Compound Van-7

Xiao-mei Mo,^{1,2} Zhan-fang Chen,² Xin Qi,¹ Yan-tuan Li,¹ and Jing Li¹

¹Key Laboratory of Marine Drugs, Ministry of Education, School of Medicine and Pharmacy, Ocean University of China, 5 Yu-Shan Road, Qingdao 266003, China

²The Department of Pharmacy, Qingdao Women and Children Hospital, 127 Liao-Yang West Road, Qingdao 266034, China

Correspondence should be addressed to Jing Li, lijing_ouc@163.com

Academic Editor: Zhe-Sheng Chen

Vanadium compounds were studied during recent years to be considered as a representative of a new class of nonplatinum metal anticancer agents in combination to its low toxicity. Here, we found a vanadium compound Van-7 as an inhibitor of Topo I other than Topo II using topoisomerase-mediated supercoiled DNA relaxation assay. Agarose gel electrophoresis and comet assay showed that Van-7 treatment did not produce cleavable complexes like HCPT, thereby suggesting that Topo I inhibition occurred upstream of the relegation step. Further studies revealed that Van-7 inhibited Topo I DNA binding involved in its intercalating DNA. Van-7 did not affect the catalytic activity of DNase I even up to 100 μM. Van-7 significantly suppressed the growth of cancer cell lines with IC₅₀ at nanomolar concentrations and arrested cell cycle of A549 cells at G2/M phase. All these results indicate that Van-7 is a potential selective Topo I inhibitor with anticancer activities as a kind of Topo I suppressor, not Topo I poison.

1. Introduction

DNA topoisomerases which catalyze the interconversions of various topological states of DNA were originally discovered as activities that change the superhelical structure of closed circular DNAs [1]. Based on their functional mechanisms, DNA topoisomerases have been classified into two types: type I DNA topoisomerases (Topo I) break and rejoin only one of the two strands during catalysis, while type II DNA topoisomerases (Topo II) break and rejoin both strands for each DNA strand-passing reaction. Studies have shown that Topo I is associated with actively transcribed genes, whereas Topo II is required for DNA replication and for successful traverse of mitosis [2, 3]. Thus DNA topoisomerases modify the topological states of DNA which facilitate various DNA transactions such as DNA replication, recombination, chromosome condensation/decondensation, and chromosome segregation. Previous studies have suggested that Topo I does not require a nucleotide cofactor or any other energy source to relax supercoiled DNA while Topo II cannot relax supercoiled DNA without ATP [4].

Studies have identified DNA topoisomerases as therapeutic targets in cancer chemotherapy [5]. Topo I is a molecular target of hydroxycamptothecine (HCPT) while Topo II is a molecular target of a number of clinically useful anticancer drugs such as etoposide (VP-16), doxorubicin, mitoxantrone and (N-[4-(9-acridinylamino)-3-methoxyphenyl] methanesulphonanilide) (m-AMSA). Other compounds such as saintopin, intoplicine, indoloquinolinedione derivatives, β-lapachone, and related naphthoquinones have been shown to act on both Topo I and Topo II [6–9].

The success of platinum as anticancer agent has stimulated a search for other metallic cytotoxic compounds with equal or greater anticancer activity and lower toxicity [10]. Three platinum-based antineoplastic agents are now in routine clinical practice: cisplatin, carboplatin, and oxaliplatin [11]. Although these heavy metal agents are active against a variety of cancers, their clinical applications are associated with severe side effects including gastrointestinal symptoms (nausea, vomiting, diarrhea, and abdominal pain), renal tubular injury, neuron-muscular complications, and ototoxicity. In addition, the use of platinum is limited in many

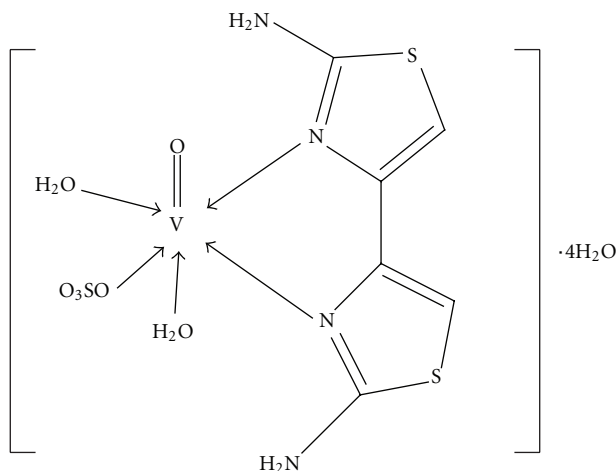


FIGURE 1: Van-7, $[\text{VO}(\text{SO}_4)(\text{C}_6\text{H}_6\text{N}_4\text{S}_2)(\text{H}_2\text{O})_2]\cdot 4\text{H}_2\text{O}$.

tumor types by primary and acquired resistance to this agent [12]. This has led to an ongoing quest for the discovery of nonplatinum metals that may extend the spectrum of activity of metal-based drugs [13]. Vanadium compounds have been widely reported to exert preventive effects against chemical carcinogenesis on animals, by modifying various xenobiotic enzymes and inhibiting carcinogen-derived active metabolites [14, 15]. In the present paper, we investigated the effects of a new vanadium compound, diaqua (2,2'-diamino-4,4'-bi-1,3-thiazole) oxosulfato-vanadium (IV) tetrahydrate (Van-7, Figure 1) [16], on the capability of inhibiting Topo I and anticancer activities in vitro. We find that the Van-7 is a potential Topo I inhibitor as a kind of Topo I suppressor other than Topo I poison.

2. Materials and Methods

2.1. Drugs and Reagents. Van-7 in light blue color crystalloid was provided by the Pharmacocchemistry Department III of Marine and Food institute, Ocean University of China and diluted in double-distilled water. The purity was determined by RP-HPLC to be more than 99.0%. Anal. Calcd for $\text{VC}_6\text{H}_{18}\text{N}_4\text{O}_{11}\text{S}_3$ (M.W. 469.36): C, 15.35; H, 3.86; N, 11.94%. Found: C, 15.30; H, 3.81; N, 11.92%. Supercoiled plasmid pBR322 was purchased from Takara Biotechnology Company (Dalian, China). 3-[4,5-dimethylthiazol-2-yl]-2,5-diphenyltetrazolium bromide (MTT), Proteinase K, and SDS were purchased from Sigma. VP16 was obtained from Pudong Pharmaceutical Factory (China) and HCPT from Feiyun Pharmaceutical Factory (China). Other chemicals used were all of analytical reagent grade. Human DNA Topo I was gifted by ZHOU Shi-Ning (Sun Yat-Sen University, China) [17].

2.2. Topo II Preparation. Topo II was extracted from L-1210 leukemic cells in peritoneal cavity 7 days after tumor inoculation following the procedure of De Isabella et al. [12, 18]. In brief, harvested L-1210 cells from DBA/2 mouse

were resuspended in 10 mL of buffer A (10 mM Tris (pH 7.5), 1.5 mM MgCl_2 , and 10 mM NaCl) and allowed to sit at 0°C for 10 min. A nonionic detergent (1 mL of 10% Nonidet P-40) was added, and the mixture gently triturated and finally left at 0°C for 15 min. The cells were then homogenized and centrifuged at 2500 rpm for 10 min, and the pellet was resuspended in 2 mL of buffer B (50 mM Tris (pH 7.5), 25 mM KCl, 2 mM CaCl_2 , 3 mM MgCl_2 , and 0.25 M sucrose). The nuclei thus obtained were layered over 0.6 mL of buffer C (buffer B with 0.6 M sucrose) and sedimented at 7000 rpm for 10 min. The pellet was resuspended in 2 mL of buffer D (buffer B without CaCl_2 , and with 5 mM MgCl_2), centrifuged at 7000 rpm for 10 min, and finally resuspended in 0.3 mL of buffer E (same as buffer D without sucrose). The solution was added 30 μL of 0.2 M EDTA (pH 8.0) and 0.66 mL of buffer F (80 mM Tris (pH 7.5), 2 mM EDTA, 1 mM DTT, 0.53 M NaCl, and 20% glycerol (v/v)). This mixture was gently triturated, left at 0°C for 30 min, and centrifuged at 40000 rpm for 20 min. The supernatant from the last centrifugation contains Topo II activity, which was examined by the DNA relaxation assay. One unit of Topo II was defined as the amount of enzyme required to fully relax 0.5 μg of supercoiled DNA under the conditions described below.

2.3. DNA Relaxation Assay. Topoisomerases were assayed by relaxation of supercoiled plasmid DNA [19, 20]. Relaxation of 250 ng of supercoiled by Topo I (2 U) was performed in 20 μL of Topo I relaxation buffer (10 mM tris-HCl, pH 7.9, 1 mM EDTA, 150 mM NaCl, 0.1% (w/v) BSA, 0.1 mM spermidine, 5% (v/v) glycerol), in the presence and absence of varying amounts of the test compounds, dissolved in dimethyl sulfoxide (5% (v/v) final concentration). Reactions were started by the addition of DNA. Control groups were either DNA alone or DNA treated with topoisomerase. Relaxation of supercoiled DNA with Topo II was performed in Topo II relaxation buffer (50 mM Tris-HCl, pH 8.0, 0.5 mM ATP, 10 mM MgCl_2 , 120 mM NaCl, and 0.5 mM dithiothreitol). DNA was added before the addition of Topo II. After 30 min at 37°C, the reaction was terminated by the addition of 1% (w/v) SDS and digested with 50 mg/mL proteinase K at 55°C for 30 min. DNA was extracted with an equal volume of chloroform/isoamyl alcohol (24 : 1) and separated on 1% (w/v) agarose gel in Tris-acetate-EDTA (TAE) buffer (40 mM trisacetate, pH 8.0, and 2 mM EDTA) at 2 V/cm for 3.5 h. Gels were stained with 5 mg/mL ethidium bromide, destained, and photographed using Polaroid 665 film or a gel-imaging system for numerical quantification by densitometry scanning (Herolab, Wiesloch, Germany).

2.4. Comet Assay. Nuclei were isolated from P388 cells by incubating whole cells in nuclear buffer (5 mM MgCl_2 , 1 mM EGTA, 1 mM KH_2PO_4 , 150 mM NaCl) for 20 min on ice with gentle rocking. Plasma membrane disruption and nuclei integrity was checked under the microscope. Isolated nuclei were exposed to Van-7 or HCPT at 40 μM for 30 min at 37°C. DNA break was detected as previously described [21]. Briefly, nuclei were embedded in agarose gel and then spread on a polylysinated microscope slide,

Nuclei were lysed in lysis buffer (2.5 M NaCl, 10 mM Tris-HCl, 100 mM Na₂EDTA, 1% Triton, 10% DMSO, pH 10) for 1 h at 4°C. After lysis, nuclei were preincubated for 20 min at 4°C in the electrophoresis buffer (0.3 M NaOH, 1 mM Na₂EDTA, pH 13.5) and then subjected to alkaline gel electrophoresis (300 mA, 4°C, 20 min). Slides were analysed by laser scanning microscopes (LSM, Zeiss Ltd.) to quantitative DNA damage. The tail moment, calculated with Komet 5.5 software (Kinetic Imaging, Bath, UK) by multiplying the total intensity of the comet tail by the migration distance from the center of the comet head, was used to measure DNA damage. Fifty nuclei for each experimental point were scored blind from two slides. The frequency distribution was defined as the percentage of number of cells with tail moment value in total cells scored.

2.5. Measurement of Topo-I Mediated DNA Cleavage. Reaction mixtures containing pBR322 DNA (250 ng) and excess of enzymes (i.e., 100 U of Topo-I) and drugs were incubated at 37°C for 30 min. Samples, which contained tested drugs, were assembled in this order: DNA, Topo-I, Van-7, or HCPT. The reactions were terminated by the adding 1% SDS and 150 mg/mL proteinase K. After the additional 30 min incubation at 37°, DNA samples were electrophoresed in 1% agarose gel containing 0.5 mg/mL ethidium bromide.

2.6. Analysis of Topo I/DNA Binding by EMSA. EMSA (electrophoretic mobility shift assay) was basically performed as described elsewhere [22]. In brief, 250 ng of supercoiled pBR322 DNA was incubated in 20 μL of relaxation Topo I buffer with or without excess of Topo I (100 U) in the presence of the test compounds at 37°C for 6 min. The reaction was started by the addition of DNA. The samples containing test compounds were assembled in the order of Topo I, HCPT, or Van-7. Samples were immediately loaded onto the 0.8% agarose gel in Tris-acetate-EDTA buffer with 1 μg/mL ethidium bromide and separated by electrophoresis for 6 h at 2 V/cm.

2.7. Ethidium Bromide Displacement Fluorescence Assay. Ethidium bromide displacement fluorescence assay [23] was employed to determine whether Van-7 binds to DNA. Fluorescence emission spectra ($\lambda_{\text{max}} = 600 \text{ nm}$, excitation wavelength 546 nm) were obtained at 25°C on a Beckman fluorescence spectrophotometer. The assays contained 1 μM ethidium bromide, 0–100 μM Van-7, and 1 μg supercoiled pBR322 DNA in 2 mL of fluorescence buffer.

2.8. Measurement of DNase I Activity. Bovine DNase I (4.0 U/mL) was incubated with 400 ng of pBR322 DNA in 20 μL of buffer (50 mM Tris-HCl, pH 7.5, 10 mM MnCl₂, and 50 μg/mL BSA) in the presence of Van-7 (50–100 μM) for 15 min at 37°C. The reaction was stopped by the addition of 25 mM EDTA (final concentration) and followed by agarose gel electrophoresis.

2.9. MTT Assay. A549, Hela, BEL-7402, P388, and L-02 cells were purchased from American Type Culture Collection

(ATCC). Culture media were selected according to ATCC suggestions. To perform growth experiments cells were seeded (10,000 cells/well) in 96-well flat bottom plates. After 24 h the media were replaced, and, after one washing, media containing the drugs were added. After 48 h incubation at 37°C, MTT solution was added at 5 mg/mL and incubated for an additional 4 h. Then culture supernate was removed, and 150 μL dimethyl sulfoxide (DMSO) was added per well to dissolve the formazan crystals. Colorimetric determination was made at 570 nm using a microplate reader (Spectra Rainbow, Austria). Six parallel samples were prepared in each group, and each experiment has been replicated for three times. A dose-response study was performed to calculate the 50% inhibiting concentration (IC₅₀) for Van-7. IC₅₀ calculated by the application of the Reed and Muench method [24] is as follows:

$$\text{IC}_{50} = \text{antilog} \left\{ A + \left[\left(\frac{B}{C} \right) D \right] \right\}, \quad (1)$$

where A is log concentration below 50% mortality, B is 50 – mortality below 50%, C is mortality above 50% – mortality below 50%, and D is log concentration above 50% – log concentration below 50%.

2.10. Flow Cytometry. A549 human lung cancer cells were seeded (300,000 cells/well) in 6-well flat bottom plates. After an incubation in F-12 medium containing 10% FCS (v/v) at 37°C for 24 h, Van-7 was added at 100 μM, 50 μM, 25 μM, 12.5 μM (final concentration), and HCPT at 40 μM except the blank control group. 48 h later, A549 cells were harvested, washed three times with phosphate-buffered saline (PBS), stained with PI for 30 min, gated and analyzed by FCM (Becton and Dickinson, Vantage, USA) with a 488 nm laser excitation and a 530 nm emission filter. Data were analyzed with Modfit 2.0 and two parallel samples were prepared in each group, and each experiment was replicated for three times.

2.11. Statistical Analysis. Comparisons of treatment outcomes were tested for statistically significant differences using Student's *t*-test for paired data. Statistical significance was assumed at **P* ≤ 0.05, ***P* ≤ 0.01, and ****P* ≤ 0.001.

3. Results

3.1. Inhibition of the Activity of Topo I but Not Topo II by Van-7. The effects of Van-7 on topoisomerases were investigated using a conventional plasmid DNA relaxation assay. HCPT, a well-known Topo I inhibitor, was employed as a positive control. A representative experiment is shown in Figure 2, the inhibition of the DNA relaxation activity of Topo I by HCPT or Van-7 was in concentration-dependent manner. We found that Van-7 at the concentration of 5 μM obviously inhibited the DNA relaxation activity of Topo I, while HCPT did not have such effect as no visible electrophoresis band of supercoiled DNA was displayed at 5 μM. In additional, Van-7 also completely inhibited the DNA relaxation activity of Topo I at the concentration of 40 μM. These results suggest that Van-7 is a more potent inhibitor of Topo I than HCPT.

TABLE 1: IC₅₀ (μ M) values obtained after 72 h of continuous Van-7 exposure.

Cell lines	P388			BEL-7402			A549			HeLa			L-02		
	0.9 ± 0.2			5.3 ± 1.1			0.1 ± 0.04			5.1 ± 1.2			60.2 ± 7.6		

The figure consists of three panels (a, b, c) showing agarose gel electrophoresis results.
 Panel (a) shows the effect of HCPT on Topo I-mediated supercoiled pBR322 relaxation. Lanes are labeled: RLX, SC, Topo I (-), Topo I (+), HCPT (40, 20, 10, 5, 2.5 μ M).
 Panel (b) shows the effect of Van-7 on Topo I-mediated supercoiled pBR322 relaxation. Lanes are labeled: RLX, SC, Topo I (-), Topo I (+), Van-7 (40, 20, 10, 5, 2.5 μ M).
 Panel (c) shows the effect of Van-7 on Topo II-mediated supercoiled pBR322 relaxation. Lanes are labeled: RLX, SC, Topo II (-), Compounds (-), VP16 (100 μ M), Van-7 (40, 80, 160 μ M).
 In all panels, RLX represents relaxed DNA and SC represents supercoiled DNA. The presence of enzyme or drug leads to a decrease in the intensity of the SC band and an increase in the RLX band. Panel (c) also includes a lane for VP16 as a reference inhibitor of Topo II.

FIGURE 2: (a) Effect of HCPT on Topo I-mediated supercoiled pBR322 relaxation. (b) Effect of Van-7 on Topo I-mediated supercoiled pBR322 relaxation. Both of the two reactions were carried out without ATP. (c) Effect of Van-7 on Topo II-mediated supercoiled pBR322 relaxation. The reaction was carried out in presence of ATP. RLX: relaxed DNA, a circular DNA molecule that has no superhelical turns. SC: supercoiled DNA, over- or underwinding of a DNA strand.

To investigate if Van-7 is a selective inhibitor of Topo I, we further tested its effect on the catalytic activity of Topo II. As shown in Figure 2(c), no inhibitory activity was observed against Topo II, even up to the concentration of 160 μ M. On the contrary, VP16, a well-known Topo II inhibitor, obviously inhibited the strand passage activity of Topo II at 100 μ M.

3.2. Van-7 Does Not Induce Cleavable Complex Formation Like HCPT. Topo I acted as a single-strand endonuclease and ligase, and HCPT inhibits ligase without affecting the cleavage step. Therefore, HCPT entraps a slow migrating complex formed by the enzyme, the drug, and DNA, named

as cleavable complex [25]. We further assessed whether Van-7 also induced the formation of the cleavable complexes. As shown in Figure 3(a), obvious increase of electrophoresis band for open circle was observed after HCPT treatment, suggesting that HCPT could induce formation of cleavable complex; however, Van-7 was not similar to HCPT as no obvious cleavable complex was found comparing with control group, suggesting that inhibitory mechanism of Van-7 against Topo I is different from that of HCPT.

To further consolidate the presumption above, the freshly isolated cell nuclei were treated for 30 min with the compound, and the occurrence of DNA breaks was assessed by comet assay (Figure 3(b)). By comet assays, HCPT was found to be able to induce DNA breaks with obvious formation of comet tail, whereas Van-7 was unable to produce a similar effect.

3.3. Van-7 Exhibits Notable DNA-Binding Activity via the Intercalative Mode. We next investigated whether Van-7 directly interfered with binding of Topo I to DNA using an EMSA assay. Here, HCPT was selected as a control because it can inhibit the ligase activity and does not interfere with the binding of the enzyme to DNA [26]. As shown in Figure 4(a), Van-7 at 100 μ M significantly hampered the binding of the enzyme to DNA, and this did not occur with HCPT as expected.

Ethidium bromide is a large, flat basic molecule that resembles a DNA base pair. Because of its chemical structure, it can intercalate (or insert) into a DNA strand. Displacement of ethidium bromide from DNA with concomitant reduction in ethidium fluorescence was used as an approach to examine whether a compound could intercalate into DNA. As shown in Figure 4(b), with the increase of Van-7, marked reduction in fluorescence intensity was found accordingly, suggesting that ethidium bromide could be displaced by Van-7 from DNA strand. This result indicates that Van-7 can intercalate into DNA and bind to DNA.

3.4. Van-7 Does Not Affect the Activity of DNase I. We further detected the effect of Van-7 on the catalytic activity of bovine DNase I. As shown in Figure 5, with Van-7 even up to 100 μ M or without Van-7, the DNase I could digest DNA indistinguishably, suggesting that Van-7 does not affect the catalytic activity of DNase I.

3.5. The Cytotoxicity Activities of Van-7 In Vitro. Van-7 was tested in four human cancer cell lines to observe its anticancer activities in vitro. Data were shown in Table 1; Van-7 was able to significantly inhibit the growth of the cancer cell lines, but show faint inhibition activity to human normal liver cell line L-02.

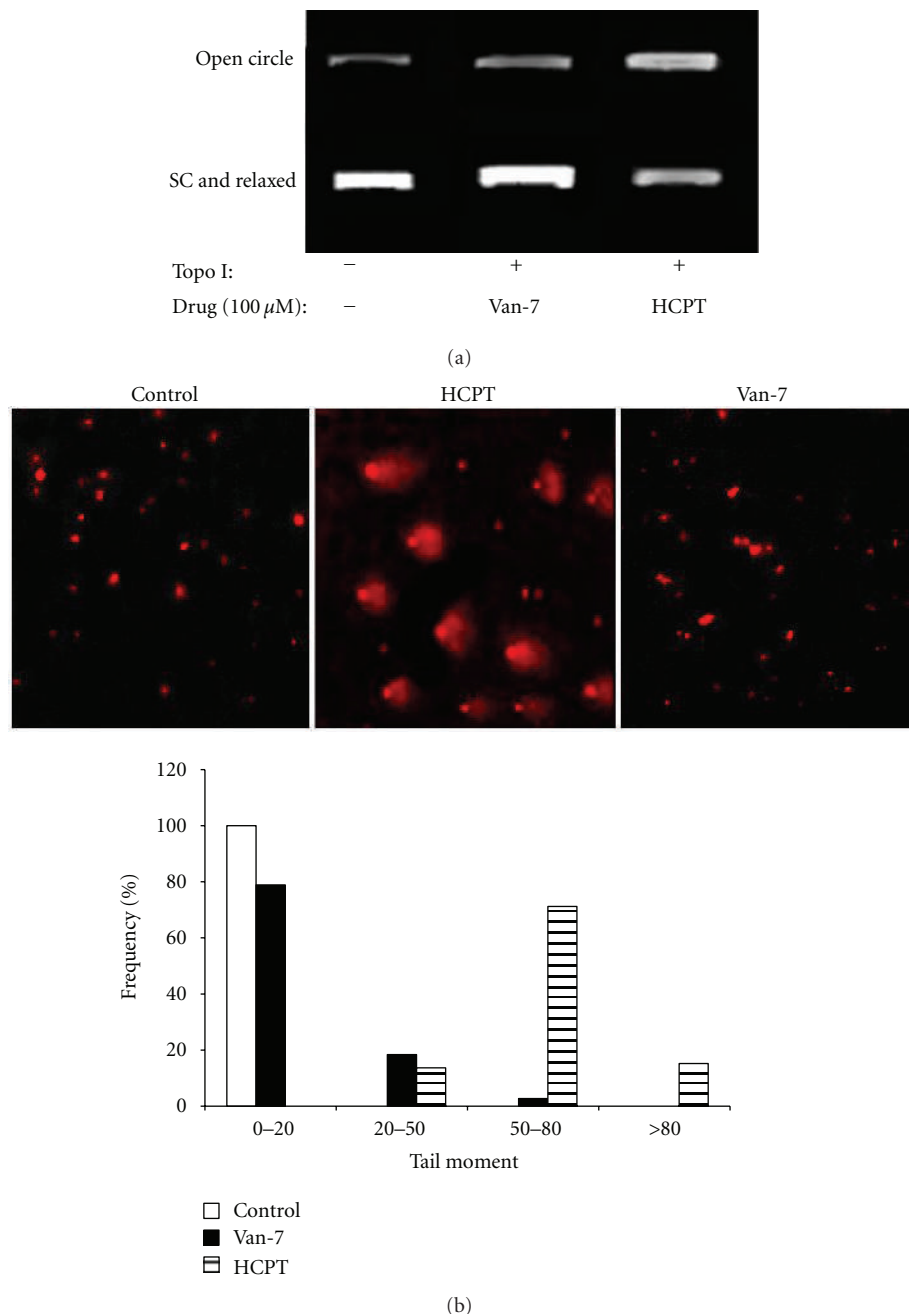


FIGURE 3: (a) Representative image of agarose gel electrophoresis of the cleavage assay. Only HCPT induced the formation of a slow migrating complex formed by enzyme, drug, and DNA, whereas Van-7 did not. (b) Comet assay performed in isolated nuclei in the presence of the vehicle, HCPT (40 μM), or Van-7 (40 μM). Tail moment for each comet was calculated. Nuclei were grouped according to the tail moment value in three groups, and the frequency distribution is shown in the bar chart. DNA damage is increased in nuclei with the highest tail moment values.

3.6. Van-7 Arrests A549 Cell Line at G2/M Phase. To clarify the pattern of Van-7-induced growth suppression, A549 cells were treated with HCPT or Van-7 for 48 hours and analyzed by flow cytometry. Flow cytometry analysis showed that Van-7 treatment resulted in the accumulation of cell populations in G2/M phase in a concentration-dependent manner (Figure 6), while HCPT blocked the cells at S phase [27]. Treatment of A549 cells with 100 μM, 50 μM, 25 μM, and 12.5 μM of Van-7 increased the percentage of cells in

the G2/M phase to 49.36%, 27.21%, 21.10%, and 15.31%, respectively.

4. Discussion

Since the discovery of *cis*-platinum, many transition metal complexes have been synthesized and assayed for antineoplastic activity. In recent years, vanadium-based molecules

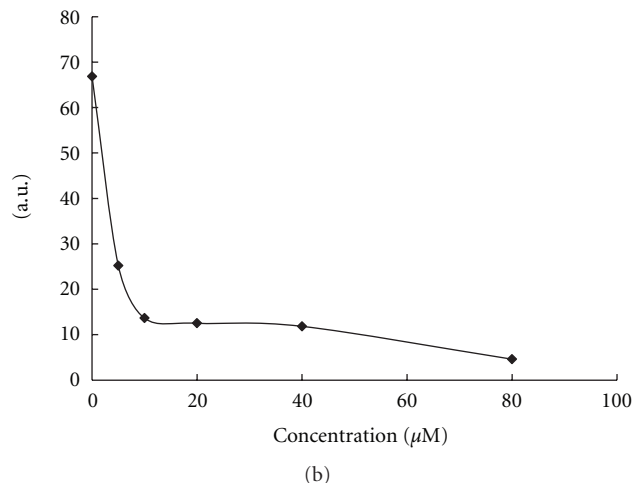
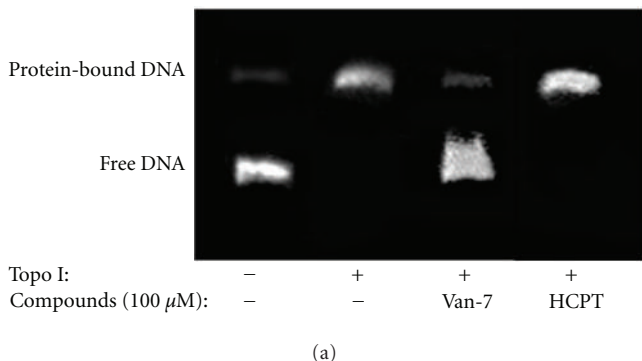


FIGURE 4: (a) Representative image of the agarose gel electrophoresis for EMSA between pBR322 DNA and Topo I. HCPT did not modulate the formation of the complex DNA/Topo 1, whereas Van-7 significantly hampered the binding of the enzyme to DNA. (b) Van-7 displaces ethidium bromide from DNA strand. The ability of Van-7 to interact with DNA was determined by a fluorescence-based ethidium bromide displacement assay. Samples contained 1 μ M ethidium bromide and 1 μ g DNA pBR322. Increasing concentrations of Van-7 were added, and decreasing ethidium fluorescence at 600 nm (λ_{max}) was monitored (546 nm excitation wavelength).

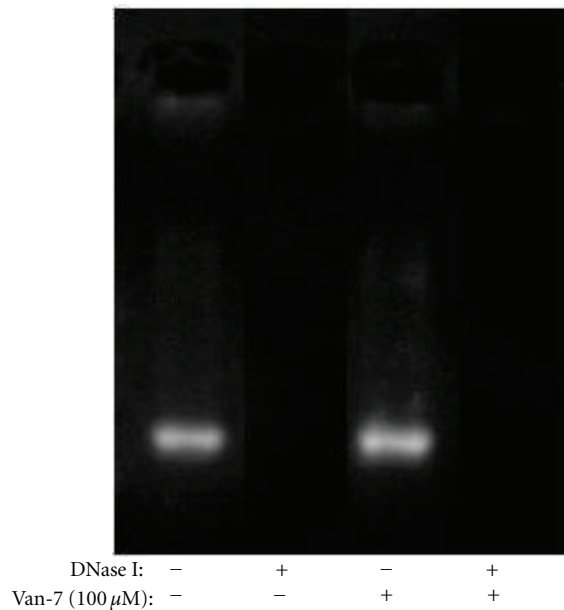


FIGURE 5: Representative image of agarose gel electrophoresis of the DNase assay. Bovine DNase I (4.0 U/mL) was incubated with 400 ng of pBR322 DNA in the presence of Van-7 (100 μ M) for 15 min at 37°C. Van-7 was unable to interfere with DNase activity. This experiment was repeated three times with similar results.

have emerged as promising anticancer and antimetastatic agents with potential application in platinum-resistant tumors or as alternatives to platinum [14]. In our screening model for inhibitor of DNA topoisomerases, we discover that Van-7, one kind of vanadium compound, has a strongly inhibitory activity to Topo I, not to Topo II.

Topo I inhibitors include Topo I poison and Topo I suppressor. Both of them are agents designed to interfere with the action of topoisomerase enzymes, but the mechanisms are different. HCPT, as a kind of camptothecin derivative, is a typical Topo I poison. HCPT can stabilize DNA Topo I, forming drug-DNA Topo I complex and inhibiting Topo I activity [28]. However, suppressor is DNA conjugant (such as Hoechst33258) or intercalator (such as aclacinomycin A). Topo I suppressor combines with DNA or deforms the structure of DNA to inhibit the catalytic activity of Topo I to result in cell death. To exert this effect, most Topo I suppressors must be in relatively high concentration, and the activity of DNA conjugant depends on its closely binding with DNA. In the present paper, Van-7 was found to inhibit the activity of Topo I obviously; however, in the test of drug-DNA Topo I complex with gel electrophoresis analysis, Van-7 was not found to form cleavable complex even up to 100 μ M. In order to further evaluate Van-7 a direct involvement in the inhibition of topoisomerase in nucleus independently on some potential interference, freshly isolated cell nuclei were used, and the probable occurrence of DNA breaks was assessed by comet assay. We found that HCPT treatment showed obvious comet tail while Van-7 did not. From the above two results, we confirm that inhibitory effect of Van-7 on Topo I activity is different from that of HCPT, and the fact that Van-7 cannot form Drug-DNA Topo I complex indicates that Van-7 is not a poison. Therefore, we presume that Van-7 acts on the upstream of catalytic reaction and probably disturbs the combination of Topo I with DNA.

DNA mobility shift assay (EMSA), also called gel retardation assay, can be used to detect DNA-protein interaction *in vitro*. In electric field, DNA fragments binding with protein migrate more slowly to positive pole than free DNA

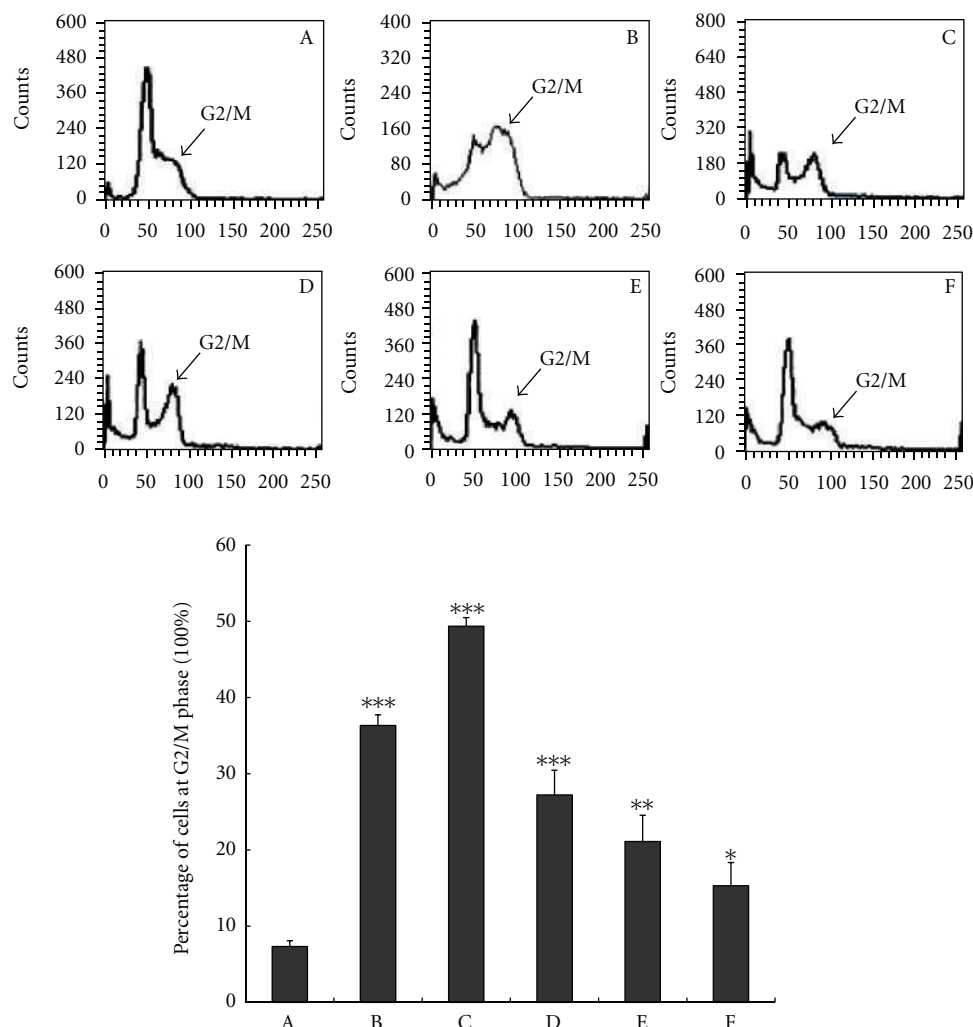


FIGURE 6: Van-7 arrested A549 cell line at G2/M phase. A: control; B: HCPT, 40 μ M; C: Van-7, 100 μ M; D: Van-7, 50 μ M; E: Van-7, 25 μ M; F: Van-7, 12.5 μ M. The percentage of G2/M, A: 7.32%; B: 36.32%; C: 49.36%; D: 27.21%; E: 21.10%; F: 15.31%. The values were the means \pm SD, $n = 3$. * $P < 0.05$, ** $P < 0.01$, *** $P < 0.001$ versus control group.

fragments. We further evaluate the effect of the compound on the binding of DNA with Topo I. In our tests, we found that Van-7 at 40 μ M obviously inhibited the binding of Topo I to DNA with free DNA fragments band in gel electrophoresis. But this phenomenon was not observed in the present of HCPT. In additional, Van-7 significantly reduced the fluorescence intensity by displacing ethidium bromide from DNA strand. All these results indicate that Van-7 intercalates to DNA and exert its inhibitory effect to Topo I.

DNase I is a nuclease that cleaves DNA preferentially at phosphodiester linkages adjacent to a pyrimidine nucleotide, yielding 5'-phosphate-terminated polynucleotide with a free hydroxyl group on position 3', which is similar to topoisomerases cutting the phosphate backbone of the DNA; however, Van-7 was not found to affect the activity of Dnase I, which indicates that Van-7 inhibits activity of Topo I with some selectivity.

Topo I has significant consequences for cancer and cancer chemotherapy via their antiproliferative or cell-differentiating action. From the results of MTT tests, Van-7 was found to strongly inhibit the growth of tumor cells, such as BEL-740A549 and Hela cells, but not normal cells. As the specific activity of Topo I was about 4-fold greater in proliferating (log phase) cells than in nonproliferating (confluent) cells, and in contrast to the changes in Topo I levels, the specific activity of Topo II showed no detectable difference in proliferating versus non-proliferating cells [29], therefore it is reasonable that Van-7 is more selective to cancer cells with proliferation rate much higher than normal cells. It is reported that the compounds exhibit a different inhibitory mechanism from camptothecin that may induce different phase cell cycle arrest, a novel Topo I inhibitor with repressing the catalytic cleavage activity of Topo I instead of forming the drug-enzyme-DNA covalent ternary complex arrested cell cycle at G2/M phase to K562 Cells [30]. Our

FACS analysis result that Van-7 in the concentration of 100 μM could block the cell cycle to G2-M other than S phase is consistent with this report.

On the whole, we consider that Van-7 is a potential Topo I inhibitor as a kind of Topo I suppressor. Van-7 can insert into DNA base pairs, resulting in DNA structure distortion, and then inhibiting the binding of DNA to Topo I, finally affecting the catalytic activity of Topo I. To the best of our knowledge, it is the first report about clarifying inhibitory ability of a vanadium metal compounds on Topo-I catalytic activity and its mechanism. However, the anticancer activity in vivo and detail mechanisms of Van-7 requires further investigation.

Abbreviations

- Topo I: Topoisomerase I
- Topo II: Topoisomerase II
- HCPT: Hydroxycamptothecine
- DMSO: Dimethylsulfoxide
- VP16: Etoposide.

Authors' Contribution

X.-m. Mo and Z.-f. Chen contributed equally to this work.

Acknowledgments

This work was supported by Grants from National High-tech R&D Program (2011AA09070104) of China and Program for Changjiang Scholars and Innovative Research Team in University (IRT0944).

References

- [1] J. C. Wang, "DNA topoisomerases," *Annual Review of Biochemistry*, vol. 65, pp. 635–692, 1996.
- [2] H. Zhang, J. C. Wang, and L. F. Liu, "Involvement of DNA topoisomerase I in transcription of human ribosomal RNA genes," *Proceedings of the National Academy of Sciences of the United States of America*, vol. 85, no. 4, pp. 1060–1064, 1988.
- [3] L. Yang, M. S. Wold, and J. J. Li, "Roles of DNA topoisomerases in simian virus 40 DNA replication in vitro," *Proceedings of the National Academy of Sciences of the United States of America*, vol. 84, no. 4, pp. 950–954, 1987.
- [4] H. J. Chen and J. Hwang, "Binding of ATP to human DNA topoisomerase I resulting in an alteration of the conformation of the enzyme," *European Journal of Biochemistry*, vol. 265, no. 1, pp. 367–375, 1999.
- [5] S. Salerno, F. Da Settimo, S. Taliani et al., "Recent advances in the development of dual topoisomerase I and II inhibitors as anticancer drugs," *Current Medicinal Chemistry*, vol. 17, no. 35, pp. 4270–4290, 2010.
- [6] J. F. Riou, P. Helissey, L. Grondard, and S. Giorgi-Renault, "Inhibition of eukaryotic DNA topoisomerase I and II activities by indoloquinolinedione derivatives," *Molecular Pharmacology*, vol. 40, no. 5, pp. 699–706, 1991.
- [7] B. Poddevin, J. F. Riou, F. Lavelle, and Y. Pommier, "Dual topoisomerase I and II inhibition by intoplicine (RP-60475), a new antitumor agent in early clinical trials," *Molecular Pharmacology*, vol. 44, no. 4, pp. 767–774, 1993.
- [8] F. Leteurtre, A. Fujimori, A. Tanizawa et al., "Saintopin, a dual inhibitor of DNA topoisomerases I and II, as a probe for drug-enzyme interactions," *Journal of Biological Chemistry*, vol. 269, no. 46, pp. 28702–28707, 1994.
- [9] B. Frydman, L. J. Marton, J. S. Sun et al., "Induction of DNA topoisomerase II-mediated DNA cleavage by β -lapachone and related naphthoquinones," *Cancer Research*, vol. 57, no. 4, pp. 620–627, 1997.
- [10] M. Galanski, M. A. Jakupc, and B. K. Keppler, "Update of the preclinical situation of anticancer platinum complexes: novel design strategies and innovative analytical approaches," *Current Medicinal Chemistry*, vol. 12, no. 18, pp. 2075–2094, 2005.
- [11] M. Galanski, "Recent developments in the field of anticancer platinum complexes," *Recent Patents on Anti-Cancer Drug Discovery*, vol. 1, no. 2, pp. 285–295, 2006.
- [12] V. Brabec and J. Kasparkova, "Modifications of DNA by platinum complexes: relation to resistance of tumors to platinum antitumor drugs," *Drug Resistance Updates*, vol. 8, no. 3, pp. 131–146, 2005.
- [13] I. Ott and R. Gust, "Non platinum metal complexes as anti-cancer drugs," *Archiv der Pharmazie*, vol. 340, no. 3, pp. 117–126, 2007.
- [14] A. M. Evangelou, "Vanadium in cancer treatment," *Critical Reviews in Oncology/Hematology*, vol. 42, no. 3, pp. 249–265, 2002.
- [15] A. Bishayee, A. Waghray, M. A. Patel, and M. Chatterjee, "Vanadium in the detection, prevention and treatment of cancer: the in vivo evidence," *Cancer Letters*, vol. 294, no. 1, pp. 1–12, 2010.
- [16] Z. Y. Wu, Y. T. Li, and D. J. Xu, "Diaqua(2,2'-diamino-4,4'-bi-1,3-thiazole)oxosulfatovanadium(IV) tetrahydrate," *Acta Crystallographica Section C*, vol. 61, no. 11, pp. m463–m465, 2005.
- [17] G. W. Yang, B. H. Yuan, K. P. Ho, X. Dai, Y. C. Lin, and S. N. Zhou, "Optimization of the expression of human DNA topoisomerase I in *Pichia pastoris*," *Sheng Wu Gong Cheng Xue Bao*, vol. 20, no. 2, pp. 181–186, 2004.
- [18] P. De Isabella, G. Capranico, M. Binaschi, S. Tinelli, and F. Zunino, "Evidence of DNA topoisomerase II-dependent mechanisms of multidrug resistance in P388 leukemia cells," *Molecular Pharmacology*, vol. 37, no. 1, pp. 11–16, 1990.
- [19] D. K. Trask, J. A. DiDonato, and M. T. Muller, "Rapid detection and isolation of covalent DNA/protein complexes: application to topoisomerase I and II," *EMBO Journal*, vol. 3, no. 3, pp. 671–676, 1984.
- [20] J. R. Spitzner, I. K. Chung, and M. T. Muller, "Eukaryotic topoisomerase II preferentially cleaves alternating purine-pyrimidine repeats," *Nucleic Acids Research*, vol. 18, no. 1, pp. 1–11, 1990.
- [21] G. Raspaglio, C. Ferlini, S. Mozzetti et al., "Thiocolchicine dimers: a novel class of topoisomerase-I inhibitors," *Biochemical Pharmacology*, vol. 69, no. 1, pp. 113–121, 2005.
- [22] F. Boege, T. Straub, A. Kehr et al., "Selected novel flavones inhibit the DNA binding or the DNA religation step of eukaryotic topoisomerase I," *Journal of Biological Chemistry*, vol. 271, no. 4, pp. 2262–2270, 1996.
- [23] B. C. Baguley and E. M. Falkenham, "The interaction of ethidium with synthetic double-stranded polynucleotides at low ionic strength," *Nucleic Acids Research*, vol. 5, no. 1, pp. 161–171, 1978.

- [24] L. Gribaldo, S. Casati, L. Figliuzzi, and E. Marafante, “In vitro myelotoxicity of environmental contaminants,” *Environmental Toxicology and Pharmacology*, vol. 6, no. 2, pp. 135–141, 1998.
- [25] C. C. Kuo, J. F. Liu, and J. Y. Chang, “DNA repair enzyme, O6-methylguanine DNA methyltransferase, modulates cytotoxicity of camptothecin-derived topoisomerase I inhibitors,” *Journal of Pharmacology and Experimental Therapeutics*, vol. 316, no. 2, pp. 946–954, 2006.
- [26] C. García-Estrada, C. F. Prada, C. Fernández-Rubio, F. Rojo-Vázquez, and R. Balaña-Fouce, “DNA topoisomerases in apicomplexan parasites: promising targets for drug discovery,” *Proceedings of the Royal Society B*, vol. 277, no. 1689, pp. 1777–1787, 2010.
- [27] L. Luo, P. Li, H. Peng, Y. Luo, and W. Tang, “Cell cycle block and apoptosis in rabbit lens epithelial cells induced by hydroxycamptothecine,” *Zhonghua Yan Ke Za Zhi*, vol. 38, no. 3, pp. 161–164, 2002.
- [28] S. Coderoni, M. Paparelli, and G. L. Gianfranceschi, “Effect of CPT on the calf thymus Topoisomerase I-mediated DNA breakage-reunion reaction: optimal conditions for the formation and reversal of the CPT trapped Topoisomerase I cleavable complex,” *Molecular Biology Reports*, vol. 17, no. 2, pp. 129–134, 1993.
- [29] J. V. Tricoli, B. M. Sahai, and P. J. McCormick, “DNA topoisomerase I and II activities during cell proliferation and the cell cycle in cultured mouse embryo fibroblast (C3H 10T1/2) cells,” *Experimental Cell Research*, vol. 158, no. 1, pp. 1–14, 1985.
- [30] N. Wu, X. W. Wu, K. Agama et al., “A novel DNA topoisomerase i inhibitor with different mechanism from camptothecin induces G2/M phase cell cycle arrest to K562 cells,” *Biochemistry*, vol. 49, no. 47, pp. 10131–10136, 2010.

Antifungal and Antioxidant Activities of Pyrrolidone Thiosemicarbazone Complexes

Ahmed A. Al-Amiry,^{1,2} Abdul Amir H. Kadhum,¹ and Abu Bakar Mohamad¹

¹Department of Chemical and Process Engineering, Faculty of Engineering and Built Environment, University of Kebangsaan Malaysia, 43600 Bangi, Selangor, Malaysia

²Biotechnology Division, Applied Science Department, University of Technology, Baghdad 10066, Iraq

Correspondence should be addressed to Ahmed A. Al-Amiry, dr.ahmed1975@gmail.com

Academic Editor: Danijela Maksimović-Ivanić

Metal complexes of (Z)-2-(pyrrolidin-2-ylidene)hydrazinecarbothioamide (L) with Cu(II), Co(II), and Ni(II) chlorides were tested against selected types of fungi and were found to have significant antifungal activities. The free-radical-scavenging ability of the metal complexes was determined by their interaction with the stable free radical 2,2''-diphenyl-1-picrylhydrazyl, and all the compounds showed encouraging antioxidant activities. DFT calculations of the Cu complex were performed using molecular structures with optimized geometries. Molecular orbital calculations provide a detailed description of the orbitals, including spatial characteristics, nodal patterns, and the contributions of individual atoms.

1. Introduction

Schiff bases have often been used as chelating ligands in the field of coordination chemistry, and their metal complexes have been of great interest to researchers for many years. It is well known that N and S atoms play a key role in the coordination of metals at the active sites of many metallo-biomolecules [1]. The importance of metal ions in biological systems is well established. One of the most interesting features of metal-coordinated systems is the concerted spatial arrangement of the ligands around the metal ion. Among metal ions of biological importance, the Cu(II) ion involved in a large number of distorted complexes [2]. Over the past two decades, considerable attention has been paid to metal complexes of Schiff bases containing nitrogen and other donor atoms [3, 4]. Bioorganometallic chemistry is dedicated to the study of metallic complexes and their biological applications [5], including the design of new drugs that are more effective than those already known. The development of the field of bioinorganic chemistry has increased the interest in Schiff base complexes, because it has been recognized that many of these complexes may serve as models for biologically important species [6–9]. Antioxidants are extensively studied for their capacity to protect organisms and cells from

damage induced by oxidative stress. Scientists in various disciplines have become more interested in new compounds, either synthesized or obtained from natural sources, that could provide active components to prevent or reduce the impact of oxidative stress on cells [10].

Thiosemicarbazones are well established as an important class of sulfur-donor Schiff base ligands that are particularly useful for transition metal ions. This is due to the remarkable biological activities observed for these compounds, which have been shown to be related to their metal-complexing ability. Thiosemicarbazone Schiff bases are an important class of compounds in the medicinal and pharmaceutical fields [11].

The work discussed herein describes the *in vitro* antioxidant and antifungal activities for metal complexes derived from (Z)-2-(pyrrolidin-2-ylidene)hydrazinecarbothioamide (L) [12].

2. Experimental

2.1. General. All chemicals used in this study were of reagent grade (supplied either by Sigma-Aldrich or Fluka) and used without further purification.

The FTIR spectra were recorded in the 4.000–200 cm⁻¹ range on cesium iodide windows using a Shimadzu FTIR 8300 spectrophotometer. Proton NMR spectra were recorded on a Bruker-DPX 300 MHz spectrometer using TMS as an internal standard. The UV-VIS spectra were measured in ethanol using the Shimadzu UV-VIS -160A spectrophotometer in the range 200–1.000 nm. Magnetic susceptibility measurements for the complexes were obtained at room temperature using a Magnetic Susceptibility Balance Model MSB-MKI. Flame atomic absorption spectra from the Shimadzu AA-670 elemental analyzer were used for metal determination. Elemental microanalysis was performed using a CHN elemental analyzer model 5500-Carlo Erba. A Gallenkamp M.F.B.600.010 F melting point apparatus was used to measure the melting points of all the synthesized compounds.

2.2. Chemistry. The ligand and metal complexes were synthesized according to reference [12], and the structures of the compounds were confirmed with elemental analyses, spectral analyses (IR, UV-VIS, ¹H-NMR), conductance experiments, and magnetic measurements.

2.2.1. DFT. The molecular sketches of the reference compounds were plotted using Visualization Materials Studio 5.5 software. All quantum chemical calculations were performed using density functional theory (DFT) methodology. The DMol3 model was employed to obtain quantum chemical parameters and optimization of the molecular geometry. Molecular atomic charges were calculated by Mulliken population analysis [13].

2.3. Pharmacology

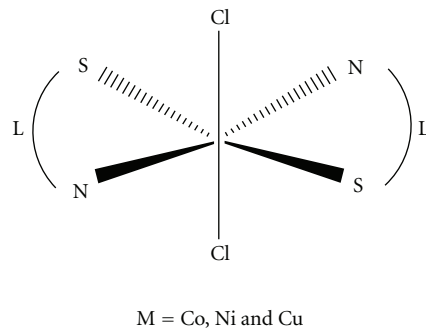
2.3.1. Evaluation of Antifungal Assay. All tests with the microorganisms (*Aspergillus niger* and *Candida albicans*) were obtained from the Biotechnology Division, Department of Applied Science, University of Technology.

Antifungal activity [14–16] was determined based on the growth inhibition rates of the mycelia of *Aspergillus niger* and *Candida albicans* strains grown in potato dextrose broth medium (PDB). Under aseptic conditions, one mL of spore suspension (5×10^6 cfu/mL) of the fungus being tested was added to 50 mL of PDB medium in a 100 mL Erlenmeyer flask. Appropriate volumes of tested metal complexes were added to produce concentrations ranging from 10 to $100 \mu\text{g mL}^{-1}$. The flasks were incubated at $27 \pm 1^\circ\text{C}$ in the dark for 5 days, at which time the mycelia were collected on filter papers. The filter papers were dried to a constant weight, and the level of inhibition relative to the control flasks was calculated from the following formula:

$$\text{percentage of inhibition} = \frac{C - T}{C} \times 100, \quad (1)$$

where T is the weight of mycelia from the test flasks and C represents the weight of mycelia from the control flasks.

A note on statistical analysis is that significant differences between values were determined by a multiple-range test ($P < 0.05$) following one-way ANOVA.



SCHEME 1: Proposed structure of the complexes.

2.3.2. Evaluation of Antioxidant Activity. A stock solution (1 mg/mL) was diluted to final concentrations of 20–100 $\mu\text{g/mL}$. An ethanolic DPPH solution (1 mL, 0.3 mmol) was added to sample solutions in DMSO (3 mL) at various concentrations (50–300 $\mu\text{g/mL}$) [17]. The mixture was shaken vigorously and allowed to stand at room temperature for 30 min. The absorbance was then measured at 517 nm using the UV-VIS spectrophotometer. Less absorbance by the reaction mixture indicates higher free-radical-scavenging activity. Ethanol was used as the solvent and ascorbic acid as the standard. The DPPH radical scavenger effect was calculated using the following equation:

$$\text{scavenging effect (\%)} = \frac{A_0 - A_1}{A_0} \times 100, \quad (2)$$

where A_0 is the absorbance of the control reaction and A_1 is the absorbance in the presence of the samples or standards.

3. Results and Discussion

3.1. Chemistry. The ligand was synthesized according to [12]. Reaction could be explained by a Schiff base mechanism.

The complexes (Scheme 1) were then synthesized by the reactions of hot ethanolic solutions of the ligand (L) with the metal ions. The ligand behaves as a bidentate ligand *via* both the thione sulfur and the azomethine nitrogen [12].

3.1.1. Density Functional Theory (DFT). DFT calculations were performed for L and CuL₂Cl₂. The optimized molecular structure of the most stable form for the Cu complex is shown in Figure 1. Orbital calculations provide a detailed description of the orbitals, including spatial characteristics, nodal patterns, and individual atomic contributions. Contour plots of the frontier orbitals for the ground state of the ligand are shown in Figure 2, including the highest occupied molecular orbital (HOMO) and the lowest unoccupied molecular orbital (LUMO) [18]. It is interesting that both orbitals are substantially distributed over the plane of conjugation. It can be seen from Figure 2 that HOMO orbitals are located on the substituted molecule whereas the LUMO orbitals resemble those obtained for the unsubstituted molecule. Therefore, the substitution has an

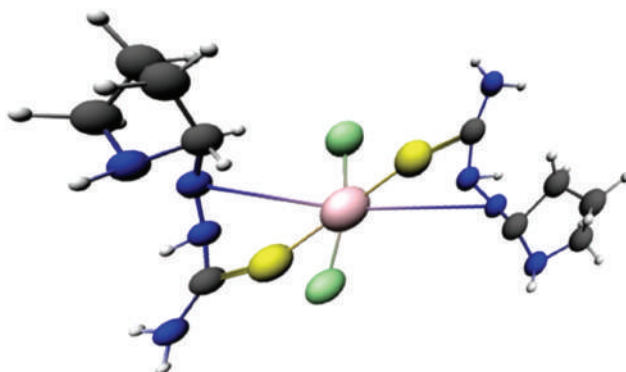
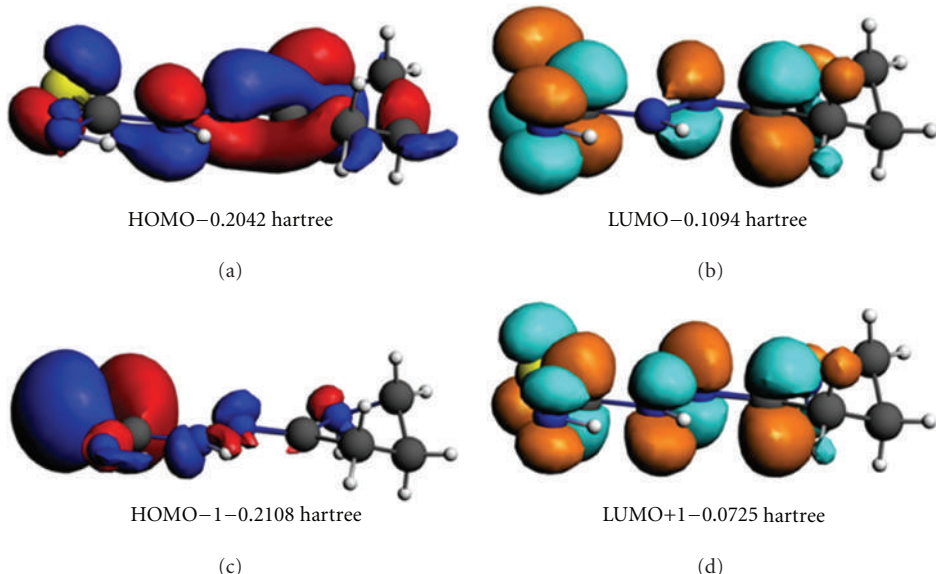
FIGURE 1: Optimized 3D structure of CuL₂Cl₂.

FIGURE 2: HOMO-LUMO energies for ligand (the energy in hartrees).

influence on the electron donation ability but only a small impact on the electron acceptance ability. The orbital energy levels of the HOMO and LUMO for the ligand are listed. It can be seen that the energy gap between the HOMO and LUMO is 0.0984 Hartrees for the ligand. The low value for the HOMO-LUMO energy gap explains the eventual charge transfer interaction taking place within these molecules.

3.1.2. Stereochemistry of the Metal Complexes. A thiosemicarbazone was first used in this study with the expectation that it would bind to the metal ion as a bidentate N,S-donor. From the preliminary characterization data, it was evident that the thiosemicarbazone ligand does indeed serve as a bidentate ligand, but the coordination mode of the ligand was not clear. The two ligands that are in the coordination sphere around the metal are significantly distorted from the ideal octahedral geometry [19]. To determine the coordination mode of the thiosemicarbazone ligand in these complexes, the structure shows that the thiosemicarbazone ligand is again coordinated to the metal in the same fashion as before. Due to

the restricted rotation around the C=N bond, the ligand may exist as two different geometric isomers. The structural determination of one representative ligand (Scheme 2) shows that the free ligand exists in the thione form.

The absence of a thiol group in both the IR and NMR spectra indicates that the ligand exists predominantly as the thione tautomeric form in solution, as shown in Scheme 2. None of the synthesized ligands or metal complexes have any bands between 2,000 and 2,500 cm⁻¹, suggesting that the ligand and metal complexes in the solid state are not in the thiol form, as shown in Scheme 2.

3.2. Pharmacology

3.2.1. Antifungal Activities. Metal ions are adsorbed on the cell walls of the microorganisms, disturbing the respiration processes of the cells and thus blocking the protein synthesis that is required for further growth of the organisms. Hence, metal ions are essential for the growth-inhibitory effects [20]. According to Overtone's concept of cell permeability, the

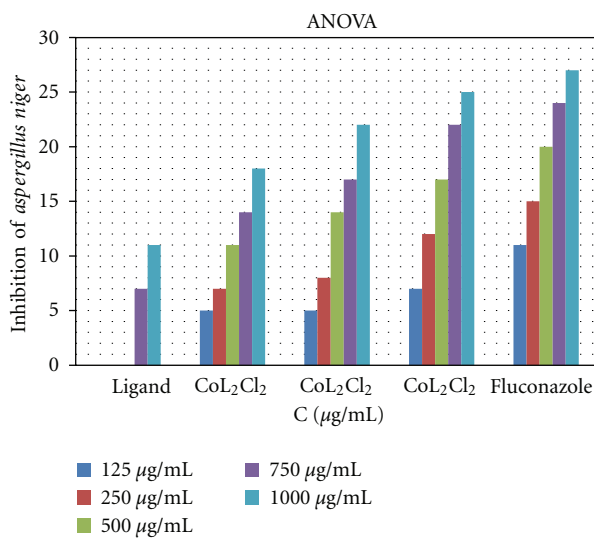


FIGURE 3: Effect of the metal complexes on *Aspergillus niger*, *P < 0.05, one way Ligand (L) = C₅H₁₀N₄S; CoL₂Cl₂ = Co(C₅H₁₀N₄S)₂Cl₂; NiL₂Cl₂ = Ni(C₅H₁₀N₄S)₂Cl₂; CuL₂Cl₂ = Cu(C₅H₁₀N₄S)₂Cl₂.

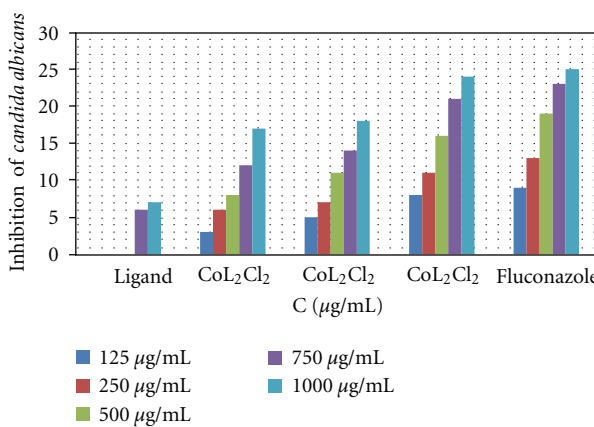


FIGURE 4: Effect of the metal complexes on *Candida albicans*, *P < 0.05, one-way ANOVA.

lipid membrane that surrounds the cell favors the passage of only lipid-soluble materials, so lipophilicity is an important factor controlling the antifungal activity. Upon chelation, the polarity of the metal ion will be reduced due to the overlap of the ligand orbitals and partial sharing of the positive charge of the metal ion with donor groups. In addition, chelation allows for the delocalization of π -electrons over the entire chelate ring and enhances the lipophilicity of the complexes. This increased lipophilicity facilitates the penetration of the complexes into lipid membranes, further restricting proliferation of the microorganisms. The variation in the effectiveness of different compounds against different organisms depends either on the impermeability of the microbial cells or on differences in the ribosomes of the cells [21]. All of the metal complexes possess higher antifungal activity than the ligand [22, 23]. Although the exact biochemical mechanism is not completely understood,

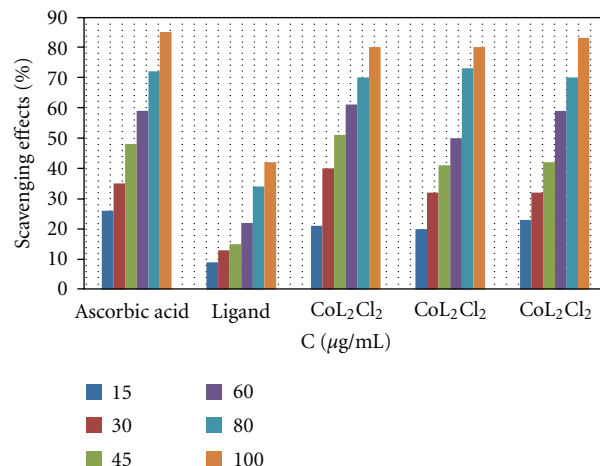


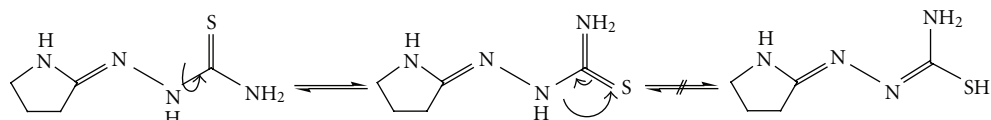
FIGURE 5: Scavenging effect of metal complexes and ascorbic acid at various concentrations, using the DPPH method.

the mode of action of antimicrobials may involve various targets in the microorganisms.

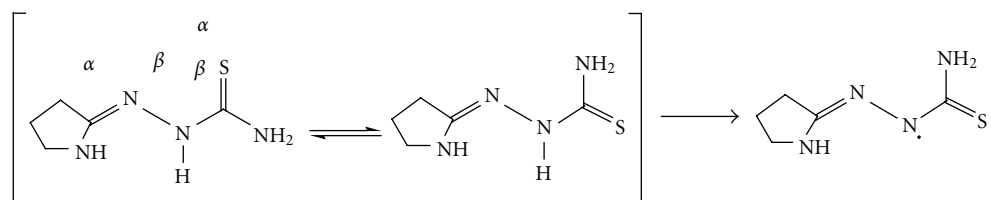
These targets include the following.

- The higher activity of the metal complexes may be due to the different properties of the metal ions upon chelation. The polarity of the metal ions will be reduced due to the overlap of the ligand orbitals and partial sharing of the positive charge of the metal ion with donor groups. Thus, chelation enhances the penetration of the complexes into lipid membranes and the blockage of metal binding sites in the enzymes of the microorganisms [24].
- Tweedy's chelation theory predicts that chelation reduces the polarity of the metal atom mainly because of partial sharing of its positive charge with donor groups and possible electron delocalization over the entire ring. This consequently increases the lipophilic character of the chelates, favoring their permeation through the lipid layers of the bacterial membrane [25].
- Interference with the synthesis of cellular walls, causing damage that can lead to altered cell permeability characteristics or disorganized lipoprotein arrangements, ultimately resulting in cell death.
- Deactivation of various cellular enzymes that play a vital role in the metabolic pathways of these microorganisms.
- Denaturation of one or more cellular proteins, causing the normal cellular processes to be impaired.
- Formation of a hydrogen bond through the azomethine group with the active centers of various cellular constituents, resulting in interference with normal cellular processes [26].

In vitro antifungal effects of the investigated compounds were tested against two fungal species (*Aspergillus niger* and *Candida albicans*). The results showed that the ligand itself



SCHEME 2



SCHEME 3: Suggested mechanism for the antioxidant activity of the ligand.

does not exhibit any antifungal activity, but all metal-ligand complexes exhibit good activities. The CuL₂Cl₂ shows more activity than NiL₂Cl₂ and CoL₂Cl₂ which may be due to the higher stability of the CuL₂Cl₂ complex (DFT studies, [12], Figures 3 and 4).

The mode of action of the compounds may involve formation of a hydrogen bond through the azomethine group (>C=N-) with the active centers of various cellular constituents, resulting in interference with normal cellular processes [27, 28].

3.2.2. Radical-Scavenging Activity. DPPH is a stable free radical that is often used for detection of the radical-scavenging activity in chemical analysis [29, 30]. The reduction capability of DPPH radicals was determined by the decrease in its absorbance at 517 nm which can be induced by antioxidants. [31]. A graph may be plotted with percentage scavenging effects on the *y*-axis and concentration ($\mu\text{g/mL}$) on the *x*-axis. The metal complexes used in the study showed good activities as a radical scavenger compared to the scavenging ability of ascorbic acid, which was used as a standard (Figure 5). These results were in agreement with previous studies of metallic complexes [32, 33] in which the ligand has antioxidant activity and it is expected that the metal moiety will increase its activity.

A postulated mechanism for the antioxidant ability of the ligand is shown in Scheme 3. The mechanism depends on the hydrogen atom of the secondary amine, which is influenced by both the allylic double bond and inductive effects. The allylic stabilization facilitates the release of hydrogen as a free radical, whereas the inductive effect from sulfur and nitrogen pushes electron density toward the free radical, resulting in a relatively stable molecule.

4. Conclusions

In this study, a ligand and its metal complexes were tested for antioxidant and antifungal activities. Of the complexes studied, CuL₂Cl₂ showed significant antifungal activities compared to either CoL₂Cl₂ or NiL₂Cl₂. In addition, all complexes were found to be superior antioxidants compared

to ascorbic acid. The synthesized compounds were studied theoretically, and the atomic charges, heat of formation, and stereochemistry were estimated. Furthermore, it was found that the compounds are not planar.

References

- [1] K. Singh, M. S. Barwa, and P. Tyagi, "Synthesis, characterization and biological studies of Co(II), Ni(II), Cu(II) and Zn(II) complexes with bidentate Schiff bases derived by heterocyclic ketone," *European Journal of Medicinal Chemistry*, vol. 41, no. 1, pp. 147–153, 2006.
- [2] J. A. Obaleyeye, J. F. Adediji, and M. A. Adebayo, "Synthesis and biological activities on metal complexes of 2,5-diamino-1,3,4-thiadiazole derived from semicarbazide hydrochloride," *Molecules*, vol. 16, no. 7, pp. 5861–5874, 2011.
- [3] X. Tai, X. Yin, Q. Chen, and M. Tan, "Synthesis of some transition metal complexes of a novel Schiff base ligand derived from 2,2'-bis(p-methoxyphenylamine) and salicylaldehyde," *Molecules*, vol. 8, no. 5, pp. 439–443, 2003.
- [4] A. A. H. Kadhum, A. B. Mohamad, A. A. Al-Amiry, and M. S. Takriff, "Antimicrobial and antioxidant activities of new metal complexes derived from 3-aminocoumarin," *Molecules*, vol. 16, no. 8, pp. 6969–6984, 2011.
- [5] A. Corona-Bustamante, J. M. Viveros-Paredes, A. Flores-Parra et al., "Antioxidant activity of butyl- and phenylstannoxanes derived from 2-, 3- and 4-pyridinecarboxylic acids," *Molecules*, vol. 15, no. 8, pp. 5445–5459, 2010.
- [6] N. H. Al-Sha'alan, "Antimicrobial activity and spectral, magnetic and thermal studies of some transition metal complexes of a Schiff base hydrazone containing a quinoline moiety," *Molecules*, vol. 12, no. 5, pp. 1080–1091, 2007.
- [7] S. Chandra, D. Jain, A. K. Sharma, and P. Sharma, "Coordination modes of a Schiff base pentadentate derivative of 4-aminoantipyrine with cobalt(II), nickel(II) and copper(II) metal ions: synthesis, spectroscopic and antimicrobial studies," *Molecules*, vol. 14, no. 1, pp. 174–190, 2009.
- [8] K. S. Prasad, L. S. Kumar, M. Prasad, and H. D. Revanasiddappa, "Novel organotin(IV)-Schiff base complexes: synthesis, characterization, antimicrobial activity, and DNA interaction studies," *Bioinorganic Chemistry and Applications*, vol. 2010, Article ID 854514, 9 pages, 2010.

- [9] H. L. Singh and A. K. Varshney, "Synthetic, structural, and biochemical studies of organotin(IV) with Schiff bases having nitrogen and sulphur donor ligands," *Bioinorganic Chemistry and Applications*, vol. 2006, Article ID 23245, 7 pages, 2006.
- [10] M. Alkan, H. Yüksek, Ö. Gürsoy-Kol, and M. Calapoğlu, "Synthesis, acidity and antioxidant properties of some novel 3,4-disubstituted-4,5-dihydro-1H-1,2,4-triazol-5-one derivatives," *Molecules*, vol. 13, no. 1, pp. 107–121, 2008.
- [11] K. S. Abou-Melha and H. Faruk, "Bimetallic complexes of schiff base bis-[4-hydroxycoumarin-3-yl]- 1N,5N-thiocarbohydrazone as a potentially dibasic pentadentate ligand. Synthesis, spectral, and antimicrobial properties," *Journal of the Iranian Chemical Society*, vol. 5, no. 1, pp. 122–134, 2008.
- [12] A. A. Al-Amiry, Y. K. Al-Majedy, H. Abdulreazak, and H. Abood, "Synthesis, characterization, theoretical crystal structure, and antibacterial activities of some transition metal complexes of the thiosemicarbazone (Z)-2-(pyrrolidin-2-ylidene)hydrazinecarbothioamide," *Bioinorganic Chemistry and Applications*, vol. 2011, Article ID 483101, 6 pages, 2011.
- [13] A. A. H. Kadhum, A. A. Al-Amiry, A. Y. Musa, and A. B. Mohamad, "The antioxidant activity of new coumarin derivatives," *International Journal of Molecular Sciences*, vol. 12, no. 9, pp. 5747–5761, 2011.
- [14] Z. Y. Daw, G. S. EL-Baroty, and A. E. Mahmoud, "Inhibition of *Aspergillus parasiticus* growth and aflatoxin production by some essential oils," *Chemie, Mikrobiologie, Technologie der Lebensmittel*, vol. 16, pp. 129–135, 1994.
- [15] S. Myiut, W. R. W. Daud, A. B. Mohamed, and A. A. H. Kadhum, "Gas chromatographic determination of eugenol in ethanolextract of cloves," *Journal of Chromatography B*, vol. 76, pp. 193–195, 1996.
- [16] A. A. Al-Amiry, "Antimicrobial and antioxidant activities of new metal complexes derived from (E)-3-(5-phenyl-1,3,4-oxadiazol-2-ylimino)methyl)naphthalen-2-ol," *Medicinal Chemistry Research*. In press.
- [17] Y. Chen, M. Wang, R. T. Rosen, and C. T. Ho, "2,2-Diphenyl-1-picrylhydrazyl radical-scavenging active components from *Polygonum multiflorum* Thunb," *Journal of Agricultural and Food Chemistry*, vol. 47, no. 6, pp. 2226–2228, 1999.
- [18] A. A. Al-Amiry, R. I. Al-Bayati, K. Y. Saour, and M. F. Radi, "Cytotoxicity, antioxidant and antimicrobial activities of novel 2-quinolone derivatives derived from coumarin," *Research on Chemical Intermediates*. In press.
- [19] A. B. P. Lever, *Lever, Inorganic Electronic Spectroscopy*, Elsevier, New York, NY, USA, 1984.
- [20] I. Pal, F. Basuli, and S. Bhattacharya, "Thiosemicarbazone complexes of the platinum metals. A story of variable coordination modes," *Proceedings of the Indian Academy of Sciences: Chemical Sciences*, vol. 114, no. 4, pp. 255–268, 2002.
- [21] Y. Anjaneyula and R. P. Rao, "Preparation, characterization and antimicrobial activity studies on some ternary complexes of Cu(II) with acetylacetone and various salicylic acids," *Synthesis and Reactivity in Inorganic and Metal-Organic Chemistry*, vol. 16, pp. 257–272, 1986.
- [22] Z. H. Chohan, M. Arif, M. A. Akhtar, and C. T. Supuran, "Metal-based antibacterial and antifungal agents: synthesis, characterization, and in vitro biological evaluation of Co(II), Cu(II), Ni(II), and Zn(II) complexes with amino acid-derived compounds," *Bioinorganic Chemistry and Applications*, vol. 2006, Article ID 83131, 13 pages, 2006.
- [23] Z. H. Chohan, A. Scozzafava, and C. T. Supuran, "Zinc complexes of benzothiazole-derived Schiff bases with antibacterial activity," *Journal of Enzyme Inhibition and Medicinal Chemistry*, vol. 18, no. 3, pp. 259–263, 2003.
- [24] K. S. Prasad, L. S. Kumar, S. C. Shekar, M. Prasad, and H. D. Revanasiddappa, "Oxovanadium complexes with bidentate N, O ligands: synthesis, characterization, DNA binding, nuclease activity and antimicrobial studies," *Chemical Sciences Journal*, vol. 12, pp. 1–10, 2011.
- [25] T. D. Thangadurai and K. Natarajan, "Mixed ligand complexes of ruthenium(II) containing α,β -unsaturated- β -ketoamines and their antibacterial activity," *Transition Metal Chemistry*, vol. 26, no. 4-5, pp. 500–504, 2001.
- [26] N. Dharmaraj, P. Viswanathamurthi, and K. Natarajan, "Ruthenium(II) complexes containing bidentate Schiff bases and their antifungal activity," *Transition Metal Chemistry*, vol. 26, no. 1-2, pp. 105–109, 2001.
- [27] R. Joseyphus and M. Nair, "Antibacterial and antifungal studies on some schiff base complexes of zinc(II)," *Mycobiology*, vol. 36, pp. 93–98, 2008.
- [28] L. Malhotra, S. Kumar, K. S. Dhindsa et al., "Synthesis, characterization and microbial activity of Co(II), Ni(II), Cu(II) and Zn(II) complexes of aryloxyacetic acid and hydrazides," *Indian Journal of Chemistry Section A*, vol. 32, pp. 457–459, 1993.
- [29] J. R. Soares, T. C. P. Dinis, A. P. Cunha, and L. M. Almeida, "Antioxidant activities of some extracts of *Thymus zygis*," *Free Radical Research*, vol. 26, no. 5, pp. 469–478, 1997.
- [30] P. D. Duh, Y. Y. Tu, and G. C. Yen, "Antioxidant activity of water extract of Harng Jyur (*Chrysanthemum morifolium* Ramat)," *Lebensmittel-Wissenschaft und-Technologie*, vol. 32, no. 5, pp. 269–277, 1999.
- [31] B. Matthäus, "Antioxidant activity of extracts obtained from residues of different oilseeds," *Journal of Agricultural and Food Chemistry*, vol. 50, no. 12, pp. 3444–3452, 2002.
- [32] S. B. Bukhari, S. Memon, M. Mahroof-Tahir, and M. I. Bhanger, "Synthesis, characterization and antioxidant activity copper-quercetin complex," *Spectrochimica Acta Part A*, vol. 71, no. 5, pp. 1901–1906, 2009.
- [33] J. Gabrielska, M. Soczyńska-Kordala, J. Hładyszowski, R. Żyłka, J. Miśkiewicz, and S. Przestalski, "Antioxidative effect of quercetin and its equimolar mixtures with phenyltin compounds on liposome membranes," *Journal of Agricultural and Food Chemistry*, vol. 54, no. 20, pp. 7735–7746, 2006.

Immobilization of Laccase in Alginate-Gelatin Mixed Gel and Decolorization of Synthetic Dyes

Mehdi Mogharabi,^{1,2} Nasser Nassiri-Koopaei,¹ Maryam Bozorgi-Koushalshahi,¹ Nastaran Nafissi-Varcheh,³ Ghodsieh Bagherzadeh,² and Mohammad Ali Faramarzi^{1,2}

¹Department of Pharmaceutical Biotechnology, Faculty of Pharmacy and Biotechnology Research Center, Tehran University of Medical Sciences, P.O. Box 14155–6451, Tehran 14174, Iran

²Department of Chemistry, Faculty of Sciences, University of Birjand, Birjand 9717853577, Iran

³Department of Pharmaceutical Biotechnology, School of Pharmacy, Shahid Beheshti University of Medical Sciences, Tehran 1457795343, Iran

Correspondence should be addressed to Mohammad Ali Faramarzi, faramarz@tums.ac.ir

Academic Editor: Spyros Perlepes

Alginate-gelatin mixed gel was applied to immobilized laccase for decolorization of some synthetic dyes including crystal violet. The immobilization procedure was accomplished by adding alginate to a gelatin solution containing the enzyme and the subsequent dropwise addition of the mixture into a stirred CaCl_2 solution. The obtained data showed that both immobilized and free enzymes acted optimally at 50°C for removal of crystal violet, but the entrapped enzyme showed higher thermal stability compared to the free enzyme. The immobilized enzyme represented optimum decolorization at pH 8. Reusability of the entrapped laccase was also studied and the results showed that *ca.* 85% activity was retained after five successive cycles. The best removal condition was applied for decolorization of seven other synthetic dyes. Results showed that the maximum and minimum dye removal was related to amido black 10B and eosin, respectively.

1. Introduction

While traditional methods in chemical processes have improved in the last decades, extensive attention has been paid to alternative techniques that utilize enzymes involving excellent characteristics, such as high activity, selectivity, and specificity. In addition, enzymes action at mild conditions of pH, pressure, and temperature proposes them as candidates for suitable catalysts in industries where low cost, energy savings, and simplicity are important [1, 2]. However, despite these advantages, some practical problems restrict their use, such as the high-cost isolation and purification process and instability in organic media and high temperatures. To overcome these limitations, several methods have been suggested and the most important of which are immobilization techniques [3, 4]. Enzyme entrapment uses natural and synthetic polymers, such as agarose, agar, and gelatin,

through thermoreversal polymerization alginate, polyvinyl acetate, acrylic acid, and β -carrageenan by ionotropic gelation [5].

Gelatin consists of proteins and peptides produced by the denaturation of collagen, which breaks down into smaller fragments. Due to its unique physical properties, such as a melting point close to physiological temperature, gelatin is used in a variety of applications, especially in the food and pharmaceutical industries [6]. Gelatin immobilization methods have been developed for entrapment of microbial cells and enzymes, especially when the enzyme is placed in a whole cell. While the gelation process is reversible with temperature and displays no efficient immobilization, other than at 30–35°C, some methods have been investigated to achieve an irreversible gelation process, such as using cross-link agents [7, 8]. Single-step immobilization is one of the most frequently used methods of entrapment, which

TABLE 1: Names, classification, maximum absorbance, and removal percentage of eight synthetic dyes using immobilized enzymes (in citrate buffer 0.1 M, pH 4.5).

Name	Classification	λ_{max}	Dye removal (%)	Removal rate (nmol/min) ^b
Amido black 10B	Diazo	618	86.9 ± 1.3 ^a	22.5 ± 2.3
Bromothymol blue	Triphenylmethan	430	53.8 ± 1.2	27.2 ± 1.4
Coomassie blue G-250	Triphenylmethan	575	71.4 ± 0.8	53.8 ± 1.5
Crystal violet	Triphenylmethan	595	58.1 ± 1.5	95.3 ± 2.8
Eosin	Heterocyclic	517	32.8 ± 1.2	20.1 ± 1.2
Malachite green	Triphenylmethan	620	76.3 ± 2.1	120.7 ± 2.5
Methyl green	Triphenylmethan	630	77.5 ± 1.5	73.4 ± 1.4
Methyl red	Azo	522	52.1 ± 1.8	147.3 ± 2.8

^aMean ± SD ($n = 3$); ^bKinetic study was performed by monitoring the loss of absorbance at λ_{max} .

could be performed by simple gelation through lowering or raising temperatures of biopolymers such as agar, agarose, κ -carrageenan, and chitosan. Although it is easy to achieve, but this kind of preparation suffers from low mechanical strength and heat damages. Therefore, alternative methods are required to produce a more porous structure with higher mechanical stability and desirable elastic behavior. There are also some techniques for stabilization of alginate suggested by Birnbaum and colleagues which consists the treatment of alginate beads with polyethyleneimine-HCl, activation of alginate with a mixture of 1-ethyl-3-(3-dimethyl-amino-propyl)-carbodiimide and N-hydroxysuccinimide, and addition of sodium metaperiodate to alginate [9].

Laccases (benzenediol : oxygen oxidoreductases, E.C. 1.10.3.2) are an interesting group of multicopper enzymes produced by higher plants and fungi that catalyze the oxidation of a wide range of organic compounds, such as phenols, in the presence of molecular oxygen [10, 11]. The most important applications discussed for laccases include pharmaceutical and food industries, textile effluent transformation, and wastewater detoxification biosensors. The unique properties of laccases, such as high stability in solution, mild reaction conditions, and selectivity for phenolic structure, make them attractive for use in chemical synthesis [12]. The mechanism of phenolic ring oxidation by laccase has been previously described. Releasing molecular nitrogen, instead of the formation of low molecular weight aromatic amines that are easily absorbed through the skin and known as powerful carcinogens and mutagens, could be considered as an advantage for using laccase for detoxification of synthetic dyes especially aromatic azo dyes [13].

Wastewater released by various industries that use synthetic dyes because of their low cost, ease of synthesis, and color variety can pollute and harm the aquatic environment. Decolorization of synthetic dyes by using special biocatalysts has received great attention because of efficient decolorization and nontoxic product generation [14, 15]. Crystal violet is a widely used synthetic pigment for dye processing. It is stable and nondegradable by conventional methods and has been identified as a main factor of industrial effluent contamination. Textile factories are under pressure to apply environmental-friendly technologies to remove it [16].

The aim of the present study was to apply alginate-gelatin mixed gel to immobilize laccase, which is further employed in the decolorization of some synthetic dyes, such as crystal violet, in aqueous solutions. Optimum pH, temperature, and proper enzyme content for decolorization by the immobilized laccase were also studied. To our knowledge, the use of alginate-gelatin mixed gel has not been examined previously for the purpose of enzyme entrapment.

2. Experimental

2.1. Chemicals and Instruments. Crystal violet, coomassie blue G-250, bromothymol blue, amido black 10B, methyl red, eosin, and malachite green (Table 1) were purchased from Sigma-Aldrich (St. Louis, MO, USA). Gelatin and sodium alginate were obtained from Merck (Darmstadt, Germany). All other reagents and chemicals were of the highest purity available. Extracellular laccase was purified from the submerged fermentation of the soil isolate ascomycete *Paraconiothyrium variabile* [10, 17, 18]. Decolorization was monitored by UV-VIS spectroscopy. Absorbance was scanned by a double-beam UV-Vis 2501 PC spectrophotometer (Shimadzu, Japan). The mechanical force to break the beads was measured with a tensiometer (Zwick/Roell 030, Germany). Optical images of the gelatin-alginate beads were taken with a USB Digital Microscope Pro (Dino-Lite, Taiwan). Scanning electron microscope (SEM, Hitachi S-2400, Japan) was applied for studying the size and surface of the beads.

2.2. Preparation of Mixed Gels, Immobilization of Laccase, and Decolorization of Crystal Violet. The gelatin-alginate mixed gel was prepared according to the method of Panouille and Larreta-Garde [19], with some modifications. Briefly, entrapment of laccase in gelatin-alginate mixed gel was performed by adding 0.1 g sodium alginate to 10 mL of a solution containing 10% (w/v) gelatin and laccase in the range of 5–50 mg (1 mg enzyme is equal to 1.25 U) under continuous stirring at room temperature. The mixture was syringed into a stirring CaCl_2 solution (200 mM), and the resulting beads were left to be harden for 1 h under the same conditions, washed three times by deionized water, and

TABLE 2: Maximum force required to rupture beads and the amount of bound protein.

Alginate	Maximum force (kgf)	Bound protein (mg/g carrier)
1%	0.125 ± 0.033 ^a	0.063 ± 0.035 ^{b,c}
2%	0.152 ± 0.041	0.094 ± 0.043
3%	0.161 ± 0.037	0.127 ± 0.080
4%	0.177 ± 0.047	0.153 ± 0.075
5%	0.204 ± 0.063	0.166 ± 0.098

^aMean ± SD ($n = 20$); ^bMean ± SD ($n = 3$); ^cBeads was washed with 50 mM citrate buffer (pH 5.0).

then stored at 4°C prior to being used in the decolorization study. The amount of bound protein was determined by Bradford's method [20], using the following equation: $Q = (Ci - Cf)/mV$, where Q was the bound enzyme (mg enzyme/g beads), Ci and Cf were the initial and final enzyme concentrations in the solution (mg/mL), V was the volume of the solution (mL), and m was the mass of the beads (g). The immobilized laccase (10 g) was transferred into a 20 mL buffer solution, at pH 3–9, containing crystal violet (final concentration 0.083 mM), at a 30–70°C temperature range, for 20 min. Maximum absorbance was monitored according to λ_{max} of the dye (Table 1). Relative decolorization was calculated by the following equation: relative decolorization (%) = $(A_{initial} - A_{final})/A_{initial} \times 100$, where $A_{initial}$ was the initial absorbance and $A_{observed}$ was the final absorbance at the given wavelength.

2.3. Optimum Temperature, PH, and Enzyme Concentration of the Immobilized Laccase. The effect of pH on the enzymatic decolorization was monitored with a dye concentration of 0.25 mg/mL at a 3–9 pH range adjusted by citrate or ammonia buffers. To determine the effect of temperature on the enzymatic decolorization, the reaction mixture was incubated at a thermal range of 30–70°C, in steps of 10°C. In order to assess the effect of enzyme quantity on decolorization, the reaction was started with different enzyme amounts, from 0.25 to 0.5 mg/mL, in 0.05 mg/mL increments. The experiments were performed in triplicate; the results shown are means ± standard deviation.

2.4. Mechanical Strength, Optical Image, and SEM. The force required to rupture the beads was recorded by compressing the beads using a tensiometer; the results are the average force from 20 independent tests. The optical microscopy was used to evaluate the shape, surface, and size of the beads, and scanning electron microscopy (SEM) was also applied to study the structure of the fabricated beads.

2.5. Reusability. Reusability of the gelatin-alginate immobilized enzyme was investigated in acetate buffer solution 0.1 M at pH 8 and 45°C. The used beads were filtered at the end of each cycle and washed three times with the same buffer to treat in the next fresh colored solution. The reusability study was performed in triplicate.

2.6. Decolorization of Synthetic Dyes. Decolorization of the other dyes from the aqueous solution—coomassie blue G-250 (0.086 mM), bromothymol blue (0.095 mM), amido black 10B (0.045 mM), methyl red (0.125 mM), eosin (0.038 mM), and malachite green (0.112 mM)—was investigated by adding 10 g immobilized laccase to 20 mL citrate buffer solution (0.1 M, pH 4.5) containing dye, at 45°C for 20 min. Relative decolorization was calculated as described above for crystal violet. Some properties of the applied synthetic dyes and the percentages of dye removal are shown in Table 1. Standard deviation and mean of the results from three independent experiments were calculated using SigmaPlot for Windows (version 10.0).

3. Results and Discussion

3.1. Effect of Experimental Parameters on Crystal Violet Decolorization. Spherical and regular-shaped gelatin-alginate beads were obtained by using ionotropic gelation; the diameters of the beads were 2.0–2.5 mm (Figure 1(a)). The results, as shown in Table 2, indicated the rupture force increase with the rise in alginate concentration. The prepared beads containing 5% alginate exhibited the highest mechanical stability. Alginate could provide a very strong network that required 0.204 kgf force to rupture. Earlier studies had also reported a direct correlation between rupture force and alginate concentration [21].

Among the investigated parameters, pH plays the key role in dye decolorization. The effect of pH on dye decolorization was examined at pH ranging from 3 to 9, using acetate (pH 3–6) and ammonia (pH 7–9) buffers. The crude enzyme significantly displayed higher decolorization activity in basic pH (Figure 2) with a sharp increase at pH values above 6 and maximum activity at pH 9. The optimal pH for the immobilized enzyme activity was 8. It shows that pH of the environment has significant effects on decolorization which suggests that the mass transfer in the gel matrix may depend on the transport of bulk H⁺ ion into the gel matrix [22].

The effect of temperature on dye decolorization was investigated by changing the reaction mixture temperatures in a 30–70°C range. The results obviously showed that decolorization increased as the temperature raised up to 50°C; at higher temperatures, decolorization efficiency remarkably decreased, which normally attributed to denaturation of enzyme. However, the comparison of decolorization results indicated high thermal stability of immobilized enzyme and confirmed the protective role of alginate-gelatin mixed gel for maintaining enzyme activity. At 50°C, the crude and immobilized enzymes exhibited more activity, as shown in Figure 3. Similarly, Forootanfar and colleagues [10] reported that the optimum temperature for laccase activity was 50°C. Other research studies have reported an optimum temperature range of 45–50°C for laccase activity immobilized by both covalent binding and adsorption [23, 24].

To determine the proper amount of enzymes required for maximum decolorization, the effect of enzyme quantity on dye decolorization was also studied. As shown in Figure 4, decolorization increased as enzyme quantity increased, from

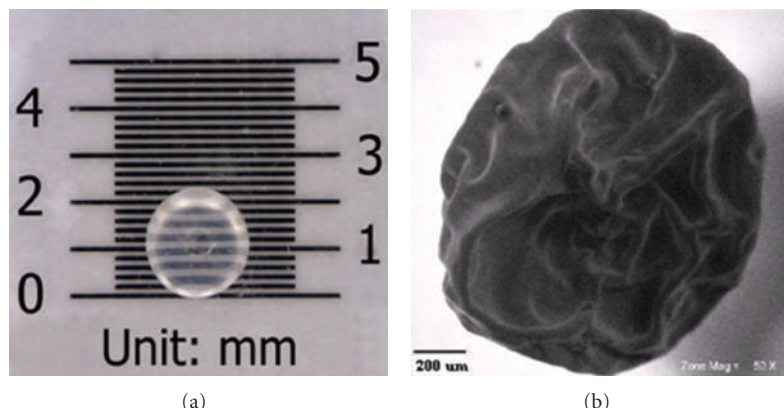


FIGURE 1: Optical image (a) and SEM of the prepared gelatin-alginate bead (b).

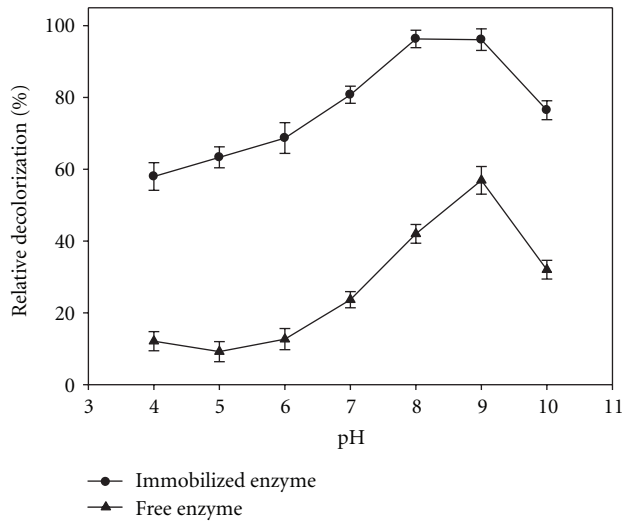


FIGURE 2: Effect of pH on relative decolorization activity of free laccase (\blacktriangle) and immobilized laccase (\bullet). Data were mean values \pm SD.

0.5 to 5 mg/mL. However, the results demonstrated that the minimum enzyme quantity to obtain maximum decolorization was 2.5 mg/mL.

The optimum conditions were obtained as described above and applied for the decolorization of other synthetic dyes (Table 1). It is notable that the efficiency of laccase enzyme for removal and detoxification of these synthetic dyes has been previously reported and discussed [13, 25, 26]. The results showed that amido black 10B and eosin exhibited maximum and minimum dye removal, respectively. It was observed that the immobilized laccase was able to decolorize more than 80% of amido black 10B, while Selvam and colleagues [27] reported 15% decolorization by laccase. However, all of the dyes were oxidized at the maximum rate in pH 8. Kinetic studies (Table 1) suggested that among the used dye substrates for the enzymatic removal, methyl red and malachite green are preferred, and, in contrast, eosin is a poor substrate [13].

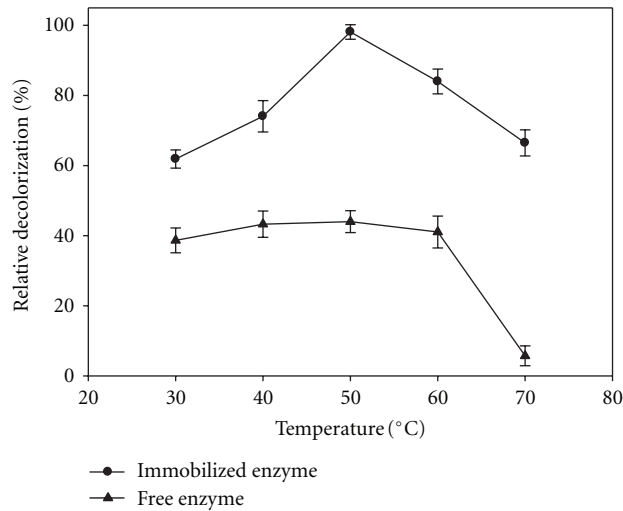


FIGURE 3: Influence of temperature on relative decolorization activity of free laccase (\blacktriangle) and immobilized laccase (\bullet). Data were mean values \pm SD.

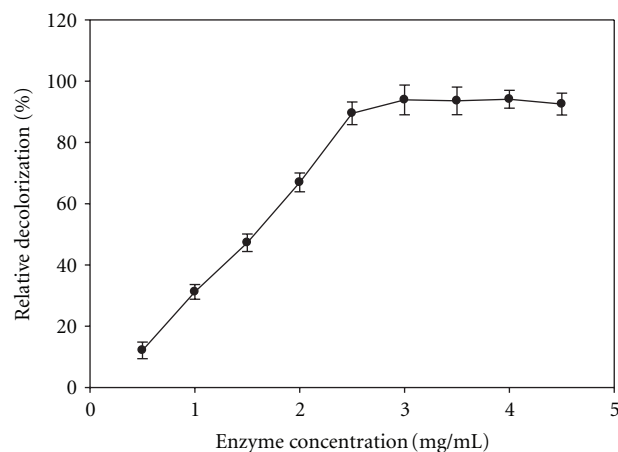


FIGURE 4: Effect of enzyme concentration on relative decolorization activity of the immobilized laccase. Data were mean values \pm SD.

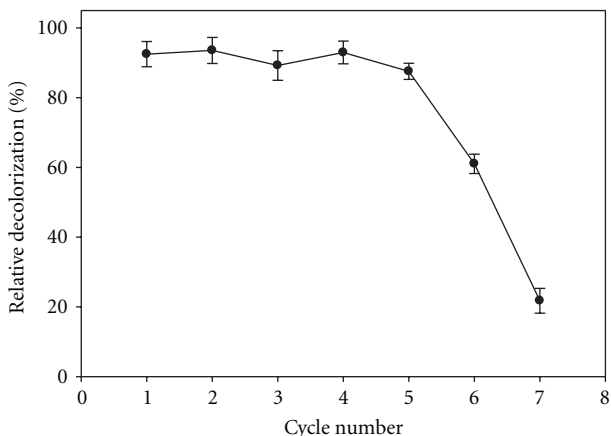


FIGURE 5: Reusability of immobilized laccase in the reaction condition. Data were mean values \pm SD.

3.2. Reusability of Immobilized Laccase. Reusability of immobilized enzymes exhibits the most important aspect for industrial applications, because immobilization of enzymes decreases the cost of production due to their repeated continuous uses. In this work, reusability of the immobilized enzyme was investigated up to seven cycles; the residual activities are presented in Figure 5. During enzymatic reactions, the alginic-gelatin mixture may cause a decrease in the pore sizes of the network, leading to difficulties in the diffusion of the substrate and product in the matrix of the gel. This restriction may cause a decrease in the efficient activity of laccase entrapped in gel after repeated use. In the literature, there are reports of successful reuses of various immobilized laccase systems, such as 60% activity after ten cycles for covalently immobilized laccase on activated polyvinyl alcohol [28–30] and 80% after five cycles for laccase immobilized on amine-terminated magnetic nanocomposites by cross-linking method [31].

4. Conclusions

Immobilization of laccase has received increasing attention in dye removal of aqueous solutions such as wastewater. Gelatin-alginic beads were prepared as a matrix system for laccase entrapment; the immobilized enzymes exhibited more stability during operation compared to free enzymes, a result that can be considered an advantage in wastewater treatment. In addition, the reusability of gelatin-alginic beads provides economic benefits when used in large-scale applications. Future investigations may focus on the decolorization of different types of dyes that are widely used in the chemical and textile industries.

Acknowledgment

This work was financially supported by Grant no. 90-04-33-16360 from Tehran University of Medical Sciences, Tehran, Iran.

References

- Z. Konsoula and M. Liakopoulou-Kyriakides, "Thermostable α -amylase production by *Bacillus subtilis* entrapped in calcium alginate gel capsules," *Enzyme and Microbial Technology*, vol. 39, no. 4, pp. 690–696, 2006.
- C. Silva, C. J. Silva, A. Zille, G. M. Guebitz, and A. Cavaco-Paulo, "Laccase immobilization on enzymatically functionalized polyamide 6,6 fibres," *Enzyme and Microbial Technology*, vol. 41, no. 6–7, pp. 867–875, 2007.
- G. D. Altun and S. A. Cetinus, "Immobilization of pepsin on chitosan beads," *Food Chemistry*, vol. 100, no. 3, pp. 964–971, 2007.
- F. Van De Velde, N. D. Lourenço, H. M. Pinheiro, and M. Bakker, "Carrageenan: a food-grade and biocompatible support for immobilization techniques," *Advanced Synthesis and Catalysis*, vol. 344, no. 8, pp. 815–835, 2002.
- S. M. Kotwal and V. Shankar, "Immobilized invertase," *Biotechnology Advances*, vol. 27, no. 4, pp. 311–322, 2009.
- C. Joly-Duhamel, D. Hellio, and M. Djabourov, "All gelatin networks: 1. Biodiversity and physical chemistry," *Langmuir*, vol. 18, no. 19, pp. 7208–7217, 2002.
- L. J. Yang and Y. C. Ou, "The micro patterning of glutaraldehyde (GA)-crosslinked gelatin and its application to cell-culture," *Lab on a Chip*, vol. 5, no. 9, pp. 979–984, 2005.
- A. Tanriseven and S. Doğan, "A novel method for the immobilization of β -galactosidase," *Process Biochemistry*, vol. 38, no. 1, pp. 27–30, 2002.
- S. Birnbaum, R. Pendleton, P. O. Larsson, and K. Mosbach, "Covalent stabilization of alginate gel for the entrapment of living whole cells," *Biotechnology Letters*, vol. 3, no. 8, pp. 393–400, 1981.
- H. Forootanfar, M. A. Faramarzi, A. R. Shahverdi, and M. T. Yazdi, "Purification and biochemical characterization of extracellular laccase from the ascomycete *Paraconiothyrium variabile*," *Bioresource Technology*, vol. 102, no. 2, pp. 1808–1814, 2011.
- H. Forootanfar, M. M. Movahednia, S. Yaghmaei et al., "Removal of chlorophenolic derivatives by soil isolated ascomycete of *Paraconiothyrium variabile* and studying the role of its extracellular laccase," *Journal of Hazardous Materials*, vol. 209–210, pp. 199–203, 2012.
- S. R. Couto and J. L. T. Herrera, "Industrial and biotechnological applications of laccases: a review," *Biotechnology Advances*, vol. 24, no. 5, pp. 500–513, 2006.
- M. Chivukula and V. Renganathan, "Phenolic azo dye oxidation by laccase from *Pyricularia oryzae*," *Applied and Environmental Microbiology*, vol. 61, no. 12, pp. 4374–4377, 1995.
- A. Kamanneni, I. Ghazi, S. Camarero, A. Ballesteros, F. J. Plou, and M. Alcalde, "Decolorization of synthetic dyes by laccase immobilized on epoxy-activated carriers," *Process Biochemistry*, vol. 43, no. 2, pp. 169–178, 2008.
- G. K. Parshetti, A. A. Telke, D. C. Kalyani, and S. P. Govindwar, "Decolorization and detoxification of sulfonated azo dye methyl orange by *Kocuria rosea* MTCC 1532," *Journal of Hazardous Materials*, vol. 176, no. 1–3, pp. 503–509, 2010.
- H. J. Fan, S. T. Huang, W. H. Chung, J. L. Jan, W. Y. Lin, and C. C. Chen, "Degradation pathways of crystal violet by Fenton and Fenton-like systems: condition optimization and intermediate separation and identification," *Journal of Hazardous Materials*, vol. 171, no. 1–3, pp. 1032–1044, 2009.
- M. A. Faramarzi and H. Forootanfar, "Biosynthesis and characterization of gold nanoparticles produced by laccase

- from *Paraconiothyrium variabile*,” *Colloids and Surfaces B*, vol. 87, no. 1, pp. 23–27, 2011.
- [18] M. Aghaie-Khouzani, H. Forootanfar, M. Moshfegh, M. R. Khoshayand, and M. A. Faramarzi, “Decolorization of some synthetic dyes using optimized culture broth of laccase producing ascomycete *Paraconiothyrium variabile*,” *Biochemical Engineering Journal*, vol. 60, no. 1, pp. 9–15, 2012.
- [19] M. Panouillé and V. Larreta-Garde, “Gelation behaviour of gelatin and alginate mixtures,” *Food Hydrocolloids*, vol. 23, no. 4, pp. 1074–1080, 2009.
- [20] M. M. Bradford, “A rapid and sensitive method for the quantitation of microgram quantities of protein utilizing the principle of protein dye binding,” *Analytical Biochemistry*, vol. 72, no. 1-2, pp. 248–254, 1976.
- [21] A. K. Anal and W. F. Stevens, “Chitosan-alginate multilayer beads for controlled release of ampicillin,” *International Journal of Pharmaceutics*, vol. 290, no. 1-2, pp. 45–54, 2005.
- [22] J. P. Chen and Y. S. Lin, “Decolorization of azo dye by immobilized *Pseudomonas luteola* entrapped in alginate-silicate sol-gel beads,” *Process Biochemistry*, vol. 42, no. 6, pp. 934–942, 2007.
- [23] X. Hu, X. Zhao, and H. M. Hwang, “Comparative study of immobilized *Trametes versicolor* laccase on nanoparticles and kaolinite,” *Chemosphere*, vol. 66, no. 9, pp. 1618–1626, 2007.
- [24] G. Hublik and F. Schinner, “Characterization and immobilization of the laccase from *Pleurotus ostreatus* and its use for the continuous elimination of phenolic pollutants,” *Enzyme and Microbial Technology*, vol. 27, no. 3–5, pp. 330–336, 2000.
- [25] X. Q. Yang, X. X. Zhao, C. Y. Liu, Y. Zheng, and S. J. Qian, “Decolorization of azo, triphenylmethane and anthraquinone dyes by a newly isolated *Trametes* sp. SQ01 and its laccase,” *Process Biochemistry*, vol. 44, no. 10, pp. 1185–1189, 2009.
- [26] G. K. Parshetti, S. G. Parshetti, A. A. Telke, D. C. Kalyani, R. A. Doong, and S. P. Govindwar, “Biodegradation of crystal violet by *Agrobacterium radiobacter*,” *Journal of Environmental Sciences*, vol. 23, no. 8, pp. 1384–1393, 2011.
- [27] K. Selvam, K. Swaminathan, and K. S. Chae, “Decolourization of azo dyes and a dye industry effluent by a white rot fungus *Thelephora* sp,” *Bioresource Technology*, vol. 88, no. 2, pp. 115–119, 2003.
- [28] D. Yinghui, W. Qiuling, and F. Shiyu, “Laccase stabilization by covalent binding immobilization on activated polyvinyl alcohol carrier,” *Letters in Applied Microbiology*, vol. 35, no. 6, pp. 451–456, 2002.
- [29] N. Vishal Gupta, D. V. Gowda, V. Balamuralidhara, and S. Mohammed Khan, “Formulation and evaluation of olanzapine matrix pellets for controlled release,” *DARU, Journal of Pharmaceutical Sciences*, vol. 19, no. 4, pp. 249–256, 2011.
- [30] F. G. Mutti, R. Pievo, M. Sgobba, M. Gullotti, and L. Santagostini, “Biomimetic modeling of copper complexes: a study of enantioselective catalytic oxidation on *D*-(+)-catechin and *L*-(-)-epicatechin with copper complexes,” *Bioinorganic Chemistry and Applications*, vol. 2008, Article ID 762029, 9 pages, 2008.
- [31] H. Y. Xiao, J. Huang, C. Liu, and D. S. Jiang, “Immobilization of laccase on amine-terminated magnetic nano-composite by glutaraldehyde crosslinking method,” *Transactions of Nonferrous Metals Society of China*, vol. 16, supplement 1, pp. s414–s418, 2006.

Analysis of the Release Characteristics of Cu-Treated Antimicrobial Implant Surfaces Using Atomic Absorption Spectrometry

Carmen Zietz,¹ Andreas Fritzsche,¹ Birgit Finke,² Vitezslav Stranak,³ Maximilian Haenle,¹ Rainer Hippler,³ Wolfram Mittelmeier,¹ and Rainer Bader¹

¹ Biomechanics and Implant Technology Research Laboratory, Department of Orthopaedics, University of Rostock, Doberaner Straße 142, 18057 Rostock, Germany

² Leibniz Institute for Plasma Science and Technology (INP e.V. Greifswald), Felix-Hausdorff-Straße 2, 17489 Greifswald, Germany

³ Institute of Physics, Ernst-Moritz-Arndt University of Greifswald, Felix-Hausdorff-Straße 6, 17487 Greifswald, Germany

Correspondence should be addressed to Carmen Zietz, carmen.zietz@med.uni-rostock.de

Academic Editor: Reinhard Paschke

New developments of antimicrobial implant surfaces doped with copper (Cu) ions may minimize the risk of implant-associated infections. However, experimental evaluation of the Cu release is influenced by various test parameters. The aim of our study was to evaluate the Cu release characteristics *in vitro* according to the storage fluid and surface roughness. Plasma immersion ion implantation of Cu (Cu-PIII) and pulsed magnetron sputtering process of a titanium copper film (Ti-Cu) were applied to titanium alloy (Ti6Al4V) samples with different surface finishing of the implant material (polished, hydroxyapatite and corundum blasted). The samples were submersed into either double-distilled water, human serum, or cell culture medium. Subsequently, the Cu concentration in the supernatant was measured using atomic absorption spectrometry. The test fluid as well as the surface roughness can alter the Cu release significantly, whereby the highest Cu release was determined for samples with corundum-blasted surfaces stored in cell medium.

1. Introduction

Total joint replacement (TJR) meets high quality and safety standards and has become a frequent surgical procedure in order to restore joint function [1]. However, implant revision remains a relevant problem in clinical use. Failure of TJR is mainly due to aseptic loosening caused by inflammatory reactions due to wear particles [2]. Postoperative implant-associated infections are rare but considered devastating complications after TJR. Although surgical techniques and environmental conditions during the surgical intervention have improved over the years, infections occur with a frequency of 0.5–2% with incisive consequences for the patients and medical costs [3]. Most implant-associated infections are caused by *Staphylococcus aureus* and *Staphylococcus epidermidis* [4, 5].

Immediately after implantation bacteria, and human host cells compete for the implant surface in the so-called

“race for the surface” [6]. If bacteria adhere to the implant surface prior to human bone cells, biofilm formation might occur and osseous integration of the implant is precarious. In terms of biofilms, the treatment of implant-associated infections can be further hindered by the thus increased bacterial resistance against antibiotics [7]. Novel developments of ion-based antimicrobial implant surfaces such as silver (Ag) [8] or copper (Cu) [9] might offer a possible solution to this problem. Various *in vitro* and *in vivo* studies confirm the antibacterial properties and cytocompatibility of Cu [10–13]. Other alternative antibacterial materials and agents are in development or already in use to prevent or treat implant-associated infections [14–18]. *In vitro* investigations of the antibacterial effects are usually performed on simplified samples and under simplified testing conditions, whereas *in vivo* tests are usually closer to the final application. *In vitro* conditions are often adjusted according to the respective test, that is, cell biological and microbiological tests are performed

with regard to their specific test protocols. Test fluids, storage times and fluid volume are essential parameters to characterise the antibacterial behaviour as well as the cytocompatibility and release kinetics of the antibacterial agents. Furthermore, the surface characteristics, such as the surface roughness, are an important aspect for coated surfaces with regard to the ion release properties [19]. Moreover, the ion release of ion-based antimicrobial coatings is of essential interest for the bactericidal activity and the cyto-compatibility of the coating.

The aim of the present study was to evaluate the Cu release characteristics of two different plasma surface treatments doped with Cu according to the storage fluid and surface roughness of the samples in order to provide an approach for possible standardised investigations in the future.

2. Materials and Methods

Titanium alloy (Ti6Al4V) discs (11 mm in diameter, 2 mm in height) were used as specimens for the investigation of ion release characteristics of Cu-doped plasma implant treatments. Two different plasma processes applying Cu were used: a plasma immersion ion implantation process (Cu-PIII) [20] and a pulsed magnetron sputtering process of a Ti-Cu film [21].

To analyse the influence of the composition of the test fluid on the Cu release, the Cu-PIII, and Ti-Cu-coated test samples were placed in 24-well plates and covered with 700 µL test fluid. Additionally, uncoated Ti6Al4V test samples were submersed as a reference. The following test fluids were used: double-distilled water (TKA Wasseraufbereitungssysteme GmbH, Niederelbert, Germany), human serum (Invitrogen, Darmstadt, Germany), and Dulbecco's Modified Eagle's medium (DMEM, Invitrogen, Carlsbad, USA) with 10% fetal calf serum (FCS Gold, PAA Laboratories GmbH, Pasching, Austria) as well as 1% gentamicin (Ratiopharm GmbH, Ulm, Germany). Subsequently, the samples were incubated at 37°C in a humidified atmosphere with 5% CO₂ for 24 h to simulate physiological conditions. All samples were corundum-blasted before plasma treating and exhibited a surface roughness after plasma treatment of Ra = 3.76 ± 0.7 µm and 2.02 ± 0.1 µm for the Cu-PIII and Ti-Cu coatings, respectively. Three samples of each coating were submersed for each test fluid configuration.

In addition, to evaluate a possible influence on the Cu release due to surface topology and roughness, three different surface treatments of the Ti6Al4V samples were performed before Cu-PIII plasma treatment: polishing (Ra = 0.09 ± 0.09 µm), hydroxyapatite (HA) blasting (Ra = 1.17 ± 0.2 µm), and corundum blasting (Ra = 4.44 ± 0.5 µm). Subsequently three Cu-PIII treated samples of each surface roughness, were immersed in double-distilled water for 5 days. Furthermore, roughness was investigated after storage in DMEM for 24 hours.

After the lapse of submersion time, the supernatants were removed from the samples and 1% nitric acid (HNO₃) was added to stabilize the released Cu ions. In addition, the supernatants were diluted for the following atomic

absorption spectrometry (AAS) analysis. By means of an AAS with electrothermal atomization (ZEEnit 650, Analytik Jena AG, Jena, Germany), the concentration of Cu ions released into the supernatants from the Cu plasma treatments was determined.

Thereby, the solutions of the different samples were evaporated in a three-step process (90°C for 20 s, 105°C for 20 s, 110°C for 10 s) followed by a pyrolysis phase at 850°C (10 s) in a platform tube. The pyrolysis phase eliminates residual organic material and combusts solid particles from the solution into ash. Using a rapid heat increase (1500°C/s), the tube was heated to 2000°C for 4 s to vaporize and convert solid particles into free atoms. This step also included the element analysis using a hollow cathode lamp with a Cu cathode radiating at 324.8 nm. Parts of the total emitted intensity were absorbed by the Cu atoms present in the tube from the diluted solution samples of the release experiments. The measured intensity was compared with the intensity of a standard Cu reference allowing the determination of the Cu concentration in the supernatants. In a final step the platform tube was cleaned by heating up to 2300°C for 4 s.

All data were stored and analyzed using the SPSS statistical package 15.0 (SPSS Inc. Chicago, Ill, USA). Descriptive statistics were computed for continuous and categorical variables [22]. The statistical data included mean and standard deviations of continuous variables, frequencies, and relative frequencies of categorical factors. Comparisons within the independent groups were achieved using the ANOVA test (Post Hoc LSD). All P values resulted from two-sided statistical tests, and values of P < 0.05 were considered to be significant.

3. Results

The uncoated Ti6Al4V control test samples showed no traces of copper in the supernatant. However, specific release characteristics were found for the analysed Cu-doped Ti6Al4V samples in different supernatants (Figure 1). Hereby, DMEM provoked the highest Cu ion release with a significant increase compared to double-distilled water (P ≤ 0.001), but no statistical significance was observed when compared to human serum (P ≥ 0.068). Higher Cu concentrations were released from the Ti-Cu films than from the Cu-PIII-treated surfaces in human serum (4.96 ± 0.22 mmol/l versus 1.25 ± 0.01 mmol/l) and in DMEM (5.27 ± 0.90 mmol/l versus 2.00 ± 0.63 mmol/l), respectively. Using double-distilled water, the observed concentration of released Cu was significantly lower (P ≤ 0.019) compared to human serum and DMEM and approximately the same for all samples with different Cu treatments (Ti-Cu: 0.20 ± 0.01 mmol/l, Cu-PIII: 0.25 ± 0.02 mmol/l).

The surface roughness did not reveal a significant influence on the Cu release in double-distilled water (Figure 2). Polished surfaces resulted in a Cu concentration in the supernatant of 0.23 ± 0.01 mmol/l. For the HA and corundum-blasted surfaces the Cu concentration is in the same dimension at 0.16 ± 0.01 mmol/l and 0.20 ± 0.01 mmol/l, respectively. In comparison to DMEM, the Cu concentrations were significantly lower (P ≤ 0.007) for all

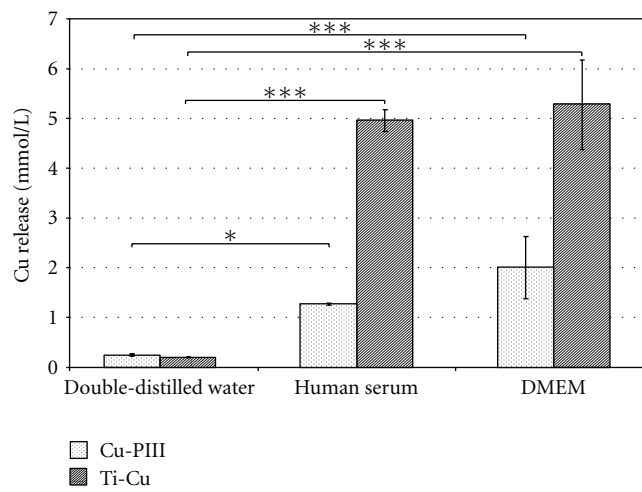


FIGURE 1: Copper concentration of Cu-PIII- and Ti-Cu-coated corundum-blasted Ti6Al4V surfaces submersed in 700 µL of different supernatants (human serum, double-distilled water, and DMEM) for 24 h at 37°C and 5% CO₂; ANOVA (Post Hoc LSD) test, *P < 0.05, ***P ≤ 0.001.

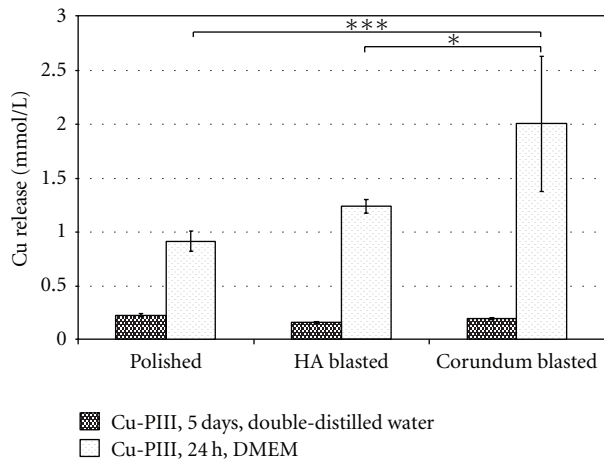


FIGURE 2: Copper concentration of Cu-PIII-treated Ti6Al4V samples with varying substrate surface roughness (polished, HA blasted, corundum blasted), submersed for 5 days in double-distilled water and 24 h in DMEM at 37°C and 5% CO₂. ANOVA (Post Hoc LSD) test, *P < 0.05, ***P ≤ 0.001.

surface topologies using double-distilled water. Corundum-blasted samples submersed in DMEM showed the highest Cu levels in the supernatant (2.00 ± 0.63 mmol/l, $P \leq 0.004$). A decrease in Cu concentration was observed for the polished samples in comparison to the HA-blasted ($P = 0.156$) and corundum-blasted ($P \leq 0.004$) samples.

4. Discussion

In order to enhance implant survival, bioactive coatings have moved into the focus of research and development. Due to the increasing risk of implant infections from multiresistant bacteria such as MRSA (multiresistant *Staphylococcus aureus*)

[10, 11, 23] or ESBL (enterobacteria producing extended spectrum beta-lactamases) [24], different antimicrobial coatings [17, 25–28] are being developed. However, the mechanical, biological and chemical properties of such innovative coatings have to be investigated thoroughly. Cu ions can be an effective antimicrobial agent to inhibit bacterial growth and biofilm formation on endoprosthetic surfaces [10, 29]. Analyses of the ion release are strictly necessary for the determination of relevant Cu concentrations required in order to regulate both antimicrobial effects and compatibility to human cells. Furthermore, the release kinetics of copper-doped surfaces needs to be investigated in standardised tests in order to ensure effective and valid ion concentrations. In this context, however, standardised test conditions have not been established so far.

The AAS is a suitable device to measure Cu concentrations in supernatants. Uncoated samples did not show any Cu in any of the analysed supernatants, whereas the Cu-treated samples revealed differences in Cu concentration. Nevertheless, using an AAS, both Cu⁺ and Cu²⁺ ions are assessed at the same time without any distinction. However, only Cu²⁺ ions cause an antimicrobial effect [30]. Hence, the concentration alone is not enough to predict the effectiveness of the coating and should be supported by microbiological tests.

Investigations of the ion release of an antimicrobial coating should coincide with cell biological tests using human cells to study biocompatibility of the coating. Furthermore, test fluid volumes should be the same for all studies, ensuring similar Cu concentrations. A test fluid volume of 700 µL was chosen to represent *in vivo* conditions. After conventional implantation technique, Wu et al. [31] observed that 40% of an uncemented femoral stem showed no bone contact with an average gap width between the bone and the femoral stem of 0.77 mm. In relation to the test samples deployed in this study, a volume of approximately 200 µL would be adequate to simulate the gap volume at the uncemented stem. However, 200 µL is not enough to cover the test samples completely, which would make *in vitro* testing impossible. Therefore, a volume of 700 µL was chosen as a compromise, which was the smallest possible volume that assured proper cell and bacterial growth in the supernatant.

The results of this study show that the amount of Cu ions released into the supernatant depends on various factors. The supernatant and its properties to dissolve Cu ions plays an important role. Surprisingly, the Cu concentration in double-distilled water for the Cu-PIII coating after 24 hours did not differ from the Cu concentration after 5 days. Therefore, double-distilled water showed an early Cu saturation for both tested coatings, whereas human serum and DMEM revealed a much higher Cu concentration in the supernatant. In fact, the highest concentration was obtained in DMEM for the Ti-Cu coating. The presence of serum proteins increases the solubility of Cu in the supernatants significantly compared to the double-distilled water because of the complex compounds between copper and amino groups found in the proteins in human serum and DMEM. Wu et al. [32] showed a higher concentration of Ag⁺ ions after 24 h in cell culture medium as in simulated body

fluid, which coincides with the Cu concentrations found in our present study. However, based on the current results, it is not possible to appoint a Cu ion saturation level for neither human serum nor DMEM. Repeated and cumulative investigations at different time periods need to be carried out and could provide a precise saturation level.

Surface roughness increases the surface area in contact with the supernatant. With rising surface roughness, an increase of the Cu concentration in the supernatant was observed. Compared to a polished surface, the corundum-blasted surface released approximately three times as many Cu ions within 24 h. In double-distilled water, the Cu concentration levels remained constant after 5 days regardless of the surface roughness, since the Cu saturation has set in within the first 24 h.

Temperature may also influence the ion release characteristic of an implant material. Therefore, the release studies should be carried out at 37°C body temperature. A time-dependant Cu release behaviour, cumulative and non cumulative, of the analysed coatings is currently under investigation. First results show that most of the Cu is released during the first 24 h, followed by a highly reduced release rate during the succeeding days. Furthermore, the effect of copper ions on human cells and tissue is currently under investigation provided by cell biological and microbiological tests as well as animal studies using an infection model.

5. Conclusion

When testing antimicrobial Cu-coated implant surfaces, it is important to apply appropriate test conditions regarding the ion release into the surrounding tissue. With respect to future clinical applications of the coated implants, a suitable test fluid such as human serum or DMEM should be used to coincide with cell biological and microbiological studies; otherwise, false conclusions may be drawn. Furthermore, it is important to use test samples with adequate surface properties close to those needed in the final application, since the surface roughness can affect the ion release dramatically.

Acknowledgments

This work was supported by the TEAM program of Mecklenburg-Vorpommern and the Helmholtz Association in Germany (UR 0402210, VH-MV1) and by the BMBF program Campus PlasmaMed (subproject PlasmaImp 13N9775, 13N11188). The authors thank Mr. U. Kellner, U. Lindemann (INP Greifswald), and L. Middelborg for the excellent technical assistance as well as Ms. A. Jonitz for the assistance in the statistical analysis.

References

- [1] C. A. Jones, L. A. Beaupre, D. W. C. Johnston, and M. E. Suarez-Almazor, "Total joint arthroplasties: current concepts of patient outcomes after surgery," *Rheumatic Disease Clinics of North America*, vol. 33, no. 1, pp. 71–86, 2007.
- [2] T. W. Bauer and J. Schils, "The pathology of total joint arthroplasty II. Mechanisms of implant failure," *Skeletal Radiology*, vol. 28, no. 9, pp. 483–497, 1999.
- [3] W. Zimmerli, A. Trampuz, and P. E. Ochsner, "Current concepts: prosthetic-joint infections," *New England Journal of Medicine*, vol. 351, no. 16, pp. 1645–1654, 2004.
- [4] A. Trampuz and W. Zimmerli, "Prosthetic joint infections: update in diagnosis and treatment," *Swiss Medical Weekly*, vol. 135, no. 17–18, pp. 243–251, 2005.
- [5] D. Campoccia, L. Montanaro, P. Speziale, and C. R. Arciola, "Antibiotic-loaded biomaterials and the risks for the spread of antibiotic resistance following their prophylactic and therapeutic clinical use," *Biomaterials*, vol. 31, no. 25, pp. 6363–6377, 2010.
- [6] A. Gristina, "Biomaterial-centered infection: microbial adhesion versus tissue integration. 1987," *Clinical Orthopaedics and Related Research*, no. 427, pp. 4–12, 2004.
- [7] J. W. Costerton, P. S. Stewart, and E. P. Greenberg, "Bacterial biofilms: a common cause of persistent infections," *Science*, vol. 284, no. 5418, pp. 1318–1322, 1999.
- [8] H. S. Ryu, I. H. Bae, and K. G. Lee, "Antibacterial effect of silver-platinumcoating for orthodontic appliances," *Angle Orthodontist*. In press.
- [9] G. Borkow and J. Gabbay, "Copper as a biocidal tool," *Current Medicinal Chemistry*, vol. 12, no. 18, pp. 2163–2175, 2005.
- [10] M. Haenle, A. Fritsche, C. Zietz et al., "An extended spectrum bactericidal titanium dioxide (TiO_2) coating for metallic implants: *in vitro* effectiveness against MRSA and mechanical properties," *Journal of Materials Science: Materials in Medicine*, vol. 22, no. 2, pp. 381–387, 2010.
- [11] L. Weaver, J. O. Noyce, H. T. Michels, and C. W. Keevil, "Potential action of copper surfaces on meticillin-resistant *Staphylococcus aureus*," *Journal of Applied Microbiology*, vol. 109, no. 6, pp. 2200–2205, 2010.
- [12] M. Yasuyuki, K. Kunihiro, S. Kurissery, N. Kanavillil, Y. Sato, and Y. Kikuchi, "Antibacterial properties of nine pure metals: a laboratory study using *Staphylococcus aureus* and *Escherichia coli*," *Biofouling*, vol. 26, no. 7, pp. 851–858, 2010.
- [13] R. Sharan, S. Chhibber, and R. H. Reed, "A murine model to study the antibacterial effect of copper on infectivity of *Salmonella enterica* serovar *Typhimurium*," *International Journal of Environmental Research and Public Health*, vol. 8, no. 1, pp. 21–36, 2011.
- [14] D. Neut, R. J. B. Dijkstra, J. I. Thompson, H. C. van der Mei, and H. J. Busscher, "Antibacterial efficacy of a new gentamicin-coating for cementless prostheses compared to gentamicin-loaded bone cement," *Journal of Orthopaedic Research*, vol. 29, no. 11, pp. 1654–1661, 2011.
- [15] L. Wang, U. J. Erasquin, M. Zhao et al., "Stability, antimicrobial activity, and cytotoxicity of poly(amidoamine) dendrimers on titanium substrates," *ACS Applied Materials & Interfaces*, vol. 3, no. 8, pp. 2885–2894, 2011.
- [16] J. Holt, B. Hertzberg, P. Weinhold, W. Storm, M. Schoenfisch, and L. Dahmers, "Decreasing bacterial colonization of external fixation pins through nitric oxide release coatings," *Journal of Orthopaedic Trauma*, vol. 25, no. 7, pp. 432–437, 2011.
- [17] E. M. Hetrick and M. H. Schoenfisch, "Reducing implant-related infections: active release strategies," *Chemical Society Reviews*, vol. 35, no. 9, pp. 780–789, 2006.
- [18] S. Chandra, S. Raizada, M. Tyagi, and A. Gautam, "Synthesis, spectroscopic, and antimicrobial studies on bivalent nickel and copper complexes of bis(thiosemicarbazone)," *Bioinorganic Chemistry and Applications*, vol. 2007, Article ID 51483, 7 page, 2007.
- [19] G. D. Christensen, L. Baldassari, and W. A. Simpson, "Methods for studying microbial colonization of plastics," *Methods in Enzymology*, vol. 253, pp. 477–500, 1995.

- [20] K. Schröder, B. Finke, M. Polak et al., "Gas-discharge plasma-assisted functionalization of titanium implant surfaces," *Materials Science Forum*, vol. 638-642, pp. 700–705, 2010.
- [21] V. Stranak, H. Wulff, H. Rebl et al., "Deposition of thin titanium-copper films with antimicrobial effect by advanced magnetron sputtering methods," *Materials Science and Engineering C*, vol. 31, no. 7, pp. 1512–1519, 2011.
- [22] R. Marcus, E. Peritz, and K. R. Gabriel, "On closed testing procedures with special reference to ordered analysis of variance," *Biometrika*, vol. 63, no. 3, pp. 655–660, 1976.
- [23] D. Ip, S. K. Yam, and C. K. Chen, "Implications of the changing pattern of bacterial infections following total joint replacements," *Journal of Orthopaedic Surgery*, vol. 13, no. 2, pp. 125–130, 2005.
- [24] M. Haenle, A. Podbielski, M. Ellenrieder et al., "Periprosthetic infections following total hip replacement with ESBL-forming bacteria importance for clinical practice," *Orthopade*, vol. 40, no. 6, pp. 528–534, 2011.
- [25] A. Ewald, S. K. Glückermann, R. Thull, and U. Gbureck, "Antimicrobial titanium/silver PVD coatings on titanium," *BioMedical Engineering Online*, vol. 5, article 22, 2006.
- [26] G. Schmidmaier, M. Lucke, B. Wildemann, N. P. Haas, and M. Raschke, "Prophylaxis and treatment of implant-related infections by antibiotic-coated implants: a review," *Injury*, vol. 37, no. 2, pp. S105–S112, 2006.
- [27] N. Y. Pfeifer, K. Hofmann-Peiker, M. Mühlé, P. H. Warnke, M. C. Weigel, and M. Kleine, "Bioactive coating of titanium surfaces with recombinant human β -defensin-2 (rHu β D2) may prevent bacterial colonization in orthopaedic surgery," *Journal of Bone and Joint Surgery. Series A*, vol. 93, no. 9, pp. 840–846, 2011.
- [28] A. Fritsche, F. Heidenau, H. G. Neumann, W. Mittelmeier, and R. Bader, "Mechanical properties of anti-infectious, bio-active and wear resistant ceramic implant surface coatings," *Key Engineering Materials*, vol. 396-398, pp. 357–360, 2009.
- [29] F. Heidenau, W. Mittelmeier, R. Detsch et al., "A novel antibacterial titania coating: metal ion toxicity and *in vitro* surface colonization," *Journal of Materials Science: Materials in Medicine*, vol. 16, no. 10, pp. 883–888, 2005.
- [30] I. Iakovidis, I. Delimaris, and S. M. Piperakis, "Copper and its complexes in medicine: a biochemical approach," *Molecular Biology International*, vol. 2011, Article ID 594529, 13 pages, 2011.
- [31] L. D. Wu, H. J. Hahne, and J. Hassenpflug, "The dimensional accuracy of preparation of femoral cavity in cementless total hip arthroplasty," *Journal of Zhejiang University Science*, vol. 5, no. 10, pp. 1270–1278, 2004.
- [32] X. Wu, J. Li, L. Wang, D. Huang, Y. Zuo, and Y. Li, "The release properties of silver ions from Ag-nHA/TiO₂/PA66 antimicrobial composite scaffolds," *Biomedical Materials*, vol. 5, no. 4, Article ID 044105, 2010.

Enhancement of Antibacterial Activity of Capped Silver Nanoparticles in Combination with Antibiotics, on Model Gram-Negative and Gram-Positive Bacteria

Aruna Jyothi Kora and Lori Rastogi

National Centre for Compositional Characterisation of Materials (NCCCM), Bhabha Atomic Research Centre,
Hyderabad 500 062, India

Correspondence should be addressed to Aruna Jyothi Kora; koramaganti@gmail.com

Academic Editor: Zhe-Sheng Chen

The nanoparticles used in this study were prepared from AgNO_3 using NaBH_4 in the presence of capping agents such as citrate, sodium dodecyl sulfate, and polyvinylpyrrolidone. The formed nanoparticles were characterized with UV-Vis, TEM, and XRD. The generation of silver nanoparticles was confirmed from the appearance of yellow colour and an absorption maximum between 399 and 404 nm. The produced nanoparticles were found to be spherical in shape and polydisperse. For citrate, SDS, and PVP capped nanoparticles, the average particle sizes were 38.3 ± 13.5 , 19.3 ± 6.0 , and 16.0 ± 4.8 nm, respectively. The crystallinity of the nanoparticles in FCC structure is confirmed from the SAED and XRD patterns. Also, the combined antibacterial activity of these differently capped nanoparticles with selected antibiotics (streptomycin, ampicillin, and tetracycline) was evaluated on model Gram-negative and Gram-positive bacteria, employing disc diffusion assay. The activity of the tested antibiotics was enhanced in combination with all the stabilized nanoparticles, against both the Gram classes of bacteria. The combined effects of silver nanoparticles and antibiotics were more prominent with PVP capped nanoparticles as compared to citrate and SDS capped ones. The results of this study demonstrate potential therapeutic applications of silver nanoparticles in combination with antibiotics.

1. Introduction

Since ancient times, silver has been known to possess antibacterial properties [1], but the solubility characteristics of silver metal and silver salts (e.g., silver nitrate) render it impractical in many clinical scenarios, that is, where silver nanoparticles (Ag NPs) have been a subject of great interest among researchers [2–4], because it is not only facile to synthesize silver nanoparticles of desired sizes [5, 6] and shapes [7–9] dispersed in aqueous/organic phases but also feasible to make films, with the composite of these particles suiting various applications in the field of medical diagnosis and therapy. The use of silver nanoparticles in materials modification for application in different fields such as clothing, semiconductor, and preparation of nanocomposite materials with improved performances has been demonstrated. For example, silver nanoparticles have been successfully coated on medical devices for infection-free transplantation [10, 11].

Silver nanoparticles have also been coated on various fabrics [12–15]; the coating of nanosilver imparts not only the metallic feature to the fibers rendering the textiles conductive but also the antibacterial property to the textiles. These studies suggest that it is possible to have extended action of silver-nanoparticle-based antibacterial activities. Moreover, it can be expected that the high specific surface area and high fraction of surface atoms of silver nanoparticles will lead to high antimicrobial activity as compared with bulk silver metal.

In recent years, resistance to antibiotics by pathogenic bacteria and fungi has been increasing at an alarming rate and has become a serious problem [16, 17]. For example, *S. typhi* has exhibited resistance to antibiotics like chloramphenicol, ampicillin, quinolone, and trimethoprim. And also *E. coli* shows resistance to a variety of antibiotics like ampicillin, kanamycin, sulfisoxazole, streptomycin, tetracycline, ticarcillin, and so forth. Silver has been thought of as

a promising agent for overcoming the resistance mechanism of antibacterial action on a range of targets as compared to a specific site of action in the case of antibiotics [18–20]. Hence, nanoparticle-based antibacterial formulations could be effective bactericidal materials as they will exhibit combined effects of silver and antibacterial agents. The enhanced activity of silver nanoparticles and antibiotics together has been reported earlier [21–25]. Herein, in this study we have compared the effect of three different capping agents citrate, sodium dodecyl sulfate, and polyvinyl pyrrolidone on the synthesis of silver nanoparticles. The nanoparticles used in this study were prepared by a common synthetic route that is borohydride reduction of silver nitrate in the presence of stabilizing agents. One of the important criterions for nanoparticle production is the prevention of particle aggregation during synthesis. The nanoparticles can be stabilized either by steric or electrostatic forces. The steric stabilization can be achieved by adsorbing polymers such as polyvinyl pyrrolidone, whereas the electrostatic stabilization can be attained by surface modifiers such as sodium dodecyl sulfate and citrate. The studies were further extended to investigate the combined antibacterial effect of these differently capped silver nanoparticles with antibiotics on both the Gram classes of bacteria.

2. Materials and Methods

2.1. Synthesis of Silver Nanoparticles. Silver nitrate (AgNO_3), sodium borohydride (NaBH_4) (E. Merck, Mumbai, India), trisodium citrate dihydrate (Finar, Hyderabad, India), sodium dodecyl sulfate (SDS) (SRL, Mumbai, India), and polyvinylpyrrolidone (PVP) with average M Wt 40,000 (Sigma-Aldrich, Mumbai, India) of analytical reagent grade were used for the synthesis. All the solutions were prepared in ultrapure water. The silver nanoparticles of 1.0 mM concentration were prepared using 6.0 mM of ice cold NaBH_4 , in the presence of 0.4 mM sodium citrate, 0.4 mM SDS, and 0.1% PVP [26], by stirring for 30 min. The produced colloidal solutions were diluted eight times with ultrapure water and the spectra were recorded.

2.2. Characterization of Synthesized Silver Nanoparticles. The UV-visible absorption spectra of the prepared colloidal solutions were recorded using an Elico SL 196 spectrophotometer (Hyderabad, India), from 250 to 800 nm, against blank. The size and shape of the nanoparticles were obtained with JEOL 2100 (Tokyo, Japan) transmission electron microscope, operating at 200 kV. The samples were prepared by depositing a drop of colloidal solution on a carbon coated copper grid and drying at room temperature. The X-ray diffraction analysis was conducted with a Rigaku, Ultima IV diffractometer (Tokyo, Japan) using monochromatic $\text{Cu K}\alpha$ radiation ($\lambda = 1.5406 \text{ \AA}$) running at 40 kV and 30 mA. The intensity data for the nanoparticle solution deposited on a glass slide was collected over a 2θ range of 35–85° with a scan rate of 1°/min. The hydrodynamic diameter and zeta potential values of the produced silver nanoparticles were assessed with a Malvern Zetasizer Nanosystem (Worcestershire, UK).

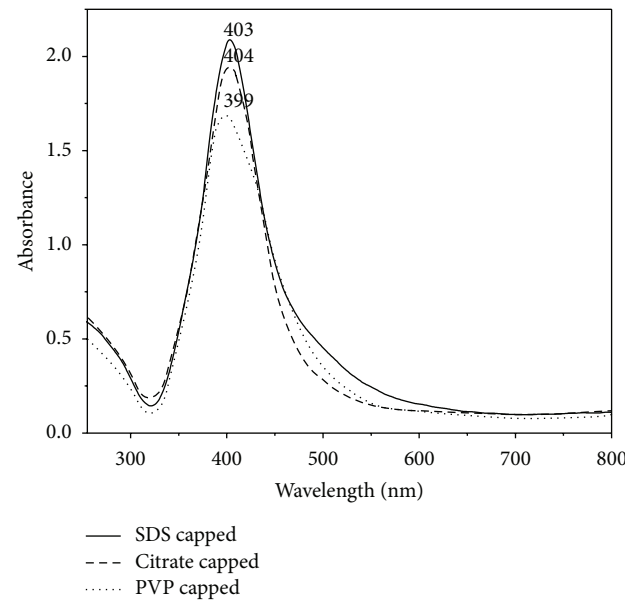


FIGURE 1: The UV-Vis absorption spectra of capped silver nanoparticles synthesized with sodium borohydride.

2.3. Disc Diffusion Assay. All the glassware and media used were sterilized in an autoclave at 121°C for 20 min. The bacterial strains *Escherichia coli* (ATCC 25922) and *Staphylococcus aureus* (ATCC 25923) were used as model test strains for Gram-negative and Gram-positive bacteria, respectively. The bacterial suspension was prepared by growing a single colony overnight in nutrient broth and by adjusting the turbidity to 0.5 McFarland standard. The disc diffusion method was used to evaluate the antibacterial activity of silver nanoparticles in combination with antibiotics. Based on the CLSI standard, the selected concentrations of antibiotics were streptomycin (10 µg), ampicillin (10 µg), and tetracycline (30 µg), respectively [27]. By using spread plate method, the Mueller-Hinton agar plates were inoculated with the turbidity adjusted bacterial suspension, and antibiotic impregnated sterile discs of 6 mm diameter (HiMedia Chemicals Pvt. Ltd., Mumbai, India) were placed on the medium surface. Also, the antibiotic discs loaded with 5 µg of nanosilver were placed on the inoculated plates to see the combined activity. The plates were maintained with discs containing silver nanoparticles and capping agents separately. These plates were incubated at 37°C for 24 h, and zone of inhibition (ZOI) was measured by subtracting the disc diameter from the total inhibition zone diameter. This assay was performed in triplicate.

3. Results and Discussion

3.1. UV-Visible Spectroscopy (UV-Vis). The appearance of yellow colour in the reaction mixtures was observed within minutes, an obvious indication for the silver nanoparticle formation. Furthermore, the nanoparticle synthesis was assured by monitoring the absorption spectra of synthesized colloidal solutions, against respective capping agent blanks (Figure 1). In the UV-Vis spectra, a single strong peak was observed for citrate, SDS, and PVP capped silver nanoparticles at 404,

403, and 399 nm, respectively, which corresponds to the typical surface plasmon resonance (SPR) of spherical silver nanoparticles. When compared to citrate and SDS stabilized, the SPR peak of PVP stabilized nanoparticles was blue shifted towards a shorter wavelength of 399 nm. The shift in SPR is determined by the capping agent due to the local nature of its effect on the surface of the nanoparticles [28].

3.2. Transmission Electron Microscopy (TEM). Figure 2 shows the TEM image of the silver nanoparticles stabilized with citrate. These nanoparticles are mostly spherical and were few square shaped, polydisperse, and showing wide range of particles from 21 to 70 nm with bimodal distribution. The smaller sized population had a mean diameter of 31.1 ± 6.2 nm (73%), while the larger sized one had a mean diameter of 57.5 ± 7.8 nm (27%). The average particle size obtained from both populations was about 38.3 ± 13.5 nm ($P \leq 0.0001$) (Figure 2(c)). Furthermore, the size of the particles was compared with SDS capped colloids (Figure 3). The nanoparticles are spherical in shape, polydisperse with bimodal distribution showing sizes of 12–34 nm. The smaller sized population had a mean diameter of 16.3 ± 3.1 nm (79%) and the larger sized one had a mean diameter of 28.1 ± 2.9 nm (21%). The average particle size of the two modes was about 19.3 ± 6.0 nm ($P \leq 0.0001$) (Figure 3(c)). Furthermore, the size was also evaluated for PVP capped colloidal solution (Figure 4). The produced nanoparticles are spherical, nonaggregated, and bimodal with a size distribution of 8.0–28 nm. The smaller and larger sized populations had mean diameters of 15.1 ± 3.7 nm (92%) and 27.2 ± 1.1 nm (8%), respectively. The average particle size obtained from both the diameter distributions was about 16.0 ± 4.8 nm ($P \leq 0.0001$) (Figure 4(c)). The bimodal distribution is likely due to the inhomogeneous growth, which is kinetically favoured. Among the preparations, the silver colloids stabilized with PVP exhibited a narrow particle size distribution. It is worth noting that with PVP, the average size of the nanoparticles formed decreased. The decrease in polydispersity and mean particle size with PVP stabilized particles was also evident from the TEM image. This is possibly due to the higher electron donating ability of PVP leading to a stronger interaction with positively charged silver ions during reduction, thereby an enhanced stabilization between capping molecules and nanoparticle surfaces [29]. The size and shape of the nanoparticles synthesized depend on many parameters such as choice of reduction technique, concentration of metal precursor, reductant, and capping agent [28].

3.3. X-Ray Diffraction (XRD). The XRD pattern of the stabilized silver nanoparticles is shown in Figure 5. There were five well-defined characteristic diffraction peaks at 38.3° , 44.5° , 64.8° , 77.6° , and 81.8° , respectively, corresponding to (111), (200), (220), (311), and (222) planes of face centered cubic (fcc) crystal structure of metallic silver. The interplanar spacing (d_{hkl}) values (2.307, 2.012, 1.437, 1.229, and 1.176 Å) and the lattice constant (4.047 Å) calculated from the XRD spectrum of silver nanoparticles are in agreement with the standard silver values (JCPDS PDF card 04-0783). Therefore,

the XRD pattern further corroborates the highly crystalline nature of nanoparticles observed from the selected-area electron diffraction (SAED) patterns depicting concentric rings with intermittent bright dots (Figures 2, 3, and 4). In addition, the broadening of the diffraction peaks was observed owing to the effect of nanosized particles. From the diffraction pattern, it is clear that the lattice plane (111) is the favored orientation for the generated nanoparticles [30].

3.4. Antibacterial Activity. In this report, the combined effect of the capped silver nanoparticles with antibiotics was assessed in comparison to antibiotics, with disc diffusion method. The concentrations of capping agents used for synthesis of nanoparticles did not show any antibacterial activity on the test strains. It was observed that the collective effect of silver nanoparticles with antibiotics was additive. The activity of the three antibiotics: streptomycin, ampicillin, and tetracycline with citrate, SDS, and PVP capped nanoparticles, against *E. coli* and *S. aureus* strains was shown as percentage enhancement in antibacterial effect. The increase in antibacterial activity of different antibiotics was quantified by the equation $(B - A)/A \times 100$, where A and B are the ZOI for antibiotic and antibiotic + silver nanoparticles, respectively. The activity of all the tested antibiotics was increased in combination with all the silver nanoparticles employed, against the test bacterial strains. For the Gram-negative *E. coli*, the highest increase was noted for tetracycline ($P \leq 0.004$) followed by ampicillin ($P \leq 0.01$) and streptomycin ($P \leq 0.05$) with citrate capped nanoparticles. For SDS capped nanoparticles, the raise in the activity was in the order of ampicillin ($P \leq 0.001$) > tetracycline ($P \leq 0.001$) > streptomycin ($P \leq 0.005$). The highest percentage of enhancement was found for ampicillin ($P \leq 0.0004$) followed by tetracycline ($P \leq 0.002$) and streptomycin ($P \leq 0.03$), with PVP capped nanoparticles (Figure 6). In the case of Gram-positive *S. aureus* strain, the order was found to be streptomycin ($P \leq 0.005$) > ampicillin ($P \leq 0.01$) > tetracycline ($P \leq 0.01$) for citrate and SDS capped nanoparticles. For the PVP capped nanoparticles, the enhancement was in the order of streptomycin ($P \leq 0.0005$) > tetracycline ($P \leq 0.001$) > ampicillin ($P \leq 0.005$) (Figure 7). Interestingly, among the selected antibiotics, streptomycin has shown the highest activity against *S. aureus* with PVP capped silver nanoparticles. The collective activity of nanoparticles capped with PVP with the antibiotics streptomycin and tetracycline against *S. aureus* was found to be the highest in comparison with citrate and SDS capped nanoparticles. With the same polymer capped nanoparticles against *E. coli*, the highest percentage of enhancement was observed for the antibiotic ampicillin (Figure 6). From the data, it is evident that antibiotic ampicillin demonstrates the highest percentage of enhancement in activity against *E. coli* with PVP and SDS capped nanoparticles. In contrast, the maximum increase in activity against *S. aureus* was observed for the streptomycin antibiotic with PVP capped nanoparticles. The differential susceptibility of Gram-negative and Gram-positive bacteria towards antibacterial agents possibly depends on their cell wall structure [31]. The results obtained in our study

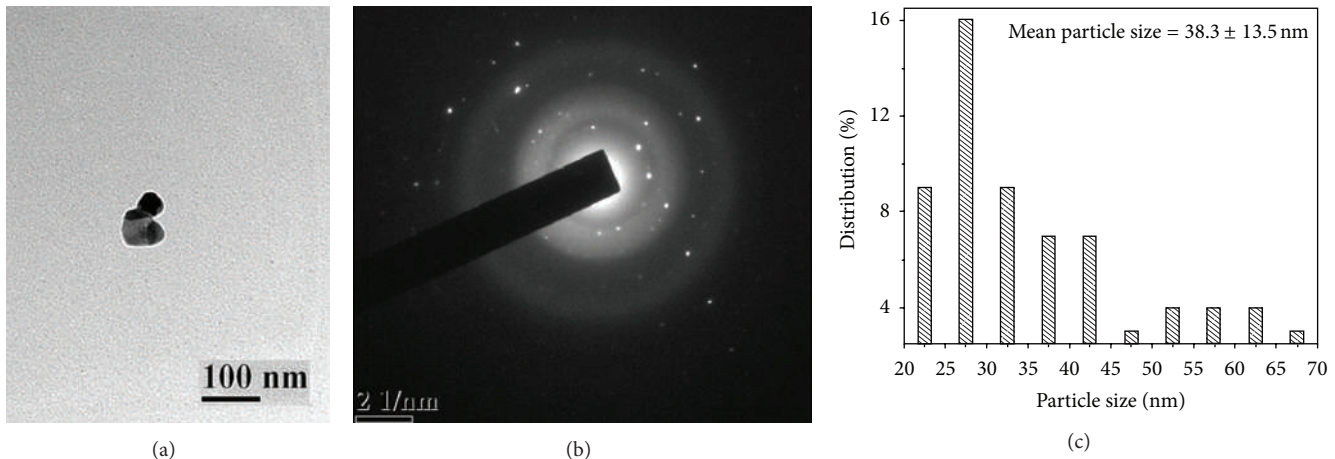


FIGURE 2: TEM images of citrate stabilized silver nanoparticle, at (a) 100 nm scale, (b) corresponding SAED pattern, and (c) histogram showing the particle size distribution.

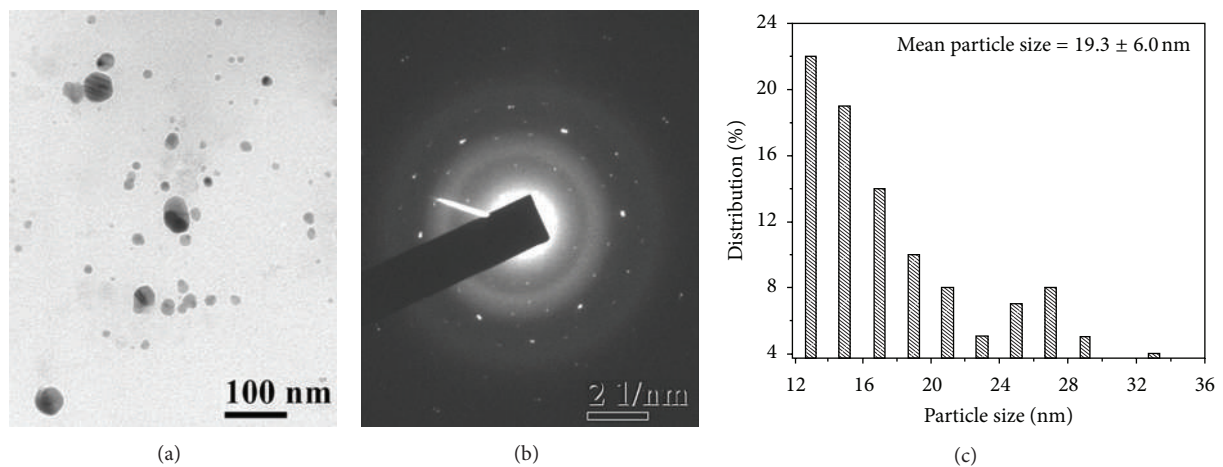


FIGURE 3: TEM images of SDS capped silver nanoparticle, at (a) 100 nm scale, (b) corresponding SAED pattern, and (c) histogram showing the particle size distribution.

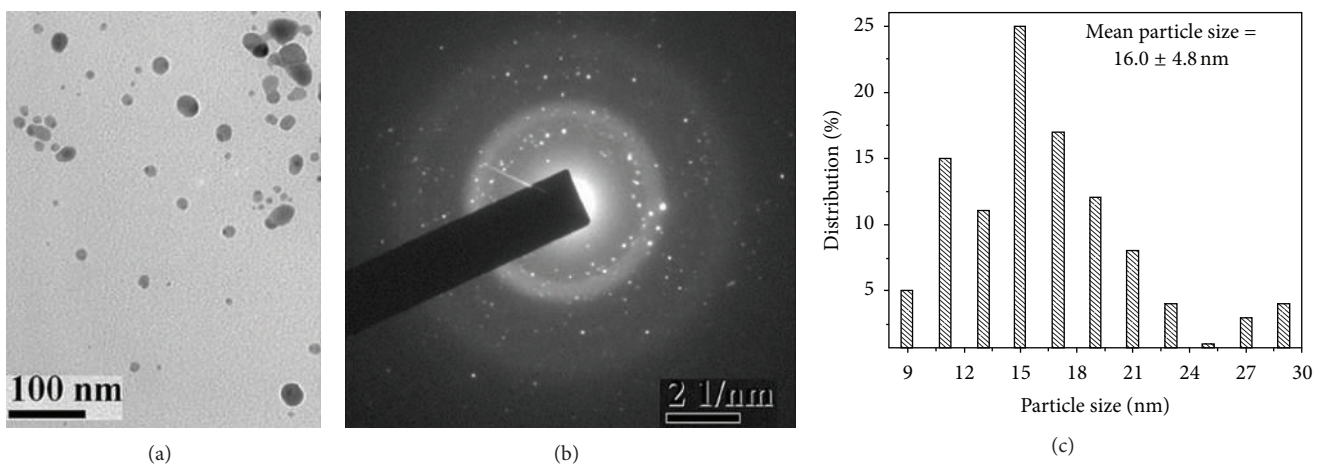


FIGURE 4: TEM images of PVP stabilized silver nanoparticle, at (a) 100 nm scale, (b) corresponding SAED pattern, and (c) histogram showing the particle size distribution.

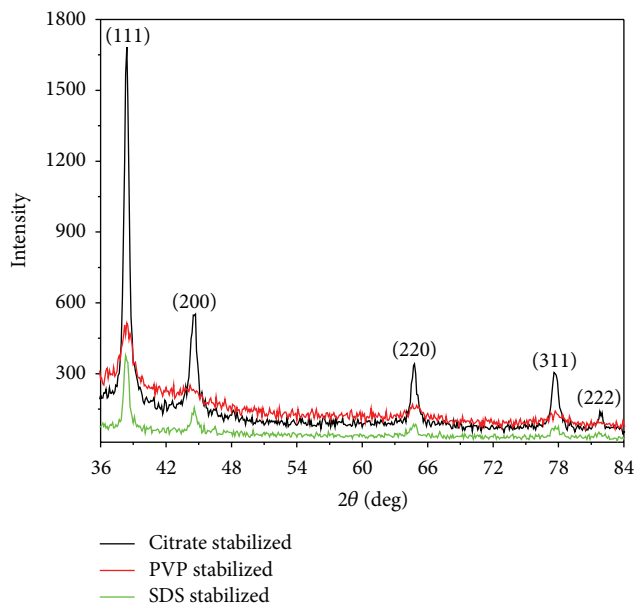


FIGURE 5: The XRD pattern of capped silver nanoparticles, indicating the face centered cubic (fcc) crystal structure.

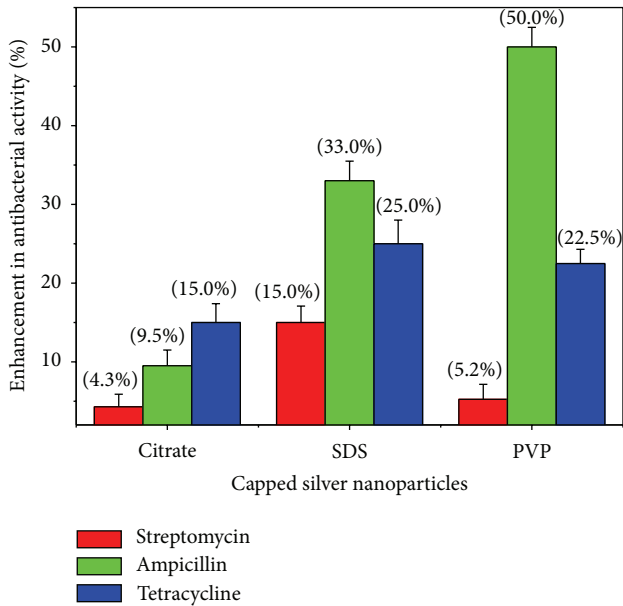


FIGURE 6: The percentage of enhancement in antibacterial activity observed for the antibiotics in combination with silver nanoparticles, against the bacterial strain *E. coli* ATCC 25922.

on collective effects of antibiotics with silver nanoparticles are in similar lines with earlier studies reported [21, 22, 24, 25, 32–34].

The data suggests that the enhancement in antibacterial activity of antibiotics with silver nanoparticles depends on the influence of the capping agent on nanoparticles. The combined effects of silver nanoparticles and antibiotics were more prominent with PVP capped nanoparticles as compared to citrate and SDS capped ones. This can be probably attributed

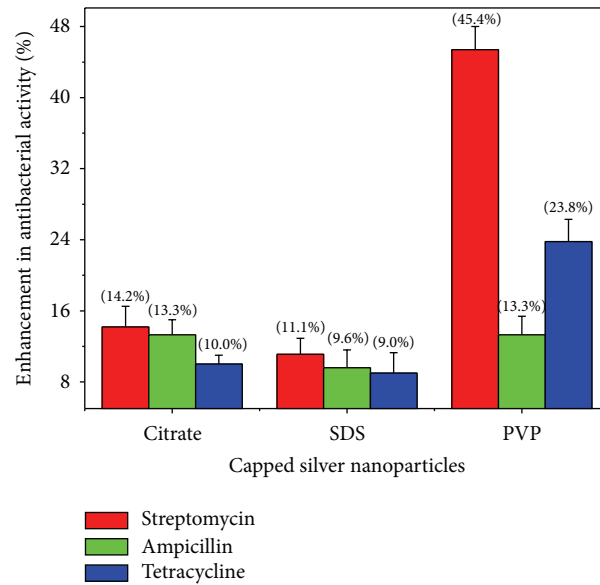


FIGURE 7: The percentage of enhancement in antibacterial activity observed for the antibiotics in combination with silver nanoparticles, against the bacterial strain *S. aureus* ATCC 25923.

to the steric stabilization of nanoparticles by the polymer PVP. It is well established that PVP capped silver and gold nanoparticles exhibit excellent stability towards changes in pH and ionic strength [35, 36]. Thus, the PVP capping on the surface of nanoparticles protects from changes in environmental conditions and prevents aggregation. In addition, the capping agent PVP is known to improve the bioavailability of the drug and the same is reported for curcumin conjugated to PVP capped gold nanoparticles [37]. The probable mechanism involved in enhanced antibacterial activity of antibiotics with silver nanoparticles can be attributed to the bonding reaction between nanoparticles and antibiotic molecules. The active functional groups of antibiotics such as hydroxyl and amino groups react with large surface area of the silver nanoparticles by chelation [22].

4. Conclusions

In this study, we have used a chemical reduction method for the synthesis of silver nanoparticles in the presence of three different capping agents. The produced nanoparticles were found to be spherical in shape and polydisperse. The antibacterial activity of the selected antibiotics was increased in the presence of these capped silver nanoparticles against test strains. The increase in activity was more pronounced with PVP capped silver nanoparticles for both Gram-negative and Gram-positive bacteria. In view of this, further studies are envisaged to explore the mechanism involved in enhanced antibacterial activity.

Conflict of Interests

The authors declare that they have no conflict of interests with any of the commercial identities mentioned in the paper.

Acknowledgments

The authors would like to thank Dr. J. Arunachalam, Former Head, NCCCM, BARC for his constant support and encouragement. The TEM support rendered by Central Research Facility at IIT, Kharagpur, India, is gratefully acknowledged.

References

- [1] S. Silver and L. T. Phung, "Bacterial heavy metal resistance: new surprises," *Annual Review of Microbiology*, vol. 50, no. 1, pp. 753–789, 1996.
- [2] M. Guzman, J. Dille, and S. Godet, "Synthesis and antibacterial activity of silver nanoparticles against gram-positive and gram-negative bacteria," *Nanomedicine: Nanotechnology, Biology, and Medicine*, vol. 8, no. 1, pp. 37–45, 2012.
- [3] V. K. Sharma, R. A. Yngard, and Y. Lin, "Silver nanoparticles: green synthesis and their antimicrobial activities," *Advances in Colloid and Interface Science*, vol. 145, no. 1-2, pp. 83–96, 2009.
- [4] I. Sondi and B. Salopek-Sondi, "Silver nanoparticles as antimicrobial agent: a case study on *E. coli* as a model for Gram-negative bacteria," *Journal of Colloid and Interface Science*, vol. 275, no. 1, pp. 177–182, 2004.
- [5] G. A. Martinez-Castanon, N. Nino-Martinez, F. Martinez-Gutierrez, J. R. Martinez-Mendoza, and F. Ruiz, "Synthesis and antibacterial activity of silver nanoparticles with different sizes," *Journal of Nanoparticle Research*, vol. 10, pp. 1343–1348, 2008.
- [6] X. Sun and Y. Luo, "Preparation and size control of silver nanoparticles by a thermal method," *Materials Letters*, vol. 59, no. 29-30, pp. 3847–3850, 2005.
- [7] Z. Shervani, Y. Ikushima, M. Sato et al., "Morphology and size-controlled synthesis of silver nanoparticles in aqueous surfactant polymer solutions," *Colloid and Polymer Science*, vol. 286, no. 4, pp. 403–410, 2008.
- [8] B. Sadeghi, F. S. Garmaroudi, M. Hashemi et al., "Comparison of the anti-bacterial activity on the nanosilver shapes: nanoparticles, nanorods and nanoplates," *Advanced Powder Technology*, vol. 23, no. 1, pp. 22–26, 2012.
- [9] S. Pal, Y. K. Tak, and J. M. Song, "Does the antibacterial activity of silver nanoparticles depend on the shape of the nanoparticle? A study of the gram-negative bacterium *Escherichia coli*," *Applied and Environmental Microbiology*, vol. 73, no. 6, pp. 1712–1720, 2007.
- [10] F. Furno, K. S. Morley, B. Wong et al., "Silver nanoparticles and polymeric medical devices: a new approach to prevention of infection?" *Journal of Antimicrobial Chemotherapy*, vol. 54, no. 6, pp. 1019–1024, 2004.
- [11] K. N. J. Stevens, S. Croes, R. S. Boersma et al., "Hydrophilic surface coatings with embedded biocidal silver nanoparticles and sodium heparin for central venous catheters," *Biomaterials*, vol. 32, no. 5, pp. 1264–1269, 2011.
- [12] M. H. El-Rafie, T. I. Shaheen, A. A. Mohamed, and A. Hebeish, "Bio-synthesis and applications of silver nanoparticles onto cotton fabrics," *Carbohydrate Polymers*, vol. 90, no. 2, pp. 915–920, 2012.
- [13] D. Hegemann, M. M. Hossain, and D. J. Balazs, "Nanostructured plasma coatings to obtain multifunctional textile surfaces," *Progress in Organic Coatings*, vol. 58, no. 2-3, pp. 237–240, 2007.
- [14] M. L. W. Knetsch and L. H. Koole, "New strategies in the development of antimicrobial coatings: the example of increasing usage of silver and silver nanoparticles," *Polymers*, vol. 3, no. 1, pp. 340–366, 2011.
- [15] F. Zhang, X. Wu, Y. Chen, and H. Lin, "Application of silver nanoparticles to cotton fabric as an antibacterial textile finish," *Fibers and Polymers*, vol. 10, no. 4, pp. 496–501, 2009.
- [16] G. D. Wright, "Resisting resistance: new chemical strategies for battling superbugs," *Chemistry and Biology*, vol. 7, no. 6, pp. R127–R132, 2000.
- [17] G. D. Wright, "Bacterial resistance to antibiotics: enzymatic degradation and modification," *Advanced Drug Delivery Reviews*, vol. 57, no. 10, pp. 1451–1470, 2005.
- [18] E. T. Hwang, J. H. Lee, Y. J. Chae et al., "Analysis of the toxic mode of action of silver nanoparticles using stress-specific bioluminescent bacteria," *Small*, vol. 4, no. 6, pp. 746–750, 2008.
- [19] W. K. Jung, H. C. Koo, K. W. Kim, S. Shin, S. H. Kim, and Y. H. Park, "Antibacterial activity and mechanism of action of the silver ion in *Staphylococcus aureus* and *Escherichia coli*," *Applied and Environmental Microbiology*, vol. 74, no. 7, pp. 2171–2178, 2008.
- [20] Z. Xiu, Q. Zhang, H. L. Puppala, V. L. Colvin, and P. J. Alvarez, "Negligible particle-specific antibacterial activity of silver nanoparticles," *Nano Letters*, vol. 12, no. 8, pp. 4271–4275, 2012.
- [21] M. A. Dar, A. Ingle, and M. Rai, "Enhanced antimicrobial activity of silver nanoparticles synthesized by *Cryphonectria* sp. evaluated singly and in combination with antibiotics," *Nanomedicine: Nanotechnology, Biology, and Medicine*, vol. 9, no. 1, pp. 105–110, 2013.
- [22] A. M. Fayaz, K. Balaji, M. Girilal, R. Yadav, P. T. Kalaichelvan, and R. Venketesan, "Biogenic synthesis of silver nanoparticles and their synergistic effect with antibiotics: a study against gram-positive and gram-negative bacteria," *Nanomedicine: Nanotechnology, Biology, and Medicine*, vol. 6, no. 1, pp. e103–e109, 2010.
- [23] G. Geoprincy, P. Saravanan, N. N. Gandhi, and S. Renganathan, "A novel approach for studying the combined antimicrobial effects of silver nanoparticles and antibiotics through agar over layer method and disk diffusion method," *Digest Journal of Nanomaterials and Biostructures*, vol. 6, no. 4, pp. 1557–1565, 2011.
- [24] A. R. Shahverdi, A. Fakhimi, H. R. Shahverdi, and S. Minaian, "Synthesis and effect of silver nanoparticles on the antibacterial activity of different antibiotics against *Staphylococcus aureus* and *Escherichia coli*," *Nanomedicine: Nanotechnology, Biology, and Medicine*, vol. 3, no. 2, pp. 168–171, 2007.
- [25] L. S. Devi and S. R. Joshi, "Antimicrobial and synergistic effects of silver nanoparticles synthesized using soil fungi of high altitudes of Eastern Himalaya," *Mycobiology*, vol. 40, no. 1, pp. 27–34, 2012.
- [26] J. S. Kim, E. Kuk, K. N. Yu et al., "Antimicrobial effects of silver nanoparticles," *Nanomedicine: Nanotechnology, Biology, and Medicine*, vol. 3, no. 1, pp. 95–101, 2007.
- [27] J. L. Watts, *Performance Standards for Antimicrobial Disk and Dilution Susceptibility Tests for Bacteria Isolated from Animals: Approved Standard*, Clinical and Laboratory Standards Institute, 3rd edition, 2008.
- [28] M. M. Chili and N. Revaprasadu, "Synthesis of anisotropic gold nanoparticles in a water-soluble polymer," *Materials Letters*, vol. 62, no. 23, pp. 3896–3899, 2008.
- [29] T. Hasell, J. Yang, W. Wang, P. D. Brown, and S. M. Howdle, "A facile synthetic route to aqueous dispersions of silver nanoparticles," *Materials Letters*, vol. 61, no. 27, pp. 4906–4910, 2007.

- [30] A. J. Kora, R. Manjusha, and J. Arunachalam, "Superior bactericidal activity of SDS capped silver nanoparticles: synthesis and characterization," *Materials Science and Engineering C*, vol. 29, no. 7, pp. 2104–2109, 2009.
- [31] S. Inphonlek, N. Pimpha, and P. Sunintaboon, "Synthesis of poly(methyl methacrylate) core/chitosan-mixed-polyethylene-imine shell nanoparticles and their antibacterial property," *Colloids and Surfaces B*, vol. 77, no. 2, pp. 219–226, 2010.
- [32] S. S. Birla, V. V. Tiwari, A. K. Gade, A. P. Ingle, A. P. Yadav, and M. K. Rai, "Fabrication of silver nanoparticles by *Phoma glomerata* and its combined effect against *Escherichia coli*, *Pseudomonas aeruginosa* and *Staphylococcus aureus*," *Letters in Applied Microbiology*, vol. 48, no. 2, pp. 173–179, 2009.
- [33] S. P. Dhas, A. Mukherjee, and N. Chandrasekaran, "Synergistic effect of biogenic silver nanocolloid in combination with antibiotics: a potent therapeutic agent," *International Journal of Pharmacy and Pharmaceutical Sciences*, vol. 5, no. 1, pp. 292–295, 2013.
- [34] A. Banu, V. Rathod, and E. Ranganath, "Silver nanoparticle production by *Rhizopus stolonifer* and its antibacterial activity against extended spectrum β -lactamase producing (ESBL) strains of Enterobacteriaceae," *Materials Research Bulletin*, vol. 46, no. 9, pp. 1417–1423, 2011.
- [35] A. M. El Badawy, T. P. Luxton, R. G. Silva, K. G. Scheckel, M. T. Suidan, and T. M. Tolaymat, "Impact of environmental conditions (pH, ionic strength, and electrolyte type) on the surface charge and aggregation of silver nanoparticles suspensions," *Environmental Science and Technology*, vol. 44, no. 4, pp. 1260–1266, 2010.
- [36] A. Hitchman, G. H. Sambrook Smith, Y. Ju-Nam, M. Sterling, and J. R. Lead, "The effect of environmentally relevant conditions on PVP stabilised gold nanoparticles," *Chemosphere*, vol. 90, no. 2, pp. 410–416, 2013.
- [37] R. K. Gangwar, V. A. Dhumale, D. Kumari et al., "Conjugation of curcumin with PVP capped gold nanoparticles for improving bioavailability," *Materials Science and Engineering: C*, vol. 32, no. 8, pp. 2659–2663, 2012.

DNA-Platinum Thin Films for Use in Chemoradiation Therapy Studies

Mohammad Rezaee, Elahe Alizadeh, Darel Hunting, and Léon Sanche

Groupe en Sciences des Radiations, Département de Médecine Nucléaire et Radiobiologie, Faculté de Médecine et des Sciences de la Santé, Université de Sherbrooke, Sherbrooke, QC, Canada J1H5N4

Correspondence should be addressed to Mohammad Rezaee, mohammad.rezaee@usherbrooke.ca

Academic Editor: Goran N. Kaluderovic

Dry films of platinum chemotherapeutic drugs covalently bound to plasmid DNA (Pt-DNA) represent a useful experimental model to investigate direct effects of radiation on DNA in close proximity to platinum chemotherapeutic agents, a situation of considerable relevance to understand the mechanisms underlying concomitant chemoradiation therapy. In the present paper we determine the optimum conditions for preparation of Pt-DNA films for use in irradiation experiments. Incubation conditions for DNA platination reactions have a substantial effect on the structure of Pt-DNA in the films. The quantity of Pt bound to DNA as a function of incubation time and temperature is measured by inductively coupled plasma mass spectroscopy. Our experiments indicate that chemical instability and damage to DNA in Pt-DNA samples increase when DNA platination occurs at 37°C for 24 hours, the condition which has been extensively used for *in vitro* studies. Platination of DNA for the formation of Pt-DNA films is optimal at room temperature for reaction times less than 2 hours. By increasing the concentration of Pt compounds relative to DNA and thus accelerating the rate of their mutual binding, it is possible to prepare Pt-DNA samples containing known concentrations of Pt while reducing DNA degradation caused by more lengthy procedures.

1. Introduction

Clinical studies have shown that concomitant treatment with chemotherapeutic drugs and radiotherapy often leads to a higher rate of survival and local tumor control compared to nonsynchronous treatments [1, 2]. Platinum chemotherapeutic drugs are commonly used in concurrent chemoradiation therapy (CRT) for treatment of solid tumors [3]. Although it is clear that platinum drugs and radiation in CRT modalities increase tumor cell killing, improve locoregional control of tumors, and enhance patient survival [4, 5], the optimum schedule of the combination and the underlying mechanisms of their synergistic action have not been yet defined [6, 7]. Since DNA is the common target of both radiation and platinum chemotherapeutic agents, most studies have focused on the structural and functional alteration of DNA resulting from the combination [8, 9]. One possible mechanism responsible for the observed synergy is enhancement in immediate (secondary) species

induced by primary radiation in the vicinity of the binding site of the platinum compounds (Pt compounds) to DNA [10, 11]. The most abundant of these secondary species are electrons with the most probable energy of 9–10 eV [12]. Studies on the interaction of secondary low energy electrons (LEEs) with DNA have elucidated some of the fundamental mechanisms leading to DNA damage [13]. However, owing to the short range (~10 nm) of LEE in biological matters, such studies must be performed on very thin DNA films of similar thickness. Pt-DNA thin films could provide an experimental approach to investigate the direct effects of the secondary electrons and other short-range particles (or secondary species) on DNA in the presence of Pt compounds. Such investigations could disclose mechanisms underlying the synergistic effect between the radiation and the drug, which may have implications for the optimization of protocols in CRT as well as in the design and development of new chemotherapeutic and radiosensitizing drugs [14].

Dry thin films of bacterial plasmid DNA in supercoiled conformation are widely used in low-energy irradiations with LEEs [15, 16], photons [17], and ions [18]. They provide a simple system to evaluate the direct interaction of short-range radiations with DNA, despite the complexity of the molecule. Although purified prokaryotic DNA differs from eukaryotic DNA in terms of supercoiling and the presence of N6-methyladenine [19, 20], supercoiled plasmid DNA offers the advantage of very high sensitivity for the detection of single- and double-strand breaks. One of the main concerns with plasmid DNA films is maintenance of the DNA integrity during film preparation [21]. When the irradiation target is supercoiled DNA, the proportion of the supercoiled configuration is often used as a measure of DNA integrity. The DNA molecule is very sensitive to conditions such as temperature, humidity, and pH, hence, the DNA films must be prepared under well-controlled conditions to minimize damage. The concentration of ions in the solution of DNA has also a considerable influence in maintaining the DNA during film preparation [21, 22]. Furthermore, the type of substrate on which DNA is deposited affects the integrity of the molecule. Among the various substrates tested including tantalum (Ta), gold and graphite, Ta induces the least damage to DNA [23].

Pt compounds such as cisplatin and carboplatin bind to the N7 atom of purine bases and produce the Pt-DNA adducts including mainly intrastrand cross-links, interstrand cross-links, and monofunctional binding to guanine [24]. The adducts distort the DNA conformation and reduce the structural stability of DNA [24, 25]. Moreover, DNA must tolerate the incubation conditions required to react with Pt compounds. In most *in vitro* studies, a DNA solution is mixed with a solution of the Pt compounds at 37°C for 24 or 48 hours [26–30]. These conditions affect the integrity of the DNA as a result of depurination and oxidation processes [31]. To maximize the amount of the Pt compounds bound to DNA while keeping the DNA intact, all parameters involved in the preparation of the films must be known and carefully controlled. In particular, experimental conditions for the reaction of Pt compounds with DNA must be determined as well as the effect of chemical binding of Pt compounds on the stability of DNA.

In the present study, we investigate the parameters of the Pt compounds and platination reactions on DNA integrity in the preparation of cisplatin/DNA and carboplatin/DNA films. Optimum experimental conditions are determined to retain a high proportion of the supercoiled form of plasmid DNA in Pt-DNA films.

2. Experimental Section

2.1. Preparation of Plasmid DNA. Plasmid DNA (pGEM-3Zf(-), 3197 base pairs, ca. 1968966 amu per plasmid) was extracted from *Escherichia coli* JM109 and purified with a HiSpeed plasmid Maxi kit (QIAGEN) [32]. The purified plasmid DNA consisted of 96% supercoiled, 2% catenameric, and 2% nicked circular forms. The concentration of DNA and the relative quantity of proteins in the plasmid

DNA solution was then calculated by measuring the ratio of ultraviolet (UV) absorption of DNA and protein at 260 nm and 280 nm, respectively, with a Synergy HT-I spectrophotometer. The ratio was 1.98 which corresponds to a purity greater than 85% [33]. The TE buffer (Tris-EDTA: 10 mM–1 mM) was separated from DNA by gel filtration with a Sephadex G-50 medium [34]. Thus the final solution consisted of DNA and ddH₂O after the filtration. To evaluate the effect of Tris on the binding of Pt compounds to DNA, two different groups of the DNA solutions were prepared. In the first group, Tris buffer was added to the DNA solution at the ratio of the one tris molecule per nucleotide, and in the second group, the DNA solution was prepared with ddH₂O alone. The DNA concentration was the same in both groups. In each group, control samples were kept in the temperature of -20°C and quantified for the analysis of temperature effect on DNA.

2.2. Platination of Plasmid DNA. The Pt compounds, cisplatin [*cis*-diamminedichloroplatinum(II)] and carboplatin [*cis*-diammine(1,1-cyclobutanedicarboxylato)platinum(II)], were purchased from Sigma-Aldrich with a stated purity of 99.9% and ≥98%, respectively, and used without further purification. Their solutions were prepared in ddH₂O in different concentrations based on their molar solubility. Reactions of cisplatin and carboplatin with the DNA solutions were performed under diverse experimental conditions. These consisted of (1) two different incubation temperatures, that is, 37°C and 25°C, (2) incubation times varying from 40 minutes to 24 hours, and (3) molar ratios between Pt compounds and DNA varying from ratios 2 : 1 up to 200 : 1. DNA platination reactions were performed in the dark to inhibit photoaquation processes as aqueous solutions of cisplatin and carboplatin are degraded via illumination, especially at wavelengths below 500 nm [35, 36]. To terminate the reactions after a given incubation time, the solutions were passed through a gel filtration medium packed into a column. By the filtration, the unbound Pt compounds, tris molecules, and complexes of tris with Pt compounds were separated from the Pt-DNA solutions. The solutions passed through the homemade column packed with Sephadex-G50 gel on a glass bead bed. Sephadex G-50 is a suitable medium for separation of the molecules having a molecular weight larger than 3×10^4 g mol⁻¹ from molecules with a molecular weight smaller than 1500 g mol⁻¹. Such filtration is expected to produce clean solutions of Pt-DNA in ddH₂O because the molecular weights of most undesired compounds and complexes found in the solutions during platination have the molecular weight smaller than 1500 g mol⁻¹.

2.3. Analysis of Platinum-DNA Binding. The concentration of platinum in the solutions was measured by Elan DRC II inductively coupled plasma mass spectroscopy (ICPMS, from Perkin Elmer) which has been used as a suitable method for measurement of platinum in many biomedical applications [37, 38]. Additionally, three control samples consisting of the Pt compounds dissolved in ddH₂O at known concentrations were also prepared to calibrate the ICPMS

measurements of Pt-DNA samples. The DNA concentration was measured by spectrophotometry. It was determined from the optical density of DNA in solution measured by UV absorption at a wavelength of 260 nm. The concentration of DNA was calculated from the reference optical density.

2.4. Preparation of Substrate, DNA, and Pt-DNA Films. The DNA and Pt-DNA samples were deposited on a Ta substrate. As shown in previous studies, the stability of supercoiled plasmid DNA on Ta substrate is acceptable for vacuum experiments on LEE-induced damage [23, 39]. The Ta substrates in the current work consist of a thin film of Ta of thickness 450 ± 50 nm evaporated onto a 0.4 mm thick silicon wafer. The surface of Ta was cleaned in pure ethanol and ddH₂O and dried with a flow of dry nitrogen. Before deposition of DNA and Pt-DNA samples onto the substrate, the TE buffer was added to the DNA and Pt-DNA solutions in the ratio of 3 : 1 (three organic ions per nucleotide). It has been shown that this ratio protects the supercoiled form of DNA during the process of DNA film preparation [22]. The volumes of 7 μ L of the latter solutions of DNA and Pt-DNA consisting of 250 ng of each complex (DNA and TE molecules as well as Pt-DNA and TE molecules) were deposited onto the cleaned Ta surface. These quantities were calculated to allow formation of a five-monolayer film (about 10 nm thickness) on the Ta substrate. Such a thickness has been widely used in DNA-LEE experiments because it is smaller than the effective range of these electrons (12–14 nm) for damaging DNA [40]. After freezing at -65°C for 10 minutes in a glove box, the samples were lyophilized (freeze-dried) under a pressure of 7 mTorr by a hydrocarbon-free turbomolecular pump for 2 hours.

2.5. Quantification of the DNA and Pt-DNA Films. The DNA and Pt-DNA films were recovered from the Ta substrates with 10 μ L of TE buffer. Comparison of the amount of recovered DNA with the original DNA solution used for deposition showed that approximately 98% of DNA was recovered by the TE buffer. Quantification of the different structural forms (e.g., supercoiled, nicked circular, linear, etc.) in the DNA and Pt-DNA samples was performed by agarose gel electrophoresis. The DNA samples and the agarose gels were stained with SYBR Green I in the concentration of 100x and 10000x, respectively. The samples were run on 1% agarose gel in 1x TAE buffer at 100 volts for 7 minutes following by 75 volts for 68 minutes (5 V cm^{-1}). The gels were then scanned by Typhoon-Trio laser scanner (from GE Healthcare) adjusted for the blue fluorescent mode at an excitation wavelength of 488 nm and filter type 520 nm-bandpass (520 BP 40) in the normal sensitivity mode. Various forms of the DNA such as supercoiled, nicked circular, etc. were analyzed by ImageQuant 5.0 (Molecular Dynamics) software. To accurately quantify, the binding efficiencies of SYBR Green I for the same amount (75 ng) of supercoiled and linear DNA were measured, and then the correction factor was determined. This factor arises from the weaker binding of SYBR Green I to supercoiled DNA than to the

nicked circular and linear forms. A correction factor of 1.2 was obtained and applied to the quantification of plasmid DNA.

2.6. Statistical Analysis. OriginPro 8.1 SR1 (OriginLab Corporation) software was used for statistical and mathematical analysis. Paired *t*-test was the statistical test in which a probability of 0.05 (5%) has been considered significant.

3. Results and Discussion

3.1. Effects of Incubation Temperature on DNA and Pt-DNA Samples. Figure 1 (panels a and b) shows a comparison of the percentage of supercoiled and nicked circular forms of the DNA in the samples that had been incubated for 24 hours at three different temperatures: -20°C , 25°C , and 37°C . For each incubation temperature, DNA analysis was performed for two types of samples: (i) “DNA solutions”, that is, samples obtained directly from the incubated solutions, and (ii) “DNA films”, that is, samples that had, after incubation, been deposited and recovered from a Ta substrate. TE buffer was added to the samples at a concentration corresponding to three organic ions per nucleotide. Increasing the incubation temperature resulted in a reduction of the supercoiled form of DNA in both the solution and the film samples. The decrease is relatively small for the DNA solution samples; the samples incubated at 25°C and 37°C show a decrease of 3.8% and 9.5%, respectively, relative to that seen in the sample maintained at -20°C . At each temperature, the DNA samples recovered from Ta show a greater loss of supercoiled DNA than do the samples analyzed directly from solution. A fraction of the supercoiled loss in the film samples is related to the damages which were induced during the incubation in solution. Consequently, for DNA recovered from Ta, a decrease in the supercoiled form with increasing temperature is also observed, and the decrease is very large for the samples incubated at 37°C . The decreases in the supercoiled form are not statistically significant among the DNA solution samples with different incubation temperatures (*P* value: 0.314, 0.106). However, the difference is statistically significant between the DNA film samples incubated at 37°C and the DNA films from samples incubated at 25°C and -20°C (*P* value: 0.012 and 0.009). Additionally, there is no significant difference between the DNA films incubated at 25°C and -20°C (*P* value: 0.136).

As expected, there are enhancements in the formation of the nicked circular form with increasing incubation temperature. The increase is small except for the DNA film samples which were incubated at 37°C . In these samples the nicked circular form increases by factors of 3.7 and 3.4 compared to those kept at -20°C and 25°C , respectively. These differences are statistically significant (*P* value: 0.02 and 0.011). The high proportion of the nicked circular form in the DNA recovered from films introduces considerable inaccuracy in the evaluation of radiation-induced DNA damage.

In vitro studies have shown that heat can induce various types of DNA damage such as depurination and guanine

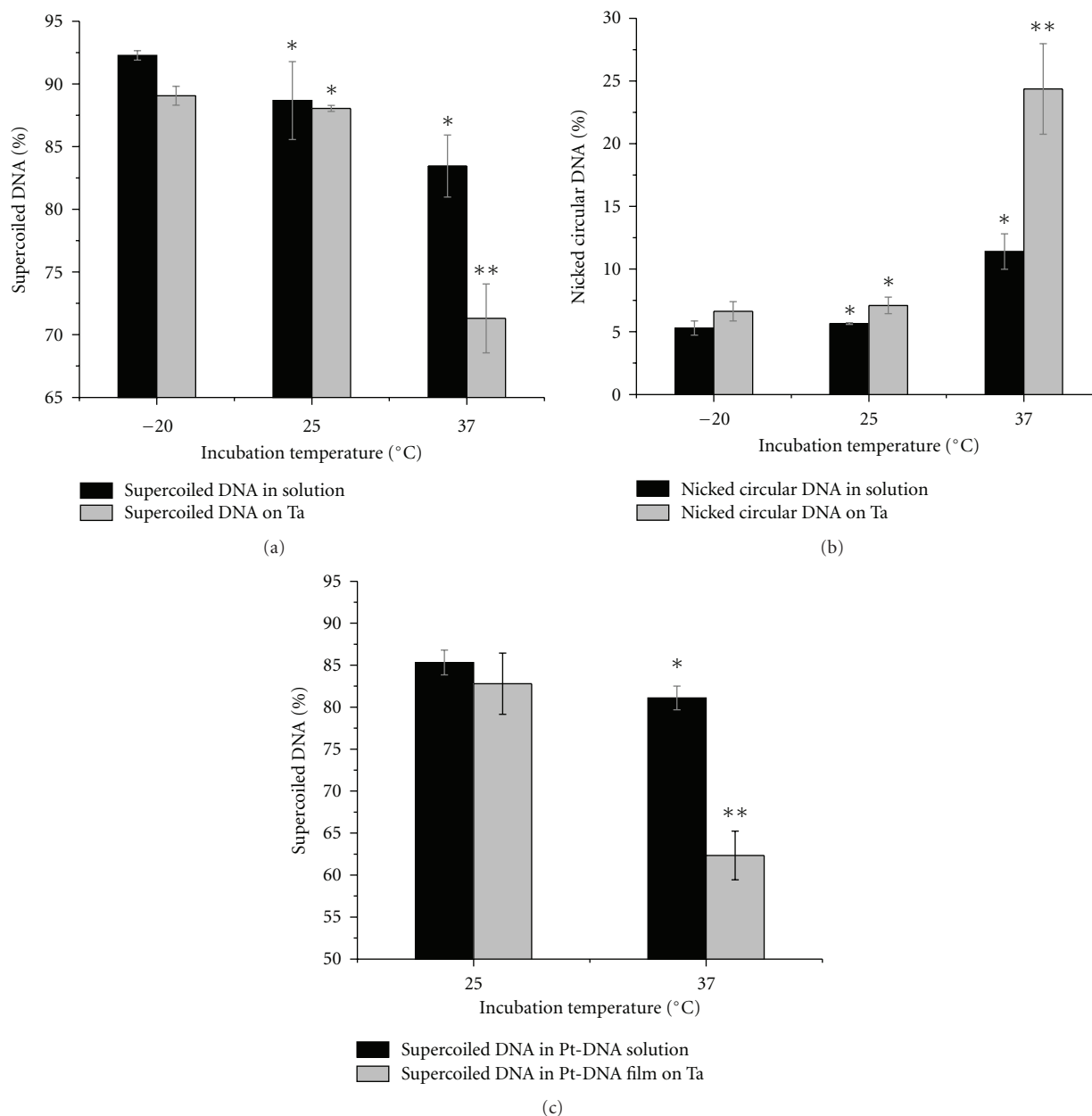


FIGURE 1: Comparison of the percentages of DNA supercoiled (a), DNA nicked circular (b), and Pt-DNA supercoiled (c) forms in the solution and film samples after incubation at -20°C, 25°C, and 37°C for 24 hours. Data in (a)–(c) are means from three independent experiments; three samples at each temperature are analyzed in each experiment; error bars show standard deviations. *indicates $P > 0.05$, **indicates $P < 0.05$.

oxidation mediated by reactive oxygen species (ROS) [31, 41]. Reaction rate constants for formation of 8-oxoguanine and guanine depurination at 37°C are $4.7 \times 10^{-10} \text{ s}^{-1}$ and $1.3 \times 10^{-9} \text{ s}^{-1}$ in DNA solutions, respectively [41]. In our experiment, each plasmid sample contained 0.065 pmole of DNA bases in a volume of 7 μL . After a 24-hour incubation of the plasmid DNA at 37°C, we can estimate that approximately 7% and 18% of the plasmid contain 8-oxoguanine molecules or have undergone guanine depurination, respectively. Such DNA molecules are more susceptible to strand breakage than the original DNA. Furthermore, evacuation

and lyophilisation during film preparation induce physical stress and can damage DNA [21]. Therefore, the DNA molecules, which have been kept at 37°C for 24 hours or more, do not have sufficient structural stability to tolerate the process of film preparation. Our results suggest that the samples incubated at 37°C are more sensitive and vulnerable to the film preparation and recovery processes than DNA samples incubated at 25°C and -20°C.

Figure 1(c) shows the comparison of the percentage concentration of supercoiled forms in samples of cisplatin-DNA complexes incubated at 25°C and 37°C for 24 hours.

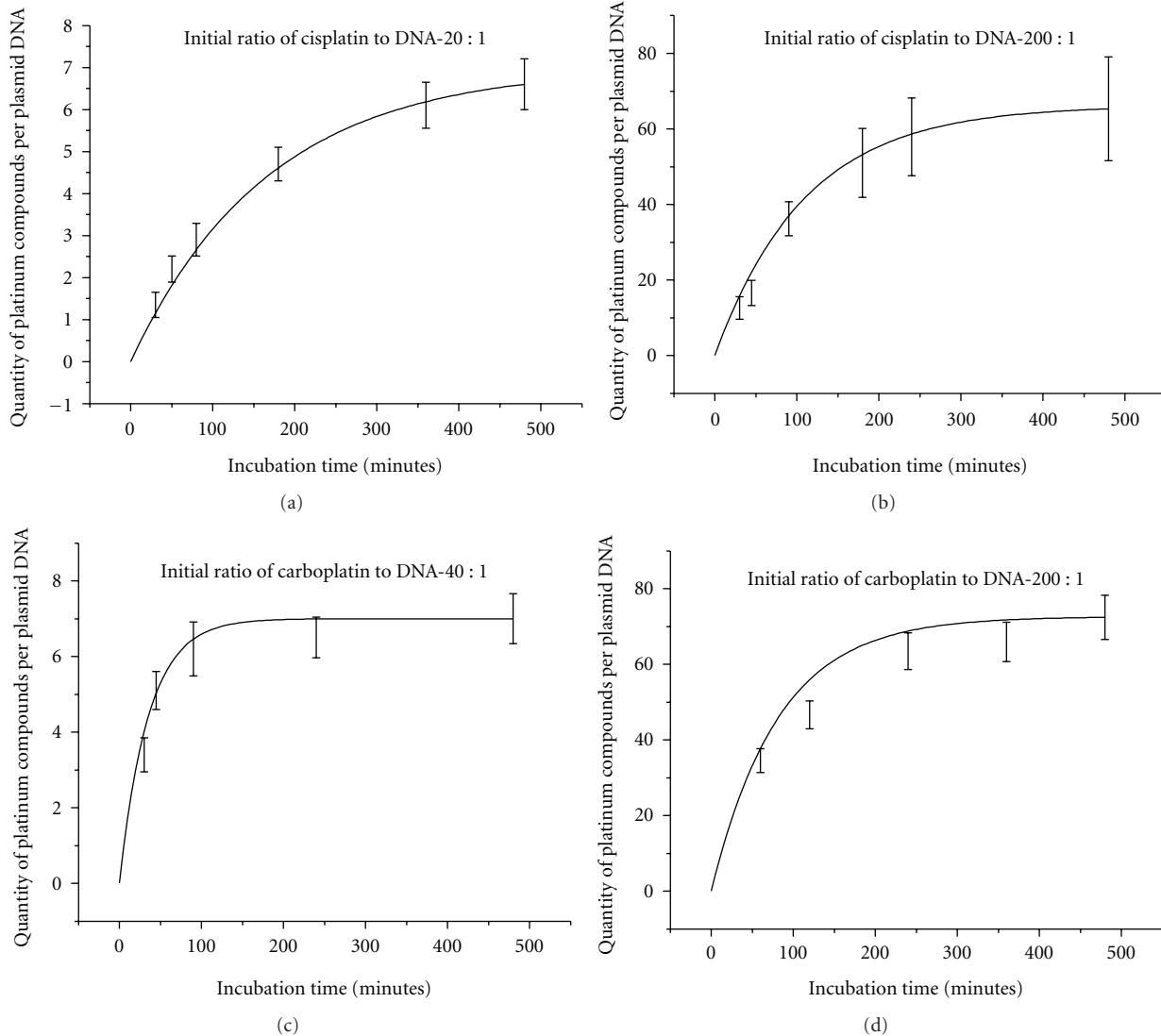


FIGURE 2: Kinetics of binding of Pt compounds to plasmid DNA. The Pt compounds are: (a) cisplatin with the initial ratios in the solution of 20 : 1, (b) 200 : 1, and (c) carboplatin with the initial ratios of 40 : 1 and (d) 200 : 1. The curves show the quantity of bound Pt compounds per DNA molecule at different incubation times at 25°C. Data in (a)–(d) are means from three measurements; error bars show standard deviations. The continuous black lines are exponential fits to the data.

Again, the analyses were performed for two groups of samples: (i) Pt-DNA solutions and (ii) Pt-DNA films on a Ta substrate. In the solution and film samples, the proportion of the supercoiled form of Pt-DNA is less than those for DNA alone. The molar ratio of cisplatin to DNA in the solutions was 2 : 1. TE buffer was added to the samples in the concentration of three organic ions per nucleotide. Predictably, in both samples the supercoiled form of DNA decreased when the incubation temperature increased. The decrease is small (4.2%) in the samples of Pt-DNA solution. In contrast, there is a large decrease in the supercoiled form of the Pt-DNA film samples (20.5%). Statistical analysis also showed that the decrease is significantly different for the Pt-DNA films with different incubation temperatures (P value: 0.0049). According to our results, the incubation

temperature during preparation of the Pt-DNA solution is a substantial factor in determining the composition of Pt-DNA films on Ta substrate for use in irradiation experiments. Moreover, the results suggest that a film composed of cisplatin-DNA complexes with a high proportion of intact DNA molecules (supercoiled form) on a Ta substrate can be obtained when DNA platination occurs at 25°C.

3.2. Kinetics of Binding Pt Compounds to DNA. Following platination at 25°C, DNA has much less damage during the process of deposition and recovery from the Ta substrate. However, the DNA platination reaction proceeds with a slower rate. Increasing the concentration of the Pt compounds can compensate for this lower rate. Figure 2 shows

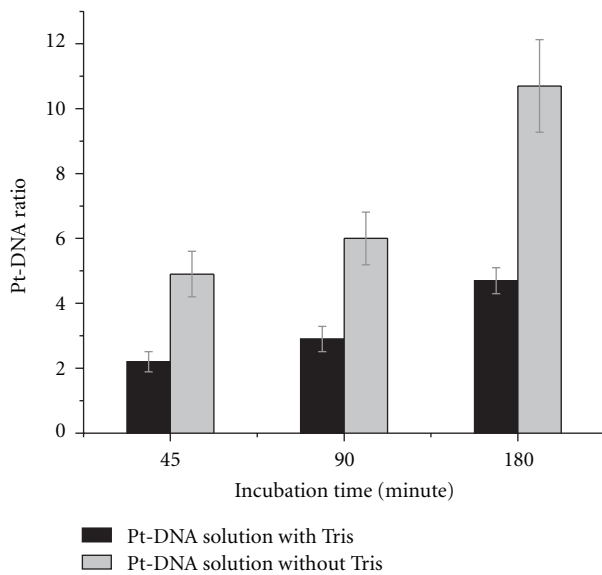


FIGURE 3: Impact of tris on the reaction of DNA platination. Pt-DNA ratios in the cisplatin-DNA solutions incubated during 45, 90, and 180 minutes at 25°C are compared in the presence and absence of tris. Data are means from three measurements; error bars show standard deviations.

the ratios of bound Pt-compound to DNA for different incubation times at 25°C when the initial concentration ratios of Pt compounds to DNA in solution are 200 : 1, 40 : 1, and 20 : 1. The solution consists of plasmid DNA, cisplatin or carboplatin, and tris with the ratio of 1 : 1 nucleotide. This amount of tris was considered as the minimum amount of buffer which can preserve the stability of DNA during the preparation process. It is clearly seen that the binding kinetics of cisplatin and carboplatin to DNA are similar and exhibit exponential behavior. These curves generally reach saturation prior to 8 hours and show a linear behaviour prior to 2 hours. For the initial concentration ratio of 200 cisplatin molecules per DNA, it is possible to have Pt-DNA samples with the ratios of bound cisplatin to DNA from 16 : 1 to 37 : 1 in 40-minute to 120-minute incubation times, respectively. For the same incubation times, the ratios are 2 : 1 and 3 : 1 when the initial ratio of cisplatin to DNA decreases an order of magnitude (20 : 1). The results demonstrate that various ratios of bound cisplatin or carboplatin to DNA can be obtained in the incubation times of less than 2 hours by increasing the initial concentration of the Pt compounds. Since the kinetics curves obey a linear fit for these incubation times, it is possible to simply extrapolate a variety of Pt-DNA ratios from this part of the curves.

Since Pt compounds can react with most buffers [42], their concentration is also a relevant parameter in the DNA platination process (i.e., buffers compete with DNA for binding Pt compounds). Tris is widely used as a buffer, especially for solutions of nucleic acids. It also reacts with Pt compounds to produce *cis*-[Pt(NH₃)₂(N-Tris)(OH)]⁺ and *cis*-[Pt(NH₃)₂(N,O-TrisH₋₁)]⁺ [43]. The bar graphs in Figure 3 show a comparison of bound Pt compounds to

DNA ratios for three different incubation times at 25°C for two different solutions: (i) a mixture of DNA, cisplatin, and ddH₂O, and (ii) a mixture of DNA, cisplatin, ddH₂O, and tris with the concentration ratio of 1 : 1 nucleotide. The initial concentration ratio of cisplatin to the DNA was 20 : 1 in the solutions. The results demonstrate that the ratio of bound cisplatin to the DNA is more than double when the platination reaction occurs in a ddH₂O solution without tris molecules.

3.3. Effects of Incubation Time on DNA and Pt-DNA Films.

The bar graphs in Figure 4 show a comparison of the percentage of supercoiled DNA and Pt-DNA samples that were incubated at 25°C for 2, 4, and 8 hours. The analyses were performed for samples that had been recovered (i) from solution, immediately after incubation (Figure 4(a)), and (ii) from films deposited on Ta (Figure 4(b)). The Pt-DNA samples were prepared with either cisplatin or carboplatin. The initial concentration ratio of the Pt compounds to DNA was 200 : 1 and that of the TE buffer was three organic ions per nucleotide. As seen from Figure 4, more than 90 percent of the DNA, in samples incubated for 2 hours, is in the supercoiled form. The proportion of supercoiled form decreases when the samples are incubated for 4 hours or more. The decrease is statistically significant in all samples except for the pure DNA solution sample. As might be expected, the decrease is greater in Pt-DNA films than in DNA samples. Thus, it is possible to prepare Pt-DNA films with a high proportion of supercoiled DNA at various ratios of bound Pt to DNA, by mixing DNA with high concentrations of Pt-compound solution and restricting the length of the incubation to less than 2 hours, as long as the incubation temperature does not exceed 25°C.

3.4. Effects of Bound Pt to DNA on Pt-DNA Samples Analysis.

The distortion of the DNA structure resulting from the formation of Pt-DNA cross-links must be considered in quantification methods such as electrophoresis. Figure 5(a) shows the migration of different forms of cisplatin-DNA in the electrophoresis gel. The mobility of the nicked circular, concatemeric, and supercoiled bands is changed with increasing numbers of bound Pt molecules per nucleotide (R_b). The change is due to distortion of the different forms of DNA by cisplatin since Pt-DNA crosslinks are known to cause conformational changes in DNA including shortening (bending) and unwinding [44, 45]. The distortion becomes greater as a function of the quantity of bound Pt molecules. Figure 5 shows the dependence of the mobility of the supercoiled, nicked circular, and concatemeric forms of cisplatin-DNA samples as a function of the ratio R_b in a 1% agarose gel. The mobility of each form of Pt-DNA is normalized to the same form of an unmodified DNA sample (Figure 5(b)). As seen from Figure 5(b), the migration of the nicked circular and supercoiled configurations generally increases with rising R_b . However, the mobility of the nicked circular form increases with a faster rate than that of the supercoiled

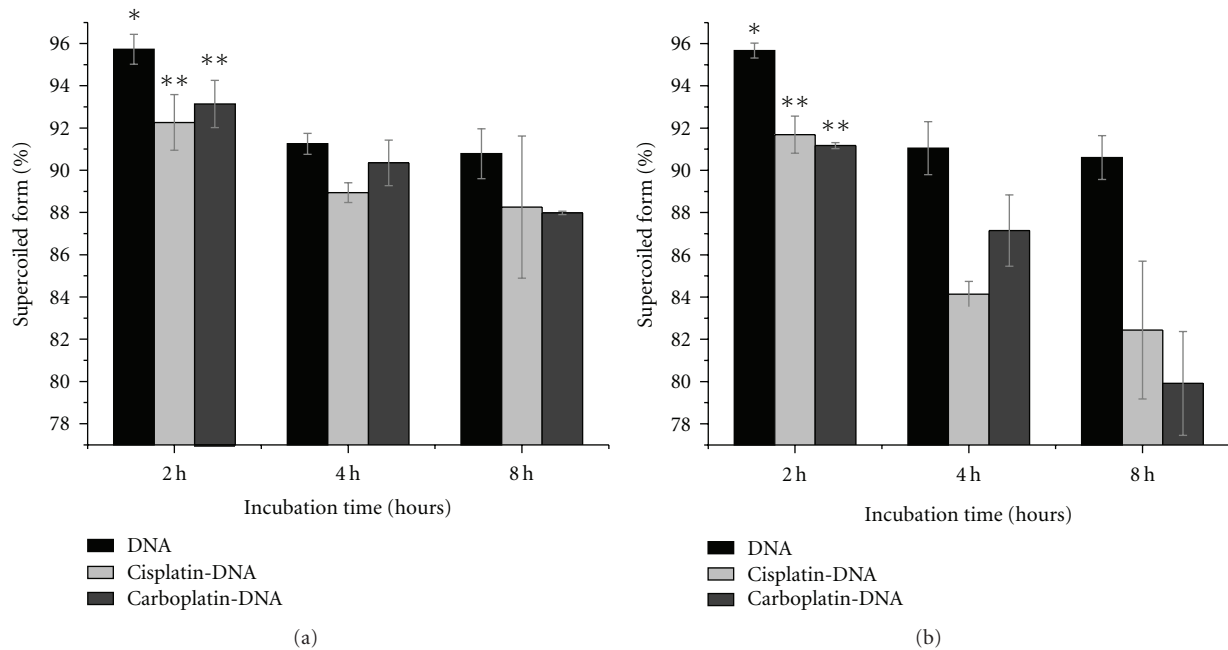


FIGURE 4: Comparison of the percentages of supercoiled forms in the samples of DNA, cisplatin-DNA, and carboplatin-DNA (a) in solution, and (b) on Ta substrate, after incubation for 2, 4, and 8 hours at 25°C. Data are means from three measurements; error bars show standard deviations.*indicates $P > 0.05$, **indicates $P < 0.05$.

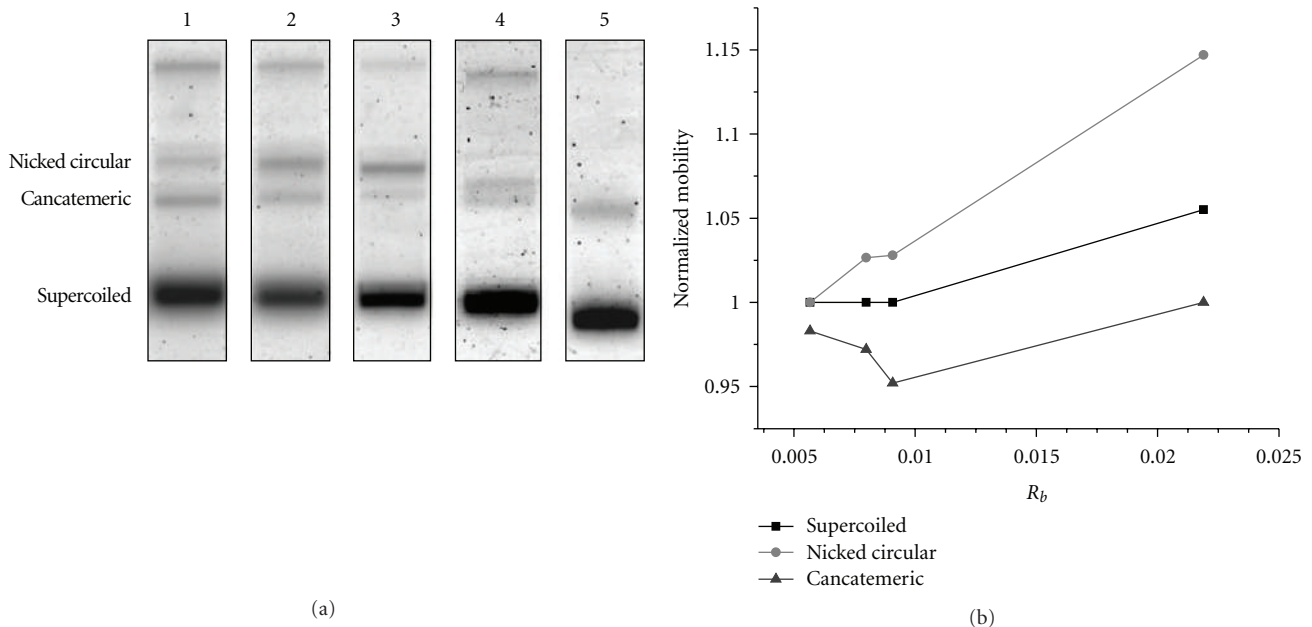


FIGURE 5: Mobility of cisplatin-DNA molecules in agarose gel. (a) Migration of the different configurations of cisplatin-DNA molecules separated by electrophoresis. Lane 1 is for a DNA sample and lanes 2–5 are for cisplatin-DNA samples with the number of bound cisplatin molecules per nucleotide, R_b , of 0.0057, 0.008, 0.0091, and 0.0219, respectively. (b) Normalized mobility of the nicked circular, supercoiled, and cconcatemeric forms of Pt-DNA samples at different R_b in gel electrophoresis.

form. Mobility of the cconcatemeric configuration decreases with rising in R_b up to 0.009 and then increases for higher R_b .

Since the number of Pt molecules per plasmid probably represents a Poisson distribution for each Pt-DNA ratio, this

would be expected to reduce the resolution of the agarose gels by increasing the dispersion within each band (i.e., the band width). The linear plasmid band lies between the nicked circular and cconcatemeric bands; thus an increase in band width could hinder precise quantification of the linear

band which usually is weaker than the others. Furthermore, the nicked circular and concatemeric bands merge owing to increased band width and form one band at $R_b = 0.022$. Our results show that the mobility changes are substantial for R_b greater than 0.005.

4. Conclusion

Thin films of platinum-DNA adducts can be considered as useful models in irradiation experiments to study the molecular mechanisms of radiosensitization which underlie concomitant chemoradiation therapy. We have investigated the optimum experimental conditions to prepare dry thin films of Pt compounds bound to plasmid DNA on a Ta substrate. Incubation conditions in DNA platination reactions have substantial effects on the stability of Pt-DNA, particularly in the thin film samples preparation. In most in vitro experiments, reaction of Pt compounds with DNA solutions has been performed at 37°C for incubation times varying from 24 to 48 hours. However, our results show that these conditions can induce damage to the DNA and highly sensitize them to manipulations required to form thin films and recover DNA from the Ta substrate. The concentration of intact DNA increases significantly in the film samples when the incubation temperature during reaction with the Pt is reduced to 25°C and the time of incubation is 2 hours. By increasing the concentration of the Pt compounds, it is possible to compensate for the reduced reaction rate at lower temperature. High levels of plasmid platination however affect the quantification of Pt-DNA samples in agarose gel electrophoresis, because Pt-DNA adducts distort the conformation of DNA molecules. Therefore, the optimum condition is obtained from an equilibrium between temperature, time, and Pt compounds concentration during the DNA platination reaction.

By recording the kinetics of binding Pt compounds to DNA, it is possible to extrapolate different Pt-DNA ratios from the kinetics curves. We have found that the proportion of supercoiled DNA is more than 90% in the Pt-DNA film when the DNA platination reaction is performed at 25°C for less than 2 hours in solutions containing the Pt compound with quantities of less than 3×10^{-2} Pt molecules per nucleotide and the minimum concentration of Tris buffer (one tris molecule per nucleotide). Under these conditions, agarose gel electrophoresis is an accurate method for quantification of DNA damage. We have also determined that the maximum number of bound Pt-compound per nucleotide is about 5×10^{-3} under our optimum conditions. This ratio is an order of magnitude higher than those found in biological studies and clinical applications [46]. These high ratios, however, are useful for in vitro mechanistic studies in which substantial quantities of product are required. Hence, we have found that by adjusting the initial concentration of Pt compounds in solution, Pt-DNA films having a known controlled ratio of platinum chemotherapeutic agents to DNA can be obtained while maintaining DNA integrity.

Acknowledgments

Financial support for this work was provided by the Canadian Institute of Health Research (CIHR) and the Marie Curie international incoming fellowship program. The authors wish to thank Dr. Andrew D. Bass, Mr. Pierre Cloutier, and Ms. Sonia Girouard for their helpful comments and suggestions.

References

- [1] H. Choy, *Chemoradiation in Cancer Therapy*, Humana Press, Totowa, NJ, USA, 2003.
- [2] V. T. DeVita Jr., S. Hellman, and S. A. Resenber, *Cancer: Principle and Practice of Oncology*, Lippincott Williams and Wilkins, New York, NY, USA, 2001.
- [3] T. Y. Seiwert, J. K. Salama, and E. E. Vokes, "The concurrent chemoradiation paradigm—general principles," *Nature Clinical Practice Oncology*, vol. 4, no. 2, pp. 86–100, 2007.
- [4] C. Schaake-Koning, W. Van den Bogaert, O. Dalesio et al., "Effects of concomitant cisplatin and radiotherapy on inoperable non-small-cell lung cancer," *The New England Journal of Medicine*, vol. 326, no. 8, pp. 524–530, 1992.
- [5] G. S. Montana, G. M. Thomas, D. H. Moore et al., "Preoperative chemo-radiation for carcinoma of the vulva with N2/N3 nodes: a gynecologic oncology group study," *International Journal of Radiation Oncology Biology Physics*, vol. 48, no. 4, pp. 1007–1013, 2000.
- [6] J. K. Salama, T. Y. Siewert, and E. E. Vokes, "Chemoradiotherapy for locally advanced head and neck cancer," *Journal of Clinical Oncology*, vol. 25, pp. 4118–4126, 2007.
- [7] C. C. E. Koning, J. S. A. Belderbos, and A. L. J. Uitterhoeve, "From cisplatin-containing sequential radiochemotherapy towards concurrent treatment for patients with inoperable locoregional non-small cell lung cancer: still unanswered questions," *Cancer Therapy Research and Practice*, vol. 2010, Article ID 506047, 5 pages, 2010.
- [8] J. W. J. Bergs, N. A. P. Franken, R. Ten Cate, C. Van Bree, and J. Haveman, "Effects of cisplatin and γ -irradiation on cell survival, the induction of chromosomal aberrations and apoptosis in SW-1573 cells," *Mutation Research*, vol. 594, no. 1–2, pp. 148–154, 2006.
- [9] G. P. Raaphorst, J. M. Leblanc, and L. F. Li, "A comparison of response to cisplatin, radiation and combined treatment for cells deficient in recombination repair pathways," *Anticancer Research*, vol. 25, no. 1, pp. 53–58, 2005.
- [10] G. D. Wilson, S. M. Bentzen, and P. M. Harari, "Biologic basis for combining drugs with radiation," *Seminars in Radiation Oncology*, vol. 16, no. 1, pp. 2–9, 2006.
- [11] L. Dewit, "Combined treatment of radiation and cisdiamminedichloroplatinum (II): a review of experimental and clinical data," *International Journal of Radiation Oncology Biology Physics*, vol. 13, no. 3, pp. 403–426, 1987.
- [12] S. M. Pimblott and J. A. LaVerne, "Production of low-energy electrons by ionizing radiation," *Radiation Physics and Chemistry*, vol. 76, no. 8–9, pp. 1244–1247, 2007.
- [13] L. Sanche, "Low-energy electron interaction with DNA: bond dissociation and formation of transient anions, radicals, and radical anions," in *Radical and Radical Ion Reactivity in Nucleic Acid Chemistry*, M. M. Greenberg, Ed., pp. 239–293, John Wiley & Sons, Hoboken, NJ, USA, 2009.
- [14] L. Sanche, "Role of secondary low energy electrons in radiobiology and chemoradiation therapy of cancer," *Chemical Physics Letters*, vol. 474, no. 1–3, pp. 1–6, 2009.

- [15] B. Boudaïffa, P. Cloutier, D. Hunting, M. A. Huels, and L. Sanche, "Resonant formation of DNA strand breaks by low-energy (3 to 20 eV) electrons," *Science*, vol. 287, no. 5458, pp. 1658–1660, 2000.
- [16] É. Brun, P. Cloutier, C. Sicard-Roselli, M. Fromm, and L. Sanche, "Damage induced to DNA by low-energy (0-30 eV) electrons under vacuum and atmospheric conditions," *Journal of Physical Chemistry B*, vol. 113, no. 29, pp. 10008–10013, 2009.
- [17] K. M. Prise, M. Folkard, B. D. Michael et al., "Critical energies for SSB and DSB induction in plasmid DNA by low-energy photons: action spectra for strand-break induction in plasmid DNA irradiated in vacuum," *International Journal of Radiation Biology*, vol. 76, no. 7, pp. 881–890, 2000.
- [18] C. A. Hunniford, R. W. McCullough, R. J. H. Davies, and D. J. Timson, "DNA damage by low-energy ions," *Biochemical Society Transactions*, vol. 37, no. 4, pp. 893–896, 2009.
- [19] G. N. Giaever, L. Snyder, and J. C. Wang, "DNA supercoiling in vivo," *Biophysical Chemistry*, vol. 29, no. 1-2, pp. 7–15, 1988.
- [20] D. M. Heithoff, R. L. Sinsheimer, D. A. Low, and M. J. Mahan, "An essential role for DNA adenine methylation in bacterial virulence," *Science*, vol. 284, no. 5416, pp. 967–970, 1999.
- [21] M. A. Smialek, R. Balog, N. C. Jones, D. Field, and N. J. Mason, "Preparation of DNA films for studies under vacuum conditions: the influence of cations in buffer solutions," *European Physical Journal D*, vol. 60, no. 1, pp. 31–36, 2010.
- [22] A. Dumont, Y. Zheng, D. Hunting, and L. Sanche, "Protection by organic ions against DNA damage induced by low energy electrons," *Journal of Chemical Physics*, vol. 132, no. 4, Article ID 045102, 2010.
- [23] L. Sanche, "Nanoscopic aspects of radiobiological damage: fragmentation induced by secondary low-energy electrons," *Mass Spectrometry Reviews*, vol. 21, no. 5, pp. 349–369, 2002.
- [24] E. R. Jamieson and S. J. Lippard, "Structure, recognition, and processing of cisplatin-DNA adducts," *Chemical Reviews*, vol. 99, no. 9, pp. 2467–2498, 1999.
- [25] S. J. Lippard, "Chemistry and molecular biology of platinum anticancer drugs," *Pure and Applied Chemistry*, vol. 59, no. 6, pp. 731–742, 1987.
- [26] C. P. Saris, P. J. M. Van de Vaart, R. C. Rietbroek, and F. A. Blommaert, "In vitro formation of DNA adducts by cisplatin, lobaplatin and oxaliplatin in calf thymus DNA in solution and in cultured human cells," *Carcinogenesis*, vol. 17, no. 12, pp. 2763–2769, 1996.
- [27] J. Malina, O. Vrana, and V. Brabec, "Mechanistic studies of the modulation of cleavage activity of topoisomerase I by DNA adducts of mono- and bi-functional PtII complexes," *Nucleic Acids Research*, vol. 37, no. 16, Article ID gkp580, pp. 5432–5442, 2009.
- [28] R. J. Knox, F. Friedlos, D. A. Lydall, and J. J. Roberts, "Mechanism of cytotoxicity of anticancer platinum drugs: evidence that cis-diamminedichloroplatinum(II) and cis-diammine-(1,1-cyclobutanedicarboxylato)platinum(II) differ only in the kinetics of their interaction with DNA," *Cancer Research*, vol. 46, no. 4, pp. 1972–1979, 1986.
- [29] G. B. Ono and V. Moreno, "Study of the modifications caused by cisplatin, transplatin, and Pd(II) and Pt(II) mepirizole derivatives on pBR322 DNA by atomic force microscopy," *International Journal of Pharmaceutics*, vol. 245, no. 1-2, pp. 55–65, 2002.
- [30] G. Natarajan, R. Malathi, and E. Holler, "Increased DNA-binding activity of cis-1,1-cyclobutanedicarboxylatodiammineplatinum(II) (carboplatin) in the presence of nucleophiles and human breast cancer MCF-7 cell cytoplasmic extracts: activation theory revisited," *Biochemical Pharmacology*, vol. 58, no. 10, pp. 1625–1629, 1999.
- [31] A. V. Chernikov, S. V. Gudkov, I. N. Shtarkman, and V. I. Bruskov, "Oxygen effect in heat-induced DNA damage," *Biophysics*, vol. 52, no. 2, pp. 185–190, 2007.
- [32] HiSpeed, *Plasmid Purification Handbook*, QIAGEN, 2005.
- [33] J. A. Glasel, "Validity of nucleic acid purities monitored by 260 nm/280 nm absorbance ratios," *BioTechniques*, vol. 18, no. 1, pp. 62–63, 1995.
- [34] *Gel Filtration- Principles and Methods Handbook*, GE Healthcare, 2007.
- [35] M. Macka, J. Borak, L. Semenkova, and F. Kiss, "Decomposition of cisplatin in aqueous solutions containing chlorides by ultrasonic energy and light," *Journal of Pharmaceutical Sciences*, vol. 83, no. 6, pp. 815–818, 1994.
- [36] M. Pujol, J. Part, M. Trillas, and X. Domènech, "Stability of aqueous carboplatin solutions under illumination," *Monatshefte für Chemie Chemical Monthly*, vol. 124, no. 11-12, pp. 1077–1081, 1993.
- [37] E. E. M. Brouwers, M. Tibben, H. Rosing, J. H. M. Schellen, and J. H. Beijnen, "The application of inductively coupled plasma mass spectrometry in clinical pharmacological oncology research," *Mass Spectrometry Reviews*, vol. 27, no. 2, pp. 67–100, 2008.
- [38] J. Huang, X. Hu, J. Zhang, K. Li, Y. Yan, and X. Xu, "The application of inductively coupled plasma mass spectrometry in pharmaceutical and biomedical analysis," *Journal of Pharmaceutical and Biomedical Analysis*, vol. 40, no. 2, pp. 227–234, 2006.
- [39] M. A. Huels, B. Boudaïffa, P. Cloutier, D. Hunting, and L. Sanche, "Single, double, and multiple double strand breaks induced in DNA by 3–100 eV electrons," *Journal of the American Chemical Society*, vol. 125, no. 15, pp. 4467–4477, 2003.
- [40] B. Boudaïffa, P. Cloutier, D. Hunting, M. A. Huels, and L. Sanche, "Cross sections for low-energy (10–50 eV) electron damage to DNA," *Radiation Research*, vol. 157, no. 3, pp. 227–234, 2002.
- [41] V. I. Bruskov, L. V. Malakhova, Z. K. Masalimov, and A. V. Chernikov, "Heat-induced formation of reactive oxygen species and 8-oxoguanine, a biomarker of damage to DNA," *Nucleic Acids Research*, vol. 30, no. 6, pp. 1354–1363, 2002.
- [42] S. J. Berners-Price and T. G. Appleton, "The chemistry of cisplatin in aqueous solution," in *Platinum-Based Drugs in Cancer Therapy*, L. R. Kelland and N. Farell, Eds., pp. 3–35, Humana Press, Totowa, NJ, USA, 2000.
- [43] P. D. Prenxler and W. D. McFadyen, "Reactions of cisplatin and the cis-diamminediaqua platinum(II) cation with tris and hepes," *Journal of Inorganic Biochemistry*, vol. 68, no. 4, pp. 279–282, 1997.
- [44] S. Kobayashi, M. Furukawa, C. Dohi, H. Hamashima, T. Arai, and A. Tanaka, "Topology effect for DNA structure of cisplatin: topological transformation of cisplatin-closed circular DNA adducts by DNA topoisomerase," *Chemical and Pharmaceutical Bulletin*, vol. 47, no. 6, pp. 783–790, 1999.
- [45] G. B. Onoa, G. Cervantes, V. Moreno, and M. J. Prieto, "Study of the interaction of DNA with cisplatin and other Pd(II) and Pt(II) complexes by atomic force microscopy," *Nucleic Acids Research*, vol. 26, no. 6, pp. 1473–1480, 1998.
- [46] T. Boulikas, G. P. Stathopoulos, N. Volakakis, and M. Vougiouka, "Systemic lipoplatin infusion results in preferential tumor uptake in human studies," *Anticancer Research*, vol. 25, no. 4, pp. 3031–3040, 2005.

Spectroscopic Characterization and Biological Activity of Mixed Ligand Complexes of Ni(II) with 1,10-Phenanthroline and Heterocyclic Schiff Bases

Y. Prashanthi,^{1,2} K. Kiranmai,¹ Ira,³ Sathish kumar K,¹ Vijay kumar Chityala,¹ and Shivaraj¹

¹Department of Chemistry, Osmania University, Hyderabad 500 007, India

²Indian Institute of Chemical Technology, Hyderabad 500 007, India

³Centre for Cellular and Molecular Biology, Hyderabad 500 007, India

Correspondence should be addressed to Shivaraj, shivaraj_sunny@yahoo.co.in

Academic Editor: Imre Sovago

Mixed ligand complexes of Ni(II) with 1,10-phenanthroline (1,10-Phen) and Schiff bases L₁(MIIMP); L₂(CMIIMP); L₃(EMIIMP); L₄(MIIMNP); L₅(MEMIIMP); L₆(BMIIMP); L₇(MMIIMP); L₈(MIIBD) have been synthesized. These metal chelates have been characterized by elemental analysis, IR, ¹H-NMR, ¹³C-NMR, Mass, UV-Vis, magnetic moments, and thermogravimetric (TG&DTA) analysis. Spectral data showed that the 1,10-phenanthroline act as neutral bidentate ligand coordinating to the metal ion through two nitrogen donor atoms and Schiff bases acts as monobasic bidentate coordinating through NO donor atoms. All Ni(II) complexes appear to have an octahedral geometry. The antimicrobial activity of mixed ligand complexes has been studied by screening against various microorganisms, it is observed that the activity enhances upon coordination. The DNA binding studies have been investigated by UV-Vis spectroscopy, and the experimental results indicate that these complexes bind to CT DNA with the intrinsic binding constant K_b = 2.5 ± 0.2 × 10⁵ M⁻¹. MTT is used to test the anticancer effect of the complexes with HL60 tumor cell. The inhibition ratio was accelerated by increasing the dosage, and it had significant positive correlation with the medication dosage.

1. Introduction

One of the major applications of the transition metal complexes is their medical testing as antibacterial and antitumor agents aiming toward the discovery of an effective and safe therapeutic regimen for the treatment of bacterial infections and cancers. In addition, many Schiff base complexes with metals have also provoked wide interest because they possess a diverse spectrum of biological and pharmaceutical activities, including antitumor, antioxidative, antifungal, and antibacterial activities [1–10]. Schiff bases and their complexes have been used as biological models to understand the structures of biomolecules and biological processes [11, 12]. The study of ternary complexes involving an aromatic Schiff base and 1,10-phenanthroline has been studied extensively [13]. To design effective chemotherapeutic agents and better anticancer drugs, it is essential to explore the interactions of

metal complexes with DNA [14]. Moreover, it is well known that some drug activities, when administered as metal complexes, are being increased, and several Schiff base complexes have also been shown to inhibit tumor growth. The incorporation of transition metal into Schiff bases enhances the biological activity of the ligand and decreases the cytotoxic effects of both the metal ion and ligand on the host [15].

In view of the wide biological activities exhibited by isoxazoles and their derivatives which include antibacterial, anticancer, anti-HIV and have applications as pesticides and insecticides, it is meaningful to extend these studies on metal complexes containing isoxazole Schiff bases. Nickel is recognized as an essential trace element for bacteria, plants, animals, and humans though the role of this metal in animal biochemistry is still not well defined.

Previously, we have reported our interesting results on the synthesis and antimicrobial activities of binary complexes

of isoxazole Schiff bases [16]. Encouraged by this result, we turned our attention towards the synthesis, biological studies, and DNA binding studies of ternary complexes. A thorough literature survey reveals that not much work has been done on the synthesis and biological studies of ternary complexes of isoxazole Schiff bases.

Hence, we are tempted to synthesize biologically important ternary Schiff base complexes. Herein, it is reported that the synthesis, spectral characterization and antimicrobial studies of ternary Schiff base complexes, and their interaction with DNA.

The following ligands which are selected in the present investigation are

- (1) 2-{[(5'-Methyl-3'-isoxazolyl)imino]methyl}phenol (MIIMP) (L_1),
- (2) 4-Chloro-2-{[(5'-Methyl-3'-isoxazolyl)imino]methyl}phenol(CMIIMP) (L_2),
- (3) 2-Ethoxy-6-{[(5'-Methyl-3'-isoxazolyl)imino]methyl}phenol(EMIIMP) (L_3),
- (4) 2-{[(5'-Methyl-3'-isoxazolyl)imino]methyl}-4-nitrophenol(MIIMNP) (L_4),
- (5) 4-Methyl-2-{[(5'-Methyl-3'-isoxazolyl)imino]methyl}phenol(MEMIIMP) (L_5),
- (6) 4-Bromo-2-{[(5'-Methyl-3'-isoxazolyl)imino]methyl}phenol(BMIIMP) (L_6),
- (7) 5-Methoxy-2-{[(5'-Methyl-3'-isoxazolyl)imino]methyl}phenol(MMIIMP) (L_7),
- (8) 4-{[(5'-Methyl-3'-isoxazolyl)imino]}-1,3-benzene-diol (MIIBD) (L_8).

2. Experimental

2.1. Materials and Methods. ^1H NMR spectra of the ligands were recorded at 200 MHz and 300 MHz on Varian Gemini Unity Spectrometer using TMS as an internal standard. ^{13}C NMR spectra were recorded at 100.6 MHz on Varian Gemini Spectrometer. The EI mass spectra were recorded on a VG micro mass 7070-H Instrument, ESI MS spectra were recorded on VG AUTOSPEC mass spectrometer. IR spectra of the ligands and complexes were recorded using KBr pellets in the range (4000–400 cm^{-1}) on Perkin-Elmer Infrared model 337. Electronic spectra of metal complexes in DMSO were recorded on Schimadzu UV-VIS 1601 spectrophotometer. Magnetic susceptibilities of the complexes were determined on Gouy balance model 7550 using $\text{Hg}[\text{Co}(\text{NCS})_4]$ as standard. The diamagnetic corrections of the complexes were computed using Pascal's constants. TGA of complexes were carried on Mettler Toledo Star system in the temperature range of 0–1000°C. Melting points of the ligands and decomposition temperature of complexes were determined on Polmon instrument (model no. MP-96). The conductivity measurements were measured in DMSO solutions (0.001 M) using Digisun Electronic Digital conductivity meter of model: DI-909 having a dip-type cell calibrated with KCl solution. The percentage composition of C, H, N for the complexes and necessary ligands were

determined by using microanalytical techniques on Perkin Elmer 240C (USA) elemental analyzer. The EPR spectra of the Copper complexes were recorded on EPR Varian-E-112 at RT. The percent composition of metal ions in solid metal complexes was determined by atomic absorption spectrophotometer.

2.2. Synthesis of Schiff Bases (L_1 – L_8) (General Method). The Schiff bases, namely L_1 , L_2 , L_3 , L_4 , L_5 , L_6 , L_7 , and L_8 , were prepared by the condensation of 3-amino-5-methyl isoxazole (5 mmol) with the respective salicyldehydes (5 mmol) was taken in methanol and refluxed for 2 h. The colored Schiff bases obtained were recrystallized from methanol and petroleum ether (8 : 2). Purity of the compound was checked by TLC. Yield: 80–85%.

2.3. Synthesis of $[\text{Ni}(L_1/L_2/L_3/L_4/L_5/L_6/L_7/L_8)(1,10\text{-phen})(\text{H}_2\text{O})_2]\text{Cl}$ Complexes. The Nickel(II) complexes were prepared by mixing the appropriate molar quantity of ligands and nickel salt using the following procedure. An ethanolic solution of Schiff base $L_1/L_2/L_3/L_4/L_5/L_6/L_7/L_8$ (10 mmol) was reflux with the ethanolic solution of Nickel(II) chloride (10 mmol) for ca 3 h. To the above mixture, an ethanolic solution of 1,10-phenanthroline(10 mmol) was added, and the reflux was continued for ca 1 h. The colored solid product formed was filtered, washed with ethanol, and dried in vacuo.

2.4. Antimicrobial Screening. The ligands and their metal complexes were screened against bacteria and fungi. Antibacterial screening was done by the paper disc method (Kirby-Bauer method) [17]. The bacterial organisms used are *Pseudomonas aeruginosa* (gram +ve) and *Escherichia coli* (gram –ve). Cultures of test organisms were maintained in nutrient agar media and subcultured in Petri dishes prior to testing. The fungal organisms used are *Aspergillus niger* and *Rhizoctonia solani*. Cultures were maintained on potato dextrose agar slants and subcultured in petri dishes prior to testing.

2.5. DNA Binding Studies. Absorption spectra were recorded on Jasco V-530 UV-visible spectrophotometer using 1 cm quartz-cuvettes. Absorption titrations were performed by keeping the concentration of the complex constant (10 μM) and by varying [CT DNA] from 0–11 μM . For $[\text{Ni}(1,10\text{-phen})(\text{EMIIMP})(\text{H}_2\text{O})_2]\text{Cl}$ complex, the binding constant (K_b), has been determined from the spectroscopic titration data using the following equation [18]:

$$\frac{[\text{DNA}]}{(\varepsilon_a - \varepsilon_f)} = \frac{[\text{DNA}]}{(\varepsilon_b - \varepsilon_f)} + \frac{1}{K_b(\varepsilon_b - \varepsilon_f)}. \quad (1)$$

The “apparent” extinction coefficient (ε_a) was obtained by calculating $A_{\text{obsd}}/[\text{Ni}]$. The terms ε_f and ε_b correspond to the extinction coefficients of free (unbound) and the fully bound complex, respectively. From plot of $[\text{DNA}] / (\varepsilon_a - \varepsilon_f)$ versus $[\text{DNA}]$ will give a slope $1/(\varepsilon_b - \varepsilon_f)$ and an intercept $1/K_b(\varepsilon_b - \varepsilon_f)$. K_b is the ratio of the slope and the intercept.

TABLE 1: Analytical data for Ternary Ni(II) complexes.

Compound	Formula	M.Wt	C %	H %	N %	M %
[Ni (1,10-phen) (MIIMP) (H ₂ O) ₂]Cl	[NiC ₂₃ H ₂₁ N ₄ O ₄ Cl]	511.2	53.99 (54.37)	4.10 (4.01)	10.95 (10.02)	11.48 (11.06)
[Ni (1,10-phen) (CMIIMP) (H ₂ O) ₂]Cl	[NiCH ₂₀ N ₄ O ₄ Cl ₂]	545.7	50.57 (50.00)	3.66 (3.27)	10.26 (10.17)	11.75 (11.27)
[Ni (1,10-phen) (EMIIMP) (H ₂ O) ₂]Cl	[NiC ₂₅ H ₂₅ N ₄ O ₅ Cl]	555.2	54.03 (53.38)	4.50 (4.41)	10.08 (10.00)	10.57 (10.27)
[Ni (1,10-phen) (MIIMNP) (H ₂ O) ₂]Cl	[NiC ₂₃ H ₂₀ N ₅ O ₆ Cl]	556.2	49.62 (51.27)	3.59 (3.24)	12.58 (12.74)	10.55 (10.72)
[Ni (1,10-phen) (MEIIMP) (H ₂ O) ₂]Cl	[NiC ₂₄ H ₂₃ N ₄ O ₄ Cl]	525.2	54.83 (54.37)	4.37 (4.21)	10.66 (10.02)	11.17 (10.95)
[Ni (1,10-phen) (MMIIMP) (H ₂ O) ₂]Cl	[NiC ₂₄ H ₂₃ N ₄ O ₅ Cl]	541.2	53.21 (52.59)	4.24 (4.20)	10.34 (10.97)	10.84 (10.37)
[Ni (1,10-phen) (BMIIMP) (H ₂ O) ₂]Cl	[NiC ₂₃ H ₂₀ N ₄ O ₄ BrCl]	590.2	46.76 (46.20)	3.38 (3.30)	9.48 (9.00)	9.93 (9.35)
[Ni (1,10-phen) (MIIBD) (H ₂ O) ₂]Cl	[NiC ₂₃ H ₂₁ N ₄ O ₅ Cl]	527.2	52.35 (52.00)	3.98 (3.20)	10.62 (10.20)	11.13 (11.02)

*The values mentioned within the bracket are calculated.

2.6. Anticancer Activity. The Ni(II) complexes are screened against HL 60 cells. The activity among these complexes are in the range of IC₅₀ (μ g/mL) are 35.48 \pm 1.12.

2.7. Methodology

2.7.1. Cell Line. Human promyelocytic leukemia (HL60) cells were cultured in RPMI-1640. The media were supplemented with 10% heat-inactivated FCS, 1 mM NaHCO₃, 200 mM L-glutamine, and penicillin-streptomycin in a humidified atmosphere of 95%, 5% CO₂ at 37°C.

2.7.2. Test Concentrations. Initially, the stock concentrations were prepared by dissolving 8 mg of each test compound in 1 mL of DMSO and further diluted to obtain a experimental stock solution of 200 μ g/mL (25 μ L of initial stock solution was diluted to 1 mL). Different aliquots of experimental stock were added to the cultured cells in the medium (final volume of 200 μ L) to attain the required test concentrations of 10, 20, 40, 60, 80, and 100 μ g/mL.

3. Results and Discussion

3.1. Characterization of Complexes. All the complexes are stable in air and have high melting points. They are freely soluble in DMSO and DMF and sparingly soluble in methanol and ethanol. The metal complexes were characterized by elemental analysis, molar conductivities, TG, DTA, IR, UV-Vis, ¹H NMR, ¹³C NMR, and Mass spectra. The analytical data of the complexes are in agreement with the experimental data. The values reveal that the metal to ligand ratio is 1 : 1 : 1 and are presented in Table 1.

3.2. Thermal Analysis. In the present investigation, the following thermoanalytical methods have been used.

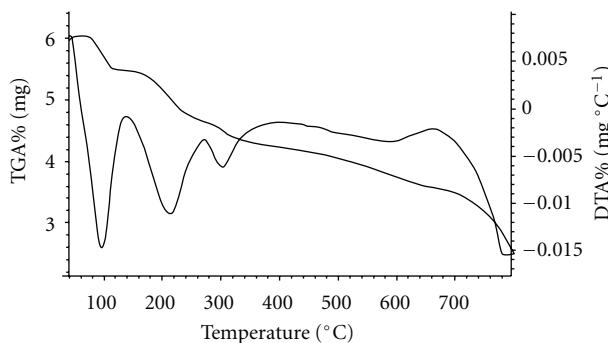
(1) *Thermogravimetric analysis (TGA) and (2) Differential Thermal Analysis (DTA).* From the thermograms of these complexes, it is concluded that the coordinated water molecules are eliminated in the temperature range of 60–1600°C. And the ligands gradually decompose to their corresponding metal oxides at higher temperatures. Presence of water molecules is further confirmed by the endothermic

bands observed in the respective DTA curve in the temperature region where the TG curves should lose weight. In addition to the endothermic bands, the DTA curves of complexes also show exothermic bands. These bands appeared at higher temperatures which represent phase transition, oxidation and/or decomposition of the compound.

The thermal decomposition process of [Ni(1,10-phen) (MIIMP)(H₂O)₂]Cl complex (Figure 1) can be divided into three stages. The first stage occurs in the range of 80–1300°C having mass loss of 12.05% (calculated 12.88%) which corresponds to the loss of two moles of coordinated water and chloride ion. In continuation to the first stage, the degradation stages occur in the range of 170–3300°C having mass loss of 38.64% (calculated 39.12%) shows partial decomposition of the ligand. The degradation stage in the range of 330 to 600°C with an estimated mass loss of 31.98% (calculated 32.48%). This mass loss corresponds to the pyrolysis of ligand molecules leaving NiO as a residue.

3.3. IR Spectra. The IR spectral data for the complexes are summarized in Table 2. A broadband at 3319–3445 cm⁻¹ due to phenolic OH group of free Schiff base disappear in their metal complexes indicating coordination through the phenolic oxygen & bands at 1601–1616 cm⁻¹ in the free ligands are due to azomethine group, which is shifted to lower frequencies in the spectra of the complexes (1570–1600 cm⁻¹) indicating involvement of azomethine nitrogen in coordination to the metal. The medium intensity bands observed for all ligands in the range 1350–1358 cm⁻¹ due to the phenolic stretching frequency, shifted to lower frequency by 10–20 cm⁻¹ in the mixed-ligand complexes suggesting involvement of the oxygen atom of the γ C–O moiety in coordination [19]. The presence of coordinated water molecules are observed by broadbands around 3342–3535 cm⁻¹ which can further confirmed by bands observed at 765–780 cm⁻¹ [20].

Shifting of bands in the region 1500–1300 cm⁻¹ of the free phenanthroline ligand is observed in the spectra. In particular, the peaks corresponding to the ring stretching frequencies ν C=C and ν C=N at 1505 and 1421 cm⁻¹ undergo shifting to higher frequencies at 1520 and 1427 cm⁻¹, indicating the coordination of the “1,10-phen” nitrogen

FIGURE 1: TGA Spectrum of $[\text{Ni}(1,10\text{-phen})(\text{MIIMP})(\text{H}_2\text{O})_2]\text{Cl}$.

atoms to the metal ion [21]. In the region $800\text{--}600\text{ cm}^{-1}$, characteristic out-of-plane hydrogen bending modes of free phenanthroline at 855 and 738 cm^{-1} , shift to frequencies of 850 and 728 cm^{-1} , respectively. Similarly, the far-infrared region of the spectra shows new peaks at $510\text{--}417\text{ cm}^{-1}$ due to the $\nu\text{M--O}$ and $\nu\text{M--N}$ vibrations, respectively [22].

3.4. Electronic Absorption Spectra and Magnetic Measurements. Absorption band assignments and magnetic measurement data of the Ni(II) complexes are given in Table 3. The electronic spectra of present Ni(II) complexes show three bands at $646\text{--}831$, $506\text{--}641$, and $356\text{--}414\text{ nm}$, presumably due to the three spin-allowed transitions. $^3\text{A}_{2g}\text{ (F)} \rightarrow ^3\text{T}_{2g}$, $^3\text{A}_{2g}\text{ (F)} \rightarrow ^3\text{T}_{1g}\text{ (F)}$ and $^3\text{A}_{2g}\text{ (F)} \rightarrow ^3\text{T}_{1g}\text{ (P)}$ transitions for octahedral structure (Scheme 1).

The Ni(II) complexes are found to have magnetic moments in the range $2.81\text{--}3.2\text{ B.M.}$, which are well within the range expected for octahedral Ni(II) complexes. The higher magnetic moments when compared to the spin-only value 2.8 B.M. , may be attributed to the slight mixing of a multiplet excited state in which spin-orbit coupling is appreciable [23].

3.5. FAB Mass Spectra. The FAB spectra of $[\text{Ni}(1,10\text{-phen})(\text{MIIMP})(\text{H}_2\text{O})_2]\text{Cl}$ have been depicted and reproduced in Figure 2. The spectrum showed a molecular ion peak M^+ at m/z 476 that is equivalent to its molecular weight $[\text{Ni}(1,10\text{-phen})(\text{MIIMP})(\text{H}_2\text{O})_2]\text{Cl}$.

The FAB spectra of $[\text{Ni}(1,10\text{-phen})(\text{MIIMNP})(\text{H}_2\text{O})_2]\text{Cl}$ showed a molecular ion M^+ peak at m/z 543 that is equivalent to its molecular weight $[(\text{Ni}(1,10\text{-phen})(\text{MIIMNP})(\text{H}_2\text{O})_2) + \text{Na}]^+$. The molecular ion by the loss of two water molecules gave a fragment ion peak at m/z 379 . All these fragments leading to the formation of the species $[\text{ML}]^+$ which undergoes demetallation to form the species $[\text{L} + \text{H}]^+$ at m/z 248 . All these spectral data which confirm the ratio of complexes are in $1:1:1$.

4. Molecular Modeling Studies

In the absence of X-ray crystal structure data the 3-dimensional structure of the molecules can not be entirely

unambiguous. The configuration possible for the Ni(II) complexes were evaluated using the semiempirical and the density functional theory calculations, respectively. The most stable structure with minimum energy among the possible ones is judged as the most probable structure as shown in Figure 3.

5. Antimicrobial Activity

The ligands and their metal complexes were screened against bacteria and fungi. Antibacterial screening was done by the paper disc method (Kirby-Bauer method). Ternary Ni(II) complexes with 1,10-phenanthroline and MIIMP, CMIIMP, EMIIMP, MIIMNP, MEMIIMP, MMIMP, BMIIMP, and MIIBD were screened against bacteria and fungi, and the results obtained are presented in Table 4. It is observed that the activity of ternary complexes is more compared to their corresponding binary complexes. This result is expected since the complexes possess a greater planar area and π -systems which make stacking more strongly. The variation in the activity of different complexes against different organisms depend either on the impermeability of the cells of the microbes or difference in ribosomes of microbial cells [24]. Comparison of the biological activity of the synthesized compounds with some known antibiotics (gentamycin) shows generally the free Schiff base ligand, and some of its complexes exhibit better activity than these antibiotics or comparable effect.

6. DNA Binding Studies

The binding of the $[\text{Ni}(1,10\text{-phen})(\text{EMIIMP})(\text{H}_2\text{O})_2]\text{Cl}$ to the CT DNA (Calf Thymus DNA) has been studied by electronic absorption spectroscopy in Figure 4. The electronic absorption spectra of $[\text{Ni}(1,10\text{-phen})(\text{EMIIMP})(\text{H}_2\text{O})_2]\text{Cl}$ in the absence and presence of CT DNA have been recorded in Tris HCl buffer at 300 K . Increasing concentration of CT DNA results in hypochromism and a red shift in the UV-Vis spectrum of complex. These spectral characteristics suggest that the π^* orbital of the intercalated ligand couples with the π orbital of base pairs, thus decreasing the $\pi\text{-}\pi^*$ transition energy and further resulting in the red shift [25]. Coupling of the π partially filled by electrons decreases the transition probabilities and concomitantly results in hypochromism. In order to compare the binding strength of the complexes with CT DNA, the intrinsic binding constants K_b are obtained by monitoring the changes in absorbance with increasing concentration of DNA. K_b is obtained from the ratio of the slope to the intercept from plots of $[\text{DNA}] / (\varepsilon_a - \varepsilon_f)$ versus $[\text{DNA}]$. The K_b value is in the order of $2.5 \pm 0.2 \times 10^5\text{ M}^{-1}$. The high K_b value is to the presence of planar structure of phen ligand which facilitates the groove binding/stacking with base pairs [26].

7. Anticancer Activity

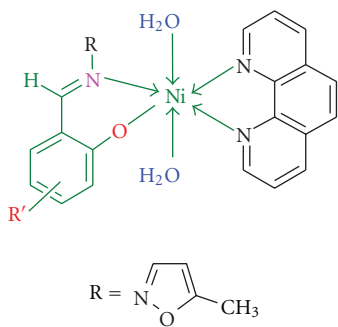
All the synthesized nickel complexes were screened for their cytotoxicity (HL60 cell). From the data, it was observed

TABLE 2: IR Absorption frequencies of Ternary Ni(II) Complexes.

Complex	ν OH	ν C=N	ν C–O	Coordinated water	ν M–O	ν M–N
[Ni (1,10-phen) (MIIMP) (H ₂ O) ₂]Cl	—	1616	1342	765	525	473
[Ni (1,10-phen) (CMIIMP) (H ₂ O) ₂]Cl	—	1570	1340	785	510	424
[Ni (1,10-phen) (EMIIMP) (H ₂ O) ₂]Cl	—	1582	1342	780	540	429
[Ni (1,10-phen) (MIIMNP) (H ₂ O) ₂]Cl	—	1604	1344	780	535	417
[Ni (1,10-phen) (MEIIMP) (H ₂ O) ₂]Cl	—	1624	1343	765	525	473
[Ni (1,10-phen) (MMIIMP) (H ₂ O) ₂]Cl	—	1620	1341	785	510	424
[Ni (1,10-phen) (BMMIIMP) (H ₂ O) ₂]Cl	—	1587	1342	779	540	429
[Ni (1,10-phen) (MIIBD) (H ₂ O) ₂]Cl	—	1616	1344	780	535	417

TABLE 3: Magnetic moments and electronic spectral data for ternary complexes.

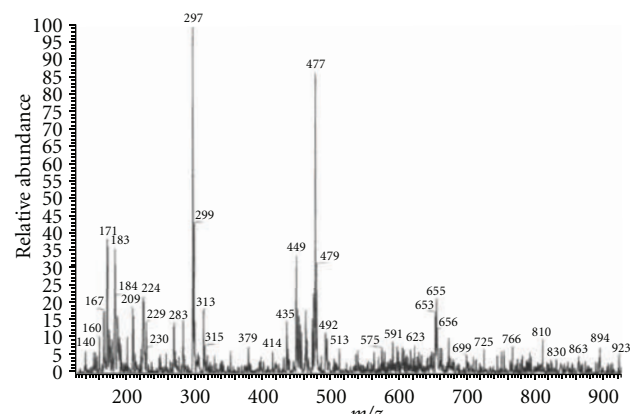
Complex	Frequency in nm ($\epsilon = 10^3 \text{ M}^{-1} \text{ cm}^{-1}$)			μ_{eff} B.M
[Ni (1,10-phen) (MIIMP) (H ₂ O) ₂]Cl	671 (0.092)	521 (0.058)	399 (0.067)	3.21
[Ni (1,10-phen) (CMIIMP) (H ₂ O) ₂]Cl	746 (0.083)	552 (0.047)	414 (0.056)	2.81
[Ni (1,10-phen) (EMIIMP) (H ₂ O) ₂]Cl	646 (0.096)	524 (0.065)	380 (0.039)	3.00
[Ni (1,10-phen) (MIIMNP) (H ₂ O) ₂]Cl	831 (0.072)	641 (0.051)	392 (0.043)	3.20
[Ni (1,10-phen) (MEIIMP) (H ₂ O) ₂]Cl	686 (0.094)	542 (0.072)	396 (0.051)	3.12
[Ni (1,10-phen) (MMIIMP) (H ₂ O) ₂]Cl	699 (0.085)	552 (0.063)	356 (0.049)	3.15
[Ni (1,10-phen) (BMMIIMP) (H ₂ O) ₂]Cl	688 (0.079)	506 (0.058)	370 (0.041)	3.05
[Ni (1,10-phen) (MIIBD) (H ₂ O) ₂]Cl	692 (0.093)	588 (0.074)	408 (0.053)	3.20



SCHEME 1: Proposed structure of the Nickel complexes.

that the complexes displayed their cytotoxic activities as IC₅₀ ($\mu\text{g}/\text{mL}$) against human promyelocytic leukemia (HL60 cells), the IC₅₀ values of all the nickel complexes are listed in Table 5.

Cell Morphological Assessment. The morphological abnormalities were studied under a phase-contrast microscope. Cells treated for 24 h showed obvious morphological changes, with chromatin condensation, fragmentation, and formation of apoptotic bodies. However, the control group (without test compound) showed normal healthy shape with intact nuclei and without any abnormalities is shown

FIGURE 2: Mass Spectrum of [Ni(1,10-phen)(MIIMP)(H₂O)₂]Cl.

in Figure 5. Most of the treated cells in all the test concentrations exhibited similar symptoms of apoptosis but the damage was severe in the cells exposed to highest concentration.

8. Conclusions

New mixed ligands and their ternary Ni(II) complexes have been designed, synthesized, and characterized. Based on analytical, conductivity, magnetic data, infrared, and electronic spectral data, they adopt octahedral geometry around Nickel(II). The TG investigations were able to evaluate the presence of water molecules in the coordination sphere.

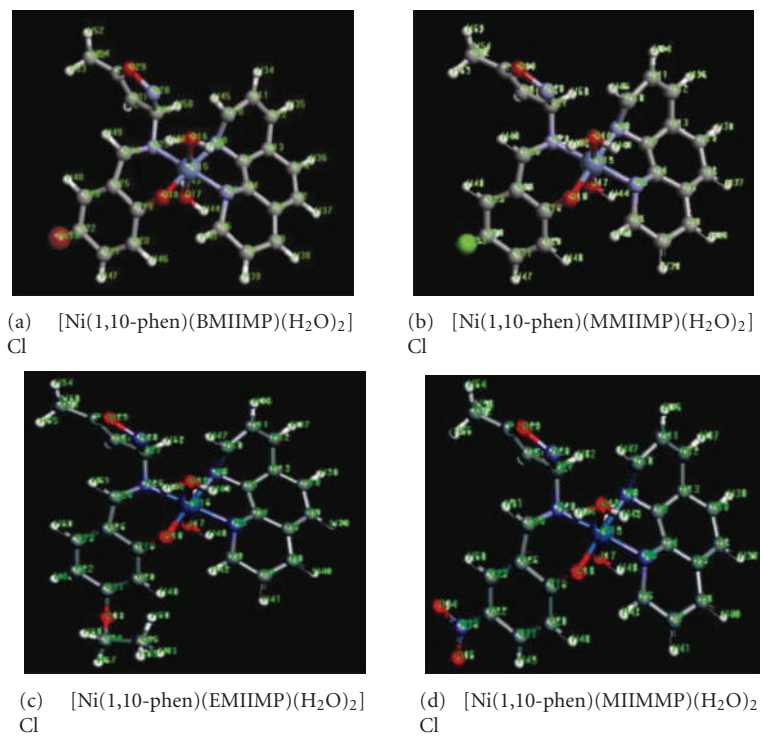


FIGURE 3: The optimized structural geometry of Ni(II) complexes.

TABLE 4: Antimicrobial activity of ternary complexes.

Complex	<i>E. coli</i>	<i>P. aeruginosa</i>	<i>R. oryzae</i>	<i>A. niger</i>
MIIMP	+	+	-	+
$[\text{Ni}(\text{MIIMP})_2(\text{H}_2\text{O})_2]$	+	+	+	+
$[\text{Ni}(1,10\text{-phen})(\text{MIIMP})(\text{H}_2\text{O})_2]\text{Cl}$	++	++	+	++
CMIIMP	+	+	+	+
$[\text{Ni}(\text{CMIIMP})_2(\text{H}_2\text{O})_2]$	+	-	+	-
$[\text{Ni}(1,10\text{-phen})(\text{CMIIMP})(\text{H}_2\text{O})_2]\text{Cl}$	++	+	+	+
EMIIMP	+	+	+	+
$[\text{Ni}(\text{EMIIMP})_2(\text{H}_2\text{O})_2]$	++	++	++	++
$[\text{Ni}(1,10\text{-phen})(\text{EMIIMP})(\text{H}_2\text{O})_2]\text{Cl}$	+++	++	+	++
MIIMNP	+	+	+	+
$[\text{Ni}(\text{MIIMNP})_2(\text{H}_2\text{O})_2]$	++	++	++	++
$[\text{Ni}(1,10\text{-phen})(\text{MIIMNP})(\text{H}_2\text{O})_2]\text{Cl}$	++	+	+	++
MEMIIMP	+	-	-	+
$[\text{Ni}(\text{MEMIIMP})_2(\text{H}_2\text{O})_2]$	+	+	+	+
$[\text{Ni}(1,10\text{-phen})(\text{MEMIIMP})(\text{H}_2\text{O})_2]\text{Cl}$	+	+	+	+
MIIMMP	+	+	+	+
$[\text{Ni}(\text{MIIMMP})_2(\text{H}_2\text{O})_2]$	++	+	-	+
$[\text{Ni}(1,10\text{-phen})(\text{MIIMMP})(\text{H}_2\text{O})_2]\text{Cl}$	+	++	+	+
BMIIMP	+	-	-	-
$[\text{Ni}(\text{BMIIMP})_2(\text{H}_2\text{O})_2]$	++	+	+	+
$[\text{Ni}(1,10\text{-phen})(\text{BMIIMP})(\text{H}_2\text{O})_2]\text{Cl}$	+++	+	+	-
MIIBD	+	+	+	+
$[\text{Ni}(\text{MIIBD})_2(\text{H}_2\text{O})_2]$	++	+	+	-
$[\text{Ni}(1,10\text{-phen})(\text{MIIBD})(\text{H}_2\text{O})_2]\text{Cl}$	++	+++	+	+
Gentamycin	++	++	-	-

Highly active: +++ (inhibition zone > 15 mm); moderately active: ++ (inhibition zone > 10 mm); slightly active: + (inhibition zone > 5 mm); inactive: - (inhibition zone < 5 mm).

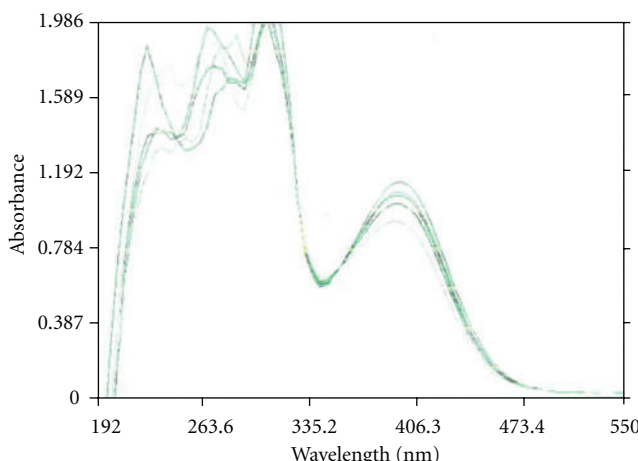
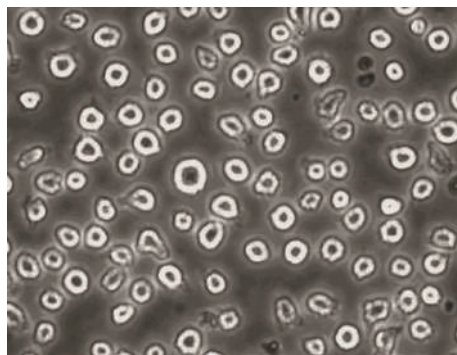
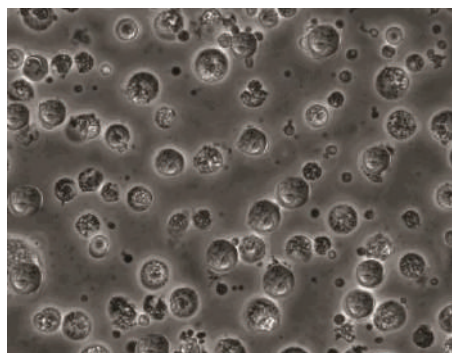


FIGURE 4: UV-Vis absorption Spectra of $[\text{Ni}(1,10\text{-phen})(\text{EMIIMP})(\text{H}_2\text{O})_2]\text{Cl}$ ($10 \mu\text{M}$) in the presence of increasing amounts of CT-DNA ; $[\text{DNA}] = 0, 10, 20, 30, 40, 50 \mu\text{M}$.



(a)



(b)

FIGURE 5: Morphological changes in HL60 cells (a) control cells with intact nuclei; (b) cell membrane blebbing, nuclear fragmentation, and chromatin condensation in presence of $[\text{Ni}(1,10\text{-phen})(\text{EMIIMP})(\text{H}_2\text{O})_2]\text{Cl}$.

Based on these observations, metal ion coordinates through phenolate oxygen, azomethine nitrogen of Schiff bases, and nitrogen atoms of phenanthroline. The antimicrobial study reveals that some of nickel complexes show better activity than the known antibiotic. The antitumor activity of complexes displayed good cytotoxic activities against human

TABLE 5: IC_{50} range of Ni(II) complexes for HeLa cells.

Complex	IC_{50} ($\mu\text{g/mL}$)
$[\text{Ni}(1,10\text{-phen})(\text{MIIMP})(\text{H}_2\text{O})_2]\text{Cl}$	65.48 ± 0.18
$[\text{Ni}(1,10\text{-phen})(\text{CMIIMP})(\text{H}_2\text{O})_2]\text{Cl}$	68.32 ± 0.21
$[\text{Ni}(1,10\text{-phen})(\text{EMIIMP})(\text{H}_2\text{O})_2]\text{Cl}$	35.48 ± 0.12
$[\text{Ni}(1,10\text{-phen})(\text{MIIMNP})(\text{H}_2\text{O})_2]\text{Cl}$	50.84 ± 0.43
$[\text{Ni}(1,10\text{-phen})(\text{MEIIMP})(\text{H}_2\text{O})_2]\text{Cl}$	47.31 ± 0.85
$[\text{Ni}(1,10\text{-phen})(\text{MMIIMP})(\text{H}_2\text{O})_2]\text{Cl}$	71.25 ± 0.42
$[\text{Ni}(1,10\text{-phen})(\text{BIIIMP})(\text{H}_2\text{O})_2]\text{Cl}$	82.30 ± 0.24
$[\text{Ni}(1,10\text{-phen})(\text{MIIBD})(\text{H}_2\text{O})_2]\text{Cl}$	52.51 ± 0.72

promyelocytic leukemia (HL60 cells). DNA binding studies of complexes reveal that presence of high K_b value facilitates the groove binding/stacking with base pairs.

Acknowledgments

The authors are grateful to the Head of the Department of Chemistry for providing the necessary facilities. The authors are thankful to the Director of IICT and the Director of CCMB and Hyderabad for providing spectral and analytical data.

References

- [1] N. Farrell, *Transition Metal Complexes as Drugs and Chemothapeutic Agents*, Kluwer Academic, Dordrecht, The Netherlands, 1989.
- [2] E. L. Hegg and J. N. Burstin, "Toward the development of metal-based synthetic nucleases and peptidases: a rationale and progress report in applying the principles of coordination chemistry," *Coordination Chemistry Reviews*, vol. 173, no. 1, pp. 133–165, 1998.
- [3] L. Casella and M. Gullotti, "Synthesis, stereochemistry, and oxygenation of cobalt(II)-pyridoxal model complexes. A new family of chiral dioxygen carriers," *Inorganic Chemistry*, vol. 25, no. 9, pp. 1293–1303, 1986.
- [4] L. Casella and M. Gullotti, "Transamination in the 2-formylpyridineamino acid-metal ion systems. Stereochemistry of zinc(II) and copper(II) complexes of N-(2-pyridylmethylidene)amino acids," *Inorganic Chemistry*, vol. 22, no. 16, pp. 2259–2266, 1983.
- [5] T. M. Aminabhavi, N. S. Biradar, S. B. Patil, V. L. Roddabasangoudar, and W. E. Rudzinski, "Amino acid schiff base complexes of dimethyldichlorosilane," *Inorganica Chimica Acta*, vol. 107, no. 4, pp. 231–234, 1985.
- [6] G. Plesch, C. Friebel, O. Švajlenová, J. Krátsmár Šmogrovic, and D. Mlynarcik, "EPR, ligand field spectra and antimicrobial activity of some N-pyruvideneglycinatocuppper(II) complexes," *Inorganica Chimica Acta*, vol. 151, no. 2, pp. 139–143, 1988.
- [7] D. Sattari, E. Alipour, S. Shirani, and J. Amighian, "Metal complexes of N-salicylideneamino acids," *Journal of Inorganic Biochemistry*, vol. 45, no. 2, pp. 115–122, 1992.
- [8] D. S. Sigman, A. Mazumder, and D. M. Perrin, "Chemical nucleases," *Chemical Reviews*, vol. 93, no. 6, pp. 2295–2316, 1993.

- [9] M. Z. Wang, Z. X. Meng, B. L. Liu, G. L. Cai, C. L. Zhang, and X. Y. Wang, "Novel tumor chemotherapeutic agents and tumor radio-imaging agents: potential tumor pharmaceuticals of ternary copper(II) complexes," *Inorganic Chemistry Communications*, vol. 8, no. 4, pp. 368–371, 2005.
- [10] V. Sharma and D. Piwnica-Worms, "Metal complexes for therapy and diagnosis of drug resistance," *Chemical Reviews*, vol. 99, no. 9, pp. 2545–2560, 1999.
- [11] A. Wolfe, G. H. Shimer Jr, and T. Meehan, "Polycyclic aromatic hydrocarbons physically intercalate into duplex regions of denatured DNA," *Biochemistry*, vol. 26, no. 20, pp. 6392–6396, 1987.
- [12] A. A. Soliman and W. Linert, "Investigations on new transition metal chelates of the 3-methoxy-salicylidene-2-aminothiophenol Schiff base," *Thermochimica Acta*, vol. 338, no. 1-2, pp. 67–75, 1999.
- [13] C. Zhang and C. Janiak, "Six-coordinated zinc complexes: $[\text{Zn}(\text{H}_2\text{O})_4(\text{phen})]\text{NO}_3 \cdot \text{H}_2\text{O}$ and $[\text{ZnNO}_3(\text{H}_2\text{O})(\text{bipy})(\text{Him})\text{NO}_3$ ($\text{phen} = 1,10\text{-phenanthroline}$, $\text{bipy} = 2,2'\text{-bipyridine}$, and $\text{Him} = \text{imidazole}$)," *Journal of Chemical Crystallography*, vol. 31, no. 1, pp. 29–35, 2001.
- [14] A. K. Patra, M. Nethaji, and A. R. Chakravarty, "Synthesis, crystal structure, DNA binding and photo-induced DNA cleavage activity of (S-methyl-l-cysteine)copper(II) complexes of heterocyclic bases," *Journal of Inorganic Biochemistry*, vol. 101, no. 2, pp. 233–244, 2007.
- [15] G. G. Mohamed, M. M. Omar, and A. A. Ibrahim, "Biological activity studies on metal complexes of novel tridentate Schiff base ligand. Spectroscopic and thermal characterization," *European Journal of Medicinal Chemistry*, vol. 44, no. 12, pp. 4801–4812, 2009.
- [16] Y. Prashanthi, K. Kiranmai, N. J. P. Subhashini, and Shivaraj, "Synthesis, potentiometric and antimicrobial studies on metal complexes of isoxazole Schiff bases," *Spectrochimica Acta A*, vol. 70, no. 1, pp. 30–35, 2008.
- [17] A. W. Bauer, W. M. Kirby, J. C. Sherris, and M. Turck, "Antibiotic susceptibility testing by a standardized single disk method.," *American Journal of Clinical Pathology*, vol. 45, no. 4, pp. 493–496, 1966.
- [18] C. V. Kumar and E. H. Asuncion, "DNA binding studies and site selective fluorescence sensitization of an anthryl probe," *Journal of the American Chemical Society*, vol. 115, no. 19, pp. 8547–8553, 1993.
- [19] V. H. Kulkarni, B. R. Patil, and B. K. Prabhakar, "IR and Möessbauer studies of Sn(IV) complexes with branched tetradentates containing N and O donor centres," *Journal of Inorganic and Nuclear Chemistry*, vol. 43, no. 1, pp. 17–21, 1981.
- [20] Z. M. Zaki and G. G. Mohamed, "Spectral and thermal studies of thiobarbituric acid complexes," *Spectrochimica Acta A*, vol. 56, no. 7, pp. 1245–1250, 2000.
- [21] A. A. Schilt and R. C. Taylor, "Infra-red spectra of 1:10-phenanthroline metal complexes in the rock salt region below 2000 cm⁻¹," *Journal of Inorganic and Nuclear Chemistry*, vol. 9, no. 3-4, pp. 211–221, 1959.
- [22] R. E. Wilde, T. K. K. Srinivasan, and S. N. Ghosh, "Mono complexes of 2,2'-bipyridine and 1,10-phenanthroline with transition metals," *Journal of Inorganic and Nuclear Chemistry*, vol. 35, no. 3, pp. 1017–1021, 1973.
- [23] A. B. P. Lever, *Inorganic Electronic Spectroscopy*, Elsevier, New York, NY, USA, 3rd edition, 1984.
- [24] C. Jayabalakrishnan and K. Natarajan, "Ruthenium(II) carbonyl complexes with tridentate Schiff bases and their antibacterial activity," *Transition Metal Chemistry*, vol. 27, no. 1, pp. 75–79, 2002.
- [25] L. Jia, X. M. Xu, J. Xu et al., "Synthesis, characterization, cytotoxic activities, and DNA-binding studies of ternary copper(II) complexes with new coumarin derivatives," *Chemical and Pharmaceutical Bulletin*, vol. 58, no. 8, pp. 1003–1008, 2010.
- [26] J. M. Kelly, A. B. Tossi, D. J. McConnell, and C. Ohuigin, "A study of the interactions of some polypyridylruthenium (II) complexes with DNA using fluorescence spectroscopy, topoisomerisation and thermal denaturation," *Nucleic Acids Research*, vol. 13, no. 17, pp. 6017–6034, 1985.

Cytotoxicity and *In Vitro* Antileishmanial Activity of Antimony (V), Bismuth (V), and Tin (IV) Complexes of Lapachol

Marcele Neves Rocha,¹ Paula Monalisa Nogueira,¹ Cynthia Demicheli,² Ludmila Gonçalvez de Oliveira,² Meiriane Mariano da Silva,² Frédéric Frézard,³ Maria Norma Melo,⁴ and Rodrigo Pedro Soares¹

¹ Centro de Pesquisas René Rachou, Fundação Oswaldo Cruz/FIOCRUZ, 30190-002 Belo Horizonte, MG, Brazil

² Departamento de Química, Instituto de Ciências Exatas, Universidade Federal de Minas Gerais, 31270-901 Belo Horizonte, MG, Brazil

³ Departamento de Fisiologia e Biofísica, Instituto de Ciências Biológicas, Universidade Federal de Minas Gerais, 31270-901 Belo Horizonte, MG, Brazil

⁴ Departamento de Parasitologia, Instituto de Ciências Biológicas, Universidade Federal de Minas Gerais, 31270-901 Belo Horizonte, MG, Brazil

Correspondence should be addressed to Rodrigo Pedro Soares; rsoares@cpqrr.fiocruz.br

Academic Editor: Patrick Bednarski

Leishmania amazonensis is the etiologic agent of the cutaneous and diffuse leishmaniasis often associated with drug resistance. Lapachol [2-hydroxy-3-(3'-methyl-2-butenyl)-1,4-naphthoquinone] displays a wide range of antimicrobial properties against many pathogens. In this study, using the classic microscopic *in vitro* model, we have analyzed the effects of a series of lapachol and chlorides complexes with antimony (V), bismuth (V), and tin (IV) against *L. amazonensis*. All seven compounds exhibited antileishmanial activity, but most of the antimony (V) and bismuth (V) complexes were toxic against human HepG2 cells and murine macrophages. The best IC₅₀ values (0.17 ± 0.03 and $0.10 \pm 0.11 \mu\text{g/mL}$) were observed for Tin (IV) complexes (3) [(Lp)(Ph₃Sn)] and (6) (Ph₃SnCl₂), respectively. Their selective indexes (SIs) were 70.65 and 120.35 for HepG2 cells, respectively. However, while analyzing murine macrophages, the SI decreased. Those compounds were moderately toxic for HepG2 cells and toxic for murine macrophages, still underlying the need of chemical modification in this class of compounds.

1. Introduction

Leishmania amazonensis, a New World species, has been identified as a dermatropic species often associated with drug resistance [1]. Current antileishmanial therapies are toxic to human and some simply fail [2, 3]. In the Americas, for over six decades, parenteral administrations of pentavalent antimonials (Sb-V), sodium stibogluconate (Pentostam), and meglumine antimoniate (Glucantime) have been used for treating leishmaniasis. In places where resistance to antimonials is common, such as India, other chemotherapeutic treatments include amphotericin B and pentamidine [2, 4]. Therefore, the absence of a low toxic and safe oral drug still underlines the need for new antileishmanial compounds.

Lapachol, [2-hydroxy-3-(3'-methyl-2-butenyl)-1,4-naphthoquinone] (Figure 1) is a natural compound extracted from the core of Bignoniaceae trees. In *Leishmania*, lapachol analogues, derivatives, and complexes have been tested by several groups. Lapachol, isolapachol, and some of their derivatives were active *in vitro* and *in vivo* against *Leishmania braziliensis* and *L. amazonensis*, respectively [5]. Bismuth (III), antimony (V), and tin (IV) complexes were active against *Helicobacter pylori*, *Leishmania major*, and *Leishmania donovani*, respectively [6–8].

The design of bifunctional metal complex, where both the ligand and the metal exert pharmacological activity, represents a promising strategy for achieving more effective and selective drugs. In the present study, lapachol was coupled

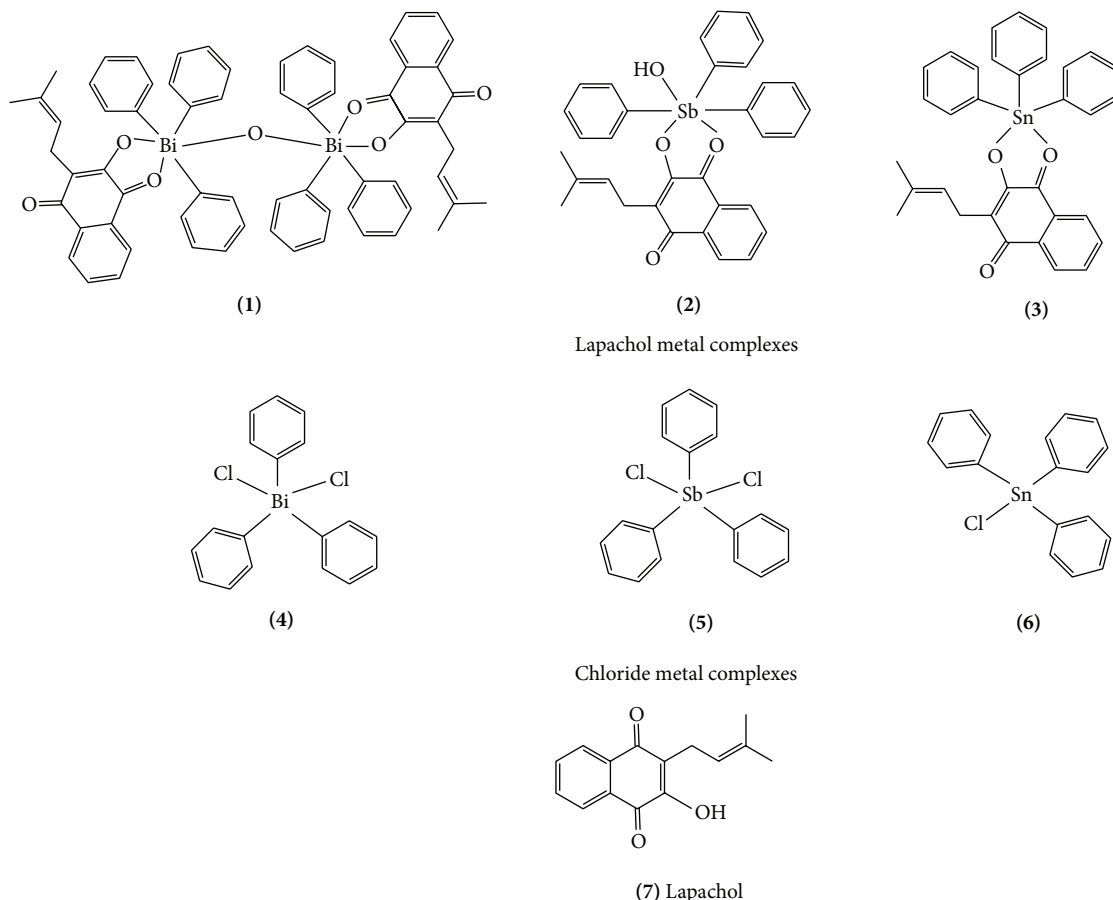


FIGURE 1: Structures of lapachol metal (Bi, Sb, and Sn) complexes (1–3) and chloride metal (Bi, Sb, and Sn) compounds (4–6) and lapachol (7). Legend: Bi = bismuth, Sb = antimony, and Sn = tin.

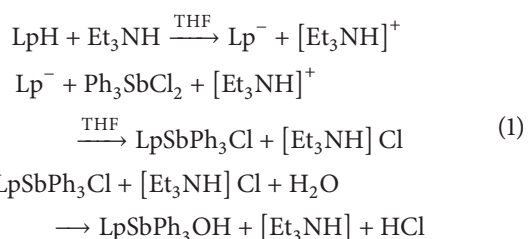
with three different metals: triphenyltin (IV), triphenylbismuth (V), and triphenylantimony (V). We have tested the *in vitro* activity and cytotoxicity of synthesized antimony (V), bismuth (V), and tin (IV) lapachol and chloride complexes against intracellular *L. amazonensis*, HepG2 cells, and murine macrophages.

2. Materials and Methods

2.1. Synthesis of the Lapachol Metal Complexes and Tested Metal Chlorides. The $(\text{Lp})(\text{Ph}_3\text{Bi})\text{O}_{0.5}$ (1) and $(\text{Lp})(\text{Ph}_3\text{Sb})\text{OH}$ (2) complexes were synthesized by following the procedure described by [9]. To prepare $(\text{Lp})(\text{Ph}_3\text{Sn})$ (3) the same procedure was used. Triethylamine ($70 \mu\text{L}$) was added to a mixture of lapachol (0.121 g , 0.5 mmol) and triphenyltin (IV) chloride (193 mg , 0.5 mmol) in chloroform (20 mL). The resulting mixture was stirred for 4 h at room temperature. Removal of the solvent under vacuum yielded a solid material. The material was subsequently dissolved in acetone and precipitated in water. The triethylammonium hydrochloride formed during the reaction was dissolved and removed by water. Elemental analyses were carried out using a Perkin-Elmer 240 Elemental Analyzer. Atomic absorption analyses of bismuth, antimony and tin contents were carried

out on a Hitachi Atomic Absorption Spectrophotometer (Model 8200).

The following equations can be proposed to illustrate the formation of $(\text{Lp})(\text{Ph}_3\text{Sb})\text{OH}$ complex as follows:



The same process can be proposed for all complexes. The yields, melting points, and elemental analyses of the compounds prepared are given in Table 1.

Triphenylbismuth dichloride (4), triphenylantimony dichloride (5), triphenyltin chloride (6), and lapachol (7) were obtained from Aldrich. Triethylamine was obtained from Sigma. The predicted structures of all tested compounds are shown in Figure 1.

2.2. Parasites. The World Health Organization (WHO) reference strain *L. amazonensis* (IFLA/BR/1967/PH8) was used and typed as previously described [10]. Promastigote forms

TABLE 1: Yields and elemental analyses of the compounds.

Compound	Yield (%)	M.p. (°C) ^a	C found (calc.) (%)	H found (calc.) (%)	Metal found (calc.) (%)	Formula for calc.
(1)	79	126–129	57.31 (57.40)	4.09 (4.23)	29.03 (29.98)	(Lp)(Ph ₃ Bi)O _{0.5}
(2)	76	154–156	65.30 (64.82)	4.52 (4.78)	20.64 (19.19)	(Lp)(Ph ₃ Sb)OH
(3)	79	107–109	66.41 (67.03)	4.40 (4.77)	21.74 (20.07)	(Lp)(Ph ₃ Sn)

^aM.p.: melting point.

were grown at 25°C in M199 medium (Sigma) supplemented with 10% heat-inactivated fetal calf serum (Cultilab), 40 mmol/L HEPES (Amersham), 0.1 mmol/L adenine (Sigma), 0.0005% hemin (Sigma), 0.0002% biotin (Sigma), 50 units/mL penicillin, and 50 mg/mL streptomycin (Invitrogen) [11].

2.3. In Vitro Classic Microscopic Tests. Animals were kept in the Animal Facility of the Centro de Pesquisas René Rachou/FIOCRUZ in strict accordance to the Guide for the Care and Use of Experimental Animals [12]. The procedures were approved by the Internal Ethics Committee in Animal Experimentation (CEUA) of Fundação Oswaldo Cruz (FIOCRUZ), Brazil (Protocol L-042/08). Mice were euthanized with CO₂ in an induction chamber prior to macrophage removal. Balb/c mice were injected intraperitoneally with 2 mL of 3% sodium thioglycollate medium. After 72 h, peritoneal macrophages were removed by washing with cold RPMI 1640 medium and enriched by adherence to round glass coverslips (13 mm) placed in a 4-well culture plate. Cells (2×10^5 cells/well) were cultured (37°C, 5% CO₂, 18 h) in RPMI supplemented with 10% heat-inactivated FBS (fetal bovine serum) prior to infection with parasites. Macrophages were exposed to stationary phase promastigotes (2×10^6 /well) at a final ratio of 1:10. The plates were incubated at 37°C, 5% CO₂, for 5 h in BOD to allow internalization of parasites [13]. Then, the medium was removed for the remaining noninternalized parasites. Negative control included only infected macrophages and medium. Incubations were tested in duplicate in two independent experiments [14, 15]. The substances were serial diluted with RPMI 1640 medium supplemented with 10% FBS at five different concentrations (50 → 3.1 µg/mL). For compounds (3) and (6), the dilution was 10 → 0.016 µg/mL. Amphotericin B was used as reference drug. Infected macrophages were exposed daily to the compounds for 3 consecutive days. After this period, coverslips were collected, stained with Panoptic (Laborclin), and subsequently mounted with Entellan (Merck) on glass slides.

2.4. Cytotoxicity Tests. The cell lineage HepG2 A16 was derived from a human hepatocellular carcinoma cell line HepG2 (ATCC HB-8065) and obtained from America Type Culture Collection line (ATCC) [16]. Balb/c murine peritoneal macrophages were obtained as described above. Cytotoxicity was determined using the MTT method (3-(4,5-dimethylthiazol-2-yl)-2,5-diphenyl tetrazolium bromide) (Sigma). HepG2 cells were kept in RPMI medium supplemented with 10% FBS, and confluent monolayers were trypsinized, washed in RPMI, and transferred to 96-well microtiter plates (4×10^4 cells/well) for 16–18 h. Murine macrophages

were used in the concentration 2×10^5 cells/well in 96-well microtiter plates. The compounds were serial diluted in different concentrations (10 → 0.16 mg/mL). In both tests, the medium was removed, and the compounds were incubated for 24 h (37°C, 5% CO₂). Colorimetric reaction was developed following the incubation with MTT (37°C, 5% CO₂, 4 h) and addition of acidified isopropanol [17]. The reaction was read spectrophotometrically (Spectramax M5, Molecular Devices, San Francisco, CA) with a 570 nm filter and a background of 670 nm. Incubations were tested in triplicate in two independent experiments. The minimum dose that killed 50% of the cells (MLD₅₀) was determined [18], and the values were plotted to generate dose-response curves using Microcal Origin Software (Northampton, MA, USA) [15, 19]. The selective indexes (SIs) of compounds were calculated using the MLD₅₀/IC₅₀ ratios to HepG2 and peritoneal macrophages [20, 21].

3. Results

The *in vitro* classic microscopic test enables direct counting to determine the percentage of infected cells and/or the number of amastigotes [22]. Here, the IC₅₀ values were calculated based on the percentage of infected macrophages [15]. The *in vitro* antileishmanial activities, cytotoxicity and selective indexes (SIs) of lapachol metal complexes and chlorides (1–6), lapachol (7) and amphotericin B are shown in Table 2. Lapachol and compounds (1), (2), and (5) were considered inactive (IC₅₀ > 10 µg/mL) and toxic (SI < 20) for HepG2 cells and macrophages [20, 21]. The tin (IV) lapachol complex (3) and chloride (6) were active against intracellular amastigote forms of *L. amazonensis* (Figures 2(a) and 2(b)) and less toxic for HepG2 cells (SIs ranging from 70.65 to 120.35) (Figures 2(d) and 2(e)) (Table 2). One triphenyl bismuth chloride (4) (Figure 2(c)) was also active and a little more toxic for HepG2 cells (Figure 2(f)) than (3) (Figure 2(d)) and (6) (Figure 2(e)) (SI = 34.03). All compounds were toxic for murine macrophages (SI < 20). Amphotericin B, an antileishmanial reference drug, exhibited an IC₅₀ value approximately fourfold higher than (3) and (6) (0.73 ± 0.60 µg/mL) (Table 2).

4. Discussion

Leishmaniasis are considered by the WHO as one of the major six important infectious diseases worldwide. Over the past years, the absence of research and development for new medicines targeting diseases affecting people in developing countries has become a global concern [23].

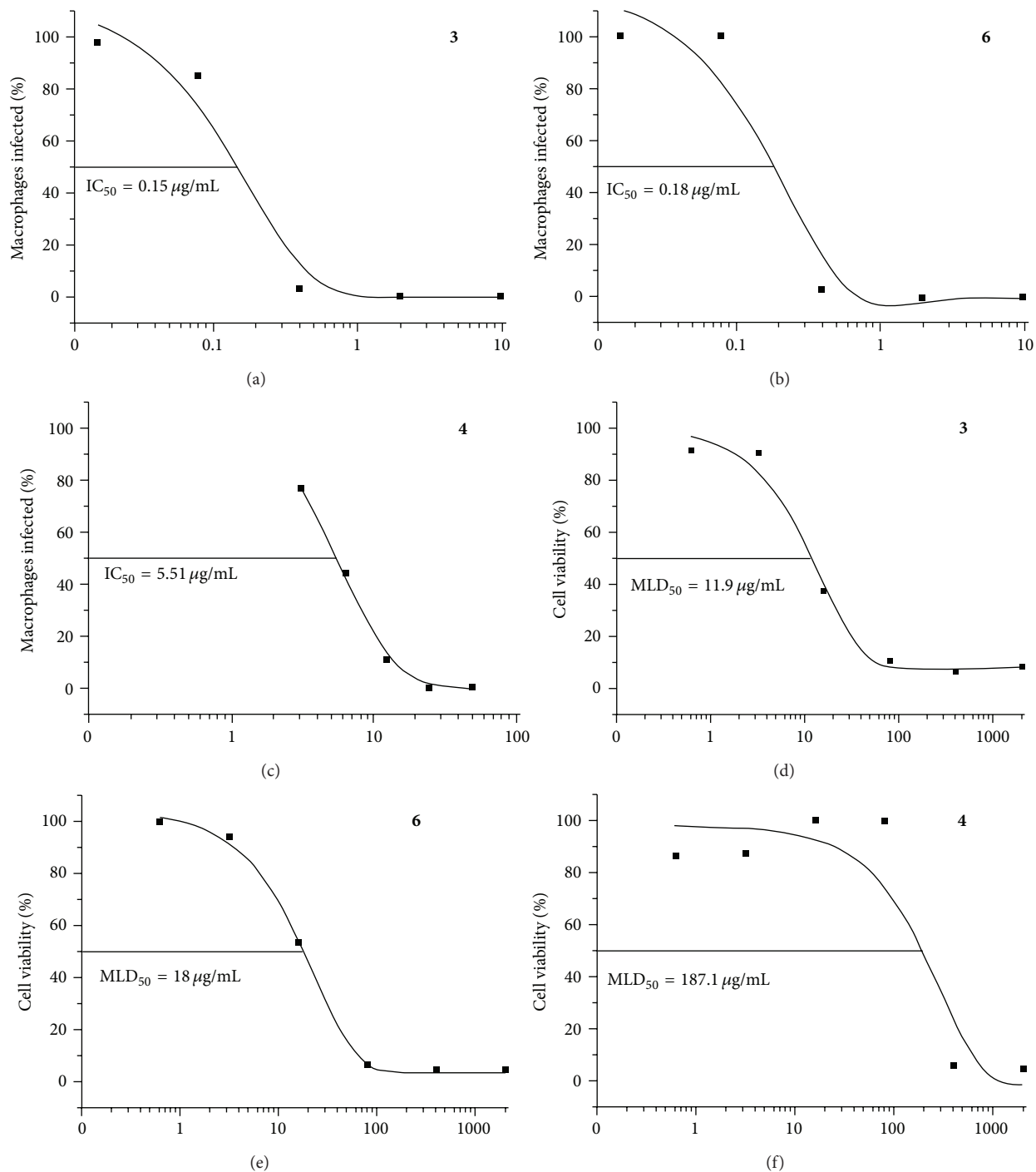


FIGURE 2: *In vitro* antileishmanial activity of compounds (3), (4), and (6) against intracellular *L. amazonensis* ((a), (b), and (c)) and cytotoxicity against hepatoma HepG2 cell ((d), (e), and (f)). Curves were obtained using Microcal Origin Software. IC_{50} = half-maximal inhibitory response; MLD_{50} = the minimum lethal dose. Figures are a representation of one experiment.

Currently, the development of new drugs, combinations, or protocols against tropical and neglected diseases is of great importance in public health [24–27]. However, side effects, treatment failure due to parasite resistance, HIV coinfection, and intravenous administration are the major concerns hindering leishmaniasis chemotherapy [2, 3].

Lapachol derivatives and complexes have exhibited anti-tumor, anti-inflammatory, antiangiogenic, analgesic, and antimicrobial properties [6, 28–32]. Lapachol and some of its analogues demonstrated activity *in vitro* against *L. braziliensis* and *L. amazonensis* [5]. The use of metal complexes against *Leishmania* may represent a potential alternative against

TABLE 2: Antileishmanial activity, cytotoxicity, and selective indexes of tested compounds for HepG2 cells and murine macrophages.

Compound	Formula	IC_{50}^a	HepG2		Macrophages	
			MLD_{50}^b	SI ^c	MLD_{50}^b	SI ^c
(1)	(Lp)(Ph ₃ Bi)O _{0.5}	29.05 ± 18.45	58.38 ± 8.47	2.01	32.4 ± 8.20	1.11
(2)	(Lp)(Ph ₃ Sb)OH	18.27 ± 5.58	325.22 ± 89.40	17.81	130.65 ± 40.52	7.15
(3)	(Lp)(Ph ₃ Sn)	0.17 ± 0.03	12.01 ± 0.17	70.65	1.6 ± 0.57	9.41
(4)	Ph ₃ BiCl ₂	5.40 ± 0.16	183.75 ± 4.77	34.03	25.15 ± 0.49	4.67
(5)	Ph ₃ SbCl ₂	11.61 ± 7.85	157.46 ± 37.13	13.56	30.75 ± 6.01	2.65
(6)	Ph ₃ SnCl ₂	0.10 ± 0.11	12.04 ± 8.42	120.35	0.73 ± 0.13	7.30
(7)	Lp ^d	15.48 ± 5.23	201.77 ± 5.32	13.03	184.65 ± 6.58	11.92
Amphotericin B		0.73 ± 0.60	644.59 ± 126.57	883.00	179.95 ± 8.84	246.51

^aIC₅₀: the inhibitory concentration that killed 50% of the *L. amazonensis* in µg/mL.

^bMLD₅₀: the minimum lethal dose that killed 50% of the cells in µg/mL.

^cSI: selective index, calculated based on the MLD₅₀/IC₅₀ ratios.

^dLp: Lapachol.

the disease since antimony-based regimens tend to be very toxic. In this context, we have explored the use of lapachol and chloride metal complexes with antimony (V), bismuth (V), and tin (IV)] against *L. amazonensis*.

In contrast to data from previous studies, lapachol (7) did not exhibit significant antileishmanial activity against *L. amazonensis* (15.48 ± 5.23 versus 5.2 ± 0.70 µg/mL) [5]. This IC₅₀ value is close to that observed for *L. braziliensis* (11.9 ± 6.9 µg/mL). This discrepancy could be attributed to the strain of *L. amazonensis* used (MHOM/BR/77/LTB0016) and experimental conditions. The highest antiproliferative activity against intracellular *L. amazonensis* was observed for tin (IV) lapachol and chloride complexes (3) and (6) (Figures 2(a) and 2(b)) and one bismuth (V) chloride compound (4) (Figure 2(c)). More importantly, compounds (3) and (6) were more active than amphotericin B and less toxic among all substances tested while using HepG2 cells (SIs of 70.65 and 120.35, resp.). Interestingly, the resulting compound of lapachol and tin (IV) showed a marked decrease in metal toxicity than lapachol alone (SIs of 70.65 versus 13.03, resp.). One of the possibilities that could justify such phenomenon could be due to an increase in the lipophilicity of the lapachol-complexed molecule. Another hypothesis is that lapachol complexation could affect the REDOX potential of the compound, thus, consequently changing its activity. Consistent with this idea, the mechanisms underlying those activities are related to the generation of reactive oxygen radicals (ROSS) induced by the bioreduction of its quinonoid nucleus through specific enzymes and oxygen [33–35]. ROS mechanisms induced by lapachol have been implicated in the chemotherapeutic activities against many protozoa such as *Trypanosoma cruzi* [30] and also tumor cells [31]. Similarly, among all metal chloride substances, the triphenyl tin (IV) chloride compound exhibited lower toxicity compared to bismuth (V) and antimony (V) chloride ones. Finally, compound (4) exhibited moderate toxicity (SI = 34.03) with an IC₅₀ value 7-fold higher than amphotericin B. However, when cytotoxicity was tested against murine macrophages, the host cells for *Leishmania*, all compounds were toxic. Those data indicate the need of chemical modifications in this class of compounds in the search of novel antileishmanial molecules.

5. Conclusions

Lapachol and a series of six lapachol and chloride metal complexes have been evaluated for their *in vitro* activity against intracellular amastigote forms of *L. amazonensis*. The tin (IV) lapachol and chloride complexes (3 and 6) exhibited higher antileishmanial activity compared to amphotericin B. The triphenyl bismuth (V) compound (4) also exhibited antileishmanial activity with moderate cytotoxicity. Lapachol compounds with bismuth (V) and tin (IV) were less toxic when compared with lapachol alone for HepG2 cells. In conclusion, tin, and in a less extent, bismuth complexes were moderately toxic for HepG2 cells and toxic for murine macrophages.

Conflict of Interests

The authors have declared that no conflict of interests exists.

Financial Support

The authors received the following funds.

Acknowledgments

R. P. Soares, C. Demicheli, F. Frézard, and M. N. Melo are supported by the National Council for the Development of Research of Brazil (CNPq) (305042/2010-6, 303866/2010-1, and 303046/2009-1). M. N. Rocha is supported by CNPq (142361/2009-7). This work was supported by Fundação de Amparo à Pesquisa do Estado de Minas Gerais (FAPEMIG) (APQ-00197-11, APQ-01123-09, PRONEX, PPM-00382-11). The authors would like to thank Dr. Deborah Sullivan-Davis for reviewing the paper.

References

- [1] A. Bittencourt, A. Barral, A. R. de Jesus, R. P. de Almeida, and G. Grimaldi Júnior, “In situ identification of *Leishmania amazonensis* associated with diffuse cutaneous leishmaniasis in

- Bahia, Brazil," *Memórias do Instituto Oswaldo Cruz*, vol. 84, no. 4, pp. 585–586, 1989.
- [2] S. L. Croft, S. Sundar, and A. H. Fairlamb, "Drug resistance in leishmaniasis," *Clinical Microbiology Reviews*, vol. 19, no. 1, pp. 111–126, 2006.
- [3] S. L. Croft, K. Seifert, and V. Yardley, "Current scenario of drug development for leishmaniasis," *Indian Journal of Medical Research*, vol. 123, no. 3, pp. 399–410, 2006.
- [4] J. Mishra, A. Saxena, and S. Singh, "Chemotherapy of leishmaniasis: past, present and future," *Current Medicinal Chemistry*, vol. 14, no. 10, pp. 1153–1169, 2007.
- [5] N. M. F. Lima, C. S. Correia, L. L. Leon et al., "Antileishmanial activity of lapachol analogues," *Memórias do Instituto Oswaldo Cruz*, vol. 99, no. 7, pp. 757–761, 2004.
- [6] P. C. Andrews, R. L. Ferrero, P. C. Junk et al., "Bismuth(III) complexes derived from non-steroidal anti-inflammatory drugs and their activity against *Helicobacter pylori*," *Dalton Transactions*, vol. 39, no. 11, pp. 2861–2868, 2010.
- [7] B. Raychaudhury, S. Banerjee, S. Gupta, R. V. Singh, and S. C. Datta, "Antiparasitic activity of a triphenyl tin complex against *Leishmania donovani*," *Acta Tropica*, vol. 95, no. 1, pp. 1–8, 2005.
- [8] P. C. Andrews, R. Frank, P. C. Junk, L. Kedzierski, I. Kumar, and J. G. MacLellan, "Anti-Leishmanial activity of homo- and heteroleptic bismuth(III) carboxylates," *Journal of Inorganic Biochemistry*, vol. 105, no. 3, pp. 454–461, 2011.
- [9] L. G. Oliveira, M. M. Silva, F. C. Paula et al., "Antimony(V) and bismuth(V) complexes of lapachol: synthesis, crystal structure and cytotoxic activity," *Molecules*, vol. 16, no. 12, pp. 10314–10323, 2011.
- [10] M. N. Rocha, C. Margonari, I. M. Presot, and R. P. Soares, "Evaluation of 4 polymerase chain reaction protocols for cultured *Leishmania* spp. typing," *Diagnostic Microbiology and Infectious Disease*, vol. 68, no. 4, pp. 401–409, 2010.
- [11] R. P. P. Soares, M. E. Macedo, C. Ropert et al., "Leishmania chagasi: lipophosphoglycan characterization and binding to the midgut of the sand fly vector *Lutzomyia longipalpis*," *Molecular and Biochemical Parasitology*, vol. 121, no. 2, pp. 213–224, 2002.
- [12] D. O. D. V. M. Ernest, M. C. D. V. M. Brenda, and A. A. McWilliam, *Guide to the Care and Use of Experimental Animals*, Canadian Council on Animal Care, 1993.
- [13] M. N. Rocha, C. M. Correa, M. N. Melo et al., "An alternative in vitro drug screening test using *Leishmania amazonensis* transfected with red fluorescent protein," *Diagnostic Microbiology and Infectious Diseases*, vol. 75, no. 3, pp. 282–291, 2013.
- [14] J. D. Berman and L. S. Lee, "Activity of antileishmanial agents against amastigotes in human monocyte-derived macrophages and in mouse peritoneal macrophages," *Journal of Parasitology*, vol. 70, no. 2, pp. 220–225, 1984.
- [15] A. C. Pinheiro, M. N. Rocha, P. M. Nogueira et al., "Synthesis, cytotoxicity, and in vitro antileishmanial activity of mono-t-butylloxycarbonyl-protected diamines," *Diagnostic Microbiology and Infectious Disease*, vol. 71, no. 3, pp. 273–278, 2011.
- [16] G. J. Darlington, J. H. Kelly, and G. J. Buffone, "Growth and hepatospecific gene expression of human hepatoma cells in a defined medium," *In Vitro Cellular & Developmental Biology*, vol. 23, no. 5, pp. 349–354, 1987.
- [17] F. Denizot and R. Lang, "Rapid colorimetric assay for cell growth and survival—modifications to the tetrazolium dye procedure giving improved sensitivity and reliability," *Journal of Immunological Methods*, vol. 89, no. 2, pp. 271–277, 1986.
- [18] M. C. Madureira, A. P. Martins, M. Gomes, J. Paiva, A. P. Cunha, and V. Rosário, "Antimalarial activity of medicinal plants used in traditional medicine in S. Tomé and Príncipe islands," *Journal of Ethnopharmacology*, vol. 81, pp. 23–29, 2002.
- [19] I. Oliveira, A. Sousa, J. S. Morais et al., "Chemical composition, and antioxidant and antimicrobial activities of three hazelnut (*Corylus avellana* L.) cultivars," *Food and Chemical Toxicology*, vol. 46, no. 5, pp. 1801–1807, 2008.
- [20] S. Nwaka and A. Hudson, "Innovative lead discovery strategies for tropical diseases," *Nature Reviews Drug Discovery*, vol. 5, no. 11, pp. 941–955, 2006.
- [21] J. R. Ioset, R. Brun, T. Wenzler, M. Kaiser, and V. Yardley, "Drug screening for kinetoplastids diseases: a training manual for screening in neglected diseases," *DNDi and Pan-Asian Screening Network*, pp. 1–74, 2009.
- [22] D. Sereno, A. Cordeiro da Silva, F. Mathieu-Daudé, and A. Ouaissi, "Advances and perspectives in *Leishmania* cell based drug-screening procedures," *Parasitology International*, vol. 56, no. 1, pp. 3–7, 2007.
- [23] P. Chirac and E. Torreele, "Global framework on essential health R&D," *The Lancet*, vol. 367, no. 9522, pp. 1560–1561, 2006.
- [24] R. Pink, A. Hudson, M. A. Mourès, and M. Bendig, "Opportunities and challenges in antiparasitic drug discovery," *Nature Reviews Drug Discovery*, vol. 4, no. 9, pp. 727–740, 2005.
- [25] M. Moran, J. Guzman, A. L. Ropars et al., "Neglected disease research and development: how much are we really spending?" *PLoS Medicine*, vol. 6, no. 2, Article ID e1000030, 2009.
- [26] J. L. Siqueira-Neto, O. R. Song, H. Oh et al., "Antileishmanial high-throughput drug screening reveals drug candidates with new scaffolds," *PLOS Neglected Tropical Diseases*, vol. 4, no. 5, article e675, 2010.
- [27] G. de Muylder, K. K. H. Ang, S. Chen, M. R. Arkin, J. C. Engel, and J. H. McKerrow, "A screen against *Leishmania* intracellular amastigotes: comparison to a promastigote screen and identification of a host cell-specific hit," *PLoS Neglected Tropical Diseases*, vol. 5, no. 7, Article ID e1253, 2011.
- [28] F. G. de Miranda, J. C. Vilar, I. A. Alves, S. C. Cavalcanti, and A. R. Antoniolli, "Antinociceptive and antiedematogenic properties and acute toxicity of *Tabebuia avellaneda* Lor. ex Griseb. inner bark aqueous extract," *BMC Pharmacology*, vol. 1, no. 1, article 6, 2001.
- [29] V. F. Andrade-Neto, M. G. L. Brandão, F. Q. Oliveira et al., "Antimalarial activity of *Bidens pilosa* L. (Asteraceae) ethanol extracts from wild plants collected in various localities or plants cultivated in humus soil," *Phytotherapy Research*, vol. 18, no. 8, pp. 634–639, 2004.
- [30] A. V. Pinto and S. L. de Castro, "The trypanocidal activity of naphthoquinones: a review," *Molecules*, vol. 14, no. 11, pp. 4570–4590, 2009.
- [31] J. M. Matés and F. M. Sánchez-Jiménez, "Role of reactive oxygen species in apoptosis: implications for cancer therapy," *The International Journal of Biochemistry & Cell Biology*, vol. 32, no. 2, pp. 157–170, 2000.
- [32] G. L. Parrilha, R. P. Vieira, P. P. Campos et al., "Coordination of lapachol to bismuth(III) improves its anti-inflammatory and anti-angiogenic activities," *BioMetals*, vol. 25, no. 1, pp. 55–62, 2012.
- [33] J. Tonholo, L. R. Freitas, F. C. de Abreu et al., "Electrochemical properties of biologically active heterocyclic naphthoquinones," *Journal of the Brazilian Chemical Society*, vol. 9, no. 2, pp. 163–169, 1998.

- [34] J. Benites, J. A. Valderrama, F. Rivera et al., “Studies on quinones—part 42: synthesis of furylquinone and hydroquinones with antiproliferative activity against human tumor cell lines,” *Bioorganic and Medicinal Chemistry*, vol. 16, no. 2, pp. 862–868, 2008.
- [35] E. A. Hillard, F. C. de Abreu, D. C. M. Ferreira, G. Jaouen, M. O. F. Goulart, and C. Amatore, “Electrochemical parameters and techniques in drug development, with an emphasis on quinones and related compounds,” *Chemical Communications*, no. 23, pp. 2612–2628, 2008.

Physicochemical Properties and Cellular Responses of Strontium-Doped Gypsum Biomaterials

**Amir Pouria,¹ Hadis Bandegani,¹ Milad Pourbaghi-Masouleh,¹
Saeed Hesaraki,¹ and Masoud Alizadeh²**

¹ Nanotechnology and Advanced Materials Department, Materials and Energy Research Center, P.O. Box 31787/316, Karaj 3177983634, Iran

² Ceramics Department, Materials and Energy Research Center, P.O. Box 31787/316, Karaj 3177983634, Iran

Correspondence should be addressed to Saeed Hesaraki, s-hesaraki@merc.ac.ir

Academic Editor: Spyros Perlepes

This paper describes some physical, structural, and biological properties of gypsum bioceramics doped with various amounts of strontium ions (0.19–2.23 wt%) and compares these properties with those of a pure gypsum as control. Strontium-doped gypsum (gypsum:Sr) was obtained by mixing calcium sulfate hemihydrate powder and solutions of strontium nitrate followed by washing the specimens with distilled water to remove residual salts. Gypsum was the only phase found in the composition of both pure and gypsum:Sr, meanwhile a shift into lower diffraction angles was observed in the X-ray diffraction patterns of doped specimens. Microstructure of all gypsum specimens consisted of many rod-like small crystals entangled to each other with more elongation and higher thickness in the case of gypsum:Sr. The Sr-doped sample exhibited higher compressive strength and lower solubility than pure gypsum. A continuous release of strontium ions was observed from the gypsum:Sr during soaking it in simulated body fluid for 14 days. Compared to pure gypsum, the osteoblasts cultured on strontium-doped samples showed better proliferation rate and higher alkaline phosphatase activity, depending on Sr concentration. These observations can predict better *in vivo* behavior of strontium-doped gypsum compared to pure one.

1. Introduction

Because strontium is chemically and physically similar to calcium, it is a trace element that accumulates in the skeleton, preferably in new trabecular bone, depending on the skeletal site. Sr content increases in the sequence diaphysis of the femur, lumbar vertebra, and iliac crest [1].

Strontium (Sr) salts were found to stimulate bone formation and inhibit bone resorption both *in vitro* and *in vivo* [2]. The oral strontium-containing drugs have recently been recommended as drug associated with treating osteoporosis [3]. The stimulatory effects of strontium on bone collagen synthesis has been reported *in vitro*, while neither calcium nor sodium salts were effective [4].

In the past decade, a wide range of bioceramics such as hydroxyapatite, tricalcium phosphate, octacalcium phosphate, and bioactive glasses have been studied for

orthopaedic applications [5–7]. Because of the beneficial effects of strontium on the treatment of bone diseases and defects, many studies have focused on synthesis, characterization, and animal modeling of strontium-containing bioceramics. Many authors attempted to incorporate Sr into crystal lattice of calcium phosphates either through a high temperature synthesis [8] or by precipitation during a setting reaction of hydroxyapatite forming cement [9]. Strontium-containing hydroxyapatite was mixed with bone cement [10, 11] to promote osteoblast attachment and mineralization *in vitro* [12] and accelerate bone growth and osteointegration *in vivo* [13]. Strontium-substituted beta-tricalcium phosphate was synthesized and used as a reactant of calcium phosphate cement with a Sr²⁺ release range of 12–30 ppm. Sr-doped hydroxyapatite was used as plasma-sprayed coating layer where a simulated cell response was observed for this layer compared to pure hydroxyapatite

TABLE 1: Details of various paste formulations for preparation of Sr-doped gypsum along with their names.

	G-0	G-Sr1	G-Sr2	G-Sr3	G-Sr4
Assumed Sr content in gypsum (%)	0	0.25	0.5	1.25	2.5
Concentration of Sr(NO ₃) solution used as liquid phase in paste (%)	0	1.36	2.80	7.04	14.08
Solid phase of paste	α-CHS	α-CHS	α-CHS	α-CHS	α-CHS

[14]. Incorporation of strontium into bioactive glasses has been also reported by some authors. Abou Neel et al. [15] reported structural and physical properties of melt-derived phosphate-based glasses in which positive effect of Sr-doped glasses on viability of human osteoblastic cells was reported. Physicochemical and in vitro cellular properties of sol-gel-derived bioactive glasses based on CaO-SrO-SiO₂-P₂O₅ system were reported by Hesaraki et al. [16].

Calcium sulfates are biocompatible and biodegradable materials used for the treatment of bone and periodontal defects for many years. Calcium sulfate can be used as a bulk material, space filler, and vehicle for a controlled release of certain drugs, associated with other graft materials [17–19]. A number of positive clinical experiences are available with calcium sulfate in bone substitution procedures [20]. Gypsum is dihydrate form of calcium sulfate (CaSO₄·2H₂O) synthetically made from Plaster of Paris, hemihydrate form of calcium sulfate (CaSO₄·1/2H₂O). Gypsum with a microstructure comprising a lot of small crystals entangled to each other, suggested that provides a more efficient environment for bone repair. It has been stated that gypsum not only is passive osteoconductive material but also might have a potential to be osteoinductive due to its special crystal structure, and high calcium content [21].

The aim of this study was to incorporate various contents of strontium ions into calcium sulfate dihydrate (gypsum) crystal lattice and to investigate the effect of this substitution on some physicochemical, structural and in vitro cellular properties of the material.

2. Materials and Methods

2.1. Starting Materials and Trade Marks. The following starting materials were used in this study: alpha-calcium sulfate hemihydrate (α-CSH, Aldrich, USA), strontium nitrate (Merck, Germany), sodium chloride (Merck, Germany), potassium chloride (Merck, Germany), calcium chloride dihydrate (Merck, Germany), sodium hydrogen carbonate (Merck, Germany), dipotassium hydrogen phosphate trihydrate (Merck, Germany), sodium sulfate decahydrate (Merck, Germany), magnesium chloride hexahydrate (Merck, Germany), tris-hydroxymethyl aminomethane (Merck, Germany), and hydrochloric acid (Merck, Germany). Except α-CSH and strontium nitrate, all the above mentioned precursors were used for the preparation of simulated body fluid (SBF) solution.

2.2. Preparation of Strontium-Doped Gypsum Specimens. Strontium-doped gypsum bioceramics (gypsum:Sr) were

prepared from the setting process of calcium sulfate hemihydrate. Calcium sulfate hemihydrate was mixed with aqueous solution of strontium nitrate at a solid to liquid loading of 2 g/mL and the obtained paste was poured into a disc-shaped Teflon mold (10 mm in diameter and 3 mm in height) and left to set. Various concentrations of strontium nitrate were used to achieve gypsum product with different concentrations of strontium doped ions. Pure distilled water was also used to fabricate gypsum product without any additive as control sample (G-0). Table 1 presents details of various paste formulations of Sr-doped gypsum specimens along with the code of each formulation. When the pastes were completely hardened (set), the specimens were taken from the mold, incubated in 100% humidified atmosphere at 37°C for 24 h, washed with distilled water for several times to remove the residuals and soluble salts, and, finally, dried at room temperature for 72 h.

2.3. Experimental Procedures

2.3.1. Concentration of Strontium in Gypsum:Sr. The concentration of strontium ions in the Sr-doped gypsum specimens was measured using inductively coupled plasma-atomic emission spectroscopy (ICP-AES) technique ARL 3410.

2.3.2. Phase Composition. Phase compositions of the specimens were determined using an X-ray diffractometer device (XRD, Philips PW 3710) with Cu-K α radiation, an operating voltage of 40 kV, and a scanning rate of 0.02 2 θ /s. For this purpose, the same weight of each specimen in powdered form was delivered to XRD unit. The XRD patterns were assessed by X'Pert HighScore software, version 1.0d, 2003 (PANalytical B.V., Almelo, The Netherlands).

2.3.3. Chemical Groups. To investigate the structural characteristics of the specimens, Fourier-transform infrared (FTIR) spectroscopy was used with KBr powder as a standard. Transparent discs were prepared by mixing the sample and the standard KBr at the KBr/sample ratio of 10 (in w/w). The FTIR spectra of the specimens were collected at 4000–400 cm⁻¹ region with 2 cm⁻¹ resolution using Bruker Vector 33.

2.3.4. Microstructural Observations and Elemental Image Analysis. The microstructure of the pure gypsum and gypsum:Sr specimens were observed using a scanning electron microscope (TESCAN, VEGA II, XMU) operated at an accelerating voltage of 40 kV and equipped with energy dispersive X-ray analyzing (EDXA) device.

2.3.5. Density. The powder density of the specimens was measured using a gas pycnometer device (Accupyc 1330, Micromeritics). For this purpose the dried hardened samples were powdered, passed through a 230 mesh sieve, and then characterized.

2.3.6. Compressive Strength. To understand the effect of incorporation of Sr^{2+} ions into gypsum on its mechanical strength, gypsum:Sr cylindrical specimens (6 mm in diameter and 12 mm in height) were fabricated in Teflon mold as described in Section 2.2. Each sample was kept in a SBF solution for 24 h and the compressive strength of wet specimens was recorded using a universal testing device (Zwick/Roell-HCR 25/400) at a crosshead speed of 1 mm/min. In this study, the SBF solution with a chemical composition resembling that of human blood plasma (solution with ionic concentration of Na^+ 142.0, K^+ 5.5, Mg^{2+} 1.5, Ca^{2+} 2.5, Cl^- 147.8, HCO_3^- 4.2, HPO_4^{2-} 1.0 and SO_4^{2-} 0.5 mM) was prepared by dissolving the chemical reagents in distilled water, buffering it with tris-hydroxymethyl aminomethane and adjusting its pH to 7.4 using hydrochloric acid [22].

2.3.7. Solubility. The solubility of gypsum and gypsum:Sr specimens were investigated through immersing disc-shaped specimens in the SBF solution at solid to solution loading of 1.6 g/100 mL and measuring the concentration of Ca and Sr ions released from the specimens into the solution (using ICP-AES instrument) as a function of time. Note that after each evaluating period, the whole volume of the SBF solution was extracted for analysis and the sample was immediately fed with a fresh solution. Cumulative concentration of each ion was calculated using the following expression:

$$[\text{Sr}]_n = \sum_{i=1}^{i=n} [\text{Sr}]_i, \quad (1)$$

where $[\text{Sr}]_n$ is cumulative concentration of Sr ions at the n th period of evaluation and i is the evaluating time interval.

2.3.8. Cell Proliferation and Alkaline Phosphatase Activity. To study the effect of incorporation of strontium into gypsum biomaterial on the viability and alkaline phosphatase activity of the osteoblastic cells, the in vitro tests were carried out using the human osteosarcoma (G-292) cells (NCBI C 116 National Cell Bank of Iran). The cells were cultured in tissue culture polystyrene (PS) flasks (Falcon, USA) at 37°C under 5% CO_2 atmosphere in Dulbecco's modified Eagle's medium (DMEM) with l-glutamine, supplemented 10% fetal bovine serum (FBS) and antibiotic antimycotic (100 units penicillin G sodium, 100 mg streptomycin sulfate, and 0.25 mg amphotericin B in saline) and harvested after the treatment with 0.05% trypsin-EDTA.

The proliferation of osteoblast cells onto the gypsum specimens was measured by MTT assay. The samples were sterilized with 70% ethanol and seeded with the cells at 3×10^4 cells/disc. Polystyrene discs with the surface area similar to gypsum specimens were prepared from the tissue culture

plate and similarly were seeded with the cells as control specimens. The specimen/cell constructs were placed into 24-wells culture plates and left undisturbed in an incubator for 4 h to allow the cells to attach to them. Then, 3 mL of culture medium was added into each well and the cell/specimen constructs were cultured in a humidified incubator at 37°C with 95% air and 5% CO_2 for 1, 3, and 7 days. The medium was changed every 3 days. After each period, the medium was removed and 2 mL of MTT, 3-(4,5-dimethylthiazol-2-yl)-2,5-diphenyl tetrazolium bromide, solution was added to each well. Following incubation at 37°C for 4 h in a fully humidified atmosphere of 5% CO_2 /95% air, MTT was taken up by active cells and reduced in the mitochondria to insoluble purple formazan granules. Subsequently, the medium was discarded and the precipitated formazan was dissolved in dimethylsulfoxide, DMSO, (150 mL/well), and optical density of the solution was read using a microplate spectrophotometer (BIO-TEK Elx 800, Highland park, USA) at a wavelength of 570 nm. The optical density (OD) was measured at the wavelength of 590 nm using a multiwell microplate reader (ICN, Switzerland).

The osteoblast activity was determined by measuring the level of alkaline phosphatase (ALP) produced by G-292 cells. The cells were seeded on the samples under the same culturing condition described above and the level of ALP activity were determined on days 1, 3, and 7. The G-292 cell lysates were frozen and thawed three times to disrupt the cell membranes. ALP activity was determined at 405 nm using p-nitrophenyl phosphate in diethanolamide buffer as chromogenic substrate.

2.3.9. Statistical Analysis. Data were processed using Microsoft Excel 2003 software and the results were produced as mean \pm standard deviation of at least 4 experiments. Significance between the mean values was calculated using standard software program (SPSS GmbH, Munich, Germany) and the $P \leq 0.05$ was considered significant.

3. Results and Discussion

3.1. Concentration of Strontium in Sr-Doped Gypsum. In this study Sr-doped gypsum was prepared through conversion of calcium sulfate hemihydrate phase into calcium sulfate dihydrate through a hydraulic reaction at the presence of Sr solution. The mechanisms of gypsum formation have been discussed elsewhere [23]. The samples were kept in a 100% humid atmosphere until all starting hemihydrate phase is converted to dihydrate form (gypsum). The samples were washed with distilled water to avoid the presence of residual soluble strontium or calcium nitrates in the formed porous matrix. Table 2 presents the concentration of Ca and Sr elements in gypsum and gypsum:Sr measured by ICP technique. The Sr content increased with increasing the amount of added Sr salt. The molar concentration of Sr in the gypsum:Sr specimens is in the range of 0.4–5.2 mol% of Ca. The normal concentration of Sr in human skeleton is ~ 3.5 mol % of Ca [24]. The results can describe why the

TABLE 2: The weight percentage of Ca and Sr elements in various Sr-doped gypsum specimens (measured by ICP-AES technique).

	G-0	G-Sr1	G-Sr2	G-Sr3	G-Sr4
Ca (%)	22.11	21.79	21.65	20.18	19.79
Sr (%)	<10 p.p.m	0.19	0.38	1.11	2.23

strontium was not added in more concentrations than the selected values.

3.2. Phase Composition. Figure 1 shows the XRD patterns of the calcium sulfate specimens with various contents of Sr dopant after hardening and washing with distilled water. All specimens show sharp and narrow peaks of gypsum and no other phases are found in the patterns. The X-ray diffraction patterns of gypsum:Sr specimens reveal a shift to lower diffraction angles when Sr concentration is increased, indicating that Sr ions are incorporated into lattice structure of gypsum crystals. In comparison with pure gypsum, the X-ray diffraction patterns of Sr-doped gypsum specimens also show an increase in the intensity of the peaks at $2\theta = 11.8^\circ$ corresponding to 020 crystal planes which is indicative of a preferred direction of gypsum crystal growth during hydration process.

3.3. Chemical Groups. The FTIR spectra of pure gypsum and Sr-doped gypsum (G-Sr4) are shown in Figure 2. The spectrum of as-set G-Sr4 specimen (hardened specimen before washing with distilled water) and its spectrum once after washing with distilled water are also shown for comparison. The FTIR spectra show the stretching bands associated to the functional groups of the gypsum components, that is, H_2O and SO_4^{2-} groups labeled in the corresponding Figures. The FTIR spectra of all other Sr-doped gypsum specimens were closely similar to that of G-Sr4 and thus have not been illustrated. Decreased intensity of nitrate band once after washing and disappearance of this band after completion of the washing procedure confirms removal of the residual additive. As it is observed, the spectrum of gypsum:Sr is similar to the spectrum of pure gypsum and no extra bands are found.

3.4. Microstructural Observations and Elemental Image Analysis. The SEM images of the specimens along with their corresponding EDXA patterns are illustrated in Figures 3 to 6. Microstructure of pure gypsum (Figure 3(a)) was found to consist of many rod-like crystals entangled to each other and its corresponding EDXA pattern (Figure 3(b)) shows the presence of calcium and sulfur as main elements of gypsum as well as gold (Au) element created from the coating layer. Micrographs of Sr-doped gypsum specimens (Figure 4: G-Sr1, Figure 5: G-Sr2 and Figure 6: G-Sr4) show thicker rod-like crystals with more elongated and compacted morphologies compared to pure gypsum. In these images, the EDXA patterns taken from that crystal marked with an arrow reveal the presence of strontium dopant element in the composition of gypsum. Regarding uniform morphology

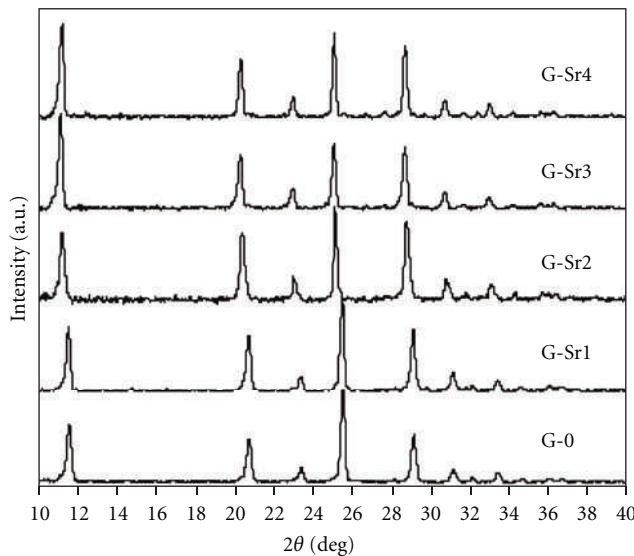


FIGURE 1: The XRD patterns of gypsum specimens with content of doped Sr.

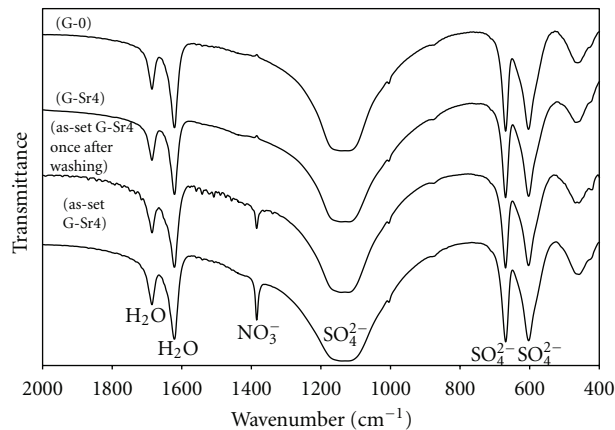


FIGURE 2: The FTIR spectra of pure gypsum (G-0) and Sr-doped gypsum (G-Sr4) in comparison with as-set G-Sr4 and G-Sr4 specimen once after washing procedure.

of the crystals and lack of other phases in the gypsum:Sr (from XRD data), these EDXA patterns can be used as complementary proofs for incorporation of Sr ions into lattice structure of gypsum.

3.5. Density. Figure 7 shows the effect of incorporation of Sr^{2+} ions into gypsum on its powder density. An increase in density of gypsum powder is observed by adding Sr in which the increase correlates with Sr concentration and the differences are statistically significant ($P < 0.05$). The increased powder density of Sr-doped gypsum in comparison with pure gypsum is due to the higher atomic weight of Sr (87.6 g/mol) compared to Ca (40.0 g/mol).

3.6. Compressive Strength. Figure 8 shows the compressive strength of the gypsum bioceramics doped with various

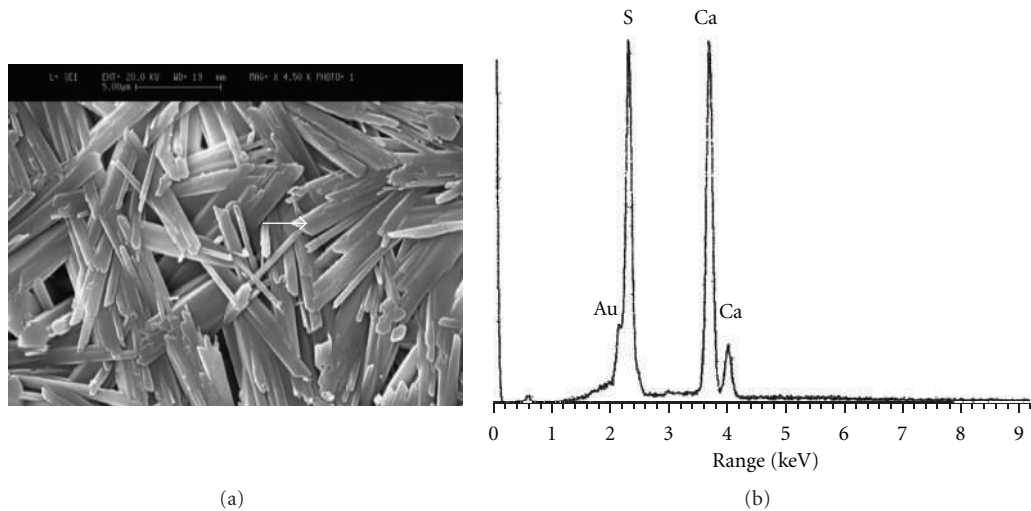


FIGURE 3: The SEM image of pure gypsum (a) along with its corresponding EDXA patterns (b).

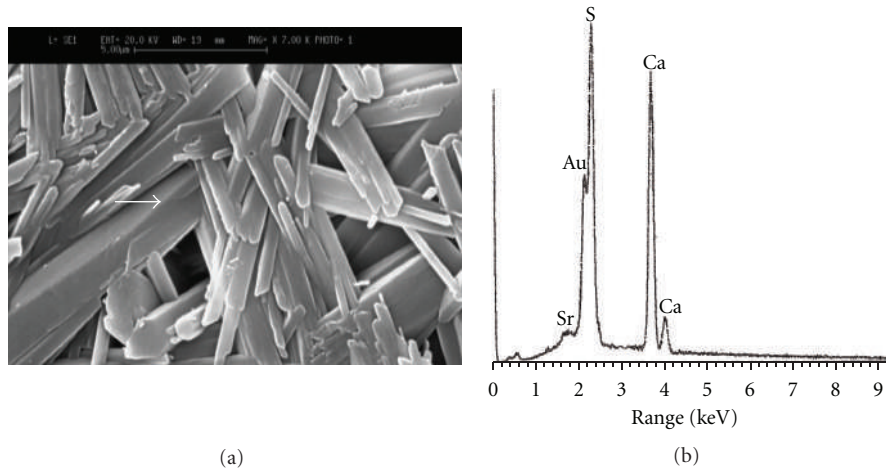


FIGURE 4: The SEM image of G-Sr1 specimen (a) along with its corresponding EDXA patterns (b).

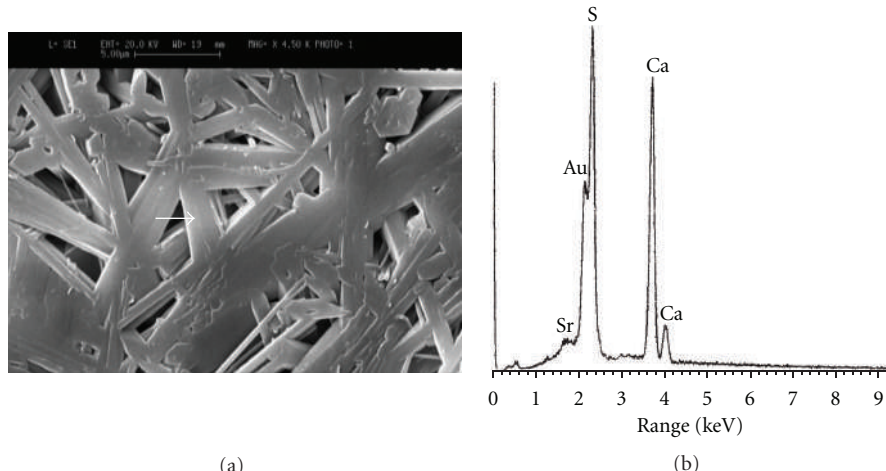


FIGURE 5: The SEM image of G-Sr2 specimen (a) along with its corresponding EDXA patterns (b).

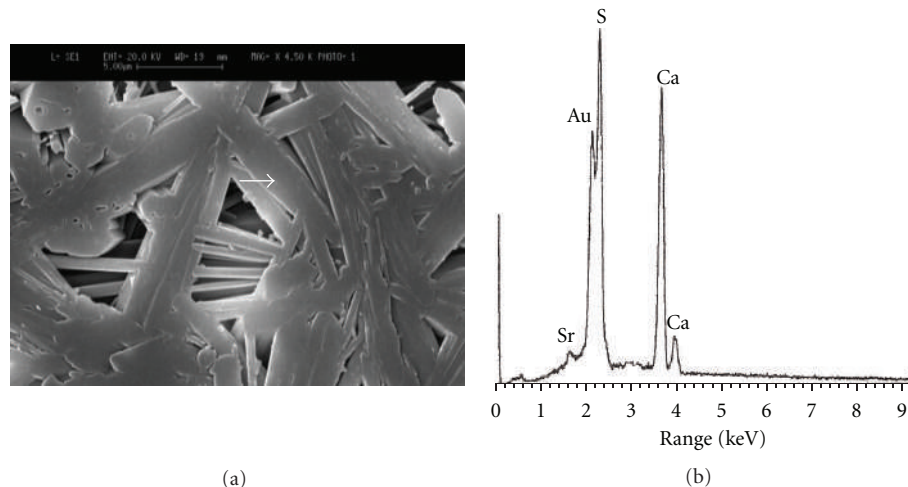


FIGURE 6: The SEM image of G-Sr4 specimen (a) along with its corresponding EDXA patterns (b).

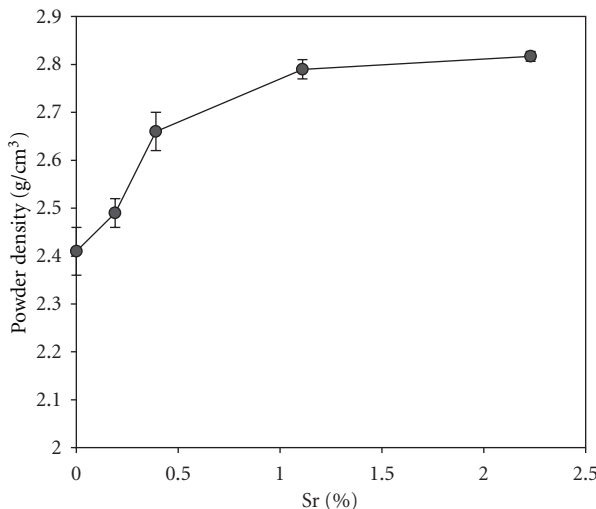


FIGURE 7: The powder density of gypsum specimens containing different contents of Sr dopant.

contents of strontium. There is no significant difference between the compressive strength values of the gypsum containing various amounts of Sr ($P > 0.05$). However the compressive strength value of pure gypsum is significantly lower than that of Sr-doped ones. Generally, mechanical strength of ceramic bodies is ruled by their microstructural features. In the case of calcium sulfate, entanglement of rod-like crystals is responsible for mechanical hardening phenomenon. These crystals are gypsum produced from conversion of calcium sulfate hemi-hydrate to calcium sulfate dihydrate through a dissolution-precipitation process [25]. The size (length and thickness) of these entangled crystals and their compression in the microstructure can affect the mechanical properties of gypsum. Note that thick and protracted crystals of gypsum:Sr tightly locked to each other (Figures 4 to 6) were to find why the compressive strength of pure gypsum is lower than that of gypsum:Sr.

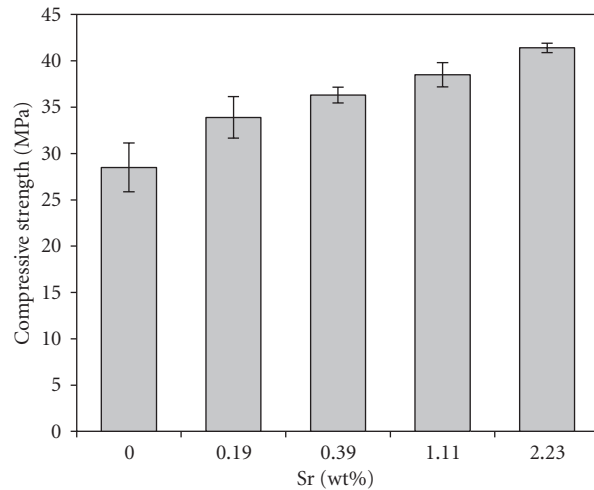


FIGURE 8: Compressive strength of gypsum specimens containing different contents of Sr dopant.

3.7. Solubility and Strontium Release. The ion release of gypsum ceramics in the SBF solution is shown in Figure 9. This experiment was carried out with periodic exchange of SBF solution and the results are presented as cumulative concentration of Ca (Figure 9(a)) and Sr (Figure 9(b)) against the immersion time. According to Figure 9(a), the concentration of Ca ions released from all gypsum specimens is much higher than that of other calcium phosphates reported in other studies [26]. It originates from the higher solubility and thus higher bioresorption rate of calcium sulfate-based materials in comparison with other well-known bioceramics such as β -tricalcium phosphate and hydroxyapatite. The concentration of Ca^{2+} ions released from pure gypsum (G-0) into the SBF solution was slightly higher than that of gypsum:Sr specimens. Since the calcium concentration is proportional to resorption rate of such bioceramics, the results demonstrate that incorporation of strontium ions

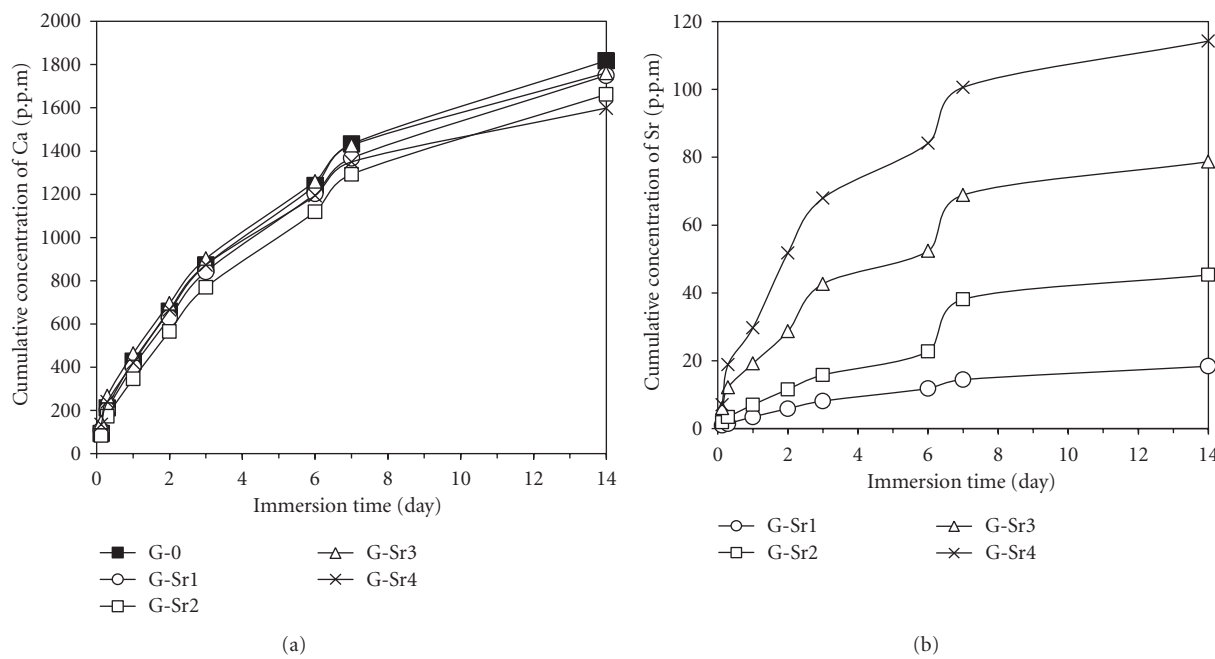


FIGURE 9: Cumulative concentration of Ca (a) and Sr (b) ions released from various Sr-doped specimens into the SBF solution.

into gypsum can diminish the biomaterial resorption rate. This decreased degradation rate of gypsum:Sr indicates higher chemical stability of these materials compared to pure gypsum. It is suggested that this is due to the complicated movement Ca ions in the crystal when encountering with Sr ions having larger atomic radius. The higher bonding strength of Sr-sulfate group in comparison with Ca-sulfate group should not be ignored too (note that Sr is more electronegative than Ca [27]). Calcium sulfate-based bioceramics have been used as potential materials for bone tissue regeneration, because of their adequate biocompatibility and osteoconductivity. However, the high degradation rate of these materials is the main practical problem [28], resulting in material to be lost in defect site before the completion of tissue repair. Incorporation of strontium into gypsum may control its too fast resorption rate to some extent.

The results clearly showed a continuous release of incorporated strontium ions into the SBF medium. It means that the gypsum can act as a suitable material for releasing Sr and stimulating osteoblastic cells and tissue repair. The concentration of Sr^{2+} ions in the SBF is proportional to the Sr content in the gypsum. At the end of the evaluation period (14 day), cumulative Sr release was 18 mg/g/L for G-Sr1 (about 4.7–8.9 mmol/g/day) and 114 mg/g/L for G-Sr4 (about 20–25 mmol/g/day). Regarding the therapeutic dose of Sr^{2+} (as strontium ranelate) which is in the range of 2.4–8.75 mmol/day (per kg of rat) for oral administration [4], the level of Sr^{2+} ions released from gypsum:Sr of this study is higher than that of Sr-substituted hydroxyapatite reported by Landi et al. [29] and comparable to that of Sr-doped betacalcium phosphate bioceramics reported by Alkhraisat et al. [26]. The concentration of the released Sr^{2+} ions should be in therapeutic range, because osteoclasts are inhibited by

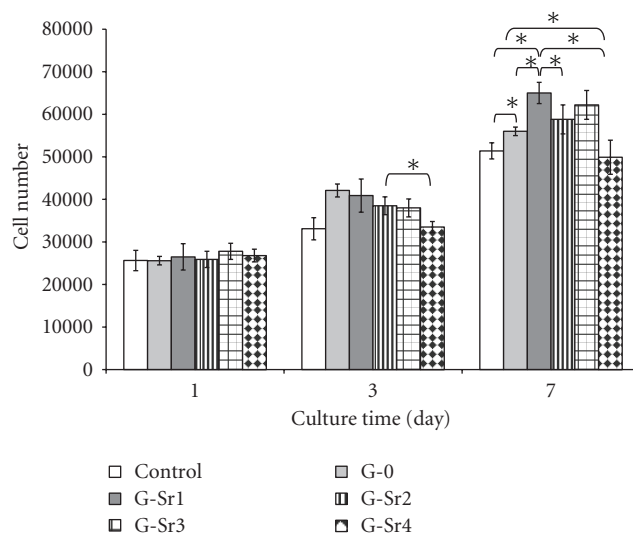


FIGURE 10: Proliferation of G-292 osteoblastic cells on gypsum specimens with various amounts of Sr dopant (* $P < 0.05$).

the effective dose of these ions. The maximum Sr/Ca molar ratio in the SBF is about 0.03, which is in the range of Sr/Ca in bone skeleton [24]. Generally, our results showed that the release of Sr^{2+} ions into an SBF and thus into a cell culture medium can be tailored by varying its concentration in gypsum crystals.

3.8. Cell Proliferation and Alkaline Phosphatase Activity. Figure 10 shows the results of G-292 cell proliferation on the polystyrene (control), pure gypsum, and Sr-doped

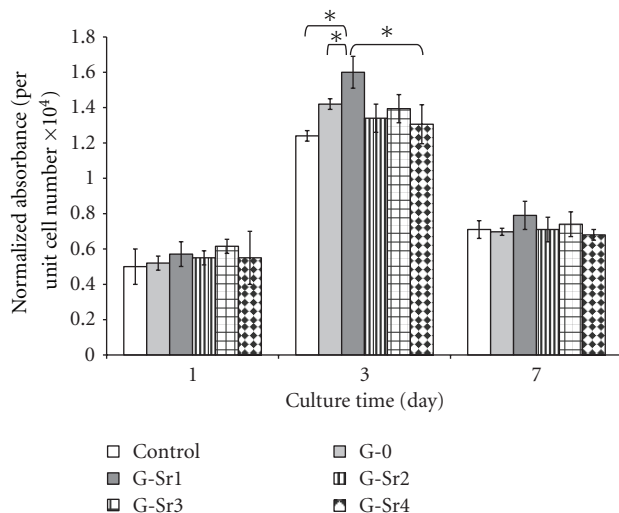


FIGURE 11: Normalized ALP activity of G-292 osteoblastic cells cultured on gypsum specimens with various amounts of Sr dopant (* $P < 0.05$).

gypsum specimens. After cell attachment, the osteoblasts proliferate on all specimens because of the difference in cell number between days 1, 3 and 7 ($P < 0.05$). In this study, it was found that the proliferation of the cells on gypsum specimens was significantly ($P < 0.05$) better than on control specimen, meanwhile the osteoblastic cells could proliferate on some gypsum:Sr discs at a significantly higher rate than on pure gypsum. Firstly, according to Lazáry et al. [21], physical structure of gypsum may be responsible for the suitable proliferation of osteoblastic cells onto the gypsum specimen. In other words, the cells can be attached onto the gypsum surfaces because it has been formed from Plaster of Paris (CaSO_4 -hemihydrate) by adding water and its microstructure is composed of too many rod-like small crystals entangled to each other to provide large specific surface area. Secondly, it has been proved that strontium ions can stimulate cellular responses and subsequently increase rate of cell proliferation process. In this study, the effect of Sr^{2+} on proliferation of osteoblastic cells was proved to be dose-dependent, because of the lower proliferation rate of the osteoblasts on G-Sr4 compared with other Sr-doped samples. It is in agreement with other studies [30].

Alkaline phosphatase is known as an early osteoblastic differentiation marker and is produced by the cells showing mineralized extracellular matrix [31]. Alkaline phosphatase activity of the osteoblasts is illustrated in Figure 11 as normalized absorbance number (per unit cell number) against the culture time. ALP activity of the osteoblasts cultured on gypsum specimens, especially G-Sr1, was better than those cultured on polystyrene. While higher ALP activity was found on G-Sr1 compared to gypsum, the difference in ALP value of pure gypsum and other Sr-doped gypsum specimens was not statistically significant ($P > 0.05$). Alkaline phosphatase activity was inhibited on day 7 for all specimens probably due to conflux of extended cell [16]. There are many studies that confirm this fact that strontium

ions incorporated into composition of bioceramics can improve proliferation and/or alkaline phosphatase activity of osteoblastic cells [32]. In this study, it was shown that the presence of Sr^{2+} ions in the lattice structure of gypsum could also play important role in proliferation and ALP activity of G-292 osteoblastic cells.

4. Conclusions

Calcium sulfate dihydrate (gypsum) bioceramics with improved compressive strength and cellular properties are obtained by doping various concentrations of strontium into crystal lattice of the material. Incorporation of strontium into gypsum affects its crystal morphology and water solubility. The Sr-doped gypsum was found to be useful as strontium releasing material with a continuous release profile in which amount of the liberated strontium is dependent of its concentration in host material. Both proliferation rate and alkaline phosphatase activity of human osteosarcoma cells on gypsum:Sr can be improved by incorporation of strontium, depending on the Sr dose in the host lattice. These observations can also predict better in vivo functions of strontium-doped gypsum compared to pure gypsum which requires more investigations.

References

- [1] S. G. Dahl, P. Allain, P. J. Marie et al., "Incorporation and distribution of strontium in bone," *Bone*, vol. 28, no. 4, pp. 446–453, 2001.
- [2] S. Pors Nielsen, "The biological role of strontium," *Bone*, vol. 35, no. 3, pp. 583–588, 2004.
- [3] R. Rizzoli, "A new treatment for post-menopausal osteoporosis: strontium ranelate," *Journal of Endocrinological Investigation*, vol. 28, no. 8, pp. 50–57, 2005.
- [4] P. J. Marie, P. Ammann, G. Boivin, and C. Rey, "Mechanisms of action and therapeutic potential of strontium in bone," *Calcified Tissue International*, vol. 69, no. 3, pp. 121–129, 2001.
- [5] O. Suzuki, H. Imaizumi, S. Kamakura, and T. Katagiri, "Bone regeneration by synthetic octacalcium phosphate and its role in biological mineralization," *Current Medicinal Chemistry*, vol. 15, no. 3, pp. 305–313, 2008.
- [6] Z. Huan and J. Chang, "Calcium-phosphate-silicate composite bone cement: self-setting properties and in vitro bioactivity," *Journal of Materials Science*, vol. 20, no. 4, pp. 833–841, 2009.
- [7] T. Yu, J. Ye, and Y. Wang, "Synthesis and property of a novel calcium phosphate cement," *Journal of Biomedical Materials Research—Part B*, vol. 90, no. 2, pp. 745–751, 2009.
- [8] A. Bigi, E. Foresti, M. Gandolfi, M. Gazzano, and N. Roveri, "Isomorphous substitutions in β -tricalcium phosphate: the different effects of zinc and strontium," *Journal of Inorganic Biochemistry*, vol. 66, no. 4, pp. 259–265, 1997.
- [9] S. Jegou Saint-Jean, C. L. Camiré, P. Nevsten, S. Hansen, and M. P. Ginebra, "Study of the reactivity and in vitro bioactivity of Sr-substituted α -TCP cements," *Journal of Materials Science*, vol. 16, no. 11, pp. 993–1001, 2005.
- [10] Y. W. Li, J. C. Y. Leong, W. W. Lu et al., "A novel injectable bioactive bone cement for spinal surgery: a developmental and preclinical study," *Journal of Biomedical Materials Research*, vol. 52, no. 1, pp. 164–170, 2000.

- [11] D. Guo, K. Xu, X. Zhao, and Y. Han, "Development of a strontium-containing hydroxyapatite bone cement," *Biomaterials*, vol. 26, no. 19, pp. 4073–4083, 2005.
- [12] K. M. C. Cheung, W. W. Lu, K. D. K. Luk et al., "Vertebraloplasty by use of a strontium-containing bioactive bone cement," *Spine*, vol. 30, no. 17, pp. S84–S91, 2005.
- [13] C. T. Wong, W. W. Lu, W. K. Chan et al., "In vivo cancellous bone remodeling on a Strontium-containing hydroxyapatite (Sr-HA) bioactive cement," *Journal of Biomedical Materials Research—Part A*, vol. 68, no. 3, pp. 513–521, 2004.
- [14] W. Xue, H. L. Hosick, A. Bandyopadhyay et al., "Preparation and cell-materials interactions of plasma sprayed strontium-containing hydroxyapatite coating," *Surface and Coatings Technology*, vol. 201, no. 8, pp. 4685–4693, 2007.
- [15] E. A. Abou Neel, W. Chrzanowski, D. M. Pickup et al., "Structure and properties of strontium-doped phosphate-based glasses," *Journal of the Royal Society Interface*, vol. 6, no. 34, pp. 435–446, 2009.
- [16] S. Hesaraki, M. Alizadeh, H. Nazarian, and D. Sharifi, "Physico-chemical and in vitro biological evaluation of strontium/calcium silicophosphate glass," *Journal of Materials Science*, vol. 21, no. 2, pp. 695–705, 2010.
- [17] D. Anson, "Using calcium sulfate in guided tissue regeneration: a recipe for success," *Compendium of Continuing Education in Dentistry*, vol. 21, no. 5, pp. 365–372, 2000.
- [18] S. J. Bier and M. C. Sinensky, "The versatility of calcium sulfate: resolving periodontal challenges," *Compendium of Continuing Education in Dentistry*, vol. 20, no. 7, pp. 655–662, 1999.
- [19] G. Pecora, S. Andreana, J. E. Margarone, U. Covani, and J. S. Sottosanti, "Bone regeneration with a calcium sulfate barrier," *Oral Surgery, Oral Medicine, Oral Pathology, Oral Radiology, and Endodontics*, vol. 84, no. 4, pp. 424–429, 1997.
- [20] S. Paderni, S. Terzi, and L. Amendola, "Major bone defect treatment with an osteoconductive bone substitute," *La Chirurgia Degli Organi di Movimento*, vol. 93, no. 2, pp. 89–96, 2009.
- [21] A. Lazáry, B. Balla, J. P. Kósa et al., "Effect of gypsum on proliferation and differentiation of MC3T3-E1 mouse osteoblastic cells," *Biomaterials*, vol. 28, no. 3, pp. 393–399, 2007.
- [22] T. Kokubo, H. Kushitani, S. Sakka, T. Kitsugi, and T. Yamamuro, "Solutions able to reproduce in vivo surface-structure changes in bioactive glass-ceramic A-W3," *Journal of Biomedical Materials Research*, vol. 24, no. 6, pp. 721–734, 1990.
- [23] S. Hesaraki, F. Moztarzadeh, and N. Nezafati, "Evaluation of a bioceramic-based nanocomposite material for controlled delivery of a non-steroidal anti-inflammatory drug," *Medical Engineering and Physics*, vol. 31, no. 10, pp. 1205–1213, 2009.
- [24] P. Fourman, P. Royer, M. Levell, and D. B. Morgan, *Calcium Metabolism and the Bone*, Blackwell, Oxford, UK, 2nd edition, 1968.
- [25] S. Hesaraki, F. Moztarzadeh, R. Nemati, and N. Nezafati, "Preparation and characterization of calcium sulfate-biomimetic apatite nanocomposites for controlled release of antibiotics," *Journal of Biomedical Materials Research—Part B*, vol. 91, no. 2, pp. 651–661, 2009.
- [26] M. Hamdan Alkhraisat, C. Moseke, L. Blanco, J. E. Barralet, E. Lopez-Carbaos, and U. Gbureck, "Strontium modified biocements with zero order release kinetics," *Biomaterials*, vol. 29, no. 35, pp. 4691–4697, 2008.
- [27] D. Boyd, M. R. Towler, S. Watts, R. G. Hill, A. W. Wren, and O. M. Clarkin, "The role of Sr²⁺ on the structure and reactivity of SrO-CaO-ZnO-SiO₂ ionomer glasses," *Journal of Materials Science*, vol. 19, no. 2, pp. 953–957, 2008.
- [28] M. A. Rauschmann, T. A. Wichelhaus, V. Stirnal et al., "Nanocrystalline hydroxyapatite and calcium sulphate as biodegradable composite carrier material for local delivery of antibiotics in bone infections," *Biomaterials*, vol. 26, no. 15, pp. 2677–2684, 2005.
- [29] E. Landi, A. Tampieri, G. Celotti, S. Sprio, M. Sandri, and G. Logroscino, "Sr-substituted hydroxyapatites for osteoporotic bone replacement," *Acta Biomaterialia*, vol. 3, no. 6, pp. 961–969, 2007.
- [30] W. Xue, J. L. Moore, H. L. Hosick et al., "Osteoprecursor cell response to strontium-containing hydroxyapatite ceramics," *Journal of Biomedical Materials Research—Part A*, vol. 79, no. 4, pp. 804–814, 2006.
- [31] G. S. Stein, J. B. Lian, and T. A. Owen, "Relationship of cell growth to the regulation of tissue-specific gene expression during osteoblast differentiation," *The FASEB Journal*, vol. 4, no. 13, pp. 3111–3123, 1990.
- [32] H. W. Kim, Y. H. Koh, Y. M. Kong, J. G. Kang, and H. E. Kim, "Strontium substituted calcium phosphate biphasic ceramics obtained by a powder precipitation method," *Journal of Materials Science*, vol. 15, no. 10, pp. 1129–1134, 2004.

Synthesis, Characterization, Mössbauer Parameters, and Antitumor Activity of Fe(III) Curcumin Complex

Mutasim Ibrahim Khalil, Aisha Mohamed Al-Zahem, and Maha Hamad Al-Qunaibit

Chemistry Department, King Saud University, Riyadh 11451, Saudi Arabia

Correspondence should be addressed to Mutasim Ibrahim Khalil; mkhalil@ksu.edu.sa

Academic Editor: Giovanni Natile

Curcumin-Fe(III) complex was prepared from $\text{Fe}(\text{NO}_3)_3 \cdot 9\text{H}_2\text{O}$ precursor and curcumin by refluxing a slightly basic methanolic solution of their mixture with the objective of investigating its cytotoxicity. The enol form of curcumin ligand was established by FTIR, UV/Vis, ^1H NMR, and ^{13}C NMR spectroscopy. The as-prepared product was characterized by elemental analysis, FTIR, UV, and Mössbauer spectroscopic techniques. An octahedral high-spin Fe(III) complex was obtained, δ , 0.37 mm s^{-1} ; Q.S., 0.79 mm s^{-1} ; no magnetic relaxation was observed at liquid N_2 temperature, neither reduction of Fe(III). The tested cytotoxicity of the as-prepared complex on four cancer cell lines indicated inhibition of the curcumin activity upon complexing with iron.

1. Introduction

The β diketone curcumin and curcuminoids (1,7-diaryl-1,6-heptadiene-3,5-diones) which are a group of naturally occurring 1,3-diketones have received considerable attention in the last few decades. This is due to the fact that they possess antitumor [1–3] and antioxidant effects [4] and have a good potential for metal ions complexation.

It has been reported that metal complexation alters the various physiological properties especially the cytotoxic and antitumor activities of many naturally occurring compounds [5]. It is demonstrated that the coordination of metal ions, for example, Cu(II), Mn(II), Au(III), and so forth, with bioactive ligands can actually improve the pharmaceutical activity of drugs [6, 7].

The Mössbauer metal isotopes, for example, Fe, Au, Ru, Ir, and so forth, form stable complexes with the curcumin ligand [8, 9]. Tonnesen and Greenhill [8] have reported the reduction of Fe(III) to Fe(II) in the presence of curcumin. However, there is no published Mössbauer data on such complexes that could shed light on iron moiety and the correlation between the magnetic, symmetry, and oxidation states of metal ions in such chelates and their biological activity. In this paper we report the Mössbauer data of $\text{Fe}(\text{curc})_3$ complex, compare it to the well-known $\text{Fe}(\text{acac})_3$

data, and identify and correlate oxidation state of the central iron metal ion, magnetic relaxation, and structural symmetry of the as-prepared complex to its antitumor cytotoxicity on four cancer cell lines.

2. Experimental

2.1. Chemicals and Materials. All solvents (Sigma-Aldrich) were reagent grades and were used without further purifications. Curcumin (Sigma-Aldrich and Acros Organics) was extensively analyzed and the Sigma sample form was established. $\text{Fe}(\text{NO}_3)_3 \cdot 9\text{H}_2\text{O}$ (BDH) laboratory reagent was used.

2.2. Analytical Instruments. FTIR spectra were recorded in the solid state (KBr pellets) in the range $250\text{--}4000 \text{ cm}^{-1}$ using a Shimadzu FTIR-8400S, Prestige-21 spectrophotometer. UV/Vis spectra were recorded on a Shimadzu UV-1650 PC spectrophotometer in the range $200\text{--}800 \text{ nm}$. ^1H and ^{13}C NMR were recorded on a Jeol Eclipse 400 MHz instrument using TMS external standard (chemical shift δ in ppm). C, H, N, O, and iron analysis was carried at Mikroanalytisches Labor Pascher, Remagen Laboratories. The ^{57}Fe Mössbauer absorption spectra were recorded at 295 K and 78 K using

TABLE 1: Mössbauer parameters of $\text{Fe}(\text{acac})_3$ and $\text{Fe}(\text{curc})_3$ complexes.

Sample/temperature	I.S. (mm/s)	Q.S. (mm/s)	Γ (mm/s)
$\text{Fe}(\text{Curcumin})_3$ (295 K)	0.37	0.79	0.51
$\text{Fe}(\text{Curcumin})_3$ (78 K)	0.46	0.96	0.62
$\text{Fe}(\text{acac})_3$ (295 K)	0.36	0.82	0.49
$\text{Fe}(\text{acac})_3$ (78 K)	0.44	0.94	0.33

a Harwell Mössbauer spectrometer. The spectra were refined using least square method.

2.3. Cytotoxic Activity Measurements. Cytotoxic activity measurements were carried out in Cairo Cancer Research Center, Egypt. The determination and counting of viable cells were achieved by adding 50 μL of 0.05% trypan blue solution to 50 μL of the single cell suspension. The cells were examined under the inverted microscope using the hemocytometer. Nonstained (viable) cells were counted and the following equation was used to calculate the cell count/mL of cell suspension:

$$\text{viable cells/mL} = \frac{\text{number of cells 4 quarters} \times 2 (\text{dilution factor}) \times 10^4}{4}. \quad (1)$$

The cells were then diluted to give the concentration of single cell suspension required for each experiment.

The percentage of cell survival was calculated as follows:

- (i) survival fraction = O.D. (treated cells)/O.D. (control cells),
- (ii) the IC_{50} values are the concentrations of thymoquinone required to produce 50 inhibitions of cell growth. The experiment was repeated 3 times for each cell line.

2.4. Synthesis of $\text{Fe}(\text{III})(\text{acac})_3$ and $\text{Fe}(\text{III})(\text{curc})_3$ Complexes. The $\text{Fe}(\text{III})(\text{acac})_3$ complex was prepared by dissolving 2.1 g of finely ground iron(III) chloride hexahydrate in 50 mL distilled water in a 250 mL beaker. 0.1 M NaOH solution was added dropwise until the brown precipitate that was formed is completely redissolved. 2.4 mL of acetylacetone in 20 mL ethanol was then added dropwise with continuous magnetic string followed by the addition of 3.3 g sodium acetate in 15 mL distilled water. The whole mixture was heated in a water bath to $\approx 80^\circ\text{C}$ and maintained at that temperature for 1 h with rapid stirring. The solution was then cooled to room temperature and cooled further in an ice bath. The red crystals were vacuum filtered and dried in a desiccator [10, 11]. The complex was characterized by elemental analysis, (found; C%, 50.6; H%, 6.3; yield%, 72), FTIR spectroscopy (see supporting information available online at <http://dx.doi.org/10.1155/2013/982423>), and Mössbauer spectroscopy, Figure 1 and Table 1. $\text{Fe}(\text{III})(\text{curc})_3$ complex was prepared by refluxing for 3 h in a methanolic mixture solution of 0.6 mmol curcumin and 0.2 mmol $\text{Fe}(\text{III})(\text{NO}_3)_3 \cdot 9\text{H}_2\text{O}$

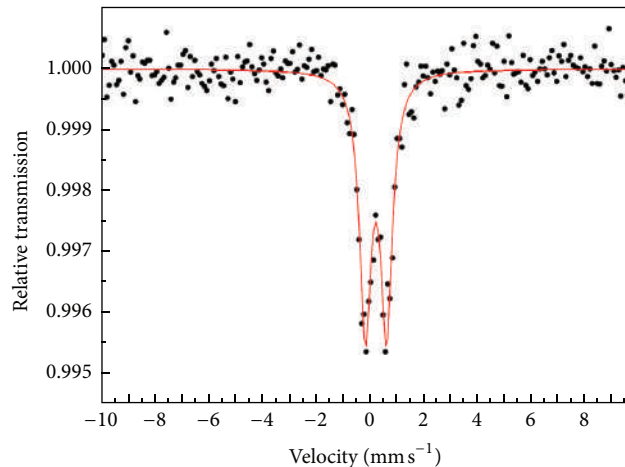


FIGURE 1: The room Temperature (295 K) Mössbauer spectrum of $\text{Fe}(\text{III})(\text{curc})_3$.

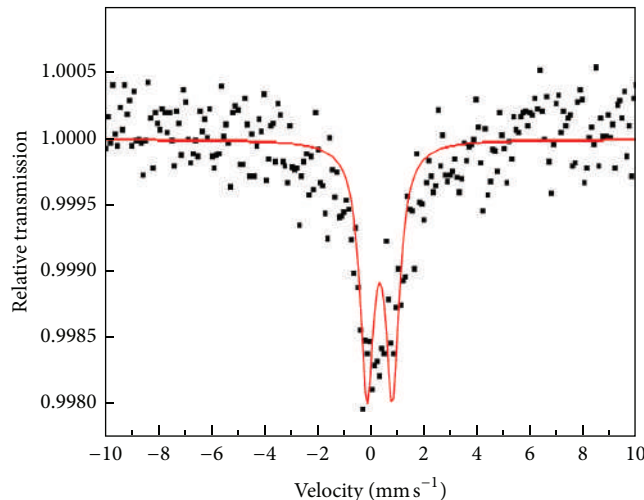


FIGURE 2: The room temperature (295 K) Mössbauer spectrum of the $\text{Fe}(\text{III})(\text{acac})_3$.

that was made slightly basic by the addition of few drops of triethylamine. The deep red brown solid product was vacuum filtered, washed with methanol, and dried in vacuum at room temperature overnight. The complex was characterized by elemental analysis, FTIR (supporting information), and Mössbauer spectroscopy, Figure 2 and Table 1. The elemental analytical data are consistent with the formulation: $\text{Fe}[\text{C}_{21}\text{H}_{19}\text{O}_6]_3 \cdot 2\text{H}_2\text{O}$. found, (calc): C%, 63.02, (63.36); H%, 5.06, (5.10); O%, 26.20, (26.79); Fe%, 5.02, (4.68).

TABLE 2: Surviving fraction of cancer cells at various concentrations ($\mu\text{g/mL}$).

Cancer line	Compound	Concentration			
		0	5	12.5	25
HCT-116	Dox	1.000000	0.321921	0.255892	0.170503
	Curcumin	1.000000	0.337999	0.210925	0.210925
	$\text{Fe}(\text{curc})_3$	1.000000	0.634077	0.596687	0.248749
HEPG2	Dox	1.000000	0.340080	0.301258	0.193985
	Curcumin	1.000000	0.293962	0.149182	0.236437
	$\text{Fe}(\text{curc})_3$	1.000000	0.969865	0.600591	0.228678
Hela	Dox	1.000000	0.203353	0.190643	0.080675
	Curcumin	1.000000	0.260466	0.164231	0.186826
	$\text{Fe}(\text{curc})_3$	1.000000	0.933095	0.679533	0.226367
MCF7	Dox	1.000000	0.194273	0.171715	0.185526
	Curcumin	1.000000	0.140455	0.118242	0.145352
	$\text{Fe}(\text{curc})_3$	1.000000	0.869626	0.737578	0.357802

3. Results and Discussion

The Mössbauer effect is the most reliable technique to identify the oxidation state of iron ions in complexes. The Mössbauer absorption spectrum of the as-prepared curcumin-iron(III) complexes is of similar pattern showing a quadrupole-split doublet of equal intensities and chemical isomer shifts characteristic of octahedral high-spin iron(III) [12–15], Figures 1 and 2 and Table 1.

The absence of any magnetic components at liquid nitrogen temperature rules out the existence of magnetic relaxation. There is no Mössbauer effect evidence that Fe(III) is reduced to Fe(II) in the presence of curcumin as reported in the literature [8]. The Fe^{2+} ion, if present, should show a doublet having an isomer shift of 1.2 mm/s and a quadrupole of 2.9 mm/s [14].

The FTIR and ^1H NMR spectroscopic measurements have confirmed the enol form of curcumin (supporting information). The FTIR spectrum of $\text{Fe}(\text{III})(\text{curc})_3$ complex lost the 3423 cm^{-1} band assigned to $\nu(\text{O}-\text{H})$ of the enol form with the persistence of the phenolic (OH) group vibrational band strongly indicating that it is not coordinated to the metal ion (supporting information). The chemistry of curcumin solution system is pH dependent. Tonnesen and Karlsen [16] have studied the stability of curcumin in the pH range from 1 to 11. They have postulated that curcumin is in equilibrium between three forms, that is, H_3Curc ; H_2Curc^- ; $\text{HC}\text{Curc}^{2-}$, at pH area 8.2–8.5. They reported a 50% degradation of curcumin in a 0.1% NaOH solution. Pineda et al. [17] measured three acidity constants for curcumin. The one corresponding to the equilibrium $\text{H}_3\text{Curc} \leftrightarrow \text{H}_2\text{Curc}^- + \text{H}^+$ [$\text{p}K_a = 8.38$] was attributed to the acetylacetone-type group. Such a dependence of curcumin system on pH of solution means that the H^+ ion is involved in reaction mechanism. However, there are some controversies on which proton(s) is involved. While Tonnesen et al. [18] concluded that complex formation between curcumin and iron and the reduction of Fe^{3+} to Fe^{2+} in the presence of curcumin are independent of the phenolic hydroxyl groups in the curcumin molecule, Barclay et al. [19] reported that synthetic nonphenolic curcumin exhibited no

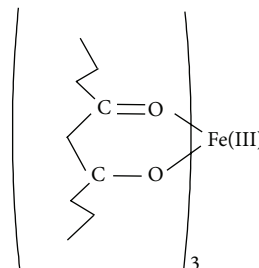


FIGURE 3: Bidentate coordination of curcumin ligand to Fe(III) ion.

antioxidant activity deducing that the H atoms are donated from the phenolic groups. On the other hand, Jovanovic et al. [20] suggested the release of H atoms from CH_2 group.

Accordingly, we envisage that the number of protons released by the curcumin enol form determines the type of product. Hence, the three curcumin ligands are coordinated to the iron(III) ion in a bidentate fashion forming the octahedral geometry indicated by the measured Mössbauer parameters, Figure 3.

The antitumor activity of such an established octahedral high-spin iron(III) complex was tested against four cancer cell lines, that is, MCT-7, HepG-2, Hela, and HCT-116. Their activities were compared to doxorubicin (DOX) and pure curcumin. The calculated IC_{50} values indicated that metal complexation inhibits the cytotoxicity of curcumin, Tables 2 and 3. Table 2 presents the survival fractions of the four cancer cell lines at different concentrations of inhibitors, and the calculated IC_{50} values are presented in Table 3.

Curcumin alone showed higher antioxidant effect towards all four tumor cell lines at IC_{50} values of 3.02 (MCF-7) , 3.43 (HepG2) , 3.43 (Hela) , and $3.81\text{ (HCT-116)}\text{ }\mu\text{g mL}^{-1}$, than both curcumin-iron(III) complexes (see supporting information). These results are in contrast with the reported concept of synergistic enhancement of ligand effects by combination with ions [5–7, 21–23]. One may relate the lower cytotoxicity of the curcumin-iron complexes compared to curcumin alone to the fact that the central carbon atom

TABLE 3: Cytotoxicity on cancer cell lines.

	IC ₅₀ value (µg/mL)			
	Cancer cells			
	MCF-7	HepG-2	HeLa	HCT-116
DOX	2.97	4.57	3.64	3.743
Curcumin	3.02	3.43	3.43	3.81
Fe(curc) ₃	20.4	15.8	17.6	16
Fe(acac) ₃	22.0	20.1	21.3	21.0

with the labile hydrogen is locked and unable to produce oxyradicals unless the curcumin ligand dissociates from the complex. It is more likely that the keto-enol function but not the phenol OH group directs curcumin cytotoxic behavior.

It is worth mentioning that metal acetates or chlorides are the reagents used by research workers for the synthesis of curcumin-metal complexes although Pineda et al. [17] did not specify the iron salt employed in their study.

Then, one cannot rule out at this stage the role of the oxidizing nitrate groups in inhibiting the reduction of Fe³⁺ ions by curcumin. It is the reaction suggested by Pineda et al. [17] to take place prior to complex formation.

The IC₅₀ values of both iron complexes, being of comparable values, could be attributed to the antioxidant potential of iron(III) ion. Hence, one can conclude that the diketone system of curcumin appears to be the part of the curcumin molecule involved in the scavenging of oxygen radicals.

Conflict of Interests

The authors declare that they have no conflict of interests arising from any financial relation with the commercial identity mentioned in this paper.

Acknowledgment

This project was supported by King Saud University, Deanship of Scientific Research, College of Science, Research Center.

References

- [1] R. H. Liu, "Potential synergy of phytochemicals in cancer prevention: mechanism of action," *Journal of Nutrition*, vol. 134, no. 12, pp. 3479S–3485S, 2004.
- [2] B. K. Adams, E. M. Ferstl, M. C. Davis et al., "Synthesis and biological evaluation of novel curcumin analogs as anti-cancer and anti-angiogenesis agents," *Bioorganic and Medicinal Chemistry*, vol. 12, no. 14, pp. 3871–3883, 2004.
- [3] E. R. Hahm, Y. S. Gho, S. Park, C. Park, K. W. Kim, and C. H. Yang, "Synthetic curcumin analogs inhibit activator protein-1 transcription and tumor-induced angiogenesis," *Biochemical and Biophysical Research Communications*, vol. 321, no. 2, pp. 337–344, 2004.
- [4] S. V. Jovanovic, C. W. Boone, S. Steenken, M. Trinoga, and R. B. Kaskey, "How curcumin works preferentially with water soluble antioxidants," *Journal of the American Chemical Society*, vol. 123, no. 13, pp. 3064–3068, 2001.
- [5] K. H. Thompson, K. Böhmerle, E. Polishchuk et al., "Complementary inhibition of synoviocyte, smooth muscle cell or mouse lymphoma cell proliferation by a vanadyl curcumin complex compared to curcumin alone," *Journal of Inorganic Biochemistry*, vol. 98, no. 12, pp. 2063–2070, 2004.
- [6] S. Zhang, C. Tu, and X. Wang, "Novel C ytotoxic Copper(II) complexes of 8-aminoquinoline derivatives: crystal structure and different reactivity towards Glu tathioneInorg," *European Journal of Chemistry*, vol. 98, pp. 4028–4035, 2004.
- [7] S. Dutta, A. Murugkar, N. Gandhe, and S. Padhye, "Enhanced antioxidant activities of metal conjugates of Curcumin derivatives," *Metal-Based Drugs*, vol. 8, no. 4, pp. 183–188, 2001.
- [8] H. H. Tonnesen and J. V. Greenhill, "Studies on curcumin and curcuminoids. XXII: curcumin as a reducing agent and as a radical scavenger," *International Journal of Pharmaceutics*, vol. 87, no. 1–3, pp. 79–87, 1992.
- [9] K. K. Sharma, S. Chandra, and D. K. Basu, "Synthesis and antiarthritic study of a new orally active diferuloyl methane (curcumin) gold complex," *Inorganica Chimica Acta*, vol. 135, no. 1, pp. 47–48, 1987.
- [10] A. Hantzsch and C. H. Desch, *Annalen*, vol. 1, American Chemical Society, Washington, DC, USA, 1902.
- [11] J. Josepg, H. A. C. Mckay, and E. J. W. Verwey, "The infrared spectra of metal acetylacetones in the sodium chloride region," *Journal of Inorganic and Nuclear Chemistry*, vol. 5, pp. 295–303, 1958.
- [12] M. I. Khalil and A. I. AL-Wassil, "The Nature of iron moiety, a mossbauer spectroscopic investigation," *Journal of the Serbian Chemical Society*, vol. 3, pp. 19–25, 1999.
- [13] M. W. Hisham and F. J. Berry, "The influence of ball milling and subsequent calcination on the formation of LiFeO₂," *Journal of Materials Science*, vol. 37, no. 21, pp. 4621–4625, 2002.
- [14] E. Murad and R. M. Taylor, "The Mossbauer spectra of hydroxycarbonate green rusts," *Clay Minerals*, vol. 19, no. 1, pp. 77–83, 1984.
- [15] C. W. Childs and J. H. Johnston, "Mossbauer spectra of proto-ferrihydrite at 77K and 295K," *Australian Journal of Soil Research*, vol. 18, pp. 245–250, 1980.
- [16] H. H. Tonnesen and J. Karlsen, "Studies on curcumin and curcuminoids," *Zeitschrift für Lebensmittel-Untersuchung und -Forschung*, vol. 180, pp. 402–404, 1985.
- [17] M. B. Pineda, M. T. R. Silva, M. R. Romo, E. G. Verqara, and A. R. Hennandez, "Spectroscopica," *Chemica Acta A*, vol. 60, no. 5, pp. 1091–1097, 2004.
- [18] H. H. Tonnesen, J. Karlsenand, and G. B. Henegouwer, "Studies on curcumin and curcuminoids VIII. Photochemical stability of curcumin," *Zeitschrift für Lebensmittel-Untersuchung und -Forschung*, vol. 183, no. 2, pp. 116–122, 1986.
- [19] L. R. C. Barclay, M. R. Vinqvist, K. Mukai et al., "On the antioxidant mechanism of curcumin: classical methods are

- needed to determine antioxidant mechanism and activity,” *Organic Letters*, vol. 2, no. 18, pp. 2841–2843, 2000.
- [20] S. V. Jovanovic, S. Steenken, C. W. Boone, and M. G. Simic, “H-atom transfer is a preferred antioxidant mechanism of curcumin,” *Journal of the American Chemical Society*, vol. 121, no. 41, pp. 9677–9681, 1999.
- [21] X. Sheng, X. M. Lu, Y. T. Chen et al., “Synthesis, DNA-binding, cleavage, and cytotoxic activity of new 1,7-dioxa-4,10-diazacyclododecane artificial receptors containing bisguanidinoethyl or diaminoethyl double side arms,” *Chemistry*, vol. 13, no. 34, pp. 9703–9712, 2007.
- [22] A. Valentini, F. Conforti, A. Crispini et al., “Synthesis, oxidant properties, and antitumoral effects of a heteroleptic palladium(II) complex of curcumin on human prostate cancer cells,” *Journal of Medicinal Chemistry*, vol. 52, pp. 484–491, 2009.
- [23] G. Federici, S. Bernadini, and D. Pucci, “Effects of a heteroleptic palladium (II) complex of curcumin on human prostate cancer cells,” *Journal of Solid State Chemistry*, vol. 160, pp. 230–236, 2002.

Thermodynamic Investigation and Mixed Ligand Complex Formation of 1,4-Bis-(3-aminopropyl)-piperazine and Biorelevant Ligands

**Ahmed A. El-Sherif, Mohamed R. Shehata, Mohamed M. Shoukry,
and Mohammad H. Barakat**

Department of Chemistry, Faculty of Science, Cairo University, Giza 12613, Egypt

Correspondence should be addressed to Ahmed A. El-Sherif, aelsherif72@yahoo.com

Academic Editor: Anastasios Keramidas

Thermodynamic parameters for protonation of 1,4-bis(3-aminopropyl)-piperazine (BAPP) and its metal complexation with some divalent metal ions were determined in aqueous solution at constant ionic strength (0.1 M NaNO₃) using a potentiometric technique. The order of $-\Delta G^{\circ}$ and $-\Delta H^{\circ}$ was found to obey Co²⁺ < Ni²⁺ < Cu²⁺ > Zn²⁺, in accordance with the Irving-Williams order. The formation equilibria of zinc (II) complexes and the ternary complexes Zn(BAPP)L, where L = amino acid, amides, or DNA constituents, have been investigated. Ternary complexes are formed by a simultaneous mechanism. The concentration distribution of the complexes in solution was evaluated as a function of pH. Stoichiometry and stability constants for the complexes formed are reported and discussed. The stability of ternary complexes was quantitatively compared with their corresponding binary complexes in terms of the parameter $\Delta \log K$.

1. Introduction

Metal complexes of biologically important ligands are sometimes more effective than free ligands [1]. It is not surprising, therefore, that many authors have studied the coordination compounds of several central atoms. Mixed ligand complexes have a key role in biological chemistry [2] because the mixed chelation occurs commonly in biological fluids as millions of potential ligands are likely to compete for metal ions *in vivo* [3]. These create specific structures [4] and have been implicated in the storage and transport of active substances through membranes. Among these ligands are piperazine and its derivatives. Some piperazine derivatives were found to inhibit acute human immune deficiency HIV virus from chronically and latently infected cells containing proviral DNA [5]. Also the antimalarial activities of piperazine derivatives are also known [6]. The investigation of metal complexes of piperazine compounds will support their

biological activity. The study of ternary complexes of transition metal ions with amino acids, peptides, or DNA units has been the focus of increasing research effort [7–10], which has revealed the role of metal ions at the molecular level. These types of complexes are implicated in the storage and transport of metal ions and of active substances through membranes. So, it is worthwhile to assemble information on their formation, stability, and structure and on the mutual influence of two ligands bound to the same metal ion. Zinc(II), among other transition metal ions, plays a vital role in biological processes. Zinc deficiency can cause unusual disorders in the development of the body, disorders in the metabolic system and prostate gland, and can result in mental retardation. Studies on model complexes of zinc(II) ions have focused to improve the understanding of the structure-reactivity relationship of the active site in zinc-enzymes [11–14]. In some of the model complexes the chelating ligands (e.g., polyamines) have been selected to

bind to three or four coordination sites of Zn^{II} via N-donor atoms, with the next sites being occupied by other ligands [15–18].

In view of the above facts and in continuation of our published work on the formation equilibria of amino acids [19, 20], amides [21, 22], and DNA units [23, 24], we report herein the protonation constants of the free ligand (BAPP) and the stepwise stability constants for its complexes with a number of 3d divalent metal ions (Zn²⁺, Co²⁺, Ni²⁺, and Cu²⁺) and the thermodynamics of these systems. This was done through calculation of stability constants for their complexes at different temperatures. This work is also extended to present some correlations between the thermodynamic functions and some of well-known properties of the metal ions. Ternary complexes involving Zn(II) ion, BAPP and amino acid, peptide, or DNA constituents are investigated.

2. Experimental

2.1. Materials and Reagents. 1,4-Bis(3-aminopropyl)-piperazine (BAPP), Ni(NO₃)₂·6H₂O, and Co(NO₃)₂·6H₂O were provided from Aldrich Chem. Co. Cu(NO₃)₂·3H₂O was provided from Fluka. Zn(NO₃)₂·6H₂O was provided from FSA supplies. The metal ion solutions were prepared by dissolving A.R. grade metal salts in deionized water. Amino acids, peptides, and DNA constituents investigated are: alanine, threonine, serine, ornithine, glutamic acid, histamine·2HCl, glycinate, glutamine, inosine, thymidine, and thymine. These materials were provided by Sigma Chem. Company and used without further purification. All solutions of the above reagents were freshly prepared in deionized water. All other chemicals used were of A.R. grade quality. Carbonate-free NaOH (titrant) was prepared and standardized against potassium hydrogen phthalate solution. The structural formula of BAPP and some selected biorelevant ligands are given in Scheme 1.

2.2. Apparatus and Procedures. Potentiometric measurements were made using a Metrohm 686 titroprocessor equipped with a 665 Dosimat (Switzerland—Herisau). A thermostatted glass-cell was used and equipped with a magnetic stirring system, a Metrohm glass electrode, a thermometric probe, a microburrette delivery tube, and a salt bridge connected with the reference cell filled with 0.1 mol·dm⁻³ KCl solution in which saturated calomel electrode was dip zped. The titroprocessor and electrode were calibrated daily with standard buffer solutions prepared according to NBS specifications at 25.0 ± 0.1°C [25] and I = 0.1 mol·dm⁻³, potassium hydrogen phthalate (pH 4.008), and a mixture of KH₂PO₄ and Na₂HPO₄ (pH 6.865). The BAPP solution was prepared in the protonated form by dissolving in HNO₃ solution. The protonation constant of the ligand was determined potentiometrically by titrating the ligand (40 cm³) solution (1.25×10^{-3} mol·dm⁻³) of constant ionic strength 0.1 mol·dm⁻³, (adjusted with NaNO₃). The stability constants of the binary complexes were determined by titrating 40 cm³ of a solution mixture of Zn^{II}, Cu^{II}, Co^{II}, or Ni^{II}

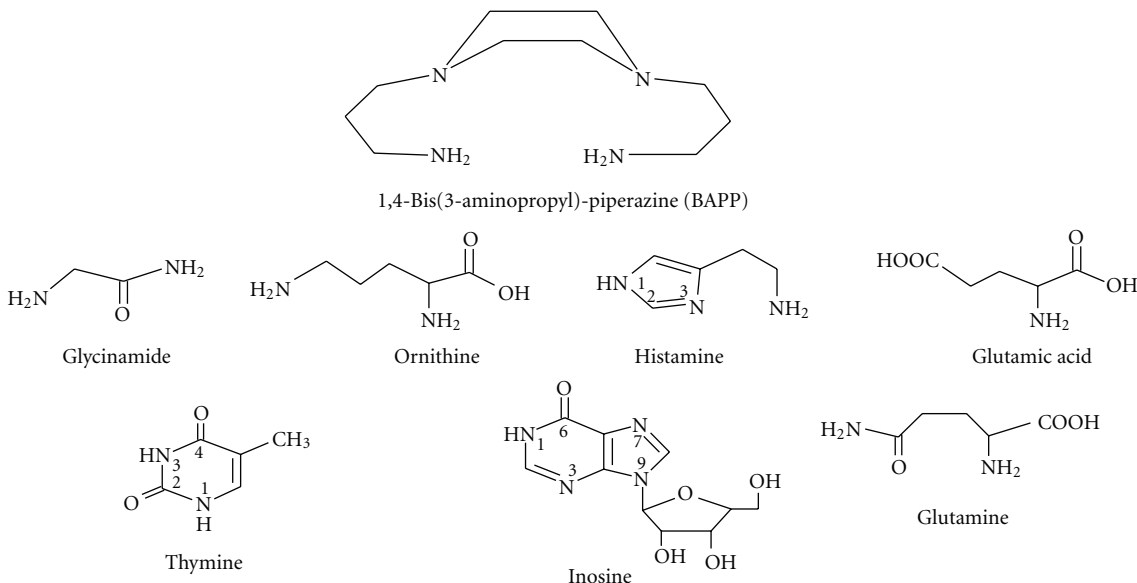
(1.25×10^{-3} mol·dm⁻³), the ligand (2.5×10^{-3} mol·dm⁻³), and NaNO₃ (0.1 mol·dm⁻³). The stability constants of the ternary complexes were determined by titrating 40 cm³ of a solution mixture of Zn^{II} (1.25×10^{-3} mol·dm⁻³), the BAPP (1.25×10^{-3} mol·dm⁻³), the ligand (1.25×10^{-3} mol·dm⁻³), and NaNO₃ (0.1 mol·dm⁻³). All titrations were performed in a purified nitrogen atmosphere, using aqueous 0.05 M NaOH as titrant. The pH meter readings were converted into hydrogen ion concentration by titrating HCl solution (0.05 mol·dm⁻³) with NaOH solution (0.05 mol·dm⁻³) at 25°C and I = 0.1 mol·dm⁻³ NaNO₃. The pH is plotted against p[H]. The relationship pH–p[H] = 0.05 was observed. [OH⁻] value was calculated using a pK_w value of 13.921 [26]. For the variable temperature studies the following values of pK_w were employed at 20°C (pK_w = 14.126) at 30°C (pK_w = 13.753), at 35°C (pK_w = 13.660).

2.3. Data Processing. The calculations were obtained from ca. 100 data points in each titration using the computer program MINIQUAD-75 [27]. The stoichiometry and stability constants of the complexes formed were determined by trying various possible composition models. The model selected gave the best statistical fit and was chemically consistent with the titration data without giving any systematic drifts in the magnitudes of various residuals, as described elsewhere [27]. The fitted model was tested by comparing the experimental titration data points and the theoretical curve calculated from the values of the acid dissociation constant of the ligand and the formation constants of the corresponding complexes. The species distribution diagrams were obtained using the program SPECIES [28] under the experimental condition employed. All measurements were carried out in our laboratory in Cairo University.

3. Results and Discussion

3.1. Protonation Constants of BAPP Ligand. The stoichiometric protonation constants of the investigated BAPP ligand were determined in aqueous solution at 25°C and these constants are tabulated in Table 1. The BAPP ligand studied here have four protonation constants. This is also illustrated in the species distribution of the BAPP ligand in Figure 1. In acidic solution (pH < 3), BAPP initially exists in the fully protonated form as H₄L⁺⁴. On rising the pH, the species (H₄L⁺⁴) lose its protons forming (H₃L⁺³), which is the predominant species in pH range 3.0–7.0. As pH increases, the second and third protons are deprotonated forming the species (H₂L⁺²) and (HL⁺) with maximum concentration percentage of 93% and 43% at pH 8.5 and 10, respectively. With further increase of pH, the fourth proton begins deprotonation to give the full deprotonated species (L) which is the predominant species at pH > 10.5.

3.2. Binary Complexes of 1,4-Bis(3-aminopropyl)piperazine (BAPP). The formation constants of M^{II}-BAPP complexes were determined. The potentiometric titration curves for Cu²⁺, Co²⁺, Ni²⁺, and Zn²⁺ with BAPP are significantly lower than the BAPP titration curve, corresponding to formation



SCHEME 1: Structural formulae of some important investigated ligands.

TABLE 1: Protonation constants of (BAPP) in aqueous solution at different temperatures (at 0.01 M ionic strength).

Temp. (°C)	$\log K_1^H$	$\log K_2^H$	$\log K_3^H$	$\log K_4^H$
20	10.41	10.01	7.09	2.78
25	10.25	9.87	6.99	2.74
30	10.1	9.73	6.91	2.71
35	9.99	9.6	6.81	2.66

$\log K_1^H$, $\log K_2^H$, $\log K_3^H$ and $\log K_4^H$ are the stepwise protonation constants.

TABLE 2: Stepwise stability constants for the complexation of (BAPP) with 3d divalent metal ions in aqueous solution at 0.1 M NaNO₃ at different temperatures.

Cations	log K^a			
	20°C	25°C	30°C	35°C
ZnL	4.74 (0.06)	4.64 (0.08)	4.55 (0.08)	4.47 (0.07)
CoL	5.59 (0.02)	5.35 (0.09)	5.12 (0.06)	4.88 (0.10)
NiL	5.88 (0.04)	5.61 (0.02)	5.33 (0.03)	5.06 (0.02)
CuL	14.26 (0.02)	13.81 (0.01)	13.42 (0.05)	13.09 (0.07)

^a Standard deviations are given in parentheses. I: BAPP.

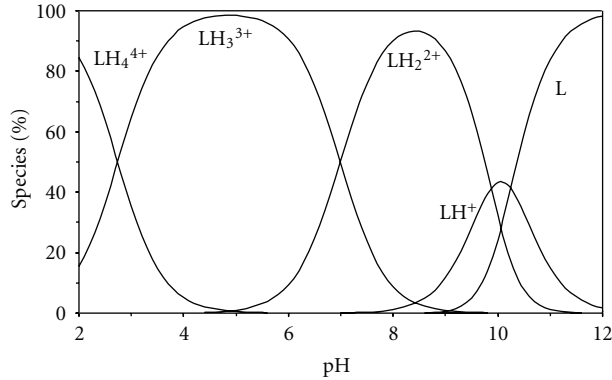


FIGURE 1: Concentration distribution of various species as a function of pH in the BAPP system (1.25 mM of BAPP).

of a complex through release of a proton. The potentiometric data of M^{II} -BAPP solution mixture were fitted assuming the formation 1:1 species but not 1:2 species. The formation of the 1:2 complex seems to be hindered because BAPP ligand is a tetradeятate ligand. The stability constants of their complexes are given in Table 2.

3.3. Correlation of the Properties of Metal Ions with the Formation Constants of Mixed Ligand Complexes. In an attempt to explain why a given ligand prefers binding to one metal rather than another, it is necessary to correlate the stability constants with the characteristic properties of the metal ions, such as the ionic radius, ionization energy, electronegativity, and the atomic number, investigated. The formation constants of M^{II} -complexes of bivalent 3d transition metal ions with BAPP as given in Table 2 are in the order: Co^{2+} ($\log \beta_{110} = 5.59$) < Ni^{2+} ($\log \beta_{110} = 5.88$) < Cu^{2+} ($\log \beta_{110} = 14.26$) > Zn^{2+} ($\log \beta_{110} = 4.74$) in accordance with Irving and Williams order [29]. Here we have discussed relationships between the properties of central metal ions reported in Table 3 [30] and the stability constants of complexes. The correlation between the $\log K_{ML}$ and the reciprocal ionic radii ($1/r$) of the studied bivalent transition metal ions was found to be almost linear (Figure 2). Also, a good linear correlation has been obtained between $\log K_{ML}$ and the electronegativities of the metal ions under study (Figure 2). This in accordance with the fact that increasing electronegativity of the metal ions (Zn^{2+} (1.65) < Co^{2+} (1.88) < Ni^{2+} (1.91) < Cu^{2+} (2.0)) will decrease the electronegativity difference between the metal

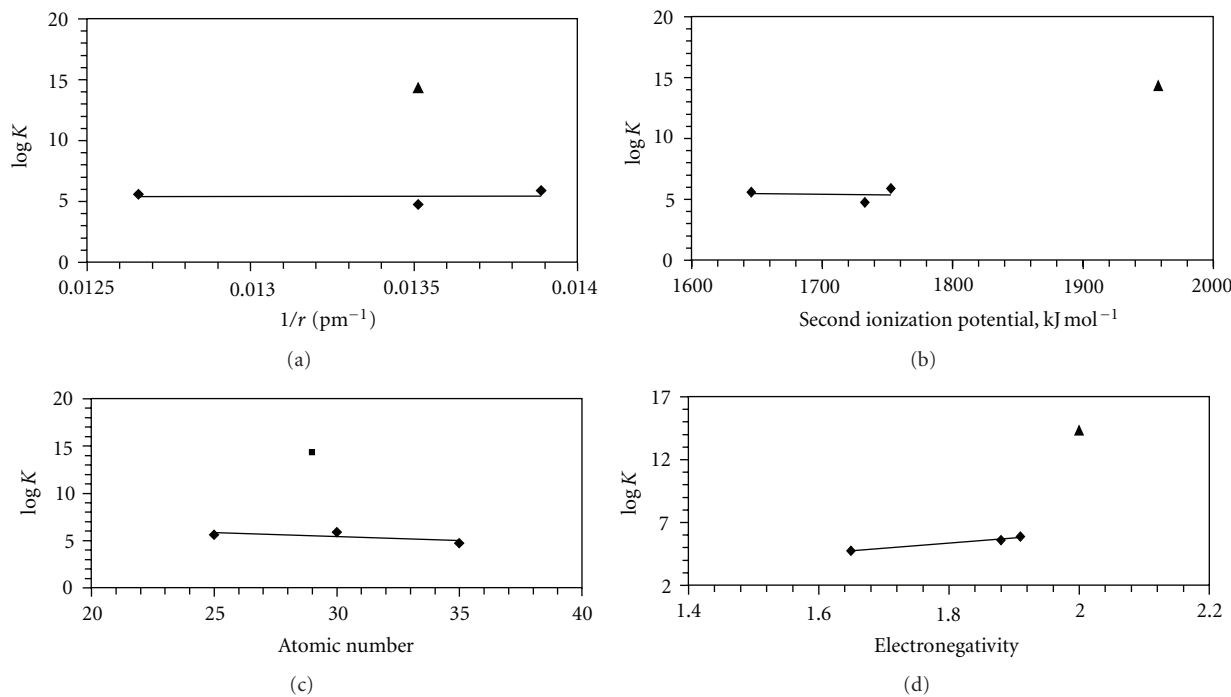


FIGURE 2: Effect of metal ion properties on the stability constants of metal complexes.

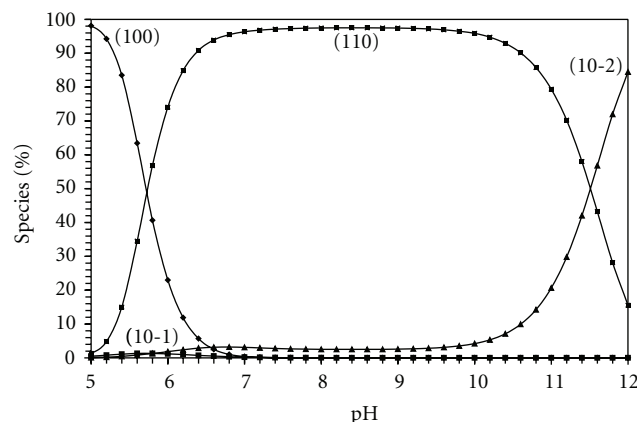
TABLE 3: Atomic number, ionic radius, electronegativity, and ionization potential of the investigated bivalent metal ion^a.

Metal ion	Co^{2+}	Ni^{2+}	Cu^{2+}	Zn^{2+}
Atomic number	27	28	29	30
Ionic radius (pm)	79	72	71	74
Electronegativity	1.88	1.91	2.00	1.65
Second ionization energy (kJ/mol)	1646	1753	1958	1733

^aValues from [30].

atom and the donor atom of the ligand. Thus, the metal-ligand bond would have more covalent character, which may lead to greater stability of the metal chelates. A good linear relationship has been obtained between $\log K_{\text{ML}}$ and the second ionization potential of the bivalent metal ions under study. In general, it is noted that the stability constant of the Cu^{2+} complex is quite large compared to the other metals. The ligand field will give Cu^{2+} some extra stabilization due to tetragonal distortion of the octahedral symmetry [31, 32]. The Cu (II) complex will be further stabilized due to the Jahn-Teller effect [31]. Thus, $\log K$ value for the Cu^{2+} -complex deviates significantly when $\log K$ values of metal chelates are plotted against properties of the metal ions.

3.4. Species Distribution Curves. Estimation of equilibrium concentrations of metal (II) complexes as a function of pH provides a useful picture of metal ion binding in solutions. The concentrations of metal-ligand complexes increase with increasing of pH. The species distribution pattern for $\text{Zn}(\text{BAPP})^{2+}$ complex, taken as a representative of metal ligand complexes, is given in Figure 3. $\text{Zn}(\text{BAPP})^{2+}$ complex

FIGURE 3: Concentration distribution of various species as a function of pH in the Zn^{2+} -BAPP system (1.25 mM of Zn^{2+} and BAPP).

starts to form at $\text{pH} \sim 5$ and reaches its maximum concentration of 98% at $\text{pH} \sim 8$.

3.5. Effect of Temperature. The values obtained for the thermodynamic parameters ΔH^0 , ΔS^0 , and ΔG^0 , associated with the protonation of BAPP and its complex formation with M(II) species, were calculated from the temperature dependence of the data. ΔH^0 and ΔS^0 were obtained by linear least square fit of $\ln K$ versus $1/T$ ($\ln K = -\Delta H^0/RT + \Delta S^0/R$) leading to an intercept $\Delta S^0/R$ and a slope $-\Delta H^0/R$, where K is the equilibrium constant, (Figures 4 and 5), The main conclusions from the data can be summarized as follows.

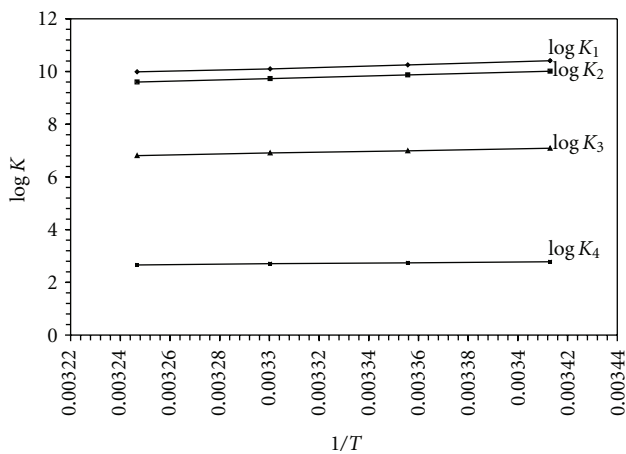


FIGURE 4: Effect of temperature on stepwise protonation constant of H_4BAPP^{+4} . Curves: $\log K_1$ corresponds to the 011 species; $\log K_2$ corresponds to 012 species; $\log K_3$ corresponds to 013 species; $\log K_4$ corresponds to 014 species.

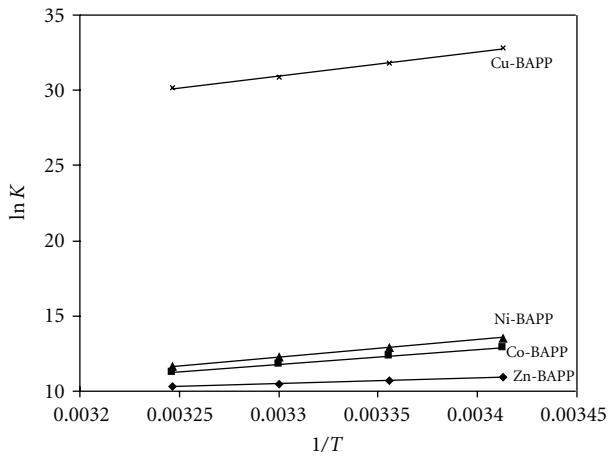


FIGURE 5: Effect of temperature on $\ln K$ of M^{2+} complexes with BAPP.

(I) The protonation reactions of the *N*-site of BAPP is exothermic and of comparable ΔH^0 and ΔS^0 with a net negative ΔG^0 (Table 4). Three factors affect the protonation reactions.

- (i) The neutralization reaction, which is an exothermic reaction process.
- (ii) Desolvation of ions, which is an endothermic process.
- (iii) The change of the configuration and the arrangements of the hydrogen bonds around the free and the protonated ligands.

The negative ΔS^0 indicates that the total number of solvent molecules bound with the dissociated ligand is greater than that originally accompanying the undissociated form.

(II) The stability constants of the complexes formed at different temperatures decreased with increasing temperature, confirming that the complexation process is more favorable at lower temperatures. The thermodynamic parameters of metal complexes were calculated by a procedure similar to that used for the protonation of BAPP and the values are recorded in Table 5. It is known that the divalent metal ions exist in solution as octahedrally hydrated species [29] and the obtained values of ΔH^0 and ΔS^0 can then be considered as sum of two contributions: (a) release of H_2O molecules and (b) metal-ligand bond formation. From these results the following conclusions can be reached.

- (1) All values of ΔG^0 for complexation are negative, indicating the spontaneity of the chelation process.
- (2) The negative values of ΔH^0 , show that the chelation process is exothermic, indicating that the complexation reactions are favored at low temperatures.

3.6. Ternary Complexes Involving Zn^{2+} , BAPP and Amino Acids, Peptides, or DNA Constituents

3.6.1. Ternary Complex Formation Equilibria Involving Amino Acids. Ternary complex formation may proceed either through a stepwise or simultaneous mechanism depending on the chelating potential of BAPP and the other ligand (*L*). The formation constant of 1:1 Zn^{II} -BAPP complex is of the same order of magnitude like Zn^{II} -ligand (*L*) complex, (Table 6). It is reasonable to propose that in presence of both ligands, the reaction proceeds by simultaneous mechanism. This assumption was supported by comparing the experimental potentiometric data with the theoretically calculated (simulated) curve, (Figure 6). Thus, the formation of ternary complex can be described by the following equilibrium (charges are omitted for simplicity):



Figure 5 represents such a comparison for threonine system, from which it follows that the experimental data coincide with the theoretical curve. This supports the validity of the ternary complex formation model. The potentiometric data of the ternary complexes involving simple amino acids best fits assuming a complex of stoichiometric coefficient 1110 species for amino acids except for glutamic acid, ornithine, and histamine, where both 1110 and 1111 species are formed. Estimation of the concentration distribution of the various species in solution provides a useful picture of metal ion binding. The speciation diagram for threonine complex, taken as a representative amino acid, is given in Figure 7. The deprotonated species 1110 attains a maximum concentration of 99% at pH 8.8, therefore the ternary complexes of amino acids predominates in the physiological pH range. The pK_a values for the histamine complex is 9.24, being higher than

TABLE 4: Thermodynamic parameters for the stepwise protonation of (BAPP) in aqueous solution (at 0.01 M ionic strength)^a.

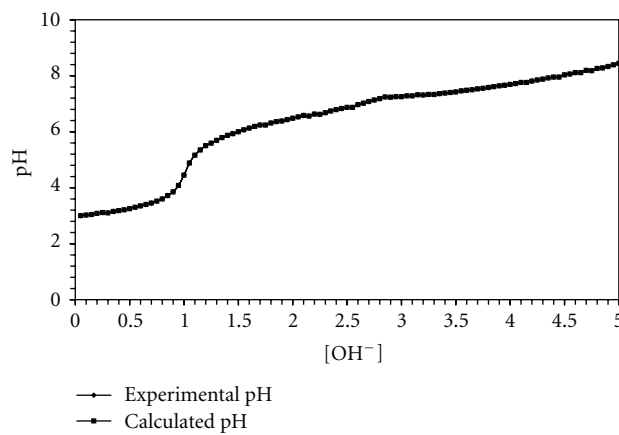
Equilibrium ^b	ΔH° kJMol ⁻¹	ΔS° JK ⁻¹ Mol ⁻¹	ΔG° kJMol ⁻¹
(1) L + H ⁺ ⇌ LH ⁺ log K_1^H	-48.8 (0.8)	32.7 (0.7)	-58.5 (0.8)
(2) LH ⁺ + H ⁺ ⇌ LH ₂ ²⁺ log K_2^H	-47.4 (0.7)	30.1 (0.6)	-56.3 (0.8)
(3) LH ₂ ²⁺ + H ⁺ ⇌ LH ₃ ³⁺ log K_3^H	-31.8 (0.6)	27.3 (0.5)	-39.9 (0.8)
(4) LH ₃ ³⁺ + H ⁺ ⇌ LH ₄ ⁴⁺ log K_4^H	-13.5 (0.3)	7.31 (0.12)	-15.6 (0.3)

^a Standard deviations are given in parentheses; ^bL, where L denotes 1,4-bis(3-aminopropyl)-piperazine (BAPP).

TABLE 5: Thermodynamic parameters for ML complexes of (BAPP) with 3d divalent metal ions in aqueous solution at 0.1 M NaNO₃ at different temperatures^a.

Equilibrium	ΔH° kJMol ⁻¹	ΔS° JK ⁻¹ Mol ⁻¹	ΔG° kJMol ⁻¹
(1) Zn ²⁺ + L ⇌ ZnL ²⁺	-31.1 (0.4)	-15.5 (0.7)	-26.5 (0.8)
(2) Co ²⁺ + L ⇌ CoL ²⁺	-81.5 (0.8)	-171.2 (1.2)	-30.5 (0.4)
(3) Ni ²⁺ + L ⇌ NiL ²⁺	-94.7 (0.9)	-210.4 (1.9)	-32.0 (0.4)
(4) Cu ²⁺ + L ⇌ CuL ²⁺	-134.5 (1.1)	-186.7 (1.5)	-78.9 (0.9)

^a Standard deviations are given in parentheses; L: BAPP.

FIGURE 6: Experimental and calculated potentiometric titration curves of the Zn^{II}-BAPP-Threonine system.

that of the protonated imidazole ($pK_a = 6.12$), but closer to that of the protonated amino group (NH_3^+) in histamine ligand ($pK_a = 9.85$). This reveals that the proton in the protonated complex would be located mainly on the amino group.

The pK_a of the protonated species of Zn(BAPP)-glutamic acid is (7.58), being higher than that of the carboxylate group ($pK_a = 4.15$), but near to that of the protonated amino group NH_3^+ ($pK_a = 9.58$), suggesting that the proton in the protonated complex would be located mainly on the amino group, considering the increase in acidity due to complex formation. The species distribution for glutamic acid complex, taken as a representative, is given in Figure 8. The protonated species 1111 complex predominates with formation percentage of (55% at pH ~7.0); the deprotonated species 1110 complex reaches the maximum concentration of 97% at

TABLE 6: Stability constants of the ternary species in the Zn^{II}-BAPP-amino acid, amide, or DNA constituent systems and proton-association constants and their binary stability constants.

<i>l p q r</i> ^a	$\log \beta^b$
	OH ⁻
	BAPP
1 0 0 -1	-7.96 (0.01)
1 0 0 -2	-15.64 (0.01)
0 1 0 1	—
0 1 0 2	10.25 (0.01)
0 1 0 3	20.12 (0.02)
0 1 0 4	27.11 (0.03)
1 1 0 0	30.26 (0.01)
1 1 0 0	4.64 (0.03)
	Alanine
0 0 1 1	9.69 (0.01)
0 0 1 2	11.88 (0.02)
1 0 1 0	4.58 (0.03)
1 0 2 0	8.71 (0.06)
1 1 1 0	14.91 (0.01)
	Threonine
0 0 1 1	9.06 (0.01)
0 0 1 2	11.03 (0.02)
1 0 1 0	4.63 (0.09)
1 0 2 0	8.62 (0.08)
1 1 1 0	14.36 (0.08)
	Serine
0 0 1 1	9.14 (0.01)
0 0 1 2	11.40 (0.01)
1 0 1 0	4.60 (0.09)
1 0 2 0	8.45 (0.08)
1 1 1 0	16.86 (0.08)
	Ornithine
0 0 1 1	10.58 (0.00)
0 0 1 2	19.43 (0.02)
0 0 1 3	21.39 (0.02)
1 0 1 0	—
1 0 2 0	—
1 1 1 0	—
1 1 1 1	—
	Glutamic acid
0 0 1 1	9.58 (0.01)
0 0 1 2	13.73 (0.01)
0 0 1 3	—
1 0 1 0	5.22 (0.02)
1 0 2 0	10.18 (0.05)
1 1 1 0	12.39 (0.10)
1 1 1 1	21.63 (0.07)
	Histamine·2HCl
0 0 1 1	10.58 (0.00)
0 0 1 2	19.43 (0.02)
0 0 1 3	21.39 (0.02)
1 0 1 0	—
1 0 2 0	—
1 1 1 0	—
1 1 1 1	—
	Glycinamide
0 0 1 1	7.60 (0.01)
1 0 1 0	3.28 (0.07)
1 1 1 0	12.47 (0.06)
	Glutamine
0 0 1 1	8.95 (0.01)
1 0 1 0	4.12 (0.06)
1 1 1 0	15.41 (0.08)
	Inosine
0 0 1 1	8.55 (0.02)
1 0 1 0	3.52 (0.10)
1 1 1 0	14.15 (0.10)
1 1 1 1	20.38 (0.10)
	Thymine
0 0 1 1	9.58 (0.02)
1 0 1 0	4.82 (0.08)
1 1 1 0	15.89 (0.10)
1 1 1 1	15.72 (0.09)
	Thymidine
0 0 1 1	9.50 (0.01)
1 0 1 0	4.47 (0.08)
1 1 1 0	15.72 (0.09)
1 1 1 1	—

^a*l, p, q* and *r* are stoichiometric coefficients corresponding to Zn^{II}, BAPP, other ligand, and H⁺, respectively.

^bStandard deviations are given in parentheses sum of square of residuals are less than 5E-7.

pH ~9.8. Therefore the species 1111 complex predominates in the physiological pH range.

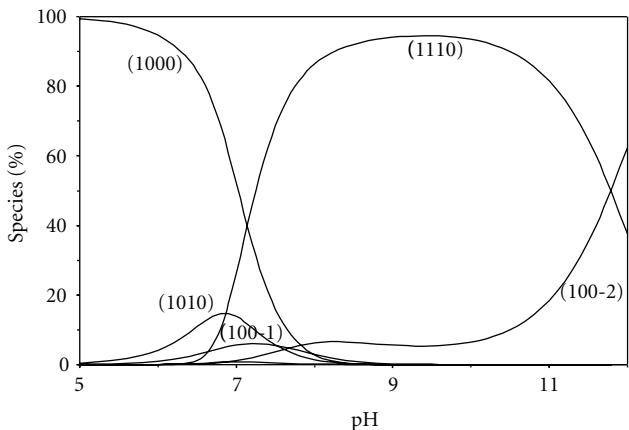


FIGURE 7: Concentration distribution of various species as a function of pH in the $[Zn(BAPP)(\text{threonine})]$ system (1.25 mM of Zn^{2+} , BAPP, and threonine).

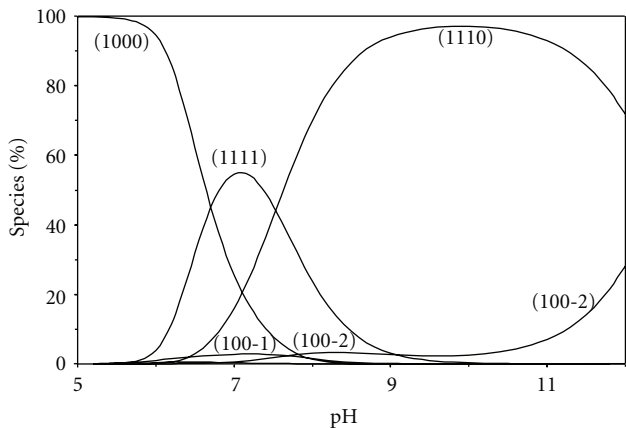


FIGURE 8: Concentration distribution of various species as a function of pH in the $[Zn(BAPP)(\text{glutamic acid})]$ system (1.25 mM of Zn^{2+} , BAPP, and glutamic acid).

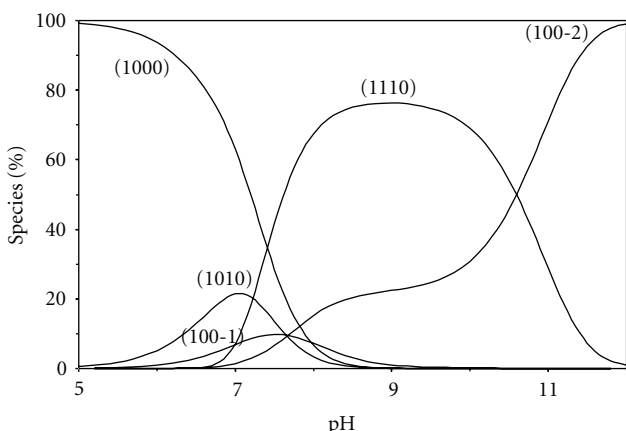


FIGURE 9: Concentration distribution of various species as a function of pH in the $[Zn(BAPP)(\text{glycinamide})]$ system (1.25 mM of Zn^{2+} , BAPP, and glycinamide).

TABLE 7: $\Delta \log K = \log \beta_{1110} - (\log \beta_{1100} + \log \beta_{1010})$.

	$\Delta \log K$
Alanine	5.69
Threonine	5.09
Serine	7.62
Ornithine	9.32
Glutamic acid	6.92
Histamine·2HCl	2.53
Glycinamide	4.55
Glutamine	6.65
Inosine	5.99
Thymidine	6.61
Thymine	6.43

Ornithine is α -amino acid having an extra amino group. Ornithine forms protonated complex 1111 species and the pK_a value amounts to 7.10. This is fairly comparable with the acid protonation constant of the δ -amino group, considering the increase in acidity due to complex formation.

3.6.2. Ternary Complex Formation Equilibria Involving Amides. Ternary complex formation of amides proceeds also through simultaneous mechanism (Table 7). The potentiometric data reported for the peptides, serine, and threonine complexes reveals the formation of $Zn(BAPP)(L)$ species rather than the $Zn(BAPP)LH_{-1}$ species which supports the view that induced ionization of peptide hydrogen would be unfavoured. This finding is in agreement with previous investigation carried out on the $Zn(\text{II})$ -diethylenetriamine-peptide and $Zn(\text{II})$ -nitrilo-tris(methyl phosphonic acid)-peptide systems [33].

The glutamine complex is more stable than the glycaminamide complex, presumably due to the fact that glutamine carries a negative charge, whereas glycaminamide is neutral. The electrostatic interaction between the glutamate and the positively charged $Zn(\text{II})$ complex would result in a lowering of the free energy of formation.

The speciation diagram of glycaminamide complex as a representative of amides is given in Figure 9. The mixed ligand species $[Zn(BAPP)L]$ (1110) starts to form at $pH \sim 6.8$ and with increasing pH, its concentration increases reaching the maximum of 76% at $pH \sim 9$. The species with concentration percentage less than 5% were neglected in the concentration distribution plot for clarity.

3.6.3. Ternary Complex Formation Equilibria Involving DNA Units. Inosine is slightly more acidic than the pyrimidinic species (thymine and thymidine). This can be related to the existence of the anion form of purinic derivatives in a higher number of resonance forms due to the presence of two condensed rings in this ligand (inosine). Based on the existing data, thymine and thymidine ligate in the deprotonated form as monoanions, through N3, and they do not form protonated complexes. As a result of the high pK_a values of pyrimidines ($pK_a \approx 9$) and the fact that they are monodentates, the complexes are formed only above pH 6, supporting the view

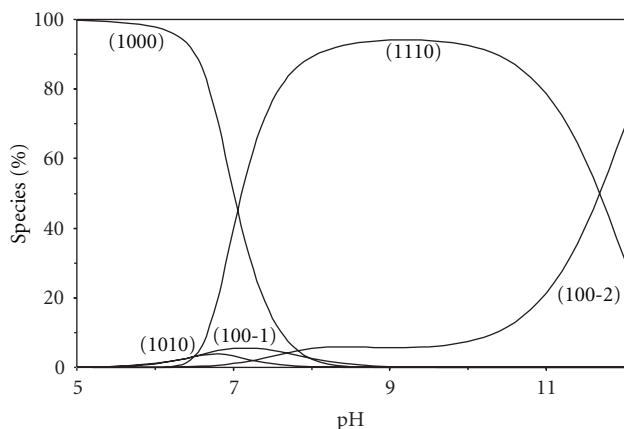


FIGURE 10: Concentration distribution of various species as a function of pH in the $[Zn(BAPP)(\text{inosine})]$ system (1.25 mM of Zn^{2+} , BAPP, and inosine).

that the negatively charged nitrogen donors of pyrimidine bases are important binding sites in the neutral and slightly basic pH ranges. The purines like inosine have two metal ion binding centres N1 and N7 nitrogens. Inosine may become protonated at N(7) with formation of $[\text{N}(1)\text{H}-\text{N}(7)\text{H}]$ monocations. In the present study, the pK_a of N(1)H was only determined since the pK_a of N(7)H is too low to be detected by the potentiometric technique. In the acidic pH-range, N1 remains protonated, while the metal ion is attached to N7. The gradual change from N7-binding to N1-binding with increasing pH has been rather extensively documented by nuclear magnetic resonance (NMR) [34] and electron paramagnetic resonance (EPR) [35] spectroscopic measurements. Consequently, it is proposed that N(1) serves as a coordination site in the mixed ligand complexes of inosine at higher pH values. The speciation of inosine complex is presented in Figure 10, where the species distribution of the complexes is plotted as a function of pH. The complex $[Zn(\text{BAPP})\text{L}]$ (1110) reaching a maximum concentration of 94% at pH 9.

3.7. Comparison of the Stability Constant of the Ternary Complexes with Those of the Binary Complexes. One of the most important parameters generally used for indicating the stabilization of the mixed complexes with respect to the binary ones namely is $\Delta \log K$. It has been widely accepted and used for many years [36] and the advantages in using $\Delta \log K$ in comparing stabilities of ternary and binary complexes have been reviewed. $\Delta \log_{10} K$, the difference between the stabilities of the binary and mixed complexes, expresses the effect of the bounded primary ligand towards an incoming secondary ligand (L). One expects to obtain negative values for $\Delta \log K$ (Table 7), since more coordination positions are available for the bonding of ligand (L) in the binary than in the ternary complexes. This indicates that the secondary ligand (L) amino acid, peptide, or DNA form more stable complexes with zinc (II) ion alone than with

Zn^{II} -BAPP complex. The $\Delta \log K$ value for deprotonated ternary complexes is given by



$$\begin{aligned} \Delta \log K_{\text{Zn}(\text{BAPP})\text{L}} = & \log \beta_{\text{Zn}(\text{BAPP})(\text{L})} - \log \beta_{\text{Zn}(\text{BAPP})} \\ & - \log \beta_{\text{Zn}(\text{L})}. \end{aligned} \quad (3)$$

All values of $\Delta \log K$ for the ternary complexes studied in this paper are listed in Table 7. It is of interest to note that for all the systems listed in Table 7, the values for $\Delta \log K$ are positive; that is, equilibrium 6 is on its right side. According to Sigel [36, 37], the relative stability of a ternary complex $\text{Zn}(\text{BAPP})\text{L}(1110)$ compared to its binary complex $\text{Zn}(\text{BAPP})$ (1100) or $\text{Zn}(\text{L})$ (1010) can be expressed quantitatively by (2) and (3). Zn-BAPP (1:1) has fewer coordination sites than the aquatic Zn^{2+} ion complex. Consequently, the secondary ligands (L) are expected to bind to the Zn-BAPP complex with a smaller stability constant than with an aquatic metal ion. Therefore, $\Delta \log_{10} K$ should be negative and generally have a value between -0.5 and -2.0 [36, 38] depending on the geometry of the complex. For Zn^{2+} ions, positive values of $\Delta \log_{10} K$ may be considered as evidence for the occurrence of enhanced stabilities. This may be explained on the premise that: a sort of hydrophobic intramolecular interaction possibly occurred between the hydrophobic moiety of BAPP and the noncoordinating hydrophobic side chain of amino acids in aqueous solutions. Such a hydrophobic interaction has been reported in literature [36, 39–41].

4. Conclusions

The present investigation describes the formation equilibria of $\text{Zn}(\text{II})$ complexes involving BAPP and some ligands of biological significance. In combination of stability constants data of such Zn^{II} complexes with amino acids, peptides, or DNA constituents, it would be possible to calculate the equilibrium distribution of the metal species in biological fluids where all types of ligands are present simultaneously. This would form a clear basis for understanding the mode of action of such metal species under physiological conditions. From the above results, it may be concluded that ternary complex formation of amino acids and peptides proceeds through simultaneous mechanism. The mixed ligand complexes are formed in the physiological pH range, indicating this interaction. The positive value of $\Delta \log K$ is attributed to the extra stability of the ternary complexes.

References

- [1] E. Jóna, M. Kubranová, P. Šimon, and J. Mrožínski, "Thermochemical investigation: $\text{Ni}(\text{II})$ -3-pyridylcarbinol (ronicol) interactions in solid halogeno and thiocyanato complexes," *Journal of Thermal Analysis*, vol. 46, no. 5, pp. 1325–1337, 1996.
- [2] A. S. Mildvan and M. Cohn, "Kinetic and magnetic resonance studies of the pyruvate kinase reaction. II. Complexes of

- enzyme, metal, and substrates," *Journal of Biological Chemistry*, vol. 241, no. 5, pp. 1178–1193, 1966.
- [3] G. M. R. Tombo and D. Bellus, "Chiralität und pflanzenschutz," *Angewandte Chemie*, vol. 103, no. 10, pp. 1219–1241, 1991.
- [4] E. Bouwman, W. L. Driessens, and J. Reedijk, "Model systems for type I copper proteins: structures of copper coordination compounds with thioether and azole-containing ligands," *Coordination Chemistry Reviews*, vol. 104, no. 1, pp. 143–172, 1990.
- [5] J. A. Turpin, R. W. Buckheit, D. Derse et al., "Inhibition of acute-, latent-, and chronic-phase human immunodeficiency virus type 1 (HIV-1) replication by a bistriazoloacridone analog that selectively inhibits HIV-1 transcription," *Antimicrobial Agents and Chemotherapy*, vol. 42, no. 3, pp. 487–494, 1998.
- [6] M. Medou, G. Priem, L. Rocheblave et al., "Synthesis and anti-HIV activity of α -thiophenoxy-hydroxyethylamide derivatives," *European Journal of Medicinal Chemistry*, vol. 34, no. 7-8, pp. 625–638, 1999.
- [7] B. Onoa and V. Moreno, "Nickel(II) and copper(II)—L-cysteine, L-methionine, L-tryptophan-nucleotide ternary complexes," *Transition Metal Chemistry*, vol. 23, no. 4, pp. 485–490, 1998.
- [8] K. Burger, *Biocoordination Chemistry: Coordination Equilibria in Biologically Active Systems*, E. Horwood, New York, NY, USA, 1990.
- [9] R. P. Bonomo, B. Di Blasio, G. Maccarrone et al., "Crystal and molecular structure of the [6-deoxy-6-[(2-(4-imidazolyl)ethyl)amino]cyclomaltoheptaose]copper(II) ternary complex with L-tryptophanate. Role of weak forces in the chiral recognition process assisted by a metalloclodextrin," *Inorganic Chemistry*, vol. 35, no. 15, pp. 4497–4504, 1996.
- [10] M. Sabat, B. Lippert, A. Sigel, and H. Sigel, *Metal Ions in Biological Systems*, vol. 33, Marcel Dekker, New York, NY, USA, 1996.
- [11] E. Kimura, T. Koike, and M. Shionoya, "Lewis acids and vanadium," in *Metal Sites in Proteins and Models. Phosphatases*, H. A. O. Hill, P. J. Sadler, and A. J. Thomson, Eds., vol. 89, no. 1, Springer, Berlin, Germany, 1997.
- [12] T. Koike, M. Inoue, E. Kimura, and M. Shiro, "Novel properties of cooperative dinuclear zinc(II) ions: The selective recognition of phosphomonoesters and their P-O ester bond cleavage by a new dinuclear zinc(II) cryptate," *Journal of the American Chemical Society*, vol. 118, no. 13, pp. 3091–3099, 1996.
- [13] T. Koike, S. Kajitani, I. Nakamura, E. Kimura, and M. Shiro, "The catalytic carboxyester hydrolysis by a new zinc(II) complex with an alcohol-pendant cyclen (1-(2-hydroxyethyl)-1,4,7,10-tetraazacyclododecane): a novel model for indirect activation of the serine nucleophile by zinc(II) in zinc enzymes," *Journal of the American Chemical Society*, vol. 117, no. 4, pp. 1210–1219, 1995.
- [14] E. Kimura, T. Koike, T. Shiota, and Y. Iitaka, "Acid properties of zinc(II) and cadmium(II) in complexation with macrocyclic oxo polyamine ligands," *Inorganic Chemistry*, vol. 29, no. 23, pp. 4621–4629, 1990.
- [15] X. Zhang and R. Van Eldik, "A functional model for carbonic anhydrase: thermodynamic and kinetic study of a tetraaza-cyclododecane complex of zinc(II)," *Inorganic Chemistry*, vol. 34, no. 22, pp. 5606–5614, 1995.
- [16] E. Kimura and K. K. Karlin, *Progress in Inorganic Chemistry*, vol. 41, Wiley, 1994.
- [17] E. Kimura, I. Nakamura, T. Koike et al., "Carboxyester hydrolysis promoted by a new zinc(II) macrocyclic triamine complex with an alkoxide pendant: a model study for the serine alkoxide nucleophile in zinc enzymes," *Journal of the American Chemical Society*, vol. 116, no. 11, pp. 4764–4771, 1994.
- [18] E. Kimura, M. Shionoya, A. Hoshino, T. Ikeda, and Y. Yamada, "A model for catalytically active zinc(II) ion in liver alcohol dehydrogenase: a novel "hydride transfer" reaction catalyzed by zinc(II)-macrocyclic polyamine complexes," *Journal of the American Chemical Society*, vol. 114, no. 26, pp. 10134–10137, 1992.
- [19] A. A. El-Sherif and M. M. Shoukry, "Ternary copper(II) complexes involving 2-(aminomethyl)-benzimidazole and some bio-relevant ligands. Equilibrium studies and kinetics of hydrolysis for glycine methyl ester under complex formation," *Inorganica Chimica Acta*, vol. 360, no. 2, pp. 473–487, 2007.
- [20] A. A. El-Sherif and M. M. Shoukry, "Copper(II) complexes of imino-bis(methyl phosphonic acid) with some bio-relevant ligands. Equilibrium studies and hydrolysis of glycine methyl ester through complex formation," *Journal of Coordination Chemistry*, vol. 58, no. 16, pp. 1401–1415, 2005.
- [21] A. A. El-Sherif and M. M. Shoukry, "Coordination properties of tridentate (N,O,O) heterocyclic alcohol (PDC) with Cu(II). Mixed ligand complex formation reactions of Cu(II) with PDC and some bio-relevant ligands," *Spectrochimica Acta A*, vol. 66, no. 3, pp. 691–700, 2007.
- [22] A. A. El-Sherif, "Mixed-ligand complexes of 2-(aminomethyl) benzimidazole palladium(II) with various biologically relevant ligands," *Journal of Solution Chemistry*, vol. 35, no. 9, pp. 1287–1301, 2006.
- [23] A. A. El-Sherif, M. M. Shoukry, and R. Van Eldik, "Complex-formation reactions and stability constants for mixed-ligand complexes of diaqua(2-picolyamine)palladium(II) with some bio-relevant ligands," *Dalton Transactions*, no. 7, pp. 1425–1432, 2003.
- [24] M. M. Shoukry, E. M. Khairy, and A. A. El-Sherif, "Ternary complexes involving copper(II) and amino acids, peptides and DNA constituents. The kinetics of hydrolysis of α -amino acid esters," *Transition Metal Chemistry*, vol. 27, no. 6, pp. 656–664, 2002.
- [25] R. G. Bates, *Determination of pH-Theory and Practice*, Wiley-Interscience, New York, NY, USA, 2nd edition, 1975.
- [26] A. A. El-Sherif, "Coordination properties of bidentate (N, O) and tridentate (N, O, O) heterocyclic alcohols with dimethyltin (IV) ion," *Journal of Coordination Chemistry*, vol. 64, no. 7, pp. 1240–1253, 2011.
- [27] P. Gans, A. Sabatini, and A. Vacca, "An improved computer program for the computation of formation constants from potentiometric data," *Inorganica Chimica Acta*, vol. 18, pp. 237–239, 1976.
- [28] L. Pettit, University of Leeds, Personal Communication.
- [29] H. M. N. H. Irving and R. J. P. Williams, "The stability of transition-metal complexes," *Journal of the Chemical Society*, pp. 3192–3210, 1952.
- [30] J. E. Huheey, *Inorganic Chemistry-Principles of Structure and Reactivity*, Harper, New York, NY, USA, 1983.
- [31] F. A. Cotton and G. Wilkinson, *Advanced Inorganic Chemistry*, Wiley, London, UK, 1962.
- [32] C. S. G. Phillips and R. J. P. Williams, *Inorganic Chemistry: Metals*, vol. 2, Oxford University Press, New York, NY, USA, 1966.
- [33] M. M. A. Mohamed and A. A. El-Sherif, "Complex formation equilibria between zinc(II), nitrilo-tris(methyl phosphonic

- acid) and some bio-relevant ligands. The kinetics and mechanism for zinc(II) ion promoted hydrolysis of glycine methyl ester," *Journal of Solution Chemistry*, vol. 39, no. 5, pp. 639–653, 2010.
- [34] K. Maskos, "The interaction of metal ions with nucleic acids. A nuclear magnetic resonance relaxation time study of the copper(II)-inosine 5'-monophosphate system in solution," *Acta Biochimica Polonica*, vol. 28, no. 2, pp. 183–200, 1981.
- [35] D. J. Hodgson, "The stereochemistry of metal complexes of nucleic acid constituents," in *Progress in Inorganic Chemistry*, S. J. Lippard, Ed., vol. 23, pp. 211–254, John Wiley, New York, NY, USA, 1977.
- [36] H. Sigel, *Coordination Chemistry*, vol. 20, Pergamon Press, Oxford, UK, 1980.
- [37] H. Sigel, *Metal Ions in Biological Systems*, vol. 2, Dekker, New York, NY, USA, 1973.
- [38] K. Maskos, "The interaction of metal ions with nucleic acids. A nuclear magnetic resonance relaxation time study of the copper(II)-inosine 5'-monophosphate system in solution," *Acta Biochimica Polonica*, vol. 28, no. 2, pp. 183–200, 1981.
- [39] O. Yamauchi and A. Odani, "Structure-stability relationship in ternary copper(II) complexes involving aromatic amines and tyrosine or related amino acids. Intramolecular aromatic ring stacking and its regulation through tyrosine phosphorylation," *Journal of the American Chemical Society*, vol. 107, no. 21, pp. 5938–5945, 1985.
- [40] B. E. Fischer and H. Sigel, "Ternary complexes in solution. 35. Intramolecular hydrophobic ligand-ligand interactions in mixed ligand complexes containing an aliphatic amino acid," *Journal of the American Chemical Society*, vol. 102, no. 9, pp. 2998–3008, 1980.
- [41] A. A. El-Sherif, "Equilibrium studies of binary and mixed-ligand complexes of zinc(II) involving 2-(aminomethyl)-benzimidazole and some bio-relevant," *Journal of Solution Chemistry*. In press.

Temporal Changes in Concentrations of Some Trace Elements in Muscle Tissue of Crayfish, *Astacus leptodactylus* (Eschscholtz, 1823), from Keban Dam Lake

Onder Aksu,¹ Ragip Adiguzel,² Veysel Demir,³ Numan Yildirim,⁴ Durali Danabas,¹ Sebahat Seker,⁵ Safak Seyhaneyildiz Can,³ and Mustafa Ates⁶

¹ Fisheries Faculty, University of Tunceli, 62000 Tunceli, Turkey

² Department of Chemical Engineering, Faculty of Engineering, University of Tunceli, 62000 Tunceli, Turkey

³ Department of Bioengineering, Faculty of Engineering, University of Tunceli, 62000 Tunceli, Turkey

⁴ Department of Environmental Engineering, Faculty of Engineering, University of Tunceli, 62000 Tunceli, Turkey

⁵ Department of Environmental Engineering, Faculty of Engineering, University of Ardahan, 75000 Ardahan, Turkey

⁶ Vocational School of Tunceli, University of Tunceli, 62000 Tunceli, Turkey

Correspondence should be addressed to Ragip Adiguzel; adiguzelragip@gmail.com

Academic Editor: Zhe-Sheng Chen

Crayfish (*Astacus leptodactylus* Eschscholtz, 1823) is the native crayfish species in Turkey. It was exported regularly to Western Europe. In this study, bioaccumulation and temporal trends of some trace elements (arsenic: As, cadmium: Cd, copper: Cu, mercury: Hg, lead: Pb, and zinc: Zn) in edible abdomen muscle of crayfish from Keban Dam Lake (Elazığ, Turkey) were investigated for the 2006–2012 period. Sequence of metal concentration levels was Zn > Cu > Hg > Pb > Cd > As in muscle tissues. The highest concentration of Zn (21.69 mg kg⁻¹) was detected in 2006, while the lowest (4.35 mg kg⁻¹) in 2009. In general, it was found that the concentrations of trace elements investigated were lower than the maximum permissible limits of the food regulations of the Ministry of Food, Agriculture, and Livestock (MFAL), the Turkish Food Codex and Commission Regulation (EC). If the crayfish selected for the study are recognized as bioindicators of environmental pollution, then it is possible to conclude that the changes in studied trace elements concentrations in the Keban Dam Lake are being steady.

1. Introduction

Many pollutants including trace elements are released from natural and anthropogenic sources into aquatic environments [1, 2]. Accumulation of these elements in sediments, aquatic biota, and edible aquatic organisms is an important concern, because they are easily involved in food chain and affect most important reactions in living organisms, even at low concentrations [1, 3, 4].

Copper (Cu) can enter the environment through releases from the mining of Cu and other metals and from factories that make or use Cu metal or Cu compounds. Copper can also enter the environment through waste dumps, domestic waste water, combustion of fossil fuels and wastes, wood production, phosphate fertilizer production, and natural

sources. One of the most commonly reported adverse health effect of Cu is gastrointestinal distress [5].

Cadmium (Cd) is emitted to soil, water, and air by nonferrous metal mining and refining, manufacture and application of phosphate fertilizers, fossil fuel combustion, and waste incineration and disposal. Cadmium can accumulate in aquatic organisms and agricultural crops. The U.S. Department of Health and Human Services (DHHS) has determined that Cd and Cd compounds are known human carcinogens [6].

Lead (Pb) and Pb alloys are commonly found in pipes, storage batteries, weights, shot and ammunition, cable covers, and sheets used to shield us from radiation. The largest use for lead is in storage batteries in cars and other vehicles. Lead compounds are used as a pigment in paints, dyes, and

ceramic glazes and in caulk. The amount of Pb used in these products has been reduced in recent years to minimize Pb's harmful effect on people and animals. Lead has long been known to alter the hematological system by inhibiting the activities of several enzymes involved in heme biosynthesis [7].

Mercury (Hg) is a naturally occurring metal and enters the environment as the result of the normal breakdown of minerals in rocks and soil from exposure to wind and water, and from volcanic activity. Approximately 80% of the Hg released from human activities are elemental Hg released to the air, primarily from fossil fuel combustion, mining, and smelting and from solid waste incineration. About 15% of the total is released to the soil from fertilizers, fungicides, and municipal solid waste (e.g., from waste that contains discarded batteries, electrical switches, or thermometers). An additional 5% is released from industrial wastewater to water in the environment [8].

Zinc (Zn) is an essential human nutrient and a cofactor for over 300 enzymes and is found in all tissues. In humans, the highest concentrations of Zn have been found in bone, muscle, prostate, liver, and kidneys [9, 10]. Large oral doses of Zn can interfere with Cu bioavailability as they compete for absorption, and clinical signs of immune dysfunction have been reported with daily doses in excess of 150 mg [11].

The most essential component of life, water, being contaminated with arsenic is a global human health hazard. Millions of the populations worldwide are exposed to arsenic-contaminated drinking water. Arsenic (As) is widely distributed in nature and released into the environment through natural sources, industrial processes, and agriculture usage [12]. Arsenic can affect human health and is considered one of the most significant environmental causes of cancer in the world [13]. Reference [14] reported that As is a unique carcinogen. It is the only known human carcinogen for which there is adequate evidence of carcinogenic risk by both inhalation and ingestion.

Some trace elements including Zn and Cu which are taken up by aquatic invertebrates both from food and solution are known to be essential elements and play important roles in biological metabolism at very low concentrations [15–18].

Others are known to be toxic, even at low concentrations, including aluminum (Al), As, Cd, chromium (Cr), iron (Fe), manganese (Mn), Hg, nickel (Ni), selenium (Se), Zn, and Pb [15, 19]. These elements can cause adverse effects on aquatic organisms, if these chemicals exist in biota and eventually build up to unacceptable levels in these organisms. Some trace elements are major contributor to crucial biochemical reactions in many living organisms such as fish and crustaceans [1, 20].

Generally crustaceans like all aquatic invertebrates accumulate metals from a wide range of sources and the trace metal concentrations within their tissues and bodies show great variability [21]. Crayfish can be used to monitor the aquatic environments for heavy metal pollution because they are solitary bottom dwellers, which keep much of their bodies in contact with surrounding objects and tend to accumulate metals in their tissues [22, 23]. These crayfish are used as a vector of contamination in many studies [3, 21, 22, 24, 25].

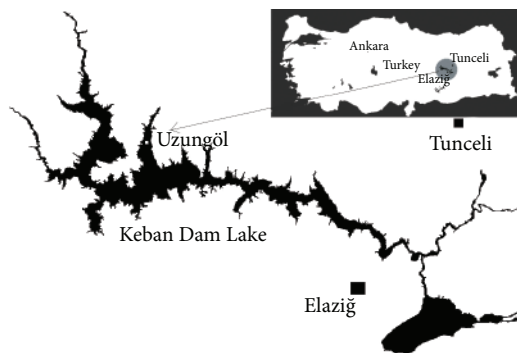


FIGURE 1: The map of sampling stations.

Due to negative effect of trace elements, their bioaccumulation in edible tissues of aquatic invertebrates needs to be monitored. The objective of this study is to determine temporally the bioaccumulation of trace elements in abdomen muscles of crayfish, *Astacus leptodactylus*, which is sea food having a great attraction in human consumption.

2. Materials and Methods

2.1. Properties of Sampling Area. The Keban Dam Lake, which is a hydroelectric dam on the river Euphrates, is located between the cities of Elazığ and Tunceli. The surface area of Keban Dam Lake is 687.31 km². It is situated at latitude 38°5' N and 38°4' E longitude at an elevation of 1134 m above sea level. This study was conducted in region with the sampling site coordinates of N 38° 57' 09" E 38° 53' 19" on Keban Dam Lake (Figure 1).

Near the sampling area, there are some metal processing industries that contribute to pollution of Keban Dam Lake. The effluent from Elazığ city sewage treatment facility is discharged to Keban Dam Lake. There are also some cage aquaculture facilities around sampling area.

2.2. Crayfish Sampling. The freshwater crayfish (*A. leptodactylus*) were caught by fyke nets in sampling area from Keban Dam Lake (Figure 1) each year in June and July from 2006 to 2012. The samples were sealed via plastic bags and transferred to the laboratory under cold chains. For each year, twenty five crayfish have approximately the same weight and length (same condition index) and were selected randomly among crayfish that is bigger than 10 cm, legal catching length, and the abdomen muscles of crayfish were dissected. The abdomen muscles of all crayfish were homogenized with tissue homogenizer and used for trace element determination.

2.3. Analysis. The concentrations of trace elements were measured with ICP MS (Perkin Elmer Germany) according to the methods (no. 161) described by NMKL [26] in Food Control Laboratory in Izmir (Turkey). The concentrations obtained from the analyses were compared with the same tissue (muscle) and species (crayfish) in MFAL and EC. The

TABLE 1: The levels of trace elements in abdomen muscles of crayfish (*A. leptodactylus* Eschscholtz, 1823) between 2006 and 2012 in Keban Dam Lake (Elazığ, Turkey).

Trace elements (mg kg ⁻¹)	Sampling periods						
	2006	2007	2008	2009	2010	2011	2012
As	0.037	UDL*	UDL	UDL	UDL	0.146	UDL
Cd	0.01	UDL	0.02	UDL	0.01	UDL	0.01
Cu	7.20	5.28	4.39	2.42	3.81	4.74	6.967
Hg	0.193	0.160	0.059	0.016	0.150	0.983	0.418
Pb	0.03	UDL	UDL	UDL	0.01	0.04	0.08
Zn	21.69	17.95	16.22	4.35	14.60	16.04	21.65

*UDL: under detection limit.

detectable limits of elements were 0.003, 0.001, 0.05, 0.01, 0.01, and 0.01 mg kg⁻¹ for As, Hg, Zn, Cd, Cu, and Pb, respectively.

3. Results and Discussions

The concentrations of trace elements in abdomen muscles of crayfish were shown in Table 1. The highest Zn and Cu accumulation was measured as 21.69 and 7.2 mg kg⁻¹, respectively, in 2006. There is a decrease in the concentration of both metals between 2006 and 2009 and an increase in following years. The levels of As were detected only in 2006 and 2011. The As, Cd, and Pb bioaccumulation levels were measured under the detectable limits for most of the samples analyzed. In general, there is an increase in mercury bioaccumulation level. The highest levels of Cu and Cd were determined in 2006 and 2008, while the lowest levels were determined in 2009. The antagonism between Cu and Cd was observed.

A. leptodactylus is the native crayfish species in Turkey. It was exported regularly to Western Europe, although domestic consumption of *A. leptodactylus* was very little. There has been an increase in the production of *A. leptodactylus* in recent years. One of the introduced populations of *A. leptodactylus* in Turkey is that in Keban Dam Lake, Elazığ [27].

Lake sediment represents an important sink for trace metals in aquatic systems, and metal concentrations in sediment can be several orders of magnitude greater than in the overlying water [28, 29]. Researchers determined some trace element concentration in water and sediment samples of Keban Dam Lake. Average Zn concentration was measured as 1.28 ppm in water samples and average concentration of Zn, Cu, Cr, Co, and Ni in sediment samples as 1473, 32.7, 198, 50, and 198 ppm, respectively [30].

In aquatic systems, crayfish have been a widespread importance to monitor metals and other contaminants [31], because of consuming widely and increasingly in human diets in the world [32]. Most crayfish are omnivorous benthic feeders living in close contact with the sediment and taking a variety of both animal and plant material [33, 34]. Few data are available on trace metal concentrations in benthic invertebrates from Keban Dam Lake, Elazığ, Turkey. In the present study, freshwater crayfish (*A. leptodactylus*) were used as the bioindicator organisms for monitoring and assessment

of the water quality of the Keban Dam Lake for trace metals. Because they are closely associated with surficial sediments, and their effective bioaccumulation capacity of toxic metals has potential for transferring contaminants up the food web to human consumers.

In this study, the concentrations of trace elements determined were at permissible levels set by Turkish legislation in all years. No distinctive bioaccumulation trend was observed among years for any trace elements studied. Bioaccumulation of cooper, zinc, and mercury has a decreasing trend between 2006 and 2009 and then periods have showed increasing trend. But, for Hg and Pb, there is an increase in bioaccumulation level in last two years. That increased level can be associated with increasing cage aquaculture facilities and agricultural activities around sampling area. Similarly [35] reported that the aquaculture industries such as cage aquaculture facilities may discharge many chemical pollutants like trace elements and PAHs to aquatic environment especially due to the use of antibiotic, agrochemicals formulated feed.

4. Conclusion

In this study, the results of trace elements concentrations in *A. leptodactylus* which were captured from Keban Dam Lake between 2006 and 2012 were reported. Our results showed that bioaccumulation can occur in edible tissues. This study will provide significant data for further water quality monitoring studies to establish effects of trace element presence on living organisms in Keban Dam Lake area.

Conflict of Interests

The authors declare that there is no conflict of interests regarding the publication of this paper.

Acknowledgments

This study was carried out by the support of the Provincial Directorate of Food, Agriculture, and Livestock in Tunceli (Turkey). The authors are thankful to all members of the Provincial Directorate of Food, Agriculture, and Livestock in Tunceli for their help and cooperation.

References

- [1] A. Suárez-Serrano, C. Alcaraz, C. Ibáñez, R. Trobajo, and C. Barata, "Procambarus clarkii as a bioindicator of heavy metal pollution sources in the lower Ebro River and Delta," *Ecotoxicology and Environmental Safety*, vol. 73, no. 3, pp. 280–286, 2010.
- [2] O. Kaplan, N. C. Yıldırım, N. Yıldırım, and M. Cimen, "Toxic elements in animal products and environmental health," *Asian Journal of Animal and Veterinary Advances*, vol. 6, no. 3, pp. 228–232, 2011.
- [3] F. J. Sánchez, M. D. G. Gil, N. P. Sánchez, and J. L. Martínez, "Determination of heavy metals in crayfish by ICP-MS with a microwave-assisted digestion treatment," *Ecotoxicology and Environmental Safety*, vol. 54, pp. 223–228, 2003.

- [4] M. Ural, N. Yildirim, D. Danabas et al., "Some heavy metals accumulation in tissues in *Capoeta umbra* (Heckel, 1843) from Uzungayir Dam Lake (Tunceli, Turkey)," *Bulletin of Environmental Contamination and Toxicology*, vol. 88, no. 2, pp. 172–176, 2012.
- [5] Agency for Toxic Substances and Disease Registry (ATSDR), *Toxicological Profile for Copper*, U.S. Department of Health and Human Services, Atlanta, Ga, USA, 2004.
- [6] Agency for Toxic Substances and Disease Registry (ATSDR), *Toxicological Profile for Cadmium*, U.S. Department of Health and Human Services, Atlanta, Ga, USA, 2011.
- [7] Agency for Toxic Substances and Disease Registry (ATSDR), *Toxicological Profile for Lead*, U.S. Department of Health and Human Services, Atlanta, Ga, USA, 2007.
- [8] Agency for Toxic Substances and Disease Registry (ATSDR), *Toxicological Profile for Mercury*, Atlanta, Ga, USA, 1999.
- [9] H. A. Schroeder, A. P. Nason, I. H. Tipton, and J. J. Balassa, "Essential trace metals in man: zinc. Relation to environmental cadmium," *Journal of Chronic Diseases*, vol. 20, no. 4, pp. 179–210, 1967.
- [10] M. E. Wastney, R. L. Aamodt, W. F. Rumble, and R. I. Henkin, "Kinetic analysis of zinc metabolism and its regulation in normal humans," *The American Journal of Physiology*, vol. 251, no. 2, pp. 398–410, 1986.
- [11] L. E. Cuevas and A. Koyanagi, "Zinc and infection: a review," *Annals of Tropical Paediatrics*, vol. 25, no. 3, pp. 149–160, 2005.
- [12] D. K. Nordstrom, "Worldwide occurrences of arsenic in ground water," *Science*, vol. 296, no. 5576, pp. 2143–2145, 2002.
- [13] A. H. Smith, C. Hopenhayn-Rich, M. N. Bates et al., "Cancer risks from arsenic in drinking water," *Environmental Health Perspectives*, vol. 97, pp. 259–267, 1992.
- [14] J. A. Centeno, P. B. Tchounwou, A. K. Patlolla et al., "Environmental pathology and health effects of arsenic poisoning: a critical review," in *Managing Arsenic in the Environment: From Soil to Human Health*, R. Naidu, E. Smith, G. Owens, P. Bhattacharya, and P. Nadebaum, Eds., pp. 311–327, CSIRO, Melbourne, Australia, 2006.
- [15] Q. D. Le, K. Shirai, D. C. Nguyen, N. Miyazaki, and T. Arai, "Heavy metals in a tropical eel *Anguilla marmorata* from the central part of vietnam," *Water, Air, and Soil Pollution*, vol. 204, no. 1–4, pp. 69–78, 2009.
- [16] G. Bagatto and M. A. Alikhan, "Copper, cadmium, and nickel accumulation in crayfish populations near copper-nickel smelters at Sudbury, Ontario, Canada," *Bulletin of Environmental Contamination and Toxicology*, vol. 38, no. 3, pp. 540–545, 1987.
- [17] D. J. H. Phillips and P. S. Rainbow, *Biomonitoring of Trace Aquatic Contaminants*, vol. 388 of *Ettore Majorana International Science Series*, Chapman and Hall, London, UK, 1993.
- [18] D. Danabas, F. Benzer, O. Kaplan, and N. C. Yildirim, "Levels of copper in liver, muscle and gill tissues in *Capoeta trutta* (Heckel, 1843) from Munzur River, Turkey," *African Journal of Agricultural Research*, vol. 6, no. 7, pp. 1909–1912, 2011.
- [19] G. B. Masters, *Introductions to Environmental Engineering and Science*, Prentice Hall, Upper Saddle River, NJ, USA, 1997.
- [20] O. Barim and M. Karatepe, "The effects of pollution on the vitamins A, E, C, β-carotene contents and oxidative stress of the freshwater crayfish, *Astacus leptodactylus*," *Ecotoxicology and Environmental Safety*, vol. 73, no. 2, pp. 138–142, 2010.
- [21] A. C. K. Benli, R. Sarıkaya, A. Sepici-Dincel, M. Selvi, D. Şahin, and F. Erkoç, "Investigation of acute toxicity of (2,4-dichlorophenoxy)acetic acid (2,4-D) herbicide on crayfish (*Astacus leptodactylus* Esch. 1823)," *Pesticide Biochemistry and Physiology*, vol. 88, no. 3, pp. 296–299, 2007.
- [22] A. T. Khan, D. M. Forester, and H. W. Mielke, "Heavy metal concentrations in two populations of crayfish," *Veterinary and Human Toxicology*, vol. 37, no. 5, pp. 426–428, 1995.
- [23] P. A. Schilderman, E. J. C. Moonen, L. M. Maas, I. Welle, and J. C. S. Kleinjans, "Use of crayfish in biomonitoring studies of environmental pollution of the river Meuse," *Ecotoxicology and Environmental Safety*, vol. 44, no. 3, pp. 241–252, 1999.
- [24] M. Guoda, "Bioaccumulation of heavy metals in noble crayfish (*Astacus astacus* L.) tissues under aquaculture conditions," *Ecologija*, vol. 2, pp. 79–82, 2002.
- [25] U. Güner, "Heavy metal effects on P, Ca, Mg, and total protein contents in embryonic pleopodal eggs and stage-1 juveniles of freshwater crayfish *Astacus leptodactylus* (Eschscholtz, 1823)," *Turkish Journal of Biology*, vol. 34, no. 4, pp. 405–412, 2010.
- [26] NMKL, "Nordic committee on food analysis," method no. 161, Postboks 8156 Dep. N-0033, Oslo, Norway, pp. 1–8, 1998.
- [27] M. M. Harlioğlu, Ö. Barim, I. Türkoglu, and A. G. Harlioğlu, "Potential fecundity of an introduced population, Keban Dam Lake, Elazığ, Turkey, of freshwater crayfish, *Astacus leptodactylus leptodactylus* (Esch., 1852)," *Aquaculture*, vol. 230, no. 1–4, pp. 189–195, 2004.
- [28] S. N. Luoma, "Bioavailability of trace metals to aquatic organisms—a review," *Science of the Total Environment*, vol. 28, pp. 1–22, 1983.
- [29] M. C. Eimers, R. D. Evans, and P. M. Welbourn, "Cadmium accumulation in the freshwater isopod *Asellus racovitzai*: the relative importance of solute and particulate sources at trace concentrations," *Environmental Pollution*, vol. 111, no. 2, pp. 247–253, 2001.
- [30] F. Kulahci and M. Doğru, "Physical and chemical investigation of water and sediment of the Keban Dam Lake, Turkey—part 2: distribution of radioactivity, heavy metals and major elements," *Journal of Radioanalytical and Nuclear Chemistry*, vol. 268, no. 3, pp. 529–537, 2006.
- [31] J. Burger, K. F. Gaines, C. S. Boring et al., "Metal levels in fish from the Savannah river: potential hazards to fish and other receptors," *Environmental Research*, vol. 89, no. 1, pp. 85–97, 2002.
- [32] Z. Zhang, L. He, J. Li, and Z. B. Wu, "Analysis of heavy metals of muscle and intestine tissue in fish—in banan section of chongqing from three gorges reservoir, China," *Polish Journal of Environmental Studies*, vol. 16, no. 6, pp. 949–958, 2007.
- [33] J. Love and J. F. Savino, "Crayfish (*Orconectes virilis*) predation on zebra mussels (*Dreissena polymorpha*)," *Journal of Freshwater Ecology*, vol. 8, pp. 253–259, 1993.
- [34] M. Matthews, J. D. Reynolds, and M. J. Keatinge, "Macrophyte reduction and benthic community alteration by the crayfish, *Austropotamobius pallipes* (Lereboullet)," *Freshwater Crayfish*, vol. 9, pp. 289–299, 1993.
- [35] Y. Shahrizat, *Distribution and accumulation of heavy metals in fish cage system in Linggi, Estuary, Malaysia [M.S. thesis]*, Faculty of Science, University of Putra Malaysia, 2005.

Synthesis, Spectral Characterization, and Antiproliferative Studies of Mixed Ligand Titanium Complexes of Adamantylamine

Raj Kaushal,¹ Nitesh Kumar,¹ Ashun Chaudhary,² Saroj Arora,² and Pamita Awasthi¹

¹ Department of Chemistry, National Institute of Technology, Hamirpur, Himachal Pradesh 177005, India

² Department of Botanical and Environmental Sciences, Guru Nanak Dev University, Amritsar, Punjab 143005, India

Correspondence should be addressed to Nitesh Kumar; niteshnit6@gmail.com

Academic Editor: Ian Butler

Titanium complexes have been synthesized by the reaction between titanium tetrachloride ($TiCl_4$), respective bidentate ligand [4,4'-dimethoxy-2,2'-bipyridine (bpome), 6,6'-dimethyl-2,2'-bipyridine (dpme), 1,2-diaminocyclohexane (dach), 1,10-phenanthroline (phen), and benzoylacetone (bzac)], and adamantylamine (ada) in 1:2:2 molar ratios, respectively. The structure of synthesized complexes was confirmed using elemental analysis, FTIR, UV-visible, 1H NMR, and mass spectrometry techniques. The nanocrystalline nature of complexes was confirmed by powder XRD study. The complexes were evaluated for cytotoxic potential in HeLa (cervical), C6 (glioma), and CHO (Chinese hamster ovarian) cell lines. The complex E was found to be more effective cytotoxic agent against HeLa cell line with an IC_{50} value of 4.06 μM . Furthermore, the effect of synthesized complexes was studied on different stages of the cell cycle in CHO cells. All complexes exhibited the dose dependent increase in cytotoxicity. The results have shown an increase in sub- G_0 population with increase in concentration which is an indicative measure of apoptosis.

1. Introduction

The discovery of cisplatin, a metal (platinum) based anti-cancer drug by Rosenberg et al. in 1965, has created interest in the development of metal based anticancer drugs [1–3]. The effect of transition metal complexes, other than platinum such as ruthenium [4–8], palladium [9–13], gold [14, 15], and titanium [16–25] has also been studied on several cancer cell lines. In addition to cisplatin, many other platinum based drugs, namely, carboplatin, oxaliplatin, tetraplatin, and satraplatin [3], and nonplatinum based drugs, namely, budotitane, titanocene dichloride [16], NAMI-A, KP1019 [26–29], and auranofin [14] have shown remarkable results. Out of these, the first nonplatinum anticancer drugs were budotitane and titanocene dichloride which are titanium based drugs [16]. These titanium complexes offer an alternative to chemotherapy, although these complexes do not follow a mechanism similar to that of other metal complexes. Previous studies have revealed that titanium compounds are effective against those cell lines which are resistant to platinum based

drugs and kill the cancer cells through apoptosis. It has also been confirmed that lability of ligand is not a mandatory condition for a compound to show cytotoxicity [30], but other ligand properties have been found to be necessary for this activity [31]. It is well established that ligands having electron donating atom(s) show increased cytotoxicity due to enhanced coordination capacity [32, 33]. Since few efforts have been made towards the synthesis and use of titanium complexes as chemotherapeutic agents, this is an important area of research. In the present work, we report the synthesis, structural characterization, and antiproliferative potential of some of titanium complexes.

2. Experimental Section

2.1. Materials and Methods. Ligands and titanium tetrachloride used were obtained from Sigma Aldrich. All the solvents were of AR grade (Merck) and purified by standard procedure before use and stored over 4 Å molecular sieves. Purity of ligands was checked by checking their melting points. Elemental

analyses were performed by using Perkin-Elmer, Series 2400. The UV-visible spectra of the complexes were recorded on Perkin Elmer Lambda 750 in the range of 200–800 nm and FTIR Spectra were recorded from 4000–200 cm⁻¹ on Perkin Elmer 1600. The mass spectrum was recorded by using the electron spray ionization technique on Waters Micromas Q Tof Micro. ¹H NMR Spectra were recorded on Brucker Avance 400 MHz spectrometer. Crystalline nature of the complexes has been confirmed by powder XRD technique on Philips 1710 X-ray diffractometer.

2.2. Synthetic Procedures (A–E)

2.2.1. Synthesis of Bis(adamantylamino)bis-(4,4'-dimethoxy-2,2'-bipyridyl)titanium(II), Ti(ada)₂(bpome)₂, (A). To a colorless solution of 4,4'-dimethoxy-2,2'-bipyridyl (0.45 g, 2.1 mmol) in 25 mL of toluene, a pale yellow colored solution of titanium tetrachloride (0.2 g, 1.05 mmol) in 25 mL of toluene was added dropwise with continuous stirring under ice cold conditions. The reaction mixture was stirred for 2 h followed by refluxing for 10 h till the evolution of chlorine gas ceased. The evolution of chlorine gas was checked by passing the gas through a potassium iodide solution which results in reddish brown color of potassium iodide due to liberation of iodine. After removing solvent through vacuum distillation compound was dried under vacuum. A light yellow colored solid compound [TiCl₂(bpome)₂] was obtained. Yield: 0.5 g (86.2%). Now, to a solution of TiCl₂(bpome)₂ (0.5 g, 0.91 mmol) in 25 mL of toluene, adamantylamine (0.27 g, 1.81 mmol) in 25 mL of toluene was added dropwise with continuous stirring. The reaction mixture was stirred for 2 h and refluxed for 14 h till the evolution of HCl gas ceased. The evolution of HCl gas was confirmed by passing the gas through an ammonia solution which results in white dense fumes of ammonium chloride. The excess solvent was removed by vacuum distillation and the compound was washed with petroleum ether. The compound was dried under vacuum. A cream colored solid powder was obtained which was recrystallised in methanol. Yield: 0.45 g (64.28%). TiC₄₄H₅₄N₆O₄: elemental anal. Calcd (%): C 67.67, H 7.17, N 10.76; found (%): C 66.71, H 7.05, N 10.52. FTIR (KBr, cm⁻¹) $\bar{\nu}$: 3388 (NH Stretching), 3015 (aromatic CH stretching), 2927 (CH stretching), 1629 (C=C stretching), 1522 (C=N stretching), 1449 (NH bending), 1313, 1229 (CH bending), 906, 809 (CH out of plane deformation), 452 (Ti–N stretching). ¹H NMR (DMSO, 400 MHz): adamantylamine δ , ppm = 2.1 (s, NH), 1.86 (d, ³J = 1.96 Hz, CH₂ protons), 1.66, 1.59, (dd, ³J = 12.36, 29.6 Hz CH protons). 4,4'-Dimethoxy-2,2'-bipyridine δ , ppm = 8.66 (d, ³J = 6.16 Hz, 4H, H⁶), 7.96 (s, 4H, H³), 7.37 (d, ³J = 8 Hz, 4H, H⁵), 4.09 (s, 12H, OCH₃).

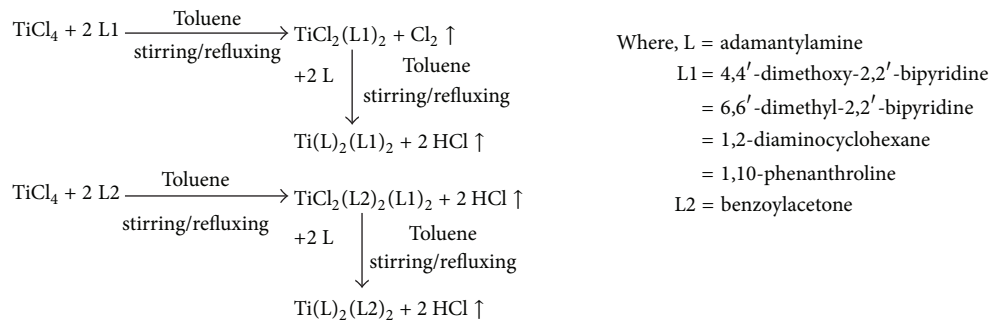
2.2.2. Synthesis of Bis(adamantylamino)bis-(6,6'-dimethyl-2,2'-bipyridyl)titanium(II), Ti(ada)₂(dpme)₂, (B). The complex was synthesized in accordance to the procedure used for complex A. Yield: 0.4 g (84.38%). TiC₄₄H₅₄N₆: elemental anal. Calcd (%): C 73.70, H 7.81, N 11.72; found (%): C 73.91, H 7.94, N 11.54. FTIR (KBr, cm⁻¹) $\bar{\nu}$: 3336 (NH stretching), 3071 (aromatic CH stretching), 2925 (CH stretching), 1644

(C=C stretching), 1506 (C=N stretching), 1441 (NH bending) 1271, 1117 (CH bending), 906, 801 (CH out of plane deformation), 404 (Ti–N stretching). ¹H NMR (DMSO, 400 MHz): adamantylamine δ , ppm = 2.12 (s, NH), 1.91 (d, ³J = 2.12 Hz, CH₂ protons), 1.69, 1.64, (dd, ³J = 12.6, 22.6 Hz CH protons). 6,6'-Dimethyl-2,2'-bipyridine δ , ppm = 8.5 (d, ³J = 7.96 Hz, 4H, H⁵), 8.23 (t, ³J = 7.8, 7.8 Hz 4H, H⁴), 7.68 (d, ³J = 7.8 Hz, 4H, H³), 2.89 (s, 12H, CH₃).

2.2.3. Synthesis of Bis(adamantylamino)bis-(1,2-diaminocyclohexane)titanium(II), Ti(ada)₂(dach)₂, (C). The complex C was synthesized similarly to complex A. Yield = 0.48 g (87.2%). TiC₃₂H₅₈N₆: elemental anal. Calcd (%): C 66.63, H 10.41, N 14.57; found (%): C 65.77, H 10.23, N 14.72. FTIR (KBr, cm⁻¹) $\bar{\nu}$: 3379 (NH stretching), 2925, 2900 (CH stretching), 1595 (C=N stretching), 1522 (NH bending), 1360, 1311 (CH bending), 1084, 1020 (CH out of plane deformation), 444 (Ti–N stretching). ¹H NMR (D₂O, 400 MHz): adamantylamine δ , ppm = 2.09 (s, NH), 1.7, ³J = 4 (d, CH₂ protons), 1.63, 1.55, (dd, ³J = 12.52, 36.76 CH protons). 1,2-Diaminocyclohexane δ , ppm = 3.63 (t, ³J = 4.8, 4.64 CH), 3.3(m, NH₂), 2.01, 1.76, 1.68, 1.3 (H³, H⁶, H⁴, H⁵).

2.2.4. Synthesis of Bis(adamantylamino)bis-(1,10-phenanthroline)titanium(II), Ti(ada)₂(phen)₂, (D). The procedure described above for complex A was followed for the synthesis of complex D. Yield: 0.42 g (87.5%). TiC₄₄H₄₆N₆: elemental anal. Calcd (%): C 74.55, H 6.77, N 11.85; found (%): C 74.46, H 6.42, N 11.52. FTIR (KBr, cm⁻¹) $\bar{\nu}$: 3412 (NH stretching), 3039 (aromatic CH stretching), 2927 (CH stretching), 1612 (C=C stretching), 1514 (N–H bending), 1449 (C=N stretching), 1368, 1319 (CH bending), 1084 (CH out of plane deformation), 411 (Ti–N stretching). ¹H NMR (D₂O, 400 MHz): adamantylamine δ , ppm = 2.04 (s, NH), 1.75 (d, ³J = 2.52, CH₂ protons), 1.61, 1.55, (dd, ³J = 24.8 CH protons). 1,10-Phenanthroline δ , ppm = 8.56 (d, ³J = 7.43, 4H, H² & H⁹), 7.7 (s, 4H, H⁵ & H⁶), 7.4 (d, ³J = 9.28, 4H, H⁴ & H⁷), 6.8 (dd, ³J = 28, 40, 4H, H³ & H⁸).

2.2.5. Synthesis of Bis(adamantylamino)bis(benzoylacetonato)titanium(IV), Ti(ada)₂(bzac)₂, (E). The procedure for the synthesis of complex A was followed for the preparation of complex E. However, there was evolution of HCl gas in both the steps. Yield: 0.43 g (86%). TiC₄₀H₄₈N₂O₂: elemental anal. Calcd (%): C 71.61, H 7.45, N 4.17; found (%): C 71.70, H 7.27, N 4.10. FTIR (KBr, cm⁻¹) $\bar{\nu}$: 3379 (NH stretching), 2933, 2866 (CH stretching), 1612 (C=O stretching), 1522 (C=C stretching), 1449 (NH bending), 1109, 1004 (C–H bending), 557 (Ti–O stretching), 427 (Ti–N stretching). ¹H NMR (D₂O, 400 MHz): adamantylamine δ , ppm = 2 (s, NH), 1.71 (d, ³J = 2.56, CH₂ protons), 1.58, 1.49, (dd, ³J = 12.56, 12.08 CH protons). Benzoylacetone δ , ppm C₆H₅: δ = 8.08 (d, ³J = 7.52, 4H, H² and H⁶), 7.96 (t, ³J = 7.16, 4.28, 4H, H³ and H⁵), 7.6 (t, ³J = 7.64, 7.28, 2H, H⁴), 3.92 (s, CH protons), 2.5 (s, CH₃ protons).



SCHEME 1: General synthetic route for mixed ligand titanium complexes of adamantylamine.

2.3. Cytotoxicity Studies

2.3.1. Cell Lines and Culture. The cytotoxic studies of synthesized complexes were performed on HeLa (cervical cancer cell line), C6 (glioma), and CHO (Chinese hamster ovarian) cell line. The cells were grown in Dulbecco's Modified Eagle's Medium (DMEM) containing fetal calf serum (FCS) (10%), penicillin (100 units/mL), and streptomycin (100 $\mu\text{g}/\text{mL}$) at 37°C with 90% humidity and 5% CO₂. The complexes were dissolved in dimethyl sulphoxide (DMSO) to prepare the solutions of different concentrations. The selected cell lines were treated with these solutions to calculate the IC₅₀ values by using MTT (3-(4,5-dimethylthiazol-2-yl)-2,5-diphenyltetrazolium bromide) assay while control cells received only DMSO.

2.3.2. MTT Assay. The growth inhibitory effect of newly synthesized titanium complexes on HeLa, C6, and CHO cells was determined by MTT assay [34]. For this, cells were supplemented in complete growth medium to get 1×10^5 cells/mL and 100 μL of cell suspension per well was seeded in tissue culture plate. The assay was carried out in 96 well plates in triplicate in which cells were treated with three different concentrations of complexes and incubated for 12 h in CO₂ incubator. Thereafter, 20 μL of freshly prepared MTT solution, 5 mgmL⁻¹ in PBS (phosphate buffered saline) after sterile filtering, was added to each well. Now, culture plates were stirred at 150 rpm for 5 min to thoroughly mix MTT into the media. The plates were further incubated for 4 h at 37°C to allow metabolism of MTT. MTT formazan crystals were resuspended in 100 μL of DMSO and plates were stirred for 20 min in order to dissolve formazan crystals and optical density was measured at 570 nm. The phase contrast imaging was done by using Nikon Eclipse TS100 inverted microscope.

2.3.3. Cell Cycle Analysis. 1×10^6 cells/dish well was plated in 24 well plates which were allowed for adhesion for 6 h and then treated with complexes at three different concentrations. After 24 h of treatment, cells were harvested from the plate. The cell suspension having 1×10^6 cells was centrifuged and the resultant cell pellet was resuspended in phosphate buffered saline (1 mL) solution. The cells were fixed in ice cold 70% ethanol and stained with propidium iodide followed by analysis on the FL-2 channel by BD Accuri C6 flow cytometer

(BD Biosciences Immunocytometry Systems, San Jose, CA). DNA content histograms and cell cycle phase distributions were modeled from at least 15,000 single events.

3. Results and Discussion

Synthesis of titanium complexes was carried out in two steps. In the first step, titanium tetrachloride reacted with respective bidentate ligand, that is, 4,4'-dimethoxy-2,2'-bipyridine, 6,6'-dimethyl-2,2'-bipyridine, 1,2-diaminocyclohexane, 1,10-phenanthroline, and benzoylacetone which are coligands in 1:2 molar ratio under continuous stirring and refluxing by using toluene as a solvent. There was evolution of chlorine gas during the course of reaction. In the next step, respective titanium complexes reacted with main ligand (adamantylamine) in 1:2 molar ratio in the same solvent, which results in evolution of HCl gas [35] as shown in Scheme 1. Elemental analysis, that is, Titanium and chlorine estimation, was performed to check the composition by gravimetric and Volhard's method, respectively, and molecular weight was determined by Rast's camphor method (Table 1). The analytical data and spectroscopic characterization of complexes confirm the proposed structure of complexes. The proposed structure of complexes and their corresponding ligands has been shown in Table 2.

3.1. FTIR Spectra. The bands of FTIR were assigned by comparing the spectra of complexes with those of free ligands and were shown in Table 3. From the spectra of complexes, we have found that wave number of $\bar{\nu}_{\text{C}-\text{H}}$ band appearing around 2900–3000 cm⁻¹ does not change much although the intensity of the band changes and gets weaker upon complexation with titanium metal. The absorption band due to $\bar{\nu}_{\text{C}=\text{C}}$ stretching at 1595, 1578, and 1603 cm⁻¹ in the bidentate ligand of complexes A, B, and D gets shifted to 1629, 1644, and 1612 cm⁻¹ (Table 3). The shift may be due to reduction in electron density after an increase in conjugation caused by complexation with titanium metal [36]. In previous studies, it has been observed that three factors, namely, field effect, steric effect, and ring strain, can cause shift in vibrational frequencies of complexes. Due to field effect [37], the value of force constant gets changed and there is change in vibration frequencies, due to steric effect [36], the conjugation in the complex is not completed which results in a shift in

TABLE 1: Physical and analytical properties of titanium complexes.

Complex	Color	Yield (%)	M.P. (°C)	Experimental (Theoretical) % Ti	Experimental (Theoretical) % MW
Ti(ada) ₂ (bpome) ₂ (A)	Cream	64.2	205–210	6.3 (6.1)	778 (780)
Ti(ada) ₂ (dpme) ₂ (B)	Cream	87.3	205–210	7.1 (6.6)	713 (716)
Ti(ada) ₂ (dach) ₂ (C)	White	87.2	225–230	8.3 (8.1)	574 (577)
Ti(ada) ₂ (phen) ₂ (D)	Cream	87.5	210–215	6.0 (6.6)	705 (708)
Ti(ada) ₂ (bzac) ₂ (E)	Light Orange	86	240–245	7.8 (7.1)	668 (670)

absorption frequencies to higher wave number, and due to ring strain in the molecule, more energy is required for vibration of bonds which results in shift of band towards higher wave number. The ring breathing vibration (around 800–900 cm⁻¹) having more intensity gets shifted to higher wave number in complexes (around 1000 cm⁻¹). All these changes can be assigned to the coordinated nature of bidentate ligand through nitrogen atoms [12, 13]. The band formed around 3350–3400 cm⁻¹ due to N–H stretching of adamantylamine ring, while the occurrence of a strong band in the region 1600–1580 cm⁻¹ in complex E may be assigned to stretching modes of $\bar{\nu}_{\text{C=O}}$ in benzoylacetone ligand. In complex E carbonyl groups are involved in bonding with the metal ion which is further supported by the appearance of an intense band at ~ 557 cm⁻¹ assignable to $\bar{\nu}_{\text{M-O}}$ vibration. Appearance of new bands at 452, 404, 444, 411, and 427 cm⁻¹ in complexes A, B, C, D, and E shows that ligands are coordinated to the metal atom through nitrogen [35, 38] and the absence of bands in the region 385–340 cm⁻¹ due to $\bar{\nu}_{\text{Ti-Cl}}$ bond in all complexes indicates the complete removal of chloride ions [39].

3.2. UV-Visible Spectra. The UV-visible spectra of the complexes (Figure 1) and ligands were recorded from a solid sample by using diffuse reflectance technique. The transitions observed in the UV-visible spectrum of complexes were due to intraligand charge transfer. The transition around 320–325 nm can be attributed to $n \rightarrow \pi^*$ transition in complexes A, B, D, and E get shifted to lower wavelength after coordination. However bands due to $\pi \rightarrow \pi^*$ around 240–245 nm remain almost at the same position even after coordination. Since in complex C both the ligands are of cyclic nature, so there is no possibility of these transitions.

3.3. ^1H NMR Study. The ^1H NMR spectra of the complexes are consistent with the structures proposed in the reaction scheme. We find that bidentate ligands of synthesized complexes show a considerable downfield shift of protons after complexation with titanium. This shift may be due to transfer of electron density from ligand protons to the metal atom [35, 40]. However, protons of adamantylamine in all complexes appearing around 1.2–2.12 ppm show a marginal chemical shift. The cyclic aliphatic nature of both the ligands in complex C creates complications in the spectrum as the peaks corresponding to these falls almost in the same region.

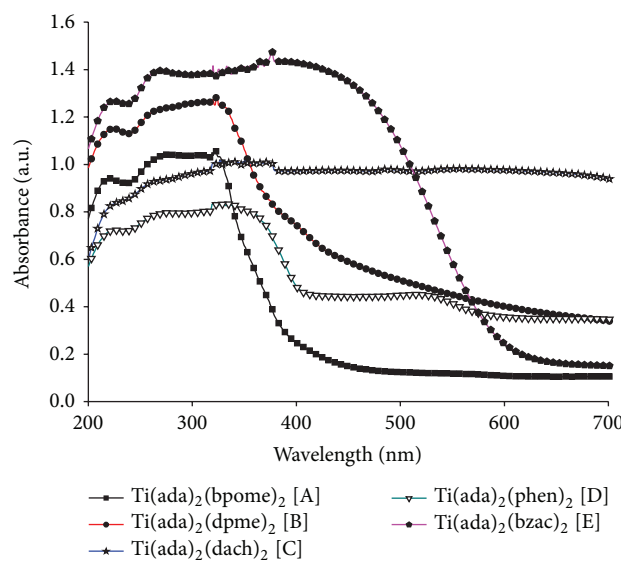


FIGURE 1: Electronic spectra of titanium complexes.

However, the integration of signals in all spectra supports the formation of proposed complexes.

3.4. Mass Spectra. The structure of complexes was further confirmed by recording electron spray mass spectrum. The complex A showed base peak at $m/z = 152$ due to $\text{C}_{10}\text{H}_{17}\text{N}$ fragment ion and 4,4'-dimethoxy-2,2'-bipyridine ligand in the complex showed peak at $m/z = 217$ with relative intensity of 25%. We find that this complex also shows a peak at $m/z = 478$ due to $\text{TiC}_{24}\text{H}_{24}\text{N}_4\text{O}_4$ fragment ion. In case of complex B, one peak at $m/z = 185$ due to $\text{C}_{12}\text{H}_{12}\text{N}_2$ fragment ion and another peak at $m/z = 152$ due to $\text{C}_{10}\text{H}_{17}\text{N}$ fragment ion were found with a relative intensity of 18%. In complex C, peaks were formed at $m/z = 98, 115, 230$ due to $\text{C}_6\text{H}_{12}\text{N}$, $\text{C}_6\text{H}_{14}\text{N}_2$, and $\text{TiC}_{10}\text{H}_{19}\text{N}_2$ fragment ions. The complex D shows peaks at $m/z = 304$ and 335 due to $\text{TiC}_{16}\text{H}_{22}\text{N}_3$ and $\text{TiC}_{16}\text{H}_{22}\text{N}_3$ fragment ions. In addition to these peaks, complex D shows a molecular ion peak at $m/z = 708$ with very low intensity. In complexes C, D, and E, formation of the base peak takes place due to $\text{C}_{10}\text{H}_{17}\text{N}$ fragment ion at $m/z = 152$. The complex E, in addition to base peak, also shows fragment ion peaks, in which one peak is formed at $m/z = 401$ due to $\text{TiC}_{22}\text{H}_{32}\text{N}_2\text{O}_2$ fragment ion. The complexes A, B, C, and E show their molecular ion peaks at $m/z = 780, 716, 577$, and 670

TABLE 2: Structure of ligands and proposed complexes.

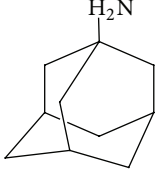
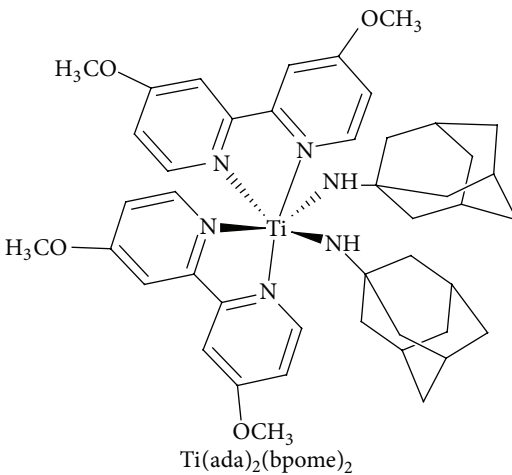
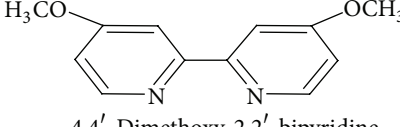
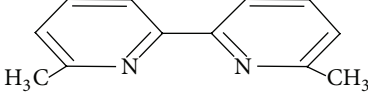
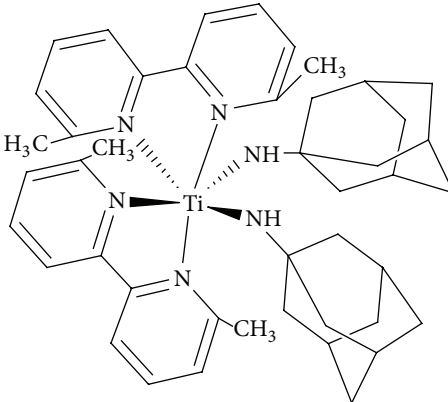
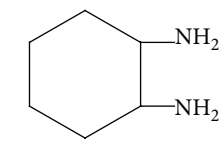
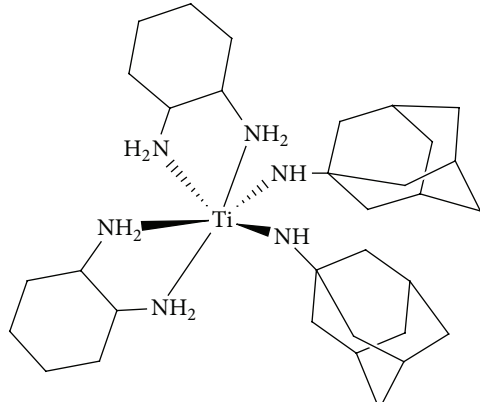
Ligands	Proposed complexes
	
	
	
	

TABLE 2: Continued.

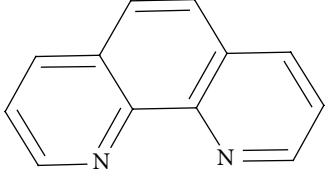
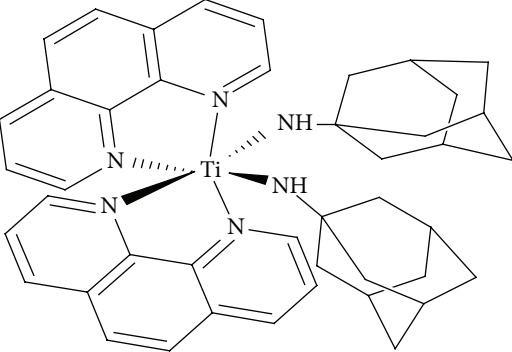
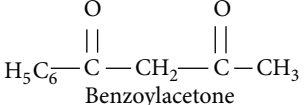
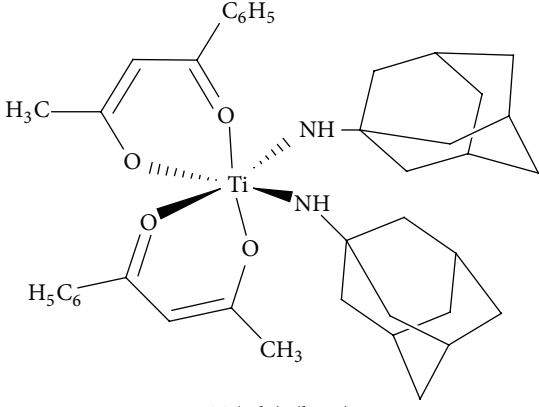
Ligands	Proposed complexes
 1,10-Phenanthroline	
 Benzoylacetone	

TABLE 3: Selected FTIR bands for titanium complexes and their corresponding ligands $\bar{\nu}$ (cm^{-1}).

Ligand/Complex	$\bar{\nu}_{\text{Ti}-\text{O}}$	$\bar{\nu}_{\text{Ti}-\text{N}}$	$\bar{\nu}_{\text{C}-\text{H}}$ bend	$\bar{\nu}_{\text{C}-\text{C/C=C}}$ stretch	$\bar{\nu}_{\text{N}-\text{H}}$ bend	$\bar{\nu}_{\text{C}-\text{H}}$ stretch	$\bar{\nu}_{\text{N}-\text{H}}$ stretch	$\bar{\nu}_{\text{C=O}}$ stretch
Ada	—	—	1132, 1108	1457	1589	2912	3345, 3372	
bpome	—	—	1303, 1230	1595	—	3071, 2974	—	
Ti(ada) ₂ (bpome) ₂	—	452	1313, 1229	1629	1449	3015, 2927	3388	
dpme	—	—	1247, 1158	1578	—	3063, 2917	—	
Ti(ada) ₂ (dpme) ₂	—	404	1271, 1117	1644	1441	3071, 2925	3336	
dach	—	—	1373, 1072	1433	1578	2924	3357, 3285	
Ti(ada) ₂ (dach) ₂	—	444	1360, 1311	1470	1522	2925, 2900	3379	
phen	—	—	1344, 1093	1603	—	3055	—	
Ti(ada) ₂ (phen) ₂	—	411	1368, 1319	1612	1514	3039, 2927	3412	
bzac			1255	1409		3063, 3006		1603
Ti(ada) ₂ (bzac) ₂	557	427	1109, 1004	1522	1449	2933, 2866	3379	1612

indicating the formation of complexes. The existence of these different fragment ion peaks, base peaks, and molecular ion peaks supports the stoichiometric formulation of synthesized complexes [35].

3.5. Powder XRD Study. The powder X-ray diffraction study was performed to understand the lattice structure of the complexes. Figure 2 shows XRD pattern obtained for all the complexes with well-defined peaks in these patterns which

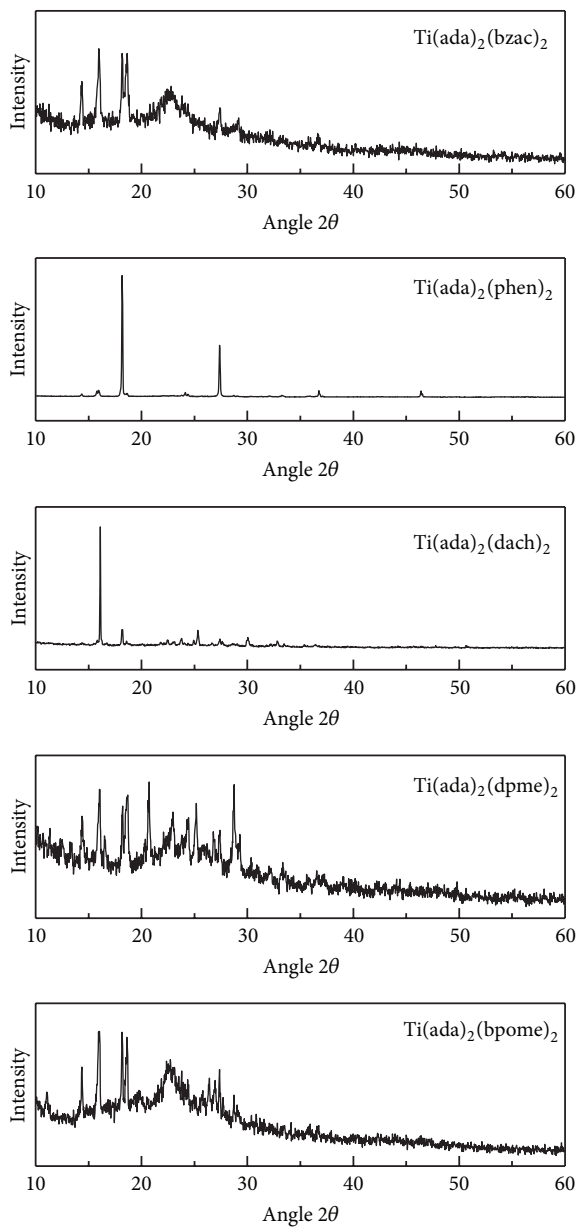


FIGURE 2: Powder XRD pattern of titanium complexes.

indicate the crystalline nature of complexes. Scherrer's equation $D = (\lambda \times 0.9)/(\beta \times \cos \theta)$ [35, 41], with D as the crystallite size of $(h k l)$ planes, λ as the wavelength of incident radiation ($\text{CuK}\alpha$, 1.54 \AA), and β as full width half maximum (FWHM), was used to calculate the crystallite size of complexes. The calculated crystallite size for complexes A, B, C, D, and E was 69, 26.5, 19.1, 115, and 76.6 nm , respectively, which falls in nanorange. Unit cell parameter of the complexes has been calculated by using Powder X software [42] and the results are summarized in Table 4. We have also observed that as the crystallite size decreases, peaks become broader as seen in Figure 2. On the basis of these different spectroscopic techniques, that is, UV-visible, FTIR, ^1H NMR, and mass spectrometry, an octahedral geometry may be proposed for the synthesized titanium complexes [43].

3.6. MTT Assay. The IC_{50} values were calculated by using best fit regression model and results have been tabulated in Table 5. The change in morphological features was observed at different concentrations of complexes, which indicates that such change in morphology is dose dependent as shown in Figure 3. The phase contrast imaging was done with a Nikon microscope at $40\times$ after harvesting stage which clearly shows the formation of small apoptotic bodies, rounding of cells, shrinkage of cells, and plasma membrane blebbing. From the calculated IC_{50} values, it has been observed that complex E with benzoylacetone ligand shows ($4.06 \mu\text{M}$) better activity than other complexes against the HeLa cell line, which is even better than known anticancer drug camptothecin as seen in Table 5. But ligands were found not much effective against the tested cancer cell lines.

TABLE 4: XRD data of titanium complexes.

Empirical formula	TiC ₄₄ H ₅₄ N ₆ O ₄ (A)	TiC ₄₄ H ₅₄ N ₆ (B)	TiC ₃₂ H ₅₈ N ₆ (C)	TiC ₄₄ H ₄₆ N ₆ (D)	TiC ₄₀ H ₄₈ N ₂ O ₂ (E)
Formula weight	780	716	576	708	670
Crystal system	Monoclinic	Monoclinic	Monoclinic	Monoclinic	Monoclinic
Lattice type	P	P	P	P	P
<i>a</i> (Å°)	17	13	16	11	17
<i>b</i> (Å°)	13	11	12	13	11
<i>c</i> (Å°)	14	20	15	14	16
α (°)	90	90	90	90	90
β (°)	91	106	113	106	85
γ (°)	90	90	90	90	90
Crystallite size (nm)	69	26.5	19.1	115	76.6
<i>V</i> (Å°) ³	3094	2860	2880	2002	2992
2 <i>θ</i> start	10	10	10	10	10
2 <i>θ</i> end	60	60	60	60	60
Radiation	Cu	Cu	Cu	Cu	Cu
Wavelength	1.54	1.54	1.54	1.54	1.54

TABLE 5: Cytotoxic studies of titanium complexes on HeLa, C6 and CHO cancer cell lines as determined by MTT assay.

Complex	Hela (cervical)	Cell line (Source)	
		C6 (Rat glioma)	CHO (Ovary)
Ti(ada) ₂ (bpome) ₂	13	17.8	19.9
Ti(ada) ₂ (dpme) ₂	74	69.8	16.1
Ti(ada) ₂ (dach) ₂	20.4	21	16.6
Ti(ada) ₂ (phen) ₂	11.1	22.1	21.5
Ti(ada) ₂ (bzac) ₂	4.06	21.8	46.1
Adamantylamine	104.5	148	123
Camptothecin	6.2	6.4	6.4

The IC₅₀ values of main ligand, that is, adamantylamine along with its complexes, has been shown in Table 5. Complexes A, C, and D with 4,4'-dimethoxy-2,2'-bipyridine, 1,2-diaminocyclohexane, and 1,10-phenanthroline ligand shows good activity against all the tested cell lines which may be due to the presence of electron withdrawing nature of methoxy group, cyclic nature of 1,2-diaminocyclohexane, and aromatic nature of 1,10-phenanthroline ligand. However, complex B with 6,6'-dimethyl-2,2'-bipyridine was not found much effective against HeLa and C6 cell lines, which may be due to the presence of electron donating methyl groups in the ligand. So, it could be summarized that electron withdrawing group present in ligand as well as cyclic and aromatic nature of ligand are responsible for the cytotoxicity of titanium complexes.

3.7. Cell Cycle Analysis Using Propidium Iodide. For cell cycle analysis, CHO cells were treated with the complexes at three concentrations almost near to their IC₅₀ values which caused the decrease in the number of cells with an increase in dose due to induction of apoptosis. It has been observed that all complexes increases cells in hypo-diploid cells of cell cycle

and also increased the cell death with increase in concentration. Among all the complexes, complex E having benzoylacetone ligand showed 44.3% cell death at 80 μM, which is the maximum for all the complexes. However, known anticancer drug Camptothecin showed 45.5% cell death at 6 μM. Abundant evidences suggest that mitochondria plays a key role in the initiation of apoptosis by releasing Cytochrome C [44, 45]. In addition to Cytochrome C, other factors such as apoptosis signaling molecules and apoptosis inducing factor (AIF) can be important triggers of apoptosis [18]. It has been confirmed from cell cycle analysis (Figure 4) that cell death occurred through increase in hypo-diploid cells (Sub-G₁ population) which indicates apoptosis. Previous studies showed that titanium affects polymerase proteins and transcription factors which inhibits protein synthesis and causes cytotoxicity [46].

4. Conclusions

We have reported the synthesis of mixed ligand titanium complexes having nitrogen containing ligands. The structure of the complexes has been confirmed by elemental analysis,

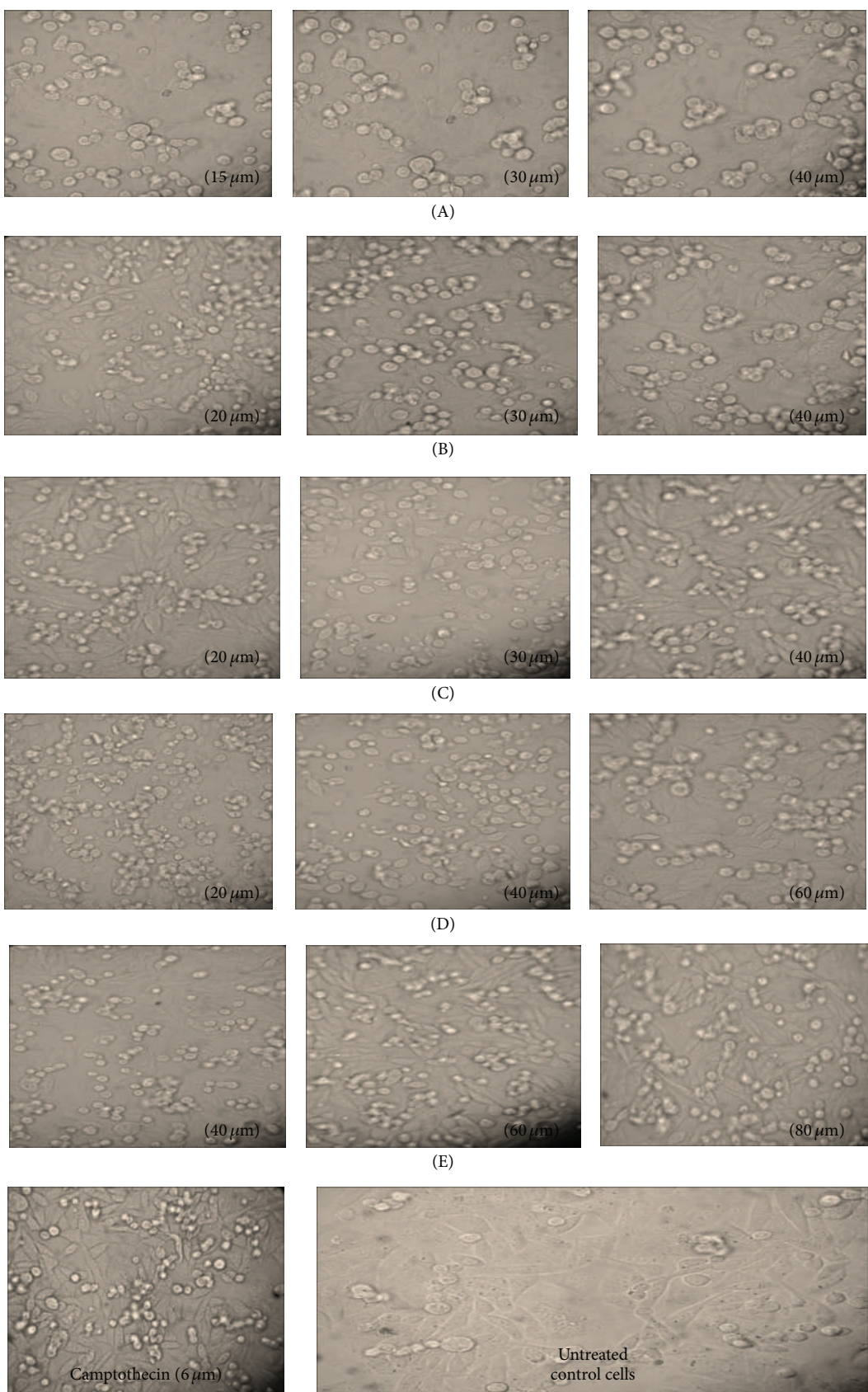


FIGURE 3: Morphology of CHO cells at different concentrations of titanium complexes.

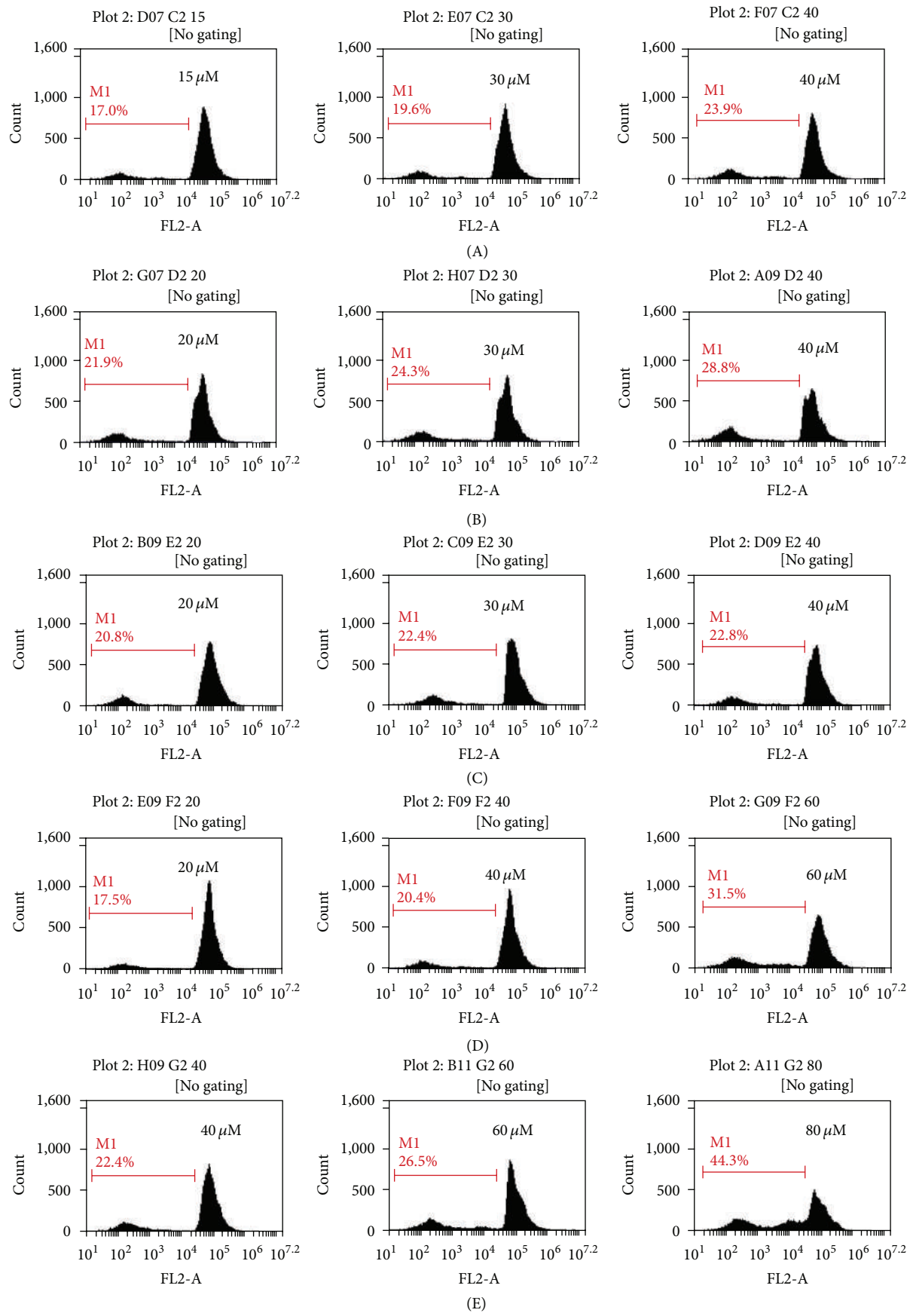


FIGURE 4: Continued.

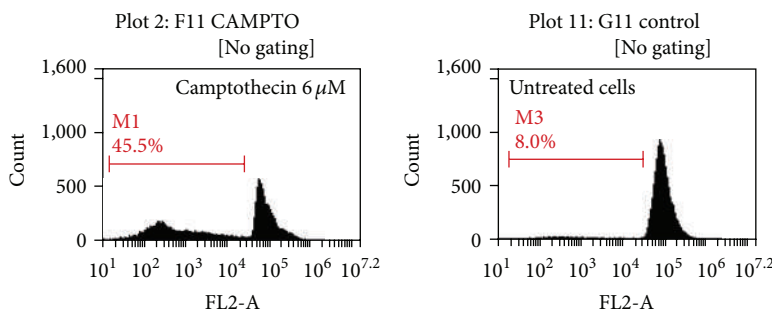


FIGURE 4: Cell cycle analysis of CHO cells exposed to different concentrations of titanium complexes that is, below IC₅₀, near IC₅₀, and above IC₅₀ on flow cytometer by staining with propidium iodide.

FTIR, UV-visible, ¹H NMR, and mass spectrometry techniques. Cytotoxic studies were done on different cell lines and it has been found that complex E with benzoylacetone ligand was a more potent cytotoxic agent. The morphological analysis on CHO cells indicates characteristics features of apoptosis and cell cycle analysis indicate increase in hypo-diploid cells. The mechanism of action has been certainly established *in vitro*; however, the efficacy of these complexes with their action mechanisms should also be demonstrated *in vivo*.

Conflict of Interests

The authors declare that there is no conflict of interests regarding the publication of this paper.

Acknowledgments

The authors would like to thank Director of National Institute of Technology, Hamirpur, India, for providing necessary laboratory facilities to carry out this work. The authors also acknowledge Head of Department of Botanical and Environmental Sciences, Guru Nanak Dev University, Amritsar, Punjab, India, for providing the necessary facilities for *in vitro* analysis.

References

- [1] E. Wiltshaw, "Cisplatin in the treatment of cancer," *Platinum Metals Review*, vol. 23, no. 3, pp. 90–98, 1979.
- [2] J. Reedijk, "Why does cisplatin reach guanine-N7 with competing S-donor ligands available in the cell?" *Chemical Reviews*, vol. 99, no. 9, pp. 2499–2510, 1999.
- [3] I. Kostova, "Platinum complexes as anticancer agents," *Recent Patents on Anti-Cancer Drug Discovery*, vol. 1, no. 1, pp. 1–22, 2006.
- [4] S. Fruhauf and W. J. Zeller, "New platinum, titanium, and ruthenium complexes with different patterns of DNA damage in rat ovarian tumor cells," *Cancer Research*, vol. 51, no. 11, pp. 2943–2948, 1991.
- [5] A. Bergamo, A. Masi, M. A. Jakupcic, B. K. Keppler, and G. Sava, "Inhibitory effects of the ruthenium complex KP1019 in models of mammary cancer cell migration and invasion," *Metal-Based Drugs*, vol. 2009, Article ID 681270, 9 pages, 2009.
- [6] M. J. Clarke, "Ruthenium in cancer chemotherapy," *Platinum Metals Review*, vol. 32, no. 4, pp. 198–199, 1988.
- [7] S. S. Anchuri, S. Thota, R. Yerra, and S. Dhulipala, "In vitro antioxidant activity of some novel synthetic mononuclear ruthenium (II) compounds," *Letters in Drug Design and Discovery*, vol. 9, no. 4, pp. 421–425, 2012.
- [8] M. Auzias, B. Therrien, G. Süss-Fink, P. Štěpnička, H. A. Wee, and P. J. Dyson, "Ferrocenoyl pyridine arene ruthenium complexes with anticancer properties: synthesis, structure, electrochemistry, and cytotoxicity," *Inorganic Chemistry*, vol. 47, no. 2, pp. 578–583, 2008.
- [9] J.-Y. Kim, "Synthesis of some Palladium(II) complexes of 1,2-Diamino cyclohexane and dicarboxylates as cis-platin analogues of palladium series," *Archives of Pharmacal Research*, vol. 15, no. 4, pp. 336–342, 1992.
- [10] A. S. Abu-Surrah, H. H. Al-Sa'doni, and M. Y. Abdalla, "Palladium based chemotherapeutic agents. Routes towards complexes with good antitumor activity," *Cancer Therapy*, vol. 6, pp. 1–10, 2008.
- [11] M. Islami-Moghaddam, H. Mansouri-Torshizi, A. Divsalar, and A. A. Saboury, "Synthesis, characterization, cytotoxic and DNA binding studies of diimine platinum(II) and palladium(II) complexes of short hydrocarbon chain ethyldithiocarbamate ligand," *Journal of the Iranian Chemical Society*, vol. 6, no. 3, pp. 552–569, 2009.
- [12] P. Chellan, N. Shunmoogam-Gounden, D. T. Hendricks et al., "Synthesis, structure and in vitro biological screening of palladium(II) complexes of functionalised salicylaldimine thiosemicarbazones as antimalarial and anticancer agents," *European Journal of Inorganic Chemistry*, no. 22, pp. 3520–3528, 2010.
- [13] A. Srivastava and D. C. Gupta, "Synthesis and structural investigations of coordination compounds of palladium(II) with 5-methyl uracil," *International Journal of Applied Engineering Research, Dindigul*, vol. 1, no. 2, pp. 222–227, 2010.
- [14] C. Gabbiani, A. Casini, and L. Messori, "Gold(III) compounds as anticancer drugs," *Gold Bulletin*, vol. 40, no. 1, pp. 73–81, 2007.
- [15] A. Casini, M. C. Diawara, R. Scopelliti, S. M. Zakeeruddin, M. Grätzel, and P. J. Dyson, "Synthesis, characterisation and biological properties of gold(iii) compounds with modified bipyridine and bipyridylamine ligands," *Dalton Transactions*, vol. 39, no. 9, pp. 2239–2245, 2010.
- [16] E. Meléndez, "Titanium complexes in cancer treatment," *Critical Reviews in Oncology/Hematology*, vol. 42, no. 3, pp. 309–315, 2002.
- [17] E. Dubler, R. Buschmann, and H. W. Schmalle, "Isomer abundance of bis(β-diketonato) complexes of titanium(IV).

- Crystal structures of the antitumor compound budotitanate $[\text{Ti}^{\text{IV}}(\text{bzac})_2(\text{OEt})_2]$ and of its dichloro-derivative $[\text{Ti}^{\text{IV}}(\text{bzac})_2\text{Cl}_2]$ (bzac = 1-phenylbutane-1,3-dionate)," *Journal of Inorganic Biochemistry*, vol. 95, no. 2-3, pp. 97–104, 2003.
- [18] K. O'Connor, C. Gill, M. Tacke et al., "Novel titanocene anti-cancer drugs and their effect on apoptosis and the apoptotic pathway in prostate cancer cells," *Apoptosis*, vol. 11, no. 7, pp. 1205–1214, 2006.
- [19] C. Pampillón, J. Claffey, M. Hogan, and M. Tacke, "Novel achiral titanocene anti-cancer drugs synthesised from bis-N,N-dimethylamino fulvene and lithiated heterocyclic compounds," *BioMetals*, vol. 21, no. 2, pp. 197–204, 2008.
- [20] S. Eger, T. A. Immel, J. Claffey et al., "Titanocene difluorides with improved cytotoxic activity," *Inorganic Chemistry*, vol. 49, no. 4, pp. 1292–1294, 2010.
- [21] L. M. Gao and E. Meléndez, "Cytotoxic properties of titanocenyl amides on breast cancer cell line MCF-7," *Metal-Based Drugs*, vol. 2010, Article ID 286298, 6 pages, 2010.
- [22] E. A. Williamson, T. J. Boyle, R. Raymond et al., "Cytotoxic activity of the titanium alkoxide $(\text{OPy})_2\text{Ti}(4\text{AP})_2$ against cancer colony forming cells," *Investigational New Drugs*, vol. 30, no. 1, pp. 114–120, 2012.
- [23] M. Tacke, L. T. Allen, L. Cuffe et al., "Novel titanocene anti-cancer drugs derived from fulvenes and titanium dichloride," *Journal of Organometallic Chemistry*, vol. 689, no. 13, pp. 2242–2249, 2004.
- [24] M. Hogan, J. Claffey, E. Fitzpatrick, T. Hickey, C. Pampillon, and M. Tacke, "Synthesis and cytotoxicity studies of titanocene C analogues," *Metal-Based Drugs*, vol. 2008, Article ID 754358, 7 pages, 2008.
- [25] F.-J. K. Rehmann, A. J. Rous, O. Mendoza et al., "A trimethoxyphenyl substituted ansa-titanocene: a possible anti-cancer drug," *Polyhedron*, vol. 24, no. 11, pp. 1250–1255, 2005.
- [26] G. Sava and A. Bergamo, "Ruthenium-based compounds and tumour growth control (review)," *International Journal of Oncology*, vol. 17, no. 2, pp. 353–365, 2000.
- [27] J. M. Rademaker-Lakhai, D. Van Den Bongard, D. Pluim, J. H. Beijnen, and J. H. M. Schellens, "A phase I and pharmacological study with imidazolium-trans-DMSO-imidazole-tetrachlororuthenate, a novel ruthenium anticancer agent," *Clinical Cancer Research*, vol. 10, no. 11, pp. 3717–3727, 2004.
- [28] G. Sava, R. Gagliardi, A. Bergamo, E. Alessio, and G. Mestroni, "Treatment of metastases of solid mouse tumours by NAMI-A: comparison with cisplatin, cyclophosphamide and dacarbazine," *Anticancer Research*, vol. 19, no. 2A, pp. 969–972, 1999.
- [29] A. Bergamo, B. Gava, E. Alessio et al., "Ruthenium-based NAMI-A type complexes with in vivo selective metastasis reduction and in vitro invasion inhibition unrelated to cell cytotoxicity," *International Journal of Oncology*, vol. 21, no. 6, pp. 1331–1338, 2002.
- [30] M. Shavit, D. Peri, A. Melman, and E. Y. Tshuva, "Antitumor reactivity of non-metallocene titanium complexes of oxygen-based ligands: is ligand lability essential?" *Journal of Biological Inorganic Chemistry*, vol. 12, no. 6, pp. 825–830, 2007.
- [31] A. D. Tinoco, H. R. Thomas, C. D. Incarvito, A. Saghatelian, and A. M. Valentine, "Cytotoxicity of a Ti(IV) compound is independent of serum proteins," *Proceedings of the National Academy of Sciences of the United States of America*, vol. 109, no. 13, pp. 5016–5021, 2012.
- [32] S. Halder, S.-M. Peng, G.-H. Lee et al., "Synthesis, structure, spectroscopic properties and cytotoxic effect of some thiosemicarbazone complexes of palladium," *New Journal of Chemistry*, vol. 32, no. 1, pp. 105–114, 2008.
- [33] D. Kovala-Demertzis, M. A. Demertzis, J. R. Miller, C. Papadopoulou, C. Dodorou, and G. Filousis, "Platinum(II) complexes with 2-acetyl pyridine thiosemicarbazone: synthesis, crystal structure, spectral properties, antimicrobial and antitumour activity," *Journal of Inorganic Biochemistry*, vol. 86, no. 2-3, pp. 555–563, 2001.
- [34] T. Mosmann, "Rapid colorimetric assay for cellular growth and survival: application to proliferation and cytotoxicity assays," *Journal of Immunological Methods*, vol. 65, no. 1-2, pp. 55–63, 1983.
- [35] R. Kaushal, N. Kumar, P. Awasthi, and K. Nehra, "Syntheses, characterization and antibacterial study of titanium complexes," *Turkish Journal of Chemistry*, vol. 37, no. 6, pp. 936–945, 2013.
- [36] X.-M. Shi, H.-Y. Wang, Y.-B. Li et al., "Spectroscopic studies on Co(II), Ni(II), Zn(II) complexes with 4,4'-bipyridine," *Chemical Research in Chinese Universities*, vol. 26, no. 6, pp. 1011–1015, 2010.
- [37] D. M. Czakis-Sulikowska, J. Radwańska-Doczekalska, and G. Sójka, "4,4'-Dipyridyl complexes of rare-earth thiocyanates," *Monatshefte für Chemie Chemical Monthly*, vol. 115, no. 8-9, pp. 961–973, 1984.
- [38] M. Gülcen, M. Sönmez, and I. Berber, "Synthesis, characterization, and antimicrobial activity of a new pyrimidine Schiff base and its Cu(II), Ni(II), Co(II), Pt(II), and Pd(II) complexes," *Turkish Journal of Chemistry*, vol. 36, no. 1, pp. 189–200, 2012.
- [39] S. Xiao, H. Lu, and M. Zhang, "Studies on $\text{TiCl}_4/\text{Mg}(\text{OEt})_2/\text{EB}$ supported catalysts for propylene polymerization," *Chinese Journal of Polymer Science*, vol. 8, no. 3, pp. 253–260, 1990.
- [40] K. Zamani, A. Mobinkhaledi, N. Foroughifar, K. Faghihi, and V. Mahdavi, " H NMR studies of some imidazole ligands coordinated to Co(III)," *Turkish Journal of Chemistry*, vol. 27, no. 1, pp. 71–75, 2003.
- [41] C. J. Dhanaraj and M. S. Nair, "Synthesis and characterization of metal(II) complexes of poly(3-nitrobenzylidene-1-naphthylamine-co-succinic anhydride)," *European Polymer Journal*, vol. 45, no. 2, pp. 565–572, 2009.
- [42] S. B. Ade, M. N. Deshpande, and D. G. Kolhatkar, "Synthesis, characterization, spectroscopic studies and antimicrobial activity of 2-[(2-Hydroxy-5-nitrobenzylidene)-amino]-4-methyl-phenol with complexes of Cd(II) and Hg(II) ions," *International Journal of ChemTech Research*, vol. 4, no. 2, pp. 474–478, 2012.
- [43] N. P. Priya, S. V. Arunachalam, N. Sathya, V. Chinnusamy, and C. Jayabalakrishnan, "Catalytic and antimicrobial studies of binuclear ruthenium(III) complexes containing bis- β -diketones," *Transition Metal Chemistry*, vol. 34, no. 4, pp. 437–445, 2009.
- [44] J. M. Penninger and G. Kroemer, "Mitochondria, AIF and caspases—rivaling for cell death execution," *Nature Cell Biology*, vol. 5, no. 2, pp. 97–99, 2003.
- [45] L. Ravagnan, T. Roumier, and G. Kroemer, "Mitochondria, the killer organelles and their weapons," *Journal of Cellular Physiology*, vol. 192, no. 2, pp. 131–137, 2002.
- [46] C. V. Christodoulou, A. G. Eliopoulos, L. S. Young, L. Hodgkins, D. R. Ferry, and D. J. Kerr, "Anti-proliferative activity and mechanism of action of titanocene dichloride," *British Journal of Cancer*, vol. 77, no. 12, pp. 2088–2097, 1998.

Evaluation of DNA Binding, Cleavage, and Cytotoxic Activity of Cu(II), Co(II), and Ni(II) Schiff Base Complexes of 1-Phenylindoline-2,3-dione with Isonicotinohydrazide

Ramadoss Gomathi,¹ Andy Ramu,¹ and Athiappan Murugan²

¹ Department of Inorganic Chemistry, School of Chemistry, Madurai Kamaraj University, Madurai, Tamil Nadu 625 021, India

² Department of Microbiology, Periyar University, Salem, Tamil Nadu 636011, India

Correspondence should be addressed to Andy Ramu; ramumku@yahoo.co.in

Academic Editor: Ian Butler

One new series of Cu(II), Co(II), and Ni(II) Schiff base complexes was prepared through the condensation reaction between 1-phenylindoline-2,3-dione with isonicotinohydrazide followed by metalation, respectively. The Schiff base ligand(L), (*E*)-N'-(2-oxo-1-phenylindolin-3-lidene)isonicotinohydrazide, and its complexes were found soluble in DMF and DMSO solvents and characterized by using the modern analytical and spectral techniques such as elemental analysis, conductivity, magnetic moments, IR, NMR, UV-visible, Mass, CV, and EPR. The elemental analysis data of ligand and their complexes were well agreed with their calculated values in which metal and ligand stoichiometry ratio 1:2 was noted. Molar conductance values indicated that all the complexes were found to be nonelectrolytes. All the complexes showed octahedral geometry around the central metal ions. Herein, we better characterized DNA binding with the complexes by UV-visible and CD spectroscopy and cyclic voltammetry techniques. The DNA cleavage experiments were carried out by Agarose gel electrophoresis method and the cytotoxicity experiments by MTT assay method. Based on the DNA binding, cleavage, and cytotoxicity studies, Cu and Ni complexes were found to be good anticancer agents against AGS-human gastric cancer cell line.

1. Introduction

Isatin(1-H indole-2,3-dione) Schiff bases are significant in therapeutic and pharmaceutical compounds in the field [1]. These complexes also exhibited their wide antibacterial [2], antifungal [3], and antitumor activity [4, 5]. Nitrogen containing heterocyclic compounds are identified as indispensable structural units for both the chemists and biochemists [6, 7]. Among the various classes of benzene fused five-membered nitrogen containing heterocyclic compounds, isatin derivatives could be used pharmacologically as an important class of active components [8–10]. The interactions of Schiff base metal complexes containing O and N coordination with DNA have been thoroughly considered [11, 12]. Recently, there has been remarkable interest in studies related to the interaction of transition metal ions with nucleic acid because of their relevance in the development of new reagents for biotechnology and medicine [13]. These

studies are also essential to understand the toxicity of drugs containing metal ions [14]. Transition metal complexes have gained significance for their applicability in the biological field [15, 16]. Some of the transition metal complexes, such as Cu(II), were known to function as specific probe for DNA bulges due its ability to cleave DNA [17]. Recently, we have reported our results on the interaction of bidentate Schiff base complexes with DNA [18, 19]. In this background, this study highlights the binding, cleavage, and cytotoxicity with the new series of transition metals N-phenylisatin-isonicotinohydrazide Schiff base complexes with calf thymus DNA and AGS cell line, respectively.

2. Experimental

2.1. Materials. All chemicals were purchased from Sigma-Aldrich, Merck-(A.R) and used as received without further purification. The isatin Schiff base was prepared according

to the literature procedure [20]. N-phenylisatin, isonicotinohydrazide, and DMSO are GR grade; CT and *p*UC-19 DNA were purchased from Genie, Bangalore. Metal chlorides [$\text{CuCl}_2 \cdot 2\text{H}_2\text{O}$, $\text{NiCl}_2 \cdot 6\text{H}_2\text{O}$, $\text{CoCl}_2 \cdot 6\text{H}_2\text{O}$] and solvents were purchased from E-Merck, A.R grade, Mumbai.

2.2. Physical Measurements. C, H, and N analyses of free Schiff base ligands and their metal complexes were performed in C, H, and N analyzer Elementar Vario EL III. Metal contents were analyzed by the standard procedures. Hand-Held Meter LF330 was used to measure the molar conductance of free Schiff base ligands and metal complexes in DMSO (1×10^{-3} M). The electronic spectra were recorded in DMSO solutions using Shimatzu Model 160 UV-visible spectrophotometer. The IR spectra of the complexes were recorded on a JASCO V-550 UV-Vis spectrophotometer in KBr pellets. NMR spectra were recorded on BRUKER DPX-300 High performance Digital FT-NMR spectrometer in DMSO-d⁶ using TMS as internal standard. Electrospray ionisation mass spectrometry (ESI-MS) analysis was performed in the positive ion mode on a liquid chromatography-ion trap mass spectrometer (LCQ Fleet), Thermo Fisher Instruments Limited, US. Magnetic susceptibility measurement of the powdered samples was carried out by the Gouy balance. EPR measurements were carried out by using a Varian E4 X-band spectrometer equipped with 100 Hz modulation. Cyclic Voltammetric measurements were carried out in a Bio-Analytical System (BAS) model CV-50W electrochemical analyzer.

2.3. DNA Binding and Cleavage

2.3.1. Electronic Absorption Studies. DNA-binding experiments were performed by UV-visible spectroscopy in Tris-HCl/NaCl buffer (5 mmol L⁻¹ Tris-HCl/50 mmol L⁻¹ NaCl buffer, pH 7.2) and used DMSO (10%) solution of metal complexes. The concentration of CT-DNA was determined from the absorption intensity at 260 nm with a value of 6600 (mol L⁻¹)⁻¹ cm⁻¹. Absorption titration experiments were made using different concentrations of CT-DNA, while keeping the complex concentration constant. Correction was made for the absorbance of the CT-DNA itself. Samples were equilibrated before recording each spectrum. For metal complexes, the intrinsic binding constant (K_b) was determined from the spectral titration data using the following equation [21]:

$$\frac{[\text{DNA}]}{(\varepsilon_a - \varepsilon_f)} = \frac{[\text{DNA}]}{(\varepsilon_b - \varepsilon_f)} + \frac{1}{K_b (\varepsilon_b - \varepsilon_f)}, \quad (1)$$

where ε_a , ε_b , and ε_f are the molar extinction coefficients of the free complexes in solution, complex in the fully bound from with CT-DNA, and complex bound to DNA at a definite concentration, respectively. In the plot of $[\text{DNA}] / (\varepsilon_a - \varepsilon_f)$ versus $[\text{DNA}]$, K_b was calculated.

2.3.2. Circular Dichroism (Cd) Measurements. Circular dichroism spectra were registered in a JASCO J-810 spectropolarimeter, using a quartz cuvette of 0.2 cm path length,

at room temperature, in the range 230–330 nm. The initial experimental DNA concentration was 800 μM , and the spectra were registered in the absence or in the presence of 10 to 50 μM of each complex studied [22].

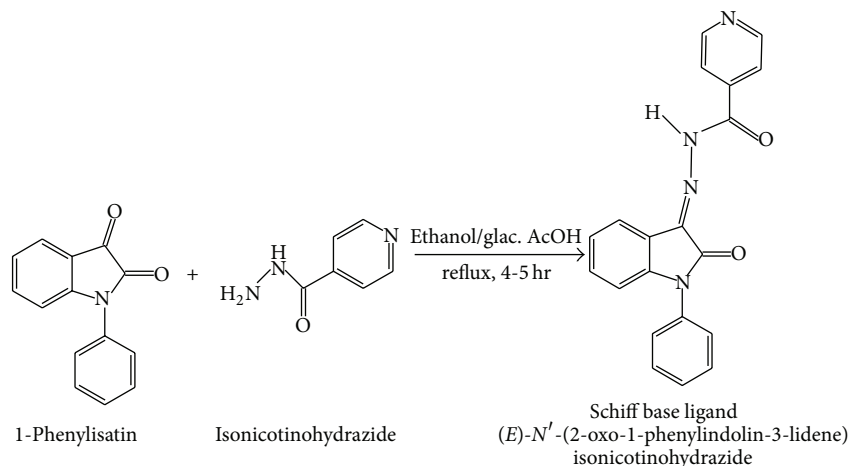
2.3.3. Electrochemical Studies. Cyclic voltammetry analysis was carried out in a Bio-Analytical System (BAS) model CV-50W electrochemical analyzer. All voltammetric experiments were performed in a single compartment cell of volume 10–15 mL containing a three electrode system comprising a carbon working electrode, Pt-wire as auxiliary electrode, and reference electrode as an Ag/AgCl.

2.3.4. DNA Cleavage Studies. pUC19 DNA at pH 7.5 in Tris-HCl buffered solution was used to perform Agarose gel electrophoresis. Oxidative cleavage of DNA was examined by keeping the concentration of the 30 μM of complexes and 2 μL of pUC19 DNA and this made up the volume to 16 μL with 5 mM Tris-HCl/5 mM NaCl buffer solution. The resulting solutions were incubated at 37°C for 2 h and electrophoresed for 2 h at 50 V in Tris-acetate-EDTA (TAE) buffer using 1% Agarose gel containing 1.0 $\mu\text{g}/\text{mL}$ ethidium bromide and photographed under UV light [23].

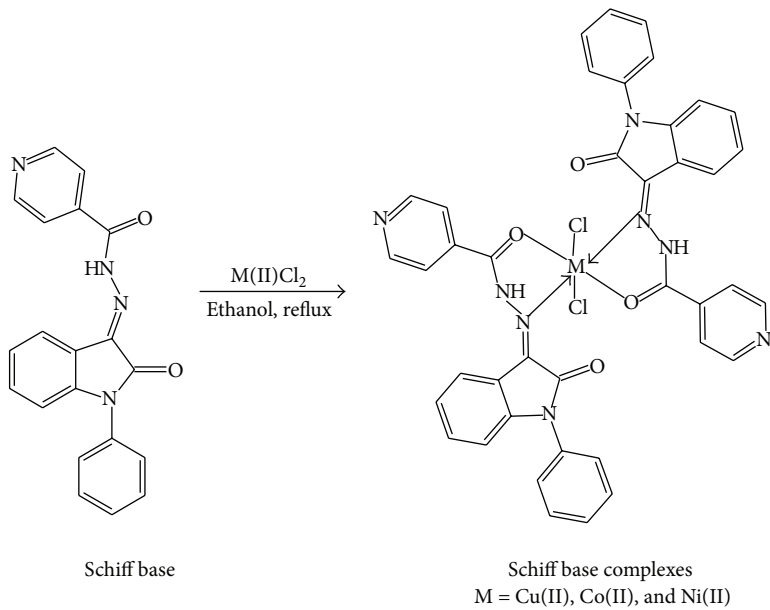
2.4. Cytotoxicity. Cytotoxicity studies were carried out using human gastric cancer cell line (designated AGS) which were obtained from National Centre for Cell Science (NCCS), Pune, India. Cell viability was carried out using the MTT assay method. The AGS cells were grown in Dulbecco's Modified Eagle's Medium (DME) and Ham's F-12 Nutrient Mixture containing 10% fetal bovine serum (FBS), 1% Glutamine, 1% antibiotic, 1% sodium bicarbonate, and 1% nonessential amino acids. For screening experiment, AGS cells were seeded into 96-well plates in 100 μL of respective medium containing 10% FBS, at plating density of 10,000 cells/well and incubated at 37°C, 5% CO_2 for 24 h prior to addition of complexes. The complexes were dissolved in DMSO and diluted in the medium. After 24 h, the medium was replaced with respective medium containing the complexes at various concentrations and incubated at 37°C, 5% CO_2 for 48 h. Triplicate was maintained. After 48 h, 10 μL of MTT (5 mg/mL) in phosphate buffered saline (PBS) was added to each well and incubated at 37°C for 4 h. The medium with MTT was then flicked off and the formed formazan crystals were dissolved in 100 μL of DMSO and then measured the absorbance at 570 nm using microplate reader. The percentage of cell inhibition was determined using the following formula and chart was plotted between percentage of cell inhibition and concentration, and from this IC_{50} value was calculated. percentage of inhibition = [mean OD of untreated cells (control)/mean OD of treated cells (control)] × 100 [24].

2.5. Chemistry of the Synthesis Compounds

2.5.1. Synthesis of (E)-N¹-(2-Oxo-1-phenylindolin-3-lidene) Isonicotinohydrazide (L). 1-Phenyl isatin (1 mMol) and isonicotinohydrazide (1 mMol) were dissolved in 50 mL of absolute ethanol; three drops of glacial acetic acid were



SCHEME 1: Synthesis of Schiff base ligand.



SCHEME 2: Synthesis of Schiff base complexes.

added and the resulting solution was refluxed for 5 h. The results compounds were precipitated upon cooling to room temperature, isolated by filtration, and recrystallized from EtOH. Yellow colored crystalline compounds were obtained (Scheme 1). These ligands were confirmed by Elemental analyzer, IR, NMR, and Mass spectra. Yield: 95%, m.p. 180°C, elemental analysis: found (calculated) (%) for L: C, 70.01 (70.14); H, 3.97 (4.12); N, 16.52 (16.37). IR (cm^{-1} in KBr pellets): 1602 (C=N), 1695 (indole-C=O), 1685 (C=O, isoniazid), 3269 (NH). ^1H NMR (300 MHz, CDCl_3 , δ/ppm): δ 14.21 (s, 1H), δ 8.80–8.78 (d, pyridine protons, 4H), 7.93–6.86 (m, aromatic protons); ^{13}C -NMR 162.15 (C=O, isatin), 161.81 (C=O, isoniazid), 134.55 (C=N, azomethine carbon), 150.91–110.12 (aromatic ring) ESI-MS = 343 (M+H).

2.5.2. Synthesis of Cu(II), Co(II), and Ni(II) Complexes. The metal(II) complexes in this study were prepared by mixing of 1 mMol of corresponding metal(II) chloride in ethanol with 2 mM of the Schiff base in the molar ratio 1:2. The reaction mixture was refluxed at 60°C for 4 hrs [25]. Then it was allowed to cool at room temperature. Powdered solid obtained was filtered, washed with ethanol, and dried under vacuum (Scheme 2). The Schiff base complexes were characterized by elemental analysis, UV-visible, infrared (IR), electron paramagnetic resonance (EPR) spectroscopy, and magnetic moment.

Complex 1. Yield: 83%, m.p. > 300°C, elemental analysis: found (calculated) (%) for L-Cu: C, 59.37 (59.03); H, 3.71 (3.75); N, 13.11 (13.43). UV-visible (in MeOH): λ_{max} (nm):

TABLE 1: Composition and physical characteristics of ligand and their complexes.

Ligand/complexes	Molecular formula	Color	Found (calculated) %			M.P (°C)	Yield (%)	Ω (Ohm $^{-1}$ cm 2 M $^{-1}$)
			M	C	H	N		
L	C ₂₀ H ₁₄ N ₄ O ₂	Crystalline yellow		70.01 (70.14)	3.97 (4.12)	16.52 (16.37)	180	95
L-Cu	C ₄₁ H ₃₁ N ₈ O ₄ Cl ₂ Cu	Green	7.51 (7.62)	59.37 (59.03)	3.71 (3.75)	13.11 (13.43)	>300	83
L-Co	C ₄₁ H ₃₁ N ₈ O ₄ Cl ₂ Co	Dark green	6.58 (7.10)	59.32 (59.36)	3.63 (3.77)	13.47 (13.51)	>285	80
L-Ni	C ₄₁ H ₃₁ N ₈ O ₄ Cl ₂ Ni	Yellow	7.31 (7.08)	59.35 (59.38)	3.68 (3.77)	13.56 (13.51)	>285	80

278(ILCT), 344(ILCT), 454(MLCT), 810(d-d). IR (cm $^{-1}$): 1612 (C=N), 1691 (indole-C=O), 1673 (-NH-C=O), 3265 (NH), 601 (M-O), 453 (M-N), $g_{\parallel} = 2.339$; $g_{\perp} = 2.05$; A $_{\parallel} = 120 \times 10^4$, μ_{eff} (300 K): 2.95 μ_B .

Complex 2. Yield: 80%. m.p. > 285°C elemental analysis: found (calculated) (%) for L-Co: C, 59.32 (59.36); H, 3.63 (3.77); N, 13.47 (13.51). UV-visible (in DMSO): λ_{max} (nm): 276(ILCT), 344(ILCT), 612, 674 (d-d). IR (cm $^{-1}$): 1612 (C=N), 1693 (indole-C=O), 1676(-NH-C=O), 3263(NH), 572(M-O), 447 (M-N), μ_{eff} (300 K): 4.52 μ_B .

Complex 3. Yield: 80%. m.p. > 285°C, elemental analysis: found (calculated) (%) for L-Ni: C, 59.35(59.38); H, 3.68 (3.77); N, 13.56 (13.51). UV-visible (in DMSO): λ_{max} (nm): 274(ILCT), 344(ILCT), 452(MLCT). IR (cm $^{-1}$): 1610(C=N), 1693 (indole-C=O), 1674 (-NH-C=O), 3268(NH), 574(M-O), 449 (M-N), μ_{eff} (300 K): 3.41 μ_B .

3. Results and Discussion

The Schiff base ligand (L) and their complexes with Cu(II), Co(II), and Ni(II) were found to be air stable, amorphous, moisture free, and soluble only in DMF and DMSO solvents and kept in vacuum desiccators under nitrogen atmosphere and used for chemical and biological studies. The experimental results are discussed under various subheadings as detailed below.

3.1. Elemental Analysis and Conductivity Measurements. Physicochemical characteristics such as melting point (m.p.), color, yield, elemental analysis, and conductivity of the ligand(L) and complexes were determined and the data shown in Table 1. The observed low conductivity values (22.0–38.40 Ω^{-1} cm 2 mol $^{-1}$) were accounted for the dissociation and hence the complexes are found as nonelectrolytes [26].

3.2. NMR Spectra. The ^1H -NMR (300 MHz, CDCl₃, δ /ppm) spectrum of the Schiff base which exhibited a signal at 14.21(s, 1H) was assigned to the NH proton of isonicotinohydrazide and the signals at 7.93–6.86 (m, 13H) were assigned to aromatic protons (Figure 1(a)). The ^{13}C NMR spectra provide further support for the structure evidence of the ligand. The signals at 162.15 and 161.81 confirm the carbonyl carbon

TABLE 2: Infrared spectral data for the free ligand and their complexes in KBr disc (cm $^{-1}$).

Compounds	C=N (imine)	C=O (isatin)	C=O (isoniazid)	NH	M-O	M-N
L	1602	1695	1685	3269	—	—
L-Cu	1612	1691	1673	3265	601	453
L-Co	1612	1693	1676	3263	572	447
L-Ni	1610	1693	1674	3268	574	449

of isatin and isonicotinohydrazide. The signals appeared at 134.55; it confirms the formation of imine carbon and signals from 150.91 to 110.12, the aromatic rings (Figure 1(b)).

3.3. Analysis of Mass Spectra. Mass spectrometry (MS) an analytical technique that measures the mass-to-charge ratio of charged particles. ESI mass spectra for ligand and complexes were recorded and are shown in Figure 2. MS[ESI (M+1)] exact mass calculated for L (a) required *m/z* 342.81 and found *m/z* 343.96 and copper(II) (b) complex required *m/z* 819.9 and found *m/z* 820. These values also confirm the formation of ligand and complexes.

3.4. Infrared Spectra. In order to study the bonding mode of ligand moiety to metal ion in the complexes, IR spectra of the free ligand were compared with those of the metal complexes. The FT-IR spectral data are summarized in Table 2. The IR spectrum of the free ligand (L) showed broadband at 3269 cm $^{-1}$, which can be attributed to NH stretching vibration of the isoniazid structural unit. The position of these bands remained at nearly the same frequency in the spectra of the metal complexes which suggests the noncoordination of this group to central metal ion in the metal complexes [27]. A sharp peak at 1602 cm $^{-1}$ was assigned to $\nu(\text{C}=\text{N})$, which is characteristic of Schiff bases. In the spectra of the complexes, this peak is slightly shifted to higher frequency around 1610–1612 cm $^{-1}$. This suggested that one point of attachment of the metal is through the azomethine nitrogen atom [28, 29]. The strong intensity bands of ligand were observed at the region 1685 cm $^{-1}$ of the spectra indicating carbonyl group. The position of these bands was shifted to lower region 1673–1676 cm $^{-1}$, indicating the involvement of $\nu(\text{C}=\text{O})$ with metal centre during complexation. The bands at 1695 cm $^{-1}$

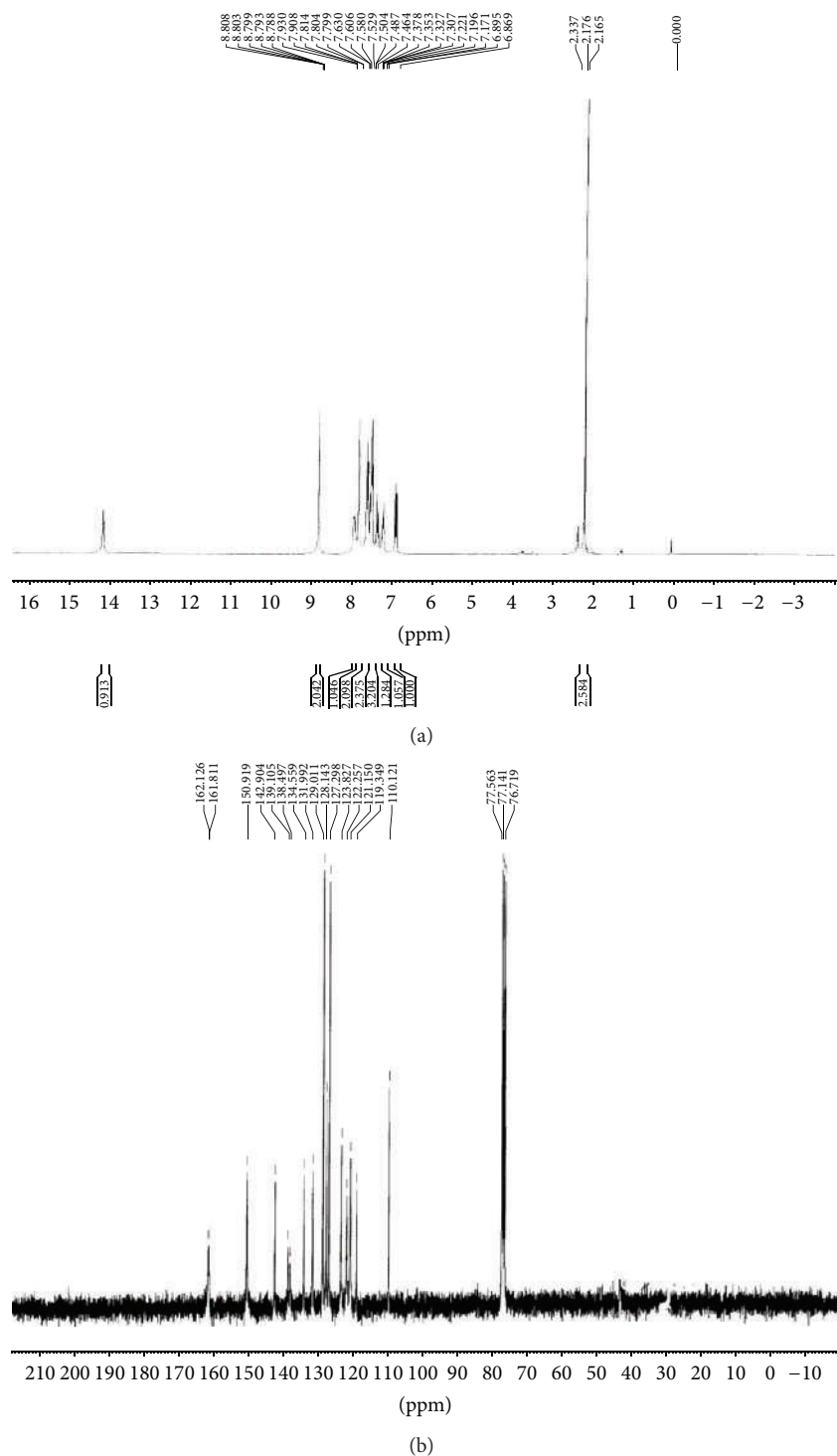


FIGURE 1: (a) ¹H NMR spectrum and (b) ¹³C NMR of ligand.

and 1691–1693 cm⁻¹ in the spectrum of the free ligand and complexes, respectively, were assigned to $\nu(\text{C}=\text{O})$ of isatin moiety. The positions of these bands were found at nearly the same frequency in spectra of the metal complexes, suggesting the uncoordination of this group. New bands observed in the 447–453 and 572–601 cm⁻¹ for the complexes were assigned to stretching frequencies of M–N and M–O, respectively

[30, 31]. Thus, the IR spectral results provide evidence for bidentate complex formation of Schiff bases with metals.

3.5. Electronic Spectra and Magnetic Moment Values. The electronic spectra of the ligand and its Cu(II), Co(II), and Ni(II) complexes were recorded in DMSO and their probable assignments are given in Table 3. The

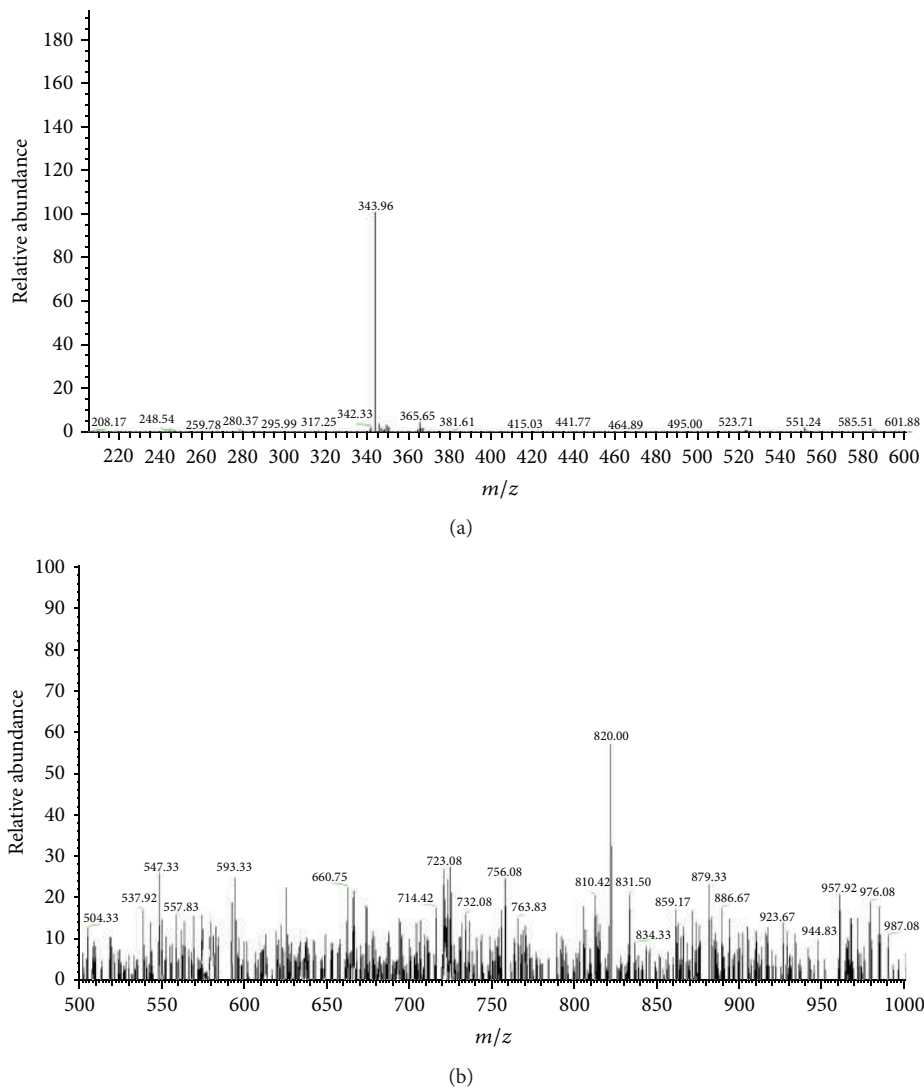


FIGURE 2: Mass spectrum of ligand (a) and copper complex (b).

TABLE 3: Electronic spectral parameters and magnetic moment with suggested geometry of the complexes.

Compound	$\pi \rightarrow \pi^*$ (cm $^{-1}$)	$n \rightarrow \pi^*$ (cm $^{-1}$)	LMCT	d-d band	Assignment	Suggested structure	μ_{eff} (B.M.)
L	36764	29239					
L-Cu	35971	29069	22026	12345	$^2\text{B}_{1g} \rightarrow ^2\text{B}_{2g}, \text{E}_g$	Distorted octahedral	4.52
L-Co	36231	29068	—	16339, 14836	$^4\text{T}_{1g}(\text{F}) \rightarrow ^4\text{T}_{1g}(\text{P})$	Octahedral	4.13
L-Ni	36496	29069	22132	—	$^3\text{A}_{2g} \rightarrow ^3\text{T}_{1g}(\text{F})$	Octahedral	3.91

absorption bands at 36764 cm $^{-1}$ and 29239 cm $^{-1}$ attributed to $\pi \rightarrow \pi^*$ and $n \rightarrow \pi^*$ transitions in the ligand(L). The Cu(II) complex showed d-d band at 12345 cm $^{-1}$. These bands may be assigned to $^2\text{B}_{1g} \rightarrow ^2\text{B}_{2g}, ^2\text{E}_g$ transitions. The position of these bands is consistent with octahedral geometry around the Cu(II) ion. The electronic spectra of Co(II) complex exhibited the absorption d-d bands at 16339 and 14836 cm $^{-1}$. These bands may be assigned to $^4\text{T}_{1g}(\text{F}) \rightarrow ^4\text{T}_{1g}(\text{P})$ and $^4\text{T}_{1g}(\text{F}) \rightarrow ^4\text{A}_{2g}$ transitions.

The position of these bands is consistent with octahedral geometry around the Co(II) ion. The Cu(II) and Co(II) complexes showed paramagnetism, 4.52 and 4.13 BM respectively [32, 33]. Similarly, the electronic spectra of Ni(II) complex exhibited absorption band at 22132 cm $^{-1}$ and assigned to be LMCT band and the d-d band suppressed by LMCT band. The position of these bands is consistent with octahedral geometry around the Ni(II) ion. The Ni(II) also showed paramagnetism, 3.91 BM [34].

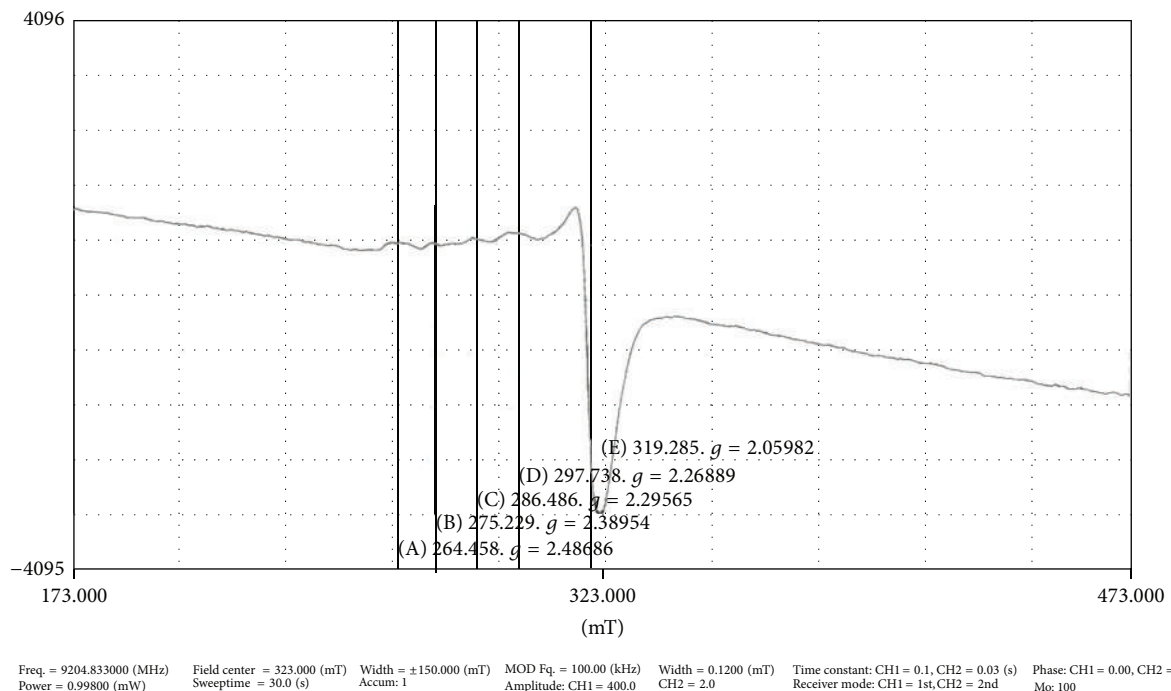


FIGURE 3: EPR spectrum of copper complex at 77 K.

TABLE 4: Electrochemical parameters for Cu(II), Co(II), and Ni(II) complexes.

Compound	Redox couple	Epa (mV)	Epc (mV)	ΔEp (mV)	Ipa/Ipc
L-Cu	Cu(II)/Cu(I)	-214	-103	111	1.03
L-Co	Co(II)/Co(I)	790	610	180	0.82
L-Ni	Ni(II)/Ni(I)	521	384	137	0.91

3.6. EPR Spectra. The X-band EPR spectrum of the copper(II) complex was recorded in the solid state at room temperature and in DMSO solvents at liquid nitrogen temperature using the DPPH radical as the *g* marker (Figure 3). The complex has a well-resolved g_{\parallel} and broadened g regions and various Hamiltonian parameters have been calculated as $g_{\parallel} = 2.339$; $g_{\perp} = 2.05$; $A_{\parallel} = 120 \times 10^4$. The trend $g_{\parallel} > g_{\perp}$ observed in this complex indicates that the unpaired electron is most likely to be in the $d_{x^2-y^2}$ orbital [35].

3.7. Cyclic Voltammetry. A cyclic voltammogram of Cu(II) complex presented in Table 4. Voltammogram (Figure 4) displays a reduction peak at $E_{pc} = -103.60$ mV, with an associated oxidation peak at $E_{pa} = -214.77$ mV at a scan rate of 50 mV/s. The peak separation of this couple (ΔE_p) is 0.77V and increases with scan rate, $I_{pa}/I_{pc} = 1.03$. Thus, the analyses of cyclic voltammetric responses at different scan rate gave the evidence for quasireversible one electron reduction. The most significant feature of the Cu(II) complex is the Cu(II)/Cu(I) couple. The ratio of cathodic-to-anodic peak height was less than one. However, the peak current

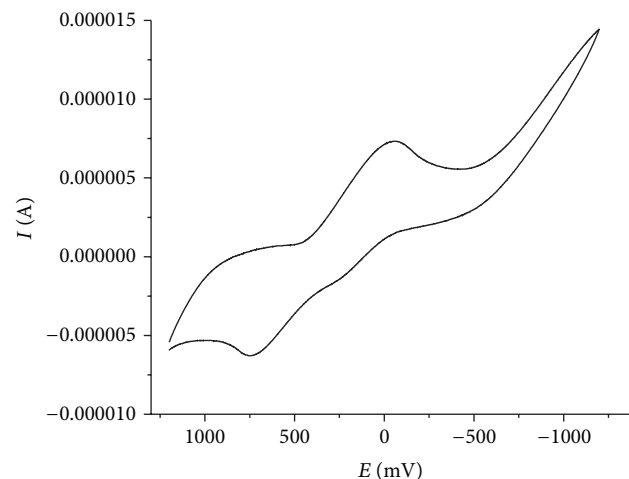
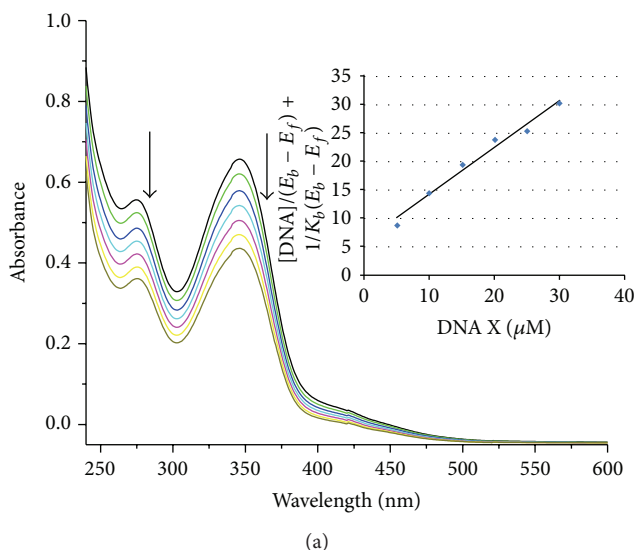
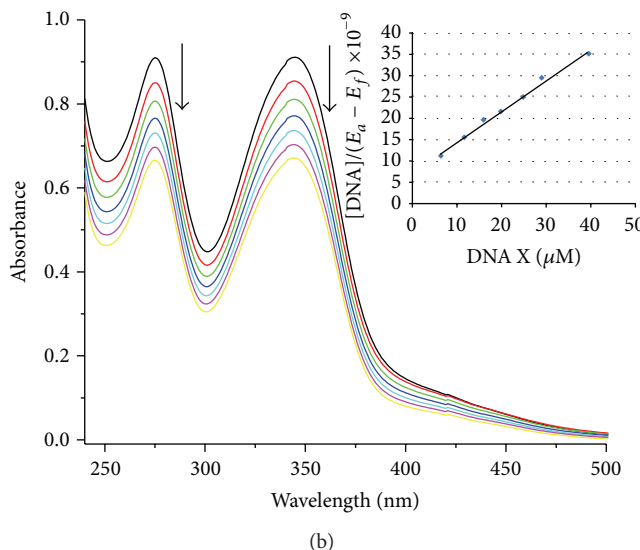


FIGURE 4: CV spectrum of Cu(II) complex.

increases with the increase of the square root of the scan rates. This establishes the electrode process as diffusion controlled [29]. In Co(II) complex shows a redox process corresponding to the Co(II)/Co(I) couple at $E_{pa} = 790$ mV and the associated cathodic peak at $E_{pc} = 610$ mV and the Ni(II) complex showed redox process corresponding to the Ni(II)/Ni(I) couple at $E_{pa} = 521$ mV and the associated cathodic peak at $E_{pc} = 384$ mV. These couples are also found to be quasi-reversible as the peak separation between the anodic and cathodic potentials. But the ratio between the anodic and cathodic currents suggests that the process is simple one-electron transfer, quasi-reversible process [36].



(a)



(b)

FIGURE 5: Absorption spectra of (a) Cu(II) and (b) Co(II) complexes in the absence and in the presence of the CT-DNA. [complex] = 30 μM , [DNA] = 0 to 30 μM . The arrow indicates absorption intensity decrease with increasing addition of the CT-DNA. Plots of $[\text{DNA}] / (\mathcal{E}_a - \mathcal{E}_f)$ versus [DNA] for the complexes with CT-DNA. The arrow indicates absorption intensity decrease with increasing addition of the CT-DNA.

3.8. DNA Interaction Studies. DNA is a molecule of great biological significance and controls the structure and function of cells [36]. These important biological activities will be started via receiving a signal to DNA, which is often in the form of a regulatory protein binding to a particular region of the DNA molecule. The binding specificity and strength of this regulatory protein may be imitated by a small molecule; consequently DNA function can be artificially modulated, inhibited, or activated by binding this molecule instead of the protein [37]. Some studies show that binding can occur between the DNA base pairs (intercalation) [38, 39], while some results are indicative of their groove binding nature [40, 41]. DNA interaction studies have been carried out with the prepared complexes by using UV-visible, CD, and CV spectral techniques and DNA cleavage activity also has been studied by gel-electrophoresis which showed significant results.

3.8.1. DNA Binding-Absorption Spectra. The change of the UV spectra of complexes in the presence of different concentrations of DNA was studied. Hypochromism and red shift in the UV absorption spectra were observed upon addition of DNA increasing concentrations to the complexes solution in the absorption intensity region 275–280 nm and 344–346 nm. These effects are particularly pronounced for intercalators. In the case of groove binders wavelength shift is usually correlated with a conformational change on binding or complex formation [42]. In general, the extent of the hypochromism indicates the interaction binding strength and intrinsic binding constant, K_b for complexes with CT-DNA was determined according to (1) [43], where [DNA] is the concentration of DNA in base pairs. \mathcal{E}_a is the extinction coefficient for APM absorption band at a given DNA concentration, \mathcal{E}_f is extinction coefficient of free complexes, and \mathcal{E}_b is the extinction coefficient of complexes when fully bound to

TABLE 5: Absorption properties of metal (II) complexes with CT-DNA.

Complexes	λ_{\max} (nm)	$\Delta\lambda$ (nm)	Hypochromicity (%)	K_b (M^{-1})
L-Cu(II)	275, 345	3	59.05, 65.45	10.50
L-Co(II)	280, 346	5	37.53, 42.18	5.88
L-Ni(II)	275, 344	2	37.53, 58.48	6.81

DNA (it is assumed when further addition of DNA does not change the absorbance).

In particular, \mathcal{E}_f was determined by a calibration curve of the isolated complexes in DMSO solution, following Beer's law. \mathcal{E}_a was determined as the ratio between the measured absorbance and the complex concentration. Plot of $[\text{DNA}] / (\mathcal{E}_a - \mathcal{E}_f)$ versus [DNA] gives a slope of $1 / (\mathcal{E}_b - \mathcal{E}_f)$ and a y -intercept equal to $1 / K_b (\mathcal{E}_b - \mathcal{E}_f)$; K_b is the ratio of the slope of the y -intercept (Figure 5 insert). The K_b value was calculated to be 10.50×10^4 , 5.88×10^4 , and $6.81 \times 10^4 \text{ M}^{-1}$ (Table 5). The K_b value obtained here is less than that of reported for classical intercalator (for ethidium bromide whose binding constants have been found to be in the order of 10^6 – 10^7 M^{-1}) [44]. In comparing the intrinsic binding constant (K_b) of Cu(II), Co(II), and Ni(II) complexes with DNA groove binders, as observed in the literature, we can deduce that this complex binds to CT-DNA via groove binding [45, 46].

3.8.2. DNA Binding-Cd Spectra. CD spectra is a useful technique in diagnosing changes in DNA morphology during drug–DNA interactions, since CD signals are quite sensitive to the mode of DNA interactions with small molecules [47]. In the case of CT-DNA interacting with metal complexes, the characteristic CD spectra showed two bands as a positive one

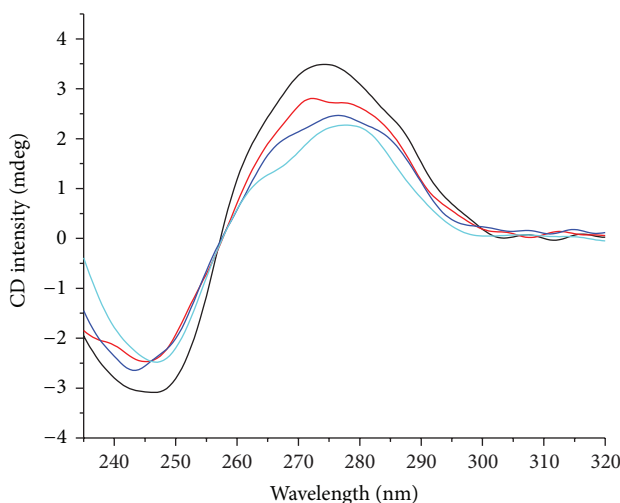


FIGURE 6: Circular dichroism spectra of DNA ($80 \mu\text{M}$) in 10 mM Tris HCl buffer, in the presence of increasing amounts of copper(II) complex.

at 275 nm due to the base stacking between the compounds and DNA bases and a negative band at 245 nm due to the right-handed helicity B form of DNA [48]. Observed changes in these CD signals of DNA are usually assigned to corresponding changes in its structure (Figure 6). The simple groove binding or electrostatic interaction between small molecules and DNA causes less or no perturbation on the base stacking and helicity bands, whereas a classical intercalation enhances both CD bands, stabilizing the CT-DNA form B conformation, as observed for intercalative ligands [49]. Complexes Cu, Co, and Ni exhibited different binding constant values, determined in UV-visible experiments. Generally the DNA of A and B forms structures which have right-handed helix; however, the helical parameters are different in helix pitch, base pair tilt, and twist angle in degrees as 28, 20, and 33 (A form) and 24, -6, and 36 (B form), respectively. B form is the major form that is found in the cell (Watson and Crick 1953). However, after the complex addition to CT-DNA it was only verified as small perturbations in negative and positive bands of CD spectra for three complexes, as shown in Figure 6. Macías et al. [50] observed an increase in both positive and negative bands after incubating complexes with DNA, attributed to a typical intercalative mode, involving $\pi \rightarrow \pi^*$ stacking and stabilization of the right-handed form of CT-DNA. Incubation of DNA with complexes shows little perturbation of the two bands, which is indicative of a nonintercalative interaction between complexes and DNA and offers another support to its groove binding nature [51].

3.8.3. DNA-Binding-Cyclic Voltammetry Study. Electrochemical investigations of metal-DNA interactions provide a useful complement to spectroscopic methods. Cyclic voltammogram of copper complex in the presence of CT-DNA in various concentrations is shown in Figure 7. CV data explored that Cu exhibited a pair of redox peaks for one

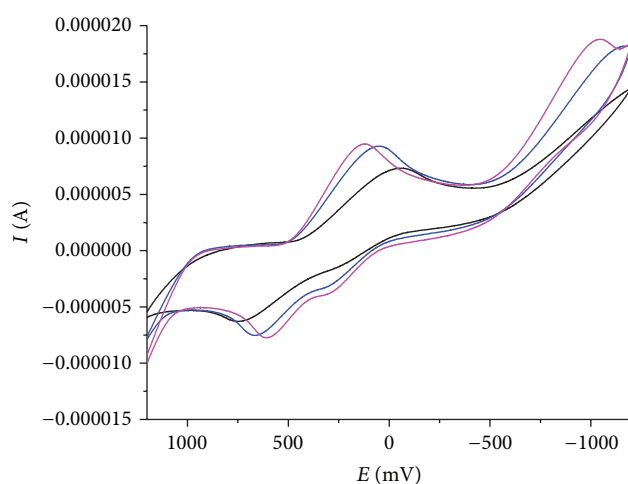


FIGURE 7: Cyclic voltammogram of copper(II) complex in the absence and presence of increasing amounts CT-DNA at room temperature in DMSO: buffer (1: 2) mixture (pH 7.2) (scan rate 0.1 Vs^{-1}).

electron transfer couple of Cu(II)/Cu(I) at the scan rate of 50 mVs (curve). The ratio of (I_{pa}/I_{pc}) value of 0.5 and the peak to peak separation (ΔE_p) of 0.44 V suggested the characteristic of the of the electrotransfer process and this was fairly common for Cu(II)/Cu(I) couple because of the reorganization of the coordination sphere. After interaction with CT-DNA, the value of ΔE_p was decreased to 0.23 V suggesting that the reversibility of the electron-transfer process of the copper complex was changed better. Moreover, both the oxidation and the reduction peak potentials underwent positive shifts accompanied by the decreases of the redox peak currents. It has pointed out that the electrochemical potential of the small molecules would shift positively when it interacted into DNA double helix, and if it bounds to DNA by groove binding only takes place. So we thought that the greater affinity of Cu with CT-DNA is most likely caused by a specific binding mode [52]. The two quasireversible redox couple for Cu(II) complex and other complexes are irreversible redox couple for Co(II) and Ni(II).

3.8.4. DNA Cleavage Studies By Agarose Gel Electrophoresis. The ability of Cu(II), Co(II), and Ni(II) complexes to perform DNA cleavage was monitored by agarose gel electrophoresis with the pUC19 plasmid DNA. The experimental results were shown in Figure 8. Two clear bands were observed for the controls in which the three complexes were absent (lane 1). The relatively fast migration is the intact super coil form (Form II) and the slower moving migration is the open circular form (Form I), which was generated from super coiled when scission occurred on its one strand [53, 54]. The amount of Form II diminished gradually and partly converted to Form I and it is obvious that the complexes have more ability to cleave the super coiled plasmid DNA.

3.9. Cytotoxicity. The cytotoxicity assay for the new complexes was assessed using the method of MTT reduction.

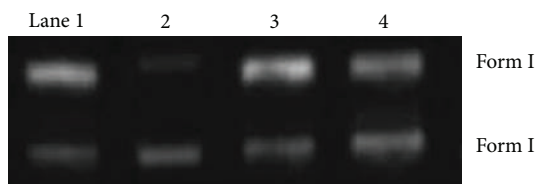


FIGURE 8: Cleavage of super coiled pUC19 ($10 \mu\text{M}$) by the Cu(II), Co(II), and Ni(II) complexes in the presence of triacetate EDTA (TEA) buffer at 37°C . Upper line: Form I and lower line: Form II; Lane 1: DNA-control; Lane 2: L-Cu; Lane 3: L-Co; Lane 4: L-Ni.

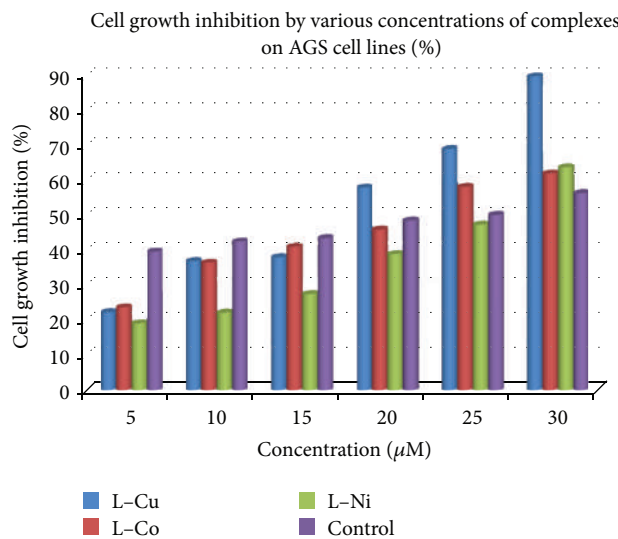


FIGURE 9: Treatment of complexes that exert an antiproliferative effect on liver cancer cell line. HepG2 cells were treated with complexes (Cu, Co, and Ni) for 48 h. Control received appropriate carriers. Cell viability was assessed by MTT cell proliferation assay.

The market reference Mitomycin-C was used as a positive control. All the ligands and complexes were found to be cytotoxic to liver cancer cell line (HepG2). The IC_{50} values (50% inhibition of cell growth for 48 h) for complexes Cu, Co, and Ni are $5 \mu\text{M}$, $10 \mu\text{M}$, $20 \mu\text{M}$, $25 \mu\text{M}$, and $30 \mu\text{M}$, respectively (Figure 9). The complexes exhibited higher cytotoxic effects on liver cancer cells with lower IC_{50} values indicating their efficiency in killing the cancer cells even at low concentrations. The ligand did not show any significant activity up to $100 \mu\text{M}$. However, cytotoxic effectiveness of the compounds with an IC_{50} of Cu and Ni complexes was higher than that of control. There are reports in the literature on the cytotoxic effects of the complexes with longer incubation time periods [55–57]. The longer incubation period may result in the development of cellular resistance for that particular complex. The complexes Cu and Ni is showed better activity than Co complex because the reduction potential of Cu(II) and Ni(II), almost in same order of magnitude; however the Co(II) is widely varied and mostly biocompatible in living system. Moreover, the IC_{50} values of our complexes are comparable with the reported IC_{50} values of standard anticancer drugs such as Mitomycin-C.

4. Conclusion

One of the most important goals of pharmacological research is the search for new molecular structures which exhibit effective antitumor activities. This has driven inorganic and organometallic chemists to look for new metal compounds with good activities, preferably against tumors that are responsible for high cancer mortality. In this study, new series of Schiff base (L) and its complexes Cu(II), Co(II), and Ni(II) showed octahedral geometry. The binding behaviors of the complexes toward CT-DNA were investigated by absorption spectroscopy, CD, and CV techniques. In conclusion competitive binding of complexes for DNA indicated that complexes could interact as a groove binder. It should be noted that the observed intrinsic binding constant ($5.88\text{--}10.50 \times 10^4 \text{ M}^{-1}$) is comparable to other groove binders as well and complexes Cu and Ni have stronger binding affinity than Co. The complexes bind to super coiled plasmid pUC19 DNA and display efficient hydrolytic cleavage and are a specific groove binder. The cytotoxic studies showed that the complexes Cu and Ni exhibit good cytotoxic activity against AGS cell line. Furthermore, these complexes have potential practical applications to formulate into an efficient drug against cancer.

Conflict of Interests

The authors declare that there is no conflict of interests regarding the publication of this paper.

Acknowledgments

The authors sincerely acknowledge the financial support received from UGC-JRF (BSR), New Delhi. The authors express their sincere thanks to Dr. Kumaresan, Department of Genetics, School of Biological Sciences, MKU, for providing necessary research facilities.

References

- [1] M. S. Karthikeyan, D. J. Prasad, B. Poojary, K. Subrahmanyam Bhat, B. S. Holla, and N. S. Kumari, "Synthesis and biological activity of Schiff and Mannich bases bearing 2,4-dichloro-5-fluorophenyl moiety," *Bioorganic and Medicinal Chemistry*, vol. 14, no. 22, pp. 7482–7489, 2006.
- [2] A. Dandia, V. Sehgal, and P. Singh, "Synthesis of fluorine containing 2-aryl-3-pyrazolyl/pyranyl/isoazolinyl-indole derivative as antifungal and antibacterial agents," *Indian Journal of Chemistry B*, vol. 32, pp. 1288–1291, 1993.
- [3] K. Singh, M. S. Barwa, and P. Tyagi, "Synthesis, characterization and biological studies of Co(II), Ni(II), Cu(II) and Zn(II) complexes with bidentate Schiff bases derived by heterocyclic ketone," *European Journal of Medicinal Chemistry*, vol. 41, no. 1, pp. 147–153, 2006.
- [4] O. M. Walsh, M. J. Meegan, R. M. Prendergast, and T. Al Nakib, "Synthesis of 3-acetoxyazetidin-2-ones and 3-hydroxyazetidin-2-ones with antifungal and antibacterial activity," *European Journal of Medicinal Chemistry*, vol. 31, no. 12, pp. 989–1000, 1996.
- [5] N. Raman, K. Pothiraj, and T. Baskaran, "DNA interaction, antimicrobial, electrochemical and spectroscopic studies of

- metal(II) complexes with tridentate heterocyclic Schiff base derived from 2'-methylacetacetanilide," *Journal of Molecular Structure*, vol. 1000, no. 1-3, pp. 135–144, 2011.
- [6] K. R. Surati and B. T. Thaker, "Synthesis, spectral, crystallography and thermal investigations of novel Schiff base complexes of manganese (III) derived from heterocyclic β -diketone with aromatic and aliphatic diamine," *Spectrochimica Acta A*, vol. 75, no. 1, pp. 235–242, 2010.
- [7] M. A. Ali, A. H. Mirza, H. J. H. A. Bakar, and P. V. Bernhardt, "Preparation and structural characterization of nickel(II), cobalt(II), zinc(II) and tin(IV) complexes of the isatin Schiff bases of S-methyl and S-benzylthiocarbazates," *Polyhedron*, vol. 30, no. 4, pp. 556–564, 2011.
- [8] G. Cerchiaro, G. A. Micke, M. F. M. Tavares, and A. M. da Costa Ferreira, "Kinetic studies of carbohydrate oxidation catalyzed by novel isatin-Schiff base copper(II) complexes," *Journal of Molecular Catalysis A*, vol. 221, no. 1-2, pp. 29–39, 2004.
- [9] Z. H. Chohan, H. Pervez, A. Rauf, K. M. Khan, and C. T. Supuran, "Isatin-derived antibacterial and antifungal compounds and their transition metal complexes," *Journal of Enzyme Inhibition and Medicinal Chemistry*, vol. 19, no. 5, pp. 417–423, 2004.
- [10] V. Arjunan, I. Saravanan, P. Ravindran, and S. Mohan, "Structural, vibrational and DFT studies on 2-chloro-1H-isoindole-1,3(2H)-dione and 2-methyl-1H-isoindole-1,3(2H)-dione," *Spectrochimica Acta A*, vol. 74, no. 3, pp. 642–649, 2009.
- [11] V. Pawar, D. Lokwani, S. Bhandari et al., "Design of potential reverse transcriptase inhibitor containing Isatin nucleus using molecular modeling studies," *Bioorganic and Medicinal Chemistry*, vol. 18, no. 9, pp. 3198–3211, 2010.
- [12] C. Metcalfe and J. A. Thomas, "Kinetically inert transition metal complexes that reversibly bind to DNA," *Chemical Society Reviews*, vol. 32, no. 4, pp. 215–224, 2003.
- [13] K. E. Erkkila, D. T. Odom, and J. K. Barton, "Recognition and reaction of metallointercalators with DNA," *Chemical Reviews*, vol. 99, no. 9, pp. 2777–2795, 1999.
- [14] V. Uma, V. G. Vaidyanathan, and B. U. Nair, "Synthesis, structure, and DNA binding studies of copper(II) complexes of terpyridine derivatives," *Bulletin of the Chemical Society of Japan*, vol. 78, no. 5, pp. 845–850, 2005.
- [15] W. Szczepanik, J. Ciesiolka, J. Wrzesiński, J. Skala, and M. Jezowska-Bojczuk, "Interaction of aminoglycosides and their copper(II) complexes with nucleic acids: implication to the toxicity of these drugs," *Dalton Transactions*, no. 8, pp. 1488–1494, 2003.
- [16] Q.-L. Li, J. Huang, Q. Wang et al., "Monometallic complexes of 1,4,7,10-tetraazacyclododecane containing an imidazolium side: synthesis, characterization, and their interaction with plasmid DNA," *Bioorganic and Medicinal Chemistry*, vol. 14, no. 12, pp. 4151–4157, 2006.
- [17] P. K. Dubey, S. Srinivas Rao, and V. Aparna, "Synthesis of some novel 3-(2-chloro-3-quinolyl)-5-phenyl [1,3] thiazolo [2,3-c] [1,2,4] triazoles," *Heterocyclic Communications*, vol. 9, no. 3, pp. 281–286, 2003.
- [18] R. Gomathi, A. Ramu, and A. Murugan, "Synthesis, spectral characterization of N-benzyl isatin schiff base Cu(II), Co(II) and Ni(II) complexes and their effect on cancer cell lines," *International Journal of Innovative Research in Science, Engineering and Technology*, vol. 2, no. 10, pp. 5156–5166, 2013.
- [19] R. Gomathi and A. Ramu, "Synthesis, DNA binding, cleavage, antibacterial and cytotoxic activity of Novel Schiff base Co(II) Complexes of substituted isatin," *International Journal of Advanced Research*, vol. 1, no. 8, pp. 556–567, 2013.
- [20] R. Hettich and H.-J. Schneider, "Cobalt(III) polyamine complexes as catalysts for the hydrolysis of phosphate esters and of DNA. A measurable 10 million-fold rate increase," *Journal of the American Chemical Society*, vol. 119, no. 24, pp. 5638–5647, 1997.
- [21] C.-C. Cheng, Y.-N. Kuo, K.-S. Chuang, C.-F. Luo, and W. J. Wang, "A new CoII complex as a bulge-specific probe for DNA," *Angewandte Chemie (International Edition)*, vol. 38, no. 9, pp. 1255–1257, 1999.
- [22] R. Gomathi and A. Ramu, "Synthesis, characterization of novel Cu(II) complexes of isatin derivatives as potential cytotoxicity, DNA binding, cleavage and antibacterial agents," *International Journal of Innovative Research in Science Engineering and Technology*, vol. 2, no. 9, pp. 4852–4486, 2013.
- [23] A. Wolfe, G. H. Shimer Jr., and T. Meehan, "Polycyclic aromatic hydrocarbons physically intercalate into duplex regions of denatured DNA," *Biochemistry*, vol. 26, no. 20, pp. 6392–6396, 1987.
- [24] F. A. Beckford, M. Shaloski Jr., G. Leblanc et al., "Microwave synthesis of mixed ligand diimine-thiosemicarbazone complexes of ruthenium(II): biophysical reactivity and cytotoxicity," *Dalton Transactions*, no. 48, pp. 10757–10764, 2009.
- [25] S. P. Hiremath, B. H. M. Mruthyunjayaswamy, and M. G. Purohit, "Synthesis of substituted 2-aminoindoles and 2-(2'-Phenyl-1',3',4'-oxadiazolyl)aminoindoles," *Indian Journal of Chemistry B*, vol. 16, pp. 789–792, 1978.
- [26] A. D. Kulkarni, S. A. Patil, and P. S. Badami, "Electrochemical properties of some transition metal complexes: synthesis, characterization and In-vitro antimicrobial studies of Co(II), Ni(II), Cu(II), Mn(II) and Fe(III) complexes," *International Journal of Electrochemical Science*, vol. 4, no. 5, pp. 717–729, 2009.
- [27] D.-D. Li, J.-L. Tian, W. Gu, X. Liu, and S.-P. Yan, "Synthesis, X-ray crystal structures, DNA binding and nuclease activities of two novel 1,2,4-triazole-based Cu^{II} complexes," *European Journal of Inorganic Chemistry*, no. 33, pp. 5036–5045, 2009.
- [28] M. P. Fitzsimons and J. K. Barton, "Design of a synthetic nuclease: DNA hydrolysis by a zinc-binding peptide tethered to a rhodium intercalator," *Journal of the American Chemical Society*, vol. 119, no. 14, pp. 3379–3380, 1997.
- [29] F. Arjmand, S. Parveen, M. Afzal, L. Toupet, and T. Ben Hadda, "Molecular drug design, synthesis and crystal structure determination of CuII-SnIV heterobimetallic core: DNA binding and cleavage studies," *European Journal of Medicinal Chemistry*, vol. 49, pp. 141–150, 2012.
- [30] P. Guerrero, S. Tamburini, and P. A. Vigato, "From mononuclear to polynuclear macrocyclic or macroacyclic complexes," *Coordination Chemistry Reviews*, vol. 139, pp. 17–243, 1995.
- [31] S. Budagumpi, G. S. Kurdekar, G. S. Hegde, N. H. Bevinahalli, and V. K. Revankar, "Versatility in the coordination behavior of a hexatopic compartmental Schiff-base ligand in the architecture of binuclear transition metal(II) complexes," *Journal of Coordination Chemistry*, vol. 63, no. 8, pp. 1430–1439, 2010.
- [32] S. Shashidhar, K. Shivakumar, P. V. Reddy, and M. B. Halli, "Synthesis and spectroscopic characterization of metal complexes with naphthofuran-2-carbohydrazide Schiff's base," *Journal of Coordination Chemistry*, vol. 60, no. 3, pp. 243–256, 2007.
- [33] H. Liu, H. Wang, F. Gao, D. Niu, and Z. Lu, "Self-assembly of copper(II) complexes with substituted arylhydrazones and monodentate N-heterocycles: synthesis, structure and properties," *Journal of Coordination Chemistry*, vol. 60, no. 24, pp. 2671–2678, 2007.

- [34] D. P. Singh, R. Kumar, V. Malik, and P. Tyagi, "Synthesis and characterization of complexes of Co(II), Ni(II), Cu(II), Zn(II), and Cd(II) with macrocycle 3,4,11,12-tetraoxo-1,2,5,6,9,10,13,14-octaaza-cyclohexadeca-6,8,14,16-tetraene and their biological screening," *Transition Metal Chemistry*, vol. 32, no. 8, pp. 1051–1055, 2007.
- [35] V. C. da Silveira, H. Benezra, J. S. Luz, R. C. Georg, C. C. Oliveira, and A. M. D. C. Ferreira, "Binding of oxindole-Schiff base copper(II) complexes to DNA and its modulation by the ligand," *Journal of Inorganic Biochemistry*, vol. 105, no. 12, pp. 1692–1703, 2011.
- [36] Y. Ni, D. Lin, and S. Kokot, "Synchronous fluorescence, UV-visible spectrophotometric, and voltammetric studies of the competitive interaction of bis(1,10-phenanthroline)copper(II) complex and neutral red with DNA," *Analytical Biochemistry*, vol. 352, no. 2, pp. 231–242, 2006.
- [37] B. W. Rossister and J. F. Hamilton, *Physical Method of Chemistry*, John Wiley & Sons, New York, NY, USA, 2nd edition, 1985.
- [38] F.-Y. Wu, F.-Y. Xie, Y.-M. Wu, and J.-I. Hong, "Interaction of a new fluorescent probe with DNA and its use in determination of DNA," *Journal of Fluorescence*, vol. 18, no. 1, pp. 175–181, 2008.
- [39] P. B. Dervan, R. M. Doss, and M. A. Marques, "Programmable DNA binding oligomers for control of transcription," *Current Medicinal Chemistry*, vol. 5, no. 4, pp. 373–387, 2005.
- [40] S. Kashanian and J. Ezzati Nazhad Dolatabadi, "In vitro study of calf thymus DNA interaction with butylated hydroxyanisole," *DNA and Cell Biology*, vol. 28, no. 10, pp. 535–540, 2009.
- [41] S. Kashanian, M. M. Khodaei, H. Roshanfekr, N. Shahabadi, A. Rezvani, and G. Mansouri, "DNA binding, DNA cleavage, and cytotoxicity studies of two new copper (II) complexes," *DNA and Cell Biology*, vol. 30, no. 5, pp. 287–296, 2011.
- [42] S. Kashanian and S. H. Zeidali, "DNA binding studies of tartrazine food additive," *DNA and Cell Biology*, vol. 30, no. 7, pp. 499–505, 2011.
- [43] S. Kashanian, Z. Shariati, H. Roshanfekr, and S. Ghobadi, "DNA binding studies of 3, 5, 6-trichloro-2-pyridinol pesticide metabolite," *DNA Cell Biology*, vol. 31, pp. 1314–1348, 2012.
- [44] R. Bera, B. K. Sahoo, K. S. Ghosh, and S. Dasgupta, "Studies on the interaction of isoxazolcurcumin with calf thymus DNA," *International Journal of Biological Macromolecules*, vol. 42, no. 1, pp. 14–21, 2008.
- [45] R. Liu, J. Yang, and X. Wu, "Study of the interaction between nucleic acid and oxytetracycline-Eu³⁺ and its analytical application," *Journal of Luminescence*, vol. 96, no. 2–4, pp. 201–209, 2002.
- [46] M. J. Waring, "Complex formation between ethidium bromide and nucleic acids," *Journal of Molecular Biology*, vol. 13, no. 1, pp. 269–282, 1965.
- [47] V. G. Vaidyanathan and B. U. Nair, "Photooxidation of DNA by a cobalt(II) tridentate complex," *Journal of Inorganic Biochemistry*, vol. 94, no. 1–2, pp. 121–126, 2003.
- [48] Z.-H. Xu, F.-J. Chen, P.-X. Xi, X.-H. Liu, and Z.-Z. Zeng, "Synthesis, characterization, and DNA-binding properties of the cobalt(II) and nickel(II) complexes with salicylaldehyde 2-phenylquinoline-4-carboxylhydrazone," *Journal of Photochemistry and Photobiology A*, vol. 196, no. 1, pp. 77–83, 2008.
- [49] L. Milne, P. Nicotera, S. Orrenius, and M. J. Burkitt, "Effects of glutathione and chelating agents on copper-mediated DNA oxidation: pro-oxidant and antioxidant properties of glutathione," *Archives of Biochemistry and Biophysics*, vol. 304, no. 1, pp. 102–109, 1993.
- [50] B. Macías, M. V. Villa, B. Gómez et al., "DNA interaction of new copper(II) complexes with new sulfoamides as ligands," *Journal of Inorganic Biochemistry*, vol. 101, pp. 441–451, 2007.
- [51] P. Uma Maheswari and M. Palaniandavar, "DNA binding and cleavage properties of certain tetrammine ruthenium(II) complexes of modified 1,10-phenanthrolines—effect of hydrogen-bonding on DNA-binding affinity," *Journal of Inorganic Biochemistry*, vol. 98, no. 2, pp. 219–230, 2004.
- [52] Z. Zhang, Y. Yang, F. Liu, X. Qian, and Q. Xu, "Study on the interaction between 4-(2-diethylamino-ethylamino)-8-oxo-8H-acenaphtho[1,2-b]pyrrole-9-carbonitrile and DNA by molecular spectra," *International Journal of Biological Macromolecules*, vol. 38, no. 1, pp. 59–64, 2006.
- [53] T. Hirohama, Y. Kuranuki, E. Ebina et al., "Copper(II) complexes of 1,10-phenanthroline-derived ligands: studies on DNA binding properties and nuclease activity," *Journal of Inorganic Biochemistry*, vol. 99, no. 5, pp. 1205–1219, 2005.
- [54] A. K. Patra, S. Dhar, M. Nethaji, and A. R. Chakravarty, "Metal-assisted red light-induced DNA cleavage by ternary L-methionine copper(II) complexes of planar heterocyclic bases," *Dalton Transactions*, no. 5, pp. 896–902, 2005.
- [55] E. Gao, Y. Sun, Q. Liu, and L. Duan, "An anticancer metallo-benzylmalonate: crystal structure and anticancer activity of a palladium complex of 2,2'-bipyridine and benzylmalonate," *Journal of Coordination Chemistry*, vol. 59, no. 11, pp. 1295–1300, 2006.
- [56] M. Ferrari, M. C. Fornasiero, and A. M. Isetta, "MTT colorimetric assay for testing macrophage cytotoxic activity in vitro," *Journal of Immunological Methods*, vol. 131, no. 2, pp. 165–172, 1990.
- [57] N. A. Rey, A. Neves, P. P. Silva et al., "A synthetic dinuclear copper(II) hydrolase and its potential as antitumoral: cytotoxicity, cellular uptake, and DNA cleavage," *Journal of Inorganic Biochemistry*, vol. 103, no. 10, pp. 1323–1330, 2009.

Novel Zinc(II) Complexes of Heterocyclic Ligands as Antimicrobial Agents: Synthesis, Characterisation, and Antimicrobial Studies

Ramesh S. Yamgar,¹ Y. Nivid,² Satish Nalawade,² Mustapha Mandewale,² R. G. Atram,² and Sudhir S. Sawant²

¹ Department of Chemistry, Chikitsak Samuha's Patkar-Varde College of Arts, Science and Commerce, Goregaon (W), Mumbai 400 062, India

² P. G. Department of Chemistry, Government of Maharashtra, Ismail Yusuf Arts, Science and Commerce College, Jogeshwari (East), Mumbai 400 060, India

Correspondence should be addressed to Sudhir S. Sawant; sawantsudhir@hotmail.com

Academic Editor: Giovanni Natile

The synthesis and antimicrobial activity of novel Zn(II) metal complexes derived from three novel heterocyclic Schiff base ligands 8-[*(Z*)-{[3-(N-methylamino)propyl]imino}methyl]-7-hydroxy-4-methyl-2*H*-chromen-2-one, 2-[*(E*)-{[4-(1*H*-1,2,4-triazol-1-ylmethyl)phenyl]imino}methyl]phenol, and (4*S*)-4-{4-[*(E*)-(2-hydroxybenzylidene)amino]benzyl}-1,3-oxazolidin-2-one have been described. These Schiff base ligands and metal complexes are characterised by spectroscopic techniques. According to these data, we propose an octahedral geometry to all the metal complexes. Antimicrobial activity of the Schiff base ligand and its metal complexes was studied against Gram negative bacteria: *E. coli* and *Pseudomonas fluorescens*, Gram positive bacteria: *Staphylococcus aureus*, and also against fungi, that is, *C. albicans* and *A. niger*. Some of the metal complexes show significant antifungal activity (MIC < 0.2 µg/mL). The “*in vitro*” data has identified [Zn(NMAPIMHMC)₂]·2H₂O, [Zn(TMPIMP)₂]·2H₂O, and [Zn(HBABO)₂]·2H₂O as potential therapeutic antifungal agents against *C. albicans* and *A. niger*.

1. Introduction

The treatment of infectious diseases still remains an important and challenging problem because of various factors like emerging infectious diseases and the increasing number of multidrug resistant microbial pathogens. In recent years, bacterial resistance to antibiotics has been a matter of great concern. Antibiotic resistance is the ability of bacteria or other microbes to resist the effects of an antibiotic. Antibiotic resistance occurs when bacteria change in some way that reduces or eliminates the effectiveness of drugs designed to cure or prevent infections. The bacteria survive and continue to multiply causing more harm [1]. Bacteria can do this through several mechanisms like mutation of their genome or by accepting antimicrobial resistant genes from other bacteria.

This usually occurs through one of several biochemical mechanisms like mutation, destruction, or inactivation and efflux.

Due to increasing resistance of these bacterial strains, effective antibacterial medicines like Vancomycin, Ciprofloxacin, Methicillin, and so forth become less effective in treatment of diseases caused by such infections. Over the past several decades, the incidence of resistant Gram positive organisms has risen in the world. Methicillin, a resistant *Staphylococcus aureus* (MRSA), is of special concern in regard to treatment because it is usually multidrug resistant. In addition to most beta-lactams, MRSA is also commonly resistant to clindamycin, erythromycin, fluoroquinolones, aminoglycosides, cotrimoxazole, and rifampicin. These situations have revealed a substantial medical need for discovery of new classes of compounds endowed with antimicrobial activities.

To overcome such challenges in treating patients with infections of such antibacterial resistant strains, new antimicrobial agents, that is, new medicines, need to be researched and continuous efforts are necessary to explore small molecular structures as new medicines. A lower molecular weight cutoff of 500 Daltons (as part of Lipinski's "rule of five") [2] has been recommended for small molecule drug development candidates based on the observation of clinical attrition rates. A small molecule is a low molecular weight (<900 Daltons) compound that may serve as a regulator of a biological process. The upper molecular weight limit for a small molecule is approximately 900 Daltons which allows for the possibility to rapidly diffuse across cell membranes so that they can reach intracellular sites of action [3, 4]. Small molecules may also be used as research tools to probe biological function as well as leads in the development of new therapeutic agents. Some can inhibit a specific function of a multi-functional protein or disrupt protein-protein interactions [5].

It is well known that the cost of developing a new medicine, that is, new chemical entity, is enormous and takes many years to develop the same due to prolonged biological safety studies and human clinical trials. It also takes a lot of research and development efforts to develop multistep synthesis process and scale up of complex molecules. The number of chiral centres in a molecule also increases its cost to develop and time to market. Hence, new cost-effective, shorter routes of synthesis and relatively small molecules are a need of hour in new chemical entity research [6].

The antimicrobial properties of metals have been recognised for centuries and have represented some of the most fundamental breakthroughs in medicinal history [7]. Several metal complexes are known to accelerate the drug action and efficacy of the organic therapeutic agent. The precious metals platinum and silver were reported to exert a toxic effect on bacteria [8, 9]. The original observations that platinum-ammine complexes had antibacterial properties led to the discovery of their antitumour properties and the development of the highly successful platinum anticancer drugs cisplatin and carboplatin [10]. Complexes of gold have also been reported to have a wide range of antimicrobial activities [11].

In order to begin our efforts for such new medicines as effective anti-infective agents against bacteria and fungi, we thought of combining heterocyclic aniline scaffold with simple ortho hydroxy benzaldehydes like salicylaldehyde to get a Schiff base and its conversion to transition metal complex like Zn(II), Cu(II), Ni(II), and Co(II). In our initial efforts, to screen compounds derived from coumarin scaffold and aliphatic diamino compound like N,N-dimethyl ethylene diamine, we got encouraging results with respect to biological assays against Gram positive bacteria and fungi [12–14].

This diverted our focus to search for new molecular structures having less complex structure and few synthesis steps. We thought of heterocyclic aniline scaffolds and condensed with salicylaldehyde to get corresponding Schiff base and then complexation with zinc metal. Schiff bases were synthesised, isolated, and characterised. Zn(II) complexes were prepared by template method and characterised. Schiff bases and their corresponding Zn(II) metal complexes were evaluated for antibacterial and antifungal activities by MIC method.

2. Experimental

All chemicals and solvents used in this work were of analytical grade. Salicylaldehyde was purchased from Merck Chemicals. Zinc chloride, DMSO, and oxalic acid were purchased from SD Fine chemicals.

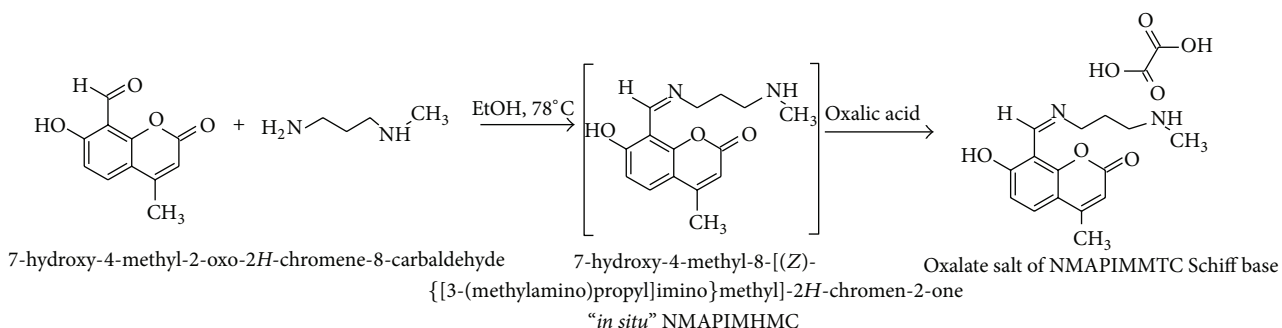
7-hydroxy-4-methyl-2-oxo-2H-chromene-8-carbaldehyde was obtained by Duff formylation procedure starting with 7-hydroxy-4-methyl-2H-chromen-2-one as per the reported method [15–17] and N-methyl propane-1,3-diamine was procured from a commercial source.

2.1. Preparation of the Schiff Base 7-Hydroxy-4-methyl-8-[(Z)-{[3-(methylamino)propyl]imino}methyl]-2H-chromen-2-one [NMAPIMHMC] Oxalate Salt (Scheme 1). The Schiff base, that is, the ligand 8-[(Z)-{[3-(N-methylamino)propyl]imino}methyl]-7-hydroxy-4-methyl-2H-chromen-2-one [NMAPIMHMC], was synthesized by the condensation of 7-hydroxy-4-methyl-2-oxo-2H-chromene-8-carbaldehyde with N-methyl propane-1,3-diamine in (1:1) molar proportion in ethanol in the presence of traces of concentrated hydrochloric acid. The reaction mixture was refluxed for an hour. On cooling, the product was isolated as yellowish brown oily mass.

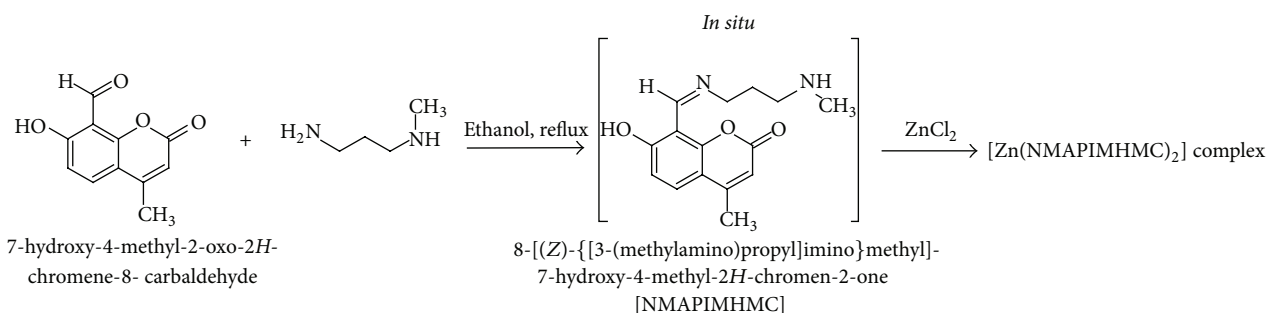
As the oily Schiff base was unstable in nature, it was difficult to characterize the compound. Therefore, its oxalate salt was prepared for spectral characterization.

4-Methyl-7-hydroxy 8-formyl coumarin (1.0 g, 0.0049 mole) was dissolved in 10 mL ethanol and N-methylpropane-1,3-diamine (0.431 g, 0.0049 mole) was added. A drop of concentrated hydrochloric acid was added and the reaction mixture was refluxed for an hour. Oxalic acid (0.555 g, 0.0041 mole, 0.9 eq.) was added and further refluxed for an hour. On cooling, the product was isolated as oxalate salt which was recrystallized from alcohol. The product was filtered and dried in oven till constant weight. Weight: 1.1 g, (yield: 70%). Colour: yellow, M.P. 205–207°C, elemental analysis observed (calculated): C 56.4% (56.02%), H 5.53% (5.69%), N 7.69% (7.22%), UV: λ_{max} 225 nm, 313 nm, MS: [M+H]⁺ 275, IR (KBr) $\nu_{\text{N-H}}$ 3468 cm⁻¹ $\nu_{\text{C=O(Lacton)}}$ 1715 cm⁻¹ $\nu_{\text{C=N}}$ 1609 cm⁻¹ $\nu_{\text{C-O-C}}$ 1076 cm⁻¹ $\nu_{\text{C-O(phenolic)}}$ 1313 cm⁻¹, ¹H NMR [DMSO(d₆), 300 MHz] 1.92 (s, 3H), 2.2–2.4 (m, 2H), 2.51 (s, 3H), 2.79 (m, 2H), 3.05 (t, 2H), 5.24 (s, 1H), 5.87 (d, 1H, J = 9.4 Hz), 6.84 (d, 1H, J = 9.4 Hz) 8.15 (s, 1H azomethine).

2.2. Preparation of the Zn(II) Complex of "In Situ" Schiff Base 7-Hydroxy-4-methyl-8-[(Z)-{[3-(methylamino)propyl]imino}methyl]-2H-chromen-2-one [NMAPIMHMC] (Scheme 2). The preparation of the Zn(II) complex was carried out by taking 7-hydroxy-4-methyl-2-oxo-2H-chromene-8-carbaldehyde (1.5 g, 0.00735 mol) in ethanol (30 mL) and N-methylpropane-1,3-diamine (0.646 g, 0.00735 mol). A drop of diluted HCl was added and the mixture was refluxed on a water bath for about an hour. The colour of solution was pale yellow. To this hot solution, zinc chloride (1.0 g, 0.00735 mol) was added. The solution was refluxed for additional three hours and TLC was checked for completion of reaction. The pale yellow precipitate formed was filtered, and washed with ethanol. Product was recrystallised in



SCHEME 1: Synthesis of Schiff base 7-hydroxy-4-methyl-8-[(Z)-{[3-(methylamino)propyl]imino}methyl]-2H-chromen-2-one [NMAPIMHMC] oxalate salt.



SCHEME 2: Synthesis of Zn(II) complex of Schiff base 7-hydroxy-4-methyl-8-[(Z)-{[3-(methylamino)propyl]imino}methyl]-2H-chromen-2-one [NMAPIMHMC].

ethanol at reflux, filtered and dried in oven at 70–80°C till constant weight. (Yield: 2.0 g, 42.0%), M.P. > 260°C, [M]⁺ 612, IR (KBr): $\nu_{\text{O-H}}$ (lattice water) 3112 cm⁻¹ $\nu_{\text{C=O}}$ (lactonyl) 1727 cm⁻¹ $\nu_{\text{C=N}}$ 1631 cm⁻¹, $\nu_{\text{C-O}}$ (phenolic) 1371 cm⁻¹, $\nu_{\text{Zn-N}}$ 543 cm⁻¹, $\nu_{\text{Zn-O}}$ 453 cm⁻¹, ¹H NMR (DMSO-d₆, 300 MHz) 2.06 (m, 2H), 2.34 (s, 3H), 2.96 (t, 2H), 3.73 (t, 2H), 5.98 (s, 1H), 6.56 (d, 2H, *J* = 8.4 Hz), 7.56 (d, *J* = 8.4 Hz) 8.83 (s, 1H azomethine).

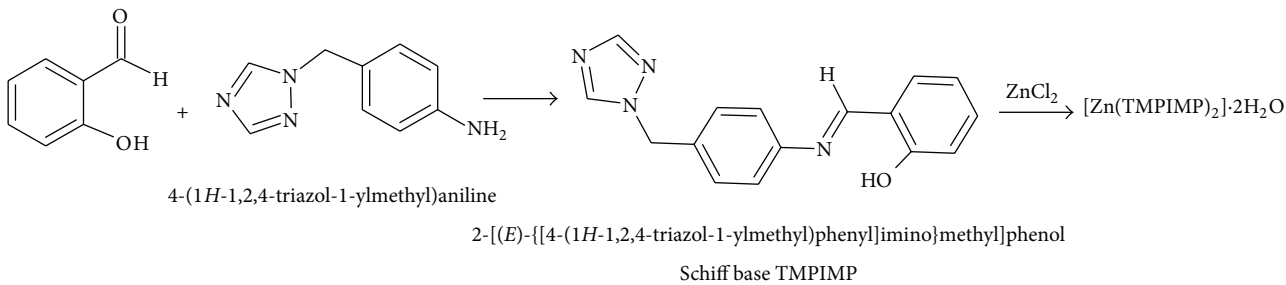
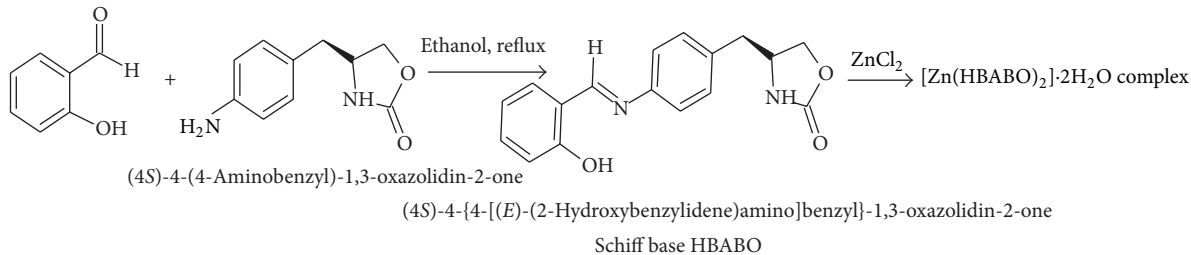
2.3. Preparation of the Schiff Base 2-[(E)-{[4-(1*H*-1,2,4-Triazol-1-ylmethyl)phenyl]imino}methyl]phenol [TMPIMP] (Scheme 3). 4-(1*H*-1,2,4-Triazol-1-ylmethyl)aniline was prepared by known method reported in literature [18] and was characterised by spectroscopic techniques. Salicylaldehyde was purchased from Merck Chemicals.

4-(1*H*-1,2,4-Triazol-1-ylmethyl)aniline (0.3 g, 0.00172 mole) was taken in 10 mL ethanol, salicylaldehyde (0.209 g, 0.00172 mole) was added, and solution was heated to reflux in water for about 2 hours. The orange coloured crystalline product was filtered and washed with ethanol. Product was dried in oven at 70–80°C till constant weight. Weight 0.278 g. Colour: yellow crystalline solid, M.P: 145°C, IR (KBr): $\nu_{\text{C=N}}$ 1621 cm⁻¹, phenolic $\nu_{\text{C-O}}$ 1143 cm⁻¹, elemental analysis: observed (calculated): C 69.1% (69.05%), H 5.2% (5.07%), N 20.52% (20.13%), MS: [M+H]⁺ 279, ¹H NMR CDCl₃ (400 MHz) 5.40 (s, 2H), 6.97 (m, 1H), 7.04 (m, 1H), 7.28–7.31 (m, 3H), 7.35–7.37 (m, 2H), 7.41–7.43 (m, 2H), 8.01 (s, 1H), 8.12 (s, 1H), 8.63 (s, 1H, -H-C=N, azomethine).

2.4. Preparation of the Zn(II) Complex of “In Situ” Schiff Base 2-[(E)-{[4-(1*H*-1,2,4-Triazol-1-ylmethyl)phenyl]imino}methyl]phenol [TMPIMP]. 4-(1*H*-1,2,4-triazol-1-ylmethyl) aniline (0.5 g, 0.00287 mol) was dissolved in ethanol (10 mL) and salicylaldehyde (0.350 g, 0.00287 mol) was added. Reaction mass colour changed to yellow. It was heated to reflux and zinc chloride (0.391 g, 0.00287 mole) added and further heated at reflux for 3 hours. Yellow precipitate of the product was filtered and washed with ethanol. It was recrystallised in ethanol and dried in oven at 70–80°C till constant weight. wt: 0.950 g (Yield: 53.3%), Colour: Yellow, M.P. 218–219°C, [M]⁺ 619, IR (KBr): $\nu_{\text{O-H}}$ (lattice water) 3312 cm⁻¹ $\nu_{\text{C=N}}$ 1619 cm⁻¹, $\nu_{\text{C-O}}$ (phenolic) 1452 cm⁻¹, $\nu_{\text{Zn-N}}$ 522 cm⁻¹, $\nu_{\text{Zn-O}}$ 447 cm⁻¹, ¹H NMR (DMSO-d₆, 300 MHz) 5.48 (s, 2H), 6.96–7.0 (m, 3H), 7.42 (m, 5H), 8.04 (s, 1H), 8.8 (s, 1H), 9.03 (s, 1H, -H-C=N, azomethine).

2.5. Preparation of the Schiff Base (4S)-4-{(E)-(2-Hydroxybenzylidene)amino}benzyl]-1,3-oxazolidin-2-one [HBABO] (Scheme 4). (4S)-4-(4-Aminobenzyl)-1,3-oxazolidin-2-one was synthesised by reported method in literature [19] and was characterised by spectroscopic techniques.

(4S)-4-(4-Aminobenzyl)-1,3-oxazolidin-2-one (0.3 g, 0.00156 mole) was taken in 10 mL ethanol, salicylaldehyde (0.190 g, 0.00156 mole) was added, and solution was heated to reflux for about 2 hours. The light orange coloured product was filtered, washed with ethanol, and again recrystallised in ethanol. Product was dried in oven at 70–80°C till

SCHEME 3: Synthesis scheme of Schiff base TMPIMP and complex $[Zn(TMPIMP)_2] \cdot 2H_2O$.SCHEME 4: Synthesis scheme of Schiff base ligand HBABO and complex $[Zn(HBABO)_2] \cdot 2H_2O$.

constant weight. Weight 0.40 g. Colour: light orange, M.P. 188–190°C, IR (KBr): ν_{N-H} 3362 cm^{-1} $\nu_{C=O}$ (oxazolidone) 1752 cm^{-1} $\nu_{C=N}$ 1644 cm^{-1} ν_{C-O-C} 1074 cm^{-1} ν_{C-O} (phenolic) 1147 cm^{-1} , elemental analysis: observed (calculated): C 68.72% (68.91%), H 5.49% (5.44%), N 9.52% (9.45%), MS: $[M+H]^+$ 297.4.

2.6. Preparation of the Zn(II) Complex of “In Situ” Schiff Base (4*S*)-4-{4-[*E*-(2-Hydroxybenzylidene)amino]benzyl}-1,3-oxazolidin-2-one [HBABO]. (4*S*)-4-(4-Aminobenzyl)-1,3-oxazolidin-2-one (0.3 g, 0.00156 mole) was dissolved in 10 mL Ethanol, salicylaldehyde (0.190 g, 0.00156 mole) was added, solution was heated to for about 30 minutes, and zinc chloride (0.212 g, 0.00156 mol) was added and further heated for 3 hours. Yellow coloured product was filtered, washed with ethanol, and recrystallised in ethanol and dried in oven till constant weight. Weight 0.80 g (yield: 78.43%), colour: yellow, M.P. 240°C (decomp.), MS: $[M+1]$ 657.

IR (KBr): ν_{O-H} (lattice water) 3282 cm^{-1} $\nu_{C=O}$ (oxazolidone) 1750 cm^{-1} $\nu_{C=N}$ 1625 cm^{-1} , ν_{C-O} (phenolic) 1446 cm^{-1} , ν_{Zn-N} 530 cm^{-1} , ν_{Zn-O} 449 cm^{-1} , elemental analysis: observed (calculated): C 59.83% (59.01), H 4.81% (4.95%), N 8.15% (8.10%), 1H NMR (DMSO-d₆, 300 MHz) 2.47–2.81 (m, 2H), 3.97–4.06 (m, 2H), 4.23–4.28 (m, 1H), 6.92–6.98 (m, 2H), 7.33–7.38 (m, 4H), 7.61 (d, 2H, $J = 7.2\text{ Hz}$), 7.81 (s, 1H N-H oxazolidinone), 8.94 (bs, 1H azomethine).

^{13}C NMR (DMSO-d₆, 75 MHz) 163.04 (-C=N azomethine), 160.26 (oxazolidone -C=O), 158.60 (-C-O phenolic), 146.43, 135.48, 133.18, 132.53, 130.49, 121.36, 119.10, 116.55, 67.97, 52.42, 39.90.

3. Results and Discussion

All the metal complexes are stable at room temperature and are nonhygroscopic in nature. On heating, they decompose at high temperatures. The complexes are insoluble in water but are soluble in DMSO. The elemental analysis, physical properties, and analytical data of the ligand and complexes are summarized below.

3.1. 1H NMR Spectra. Due to the diamagnetic nature of Zn(II) metal complexes, it was possible to scan 1H NMR spectrum in DMSO-d₆. Diamagnetic zinc metal complexes do not interfere in magnetic field of NMR instrument; however, paramagnetic metal complexes interfere and it is not possible to lock NMR instrument for scanning samples.

It was observed that the azomethine proton in $[Zn(NMAPIMMTC)_2] \cdot 2H_2O$ complex appeared at 8.83 ppm after complexation with zinc metal. It was shifted significantly downfield due to deshielding effect exerted by zinc metal atom. Apart from the downfield shift of azomethine, following other interesting observations were also made. Aromatic protons of coumarin ring were observed at 6.56 ppm and 7.56 ppm as doublets due to the electron withdrawing mesomeric effect exerted by central zinc metal atom. Olefinic proton of coumarin ring was also shifted downfield to 5.98 ppm due to electron withdrawing mesomeric effect operating through the conjugation across the aromatic ring over the α,β -unsaturated double bond of coumarin ring.

The azomethine proton in $[Zn(TMPIMP)_2] \cdot 2H_2O$ complex was observed at 8.63 ppm and that of $[Zn(HBABO)_2] \cdot 2H_2O$ was observed at 8.94 ppm.

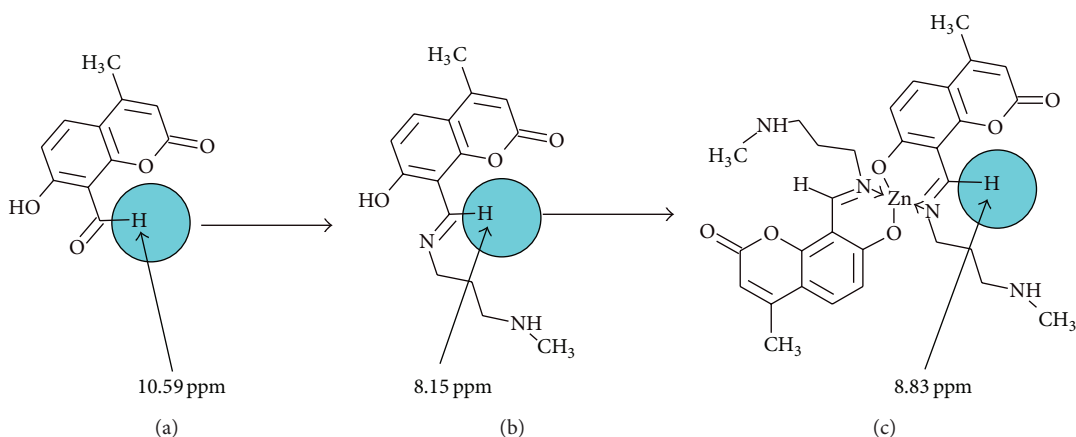


FIGURE 1: Azomethine proton shift values before and after complexation with Zn(II) metal atom.

Thus, the azomethine H-C=N protons which appeared at about 8.83 to 9.12 in free Schiff bases were shifted to downfield to 8.63 to 8.94 due to electron withdrawing effect of central metal atom (see Figure 1). The integration of all the proton indicated Zn : (L), stoichiometry of the complexes.

3.2. ^{13}C NMR Spectra. The azomethine carbon atom appeared most downfield as reported in literature values. In $[\text{Zn}(\text{NMAPIMMTC})_2] \cdot 2\text{H}_2\text{O}$ complex, it was observed at 162.73 ppm, in $[\text{Zn}(\text{HBABO})_2] \cdot 2\text{H}_2\text{O}$ complex, it was observed at 163.04 ppm, and, in $[\text{Zn}(\text{TMPIMP})_2] \cdot 2\text{H}_2\text{O}$ complex, it appeared at 163.70 ppm (Table 1).

Normally carbon attached to phenolic -OH group appears at about 155 ppm, but, in these complexes, it was observed at 155–160 ppm which may be due to electron deshielding effect of zinc metal atom.

In $[\text{Zn}(\text{NMAPIMMTC})_2] \cdot 2\text{H}_2\text{O}$, lactonyl carbon appeared at 173.63 ppm, and, in $[\text{Zn}(\text{HBABO})_2] \cdot 2\text{H}_2\text{O}$ complex, the oxazolidinone carbonyl carbon appeared at 160.26 ppm.

3.3. Mass Spectra. The formation of Schiff bases is confirmed by the presence of intense molecular ion peak in the mass spectra of Schiff base metal complexes such as $[\text{Zn}(\text{NMAPIMMTC})_2] \cdot 2\text{H}_2\text{O}$, $[\text{Zn}(\text{HBABO})_2] \cdot 2\text{H}_2\text{O}$, and $[\text{Zn}(\text{TMPIMP})_2] \cdot 2\text{H}_2\text{O}$. Other prominent peaks may be due to the elimination of CH_3NH , $-\text{CH}_2-\text{CH}_2-\text{CH}_2-$ units of propyl side chain in case of $[\text{Zn}(\text{NMAPIMMTC})_2] \cdot 2\text{H}_2\text{O}$. In other complexes, prominent peaks may be due to the fragmentation of heterocyclic rings in the molecules.

Some other peaks may be due to loss of tropylium ion and so forth from the parent ion and subsequent fragmentation. The mass spectra of the Zn(II) complexes showed molecular ion peaks corresponding to $[M(L)_2]$ stoichiometry. Peaks corresponding to L^+ and fragments of L^+ are also present in the spectra. Detection of $[M^+]$ and $[M+1]^+$ peaks in mass spectra indicated and confirmed $Zn : (L)_2$ stoichiometry of the complexes.

3.3.1. Infrared Spectra. The interpretation of IR spectra provides valuable information regarding the nature of functional

group attached to the metal atom and helped in confirmation of bond formation. In order to study the bonding mode of Schiff base ligand to the central metal atom, the IR spectra of the free ligands were compared with the spectra of the complexes. The main IR bands and their assignments are listed in Table 2.

The Schiff base HBABO has an oxazolidinone –N=C=O functional group and it has been observed as carbonyl stretching band at 1737 cm^{-1} in $[\text{Cu}(\text{HBABO})_2]\cdot 2\text{H}_2\text{O}$ complex and at 1750 cm^{-1} in $[\text{Zn}(\text{HBABO})_2]\cdot 2\text{H}_2\text{O}$ complex. All the above metal complexes have also shown absorption bands in the region $3400\text{--}3500\text{ cm}^{-1}$ due to coordinated water molecules Table 2.

- (i) The phenolic -OH band does not appear in metal complexes spectra. However new bands have appeared at 1621 cm^{-1} to 1639 cm^{-1} due to new -C=N, that is, azomethine double bond, which is characteristic of Schiff base and confirms the formation of Schiff bases and further complexation with central metal atom.
 - (ii) The IR spectra of all the metal complexes show prominent band at about 1240 – 1280 cm^{-1} due to $\nu_{\text{C}-\text{N}}$ stretching.
 - (iii) There are no prominent bands appearing in the 1600 – 1800 cm^{-1} region of the spectra indicating participation of the azomethine nitrogen and phenolic oxygen atom in coordination with the metal atom [20].
 - (iv) The broad signals in the region of 2500 cm^{-1} to 3500 cm^{-1} of the Schiff base ligands disappeared in the spectra of all the metal complexes indicating complexation with central metal cation. However, the spectra of the metal complexes in this region show a number of signals arising from $\nu_{\text{C}-\text{H}}$ and vibrations due to coordinated H_2O molecules.
 - (v) The low frequency region of the spectra indicated the presence of two new medium intensity bands at about 450 cm^{-1} to 470 cm^{-1} due to $\nu_{\text{M}-\text{O}}$ vibrations and at 530 cm^{-1} to 550 cm^{-1} due to $\nu_{\text{M}-\text{N}}$ vibrations [21].

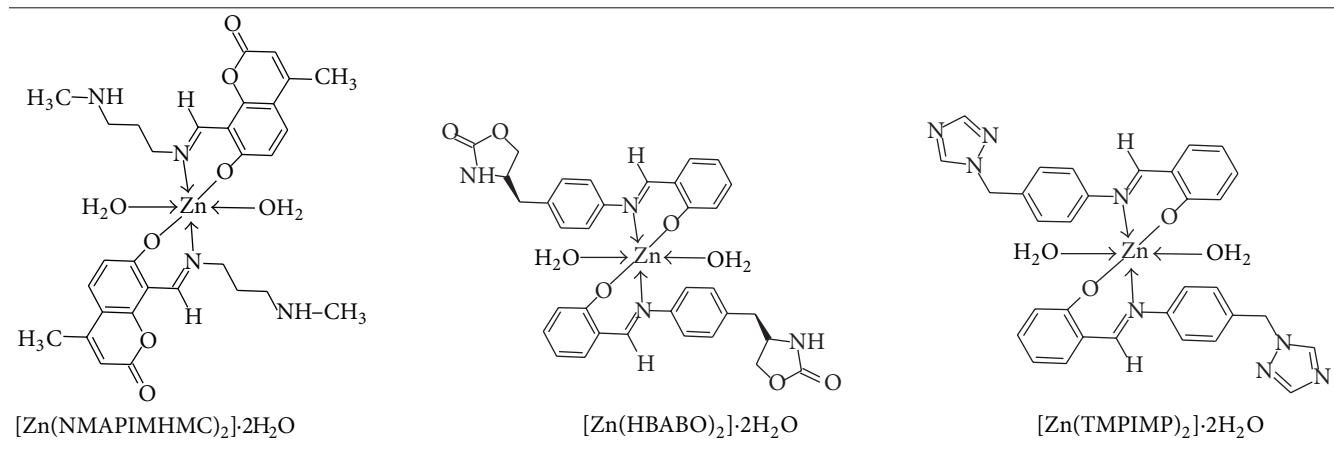
TABLE 1: ^{13}C NMR assignments of metal complexes.

	Atom number	Group	^{13}C ppm
	2, 2'	C	162.733
	3, 3'	CH	107.248
	4, 4'	C	106.985
	4a, 4a'	C	106.322
	5, 5'	CH	130.107
	6, 6'	CH	120.355
	7, 7'	C	154.867
	8, 8'	C	156.861
	8a, 8a'	C	160.229
	9, 9'	C	173.636
	10, 10'	CH ₂	58.48
	11, 11'	CH ₂	33.582
	12, 12'	CH ₂	47.342
	13, 13'	CH ₃	27.064
	14, 14'	CH ₃	18.892
	14, 14'	HC=N	163.04
	5, 5'	C=O	160.26
	20, 20'	C-O-Zn	158.60
	10, 10'	C	146.43
	7, 7'	C	135.48
	16, 16'	CH	133.18
	18, 18'	CH	132.53
	8, 8', 12, 12'	CH	130.49
	9, 9', 11, 11'	CH	121.36
	15, 15'	C	119.27
	19, 19'	CH	119.10
	17, 17'	CH	116.55
	2, 2'	CH ₂	67.97
	3, 3'	CH	52.42
	6, 6'	CH ₂	39.90
	14, 14'	HC=N	163.70
	20, 20'	C-O-Zn	160.23
	2, 2'	CH	151.44
	10, 10'	C	147.82
	5, 5'	CH	144.20
	7, 7'	C	134.69
	16, 16'	CH	133.37
	18, 18'	CH	132.52
	8, 8', 12, 12'	CH	129.12
	9, 9', 11, 11'	CH	121.60
	15, 15'	C	119.24
	17, 17'	CH	119.16
	19, 19'	CH	116.58
	6, 6'	CH ₂	51.77

TABLE 2: FT-IR bands for metal complexes and their assignments.

Complex	Lattice water $\nu_{(\text{OH})}$ cm ⁻¹	$\nu_{\text{C=O}}$ cm ⁻¹	$\nu_{\text{C=N}}$ cm ⁻¹	Phenolic $\nu_{\text{C-O}}$ cm ⁻¹	$\nu_{\text{M-N}}$ cm ⁻¹	$\nu_{\text{M-O}}$ cm ⁻¹
[Zn(NMAPIMHMC) ₂]·2H ₂ O	3122	1727 (lactone)	1631	1371	543	453
[Zn(HBABO) ₂]·2H ₂ O	3282	1750 (Oxazolidinone)	1625	1446	530	449
[Zn(TMPIMP) ₂]·2H ₂ O	3312	NA	1619	1452	522	447

TABLE 3: Proposed structure of [Zn(L)₂]·2H₂O complexes.



3.3.2. Thermogravimetric Analysis. Thermogravimetric analysis showed a loss of about 5.5% in weight corresponding to weight of two water molecules from the compound. This is water coordinated to central metal atom. Further heating resulted in continuous loss in weight with rise in temperature indicating decomposition of samples above 250°C.

It is clear from the data presented above that the experimental values of each compound are in good agreement with the theoretical values calculated for 1:2 ratio of metal:ligand stoichiometry. This is confirmed by M+ and [M+1] peaks in high resolution mass spectra.

From the discussion of the results of various spectroscopic details presented above, it may be concluded that the proposed geometry for the transition metal complexes with general formula ML₂·2H₂O is octahedral for Zn(II) complexes. The probable structures are shown in Table 3.

3.4. Biological Assay

3.4.1. Antibacterial Studies. Antimicrobial activity of the Schiff base ligand and its metal complexes was screened against two Gram negative bacteria: *E. coli* and *Pseudomonas fluorescens*, one Gram positive bacteria: *Staphylococcus aureus*, and against two fungi, that is, *C. albicans* and *A. niger* to assess their potential as antimicrobial agent by MIC method.

3.4.2. Microbiological Method [22]: MIC Procedure (for Bacteria and Fungus). The following ATCC strains were procured from Institute of Microbial Technology, Chandigarh, India: *E. coli*: ATCC no. 25922, *P. aeruginosa*: ATCC no. 25619, *S. aureus*: ATCC no. 12598, *Candida albicans*: ATCC no. 2091, *Aspergillus niger*: ATCC no. 9029.

Inoculum used was matched with 0.5 Mac Farland standard, that is, equal to 3×10^5 CFU/mL.

DMSO was used as solvent control. The solvent DMSO had no antimicrobial effect at the concentrations employed. DMSO used was commercially available. 10 mg of the test compound was dissolved in 1 mL of DMSO and this solution was used as stock solution for the test.

Nine dilutions of each drug were done with brain heart infusion (BHI) for MIC. In the initial tube, 20 μ L of above drug stock solution (10 mg/mL) was added into the 380 μ L of BHI broth. For dilutions, 200 μ L of BHI broth was added into the next 9 tubes separately. Then, from the initial tube, 200 μ L was transferred to the first tube containing 200 μ L of BHI broth. This was considered as 1×10^{-1} dilution. From 1×10^{-1} diluted tube, 200 μ L was transferred to second tube to make 1×10^{-2} dilution. The serial dilution was repeated up to 1×10^{-9} dilution for each drug. From the maintained stock cultures of required organisms, 5 μ L was taken and added into 2 mL of BHI (brain heart infusion) broth. In each serially diluted tube, 200 μ L of above culture suspension was added. The tubes were incubated for 24 hours at 37°C in the incubator and observed for turbidity. (Note: for facultative anaerobes, tubes were incubated at 37°C for 48–72 hrs in CO₂ Jar.)

Ciprofloxacin and Fluconazole were used as standards. Microbroth dilution method was used for the standard drugs.

Antifungal activity was carried out in a biosafety cabinet to avoid the contamination.

3.5. In Vitro Antimicrobial Activity. A comparative study of MIC values of Schiff base and its complexes indicated that metal complexes exhibit higher antimicrobial activity than the free Schiff base ligands and the same is indicated from the results given in Table 4.

TABLE 4: Showing comparative antibacterial and antifungal screening results by MIC method.

Test compounds	<i>E. coli</i>	<i>P. aeruginosa</i>	<i>S. aureus</i>	<i>C. albicans</i>	<i>A. niger</i>
NMAPIMHMC.oxalate	50	50	50	50	0.8
[Zn(NMAPIMHMC) ₂]·2H ₂ O	50	50	12.5	3.12	0.8
TMPIMP	100	50	12.5	50	1.6
[Zn(TMPIMP) ₂]·2H ₂ O	100	100	6.25	3.12	3.12
HBABO	100	100	6.25	12.5	6.25
[Zn(HBABO) ₂]·2H ₂ O	100	100	12.5	25	3.12
Standard Ciprofloxacin	2	<4	2	—	—
Standard Fluconazole	—	—	—	16	8

There was no promising antibacterial activity observed against Gram negative bacteria, that is, *E. coli* and *Pseudomonas*. It was in the range of MIC value of 50–100 µg/mL concentration compared to standard antibiotic Ciprofloxacin having MIC of 2 µg/mL. This may be due to effective barrier of an outer membrane of Gram negative bacteria, towards intake of external substances like test compounds under this study.

The sensitivity of the test organisms to the test compounds may also be associated with cell wall structure. The major role of action involves highly specific coordination of metal ion to thiol groups on proteins containing L-cysteine [7]. The reduced activity of the test compounds may be due to lack of such coordination of Zn(II) to form a specific complex with cell wall protein thiol groups.

However, in case of *S. aureus*, [Zn(NMAPIMHMC)₂]·2H₂O complex showed moderate activity up to MIC value of 12.5 µg/mL and [Zn(TMPIMP)₂]·2H₂O complex showed activity up to MIC value of 6.25 µg/mL. This could be due to coordination of Zn(II) atom to form a specific complex with cell wall protein thiol groups and ultimately interfering in cell wall synthesis of *S. aureus* during cell multiplication phase. The observed activity of the test compounds indicates the future potential for the development of metal coordination complexes to overcome the limitations due to currently available antibiotics to treat MSRA.

In case of antifungal activity against *C. albicans*, [Zn(NMAPIMHMC)₂]·2H₂O and [Zn(TMPIMP)₂]·2H₂O complexes showed most promising activity up to MIC value of 3.12 µg/mL, compared to standard Fluconazole having MIC value 16 µg/mL.

However, in case of antifungal activity against *A. niger*, [Zn(NMAPIMHMC)₂]·2H₂O showed the most promising activity up to MIC value of 0.8 µg/mL compared with standard Fluconazole having MIC value of 8 µg/mL. [Zn(TMPIMP)₂]·2H₂O and [Zn(HBABO)₂]·2H₂O complexes also showed better activity up to MIC value of 3.12 µg/mL.

In almost all the comparative studies done, metal complexes showed enhanced activity compared with Schiff base ligand. These observations are due to heterocyclic rings of coumarin moiety, triazole heterocyclic ring, and oxathiazolidinone heterocyclic ring incorporated in the molecular structure of the metal complexes. These structural scaffolds might interfere in the mechanism of cell multiplication as discussed above and hence stop further growth of fungus.

It is known that chelation tends to make the ligand act as more powerful and potent bacterial agent. This may be probably due to the greater lipophilic nature of the complexes. Such increased activity of the metal chelates can be explained on the basis of chelation theory [23]. As per Overton's concept of cell permeability, the lipid membrane that surrounds the cell favours the passage of only lipid soluble materials. Liposolubility of a molecule is an important factor which controls the antimicrobial activity. On chelation, the polarity of the metal ion is reduced to a greater extent due to overlap of the ligand orbital and partial sharing of positive charge of metal ion with donor groups of the Schiff base ligand [24, 25]. As a result, due to increased delocalization of the π electrons over the whole chelate ring, the lipophilicity of the complex is increased. This increased lipophilicity facilitates the penetration of the complexes into lipid membrane and then blocks the metal binding sites on enzymes of microorganisms [26]. These metal complexes also disturb the respiration process of the cell and thus block the synthesis of proteins. As synthesis of proteins is blocked, bacterial cell wall formation is not possible; hence, it results in cell death and ultimately restricts further growth of the organism [27].

According to yet another plausible mechanism, these complexes might be inhibiting DNA gyrase enzyme, which is responsible for DNA multiplication phases. Since DNA gyrase is inhibited by metal complexes, multiplication of bacterial cells is stopped, ultimately resulting in antibacterial activity [7, 28, 29].

4. Conclusion

Three novel Schiff bases 8-[*(Z*)-{[3-(N-methylamino)propyl]imino}methyl]-7-hydroxy-4-methyl-2*H*-chromen-2-one, 2-[*(E*)-{[4-(1*H*-1,2,4-triazol-1-ylmethyl)phenyl]imino}methyl]phenol, and (4*S*)-4-{4-[*(E*)-(2-hydroxybenzylidene)amino]benzyl}-1,3-oxazolidin-2-one have been synthesised and structurally characterised. Novel transition metal complexes derived from these Schiff bases have been synthesised and characterised by spectroscopic techniques.

The physical and spectral analytical data show that the metal ligand stoichiometry in all these complexes is 1:2. The spectral data show that the ligand is bidentate which coordinates through the azomethine nitrogen of Schiff base ligand and oxygen atom of salicylaldehyde fragment. Based

on analytical and spectral data, all these complexes are assigned to be in octahedral geometry.

Some of the Zn(II) metal complexes have shown significant antifungal activities compared to its Schiff base ligand and moderate antibacterial activity. Schiff base Zn(II) metal coordination complexes can be used not only as an approach to enhance their activity but also to overcome the drug resistance.

In conclusion, the “*in vitro*” data presented here has identified Zn(NMAPIMHMC)₂·2H₂O, [Zn(TMPLIC)₂]·2H₂O, and [Zn(HBABO)₂]·2H₂O as a metal containing complex of potential therapeutic benefit, particularly for the topical treatment as antifungal agent against *C. albicans* and *A. niger*.

Conflict of Interests

The authors declare that there is no conflict of interests regarding the publication of this paper.

Acknowledgment

The authors thank Dr. Kishore Bhat of Governmental Dental College, Belgaum, for facilitating antimicrobial assays and providing the procedure for the same. They also thank Dr. Ranjan Das and Ajay Patil of TIFR, Mumbai, Dr. Moneesha Fernandes of NCL, Pune, and Dr. Avinash Kumbhar of Department of Chemistry, University of Pune, for supporting with ¹H and ¹³C NMR spectra; without these supports, this work would not have been complete. They also thank the management of Patkar-Varde College, Goregaon (W), Mumbai, for constant encouragement throughout this work.

References

- [1] “Antibiotic Resistance Questions & Answers”, *Get Smart: Know When Antibiotics Work*, Center for Disease Control and Prevention, Atlanta, Ga, USA, 2013.
- [2] C. A. Lipinski, “Lead- and drug-like compounds: the rule-of-five revolution,” *Drug Discovery Today: Technologies*, vol. 1, no. 4, pp. 337–341, 2004.
- [3] M. J. Macielag, “Chemical properties of antibacterials and their uniqueness,” in *Antibiotic Discovery and Development*, T. J. Dougherty and M. J. Pucci, Eds., pp. 801–802, 2012.
- [4] D. F. Veber, S. R. Johnson, H.-Y. Cheng, B. R. Smith, K. W. Ward, and K. D. Kopple, “Molecular properties that influence the oral bioavailability of drug candidates,” *Journal of Medicinal Chemistry*, vol. 45, no. 12, pp. 2615–2623, 2002.
- [5] M. M. R. Arkin and J. A. Wells, “Small-molecule inhibitors of protein-protein interactions: progressing towards the dream,” *Nature Reviews Drug Discovery*, vol. 3, no. 4, pp. 301–317, 2004.
- [6] M. Rizzotto, “Metal complexes as antimicrobial agents,” 2013, <http://www.intechopen.com/download/pdf/39255>.
- [7] A. M. Elsome, J. M. T. Hamilton-Miller, W. Brumfitt, and W. C. Noble, “Antimicrobial activities *in vitro* and *in vivo* of transition element complexes containing gold(I) and osmium(VI),” *Journal of Antimicrobial Chemotherapy*, vol. 37, no. 5, pp. 911–918, 1996.
- [8] C. A. Ferguson, R. G. E. Murray, and P. Lancy Jr., “Effects of some platinum IV complexes on cell division of *Escherichia coli*,” *Canadian Journal of Microbiology*, vol. 25, no. 5, pp. 545–559, 1979.
- [9] R. B. Thurman and C. P. Gerba, “The molecular mechanisms of copper and silver ion disinfection of bacteria and viruses,” *Critical Reviews in Environmental Control*, vol. 18, no. 4, pp. 295–315, 1988.
- [10] B. Rosenberg, E. Renshaw, L. Vancamp, J. Hartwick, and J. Drobniak, “Platinum-induced filamentous growth in *Escherichia coli*,” *Journal of Bacteriology*, vol. 93, no. 2, pp. 716–721, 1967.
- [11] A. M. Elsome, W. Brumfitt, J. M. T. Hamilton-Miller, P. D. Savage, R. O. King, and S. Frickcr, “Antimicrobial activity and potential therapeutic use of new gold coordination complexes,” in *Program and Abstracts of the 31st Interscience Conference on Anti-Microbial Agents and Chemotherapy*, American Society for Microbiology, Chicago, Ill, USA, abstract 387, 1991.
- [12] V. Pawar, S. V. Chavan, R. S. Yamgar et al., “Synthesis and characterization of novel transition metal complexes of 4-methyl-7-hydroxy 8-formyl coumarin and their biological activities,” *Asian Journal of Research in Chemistry*, vol. 4, no. 8, pp. 1238–1242, 2011.
- [13] M. Mustapha, B. R. Thorat, S. Sawant, R. G. Atram, and R. Yamgar, “Synthesis of novel schiff bases and its transition metal complexes,” *Journal of Chemical and Pharmaceutical Research*, vol. 3, no. 4, pp. 5–9, 2011.
- [14] S. S. Sawant, V. Pawar, S. Janrao, S. R. Yamgar, and Y. Nivid, “Synthesis characterization of transition metal complexes of novel schiff base 8-[{(z)-{[3-(N-methylamino)propyl] imino}methyl]-7-hydroxy-4-methyl-2h-chromen-2-one] [NMAPIMHMC] and their biological activities,” *International Journal of Research in Pharmacy and Chemistry*, vol. 3, no. 3, pp. 636–644, 2013.
- [15] A. I. Vogel, A. R. Tatchell, B. S. Furnis, A. J. Hannaford, and P. W. G. Smith, *Vogel's Text Book of Practical Organic Chemistry*, ELBS, 5th edition, 1996.
- [16] A. Kulkarni, S. A. Patil, and P. S. Badami, “Synthesis, characterization, DNA cleavage and *in vitro* antimicrobial studies of La(III), Th(IV) and VO(IV) complexes with Schiff bases of coumarin derivatives,” *European Journal of Medicinal Chemistry*, vol. 44, no. 7, pp. 2904–2912, 2009.
- [17] G. B. Bagihalli, P. G. Avaji, P. S. Badami, and S. A. Patil, “Synthesis, spectral characterization, electrochemical and biological studies of Co(II), Ni(II) and Cu(II) complexes with thiocarbohydrazone,” *Journal of Coordination Chemistry*, vol. 61, no. 17, pp. 2793–2806, 2008.
- [18] R. Baker, V. G. Matassa, and L. J. Street, “Imidazole, triazole and tetrazole derivatives,” patent no. US5602162 of Merck Sharp & Dohme Ltd.
- [19] P. Rajnikant, “A process for the purification of (S)-4-((3-(dimethylamino)ethyl)-1H-indol-5yl)-methyl)-2-oxazolidinone,” European patent no. EPI227095B1 of AstraZeneca AB ,1996.
- [20] L. J. Bellamy, *The Infrared Spectra of Complex Molecules*, Chapman and Hall, London, UK, 1980.
- [21] K. Nakamoto, *Infrared Spectra and Raman Spectra of Inorganic and Coordination Compounds*, Wiley & Sons, New York, NY, USA, 1997.
- [22] R. Schwalbe, L. Steele-Moore, and A. C. Goodwin, *Antimicrobial Susceptibility Testing Protocols*, CRC Press, 2007.
- [23] B. G. Tweedy, “Possible mechanism for reduction of elemental sulfur by monilia fructicola,” *Phytopathology*, vol. 55, pp. 910–914, 1964.

- [24] A. K. Králová, K. Kissová, O. Švajlenová, and J. Vančo, "Biological activity of copper(II) N-salicylideneaminoacidato complexes. Reduction of chlorophyll content in freshwater alga Chlorella vulgaris and inhibition of photosynthetic electron transport in spinach chloroplasts," *Chemical Papers*, vol. 58, no. 5, pp. 357–361, 2004.
- [25] J. Parekh, P. Inamdar, R. Nair, S. Baluja, and S. Chanda, "Synthesis and antibacterial activity of some Schiff bases derived from 4-aminobenzoic acid," *Journal of the Serbian Chemical Society*, vol. 70, no. 10, pp. 1155–1161, 2005.
- [26] Y. Vaghisia, R. Nair, M. Soni, S. Baluja, and S. Chanda, "Synthesis, structural determination and antibacterial activity of compounds derived from vanillin and 4-aminoantipyrine," *Journal of the Serbian Chemical Society*, vol. 69, no. 12, pp. 991–998, 2004.
- [27] N. Raman, "Antibacterial study of the Mannich base, N-(1-morpholino-benzyl) semicarbazide and its transition metal(II) complexes," *Research Journal of Chemistry and Environment*, vol. 4, p. 9, 2005.
- [28] U. Galm, S. Heller, S. Shapiro, M. Page, S.-M. Li, and L. Heide, "Antimicrobial and DNA gyrase-inhibitory activities of novel clorobiocin derivatives produced by mutasynthesis," *Antimicrobial Agents and Chemotherapy*, vol. 48, no. 4, pp. 1307–1312, 2004.
- [29] E. J. Alvarez, V. H. Vartanian, and J. S. Brodbelt, "Metal complexation reactions of quinolone antibiotics in a quadrupole ion trap," *Analytical Chemistry*, vol. 69, no. 6, pp. 1147–1155, 1997.

Synthesis, Characterization, Antimicrobial, DNA Cleavage, and *In Vitro* Cytotoxic Studies of Some Metal Complexes of Schiff Base Ligand Derived from Thiazole and Quinoline Moiety

Nagesh Gunvanthrao Yernale and Mruthyunjayaswamy Bennikallu Hire Mathada

Department of Studies and Research in Chemistry, Gulbarga University, GULBARGA, Karnataka 585 106, India

Correspondence should be addressed to Mruthyunjayaswamy Bennikallu Hire Mathada; bhmmswamy53@rediffmail.com

Academic Editor: Claudio Pettinari

A novel Schiff base ligand *N*-(4-phenylthiazol-2-yl)-2-((2-thiaxo-1,2-dihydroquinolin-3-yl)methylene)hydrazinecarboxamide (**L**) obtained by the condensation of *N*-(4-phenylthiazol-2-yl)hydrazinecarboxamide with 2-thioxo-1,2-dihydroquinoline-3-carbaldehyde and its newly synthesized Cu(II), Co(II), Ni(II), and Zn(II) complexes have been characterized by elemental analysis and various spectral studies like FT-IR, ¹H NMR, ESI mass, UV-Visible, ESR, TGA/DTA, and powder X-ray diffraction studies. The Schiff base ligand (**L**) behaves as tridentate ONS donor and forms the complexes of type [ML(Cl)₂] with square pyramidal geometry. The Schiff base ligand (**L**) and its metal complexes have been screened *in vitro* for their antibacterial and antifungal activities by minimum inhibitory concentration (MIC) method. The DNA cleavage activity of ligand and its metal complexes were studied using plasmid DNA pBR322 as a target molecule by gel electrophoresis method. The brine shrimp bioassay was also carried out to study the *in vitro* cytotoxicity properties for the ligand and its metal complexes against *Artemia salina*. The results showed that the biological activities of the ligand were found to be increased on complexation.

1. Introduction

Schiff bases are important classes of ligands that coordinate with metal ions *via* azomethine nitrogen and have been studied extensively because of increasing recognition of their role in biological system [1]. The Schiff bases containing ONS donor atoms act as superior chelating agents for the transition and nontransition metal ions and showed remarkable biological activities [2, 3]. Coordination of these compounds with metal ions, such as copper and nickel, often enhance their activities [4]. Bonding between azomethine nitrogen and metal ion was found to be important for biological activity. Several azomethines were reported to possess important antibacterial [5], antifungal [6], anticancer [7], and diuretic activities [8].

Thiazoles are one of the most important classes of heterocycles that have attracted a great deal of interest owing to their wide range of biological properties such as antiprotozoal [9], antimicrobial [10], anti-inflammatory [11], CNS depressant [12], antitubercular [13], antitumor [14, 15], anthelmintic

[16, 17], antidiabetics [18], and herbicidal [19, 20] activities. Thus, thiazole nucleus has been much studied in the field of medicinal chemistry. Quinolines are a class of nitrogen heterocycles, present in large number of natural and synthetic compounds which exhibit strong biological activities such as antibacterial [21], antifungal [22], antiamoebic [23], antileishmanial [24], antimalarial [25], antitumor [26], immunosuppressive [27], analgesic, vasorelaxing [28], antiplasmodial [29], anticonvulsant, and antihypertensive [30] activities.

A lot of work has been done on the synthesis of compounds using substituted thiazole and quinoline moieties [31, 32]. Literature survey reveals that not much work has been carried out on Schiff base ligand derived from 2-thioxo-1,2-dihydroquinoline-3-carbaldehyde. In view of the above findings and in continuation of our research work on synthesis and characterization of new Schiff base ligands and their metal complexes, we hereby report the synthesis of a novel Schiff base ligand *N*-(4-phenylthiazol-2-yl)-2-((2-thiaxo-1,2-dihydroquinolin-3-yl)methylene) hydrazine carboxamide (**L**) and its Cu(II), Co(II), Ni(II), and Zn(II)

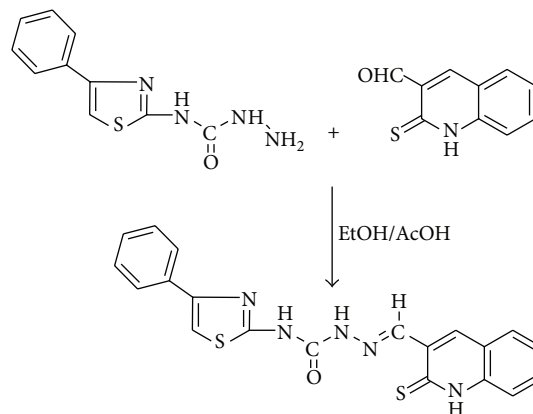
complexes, their characterization by various spectroscopic techniques, and their antimicrobial, DNA cleavage, and *in vitro* cytotoxicity property.

2. Materials and Methods

2.1. Reagents and Instruments. Elemental analysis (C, H, and N) was performed on a Vario EL III CHNS analyzer. IR spectra were recorded on a Perkin Elmer-Spectrum RX-I FTIR spectrophotometer using KBr disc technique in the 4000 to 250 cm⁻¹ region. ¹H NMR spectra were recorded on Bruker Avance II 400 MHz NMR Spectrometer in *d*₆-DMSO using TMS as an internal standard. ESI mass spectra were recorded by electrospray ionization (ESI) on a Waters Micromass Q-ToF Micro spectrometer. Electronic spectra of the Cu(II), Co(II), and Ni(II) complexes were recorded at 25°C on a Elico-SL 164 double beam spectrometer in quartz cells in the range 200–1000 nm using ca. 10⁻³ M solution in DMF. Molar conductance was measured on the ELICO (CM-185) conductivity bridge using ca. 10⁻³ M solution in dry DMF by dip-type conductivity cell fitted with a platinum electrode. Magnetic susceptibility measurements were measured on a Gouy balance using Hg [Co(NCS)₄] as the calibrant at room temperature. ESR measurement of Cu(II) complex in polycrystalline state was carried out on a JES-FA200 ESR spectrometer with X and Q band working at microwave frequency of 8.75–9.65 GHz. Thermal analysis of the complexes was carried out on a Perkin Elmer STA 6000 thermal analyzer in static air with a heating rate of 10°C/min. Powder X-ray diffraction spectrum of the complexes were recorded on Bruker AXS D8 Advance diffractometer at a wavelength 1.54 Å. All chemicals were used as received from commercial sources and solvents are purified according to the literature methods [33]. The melting points of newly synthesized compounds were determined in open glass capillary tubes and are uncorrected. Purity of the compounds was checked by TLC and the spots were observed in iodine vapor. The presence of metal and chloride contents was determined according to standard procedures [33].

Compounds, 2-thioxo-1,2-dihydroquinoline-3-carbaldehyde, and *N*-(4-phenylthiazol-2-yl)hydrazinecarboxamide were prepared according to the reported methods [31, 32].

2.2. Synthesis of Schiff Base Ligand (L). An equimolar mixture of *N*-(4-phenylthiazol-2-yl)hydrazinecarboxamide (0.234 g, 0.001 mol) and 2-thioxo-1,2-dihydroquinoline-3-carbaldehyde (0.189 g, 0.001 mol) in ethanol (25 mL) was refluxed with a catalytic amount of glacial acetic acid (1-2 drops) for about 7-8 h on a water bath. The reaction was monitored by TLC. The reaction mixture was cooled to room temperature; pale yellow colored solid separated was filtered, washed with hot ethanol, recrystallized from 1, 4-dioxane, and dried in a desiccator over anhydrous calcium chloride at room temperature (Scheme 1). Yield: 72%; m.p. 298°C. Anal. Calc. for C₂₀H₁₅N₅OS₂ (M.W. = 405): C, 59.25; H, 3.70; N, 17.28%. Found: C, 59.18; H, 3.73; N, 17.21%. IR data (ν cm⁻¹, KBr): ν (NH quinoline) 3393; ν (NH amide) 3259; ν (NH thiazole) 3119; ν (C=O) 1688; ν (C=N) 1620; ν (C=S) 1225. ¹H NMR (*d*₆-DMSO; δ ppm): 13.95 (s, 1H, Quinoline NH); 10.78 (s, 1H,



SCHEME 1: Synthesis of Schiff base ligand (L).

CONH); 8.91 (s, 1H, CONH); 8.35 (s, 1H, CH=N); 7.38–8.25 (m, 11H, ArH).

2.3. Preparation of Cu(II), Co(II), Ni(II) and Zn(II) Complexes. Hot ethanolic solution (15 mL) of the respective metal chlorides (0.001 mol) and the Schiff base ligand (0.001 mol) in ethanol (30 mL) were refluxed for about 4-5 h on a water bath and the pH of the reaction mixture was adjusted ca. 7.0–7.5 by adding alcoholic solution of sodium acetate (0.5 g). The reaction mixture was cooled to room temperature and poured in to distilled water. Metal chelates separated were collected by filtration, washed with sufficient quantity of distilled water then with hot ethanol, and finally dried in a desiccator over anhydrous calcium chloride at room temperature.

2.3.1. [Cu(C₂₀H₁₅N₅OS₂)(Cl₂)]: Green Solid. Yield: 73%; m.p. >320°C; Anal. Calc. for [Cu(C₂₀H₁₅N₅OS₂)(Cl₂)] (M.W. = 539.44): C, 44.49; H, 2.78; N, 12.97; Cl, 13.14; Cu, 11.77%; Found: C, 44.41; H, 2.80; N, 12.93; Cl, 13.17; Cu, 11.79%. IR data (ν cm⁻¹, KBr): ν (NH quinoline) 3366; ν (NH amide) 3200; ν (NH thiazole) 3089; ν (C=O) 1656; ν (C=N) 1585; ν (C=S) 1188; ν (M–O), 514; ν (M–N), 454; ν (M–S), 372; ν (M–Cl), 327.

2.3.2. [Co(C₂₀H₁₅N₅OS₂)(Cl₂)]: Brown Solid. Yield: 71%; m.p. >324°C; Anal. Calc. for [Co(C₂₀H₁₅N₅OS₂)(Cl₂)] (M.W. = 534.83): C, 44.87; H, 2.80; N, 13.08; Cl, 13.25; Co, 11.01%. Found: C, 44.95; H, 2.82; N, 13.15; Cl, 13.21; Co, 11.09%. IR data (ν cm⁻¹, KBr): ν (NH quinoline) 3295; ν (NH amide) 3192; ν (NH thiazole) 3175; ν (C=O) 1633; ν (C=N) 1553; ν (C=S) 1215; ν (M–O), 536; ν (M–N), 448; ν (M–S), 356; ν (M–Cl), 316.

2.3.3. [Ni(C₂₀H₁₅N₅OS₂)(Cl₂)]: Brown Solid. Yield: 69%; m.p. >320°C; Anal. Calc. for [Ni(C₂₀H₁₅N₅OS₂)(Cl₂)] (M.W. = 534.59): C, 44.89; H, 2.80; N, 13.09; Cl, 13.26; Ni, 10.97%. Found: C, 44.85; H, 2.75; N, 13.12; Cl, 13.30; Ni, 10.92%. IR data (ν cm⁻¹, KBr): ν (NH quinoline) 3356; ν (NH amide) 3212; ν (NH thiazole) 3090; ν (C=O) 1656; ν (C=N) 1570; ν (C=S) 1216; ν (M–O), 522; ν (M–N), 476; ν (M–S), 337; ν (M–Cl), 320.

2.3.4. $[Zn(C_{20}H_{15}N_5OS_2)(Cl_2)]$: Orange Yellow Solid. Yield: 70%; m.p. $>310^\circ\text{C}$; Anal. Calc. for $[Zn(C_{20}H_{15}N_5OS_2)(Cl_2)]$ (M.W. = 541.30): C, 44.33; H, 2.77; N, 12.93; Cl, 13.09; Zn, 12.08%. Found: C, 44.39; H, 2.72; N, 12.92; Cl, 13.15; Zn, 12.03%. IR data ($\nu \text{ cm}^{-1}$, KBr): $\nu(\text{NH quinoline})$ 3296; $\nu(\text{NH amide})$ 3189; $\nu(\text{NH thiazole})$ 3103; $\nu(\text{C=O})$ 1654; $\nu(\text{C=N})$ 1593; $\nu(\text{C=S})$ 1216; $\nu(\text{M-O})$, 540; $\nu(\text{M-N})$, 485; $\nu(\text{M-S})$, 359; $\nu(\text{M-Cl})$, 312. ^1H NMR (d_6 -DMSO; δ ppm): 11.85 (s, 1H, Quinoline NH); 9.25 (s, 1H, CONH); 8.37 (s, 1H, CONH); 8.19 (s, 1H, CH=N); 7.08–8.09 (m, 11H, ArH).

2.4. Biological Evaluation

2.4.1. *In Vitro Antimicrobial Assay.* The *in vitro* antimicrobial activity of the synthesized Schiff base ligand (**L**) and its Cu(II), Co(II), Ni(II), and Zn(II) complexes were assayed against two gram negative bacterial strains *Enterobacter aerogenes* (MTCC 111) and *Pseudomonas aeruginosa* (MTCC 424) and two fungal strains *Aspergillus niger* (MTCC 282) and *Aspergillus flavus* (MTCC 277). The above organisms were obtained from the Department of Microbiology and Biotechnology, Gulbarga University, Gulbarga, Karnataka, India, which are previously procured from Institute of Microbial Technology Chandigarh, India. The stock solutions were prepared by dissolving 10 mg of each test compound in 10 mL of freshly distilled DMSO. The various concentrations of the test compounds (100, 50 and 25 $\mu\text{g mL}^{-1}$) were prepared by diluting the stock solution with the required volume of freshly distilled DMSO. The diameter of the zone of inhibition generated by each of the test compounds against bacterial and fungal growth was measured using antibiogram zone measuring scale.

(1) *Agar Well Diffusion Assay.* *In vitro* antibacterial and antifungal activities of synthesized Schiff base ligand (**L**) and its Cu(II), Co(II), Ni(II), and Zn(II) complexes were determined by standard agar well diffusion assay. Mueller-Hinton agar media were used for antibacterial studies. The pure dehydrated Mueller-Hilton agar (38 g) dissolved in 1000 mL of distilled water. The pure cultures of the bacterial strains *Enterobacter aerogenes* and *Pseudomonas aeruginosa* were subcultured by inoculating in the nutrient broth and were incubated at 37°C for about 18 h. The agar plates were prepared by using the above media and wells were dug with the help of 6 mm sterile metallic cork borer. Each plate was inoculated with 18 h old bacterial culture (100 μL) using a micropipette and spread uniformly using bent glass rod on each plate. Different concentrations of the test compounds (100, 50, and 25 $\mu\text{g mL}^{-1}$) were incorporated into the wells using micropipette and the plates were kept for incubation at 37°C for 24 h. After the completion of incubation period, the diameters of the inhibition zones generated by each test compound against bacterial growth were measured using antibiogram zone measuring scale. The experiment done in triplicate and the average values were calculated for antibacterial activity.

Potato dextrose agar (PDA) media were used for the antifungal studies. The following ingredients were used to prepare the medium. Potatoes (sliced, washed, unpeeled 200 g), dextrose (20 g), agar (20 g) in 1000 mL distilled water.

The pure cultures *Aspergillus niger* and *Aspergillus flavus* were inoculated on PDA slants. These slants were incubated at 32°C for 7 days. To these 7-day-old slants of fungal strains, 10 mL of 0.1% tween-80 solution was added and the culture was scraped with sterile inoculating loop to get uniform spore suspension. The agar plates were prepared by using the above potato dextrose agar media and wells were dug with the help of 6 mm sterile metallic cork borer. Each plate was inoculated with 7-day-old spore suspension of each fungal culture (100 μL) using a micropipette and spread uniformly using bent glass rod on each plates. Each well was incorporated with the test compound solution of different concentrations (100, 50, and 25 $\mu\text{g mL}^{-1}$). All the inoculated plates were incubated at 32°C for about 48 h. After the completion of incubation period, the diameters of the inhibition zones generated by each test compound against fungal growth were measured using antibiogram zone measuring scale. The experiment done in triplicate and the average values were calculated for antifungal activity.

(2) *Minimum Inhibitory Concentration (MIC).* Minimum inhibitory concentration (MIC) was defined as the lowest concentration where no visible turbidity was observed in the test tubes [34, 35]. Minimum inhibitory concentration of the compounds was determined in nutrient agar plate by microdilution method according to the National Committee for Clinical Laboratory Standards [36]. Standardized suspension of test organisms (0.1 mL, 10^6 cfu/mL) and synthesized Schiff base ligand (**L**) and its Cu(II), Co(II), Ni(II), and Zn(II) complexes in different concentrations (100, 50, 25, 12.50, 6.25, 3.125, 1.563, 0.78, 0.39, and 0.195 $\mu\text{g/mL}$) were taken in test tubes and test tubes with Gentamycin and Fluconazole as positive control for bacterial and fungal strains, respectively. DMSO is used as a negative control for antibacterial and antifungal, respectively. The bacterial tubes were incubated at 37°C for 18 h and fungal tubes were incubated at 32°C for 48 h. The lowest concentration that produced no visible bacterial growth compared with the control tubes was regarded as MIC.

2.4.2. *DNA Cleavage Activity.* In order to study whether newly synthesized Schiff base ligand and its metal complexes could behave as DNA cleaving agents or not, they were examined using plasmid pBR322 DNA (Bangal re Genei, Bengaluru, Cat. No 105850) as a target molecule according to the literature method [37].

The cleavage activity of the test compounds was analyzed by agarose gel electrophoresis method. The 600 mg of agarose was dissolved in 60 mL of TAE buffer (4.84 g Tris base, pH 8.0, 0.5 M EDTA) by boiling. When the gel attains approximately 55°C , it was poured into the gel cassette fitted with comb. The gel was allowed to solidify and then carefully the comb was removed. The gel was placed in the electrophoresis chamber flooded with TAE buffer. Test compounds were prepared in DMSO (1 mg mL^{-1}). The test compounds were added separately to the isolated plasmid pBR322 DNA (225 ng) and incubated for 2 h at 37°C . After the incubation period, the 20 μL of DNA sample (mixed with bromophenol blue dye at a 1:1 ratio) was loaded carefully into the electrophoresis chamber wells along with standard DNA marker and

a constant electricity of 50 V passed for about 30 min. The gel was removed carefully and stained with Ethidium bromide (EtBr) solution (10 µg/mL) for 10–15 min. The bands were observed under UV transilluminator (UVP, Germany) and photographed to determine the extent of DNA cleavage, and the results were compared with those of a standard DNA marker.

2.4.3. In Vitro Cytotoxicity. The brine shrimp lethality bioassay has been chosen to evaluate the *in vitro* cytotoxic effect of the newly synthesized Schiff base ligand (**L**) and its Cu(II), Co(II), Ni(II), and Zn(II) complexes by using the protocol of Meyer et al. [38]. This is an efficient, rapid, inexpensive test and has a good correlation with cytotoxic activity.

Brine shrimp (*Artemia salina*) eggs were hatched in a shallow rectangular plastic dish (22 × 32 cm) filled with artificial seawater, which was prepared with a commercial salt mixture and double distilled water. An unequal partition was made in the plastic dish with the help of a perforated device. Approximately 50 mg of eggs were sprinkled into the large compartment, which was darkened while the minor compartment was open to ordinary light. After two days nauplii were collected by a pipette from the lighted side. A sample of the test compound was prepared by dissolving 20 mg of each compound in 2 mL of DMSO. From this stock solution 100, 50, and 25 µg mL⁻¹ were transferred to nine vials (three for each dilution were used for each test sample and LD₅₀ is the mean of three values) and one vial was kept as control having 2 mL of DMSO only. The solvent was allowed to evaporate overnight. After two days, when shrimp larvae were ready, 1 mL of seawater and 10 shrimps were added to each vial (30 shrimps/dilution) and the volume was adjusted with seawater to 10 mL per vial. After 24 h the number of survivors was counted. Data were analysed by a Finney computer program to determine the LD₅₀ values [39].

3. Results and Discussion

The reaction of Schiff base ligand (**L**) with Cu(II), Co(II), Ni(II), and Zn(II) ions in 1:1 ratio resulted in the complex of the type [ML(Cl)₂]. The physical and analytical data agree well with the proposed composition of Schiff base ligand and its Cu(II), Co(II), Ni(II), and Zn(II) complexes. The newly synthesized complexes are colored solids, stable in air, and insoluble in water and common organic solvents but completely soluble in DMF and DMSO. The molar conductance data of the complexes was measured in DMF at ca. 10⁻³ M and all the complexes showed conductance in the range of 50–61 Ohm⁻¹ cm² mol⁻¹ at room temperature indicating non-electrolytic nature of the complexes suggesting that the Cl⁻ anion is coordinated to metal ion. This was further supported by the proposed general formula of the complexes based upon the results of elemental analysis (Table 1) and spectral data.

3.1. IR Spectra. IR spectrum of the ligand showed a high intensity band at 1688 cm⁻¹ due to ν(C=O) and three absorption bands at 3393, 3259, and 3119 cm⁻¹ due to quinoline NH, amide NH, and NH attached to thiazole moiety, respectively.

A high intensity band observed at 1620 cm⁻¹ is attributed to the azomethine ν(C=N) vibration and a band at 1225 cm⁻¹ to ν(C=S) functioning at 2-position of quinoline moiety.

In order to study the binding mode of the Schiff base to the metal ion in complexes, the IR spectrum of the free ligand was compared with the spectra of the complexes. In the IR spectra of the complexes, medium intensity weak bands at 3366–3295, 3212–3189, and 3175–3089 cm⁻¹ were due to quinoline NH, amide NH, and NH attached to thiazole moiety, respectively, which appeared at about the same region as in the case of ligand indicating their noninvolvement in coordination. The shift of amide carbonyl ν(C=O) to lower frequency side about 55–32 cm⁻¹ which appeared in the region 1656–1633 cm⁻¹ in all the complexes confirms the coordination of oxygen atom of amide C=O with the metal ions as such without undergoing enolization [40]. The IR spectrum of all the complexes showed a shift of the azomethine ν(C=N) band towards lower frequency side about 67–27 cm⁻¹ and appeared in the region 1593–1553 cm⁻¹ when compared with the free ligand indicating the coordination of the azomethine nitrogen to the metal ions [41]. The shift of band due to ν(C=S) in all the complexes towards lower frequency side by 37–9 cm⁻¹ when compared to the ligand, which appeared in the region 1215–1188 cm⁻¹, proves the coordination of the sulfur atom of quinoline 2-thione to metal ions. The formation of complex was further confirmed by the appearance of new bands in the regions 540–514, 485–448, 372–337, and 327–312 cm⁻¹ in all the complexes due to skeletal metal-oxygen, metal-nitrogen, metal-sulfur, and metal-chloride vibrations, respectively. The important IR spectral data of the Schiff base ligand and its metal complexes are represented in Table 2.

3.2. ¹H NMR Spectra. The ¹H NMR spectrum of ligand displayed four distinct singlets at δ 13.95 (s, 1H, quinoline NH), δ 10.78 (s, 1H, CONH), δ 8.91 (s, 1H, CONH), and δ 8.35 (s, 1H, CH=N) and eleven aromatic protons as multiplets in the region δ 7.38–8.25 (m, 11H, ArH).

The ¹H NMR of Zn(II) complex displayed four distinct singlets at δ 11.85 (s, 1H, quinoline NH), δ 9.25 (s, 1H, CONH), 8.37 (s, 1H, CONH), and 8.19 (s, 1H, CH=N) and eleven aromatic protons as multiplets in the region 7.08–8.09 (m, 11H, ArH). The ¹H NMR spectral data of Schiff base ligand and its Zn(II) complex confirm the formation of Zn(II) complex with the ligand.

3.3. ESI Mass Spectral Data. The ESI mass spectra of the Schiff base ligand (**L**) and its Co(II) and Ni(II) complexes are performed to determine their molecular weight and study their fragmentation pattern. The mass spectrum of ligand showed a peak recorded at *m/z* 406 (3.93%) due to M⁺ + 1 (Figure 1). This on loss of hydrogen radical gave a peak at *m/z* 405 (2.36%) which is equivalent to its molecular weight (M.W. = 405). Further, this molecular ion underwent fragmentation by two routes. First, on loss of SH radical, it gave a fragment ion peak recorded at *m/z* 372 (2.36%), followed by expulsion of C₁₀H₆N₂ molecule which gave a fragment ion peak

TABLE I: Physical, Analytical and Molar conductance data of Schiff base ligand (L) and its metal complexes.

Compound	M.W. ^a	M.P. (°C) ^b	M	Elemental Analysis, found (Calc.) [%]			λ_m (cm ² Ω ⁻¹ mol ⁻¹)	μ_{eff} (BM)	Color
				C	H	N	Cl		
$C_{20}H_{15}N_5OS_2$	405	298	—	59.18 (59.25)	3.73 (3.70)	17.21 (17.28)	—	—	Yellow
$[Cu(C_{20}H_{15}N_5OS_2)(Cl_2)]$	539.44	>320	11.79 (11.77)	44.41 (44.49)	2.80 (2.78)	12.93 (12.97)	13.17 (13.14)	50	—
$[Co(C_{20}H_{15}N_5OS_2)(Cl_2)]$	534.83	>324	11.09 (11.01)	44.95 (44.87)	2.82 (2.80)	13.15 (13.08)	13.21 (13.25)	61	Green
$[Ni(C_{20}H_{15}N_5OS_2)(Cl_2)]$	534.59	>320	10.92 (10.97)	44.85 (44.89)	2.75 (2.80)	13.12 (13.09)	13.30 (13.26)	56	Brown
$[Zn(C_{20}H_{15}N_5OS_2)(Cl_2)]$	541.30	>310	12.03 (12.08)	44.39 (44.33)	2.72 (2.77)	12.92 (12.93)	13.15 (13.09)	55	Brown

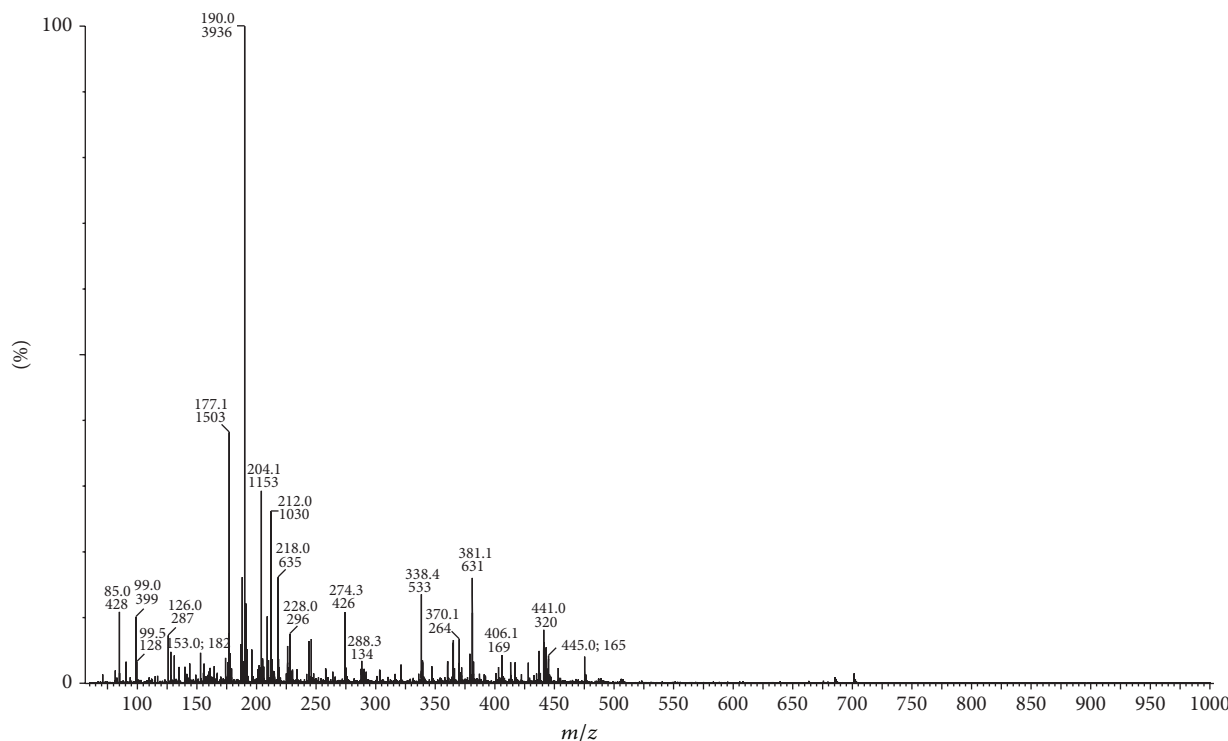
^aMolecular weight of the compounds.

^bMelting point of the compounds at their decomposition.

^cDiamagnetic.

TABLE 2: IR spectral data of Schiff base ligand (**L**) and its metal complexes.

Compounds	Quinoline $\nu_{(\text{NH})}$ cm $^{-1}$	Amide $\nu_{(\text{NH})}$ cm $^{-1}$	Thiazole $\nu_{(\text{NH})}$ cm $^{-1}$	$\nu_{(\text{C=O})}$ cm $^{-1}$	$\nu_{(\text{C=N})}$ cm $^{-1}$	$\nu_{(\text{C=S})}$ cm $^{-1}$	$\nu_{(\text{M-O})}$ cm $^{-1}$	$\nu_{(\text{M-N})}$ cm $^{-1}$	$\nu_{(\text{M-S})}$ cm $^{-1}$	$\nu_{(\text{M-Cl})}$ cm $^{-1}$
C ₂₀ H ₁₅ N ₅ OS ₂	3393	3259	3119	1688	1620	1225	—	—	—	—
[Cu(C ₂₀ H ₁₅ N ₅ OS ₂)(Cl ₂)]	3366	3200	3089	1656	1585	1188	514	454	372	327
[Co(C ₂₀ H ₁₅ N ₅ OS ₂)(Cl ₂)]	3295	3192	3175	1633	1553	1215	536	448	356	316
[Ni(C ₂₀ H ₁₅ N ₅ OS ₂)(Cl ₂)]	3356	3212	3090	1656	1570	1216	522	476	337	320
[Zn(C ₂₀ H ₁₅ N ₅ OS ₂)(Cl ₂)]	3296	3189	3103	1654	1593	1216	540	485	359	312

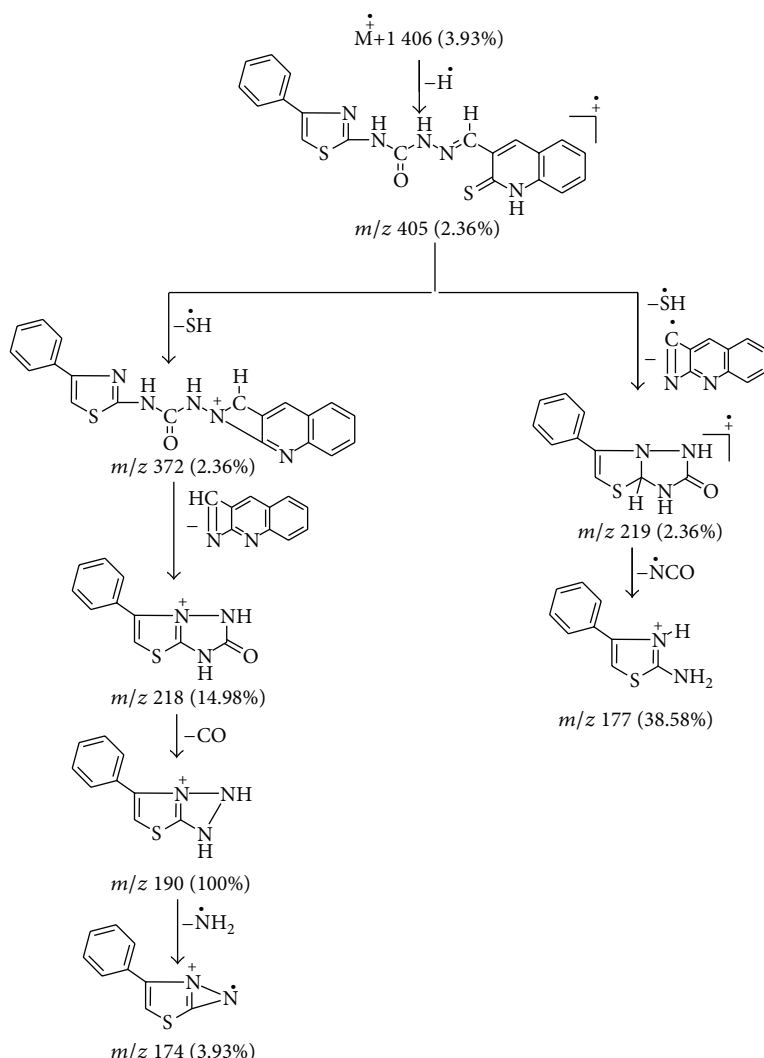
FIGURE 1: ESI mass spectrum of Schiff base ligand (**L**).

recorded at m/z 218 (14.98%). This fragment ion on further expulsion of CO molecule gave a fragment ion peak at m/z 190 (100%) which is also a base peak. This base peak on loss of NH₂ radical gives a fragment ion peak recorded at m/z 174 (3.93%). The molecular ion underwent fragmentation in another route wherein it losses SH radical and C₁₀H₅N₂ radical simultaneously giving a fragment ion peak recorded at m/z 219 (2.36%). This fragment ion on further loss of NCO radical gave a fragment ion peak recorded at m/z 177 (38.58%). This schematic mass spectral fragmentation pattern of ligand is in consistency with its structure which is depicted in Scheme 2.

The ESI mass spectrum of Co(II) complex exhibited a peak due to M⁺ + 1 at m/z 534 (5.51%). This on loss of hydrogen radical gave a peak at m/z 533 (2.30%), which is equivalent to its molecular weight (M.W. = 533). This molecular ion underwent fragmentation by two routes. First, on simultaneous loss of chlorine molecule, N=C=S radical, C₉H₅ radical, and C₈H₅N species gave a fragment ion peak recorded at m/z

177 (100%) which is also a base peak. In another route, the molecular ion peak on loss of N=C=S radical gave a fragment ion peak recorded at m/z 475 (35.43%). The schematic mass spectral fragmentation pattern of Co(II) complex of ligand is in consistency with its structure which is depicted in Scheme 3.

Similarly, the mass spectra of Ni(II) complex exhibited a peak at m/z 534 (4.72%) due to M⁺ + 1 (Figure 2). This is on loss of hydrogen radical gave the fragment ion peak recorded at m/z 533 (2.23%), which is equivalent to its molecular weight (M.W. = 533). Further this molecular ion underwent fragmentation by the loss of hydrogen radical and chlorine molecule simultaneously giving a fragment ion peak recorded at m/z 462 (29.92%). This on further loss of C₇H₅N molecule gave a fragment ion peak recorded at m/z 359 (3.14%), which underwent fragmentation by two routes. First, on loss of H-C≡C radical and two hydrogen radicals it simultaneously gave a fragment ion peak recorded at m/z 332 (21.25%), which on further expulsion of C=S molecule gave a fragment ion peak



SCHEME 2: Mass fragmentation pattern of Schiff base ligand (L).

recorded at m/z 288 (6.29%). In another route, fragment ion peak recorded at m/z 359 (3.14%) on simultaneous loss of C_9H_4NS radical and $C\equiv C-H$ radical gave a fragment ion peak recorded at m/z 177 (100%) which is also a base peak. The schematic mass spectral fragmentation pattern of Ni(II) is in consistency with its structure which is depicted in Scheme 4.

3.4. Electronic Spectra and Magnetic Susceptibility. The electronic spectra of the Cu(II), Co(II), and Ni(II) complexes were recorded in DMF solution at ca. 10^{-3} M at room temperature. The band positions of absorption band maxima assignments are listed in Table 3. The electronic spectra of green colored Cu(II) complex showed three absorption bands around 9993 cm^{-1} , 14595 cm^{-1} , and 18045 cm^{-1} which are assigned to $^2B_1 \rightarrow ^2A_1(\nu_1)$, $^2B_1 \rightarrow ^2B_2(\nu_2)$, and $^2B_1 \rightarrow ^2E(\nu_3)$ transitions, respectively. The observed transitions for Cu(II) complex are well within the ranges of $9000\text{--}10000\text{ cm}^{-1}(\nu_1)$, $11500\text{--}16000\text{ cm}^{-1}(\nu_2)$, and $15000\text{--}19000\text{ cm}^{-1}(\nu_3)$ for Cu(II) complexes of square pyramidal geometry [42, 43]. The electronic spectra of brown colored Co(II) complex displayed

three absorption bands at 11098 cm^{-1} , 17675 cm^{-1} , and 20180 cm^{-1} which are assigned to $^4A_2 + ^4E \rightarrow ^4B_1(\nu_1)$, $^4A_2 + ^4E \rightarrow ^4E(P)(\nu_2)$, and $^4A_2 + ^4E \rightarrow ^4A_2(P)(\nu_3)$ transitions, respectively, suggesting the square pyramidal geometry of the Co(II) complex [44]. The brown colored Ni(II) complex under present investigation displayed three absorption band at 10000 cm^{-1} , 13543 cm^{-1} , and 22307 cm^{-1} which are assigned to transitions $^3B_1 \rightarrow ^3E^a(\nu_1)$, $^2B_1 \rightarrow ^3A_2(\nu_2)$, and $^3B_1 \rightarrow ^3E^b(\nu_3)$, respectively, indicating the square pyramidal geometry of the Ni(II) complex [45].

The magnetic moment value for Cu(II) complex was found to be 1.73 BM which is in the range of 1.71–1.76 BM, agreeing well with the spin value of $S = 1/2$, as usually observed for Cu(II) complex, which supports its square pyramidal geometry [46]. The magnetic moment value for Co(II) complex was found to be 4.31 BM which is in the range 4.3–4.6 BM, for five coordinate square pyramidal geometries of Co(II) complex [47]. The magnetic moment of Ni(II) complex was found to be 2.78 BM, which is well within the range

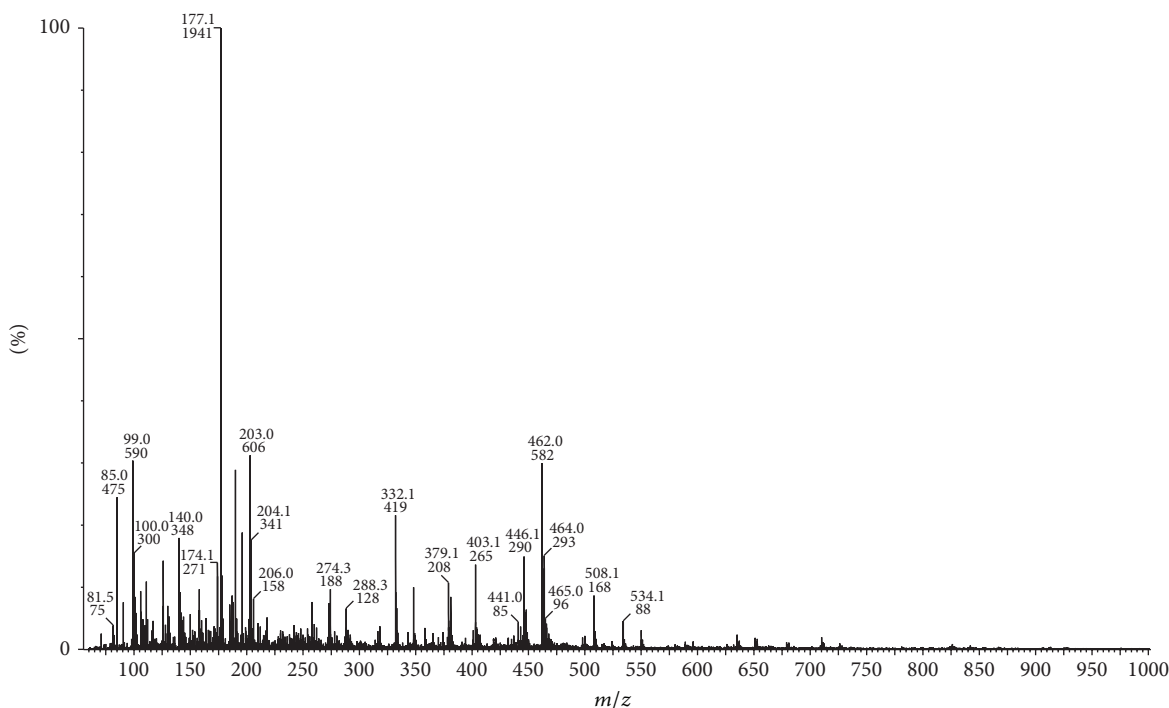
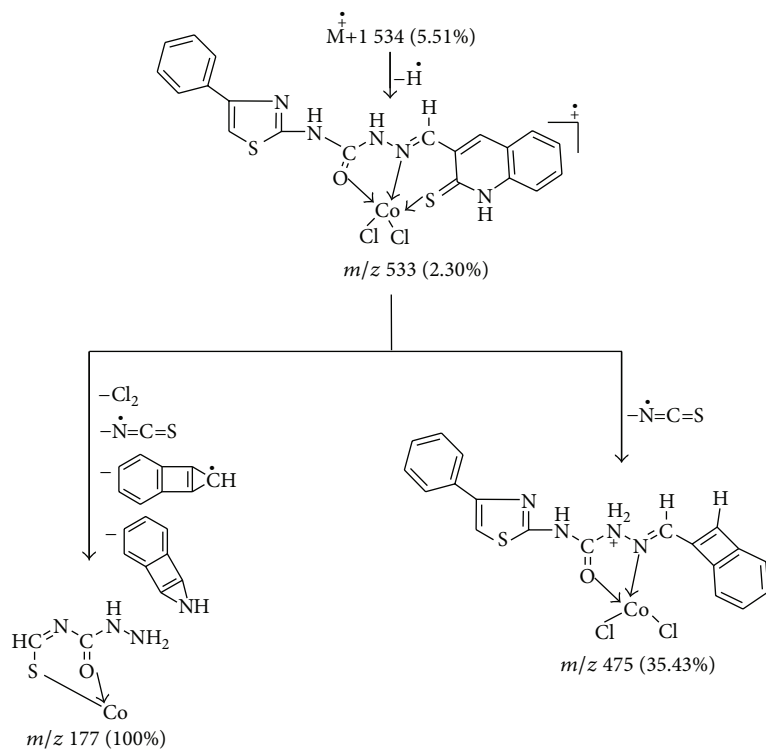


FIGURE 2: ESI mass spectrum of Ni(II) complex.



SCHEME 3: Mass fragmentation pattern of Co(II) complex.

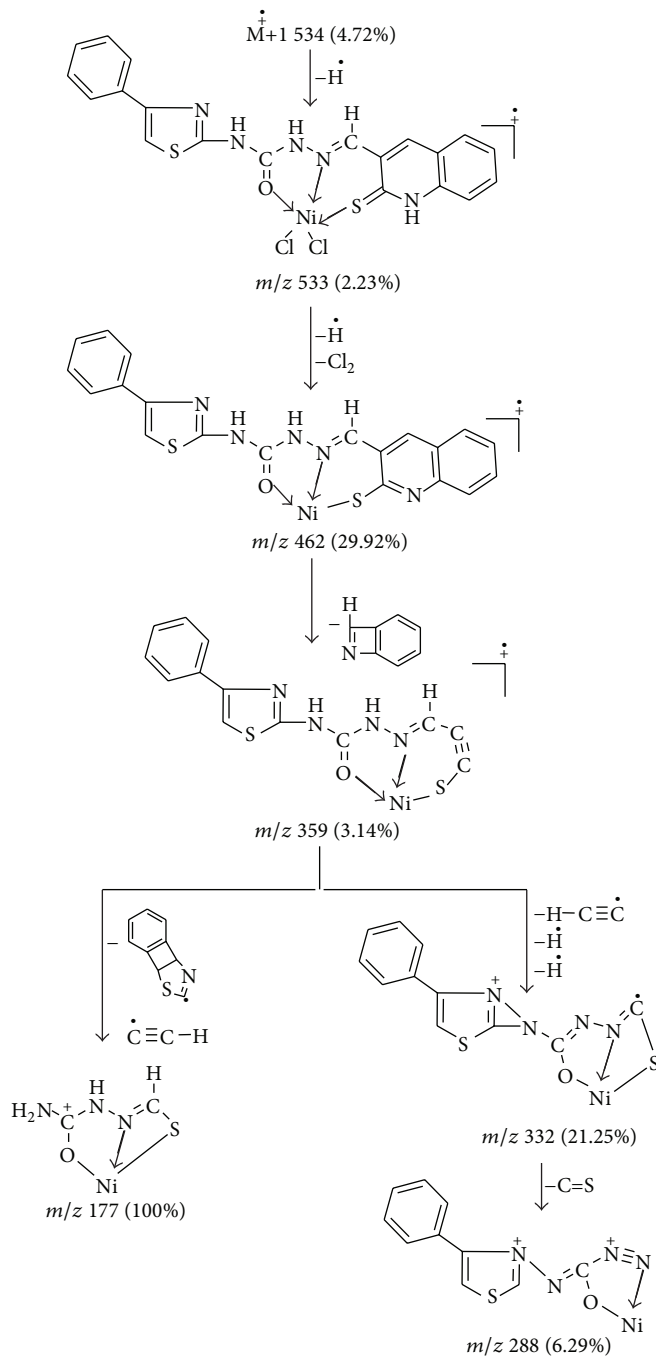
known for five coordinated square pyramidal geometries of Ni(II) complex [45].

3.5. ESR Spectra. In order to obtain further information about the stereochemistry and site of the metal-ligand bonding and determine the magnetic interaction in the metal

complexes, the X-band ESR spectrum of Cu(II) complex has been recorded in the polycrystalline state at room temperature using DPPH as a standard. The ESR spectrum of Cu(II) complex exhibited a single broad signal (Figure 3) due to dipolar broadening and enhanced spin lattice relaxation. The ESR spectra of Cu(II) complex exhibited auxiliary symmetric

TABLE 3: Electronic and ESR spectral data.

Complexes	Electronic spectra			ESR spectral data		
	Absorption (cm ⁻¹)	Band assignment	g_{\perp}	g_{\parallel}	g_{avg}	G
[Cu(C ₂₀ H ₁₅ N ₅ OS ₂)(Cl ₂)]	9993	² B ₁ → ² A ₁ (ν_1)	2.03	2.16	2.07	5.01
	14595	² B ₁ → ² B ₂ (ν_2)				
	18045	² B ₁ → ² E (ν_3)				
[Co(C ₂₀ H ₁₅ N ₅ OS ₂)(Cl ₂)]	11098	⁴ A ₂ + ⁴ E → ⁴ B ₁ (ν_1)				
	17675	⁴ A ₂ + ⁴ E → ⁴ E (P) (ν_2)				
	20180	⁴ A ₂ + ⁴ E → ⁴ A ₂ (P) (ν_3)				
[Ni(C ₂₀ H ₁₅ N ₅ OS ₂)(Cl ₂)]	10000	³ B ₁ → ³ E ^a (ν_1)				
	13543	² B ₁ → ³ A ₂ (ν_2)				
	22307	³ B ₁ → ³ E ^b (ν_3)				



SCHEME 4: Mass fragmentation pattern of Ni(II) complex.

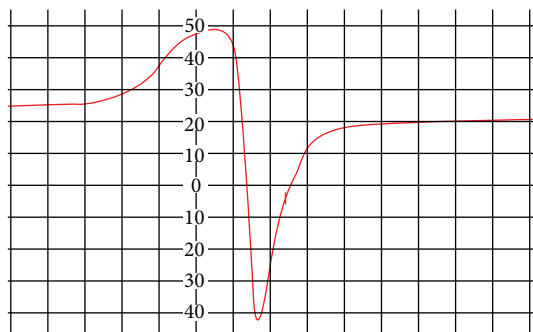


FIGURE 3: ESR spectrum of Cu(II) complex.

g-tensor parameter with $g_{\parallel}(2.16) > g_{\perp}(2.03) > 2.0023$, indicating presence of unpaired electron in $d_{x^2-y^2}$ ground state characteristic of square pyramidal geometry. The averaged “*g*” value for overall distortion is calculated using the equation: $g_{\text{avg}} = (1/3)(2g_{\perp} + g_{\parallel})$. The exchange interaction parameter *G* is calculated using the equation: $G = g_{\parallel} - 2.0023/g_{\perp} - 2.0023$. According to Hathaway and Billing [48], if the value of *G* is more than four, the exchange interaction between the Cu centres is negligible. In the present case the *G* value of 5.01 confirms the that exchange interactions between Cu(II) centers in solid state are negligible [49].

3.6. Thermal Studies. In order to examine the thermal stability of the complexes, thermo gravimetric (TG) and differential thermal analyses (DTA) were carried out for Cu(II), Co(II), and Zn(II) complexes in static air at a temperature range between 40 to 750°C at the heating rate of 10°C min⁻¹. The proposed stepwise thermal degradation pattern of complexes with temperature and formation of metal oxides is given in Table 4.

3.6.1. Cu(II) Complex. TGA and DTA curves of Cu(II) complex (Figure 4) showed that the complex is stable up to 237°C and no weight loss is observed before this temperature. The first stage of degradation occurred at 237.6°C, with the loss of the two chlorine atoms with a practical weight loss of 11.96% (Calc. 12.99%). The resultant complex on further degradation gave a break at 291°C by the loss of NCS species of quinoline moiety with a practical weight loss of 11.41% (Calc. 12.37%). The resultant complex underwent third stage of decomposition at 341°C due to loss of C₉H₇ molecule of quinoline and C₆H₆ molecule of thiazole moiety simultaneously with a practical weight loss of 47.96% (Calc. 47.01%). Further, complex showed decomposition up to 493°C due to the loss of remaining organic moiety. The final weight of the residue corresponds to cupric oxide.

3.6.2. Co(II) Complex. The thermogram of Co(II) complex showed first stage of decomposition due to loss of NCS species of quinoline moiety at 258°C with a practical weight loss of 9.66% (Calc. 10.86%). The resultant complex on further degradation gave a break at 320°C by the loss of C₈H₆ molecule of quinoline moiety with a practical weight loss of 22.22% (Calc. 21.43%), which on further degradation gave

a break at 458°C due to loss of remaining thiazole moiety (C₉H₇N₂S), two chlorine atoms, and HC=N-N-NH group simultaneously with a practical weight loss of 78.02% (Calc. 76.75%). After this, the complex showed a gradual decomposition up to 697°C by the loss of remaining organic moiety. The final weight of the residue corresponds to cobalt oxide.

3.6.3. Zn(II) Complex. The thermogram of Zn(II) complex showed first stage of decomposition due to loss of C₆H₇ species of thiazole and two chlorine atoms at 270°C with a practical weight loss of 28.71% (Calc. 27.57%). This on further loss due to C₁₀H₆NS of quinoline and CH=CH molecule of thiazole moiety gave a break at 320°C with a practical weight loss of 51.58% (Calc. 50.58%). After this, the complex showed a gradual decomposition up to 351°C by the loss of remaining organic moiety. The final weight of the residue corresponds to respective metal oxide.

3.7. Powder X-Ray Diffraction Studies. The synthesized Cu(II), Co(II), Ni(II), and Zn(II) complexes of Schiff base ligand (**L**) were soluble in some polar organic solvents (DMSO and DMF). The crystals that are suitable for single crystal studies are not obtained. In order to test the degree of crystallinity of the synthesized metal complexes, we obtained the powder X-ray diffraction pattern of the above complexes. The X-ray diffraction of Cu(II), Co(II), Ni(II), and Zn(II) complexes was scanned in the range 3–80°(θ) at wave length 1.54 Å. In all the complexes, the trend of the curves decreases from maximum to minimum intensity indicating the amorphous nature of the complexes in the present metal-ligand formation.

The X-ray diffraction pattern of Cu(II) complex records eight reflections between the range 3–80°(2 θ), which arise from diffraction of X-ray by the plane of the complex (Figure 5). The interplanar spacing (*d*-values) has been calculated by using Bragg's equation: $n\lambda = 2d \sin \theta$. The unit cell calculations have been done for cubic symmetry from the all-important peaks and the methods yielded *h k l* (Miller indices) unit cell parameter values and depicted in Table 5. The observed interplanar *d*-spacing values have been compared with the calculated ones and found to be in good agreement. The $h^2 + k^2 + l^2$ values are 1, 21, 25, 37, 53, 66, 81, and 92. It was observed that the presence of forbidden number 92 indicates that the Cu(II) complex may belong to hexagonal or tetragonal system.

The X-ray diffraction pattern of Ni(II) complex records nine reflections between the range 3–80°(2 θ), which arise from diffraction of X-ray by the plane of the complex (Figure 6). The interplanar spacing (*d*-values) has been calculated by using Bragg's equation: $n\lambda = 2d \sin \theta$. The unit cell calculations have been done for cubic symmetry from the all-important peaks and the methods yielded *h k l* (Miller indices) unit cell parameter values depicted in Table 6. The observed interplanar *d*-spacing values have been compared with the calculated ones and found to be in good agreement. The $h^2 + k^2 + l^2$ values are 1, 19, 23, 33, 43, 47, 72, 75, and 78. It was observed that the presence of forbidden numbers 23, 43, and 47 indicates that the Ni(II) complex may belong to hexagonal or tetragonal system.

TABLE 4: Thermal data of Cu(II), Co(II) and Zn(II) complex.

Complex	Decomposition temp. (°C)	Weight loss (%)		Metal oxide (%)		Inference
		Obsd.	Calc.	Obsd.	Calc.	
[Cu(C ₂₀ H ₁₅ N ₅ OS ₂)(Cl ₂)]	237.6	11.96	12.99	—	—	Loss due to two chlorine atoms
	291	11.41	12.37	—	—	Loss due to NCS species
	341	47.96	47.01	—	—	Loss due to C ₉ H ₇ molecule of quinoline and C ₆ H ₆ molecule of thiazole moiety
	Up to 493	—	—	15.92	15.65	Loss due to remaining organic moiety
[Co(C ₂₀ H ₁₅ N ₅ OS ₂)(Cl ₂)]	258	9.66	10.86	—	—	Loss due to NCS species
	320	22.22	21.43	—	—	Loss due to C ₈ H ₆ molecule of quinoline moiety
	458	78.02	76.75	—	—	Loss due to C ₉ H ₇ N ₂ S of thiazole moiety, two chlorine atoms and HC=N-NH group
	Up to 697			17.15	17.56	Loss due to remaining organic moiety
[Zn(C ₂₀ H ₁₅ N ₅ OS ₂)(Cl ₂)]	270	28.71	27.57	—	—	Loss due C ₆ H ₇ species of thiazole and two chlorine atoms
	320	51.58	50.58	—	—	Loss due to C ₁₀ H ₆ NS molecule of quinoline and CH=CH molecule of thiazole moiety
	Up to 351	—	—	16.25	17.13	Loss due to remaining organic moiety

TABLE 5: Powder X-ray data of Cu(II) complex.

Peak	2θ	θ	sin θ	sin ² θ	1000sin ² θ	1000sin ² θ/CF (h ² + k ² + l ²)	h k l	d		
								Obs.	Calc.	a in Å
1	5.758	2.879	0.050	0.0025	2.52	1.00 (1)	(1 0 0)	15.335	15.338	15.330
2	26.804	13.402	0.231	0.0536	53.68	21.301 (21)	(4 2 1)	3.323	3.323	15.338
3	28.790	14.395	0.248	0.0618	61.80	24.523 (25)	(4 3 0)	3.098	3.097	15.338
4	35.480	17.74	0.304	0.0927	92.78	36.817 (37)	(6 1 0)	2.528	2.527	15.338
5	42.777	21.388	0.364	0.1329	132.93	52.750 (53)	(6 4 1)	2.112	2.111	15.338
6	48.302	24.151	0.409	0.1673	167.36	66.412 (66)	(5 5 4)	1.882	1.882	15.338
7	53.771	26.885	0.452	0.2044	204.48	81.142 (81)	(8 4 1)	1.703	1.702	15.338
8	57.486	28.743	0.480	0.2311	231.16	91.733 (92)	(— — —)	1.601	1.601	15.339

TABLE 6: Powder X-ray data of Ni(II) complex.

Peak	2θ	θ	sin θ	sin ² θ	1000sin ² θ	1000sin ² θ/CF (h ² + k ² + l ²)	h k l	d		
								Obs.	Calc.	a in Å
1	6.099	3.049	0.053	0.0028	2.83	1.00 (1)	(1 0 0)	14.480	14.476	14.474
2	26.903	13.451	0.232	0.0541	54.11	19.120 (19)	(3 3 1)	3.311	3.310	14.475
3	29.603	14.801	0.255	0.0652	65.26	23.061 (23)	(— — —)	3.015	3.014	14.481
4	35.529	17.764	0.305	0.0930	93.08	32.892 (33)	(5 2 2)	2.524	2.523	14.480
5	40.704	20.352	0.347	0.1209	120.95	42.738 (43)	(— — —)	2.214	2.214	14.477
6	42.874	21.437	0.365	0.1335	133.57	47.197 (47)	(— — —)	2.107	2.107	14.477
7	53.747	26.873	0.452	0.2043	204.32	72.196 (72)	(6 6 0)	1.704	1.703	14.474
8	54.889	27.444	0.460	0.2124	212.418	75.057 (75)	(7 5 1)	1.671	1.671	14.474
9	56.054	28.027	0.469	0.2207	220.794	78.016 (78)	(7 5 2)	1.639	1.638	14.477

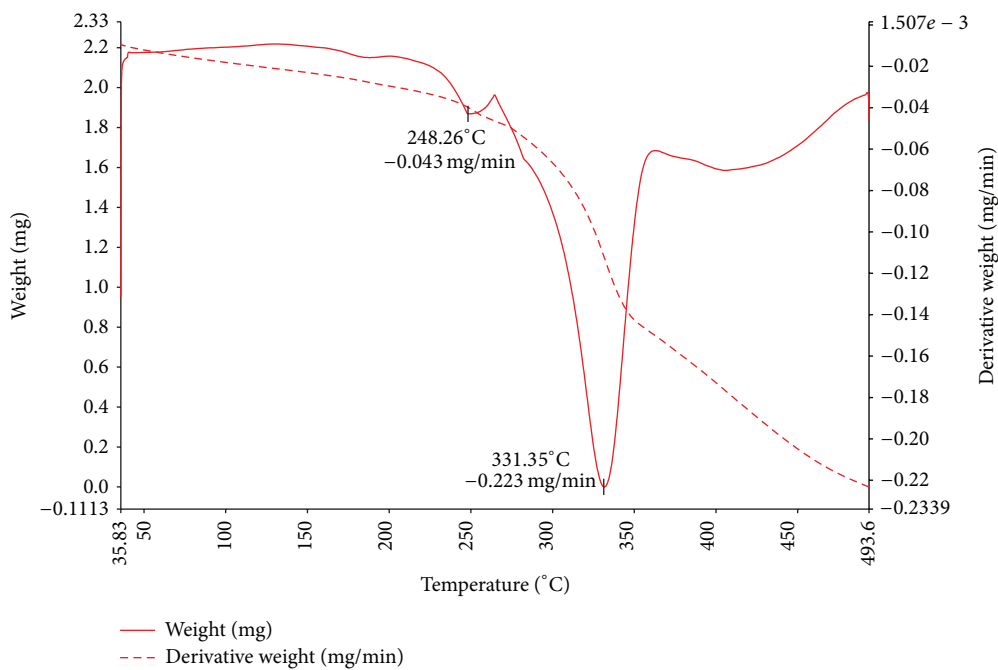


FIGURE 4: TGA and DTA curve of Cu(II) complex.

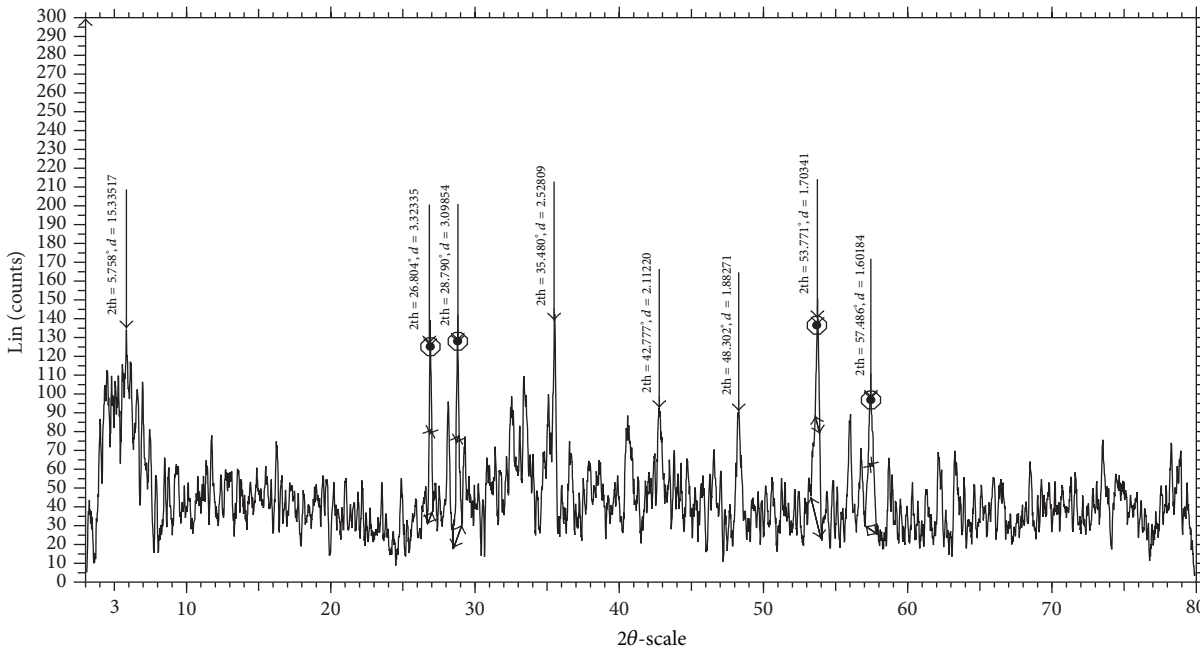


FIGURE 5: Powder XRD spectrum of Cu(II) complex.

Similar calculations were done for Co(II) and Zn(II) complexes. The Co(II) complex showed seven reflections and Zn(II) complex showed five reflections between the range 3–80°(2θ). For all the complexes, the interplanar spacing (d -values) and unit cell calculations have been done for cubic symmetry from the all-important peaks and the method yielded $h\ k\ l$ (Miller indices) units cell parameter values. The $h^2 + k^2 + l^2$ values for Co(II) complex are 1, 5, 7, and 10 and for the Zn(II) complex 1, 2, 29, 37, and 63, respectively. It was observed that the presence of forbidden number 7 in

Co(II) complex and forbidden number 63 in Zn(II) complex, respectively, indicates that these complexes may belong to hexagonal or tetragonal system.

3.8. Biological Evaluation

3.8.1. In Vitro Antibacterial and Antifungal Activities. The *in vitro* antimicrobial activity of all the synthesized compounds was screened against *Enterobacter aerogenes* and *Pseudomonas aeruginosa* bacteria and *Aspergillus niger* and

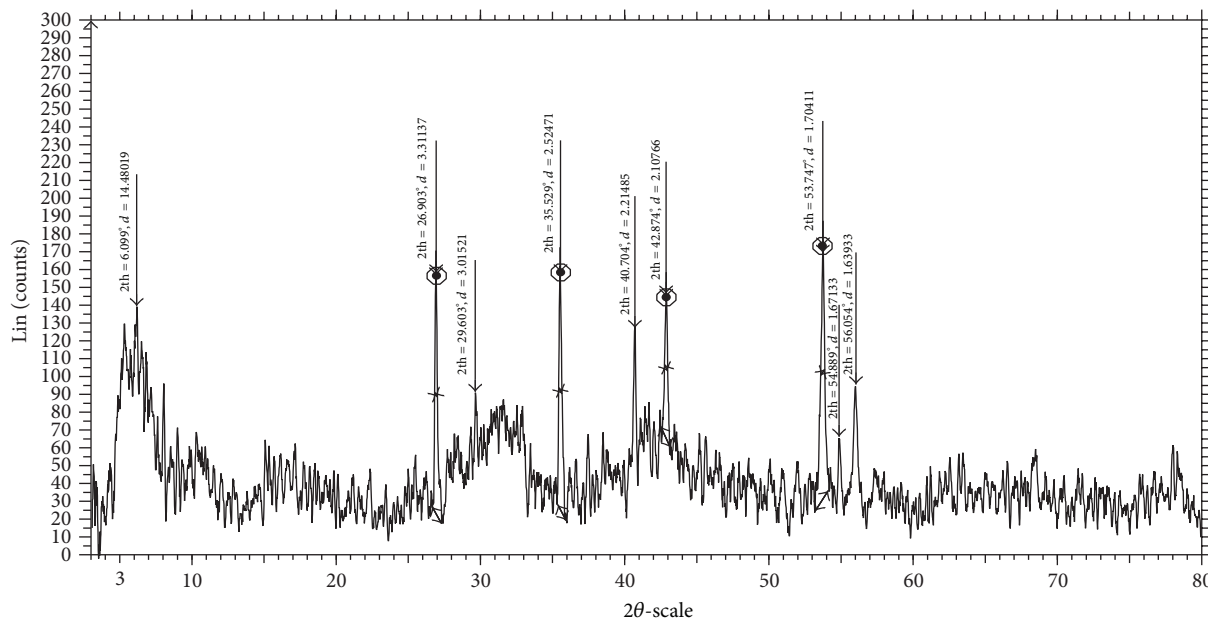


FIGURE 6: Powder XRD spectrum of Ni(II) complex.

Aspergillus flavus fungal strains by minimum inhibitory concentration (MIC) method. The minimum inhibitory concentration (MIC) profiles of all the compounds against bacteria and fungi are summarized in Table 7.

The MIC values indicated that all the complexes exhibited promising results compared to the ligand against mentioned microorganisms, and this activity is found to be enhanced on coordination with the metal ions. This enhancement in the activity may be rationalized on the basis that ligands mainly possess C=N bond. The enhanced activity of the complexes over the ligand can be explained on the basis of chelation theory [50, 51]. It is observed that, in a complex, the positive charge of the metal is partially shared with the donor atoms present in the ligand, and there may be π -electron delocalization over the whole chelate [52]. This increases the lipophilic character of the metal chelate and favors its permeation through the lipid layer of the bacterial membranes. The heterocyclic Schiff bases with different functional groups have greater tendency to interact with nucleoside bases even after complexation with metal ion or with the essential metal ions present in the biosystem can act as a promising bactericides because they always tend to interact with enzymatic functional groups in order to achieve higher coordination numbers [53]. There are also other factors which increase the activity, namely, solubility, conductivity, and bond length between the metal and the ligand.

3.8.2. DNA Cleavage Activity. The interaction of plasmid pBR322 DNA with newly synthesized ligand L and its Cu(II), Co(II), Ni(II), and Zn(II) complexes was studied using agarose gel electrophoresis method. The gel picture showing the cleavage of plasmid pBR322 DNA is depicted in Figure 7. The characterization of DNA recognition by transition metal complex has been aided by the DNA cleavage chemistry associated with redox-active or photo activated metal complexes [54]. The electrophoresis analysis clearly revealed that

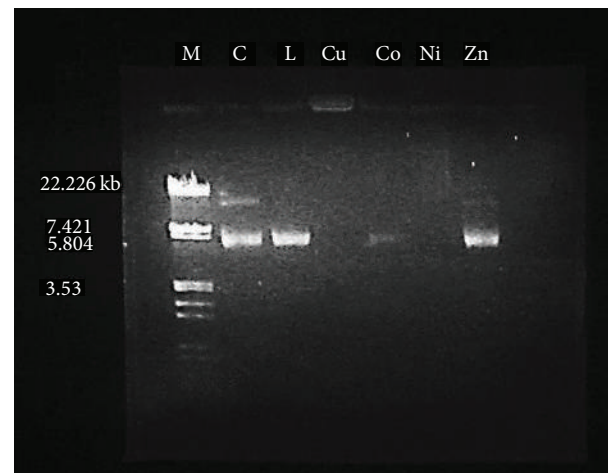


FIGURE 7: DNA cleavage on plasmid pBR 322: M: Standard DNA, C: Control DNA (untreated pBR 322), L: Schiff base ligand, Cu: Cu(II) complex, Co: Co(II) complex, Ni: Ni(II) complex, and Zn: Zn(II) complex.

the ligand and its metal complexes have acted on DNA because of a difference in molecular weight between the control and the treated DNA samples. The difference was observed in the bands of lanes of complexes compared with the control DNA of pBR322 due to the relaxation of circular DNA into linear form. This shows that the control DNA alone does not show any apparent cleavage, whereas the ligand and its metal complexes do show. In the present study, the Ethidium bromide (EtBr) stained banding pattern of plasmid pBR322 DNA was tested with newly synthesized ligand and its metal complexes. In the present case, the ligand and its Cu(II), Co(II), and Zn(II) complex showed complete cleavage of super coiled DNA and the Ni(II) complex showed

TABLE 7: Minimum Inhibitory Concentration (MIC in $\mu\text{g/mL}$) of Schiff base ligand (**L**) and its metal complexes.

Organisms	Compounds	Concentration ($\mu\text{g/mL}$)									
		0.195	0.39	0.78	1.563	3.125	6.25	12.50	25	50	100
<i>Enterobacter aerogenes</i>	Ligand (L)	+	+	+	+	***	-	-	-	-	-
	Cu-Complex	+	+	+	***	-	-	-	-	-	-
	Co-Complex	+	+	+	***	-	-	-	-	-	-
	Ni-Complex	+	+	+	+	***	-	-	-	-	-
	Zn-Complex	+	+	+	***	-	-	-	-	-	-
<i>Pseudomonas aeruginosa</i>	Ligand (L)	+	+	+	+	+	***	-	-	-	-
	Cu-Complex	+	+	***	-	-	-	-	-	-	-
	Co-Complex	+	+	***	-	-	-	-	-	-	-
	Ni-Complex	+	+	+	***	-	-	-	-	-	-
	Zn-Complex	+	+	***	-	-	-	-	-	-	-
<i>Aspergillus niger</i>	Ligand (L)	+	+	+	+	+	+	***	-	-	-
	Cu-Complex	+	+	+	***	-	-	-	-	-	-
	Co-Complex	+	+	+	+	+	***	-	-	-	-
	Ni-Complex	+	+	+	***	-	-	-	-	-	-
	Zn-Complex	+	+	+	+	***	-	-	-	-	-
<i>Aspergillus flavus</i>	Ligand (L)	+	+	+	+	+	***	-	-	-	-
	Cu-Complex	+	+	+	+	***	-	-	-	-	-
	Co-Complex	+	+	+	+	+	+	+	***	-	-
	Ni-Complex	+	+	+	+	***	-	-	-	-	-
	Zn-Complex	+	+	+	+	***	-	-	-	-	-

⁺ indicates turbidity is observed.

⁻ indicates turbidity is not observed.

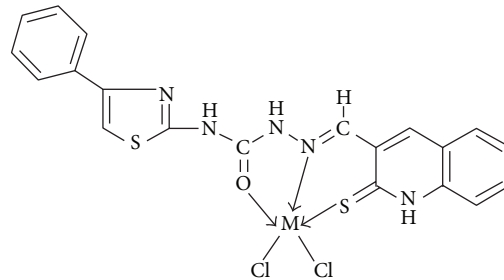
*** represents the MIC value.

TABLE 8: Brine shrimp bioassay data of the Schiff base ligand (**L**) and its metal complexes.

Compound	LD_{50} (M/mL)
Ligand (L)	2.470×10^{-4}
Cu-Complex	1.387×10^{-4}
Co-Complex	1.168×10^{-4}
Ni-Complex	1.074×10^{-4}
Zn-Complex	2.308×10^{-4}

partial cleavage of relaxed DNA and complete cleavage of supercoiled DNA. This clearly reveals the important role of coordination of O, N, and S groups to the metal ion in these DNA cleavage activities. On the basis of these findings, it can be concluded that all the newly synthesized compounds under present study are good pathogenic microorganism inhibitor; as evident on the DNA cleavage of pBR322.

3.8.3. In Vitro Cytotoxicity. All the synthesized compounds were screened for their cytotoxicity (brine shrimp bioassay) using the protocol of Meyer et al. [38]. From the data recorded in Table 8, it is evident that all the newly synthesized metal complexes exhibited potent activity when compared to the free ligand. The Co(II) and Ni(II) complexes displayed significant potent cytotoxic activity as $\text{LD}_{50} = 1.168 \times 10^{-4}$ and 1.074×10^{-4} M/mL, respectively, against *Artemia salina*.



M = Cu(II), Co(II), Ni(II), and Zn(II)

FIGURE 8: Proposed structure of the complexes.

4. Conclusions

The newly synthesized Schiff base ligand *N*-(4-phenylthiazol-2-yl)-2-((2-thioxo-1,2-dihydroquinolin-3-yl)methylene)hydrazinecarboxamide behaves as tridentate ONS donor and forms the complexes of type $[\text{ML}(\text{Cl})_2]$. With the help of various physicochemical and spectroscopic methods such as IR, ^1H NMR, UV-Visible, and ESR, the square pyramidal geometries of the Cu(II), Co(II), Ni(II), and Zn(II) complexes have been proposed (Figure 8). The newly synthesized metal complexes showed good antimicrobial activity when compared to the free ligand. The DNA cleavage activity

of all the synthesized compounds showed the cleavage of plasmid DNA pBR 322 and the cytotoxicities of Co(II) and Ni(II) complexes indicate potent cytotoxic agents that might become potent anticancer agent in clinical trials.

Conflict of Interests

The authors do not have any agreement, financial assistance, or sponsorship from any institution except providing the data which are of purely academic interest and to encourage young researchers in India. The IR spectra of compounds were recorded on Perkin Elmer-Spectrum RX-I FTIR spectrophotometer using KBr disc technique, ^1H NMR spectra were recorded on Bruker Avance II 400 MHz NMR Spectrometer in d_6 -DMSO using TMS as an internal standard, ESI mass spectra were recorded by electrospray ionization (ESI) on a Waters Micromass Q-ToF Micro spectrometer, ESR spectrum was recorded on JES-FA200 ESR spectrometer, and so forth. These names are mentioned in the experimental protocol as these are the instrument models, and it is mandatory for authors to mention the instrument models used to scan the spectra of unknown compounds. Otherwise, the corresponding author or coauthor has no-direct financial relationship with the commercial identity in any form of the institutes mentioned in our paper.

Acknowledgments

Authors are thankful to the Professor and Chairman of Department of Chemistry, Gulbarga University, Gulbarga, for providing necessary facilities for research. Authors extend their thanks to SAIF Punjab University, Chandigarh, for providing FT-IR, ^1H NMR and ESI mass spectral data, IIT Bombay for providing ESR spectral data, and STIC Cochin University for providing TG/DTA and powder X-ray data. Authors are also thankful to BioGenics Research and Training Centre in Biotechnology, Hubli, for biological studies. One of the authors (Nagesh G. Yernale) is grateful to Department of Science and Technology (DST), New Delhi, for the award of DST-INSPIRE Research fellowship.

References

- [1] P. A. Vigato and S. Tamburini, "The challenge of cyclic and acyclic Schiff bases and related derivatives," *Coordination Chemistry Reviews*, vol. 248, no. 17–20, pp. 1717–2128, 2004.
- [2] N. K. Kaushik and A. K. Mishra, "Synthesis, characterization and thermal studies of some new organotin (IV) complexes with aniline *N*-thiohydrazide and benzaldehyde aniline *N*-thiohydrazone," *Indian Journal of Chemistry A*, vol. 42, no. 11, pp. 2762–2766, 2003.
- [3] M. S. Saraiva, S. Quintal, F. C. M. Portugal et al., "Nitrogen donor ligands bearing N-H groups: effect on catalytic and cytotoxic activity of molybdenum η^3 -allyldicarbonyl complexes," *Journal of Organometallic Chemistry*, vol. 693, no. 21–22, pp. 3411–3418, 2008.
- [4] N. K. Singh, A. Srivastava, A. Sodhi, and P. Ranjan, "*In vitro* and *in vivo* antitumour studies of a new thiosemicarbazide derivative and its complexes with 3D-metal ions," *Transition Metal Chemistry*, vol. 25, no. 2, pp. 133–140, 2000.
- [5] Y. K. Vaghasiya, R. Nair, M. Soni, S. Baluja, and S. Chanda, "Synthesis, structural determination and antibacterial activity of compounds derived from vanillin and 4-aminoantipyrine," *Journal of the Serbian Chemical Society*, vol. 69, no. 12, pp. 991–998, 2004.
- [6] M. E. Hossain, M. N. Alam, J. Begum et al., "The preparation, characterization, crystal structure and biological activities of some copper(II) complexes of the 2-benzoylpyridine Schiff bases of S-methyl- and S-benzylidithiocarbazate," *Inorganica Chimica Acta*, vol. 249, no. 2, pp. 207–213, 1996.
- [7] V. E. Kuz'min, A. G. Artemenko, R. N. Loztska et al., "Investigation of anticancer activity of macrocyclic Schiff bases by means of 4D-QSAR based on simplex representation of molecular structure," *SAR and QSAR in Environmental Research*, vol. 16, no. 3, pp. 219–230, 2005.
- [8] C. T. Supuran, M. Barboiu, C. Luca, E. Pop, M. E. Brewster, and A. Dinculescu, "Carbonic anhydrase activators. Part 14. Syntheses of mono and *bis* pyridinium salt derivatives of 2-amino-5-(2-aminoethyl)- and 2-amino-5-(3-aminopropyl)-1,3,4-thiadiazole and their interaction with isozyme II," *European Journal of Medicinal Chemistry*, vol. 31, no. 7–8, pp. 597–606, 1996.
- [9] D. Branowska, A. A. Farahat, A. Kumar et al., "Synthesis and antiprotozoal activity of 2,5-*bis*[amidinoaryl]thiazoles," *Bioorganic & Medicinal Chemistry*, vol. 18, no. 10, pp. 3551–3558, 2010.
- [10] F. Rahaman, B. Hiremath, S. M. Basavarajaiah, B. H. M. Jayakumarswamy, and B. H. M. Mruthyunjayaswamy, "Synthetic, spectral, thermal and antimicrobial activity studies of some transition metal complexes derived from 2-hydroxy-methylbenzaldehyde N-(4'-phenyl-1',3',5'-thiazol-2'-yl)semicarbazone," *Journal of the Indian Chemical Society*, vol. 85, no. 4, pp. 381–386, 2008.
- [11] B. S. Holla, K. V. Malini, B. S. Rao, B. K. Sarojini, and N. S. Kumari, "Synthesis of some new 2,4-disubstituted thiazoles as possible antibacterial and anti-inflammatory agents," *European Journal of Medicinal Chemistry*, vol. 38, no. 3, pp. 313–318, 2003.
- [12] V. Banewar, "Green synthesis and *in vitro* biological evaluation of heteroaryl chalcones and pyrazolines of medicinal interest," *Journal of Chemistry*, vol. 2013, Article ID 542973, 4 pages, 2013.
- [13] A. Andreani, M. Granaiola, A. Leoni, A. Locatelli, R. Morigi, and M. Rambaldi, "Synthesis and antitubercular activity of imidazo[2,1-b]thiazoles," *European Journal of Medicinal Chemistry*, vol. 36, no. 9, pp. 743–746, 2001.
- [14] E. M. Hodnett and P. D. Mooney, "Antitumor activities of some Schiff bases," *Journal of Medicinal Chemistry*, vol. 13, no. 4, p. 786, 1970.
- [15] G. S. Hassan, S. M. El-Messery, F. A. Al-Omary, and H. I. El-Subbagh, "Substituted thiazoles VII. Synthesis and antitumor activity of certain 2-(substituted amino)-4-phenyl-1,3-thiazole analogs," *Bioorganic & Medicinal Chemistry Letters*, vol. 22, no. 20, pp. 6318–6323, 2012.
- [16] R. K. Robins and G. H. Hitchings, "Studies on condensed pyrimidine systems. XIX. A new synthesis of pyrido[2,3-d]pyrimidines. The condensation of 1,3-diketones and 3-ketoaldehydes with 4-aminopyrimidines," *Journal of the American Chemical Society*, vol. 80, no. 13, pp. 3449–3457, 1958.
- [17] A. H. M. Raeymaekers, F. T. N. Allewijn, J. Vandenbergk, P. J. A. Demoen, T. T. T. van Offenwert, and P. A. J. Janssen, "Novel

- broad-spectrum anthelmintics. Tetramisole and related derivatives of 6-arylimidazo[2,1-b]thiazole," *Journal of Medicinal Chemistry*, vol. 9, no. 4, pp. 545–551, 1966.
- [18] S. R. Pattan, C. Suresh, V. D. Pujar, V. V. K. Reddy, V. P. Rasal, and B. C. Koti, "Synthesis and antidiabetic activity of 2-amino [5'(4-sulphonylbenzylidene)-2,4-thiazolidinedione]-7-chloro-6-fluorobenzothiazole," *Indian Journal of Chemistry B*, vol. 44, no. 11, pp. 2404–2408, 2005.
- [19] S. Samadhiya and A. Halve, "Synthetic utility of Schiff bases as potential herbicidal agents," *Oriental Journal of Chemistry*, vol. 17, pp. 119–122, 2001.
- [20] Z.-H. Yu and D.-Q. Shi, "Synthesis and herbicidal activity of amino phosphonate derivatives containing thiazole and pyrazole moieties," *Phosphorus, Sulfur and Silicon and the Related Elements*, vol. 185, no. 8, pp. 1746–1752, 2010.
- [21] M.-G. Kayirere, A. Mahamoud, J. Chevalier, J.-C. Soyfer, A. Crémieux, and J. Barbe, "Synthesis and antibacterial activity of new 4-alkoxy, 4-aminoalkyl and 4-alkylthioquinoline derivatives," *European Journal of Medicinal Chemistry*, vol. 33, no. 1, pp. 55–63, 1998.
- [22] R. Musiol, J. Jampilek, V. Buchta et al., "Antifungal properties of new series of quinoline derivatives," *Bioorganic & Medicinal Chemistry*, vol. 14, no. 10, pp. 3592–3598, 2006.
- [23] J. H. Burckhalter and W. H. Edgerton, "A new type of 8-quinalinol amebacidal agent," *Journal of the American Chemical Society*, vol. 73, no. 10, pp. 4837–4839, 1951.
- [24] M. Jain, S. I. Khan, B. L. Tekwani et al., "Synthesis, antimarial, antileishmanial, and antimicrobial activities of some 8-quinalamine analogues," *Bioorganic & Medicinal Chemistry*, vol. 13, no. 14, pp. 4458–4466, 2005.
- [25] W. Cunico, C. A. Cechinel, H. G. Bonacorso et al., "Antimalarial activity of 4-(5-trifluoromethyl-1*H*-pyrazol-1-yl)-chloroquine analogues," *Bioorganic and Medicinal Chemistry Letters*, vol. 16, no. 3, pp. 649–653, 2006.
- [26] Y.-L. Chen, C.-J. Huang, Z.-Y. Huang et al., "Synthesis and anti-proliferative evaluation of certain 4-anilino-8-methoxy-2-phenylquinoline and 4-anilino-8-hydroxy-2-phenylquinoline derivatives," *Bioorganic & Medicinal Chemistry*, vol. 14, no. 9, pp. 3098–3105, 2006.
- [27] C. Papageorgiou, A. Von Matt, J. Joergensen et al., "Aromatic quinolinecarboxamides as selective, orally active antibody production inhibitors for prevention of acute xenograft rejection," *Journal of Medicinal Chemistry*, vol. 44, no. 12, pp. 1986–1992, 2001.
- [28] H. Shinkai, T. Ito, T. Iida, Y. Kitao, H. Yamada, and I. Uchida, "4-aminoquinolines: novel nociceptin antagonists with analgesic activity," *Journal of Medicinal Chemistry*, vol. 43, no. 24, pp. 4667–4677, 2000.
- [29] C. H. Kaschula, T. J. Egan, R. Hunter et al., "Structure–activity relationships in 4-aminoquinoline antiplasmodials. The role of the group at the 7-position," *Journal of Medicinal Chemistry*, vol. 45, no. 16, pp. 3531–3539, 2002.
- [30] N. Muruganantham, R. Sivakumar, N. Anbalagan, V. Gunasekaran, and J. T. Leonard, "Synthesis, anticonvulsant and anti-hypertensive activities of 8-substituted quinoline derivatives," *Biological and Pharmaceutical Bulletin*, vol. 27, no. 10, pp. 1683–1687, 2004.
- [31] B. H. M. Mruthyunjayaswamy and S. M. Basavarajaiah, "Synthesis and antimicrobial activity of novel ethyl-5-(ethoxycarbonyl)-4methylthiazol-2-yl-carbamate compounds," *Indian Journal of Chemistry B*, vol. 48, no. 9, pp. 1274–1278, 2009.
- [32] D. B. Vivekanand and B. H. M. Mruthyunjayaswamy, "Synthesis characterization and antimicrobial activity studies of some transition metal complexes derived from 5-chloro-3-phenyl-N1-((2-thioxo-1,2-dihydroquinoline-3-yl)methylene)-1*H*-indole-2-carbohydrazide," *International Journal of Chemical Science and Research*, vol. 2, pp. 29–48, 2012.
- [33] J. Mendham, R. C. Denney, J. D. Barnes, and M. J. K. Thomas, *Vogel's Quantitative Chemical Analysis*, Prentice Hall, London, UK, 6th edition, 1999.
- [34] M. R. Karekal and B. H. M. Mruthyunjayaswamy, "Synthesis, spectroscopic characterization, and biological screening of binuclear transition metal complexes of bicompartimental Schiff bases containing indole and resorcinol moieties," *Turkish Journal of Chemistry*, vol. 37, pp. 775–795, 2013.
- [35] L. L. Ramesh, M. K. Umesh, S. Kirankumar, and V. H. Jayashree, "Phytochemical screening and *in vitro* antimicrobial activity of *Typha angustifolia* Linn leaves extract against pathogenic gram negative microorganisms," *Journal of Pharmacy Research*, vol. 6, pp. 280–283, 2013.
- [36] NCCLS (National Committee for Clinical Laboratory Standards), *Performance Standards for Antimicrobial Disc Susceptibility Test*, Approved Standard M2-A6, NCCLS, Wayne, PA, USA, 6th edition, 1997.
- [37] J. Sambrook, E. F. Fritsch, and T. Maniatis, *Molecular Cloning, a Laboratory Manual*, Cold Spring Harbor, New York, NY, USA, 2nd edition, 1989.
- [38] B. N. Meyer, N. R. Ferrigni, and J. E. Putnam, "Brine shrimp: a convenient general bioassay for active plant constituents," *Planta Medica*, vol. 45, no. 1, pp. 31–34, 1982.
- [39] D. J. Finney, *Probit Analysis*, Cambridge University Press, Cambridge, UK, 3rd edition, 1971.
- [40] F. Rahaman, O. B. Ijare, Y. Jadegowd, and B. H. M. Mruthyunjayaswamy, "Phenoxy-bridged symmetrical homobinuclear complexes derived from an "end-off" compartmental ligand, 2,6-bis[5'-chloro-3'-phenyl-1*H*-indole-2'-carboxamidyl-iminomethyl]-4-methylphenol," *Journal of Coordination Chemistry*, vol. 62, no. 9, pp. 1457–1467, 2009.
- [41] U. B. Gangadharmath, V. K. Revankar, and V. B. Mahale, "Synthesis and spectroscopic characterization of cationic mononuclear oxovanadium(IV) complexes with tetridentate Schiff bases as ligands," *Spectrochimica Acta A*, vol. 58, no. 12, pp. 2651–2657, 2002.
- [42] R. Kannappan, R. Mahalakshmy, T. M. Rajendiran, R. Venkatesan, and P. Sambasiva Rao, "Magnetic, catalytic, EPR and electrochemical studies on binuclear copper(II) complexes derived from 3,4-disubstituted phenol," *Proceedings of the Indian Academy of Sciences*, vol. 115, no. 1, pp. 1–14, 2003.
- [43] D. N. Satyanarayana, *Electronic Absorption Spectroscopy and Related Techniques*, Universities Press, India, 2001.
- [44] Y. Jadegovd, O. B. Ijare, B. S. Somashekar, G. A. N. Gowda, and B. H. M. Mruthyunjayaswamy, "Synthesis, characterization and antimicrobial activity of homodinuclear complexes derived from 2,6-bis[3'-methyl-2'-carboxamidyl-iminomethyl(6',7')benzindole]-4-methylphenol, an end-off compartmental ligand," *Journal of Coordination Chemistry*, vol. 61, no. 4, pp. 508–527, 2008.
- [45] A. A. El-Binary and A. Z. El-Sonbaty, "Synthesis and properties of complexes of copper(II), nickel(II), cobalt(II) and uranyl ions with 3-(p-tolylsulphonamido)rhodanine," *Polish Journal of Chemistry*, vol. 74, no. 5, pp. 615–620, 2000.
- [46] F. A. Cotton and G. Wilkinson, *Advanced Inorganic Chemistry*, John Wiley & Sons, New York, NY, USA, 3rd edition, 1972.

- [47] N. H. Pilkington and R. Robson, "Corrigenda—complexes of binucleating ligands. III. Novel complexes of a macrocyclic binucleating ligand," *Australian Journal of Chemistry*, vol. 23, pp. 2225–2236, 1970.
- [48] B. J. Hathaway and D. E. Billing, "The electronic properties and stereochemistry of mono-nuclear complexes of the copper(II) ion," *Coordination Chemistry Reviews*, vol. 5, no. 2, pp. 143–207, 1970.
- [49] V. P. Singh, P. Singh, and A. K. Singh, "Synthesis, structural and corrosion inhibition studies on cobalt(II), nickel(II), copper(II) and zinc(II) complexes with 2-acetylthiophene benzoylhydrazone," *Inorganica Chimica Acta*, vol. 379, no. 1, pp. 56–63, 2011.
- [50] A. K. Sharma and S. Chandra, "Complexation of nitrogen and sulphur donor Schiff's base ligand to Cr(III) and Ni(II) metal ions: synthesis, spectroscopic and antipathogenic studies," *Spectrochimica Acta A*, vol. 78, no. 1, pp. 337–342, 2011.
- [51] Z. H. Chohan, M. Arif, M. A. Akhtar, and C. T. Supuran, "Metal-based antibacterial and antifungal agents: synthesis, characterization, and *in vitro* biological evaluation of Co(II), Cu(II), Ni(II), and Zn(II) complexes with amino acid-derived compounds," *Bioinorganic Chemistry and Applications*, vol. 2006, Article ID 83131, 13 pages, 2006.
- [52] Z. H. A. El-Wahab, M. M. Mashaly, A. A. Salman, B. A. El-Shetary, and A. A. Faheim, "Co(II), Ce(III) and UO₂(VI) bis-salicylatothiosemicarbazide complexes: binary and ternary complexes, thermal studies and antimicrobial activity," *Spectrochimica Acta A*, vol. 60, no. 12, pp. 2861–2873, 2004.
- [53] K. R. K. Reddy, P. Suneetha, C. S. Karigar, N. H. Manjunath, and K. N. Mahendra, "Cobalt(II), Ni(II), Cu(II), Zn(II), Cd(II), Hg(II), UO₂(VI) and th(IV) complexes from ONNN Schiff base ligand," *Journal of the Chilean Chemical Society*, vol. 53, no. 4, pp. 1653–1657, 2008.
- [54] A. Sitrani, E. C. Long, A. M. Pyle, and J. K. Barton, "DNA photocleavage by phenanthrenequinone diimine complexes of rhodium(III): shape-selective recognition and reaction," *Journal of the American Chemical Society*, vol. 114, no. 7, pp. 2303–2312, 1992.

Permissions

The contributors of this book come from diverse backgrounds, making this book a truly international effort. This book will bring forth new frontiers with its revolutionizing research information and detailed analysis of the nascent developments around the world.

We would like to thank all the contributing authors for lending their expertise to make the book truly unique. They have played a crucial role in the development of this book. Without their invaluable contributions this book wouldn't have been possible. They have made vital efforts to compile up to date information on the varied aspects of this subject to make this book a valuable addition to the collection of many professionals and students.

This book was conceptualized with the vision of imparting up-to-date information and advanced data in this field. To ensure the same, a matchless editorial board was set up. Every individual on the board went through rigorous rounds of assessment to prove their worth. After which they invested a large part of their time researching and compiling the most relevant data for our readers. Conferences and sessions were held from time to time between the editorial board and the contributing authors to present the data in the most comprehensible form. The editorial team has worked tirelessly to provide valuable and valid information to help people across the globe.

Every chapter published in this book has been scrutinized by our experts. Their significance has been extensively debated. The topics covered herein carry significant findings which will fuel the growth of the discipline. They may even be implemented as practical applications or may be referred to as a beginning point for another development. Chapters in this book were first published by Hindawi Publishing Corporation; hereby published with permission under the Creative Commons Attribution License or equivalent.

The editorial board has been involved in producing this book since its inception. They have spent rigorous hours researching and exploring the diverse topics which have resulted in the successful publishing of this book. They have passed on their knowledge of decades through this book. To expedite this challenging task, the publisher supported the team at every step. A small team of assistant editors was also appointed to further simplify the editing procedure and attain best results for the readers.

Our editorial team has been hand-picked from every corner of the world. Their multi-ethnicity adds dynamic inputs to the discussions which result in innovative outcomes. These outcomes are then further discussed with the researchers and contributors who give their valuable feedback and opinion regarding the same. The feedback is then collaborated with the researchers and they are edited in a comprehensive manner to aid the understanding of the subject.

Apart from the editorial board, the designing team has also invested a significant amount of their time in understanding the subject and creating the most relevant covers. They scrutinized every image to scout for the most suitable representation of the subject and create an appropriate cover for the book.

The publishing team has been involved in this book since its early stages. They were actively engaged in every process, be it collecting the data, connecting with the contributors or procuring relevant information. The team has been an ardent support to the editorial, designing and production team. Their endless efforts to recruit the best for this project, has resulted in the accomplishment of this book. They are a veteran in the field of academics and their pool of knowledge is as vast as their experience in printing. Their expertise and guidance has proved useful at every step. Their uncompromising quality standards have made this book an exceptional effort. Their encouragement from time to time has been an inspiration for everyone.

The publisher and the editorial board hope that this book will prove to be a valuable piece of knowledge for researchers, students, practitioners and scholars across the globe.

List of Contributors

Fangxing Xiao, Xiaobin Yao, Qianhong Bao, Danzhen Li and Yi Zheng

State Key Laboratory Breeding Base of Photocatalysis, Research Institute of Photocatalysis, College of Chemistry and Chemical Engineering, Fuzhou University, Fuzhou 350002, China

Manuel Alvarado Jr. and Russell C. Chianelli

Materials Research and Technology Institute, The University of Texas at El Paso, El Paso, TX 79912, USA

Roy M. Arrowood

Department of Metallurgical & Materials Engineering, The University of Texas at El Paso, El Paso, TX 79912, USA

Yin-Lai Wang

Department of Dentistry, Kaohsiung Armed Forces General Hospital, Kaohsiung 802, Taiwan

Fu-Yuan Teng

Department of Dentistry, Kaohsiung Armed Forces General Hospital, Kaohsiung 802, Taiwan

School of Dentistry, College of Dental Medicine, Kaohsiung Medical University, Kaohsiung 807, Taiwan

Chia-Ling Ko, Chun-Cheng Hung and Cheng-Yi Cheng

School of Dentistry, College of Dental Medicine, Kaohsiung Medical University, Kaohsiung 807, Taiwan

Hsien-Nan Kuo

Medical Device Development Division, Metal Industries Research & Development Centre, Kaohsiung 82151, Taiwan

Jin-Jia Hu

Department of Biomedical Engineering, National Cheng Kung University, Tainan 701, Taiwan

Jia-Horng Lin

Laboratory of Fiber Application and Manufacturing, Department of Fiber and Composite Materials, Feng Chia University, School of Chinese Medicine, China Medical University, Taichung 40724, Taiwan

Ching-Wen Lou

Institute of Biomedical Engineering and Material Science, Central Taiwan University of Science and Technology, Taichung 40601, Taiwan

Wen-Cheng Chen

Department of Fiber and Composite Materials, College of Engineering, Feng Chia University, 100 Wenhwa Road, Seatwen, Taichung 40724, Taiwan

M. A. Salam, M. A. Affan, Fasihuddin B. Ahmad and Norrihan Sam

Faculty of Resource Science and Technology, Universiti Malaysia Sarawak, 94300 Kota Samarahan, Sarawak, Malaysia

Ramkrishna Saha

Department of Chemistry, Shahjalal University of Science and Technology, Sylhet 3114, Bangladesh

Radka Novotná, Zdeněk Trávníček and Radovan Herchel

Department of Inorganic Chemistry, Regional Centre of Advanced Technologies and Materials, Faculty of Science, Palacký University, 17. Listopadu 12, 771 46 Olomouc, Czech Republic

T. G. Costa and B. Szpoganicz

Department of Chemistry, Federal University of Santa Catarina, CP476, 88040-900 Florianópolis, SC, Brazil

R. Younger

Department of Chemistry, University of California, Irvine, Irvine, CA 96729, USA

C. Poe and P. J. Farmer

Department of Chemistry and Biochemistry, Baylor University, Waco, TX 76706, USA

Kiran Singh, Yogender Kumar and Parvesh Puri

Department of Chemistry, Kurukshetra University, Kurukshetra 136 119, India

Gulab Singh

Department of Microbiology, Kurukshetra University, Kurukshetra 136 119, India

Kensuke Kuroda and Masazumi Okido

Department of Materials Science and Engineering, Graduate School of Engineering, Nagoya University, Nagoya 464-8603, Japan

Xiao-mei Mo

Key Laboratory of Marine Drugs, Ministry of Education, School of Medicine and Pharmacy, Ocean University of China, 5 Yu-Shan Road, Qingdao 266003, China

The Department of Pharmacy, Qingdao Women and Children Hospital, 127 Liao-Yang West Road, Qingdao 266034, China

Xin Qi, Yan-tuan Li and Jing Li

Key Laboratory of Marine Drugs, Ministry of Education, School of Medicine and Pharmacy, Ocean University of China, 5 Yu-Shan Road, Qingdao 266003, China

Zhan-fang Chen

The Department of Pharmacy, Qingdao Women and Children Hospital, 127 Liao-Yang West Road, Qingdao 266034, China

Abdul Amir H. Kadhum and Abu Bakar Mohamad

Department of Chemical and Process Engineering, Faculty of Engineering and Built Environment, University of Kebangsaan Malaysia, 43600 Bangi, Selangor, Malaysia

Ahmed A. Al-Amriery

Department of Chemical and Process Engineering, Faculty of Engineering and Built Environment,

University of Kebangsaan Malaysia, 43600 Bangi, Selangor, Malaysia

Biotechnology Division, Applied Science Department, University of Technology, Baghdad 10066, Iraq

Mehdi Mogharabi and Mohammad Ali Faramarzi

Department of Pharmaceutical Biotechnology, Faculty of Pharmacy and Biotechnology Research Center, Tehran University of Medical Sciences, P.O. Box 14155-6451, Tehran 14174, Iran

Department of Chemistry, Faculty of Sciences, University of Birjand, Birjand 9717853577, Iran

Nasser Nassiri-Koopaei and Maryam Bozorgi-Koushalshahi

Department of Pharmaceutical Biotechnology, Faculty of Pharmacy and Biotechnology Research Center, Tehran University of Medical Sciences, P.O. Box 14155-6451, Tehran 14174, Iran

Ghodsieh Bagherzadeh

Department of Chemistry, Faculty of Sciences, University of Birjand, Birjand 9717853577, Iran

Nastaran Nafissi-Varcheh

Department of Pharmaceutical Biotechnology, School of Pharmacy, Shahid Beheshti University of Medical Sciences, Tehran 1457795343, Iran

Carmen Zietz, Andreas Fritzsche, Maximilian Haenle, Wolfram Mittelmeier and Rainer Bader

Biomechanics and Implant Technology Research Laboratory, Department of Ortopedics, University of Rostock, Doberaner Straße 142, 18057 Rostock, Germany

Birgit Finke

Leibniz Institute for Plasma Science and Technology (INP e.V. Greifswald), Felix-Hausdorff-Straße 2, 17489 Greifswald, Germany

Vitezslav Stranak and Rainer Hippler

Institute of Physics, Ernst-Moritz-Arndt University of Greifswald, Felix-Hausdorff-Straße 6, 17487 Greifswald, Germany

Aruna Jyothi Kora and Lori Rastogi

National Centre for Compositional Characterization of Materials (NCCCM), Bhabha Atomic Research Centre, Hyderabad 500 062, India

Mohammad Rezaee, Elahe Alizadeh, Darel Hunting and Léon Sanche

Groupe en Sciences des Radiations, D'epartement deM'edecineNucl'eaire et Radiobiologie, Facult'e deM'edecine et des Sciences de la Sant'e, Universit'e de Sherbrooke, Sherbrooke, QC, Canada J1H5N4

Y. Prashanthi

Department of Chemistry, Osmania University, Hyderabad 500 007, India
Indian Institute of Chemical Technology, Hyderabad 500 007, India

K. Kiranmai, Sathish kumar K, Vijay kumar Chityala and Shivaraj

Department of Chemistry, Osmania University, Hyderabad 500 007, India

Ira

Centre for Cellular and Molecular Biology, Hyderabad 500 007, India

Marcelo Neves Rocha, Paula Monalisa Nogueira and Rodrigo Pedro Soares

Centro de Pesquisas Ren'e Rachou, Fundac,ao Oswaldo Cruz/FIOCRUZ, 30190-002 Belo Horizonte, MG, Brazil

Cynthia Demicheli, Ludmila Goncalvez de Oliveira and Meiriane Mariano da Silva

Departamento de Química, Instituto de Ciências Exatas, Universidade Federal de Minas Gerais, 31270-901 Belo Horizonte, MG, Brazil

Frédéric Frézard

Departamento de Fisiologia e Biofísica, Instituto de Ciencias Biologicas, Universidade Federal de Minas Gerais, 31270-901 Belo Horizonte, MG, Brazil

Maria Norma Melo

Departamento de Parasitologia, Instituto de Ciencias Biologicas, Universidade Federal de Minas Gerais, 31270-901 Belo Horizonte, MG, Brazil

Amir Pouria, Hadis Bandegani, Milad Pourbaghi-Masouleh and Saeed Hesaraki

Nanotechnology and Advanced Materials Department, Materials and Energy Research Center, P.O. Box 31787/316, Karaj 3177983634, Iran

Masoud Alizadeh

Ceramics Department, Materials and Energy Reserach Center, P.O. Box 31787/316, Karaj 3177983634, Iran

Mutasim Ibrahim Khalil, Aisha Mohamed Al-Zahem and Maha Hamad Al-Qunaibit

Chemistry Department, King Saud University, Riyadh 11451, Saudi Arabia

Ahmed A. El-Sherif, Mohamed R. Shehata, Mohamed M. Shoukry and Mohammad H. Barakat

Department of Chemistry, Faculty of Science, Cairo University, Giza 12613, Egypt

Onder Aksu and Durali Danabas

Fisheries Faculty, University of Tunceli, 62000 Tunceli, Turkey

Ragip Adiguzel

Department of Chemical Engineering, Faculty of Engineering, University of Tunceli, 62000 Tunceli, Turkey

Veysel Demir and Safak Seyhaneyildiz Can

Department of Bioengineering, Faculty of Engineering, University of Tunceli, 62000 Tunceli, Turkey

Numan Yildirim

Department of Environmental Engineering, Faculty of Engineering, University of Tunceli, 62000 Tunceli, Turkey

Sebahat Seker

Department of Environmental Engineering, Faculty of Engineering, University of Ardahan, 75000 Ardahan, Turkey

Mustafa Ates

Vocational School of Tunceli, University of Tunceli, 62000 Tunceli, Turkey

Raj Kaushal, Nitesh Kumar and Pamita Awasthi

Department of Chemistry, National Institute of Technology, Hamirpur, Himachal Pradesh 177005, India

Ashun Chaudhary and Saroj Arora

Department of Botanical and Environmental Sciences, Guru Nanak Dev University, Amritsar, Punjab 143005, India

Ramadoss Gomathi and Andy Ramu

Department of Inorganic Chemistry, School of Chemistry, Madurai Kamaraj University, Madurai, Tamil Nadu 625 021, India

Athiappan Murugan

Department of Microbiology, Periyar University, Salem, Tamil Nadu 636011, India

Ramesh S. Yamgar

Department of Chemistry, Chikitsak Samuha's Patkar-Varde College of Arts, Science and Commerce, Goregaon (W), Mumbai 400 062, India

Y. Nivid, Satish Nalawade, Mustapha Mandewale, R. G. Atram and Sudhir S. Sawant

P. G. Department of Chemistry, Government of Maharashtra, Ismail Yusuf Arts, Science and Commerce College, Jogeshwari (East), Mumbai 400 060, India

Nagesh Gunvanthrao Yernale and Mruthyunjayaswamy Bennikallu Hire Mathada

Department of Studies and Research in Chemistry, Gulbarga University, GULBARGA, Karnataka 585 106, India